Development of a Piezoelectric Micromachined Ultrasonic Transducer Optimised to Operate in the Pore Solution of Reinforced Concrete Structures.

Stephen Sammut

Department of Microelectronics & Nanoelectronics

Faculty of Information and Communication Technology

University of Malta

October 2023

Submitted in partial fulfilment of the requirements for the degree of Doctor of Philosophy (Microelectronics and Nanoelectronics)

The research work disclosed in this publication is partially funded by the Tertiary Education Scholarships Scheme (TESS) Malta 2015, financed by the Ministry for Education and Employment in Malta. TESS seeks to contribute towards the Maltese labour market and economy.

The studies were also supported by the Malta College of Arts, Science and Technology (MCAST).

Copyright Notice

Declaration of Authenticity

Student ID: [redacted]

Student Name: Stephen Sammut

Course of Study: Doctor of Philosophy (Faculty of ICT)

Title of Dissertation: Development of a Piezoelectric Micromachined Ultrasonic Transducer Optimised to Operate in the Pore Solution of Reinforced Concrete Structures.

(a) Authenticity of Dissertation

I hereby declare that I am the legitimate author of this dissertation and that it is my original work. No portion of this work has been submitted in support of an application for another degree or qualification of this or any other university or institution of higher education. I hold the University of Malta harmless against any third party claims with regard to copyright violation, breach of confidentiality, defamation and any other third party right infringement.

(b) Research Code of Practice and Ethics Review Procedure

I declare that I have abided by the University's Research Ethics Review Procedures. As a Ph.D. student, as per Regulation 49 of the Doctor of Philosophy Regulations, I accept that my thesis be made publicly available on the University of Malta Institutional Repository.

[redacted]

Stephen Sammut

17/10/2023

Date

List of publications by author in the area.

1. **The Dynamics of Piezoelectric Micromachined Ultrasonic Transducer arrays embedded in reinforced concrete**. –CSMS 2023 Concrete Sustainability Conference 21st November –FIB S.Sammut, E.Gatt, RP Borg
2. **Low frequency Piezoelectric Micromachined Ultrasonic Transducers optimized for concrete structures.** – 25-29th September 2023 Published in Eurostruct 2023 and ce/papers Wiley Online library –S.Sammut, E.Gatt, RP Borg
3. **Modelling and experimental verification of a 350µm diameter PMUT operating in Isopropanol.** Published at the Symposium on Design, Test, Integration and Packaging of MEMS/MOEMS Symposium (DTIP'2023). Included in the Symposium proceedings and in the IEEE Xplore database. 28-31st May 2023 –S.Sammut, E.Gatt, RP Borg
4. **Microscale miniaturisation of chloride ion detection sensors for long-term embedding in reinforced concrete structures**. Published in Structural Control Health Monitoring - The Journal of the International Association for Structural Control and Monitoring – First Published on 5th September 2021– S.Sammut, E.Gatt, RP Borg.
5. **Design of the data transmission component of a micrometre scale chloride ion sensor embedded inside a concrete structure.** Published in Eurostruct 2021 Conference 30th August 2021- Padova – S.Sammut, E.Gatt, RP Borg.
6. **Current density and oxygen depletion in a galvanic pair embedded in Concrete**. - SB19 conference 22/11/2019. Authors- S.Sammut, E.Gatt, R.P. Borg
7. **Chloride ion detection through the voltage response of a galvanic pair.** FIB Malta International Conference 10th April 2018 -Sustainable Concrete Materials & Structures. Published in journal Sustainable Concrete Materials & Structures. Authors – S.Sammut, E. Gatt, R.P. Borg
8. **Chloride ion detection in concrete through Galvanic and Resistivity methods.** –Published in SCOPUS Journal: JJCE Journal Jordan Journal of Civil Engineering (Vol. 11, No. 04,2017 – Oct.1, 2017). Authors – S.Sammut, E. Gatt, R.P. Borg
9. **Other papers being prepared.**

ABSTRACT

Structural Health Monitoring (SHM) of Reinforced Concrete (RC) is important to ensure that necessary interventions on concrete structures are conducted in a timely manner. Structural integrity may be effected by various chemical substances such as chloride ions which ingress the concrete's pore structure and corrode the rebar. Timely detection of such chemical substances and subsequent intervention can avoid potential structural deterioration with ensuing potentially disastrous consequences. The conduct of an effective Structural Health Monitoring regime on civil engineering structures such as bridge decks, can be challenging due to inherent difficulties required to access specific, inaccessible parts of the structure, such as the underside of a bridge deck. This points to the setup of a SHM system, through a microscale distributed sensor network as being an effective proposition. Such a system can be made up of Micro Electromechanical Systems (MEMS) devices. The sensory elements forming the distributed network would be embedded within the concrete structure during the construction phase.

To achieve a durable system which is also easy to install during the structure's construction phase, communication between the sensory elements would need to be conducted through wireless means. This dissertation explored the possibility of using microscale ultrasonic transducers as a means of implementing the inter device wireless communication channel required to achieve a viable distributed sensor system. This work's primary contribution to the body of knowledge was therefore the development of the devices required to build the ultrasonic transmission path required to form the wireless communication channel. It needs to be clear that while the author has conducted prior work focusing on the sensory part of the system and also published papers in fields such as, the use of galvanic methods for detecting chloride ion ingress, research on the sensory system itself does not form part of this dissertation.

Reviewed literature indicated that for microscale ultrasonic devices to operate within an RC structure, two particular components needed to be considered. Firstly, liquid coupling was needed to effectively couple the transducer to the concrete structure. Secondly the frequency of the PMUTs' operation needed to be in the region of 100 kHz and below. The focus of this dissertation was therefore the development of Piezoelectric Micromachined Ultrasonic Transducers (PMUTs) optimised to operate inside a liquid coupling fluid at this particular frequency range. This was found to be an area in which very sparse background research had been conducted and therefore it must be said that the nature of most of the research conducted in this dissertation was novel. This makes this dissertation a valuable tool which can act as an important background to other researchers in fields involving PMUTs deployed in liquid coupling fluids. Applications that may potentially utilise such technology are not limited to civil engineering but also encompasses areas such as the biomedical and marine engineering fields.

This dissertation outlines the extensive analytical, Finite Element Modelling (FEM) and experimental work conducted to explore the dynamics of PMUT design and operation. This included studies conducted with various variables being modified such as, filling

the PMUT cavity with gas or liquid, the utilisation of different excitation frequencies, and also the utilisation of coupling fluids having different densities such as isopropanol or glycerine.

Furthermore this dissertation also presents the development of various novel PMUT designs which were found to provide enhancements in ultrasonic reception or transmission performance. Such enhancements were based on designs such as multi electrode patterns and modified diaphragm structures. The devices developed in this dissertation were based on the PiezoMUMPS^{TM} Multi Project Wafer (MPW) design concept. Aluminium nitride was used as the piezoelectric material found at the core of the devices' operational dynamics.

ACKNOWLEDGEMENTS

I would like to start by thanking my principle supervisor Prof Edward Gatt without whose constant technical and moral support this dissertation would not have been possible. Thanks also go to my co supervisor Prof Ruben P. Borg for his important support and input in the civil engineering field. It is also important to thank all the academics, systems engineer and research officers at the faculty for their advice and help with technical issues.

My special thanks go to my family, work colleagues and friends for their constant encouragement especially my wife Charmaine and daughter Maria for their support throughout the whole PhD journey.

Contents

List of Figures

List of Tables

List of Abbreviations

ASIC	Application Specific Integrated Circuit
CFD	Computational Fluid Dynamics
CMUT	Capacitive Micromachined Ultrasonic Transducer
FFT	Fast Fourier Transform
IC	Integrated Circuit
KED	Kinetic Energy Density
PML	Perfectly Matched Layer
PMUT	Piezoelectric Micromachined Ultrasonic Transducer
RC	Reinforced Concrete
RTP	Room Temperature and Pressure
SHM	Structural Health Monitoring
SOI	Silicon On Insulator
SPL	Sound Pressure Level
TCP	Thin Circular Plate
USCM	Uniformly Stretched Circular Membrane

Chapter 1: Introduction

Reinforced concrete is amongst the most important structural components in use in today's civil engineering projects. As a structural material concrete is strong in compression but weak in tension. Therefore the concrete material is reinforced with steel rebar to make it strong in tension too. Reinforced concrete is a complex composite material which is changing properties with time as chemical and physical processes are ongoing within the structure itself. The complexity is further exacerbated due to the porous nature of concrete. This property of, porosity allows the ingress of substances from the surrounding environment. Gasses may diffuse readily into the pore structure however it is also pertinent to note that the pore structure has a fraction of it filled with liquid, mostly water.

It is therefore also possible for substances, especially those with readily soluble ionic structures to dissolve in the water which is inside the concrete pores. When dissolved the ions can readily flow into the reinforced structure's interior. Such substances may then interact with the reinforced concrete's interior constituent chemistry thereby causing chemical changes to the structural materials which in turn results in physical changes (deterioration) of the civil engineering system itself. The pore solution pH is normally alkaline. This alkalinity keeps the oxides and hydroxides of iron in the solid state which means that these do not dissolve thereby allowing the steel structure to remain protected by a passivation layer from corrosion.

A substance which is capable of defeating the passivation layer and initiating corrosion is the chloride ion which is prevalent especially in the case of infrastructures built near marine environments as well as road infrastructure where sodium chloride is commonly used as de-icing agent. Since chloride ions are highly soluble it is therefore possible for chloride ions to dissolve in the pore solution and diffuse into the interior of the concrete thereby coming into contact with the rebar [1] [2] [3]. Ideally chloride ions should be monitored in a diffuse way throughout the structure in a way as to detect any forward moving diffusion gradient as well as any transport due to bulk defects. If chloride ion concentration is to be monitored close to the rebar, it is important to position the sensory systems on the inside of the concrete structure, where they can directly sample the pore solution touching the rebar [4] [5] [6].

As civil infrastructure continues to be built in areas of high salinity, structures such as bridges, road structures, land reclamation projects, leisure areas such as hotels, and maritime infrastructures continuing in the drive to become more complex in design. The positioning of such structures as well as their exposure to the elements make them much more difficult to be manually monitored so as to ensure structural integrity. Inspection of such structures often involves intensive labour to allow for teams of operatives to be able to access the construction and inspect it in minute detail. Work could also involve taking samples of concrete to the lab and then analysing such samples through extensive analytical chemical work which may include argentometric titrations to deduce the molarity of chloride ions present.

As an example one can cite structures such as those depicted in Figure 1.1(a) which shows the Natchez Trace Parkway Double Arch Bridge. This is a concrete bridge which is 502 meters long and 47 meters above valley floor. Similarly inaccessible for inspection is the structure shown in Figure 1.1(b) which is the Bennett Bay Centennial Bridge in Idaho with a continuous box girder concrete structure spanning 527 meters.

(a) (b)

Figure 1.1 ~ The Natchez Trace Parkway Double Arch Bridge, Tennessee [7], (b) Bennett Bay Centennial Bridge Idaho [8] .

Designing systems which need to be positioned in the corrosive environment of the pore solution presents several technical challenges especially the physics which needs to be adopted for data transmission.

Due to the fact that the proposed sensory system would be distributed throughout the reinforced concrete structure, the sensors need to have a data transmission capability if they are to be of any use. They would need to be able to connect to the outside world in such a way as to be able to transmit the data (such as ionic concentration) detected by the sensors. The data communication path could be a direct path where each sensor connects directly to the central location outside of the structure. On the other hand the sensors can be set up as a distributed sensor network where each sensor is transmitting data to other sensors which in turn are communicating with others and so on until the signal arrives at a point outside of the structure.

It is also pertinent to state that it is not desirable to use wired connections to link the sensors together. The reason for this being that wired systems have inherent fragility in their physical links especially when the network is connected by construction workers who are not knowledgeable or accustomed to handing electronics systems. It was therefore for this reason that this dissertation looked at a wireless means of communication, namely ultrasonic data transmission as a potential means of communication between the sensors.

Another possible wireless data transmission method could be radio frequency transmission. However radio frequency devices' sizes are constrained by the size of their antenna which in turn is sized in relation to the operating frequency. This would mean that for a micrometer sized circuitry one would be required to go for very high frequencies. Examples of miniature systems reviewed in literature (not for same application) were utilising frequencies in the GHz range. It is important to note that even a system using a resonant frequency of 1.06 GHz needed an antenna with a length

of 6 mm [9]. Apart from the size of the antenna basically impeding micron size devices, the reinforced concrete rf transmission characteristics precludes any data transmission at such high frequencies [10].

Other types of radiation which could be evaluated for data transmission through concrete could be x rays and neutron beams.

With regards to X rays, sources of a miniature size have been developed for use in medicine. However even the smallest sources weigh more than 100 g [11]. It is also pertinent to note that X-ray radiation causes health issues to exposed orgnisms. Apart from the ever present safety issues one would also need to factor in public perception when using such a system. Surveys reviewed in literature, indicated that more than 90% of respondents believe that X-ray radiation causes health problems [12] [13].

With regards to Neutron sources one must start by noting that these are relatively large in size. Even though the use of compact neutron beam sources is being evaluated for the conduct of materials research, the beam including the ion source still remains complex with magnets being needed. Apart from this, requirements for having a vacuum chamber and an ion source also remain thus precluding possible micro sized neutron beam sources [14]. As is the case for X rays, high energy neutron sources are also a danger to human health and safety as these sources increase the risk of carcinogenesis [15].

It is therefore for these reasons that this dissertation will focus on ultrasonic radiation as a means of conducting data transmission through the reinforced concrete structure. This dissertation will look at both the transmitting and receiving components and will seek to guide the reader through the extensive mathematical modelling and lab work required to achieve the final device designs.

The work presented in this dissertation is novel in most of its aspects. Even the application itself is inherently novel as no instances of the use of microscale ultrasonic transducers as a wireless sensor network deployed in concrete have been found in literature. All of the ultrasonic systems reviewed in literature are not in the microscale but are at best handheld devices. The smallest examples of ultrasonic systems optimised for use in concrete structures, as found in literature, have a diameter in the range of 20 mm and a length of 35 mm [16]. Ultrasonic radiation is non ionising radiation and therefore considered much safer than other radiation types such as X-rays. Even high power sonars such as those used in the sea are considered safe when a person is 1m or more away from the source [17].

It is to indeed be noted that evidence of a macro scale ultrasonic transmitter which can be embedded into concrete has been presented in published literature. This operates at frequencies of around 62 kHz [16]. Further literature which was reviewed indicated the development of small sized (not microscale) transducers with a transmission range of at least 3 meters in concrete [18].

The application of microscale ultrasonic transducers in reinforced concrete structures as a communication system for distributed sensor networks is in itself a novel and challenging application, especially since transmission parameters such as resonant

frequency would need to match the parametric constraints which the communication channel imposes.

Figure 1.2 shows a conceptual design for a potential ultrasonic transmission based distributed sensor system. The conceptual system presented in this figure had separate transmit and receive components. In this dissertation the possibility of having both functions combined in a bidirectional system was also evaluated.

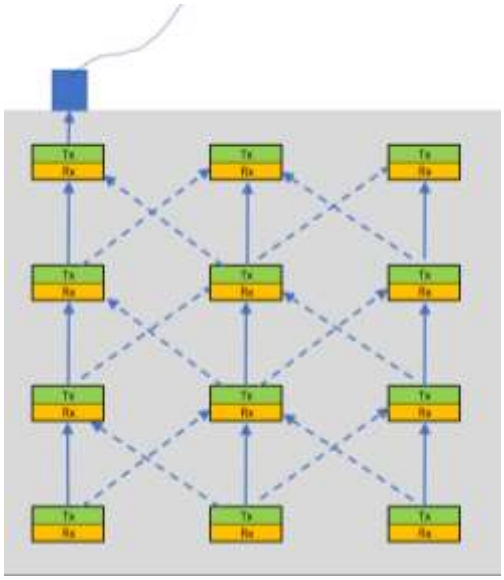

Figure 1.2 ~ A conceptual drawing showing a distributed sensory system. The grey shaded area symbolises the concrete structure itself. The sensory devices are distributed throughout the structure with each device having a transmitting part (green) and a receiving part (yellow). The wired device shown in blue is the receiving device at the surface of the structure.

The receiving device shown at the surface of the structure in Figure 1.2 would be used to transmit data through systems such as the mobile telephone network to offsite data analysis centres where decisions with regards to any structural interventions required would be taken.

Apart from this novel application of ultrasonic data transmission in the civil engineering field, this dissertation also reviews novel studies and design work on microscale ultrasonic transducers which are operating at relatively low frequencies. It is also envisaged that the technology being developed in this project would have uses in other sectors such as the biomedical field.

Novel device designs will also be presented in this dissertation such as a highly sensitive microscale ultrasonic radiation receiving device and an electrode design which increases a transmitting device's performance.

Research has indicated that publications in this area of ultrasonic application are very limited [19] [20] [21]. This dissertation utilises Piezoelectric Micromachined Ultrasonic Transducer (PMUT) technology as the basis of the ultrasonic system [22]. From literature review carried out it was evident that published research in the area of PMUTs

operating in liquid environments was even more limited and constrained to only a handful of papers. This is due to the fact that most of the PMUT devices reviewed were designed to operate in air [23] [24] [25] [26]. Evidence of research in the particular frequency range which is the subject of this dissertation, was quasi non-existent.

Due to the very limited prior literature material, extensive and reliable mathematical modelling had to be conducted to provide a reliable understanding of the underlying physics thus providing a solid background on which to base the experimental designs. It is envisaged that the theoretical and experimental work outlined in this dissertation will act as an important reference text forming the basis for future research in this field.

1.1 Key improvements achieved over the state- of the art

One of the key contributions of this dissertation was to expand the body of knowledge in the area of liquid deployed PMUTs operating with a low resonant frequency, especially those built using the PiezoMUMPS^{TM} process. An important process conducted in this dissertation was the establishment of a mathematical identity which linked a PMUT's diameter to its resonant frequency. Apart from the effect imparted by a PMUT diametric size, this project also studied how a diaphragm's circumferential geometry effected the PMUT's dynamics. This study included PMUTs having a hexagonally shaped outer diaphragm envelope rather than a "standard" circular circumference.

Another important contribution of this work on the current state of the art, was the development of modified diaphragm designs such as a PMUT having a central diaphragm held in place by suspended arms. This work demonstrated that by modifying the geometry of a PMUT's diaphragm, its dynamics including the resonant frequency can be modified. Furthermore through the experimental and FEM work presented in this dissertation it was also shown to be possible to make a PMUT more receptive to incoming acoustic radiation or become a better ultrasonic transmitter through such diaphragm modifications.

This dissertation also established parameters which were not readily available for PiezoMUMPS^{TM} devices. Examples of such established parameters were a reliable Young's Modulus value for the doped silicon forming the diaphragm as well as the Rayleigh damping coefficients which define a PMUT's dynamics when deployed in its fluidic environment. Another area of improvement over the state of the art was in the PMUT's upper electrode design. In this particular field the project also studied how changing the electrode's radial coverage area effected a PMUT's movements especially its displacement. The contribution of different electrode configurations including the use of multiple electrode shapes was also studied.

Further knowledge was also gained in the area of cavity fluid dynamics especially how different cavity fluids effected the PMUT's dynamics. Finally FEM and lab work was conducted to study how a number of PMUTs can eventually operate together in an array to increase the output pressure and hence the PMUT's ultrasonic transmission range.

1.2 Chapter Outline.

This section will provide a brief summary of each chapter to assist the reader get a broad overview of the research direction of the work presented in this dissertation.

1.2.1. Outline of Chapter 2 – Literature Review of the theory of ultrasonic physics and transducer design.

Chapter 2 presents the material covered in the extensive literature review which was carried out throughout this work. This literature review focused on two main areas of theory namely those underlining the Physics of Ultrasonics and the Design of Microscale Ultrasonic Transducers.

A proper understanding of the underlying physics of ultrasonics was deemed to be essential both for the correct interpretation of the results achieved as well as to effectively set up the experiments. Ultrasonic radiation propagates in waves which interact not only with the PMUT's structure itself but also with the surrounding fluid, containment vessel and probe needles through mechanisms such as reflection, diffraction and attenuation.

The second part of the literature review chapter, focused on the MUT technology itself. The section studied the differences between CMUT and PMUT technologies outlining the physics and mathematical modelling required for each configuration. This mathematical treatment together with the theory underlining the electrode's design engineering was then linked to the PMUT equivalent model and eventually to the expected dynamic performance.

Finally the chapter looks at the PiezoMUMPS^{TM} MEMs fabrication process used to manufacture the PMUT and array theory through which multiple PMUTs can be made to operate together to achieve the required pressures.

1.2.2. Outline of Chapter 3- Finite Element Analysis.

Due to the fact that the manufacturing of ICs is a complex and expensive process, extensive Finite Element Analysis needed to be carried out prior to producing the masks needed for the actual MEMs devices to be manufactured. In this dissertation the predominant FEA tool which was used, was multiphysics FEM using COMSOL Multiphysics. This modelling was carried out using solid mechanics and piezoelectric physics conducted in conjunction with CFD. The latter was used to model the interaction of the PMUT with the surrounding fluidic environment and create the ultrasonic environment.

Apart from modelling the PMUT's behaviour, FEA was also used in conjunction with experimental physics as a very important tool to determine critical material specific parameters such as the Young's Modulus and damping coefficients.

This chapter also looks at the modelling, which was conducted to study how changes to a PMUT's geometry can have an effect on either the reception or the transmission of ultrasonic radiation. Similarly innovative devices were modelled to predict how they would be expected to operate once manufactured. The modelling then used the physics of ultrasonics itself to model the ultrasonic transmission path through the concrete structure.

Finally the chapter describes the mask design process which was conducted to design the five masks required to build the device. These were designed following the PiezoMUMPS^{TM} design rules.

1.2.3. Outline of Chapter 4 – The Experimental Process.

The experimental process carried out in this project was conducted through three main methodologies. These were Laser Diffraction, Laser Vibrometery and finally Ultrasonic Dynamics work.

The first values of resonant frequency for the various PMUT geometries, were established through Laser Diffraction methods. This work involved the study of patterns created by the laser light interacting with the vibrating PMUT.

Subsequently, through Laser Vibrometer work conducted in conjunction with Polytec, the diaphragm dynamics of the various PMUTs was studied in greater detail especially with respect to parameters such as displacement, velocity and acceleration.

Finally the ultrasonic dynamics experimental work was conducted having two main objectives, namely to study ultrasonic transmission and reception. The first objective focused on the study of the pressure induced in the coupling fluid by the PMUTs movements. This pressure was measured through a specifically procured hydrophone and as mentioned, was conducted to study the transducer's capabilities when it was operating in transmission mode. The second objective involved the study of a PMUTs capability of operating in ultrasonic reception mode by using the hydrophone as an ultrasonic projector. In this case the voltage generated by the PMUT was measured to study its reaction to incoming ultrasonic radiation.

1.2.4. Outline of Chapter 5 - Result Analysis and Conclusions.

This chapter outlines and explains the conclusions reached through this project. These eleven conclusions were the most important novel contributions of this work to the body of knowledge. These conclusions range from the physical observations focusing on the devices' chemical interaction with the surrounding fluidic environment to conclusions

relating the PMUT's dynamics to its geometry and design. The geometries which were considered included various categories relating to both the PMUT diaphragm's diameter and shape, as well as the electrode's diameter and shape. One such geometrical conclusion focused on the establishment of an equation linking a PMUT's diameter to its resonant frequency when deployed in isopropanol coupling fluid and constructed using the PiezoMUMPS^{TM} process.

Presented in this chapter are also the conclusions related to fluid dynamics which guide the interaction of a PMUT with its fluidic environment. This fluidic environment encompasses the cavity and coupling regions, both of which have a highly significant effect on PMUT dynamics including its resonant frequency.

Chapter 2: Literature review of the theory of ultrasonic physics and transducer design.

2.1 The physics of ultrasonic radiation.

Sound waves travel through all matter be it solid, liquid or gas. The travelling sound waves move through matter via the oscillations of the particles forming the material itself [27]. Unlike electromagnetic radiation sound always requires a medium through which it can travel as sonic energy is the transfer of vibrations from one particle to the next. Sound travels through matter in two modes namely in longitudinal (or compression) pressure waves and transverse (or shear) pressure waves.

Pressure is the most important parameter involved in ultrasonic transmission physics. The molecular motion towards and away from each other causes areas of high and low pressure within matter. Pressure waves are produced at the transducer and move through the fluid in spherical fashion. An important concept is the logarithmic Sound Pressure Level (SPL) which is in decibels (dB) rather than Pascal. The equation is as shown in (2.1)) [28] [29].

$$\text{SPL}=20\log\left(\frac{p}{p_0}\right) \tag{2.1}$$

where

p_0 is the reference pressure level. In this text 20 μPa was used for air and 1μPa was used as reference pressure for liquids [28].

Another important parameter is the propagation speed where the group velocity, also known as the bulk velocity of sound refers to the velocity of an amplitude modulated sound wave passing through a medium [30]. The equation which equates the wavelength with the frequency is shown in (2.2) [31].

$$\lambda = v/f \tag{2.2}$$

where

λ is the wavelength
v is the speed of sound in the medium
f is the frequency of the radiation

Sound travels at different velocities when travelling through different substances. Each substance has a different acoustic impedance which is calculated as shown in equation (2.3).

$$Z_s = r_0 v \tag{2.3}$$

where

Z_s is the acoustic impedance of the substance
r_0 is the density of the substance

Gases normally present low values of acoustic impedances, with air having an acoustic impedance of 0.0004 $x10^6$ $kgm^{-2}s^{-1}$. This is a much smaller value than the acoustic impedance of solids and liquids. It is for this reason that in finite element modelling the solid or liquid to air boundaries are considered as free, i.e. acting in similar fashion to a vacuum [27].

Liquids have a much higher acoustic impedance with pure water having an acoustic impedance of $1.483x10^6$ $kgm^{-2}s^{-1}$. Isopropanol a liquid used extensively in this dissertation has a lower acoustic impedance of 0.912 $x10^6$ $kgm^{-2}s^{-1}$ [32]. Glycerine another fluid used in this dissertation has an acoustic impedance of $2.42x10^6$ $kgm^{-2}s^{-1}$ [33]. This value closely matches the acoustic impedance of low density solids such as plastics. The longitudinal wave velocity of sound in glycerine is 1,964 ms^{-1} with the density being 1.260 gcm^{-3} [34].

Solids on the other hand demonstrate an extensive range of densities with longitudinal wave velocities varying from 510 ms^{-1} in a low density substance such as cork (having a density of 0.24 gcm^{-3}) to 6,100 ms^{-1} in metals such as titanium, 7,390 ms^{-1} in some stainless steels and up to 12,800 ms^{-1} in beryllium [35]. Stainless steel has an acoustic impedance of $40.7x10^6$ $kgm^{-2}s^{-1}$ [36]. Hardened concrete on the other hand exhibits an acoustic impedance of 8.57 $x10^6$ $kgm^{-2}s^{-1}$ [37].

In a fluid longitudinal waves are created through vibrations occurring at the surface of the medium. To ensure that the highest amount of energy is conserved in a beam of ultrasonic radiation, it is essential to keep a particular ratio of the frequency to the beam area surface area [30] [38].

In fluids sound waves travel mostly as longitudinal waves as fluids do not have high shear strength to support the propagation of transverse pressure waves [28]. However in very viscous liquids transverse waves may indeed occur. In the latter the displacement of the particles would be at a right angle from the direction of propagation [39].

The speed of sound in gasses varies according to factors such as temperature and air pressure. In this dissertation the only gas used will be air and hence with respect to gasses this dissertation shall focus exclusively on air. At atmospheric pressure air molecules are very poorly spaced together with 0.33 nm diameter molecules being 3.3 nm apart thus only filling 0.1% of the available space. Rather than the packing of the molecules themselves the pressure which a body experiences is due to the molecular collisions which occur constantly with air molecules travelling at 500 m/s at RTP. A molecule would typically sustain around $8.3x10^9$ collisions every second.

Change in the volume of the enclosure holding the air molecules results in an increase in air pressure. This increase in pressure would be directly proportional to the change in volume, however the speed at which the compression takes place is also very important.

The equation which gives the value for the change in pressure with a slow change in volume is given by equation (2.4). This is known as an isothermal process [40].

$$\Delta P = -K\Delta V \tag{2.4}$$

On the other hand rapid changes in volume cause adiabatic compression to occur which follows equation (2.5) [40]

$$\Delta P = -\gamma K\Delta V \tag{2.5}$$

where

K is a constant
γ is equal to 1.4 in the case of diatomic gases such as O_2 and N_2 which make up air.

The reason for this is that in very rapid compression fluctuations the temperature created cannot move away with the same rapidity thereby causing a temperature increase, which in turn results in a pressure increase. This makes the gas "stiffer" as time goes by changes the acoustic properties of the devices.

Another point of importance is that particle displacement is not in phase with the magnitude of pressure as can be seen in Figure 2.1.

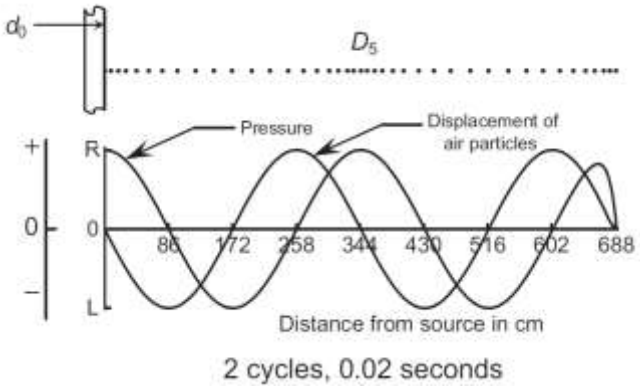

Figure 2.1 ~ Pressure and particle displacement curves of a sound waveform created by a wall which is vibrating at 100 Hz touching a body of gas. The crowded dots showing areas of high pressure [40].

Therefore if the pressure wave is following the time varying relationship cos 2πft, particle displacement would follow the sinusoidal relationship sin 2πft. The particle velocity is in phase with the pressure since velocity is the derivative of displacement.

2.1.1 Reinforced Concrete as an acoustic medium.

At these initial stages of this dissertation it is important to look at reinforced concrete as a composite material and review its acoustic characteristics in view of identifying the ideal parameters for the proposed microscale ultrasonic transmission system to operate within. This as devices designed as part of this project would need to be optimised to operate within the reinforced concrete structures.

At this stage one needs to understand the constituent materials of reinforced concrete and understand how each of these materials effect the transmission paths.

Reinforced Concrete contains many constituent components including cement, aggregate, water and of course steel reinforcement. It is therefore definitely not a homogenous transmission path for acoustic transmission. The heterogeneous composite reinforced concrete structure means that ultrasonic radiation travelling through the concrete is subject to reflections and scattering as well as attenuation by the internal geometry and materials forming the concrete.

The velocity and amplitude of the ultrasonic radiation is affected by factors such as the type of concrete, the compressive strength, moisture and concrete degradation. Propagation of ultrasonic radiation through the concrete can proceed through both shear and compression waves [18].

Various reviewed papers indicated that the frequency range of acoustic emission devices used to detect internal structural issues within reinforced concrete structures such as shear and tensile cracks, was between 40 to 100 kHz. On the other hand ultrasonic systems used to investigate structural issues within metals utilised higher frequencies. Reviewed literature specified frequencies between 100 and 900 kHz for metals [41].

To arrive to the final choice for the best frequency to use for transmission through concrete one needs to look at several factors including the thickness and the material composition making up the reinforced concrete. The distance between the transmitter and receiver, as well as the required data rate are also important factors.

Literature has also indicated that, higher frequency ultrasonic radiation is more attenuated by concrete than lower frequency radiation. This means that high frequency ultrasonic radiation is absorbed and scattered more quickly in its transit through the material thus limiting the range and quality of the transmitted signal. On the other hand when using lower frequencies which have higher wavelengths the incident waves would be affected more extensively by interference phenomena and signal distortion caused presence of other materials, such as aggregate, and rebar.

2.1.1.1. Cement.

Cement is the most important constituent component of reinforced concrete. There are several cement types available for structural engineering works. The most inexpensive and therefore most widely used was Portland cement [42]. Cement mortar composition including entrapped air causes dissipative losses in the ultrasonic transmission path. These losses are a function of the cement composition and microstructure [43] [44].

2.1.1.2. Aggregate.

Various aggregate sizes are used in the manufacture of concrete, some of which are shown in Figure 2.2.

(a) (b) (c) (d) (e) (f)

Figure 2.2 ~ Aggregate sizes showing (a) 05-1mm, (b) 1-2mm, (c) 2-5mm, (d) 5-10mm, (e) 10-15mm, (f) 15-20mm [45].

Aggregate sizes are subdivided into two broad categories, namely fine and course aggregates. For fine aggregate, normally sands are used while for coarse gravel one usually either crushed rocks or else uses gravel which has been water eroded.

Further literature review indicated that there are three categories of wave frequencies which can be considered when discussing the effects which the aggregate has on the ultrasonic transmission. This would be based on the ratio of the wavelength and the size of the potential obstructions which may scatter the waves.

These categories are as follows:

- Rayleigh Regime. This is defined by radiation having wavelengths which are much shorter than the structure's size but much larger than the aggregate size. In this region waves are coherent, which means that there is a constant phase difference between the waves. For concrete this would normally be in the region between 20 to 150 kHz [46]. To illustrate, a 100 kHz signal would have a wavelength of roughly 33 mm in concrete since sound would be travelling at around 3,300 ms^{-1} as outlined in Appendix A.
- Stochastic Regime. This occurs in the frequency range starting from 150 kHz up to around 1 MHz in concrete. In this region there is a reduction in coherent waves and an increase in incoherent waves [46]. Incoherent waves deviate in terms of critical parameters such as the phase difference between the waves. The upper usable frequency possible, due to the aggregate would normally be 500 kHz which equates to around a 10 mm wavelength being in the size range the course aggregate. At this frequency a path length of several centimetres would be reasonable to expect before scattering occurs [47].
- Geometric Regime. This regime involves radiation having frequency above 1 MHz where the heavy attenuation of ultrasonic radiation occurs in concrete. This frequency is therefore not utilised in applications which use ultrasonic radiation to study concrete [46]

The type and the composition of concrete, influences the ultrasonic attenuation coefficient. As an example, literature outlined that concrete with a water/cement ratio of 0.45 had an attenuation coefficient of 7.2176 dB/m, while an attenuation of 8.1914 dB/m was observed in concrete with water/cement ration of 0.4. The attenuation coefficient was also affected by the mix design especially the proportion of fine aggregate to coarse aggregate in the mix [47] .

For example, concrete with a 30:15 weight proportion of coarse to fine aggregate had an attenuation coefficient of 7.2 dB/m while concrete with a 40:55 ratio had an attenuation coefficient of 16.6 dB/m. In this case the ultrasonic vibrations in the concrete structure was detected through a laser Doppler vibrometer.

From an aggregate point of view therefore, a lower frequency increases the transmission range. As an example a macro scale transducer operating at 20 kHz can traverse around 10 m of concrete. A 60 kHz macro scale transducer on the other hand was found to be used in operations involving a path range of between 10 to 70 cm [47].

2.1.1.3. Water.

Water is another constituent of reinforced concrete. Like all other materials, water also absorbs ultrasonic radiation. A literature review conducted of experimental data from ultrasonic transmission has shown the best frequency for transmission of ultrasonic radiation through water to be 136 kHz [48].

This can vary greatly in practice as the absorption of sound by water is also greatly affected by temperature, pressure and dissolved solids. The interface between the solid structure and the liquid also effects the transmission of ultrasonic radiation [49].

2.1.1.4. Rebar.

Reinforcement bars are used inside reinforced concrete to give the RC material its tensile strength. Reinforcement bars are a significant factor which influences ultrasonic radiation given that the pulse velocity in steel is 1.4 to 1.7 times faster than in the concrete itself. In current applications the recommendation is that for applications requiring ultrasonic pulse velocity reading (for structural health monitoring purposes) test readings should avoid rebar to avoid signal being affected by it [47] [50] [51].

In this case higher frequencies would therefore be favourable towards a successful ultrasonic communication channel. This as a shorter wavelength radiation beam would be able to navigate in an easier fashion round the rebar and steel meshes than would a long wavelength (low frequency) signal.

2.1.1.5. Target frequency for this project.

As seen from the above literature discussion there are various components making up a reinforced concrete structure each of which has its own particular ultrasonic radiation absorption characteristics. Since each reinforced concrete type presents its particular absorption characteristics, a particular system would have to be designed to operate specifically for that structure. So as an example a bridge with a particular concrete type might require a monitoring system operating at a particular frequency while another structure might require a monitoring system operating at another frequency. The Finite Element Modelling and experimental work conducted in this dissertation was aimed at presenting important data and design concepts which can be used to set up any ultrasonic

transmission/reception systems operating in a range between 10 kHz to 400 kHz as required.

As discussed in view of the complex mix of materials making up concrete the acoustic model it presents, is has a very complex acoustic characteristic behaviour. Studies have been conducted to try to identify how acoustic attenuation varies with frequency as shown in Figure 2.3. Most current transducers designed for concrete ultrasonic testing operate between 25 and 100 kHz [52].

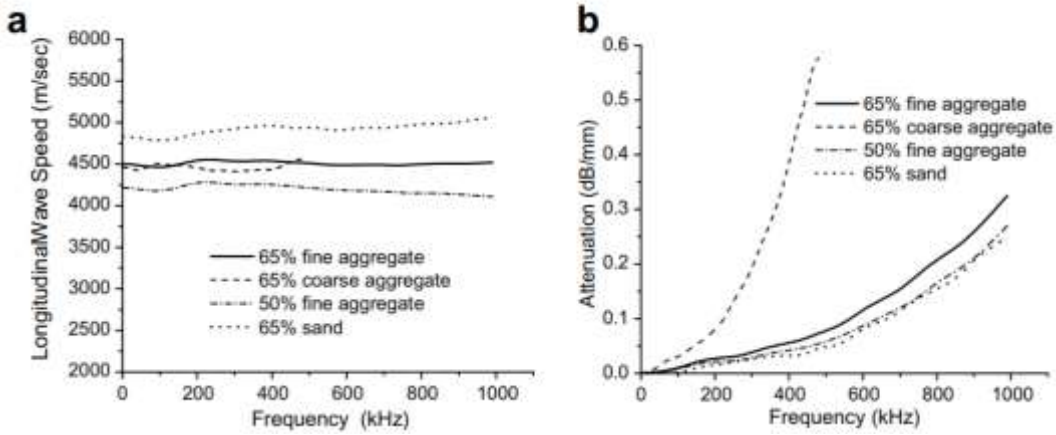

Figure 2.3 ~ (a) Graph showing wave speed against frequency and (b) attenuation vs frequency of different concrete specimens having different aggregate compositions [52].

Figure 2.3 (a) shows that the velocity of sound inside concrete does not change significantly with frequency and only varies with composition of the concrete itself. Attenuation on the other hand increases drastically beyond the 200 kHz mark as can be seen Figure 2.3 (b). This project will therefore focus on frequencies below the 200 kHz, with emphasis on the below 100 KHz range to achieve even better attenuation characteristics.

Further acoustic theory important to comprehend the fundamentals underpinning this dissertation can be reviewed in the Appendices.

2.2. Microscale Ultrasonic Transducers (MUTs).

The next section of the literature research was to look at the different types of technology available on which to base the construction of the microscale ultrasonic transducers. Literature research indicated that there are two main technologies which have been developed and used for the construction of microscale ultrasonic transducers.

These are:

- Capacitive Micromachined Ultrasonic Transducers (CMUTs)
- Piezoelectric Micromachined Ultrasonic Transducers (PMUTs)

A third technology, namely thermal actuation was also looked at for potential in the design of microscale ultrasonic transducers.

2.2.1 Capacitive Micromachined Ultrasonic Transducers (CMUTs).

As can be seen in Figure 2.4 the operation of a CMUT is based on the principle of a parallel plate capacitor in which one plate is fixed while the other plate is a flexible membrane.

(a) (b)

Figure 2.4 ~ Principles of operation of a CMUT showing operations in (a) ultrasonic reception and (b) ultrasonic transmission [53].

When the membrane moves under the influence of an incident ultrasonic wave, the distance between the two plates, changes and this change in capacitance can be detected and translated into a voltage. The CMUT can also be used to transmit data with an alternating voltage being used to cause vibration of the membrane and hence produce an ultrasonic pressure output [53]. It is important to note that CMUTs require DC bias voltages to operate. Projects reviewed in literature mention bias voltages of around 100 V to 160 V [54] while others used voltages ranging from 65 V to 75 V [55].

2.2.2 Piezoelectric Micromachined Ultrasonic Transducers (PMUTs).

Piezoelectric materials are special materials which undergo a reversible process where an applied stress creates an electrical dipole and therefore when strained piezoelectric material become electrically polarised. In this case the deformation of a solid crystal cell unit causes a moment of the dipole due to a displacement of the charged atoms which produces a net polarization. Net polarization occurs because in piezoelectric crystals the charge movements combine, as to produce a dipole moment which is macroscopic. The opposite is also true where an applied electrical field causes a strain in the material. This relationship is represented in the Heckmann diagram shown in Figure 2.5.

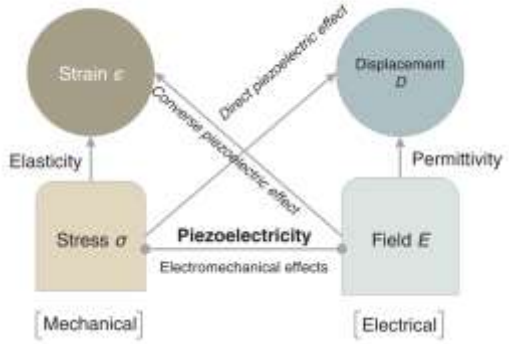

Figure 2.5 ~ A Heckmann diagram depicting the relationship between the mechanical and electrical properties [56].

Piezoelectric materials are used in numerous applications including in actuators and sensors especially through the use of PMUT structures. Examples of piezoelectric materials are barium titanate ($BaTiO_3$), lead (II) titanate ($PbTiO_3$), aluminium nitride (AlN) and lead zirconium titanate (PZT), the latter being amongst the most commonly used piezoelectric materials [57] [56].

In PMUTs the movement of a diaphragm and therefore the operation of the PMUT itself is driven by the electrically stimulated movements of the piezoelectric layer which is layered over the diaphragm [58]. The converse is also true, and PMUTs produce an output voltage when the diaphragm is perturbed.

Figure 2.6 presents a cross section of a PMUT. The areas shaded grey shows the metal layers, turquoise shows the piezoelectric layer, red shows the doped silicon layer forming the diaphragm and yellow is the insulating silicon oxide layer.

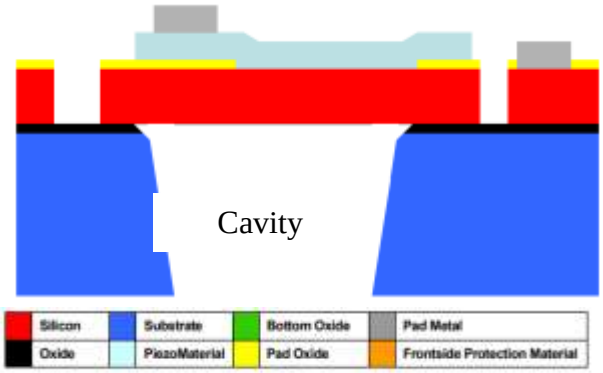

Figure 2.6 ~ Cross section showing structure of a PMUT following the PiezoMUMPs™ process [59].

The blue region is the wafer substrate. The trench forming the cavity can be seen in the wafer substrate region.

PMUTs design still presents some technical challenges one of which is that their frequency is sensitive to the active layer stress. PMUT fabrication is challenging with PMUTs sometimes having a different performance than what is postulated theoretically. Another issue is that PMUTs exhibit narrow bandwidths when compared to CMUTs. On the positive side is that PMUTs are easy to integrate with Application Specific

Integrated Circuits (ASIC) [60]. PMUTs also do not need bias voltages to operate and therefore can operate at lower voltages.

2.2.3 Decision on whether to select PMUT or CMUT technology for use in this project.

Further possible actuation mechanisms such as thermal actuation were also reviewed and feasibility studied through FEM. However research on this actuation mechanism was not taken further as devices based on thermal actuation had a speed of operation which was deemed as being too slow to be used as a basis on which to build an effective ultrasonic transducer. Hence the final decision on which transducer technology to use for this project rested on either CMUT or PMUT technologies.

CMUT technology does indeed offer some advantages over its PMUT counterpart especially when operating at high frequencies (above 20 MHz) such as those used in medical applications. CMUT manufacturing process can be more tightly controlled, and negligible spacing between elements is readily achieved [61].

Since this project would be operating at relatively low frequencies, the high frequency advantages of CMUTs would not be relevant in this project since proposed devices would be operating at frequencies below 200 kHz. The biggest advantage of PMUTs over CMUTs on the other hand is that the former do not require a high static DC bias voltage to operate [57]. The provision of the high bias voltages needed would not be a possibility in the application envisaged, since the project envisages micro sized sensors embedded in concrete for a number of years. PMUTs operate at voltages in the range of 20 V and even lower as opposed to the high bias voltages needed by CMUTs for their correct operation. This gives PMUTs the possibility of operating off galvanic processes (such as from the galvanic pair making up the sensory part for a chloride ion detector) or energy scavenging mechanisms.

2.2.4 PMUT behaviour as Membrane or Plate.

In order to conduct effective PMUT finite element modelling it is important to determination if its operation follows that of a Thin Circular Plate (TCP) or of a Uniformly Stretched Circular Membrane (USCM). The relevant theory explaining the difference between both types may be seen in Appendix B.

The fabrication process is crucial in the determination of the diaphragm's behaviour with respect to parameters such as its resonant frequency. Should the diaphragm be imparted with an intrinsic stress which is low, the behaviour would follow that of plate in which the resonant frequency is given by the equation (2.6) [19] [62] [63] [64].

$$f = \frac{\alpha}{2\pi r^2}\sqrt{\frac{D_E}{\rho h}} \tag{2.6}$$

where

$$D_E = \frac{Eh^3}{12(1-\upsilon^2)} \tag{2.7}$$

On the other hand high intrinsic stress would mean that the tensional stress will dominate the PMUTs behaviour while flexural rigidity would not have a pronounced effect on the resonant frequency [19]. In this case the diaphragm would operate as a membrane and the resonant frequency would follow the relationship outlined in (2.8).

$$f = \frac{\alpha}{2\pi r}\sqrt{\frac{T}{\rho h}} \tag{2.8}$$

where

T is the intrinsic stress causing the membrane tension
α is a constant denoting the mode of resonance
r is the diaphragm radius
D_E is the flexural rigidity
h is the thickness of the diaphragm
ρ is the density of the diaphragm

In the case of this dissertation the modelling, both analytical and finite element, was carried on the basis of the PMUT being a Thin Circular Plate with the restoring force being due to the diaphragm's stiffness rather than the application of tension [65].

The correctness of this decision was further reinforced through the Finite Element Modelling carried out and also the experimental work conducted. These have shown that the plate thickness does not change significantly as it is deforming. This is a main fundamental assumption for Kirchhoff Love Plate theory (or classical plate theory) to hold [66].

The diaphragm's modes of operation can take on the modes shown in Figure 2.7 when operating at different frequencies in different coupling fluids.

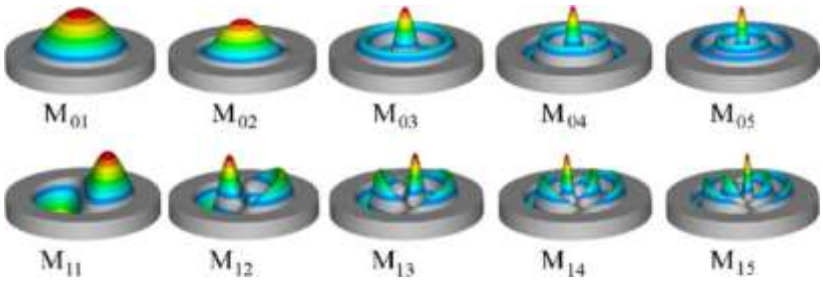

Figure 2.7 ~ 3D view of different modal shapes [67].

2.2.5 Resonant frequency determination of vibrating plates.

A plate vibrating in a fluid causes the motion of the fluid particles thereby displacing the fluid which is in contact with it. This causes the creation of sonic waves, which carry energy away from the vibrating surface. The transfer of energy from the vibrating surface causes a damping effect on the diaphragm and imposes an equivalent mass on the membrane's vibrational mechanics [68]. Such an imposed mass causes a drop in the resonant frequency of the membrane as underlined by the Lamb theoretical model. This outlines the effect which an incompressible fluid has on a diaphragm's resonant point when the fluid is present to one side of it [69].

Lamb studied the performance of plates which on the one side are in contact with an infinite body of liquid while on the other side are in contact with a gaseous fluidic substance such as air. The plates are assumed to be clamped and not able to move along their circumference. Through the derived equations outlined below approximate values for the resonant frequency of a circular plate produced from thin linearly elastic isotropic material of homogenous section can be achieved. For the purpose of these derivations the plate will have:

The radius denoted by a
The thickness denoted by h
r_p denoting the mass density of the plate's material

The analytical exercise starts with the Lamb equation derived in 1920 to approximate the profile of the displacement of the plate. This equation is shown in (2.9) below [70].

$$w(r,t) = C(t)\left(1 - \frac{r^2}{a^2}\right)^2 \tag{2.9}$$

where

$w(r,t)$ would be the membrane's normal displacement at a radial distance r (from centre)
C(t) is time dependant function representing the amplitude of the plate's normal displacement. As r tends to a, i.e. the midpoint, the value of w would tend to C and achieve its maximum value.

This mode shape is an approximation as the exact shape of a plate vibrating in a vacuum is an actual combination of Bessel functions.

2.2.5.1 Resonant frequency of plates vibrating in vacuum.

The equations denoting the maximum kinetic energy (equation (2.10) and potential energy (equation (2.11) for the vibrating membrane can be derived from the approximation presented above [70].

$$KE_{plate} = \frac{\pi r_p h a^2}{10}\left(\frac{dC}{dt}\right)^2_{max} \tag{2.10}$$

$$PE_{plate} = \frac{8\pi E h^3}{9(1-u^2)a^2}C^2 \tag{2.11}$$

where

E is the young's modulus of the plate material
u is the poisson's ratio of the plate material

The equation for the resonant frequency of the diaphragm in a vacuum is achieved from the equations of the kinetic and potential energies via the Rayleigh method and the equation is shown in equation (2.12).

$$f_{vac} = 0.4745\frac{hc_p}{a^2} \tag{2.12}$$

where

c_p which is the velocity of propagation of waves in plate is found through the equation:

$$C_p = \sqrt{\frac{E_p}{(1-u^2)r_p}}$$

The equation for the resonant frequency here presented, is for a plate vibrating in a vacuum. This needs to be developed further to also model the interaction which the surrounding fluid would have on a vibrating plate. This fluid - structure interaction will be tackled in the next section.

2.2.5.2 Resonant frequency of plates with one side in liquid.

In comparison to a plate resonating in a vacuum, plates resonating in fluids present lower resonant frequencies. As an example a plate resonating with one side in air and the other side in a liquid would resonate at a lower frequency than it would in a vacuum. The reason for this being that the presence of a liquid on one side of a plate has the effect of lowering the resonant frequency on account of an increase in the system's inertia. It is also important to note that the amplitude of the vibrations themselves is also reduced

from what one may measure in a vacuum due to the fact that energy is taken off into the liquid to produce sound waves [69]. It is also important to note that liquids have a much more noticeable effect on the resonant parameters of vibrating discs than do gasses.

There are also the damping effects which must be factored in but these are the subject of another section of this dissertation. The fundamental frequency for a circular vibrating plate is calculated by using the formula (2.13) [71]

$$\omega a^2\sqrt{\rho/D}=\frac{10.33}{\sqrt{1+0.6689\left(\frac{\Upsilon_\omega}{\Upsilon}\right)\left(\frac{a}{h}\right)}} \tag{2.13}$$

where

$\frac{\Upsilon_\omega}{\Upsilon}$ is the mass density of the liquid divided by the mass density of the plate
$\frac{a}{h}$ is ratio of the radius to the thickness of the plate

The PMUT structures discussed in this paper are based on the model of a solid circular plate clamped along its circumference. Equation (2.14) calculates the resonant frequency of a circular plate made of silicon in a water fluidic environment [69] [72].

$$f_{res,liquid} \approx \frac{f_{res,air}}{\sqrt{1+\frac{0.67}{2}\frac{\rho_{liquid}}{\rho_{si}}\frac{D_{eff}}{\left(T_{si}+T_{corr,\rho}\right)}}} \tag{2.14}$$

where

$$f_{res,air} \approx \frac{2\lambda_{io}{}^2}{\pi\sqrt{12}}\sqrt{\frac{Y_{si}}{\rho_{si}(1-\nu^2)}}\frac{T_{si}}{D_{eff}{}^2}C_{corr}$$

$$C_{corr}=\sqrt{\frac{T_{si}+3T_{corr,Y}\left(1+2\frac{T_{si}-T}{T_{si}}-\frac{T_{corr,Y}}{T_{si}}\right)}{T_{si}+T_{corr,\rho}}}$$

D_{eff} =D + 1.5 T

λ_{io} is a parameter which is dependent on the shape of the PMUT and its state such as if it is clamped or not. The values are obtained from tables in literature [71].
T_{si} is the thickness of the diaphragm
Y_{si} is the silicon's young's modulus
ρ_{si} is the density of silicon
D is the PMUT diameter
T is the total diaphragm thickness.

Analytical calculations based on equation (2.14) were very important in the early stages

of this project as they were used to achieve confidence in the finite element mathematical models which were designed. This margin of confidence was required to establish that the modelling conducted before proceeding to the prototype production was well grounded. It was also important to establish rough values for parameters needed to conduct Computational Fluid Dynamics.

A table comparing the resonant frequency calculated through analytical methods compared with experimental values is presented in Chapter 5 - Table 5.1. This showed a good correlation between the resonant frequency achieved analytically and that achieved experimentally.

2.2.5.3 The effect on PMUT dynamics by the fluid inside the PMUT cavity.

This section will start by taking a close look at the cavity shown in Figure 2.6 viewing it as an enclosed fluidic space. When looking at the dynamics of a diaphragm which is stretched over an enclosed fluid body, one needs to factor in the forces acting on it due to the pressure imparted by the change in volume of the trapped fluid created by the motion of the diaphragm itself. Hence apart from the inertial and damping forces acting on a vibrating membrane the air enclosure is also important in establishing the exact resonant frequency [65]. This interplay is similar to what one may find in a kettle drum.

A kettle drum has an enclosed air space which has an effect on its musical properties. As an example one may compare the resonant frequencies of a kettle drum to that of a common open drum (column showing drumhead acting alone) and an ideal membrane as shown in Table 2.1.

Table 2.1 ~ Comparison of the resonant frequencies of kettledrum, compared with the drumhead acting alone (without the enclosed air) and that of a theoretical ideal membrane. [73]

Mode	**Kettledrum**		**Drumhead**		**Membrane (Ideal)**
	F[Hz]	f/f_{11}	F[Hz]	f/f_{11}	f/f_{11}
01	127	0.85	82	0.53	0.63
11	150	1.00	155	1.00	1.00
21	227	1.51	229	1.48	1.34

Drums in general, are built out of a tight diaphragm stretched over an enclosure. The diaphragm vibrates over a mass of air, with the air moving back and forth. As can be seen from the table in the case of the kettle drum the enclosed air increases the frequency of the fundamental mode, mode M_{01}, and also the other modes which are symmetrical, such as M_{02}, and M_{03}. This is similar to how the resonant frequency of a loudspeaker installed in an airtight box would increase. Due to zero net displacement of air for the other modes, these would not be effected [73].

In loudspeakers this phenomenon can also be used to provide more restorative force than the cone's suspension itself. This allows better transmission and better performance for speakers which are smaller in size [73].

The movement of the diaphragm is also damped through the interaction of the PMUT with the fluids present above and below it. Figure 2.8 shows a side view of a circular plate with the outer circumference constrained from moving. The system is damped both in the upwards and downwards movement through the interaction with the fluid. The dynamics are represented by the action of a spring and a damper as shown in Figure 2.8.

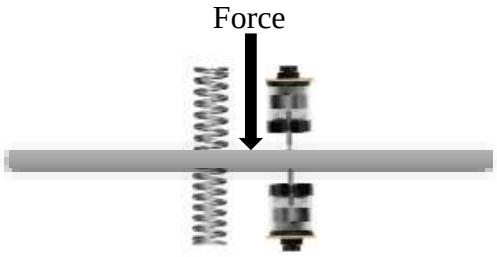

Figure 2.8 ~ Spring and damper representation of PMUT diaphragm vibrating in fluid.

Each of the springs and dampers can be represented by constants which are then used in the modelling.

Apart from the direct damping interaction of the fluids with the vibrating diaphragm, the cavity also interacts indirectly with the diaphragm through the wave movement formed inside it during the PMUT's operation. When the cavity is filled with fluid it acts as a Closed Pipe Resonator and also has an effect on the system's frequency. The theory behind the mechanics involved will be treated in the next section.

The cavity as a closed pipe gas filled resonator

Figure 2.9 shows fluid filled closed pipe resonators with a diaphragm closing one end. A standing wave is formed in the tube which has an antinode of maximum displacement of the air molecules at the open end. A node would be formed at the closed end where there is no displacement of the air. Figure 2.9 shows the formation of the nodes and antinodes.

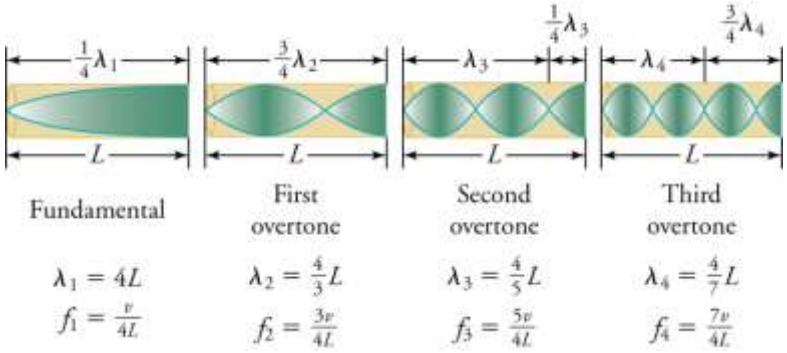

Figure 2.9 ~ Figure showing the fundamental and overtones (lowest) for a tube which is closed at the end. Maximum air displacement occurs at the open end with zero displacement at the closed end [74].

The fundamental frequency of the system is the lowest resonant frequency possible. A system has a natural frequency which is the frequency at which it would oscillate if no forces are acting on it both to drive it and to damp it. At this frequency the system would resonate and peak oscillations would be registered. Equation (2.15) below ties the natural frequencies achieved with the speed of sound in the gas and the length of the tube.

$$f_n = n\frac{v}{4L}, n = 1,3,5 \ldots \ldots, \qquad (2.15)$$

where

f_n	represents the resonant frequencies, f_1 being the fundamental
n	represents the fundamental and overtones, with 1 being the fundamental and 2 being the first overtone.
v	represents the speed of sound in the fluid
L	represents the length of the tube.

The movement of the waves inside the trapped air in a PMUT cavity was extensively modelled in the time domain and the results are presented in Appendix I.

As previously mentioned this project also looked closely at PMUTs operating with both sides in liquid by having a liquid filled cavity. This was done to establish the feasibility of bidirectional PMUT ultrasonic transmission in liquids and is looked at in detail in the next section.

The cavity acting as a closed pipe liquid filled resonator

As discussed in the previous section the cavity is an important component in the establishment of the resonant frequency. When filled with liquid the resonant frequency of the device changes. The calculation of the resonant frequency involves more complex calculations than just using the equation for an air filled cavity as provided before. Such calculations involve specifics of the geometry of the tube, the boundary conditions and also the liquid itself.

Taking a rough rule of thumb one must start by noting that as discussed before the speed of sound is faster in liquids than in gasses such as air since liquids are denser than gases. As outlined in Appendix A, the speed of sound in air is 343.2 m/s while that in isopropanol it is 1207 m/s. This 3.5 times increase in velocity, brings about an increase in the resonant frequency. However the mechanisms at play are very complex as damping due to the liquid forms a large part of the diaphragm kinematic equation apart from wave interaction with it.

The mathematical treatment involved in finding the resonant frequency of PMUTs with liquid filled cavities is certainly more challenging than that expressed so far with PMUTs operating in liquid coupling fluids with a gas filled cavity. The behaviour of

such PMUTs has been shown to have close correlation with mathematical models based on classical plate theory.

For plates with both sides in liquid equation (2.13) is used again but the term 0.6689 is multiplied by two to obtain equation (2.16) [71].

$$\omega a^2\sqrt{\rho/D}=\frac{10.33}{\sqrt{1+1.3378\left(\frac{\Upsilon_\omega}{\Upsilon}\right)\left(\frac{a}{h}\right)}} \tag{2.16}$$

The height of the fluid column above the PMUT is also a factor which needs to be taken into account when calculating the resonant frequency of a totally submerged device. However reviewed literature studying the natural frequencies of plates at different heights has indicated that the natural frequency for the first three modes of vibration is independent of the fluid level when the column reaches a height which is greater than 50% of the length of the plate length [75].

To determine the resonant frequency of a plate with both sides in liquid one needs to consider the different boundary conditions at play. It is also important to view their effect on the vibration modes of the plate which again impact the resonant frequency.

During vibration, a plate is generating standing waves, which are characterized by nodes being the points of minimal displacement and the antinodes being the points of maximum displacement. The resonant frequency corresponds to the frequency at which the plate exhibits maximum vibration which would be when the standing waves would have achieved the greatest amplitude. In this case where the plate has both sides fully immersed in the liquid, one can assume that there would be the imposition of a resistance to plate motion on either side. Such resistance would be higher than in the case were one side is bounded by air, since the liquid, being denser than air, provides a higher resistance to plate motion than would air.

It was also assumed that the increased resistance imparted by the liquid would increase the stiffness of the plate which would effectively therefore achieve a higher effective spring constant for the plate. Consequently, the hypothesis formed was that the resonant frequency of a plate with both sides in liquid would be higher than the resonant frequency for a plate with ones side in air and the other in liquid. Inversely a plate with one side in air can be hypothesised as having a lower spring constant and therefore a lower resonant frequency than one with both sides in water. This would be due to the plate having a lower level of stiffness than one with both sides in liquid.

Plate resonant frequency can be technically be determined mathematically, through the derivation of an analytical equation which considers the plate's physical properties and all boundary conditions. These would be parameters, such as the plate’s dimensions, the properties of the materials out of which it is made as well as the properties of the fluids making contact with it. However the exact equations governing the resonant frequencies of a plate especially those in the microscale are quite complex since there are many parameters at play such as the plate’s specific geometry and its mode of vibration just to name a few. Different plate theories, such as Kirchhoff plate theory or Mindlin plate theory would also be relevant in this case.

For this reason the mechanisms underpinning the dynamics of PMUT operations needed to be studied further through finite element modelling processes. Through such processes important parameters such as the amplitude of vibration, resonant frequencies and the velocity of the PMUTS motion could be studied in detail. The detailed finite element modelling which was conducted to study the effect of liquid filled cavities on PMUT dynamics is covered in detail in Appendix G.

2.2.6 On the effect of diaphragm slots on PMUT dynamics.

Literature reviewed has indicated macro scale projects were slots were cut in vibrating plates to achieve different resonant frequencies to that which would be expected for a plate without slots [76] [77]. Slots in a plate have a profound effect on the mass and stiffness distribution and can also contribute towards changing the plate's moment of inertia. This in turn influences the plate's resonant frequency points.

Based on the model established in Figure 2.8 a homogenous plate can be represented as having periodically distributed resonators. Such a setup is shown in Figure 2.10.

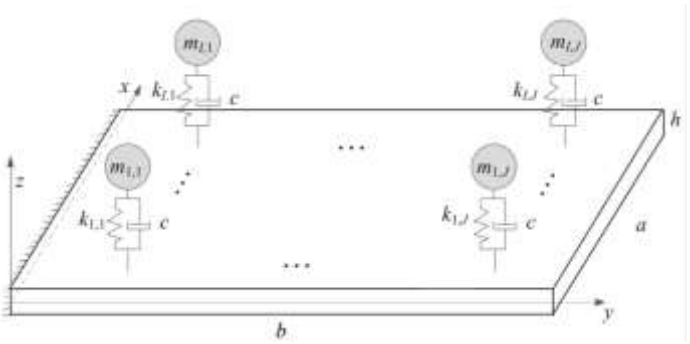

Figure 2.10 ~ Schematic of a rectangular cantilever plate showing the resonators which are periodically distributed around the plate [78].

Each of the resonators consists of a mass labelled m_{ij}, a spring labelled k_{ij}, and a damper labelled c in the diagram [78]. Changes in the shape and clamping of the structure moves the position and changes the magnitudes of the springs, dampers and masses shown in the model. Similarly the introduction of holes and cut-outs results in shifts of the structure's natural frequency as well as mode shapes which can be attained by the plates, thus changing the structure's dynamic responses to any excitation [79] [80].

Literature has indicated that cut-outs and holes are also sources of stress concentrations which have been studied through finite element methods using different plate theories and methods such as domain decomposition which was used to study the vibration responses of thin isotropic plates [80]. Reviewed literature has also indicated that experimental processes on plates using holes drilled in various locations on a plate to study changes in the structure's natural frequency have also been carried out as shown in Figure 2.11.

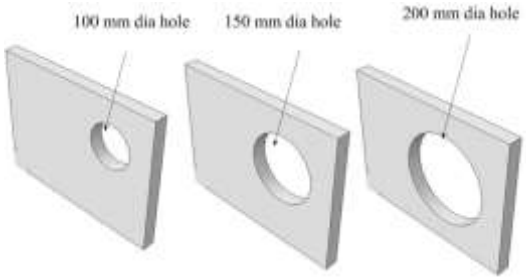

Figure 2.11 ~ Different positioning of holes in a plate [79].

In the reviewed work different sized holes were drilled in the plate shown in Figure 2.11 and the frequency of oscillation was observed. As an example it can be sited that a plate without the hole oscillated at 429.56 Hz, a plate with a 100 mm diameter hole oscillated at 382.55Hz, a plate with a 150 mm diameter hole oscillated at 334.07Hz while a plate with a 200mm diameter hole oscillated at 266.81 Hz. The position of the hole also effected the resonant frequency [79].

The study showed that the frequency reduces as the hole was moved off centre towards the plate's longer side [79]. There is a general lack of literature which reports on the evaluation of resonant frequencies of plates with cut outs. Most of the literature reviewed indicated that the natural frequencies of macro scale mechanical plates were evaluated through the use of finite element methods [81] [82] [83] [84] [85] [86].

Methods for the determination of resonant frequencies and vibration modes through analytical methods were also reviewed although these were found to be generally too cumbersome to use for the analysis of complex structures. An examples of such a method would be the Rayleigh Ritz method. Through the use of the coordinate system global coordinates can be used with to address the whole body with local coordinates being used for the hole. In this way the vibration energy of the hole is calculated and reduced from the vibration energy of the whole plate. A reviewed paper utilised a method with the name of "Independent Coordinate Coupling Method". Other methods proceeded with integration processes. The kinetic and potential energies for the circular plate are determined through (2.17) and (2.18) respectively [87].

$$T_c = \frac{1}{2}\rho h \int_0^{2\pi} \int_0^R \dot{w}_c^2 r dr d\theta \tag{2.17}$$

$$\begin{aligned} V_c = \frac{1}{2} D \int_0^{2\pi} \int_0^R \Bigg\{ & \left(\frac{\partial^2 w_c}{\partial r^2} + \frac{1}{r}\frac{\partial w_c}{\partial r} + \frac{1}{r^2}\frac{\partial^2 w_c}{\partial \theta^2} \right)^2 - 2(1 \\ & - v) \left[\left(\frac{\partial^2 w_c}{\partial r^2} \right) \left(\frac{1}{r}\frac{\partial w_c}{\partial r} + \frac{1}{r^2}\frac{\partial^2 w_c}{\partial \theta^2} \right) \right. \\ & \left. - \left(\frac{1}{r}\frac{\partial^2}{\partial r \partial \theta} - \frac{1}{r^2}\frac{\partial^2 w_c}{\partial \theta^2} \right)^2 \right] \Bigg\} r dr d\theta \end{aligned} \tag{2.18}$$

Through these equations the circular plate deflection can be computed and similarly the displacement inside the hole domain can be computed which can then be deducted mathematically. It is naturally quite possible to use such mathematical manipulations for a plate with a single hole however not so readily possible and indeed ideal to get accurate results for complex shapes such as those envisaged to be designed and studied for this project.

Literature has indicated that the natural frequencies of plates may decrease or increase with cut-outs in the plates due to the changes discussed in mass and stiffness [88]. It was therefore deemed important to explore this area further to explore potential which such modifications to the plates can provide. From the literature review it was deemed that three possibilities could be explored further through the implementation of modifications to the PMUTs:

- Possibility of reduction in the PMUT's resonant frequency. The possibility of achieving a point of resonance at a lower resonant frequency than would be expected for a device at that particular diameter. This would allow more PMUTs (operating at the same resonant frequency as larger diameter devices) to be fitted in a device of a particular surface area.
- Possibility of increasing sensitivity of device in reception of ultrasonic radiation thereby having a better dynamic performance when under the influence of an incoming ultrasonic radiation flux.
- Possibility of improving device performance when operating in liquids and especially in dense liquids.

For this reason Finite Element Modelling was conducted to explore the impact which modifications such as slots and holes can impart to a device.

2.2.7 Electrode design – coupling the electrical and mechanical domains.

Starting by looking at the simplest electrode type, i.e. a single electrode, extensive literature review was conducted to determine the best electrode coverage possible to achieve optimal power output from the transmitting PMUT devices.

One of the best papers reviewed indicated that the PMUT's deflection was at a maximum point when utilising electrodes with a radial coverage (with respect to the PMUT's diaphragm) of circa 60% [89]. This was due to the fact that at this value the electrode would achieve the best transformational coupling between the electrical and the mechanical domains, with reference to the PMUT equivalent circuit shown in Figure 2.14. The relationship between radial coverage and the coupling constant is shown in Figure 2.12.

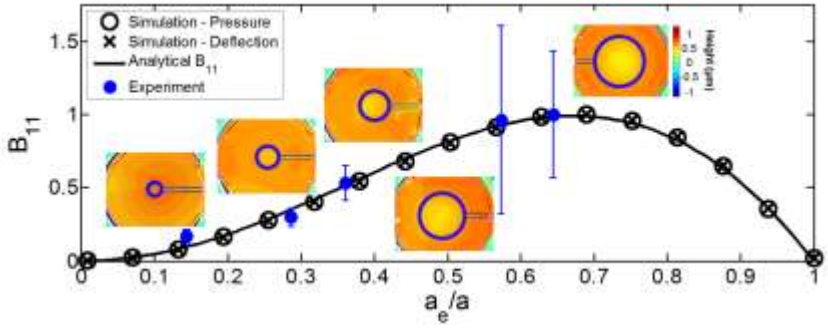

Figure 2.12 ~ Diagram showing relationship between the radial coverage of the electrode and the B11 coupling constant for a PZT PMUT with 139.5um radius [89].

A further paper reviewed simulation work conducted to establish links between electrode radial cover and the coupling between the electrical and mechanical domains. This paper discussed a PMUT having a diaphragm with a 107 μm radius and with a 71 μm top electrode radius [90]. The best value for radial electrode cover varied between another two reviewed projects. These again focused on PMUTs utilising air as coupling fluid and indicated that for the best coupling the top electrode diameter should be equal to 70% the PMUT's diameter [91] [92].

However it is also pertinent to note that the devices used in reviewed project in this case, had important differences from the devices used in the project which is the subject of this dissertation. As an example it was noted that most of the reviewed projects had used PMUTs with a piezoelectric layer made up of $Pb(Zr_{0.52})\ Ti_{04}8O_3$ known as PZT. This project, on the other hand is utilising AlN as the piezoelectric layer. It was also noted that none of the reviewed papers mentioned that experimental work was carried out in the same liquid coupling fluids used in this project namely glycerine and isopropanol. Moreover by reviewing the literature supporting Figure 2.12, it was evident that experimental verification was only conducted from a_e/a slightly above 0.1 up to slightly above 0.6 [89]. There are no tabulated experimental values for higher values of a_e/a as can be seen in Figure 2.12.

Hence, it was concluded that literature reviewed did not show sufficient mathematical and more importantly experimental data to support electrode size considerations for devices which are of the same size, and type, as those used in this project. Furthermore most of the work found was based on air or different coupling fluids than those used in the project.

Therefore as part of this project, the electrode size versus PMUT operational dynamics was studied for glycerine and isopropanol, both through extensive finite element models and also through experimental procedures which will be outlined in the sections below.

2.2.8 The PMUT Equivalent circuit.

Apart from Finite Element modelling another tool to help visualise and understand the operations of the PMUT is the lumped circuit model. This utilises analogies to impedance to represent all the PMUT's parameters be they:

- Electrical
- Mechanical
- Acoustic [93]

One such simplified equivalent circuit can be seen in Figure 2.13 which models the complete PMUT including the electrical part, the mechanical impedance and also the acoustic part.

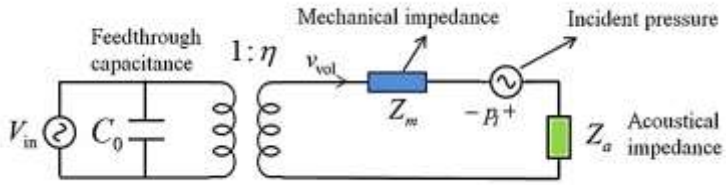

Figure 2.13 ~ A simplified PMUT equivalent circuit [94].

With respect to Figure 2.13, V_{in} would be the voltage driving with the feed in capacitance being represented by C_0. The transformer element with turn ratio 1:η represents the electromechanical coupling ratio.

This equivalent circuit model can be further enhanced with other elements as well as showing both the transmission and reception stages. The enhanced model is shown in Figure 2.14.

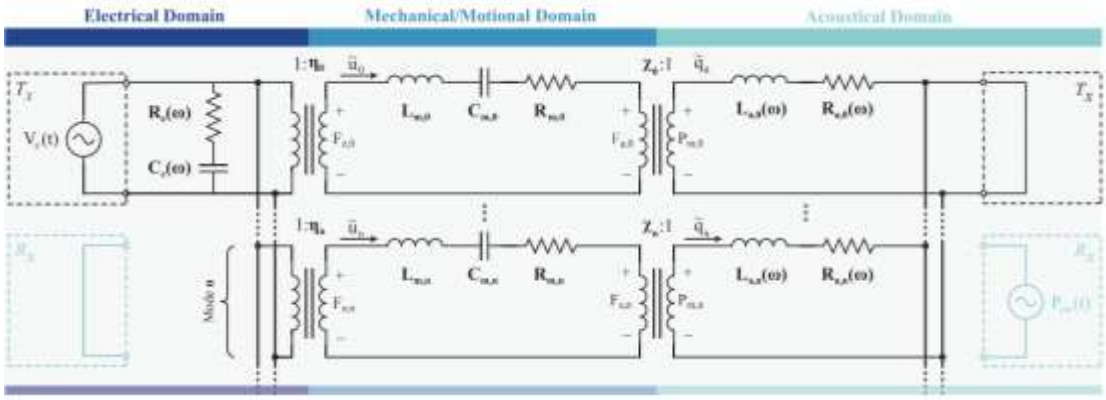

Figure 2.14 ~ Comprehensive model showing the lumped electromechanical circuit model of a PMUT [95].

With reference to Figure 2.14 in the electrical domain one can see the addition of the resistance $R_e(\omega)$ which represents energy dissipation due to the dielectric. The mechanical impedance is represented by the mid part of the circuit which is set up as spring-mass-damper [96]. A representation of such a set-up is shown in Figure 2.15. In

this case m represents the mass which is attached to a spring and oscillating under the influence of the external forces. The term k represents the spring stiffness while c represents the membrane deflection's damping coefficient.

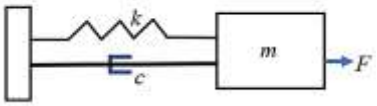

Figure 2.15 ~ A simple representation of a spring-mass-damper setup [97].

Referring back to Figure 2.14, the ratio X0:1 is the coupling representing the effective radiation area coupling the PMUT's mechanical and acoustic domains. Together L_a and R_a represent the PMUT's self-radiation impedance [96].

2.3 The PiezoMUMPs^{TM} MEMS fabrication process.

Various IC manufacturers were evaluated to determine which process to adopt for the construction of the prototype device. Due to agreements in place with the University of Malta it was however decided to look at utilising the MUMPSS multi- user MEMS process. The MUMPS program by Europractice is a program specifically designed for prototype MEMS fabrication whereby a wafer can be shared between many clients (a multi project wafer run) in order to keep the fabrication costs low. The production of the devices was coordinated with IMEC a world leading electronics research organisation.

Four MUMPS processes were evaluated for suitability namely PolyMUMPs^{TM}, MetalMUMPs^{TM}, SoiMUMPs^{TM} and PiezoMUMPs^{TM}. The PolyMUMPs^{TM} process is a process which is based on a three layer process while the MetalMUMPs^{TM} process also adopts electroplated nickel in the manufacturing. The SoiMUMPs^{TM} process is a micromachining process which utilises silicon on insulator. None of these processes produced a piezoelectric layer and therefore were not applicable for this project.

It was therefore decided to utilise the PiezoMUMPs^{TM} process which had an integral piezoelectric layer in the process. The piezoelectric layer is made up through an AlN layer with a d_{33} strain coefficient at circa 3.4-6.5 pCN^{-1} [59] .

The PiezoMUMPs^{TM} process utilises a Silicon On Insulator (SOI) 150 mm wafer. A section of a PMUT design constructed with the PiezoMUMPs^{TM} process is shown in Figure 2.6. The wafer is 400 µm thick topped by a silicon thickness of 10 µm, and an oxide thickness of 1µm.

Table 2.2 summarises the various layers forming the PiezoMUMPs^{TM} process and the thickness of each layer.

Table 2.2 ~ Summary of the layers forming a PiezoMUMPs™ device and their thickness [59] .

Layer	Mask Level	Material	Thickness
Substrate		Silicon	400±5µm
Oxide		Silicon Oxide	1±0.05µm
Silicon		Silicon doped with phosphorus	10±1 µm
Thermal Oxide	PADOXIDE	Silicon Oxide	2,000 Angstrom
Piezomaterial	PZFILM	Aluminium Nitride	0.5 µm
Pad Metal(Chrome)	PADMETAL	Chrome	20 nm
Pad Metal(Aluminium)	PADMETAL	Aluminium	1,000 nm

A final mask level in the series, is the TRENCH mask level which is used for the substrate patterning. During this process the die backside is etched through ion etching processes to form the cavity and free the diaphragm.

The structural geometries and design rules for the fabrication process will be discussed further in Appendices A and P.

2.4 Array theory.

One individual PMUT's output would be of limited value for the establishment of an operational transmission system since the sonic output power level would be very low. It is therefore normal, in applications such as ultrasound devices, that many individual ultrasonic transducers are organised to work together in the form of an array. Through such an arrangement an array of PMUTs operating together would significantly increase their output acoustic pressure level. Inversely arrays can also be used to increase the performance in terms of ultrasonic reception rather than transmission [98].

One ultrasonic source provides a circular shaped wave output. However when one has two or more sources working together the waves start to overlap and interact thus changing the waveform shape. The interaction of two waveforms depends on the phase difference in existence between them two. With reference to the concept shown in Figure 2.16, should two crests or two troughs come together, the waves would tend to amplify each other. On the other hand in the event of two crests meeting together, destructive interference occurs leading to the extinction of the waveform, if the two crests be of equal amplitude.

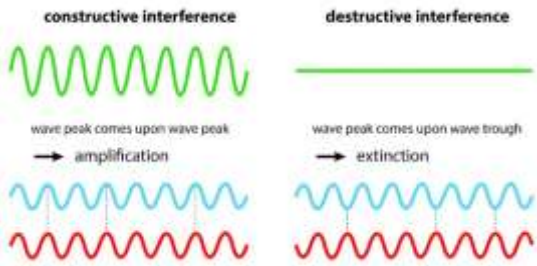

Figure 2.16 ~ The principles of constructive and destructive interference [99].

By adding more sources to the array, and introducing precise phase shifts to each source, the quality of the acoustic beam formed can be enhanced further. The beam can be made

to focus at particular points and also be steered to point at particular directions. This steering would be conducted electronically by shifting the phase of the signal being fed to each source. This is the reason why such an array is known as a Phased Array. Literature reviewed showed that each of the transmitting hydrophone antennas can be ideally spaced at ½ wavelength spacing between each other [100] [101]. Spacing the transducers further to separations such as 1.5 wavelength creates side lobes known as grating lobes. These would present a gain which would be comparable to that observed on the main lobe [102].

With multiple ultrasonic transducers spaced closer together say at the ideal ½ λ separation distance one would still get side lobes, but with a gain which is much lower than that of the main beam. Reviewed projects have also gone below the ½ λ distance between transducers which reduces the side lobes further [103]. On the other hand having the sources very close together might cause their transmission to suffer from the near field effect, which disappears if the inter source distance is a multiple integral of λ/2. This occurs especially for sources which are in phase [28].

Various ultrasonic projects utilising arrays have been reviewed some indicating array sizes having more than three hundred elements [104]. Literature has also indicated that the applications utilising arrays varied such as for example, fingerprint sensors using arrays with 42 x 65 elements [105]. Another reviewed project utilised a 110 x 56 array which operated in air at a frequency of 14 MHz. This developed an acoustic pressure of 25 kPa at a point 100 μm away from the array [106].

Every element forming the Phased Array is operated at a specific values of amplitude and the signal to each element can be timed exactly in a way as to create a specific beam with a wave front which is formed by the waves emanating from each PMUT [107]. A phased array of PMUTS can therefore perform functions such as:

- A linear scan of the neighbouring material inside the RC structure.
- Dynamic depth focusing of the beam.
- Sectorial scans where the beam can sweep over an angle.

Appendix K elaborates the area of array theory further.

2.5 Conclusions from the literature review.

As outlined in the sections above, various decisions with regards to the routes to be followed in both the mathematical modelling as well as the experimental processes, were taken after the extensive literature review which was conducted.

One of the most significant decisions taken was to base the project on PMUT technology rather than CMUT or other types of ultrasonic transducers. The details behind this decision were outlined in section 2.2.3. and the PMUT test devices were eventually built using the PiezoMUMPs ™ process.

With regards to the mathematical modelling approach to be followed, the literature review process also contributed by indicating that the best way to model the diaphragm was to treat it as a thin circular plate rather than as a membrane. This approach was followed in both the Finite Element Modelling as well as the analytical approaches outlined in this text.

Another decision with regards to PMUT geometry implemented based on literature reviewed, was the percentage radial cover size of the upper electrode. Literature reviewed indicated that a 66% electrode radial coverage was the most effective and therefore this size was taken as starting basis for the FEM and experimental work.

Last but not least in order of importance, one must also list the extensive literature list reviewed, regarding the effect which slots in a vibrating object have on its dynamic response. This literature influenced work on the development of PMUTs with modified diaphragms. The modified diaphragms were designed specifically to reduce the resonant frequency and improve reception capabilities.

The next chapter details the Finite Element Modelling which was conducted.

Chapter 3: Finite Element Analysis and design of the experimental IC.

3.1 Introduction to the Finite Element Analysis (FEA) chapter.

The underlying dynamics and performance characteristics of PMUT structures are too complex to review solely with a pure mathematical approach. Various extensive finite element analysis series were therefore developed to study the complex phenomena and set up models through which the prototype devices could then be designed prior to being fabricated [108].

This section will be therefore outlining and discussing the Finite Element Analysis which was conducted in this project. To combine all the Finite Element Modelling carried out under one chapter the author has also included modelling which was carried out post experimental phase. This modelling utilised results achieved from the experimental processes to calibrate the models thereby achieving more effective and accurate models.

Various types of Finite Element Models were designed to study the principles underlying the complex physics of the PMUT design and operation. These include both 3D, and 2D axisymmetric model types which were created in either the frequency or the time domain. For ease of understanding the various finite element models conducted are outlined in Table 3.1.

Table 3.1 ~ List of Finite element modelling conducted and discussed in this Chapter.

FEA nº	**Scope of Finite element model**	**Type of model**	**Frequency or Time Domain**
I	Determination of the Young's Modulus for phosphorous doped silicon produced by the SOI process and establishment of the resonant frequencies for PMUTs having different diameters.	2D Axisymmetric	Frequency
II	Determination of the effect which the voltage across the piezo electric layer has on the resonant frequency.	2D Axisymmetric	Frequency
III	Determination of the damping coefficients.	2D Axisymmetric	Frequency
IV	Electrode radial coverage effect on PMUT dynamics	2D Axisymmetric	Frequency
V	Determination of the effect which the cavity fluid has on PMUT dynamics.	2D Axisymmetric	Frequency and Time
VI	Acoustic pressure produced in the coupling fluid by various PMUT configurations.	2D Axisymmetric	Frequency and Time.
VII	FEM of a novel multiple electrode design.	3D and 2D Axisymmetric	Frequency and Time
VIII	FEM to determine effect on PMUT dynamics induced by diaphragm modifications.	3D	Frequency

IX	FEM to determine effect which an octagonal shaped diaphragm and cavity has on PMUT dynamics.	3D	Frequency
X	FEM of the array design	3D and 2D Axisymmetric	Time

During this project the initial Finite Element Analysis work which was conducted utilised the CoventorWare® software which was available at the University. However as the development of the models proceeded it became evident that CoventorWare® was not suitable for this project, since it did not successfully integrate the device being studied into an environment which could be designed and configured. As an example one can cite that it was not possible to utilise different coupling fluids as part of the models when using CoventorWare®. Hence the decision was taken to proceed with COMSOL as the FEA software through which to conduct finite element modelling.

3.2 FEA I ~ Determination of the Young's Modulus for phosphorous doped silicon produced by the SOI process and establishment of the resonant frequencies for PMUTs having different diameters.

Apart from the PMUTs' structural geometries and their deployment environment, the properties of the materials used to manufacture the MEMs device are extremely important to establish realistic FEMs. It is therefore important to establish these properties as accurately as possible.

Since the PiezoMUMPs™ process is not a production process but more of a prototyping fabrication system, data forthcoming from the manufacturer was lacking in completeness and therefore further literature had to be reviewed. Where necessary Finite Element Modelling combined with experimental data had to be used to calculate the exact material parameter values. One of the most important parameters required to be determined accurately for effective finite element modelling to be conducted was the Young's Modulus or modulus of elasticity which defines the stress - strain relationship.

The imposition of a stress on a structure causes strains (deformation). For many materials such as metals and semiconductors such as silicon, Hooke's law defines the relationship between stress and strain as shown in (3.1) [109]

$$s = E\hat{I} \tag{3.1}$$

where

E is the modulus of Elasticity (Young's Modulus)
s is the tensile stress
$\hat{I}$ is the engineering strain which is defined by the equation (3.2) [109]

$$\hat{\mathrm{I}} = \frac{l_i - l_0}{l_0} = \frac{\Delta l}{l_0} \tag{3.2}$$

where

l_0 is the original length before the application of loading
l_i is the length measured when loaded (instantaneous)

Various values for Young's modulus of silicon abound in literature. A reviewed paper stated that polysilicon semiconductor structures present average values of Young's modulus of 160 GPa while another stated 170 GPa as the average value [110]. Further literature studied indicate that possible values of Young's Modulus vary in a range between 130 and 188 GPa. Such values are however dependent on the deposition process [111]. The SOI wafer orientation used for the PiezoMUMPs^{TM} process was <100>.

In the case of the PiezoMUMPs^{TM} process the silicon used to form the PMUTs' diaphragms are phosphorous doped. Dopants further compound the problem of finding the exact values of the Young's modulus for the device we are testing in this project. As an example literature has shown that boron doped <100> silicon may have value ranging from 125 GPa down to 62 GPa [112]. Figure 3.1 presents experimental and modelling data found in literature showing how the Young's modulus of silicon is dependent on the crystal direction of silicon.

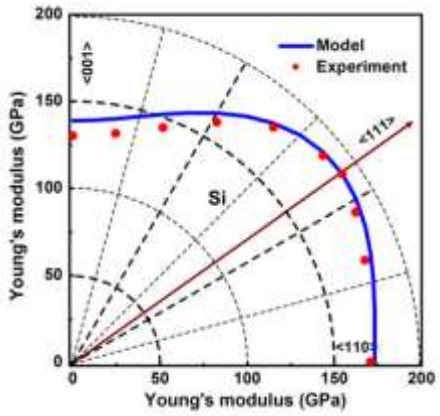

Figure 3.1 ~ Young's modulus values with the plane direction of the silicon crystal function [113].

The combination of the Young's modulus and the Poisson's ratio as elastic constants is sufficient to fully describe the isotropic materials elastic deformation parameters [114]. Therefore to build effective finite element models it is essential to establish reliable values of the Young's modulus and Poisson ratio pair. As discussed in Appendix A, the Poisson ratio for Silicon, was set at 0.28 for the simulation work conducted. The values for the Poisson ration as found in literature were quite tight and therefore this particular value was selected for silicon used in this project (<100> orientation).

On the other hand to achieve the actual value for the Young's modulus which was relevant to the doped silicon used in the PiezoMUMPS^{TM} process, finite element modelling was carried out. This was very important as only with a Young's Modulus

value which matches reality can exact diaphragm dynamics can be modelled. The axisymmetric finite element model utilised for this analysis is shown in Figure 3.2.

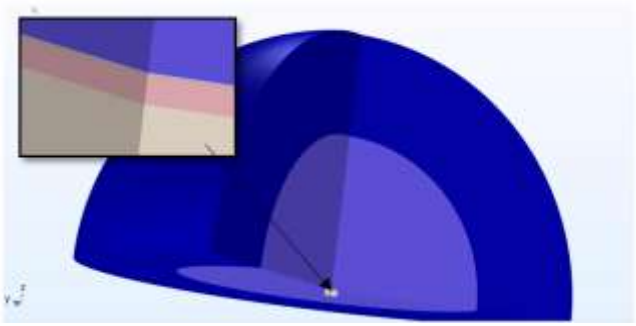

Figure 3.2 ~ Overview of the axisymmetric model developed in 3D space. Insert is the section showing cavity fluid (lower layer), overlaid by diaphragm (pink), with the electrode and coupling fluid layers next. The piezo layer sandwiched between the electrode and the diaphragm is not visible due to its small 0.5 μm size.

The details and geometry underlining the 2D models are shown in Appendix E, which the reader may review to understand the details behind the Finite Element Modelling using 2 D axisymmetric modelling.

The modelling procedure started by setting the damping parameters to zero. The next stage involved setting the Poisson's ratio to 0.28, a value fitting the window found in literature for <100> silicon.

To get to the best value of the Young's modulus an extensive number of finite element models were carried out for various sizes of PMUTs, seeing which value of Young's modulus best fits the experimental results for the resonant frequencies achieved. Through this modelling series, the value of Young's modulus which gave the closest results of resonant frequency when comparing between the FEM and experimental results for various PMUT diameters, was selected.

The PML layer's thickness was calculated by multiplying the diameter of the transducer by 15. This was done to ensure that all reflections and harmonics which would make the interpretation of the results difficult, would be adequately absorbed. The frequency domain modelling was then conducted through which the models were perturbed with a 14 $V_{p\text{-}p}$ excitation voltage. This was taken arbitrarily since the excitation voltage does not have a bearing on the resonant frequency as will be shown further below in another section.

The values for Young's modulus were varied through a parametric sweep function sweeping between 90 to 170 GPa in steps of 10 GPa. For each of the values of Young's modulus a frequency sweep was conducted to determine the device's resonant point with that particular value of Young's modulus. An example of the results achieved is shown in Figure 3.3. This shows the results of the combined parametric and frequency sweeps conducted on a circular diaphragm PMUT with a 700 μm diameter.

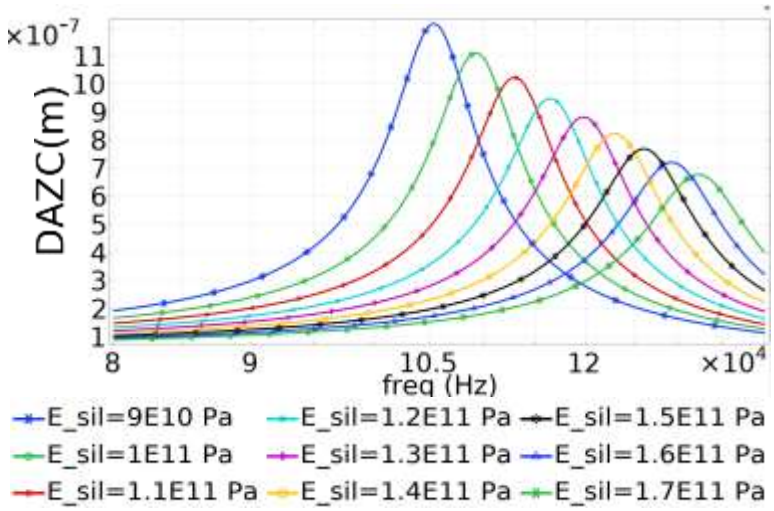

Figure 3.3 ~ PMUT Displacement Amplitude Z Component (DAZC) at the centre of the membrane for 700 µm diameter device. Damping was set to zero and Poisson ratio of Silicon was set to 0.28. The finite element frequency stepping was conducted at 100 Hz steps. Coupling fluid used was isopropanol and cavity fluid was air.

As can be seen from Figure 3.3 varying the Young's modulus has an important effect on the value of the resonant frequency as well as the amplitude. Through extensive Finite Element Analysis, the resonant frequency value was deemed as a more important and exact parameter useful to determine the silicon's Young's modulus rather than the amplitude. The reason being that the amplitude is also very dependent on damping and it can be calibrated at a later stage with the experimental values through the application of the damping coefficients. This will be discussed further in another Finite Element Modelling series. This series of parametric and frequency sweeps were carried out for various PMUT diameters and the results were tabulated as indicated in Table 3.2.

Table 3.2 ~ Actual and Finite element model resonant frequencies with different values of the Silicon Diaphragm's Young's Modulus for an Air filled Cavity and isopropanol coupling fluid PMUT. FEM step size modular between 50 and 100Hz.

DNº	D	E	F90	D90	F100	D100	F110	D110	F120	D120	F130	D130	F140	D140	F150	D150	F160	D160	F170	D170
4	550	187.7	187.4	0.14	197.0	-4.86	202.0	-7.36	206.0	-9.32	216.4	-14.23	219.8	-15.78	223.0	-17.21	230.0	-20.28	236.6	-23.07
44	600	152.0	152.7	-0.46	158.6	-4.25	164.0	-7.59	168.7	-10.41	173.7	-13.33	178.9	-16.26	183.2	-18.62	187.2	-20.75	190.5	-22.48
49	650	124.0	126.0	-1.60	130.0	-4.72	135.0	-8.49	139.0	-11.41	143.0	-14.23	147.0	-16.97	151.0	-19.64	154.5	-21.90	158.0	-24.11
56	700†1	115.86	105.0	5.56	109.2	1.63	112.9	-1.70	116.4	-4.75	119.8	-7.63	123.0	-10.26	126.2	-12.82	129.2	-15.15	132.2	-17.43
39	900	62.0	57.5	7.58	59.1	4.84	60.6	2.33	61.9	0.21	62.9	-1.39	63.7	-2.66	64.3	-3.59	64.7	-4.21	65.0	-4.68
26	1000	53.1	44.4	17.88	46.0	14.37	47.5	11.17	48.9	8.27	50.3	5.45	51.6	2.90	53.0	0.23	54.3	-2.20	55.5	-4.38
29	1800	12.7	10.8	16.09	11.2	12.47	11.6	8.97	11.9	6.43	12.2	3.94	12.5	1.51	12.8	-0.86	13.1	-3.18	13.4	-5.44
33	2000	9.4†2	8.5	10.06	8.8	6.59	9.1	3.24	9.4	0.00	9.6	-1.79	9.8	-4.17	10.0	-6.19	10.3	-8.65	10.5	-11.06
Average difference between experimental and theoretical values			7.44		3.79		0.61		-2.09		-4.87		-7.18		-9.30		-11.51		-13.55	
Average difference between experimental and theoretical absolute values			7.96		7.25		6.47		5.81		7.21		8.28		9.36		11.51		13.55	
Average error (absolute) for large ϕ (700µm to 2000µm) PMUTs only.			12.29		8.84		5.66		3.07		3.18		3.44		3.88		5.83		7.75	

Notes:

DNº	Experimental values achieved by laser vibrometer and/or laser diffraction	D	Difference between theoretical (FEM) and experimental value [%] (Young's modulus value)
D	Nominal PMUT diameter [µm]	†1	The experimental values of the vibrometer reading was an average value for the resonant frequency from three 700 µm PMUTs 56, 58 and 59.
E	Experimental value [kHz]	†2	The vibrometer value for the 2,000 µm ϕ device was discarded and the laser diffraction as well as audio confirmation results were used hence resonance being set at 10.2kHz.
F[E]	F with the value for Young's Modulus value written behind. Finite element value of resonant frequency with young's modulus set at the number written in the heading example 90 GPa [kHz]		

The value of Young's modulus which best fitted the data was selected from the results tabulated in Table 3.2. The selection process to choose the optimal value for the Young's modulus was based on four parameters as shown in Table 3.3

Table 3.3 ~ The final Young's modulus value selection process.

Parameters used to determine optimal value of Young's modulus.	**Rank order for Value of Young's modulus [GPa] which obtained the best results and average percentage difference between experimental and theoretical values.**
Young's modulus value which obtained the best average difference between the experimental and theoretical values.	1st Place 110 GPa ~ 0.61% 2nd Place 120 GPa ~ -2.09%
Young's modulus value which obtained the best average difference between the experimental and theoretical absolute values.	1st Place 120 GPa ~ 5.81% 2nd Place 110 GPa ~ 6.47%
Young's Modulus which obtained the best average error (absolute) for large ϕ (700 µm to 2,000 µm) PMUTs only.	1st Place 120 GPa ~3.07% 2nd Place 130 GPa ~3.18%
Young's modulus which obtained results closest to the audio confirmation of the resonant frequency for the 2,000 µm ϕ PMUT.	1st Place 120 GPa ~ 0% 2nd Place 130 GPa ~ -1.79%

The value of the young's modulus which therefore best fitted the parameters of the doped silicon used in the PiezoMUMPs^{TM} device fabrication was **120 GPa**. This value was in line with an experimental value found in literature indicating a Young's modulus of 130 GPa for the undoped <100> silicon used for MEMs fabrication (not PiezoMUMPS^{TM}) [113]. The circa 8% reduction between the literature value and the result calculated here can be attributed to the phosphorous dopant as discussed above.

3.3 FEA II ~ Determination of the effect which the voltage across the piezo electric layer has on the resonant frequency.

This Finite Element Analysis series was conducted to study the effect of the excitation voltage on PMUT dynamics. No literature which indicated the peak voltage the aluminium nitride could endure was evidenced. Through discussion with MEMSCAPE, and after some estimation, it was decided to keep to an excitation voltage of 20 V_{p-p} as the maximum excitation voltage. Since prototypes are expensive and take time to prepare, it was decided to utilise 14 V_{p-p} for experimental work and only utilise 19 to 18 V_{p-p} for final testing. Simulations were therefore conducted using a similar range of voltage levels. When simulations needed to be compared to experimental data 14 V_{p-p} or 18 V_{p-p} were used. On the other hand other voltages such as 20 V_{p-p} were used when indicated in the text, as a means of establishing the maximum performance dynamics for the PMUTs.

To be able to conduct the laboratory testing at these reduced voltages with the required confidence of being able to predict PMUT dynamics at higher voltages, the effect which the voltage level across the AlN had on the resonant frequency had to first be determined.

For this study FEMs of a 700 μm diameter PMUT was set up and operated at both a low voltage of 7 V_{p-p} and also at the maximum voltage of 20 V_{p-p}. In similar fashion as the FEA conducted in the section before, the values for the Young's modulus were cycled from $0.9x10^{11}$ Pa to $1.7x10^{11}$ Pa. The damping parameters were set to zero with the PMUT dynamics being regulated solely by the pressure acoustics physics. Figure 3.4 shows the PMUT displacement when excited with a voltage of 7 V_{p-p}.

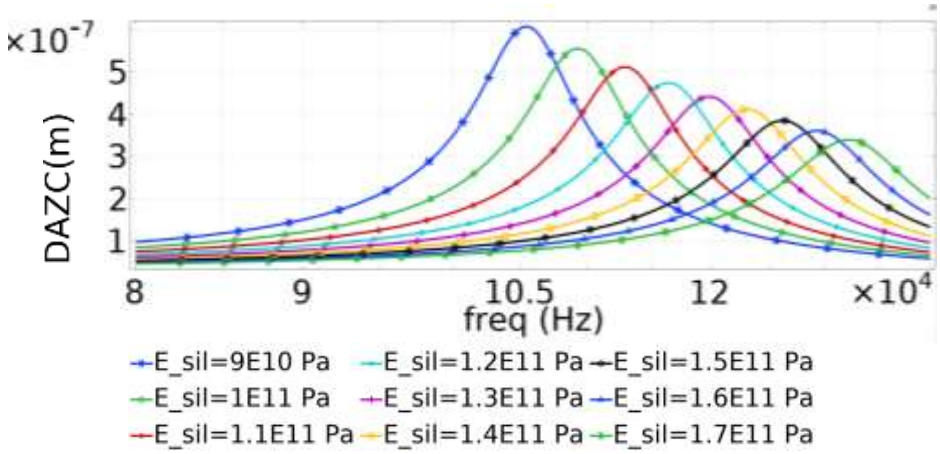

Figure 3.4 ~ Displacement Amplitude Z Component (DAZC) at the centre of the membrane for 700 μm diameter device. Damping was set to zero and Poisson ratio of Silicon was set to 0.28. The finite element frequency stepping was conducted at 100 Hz steps. Coupling fluid isopropanol and cavity fluid air.

The values of resonant frequency achieved from the models with the applied voltage across the piezoelectric layer 7 and 20 V_{p-p} finite element models were compared to the resonant frequency values achieved from being 14 V_{p-p} used in FEA I. The comparison is shown in Table 3.4.

Table 3.4 ~ Values of resonant frequency at different values of Young's Modulus with two different voltages across the AlN layer, namely 7, 14 and 20 V_{p-p}.

Young's Modulus of Silicon [x10^{11} Pa]	**Voltage across AlN 7 & 20 V_{p-p} Resonant Frequency [x10^5 Hz]**	**Voltage across AlN 14 V_{p-p} Resonant Frequency [x10^5 Hz]**
0.9	1.053	1.053
1	1.092	1.092
1.1	1.129	1.129
1.2	1.164	1.164
1.3	1.198	1.198
1.4	1.230	1.230
1.5	1.262	1.262
1.6	1.292	1.292
1.7	1.322	1.322

From the results achieved through these finite element models it has been shown that the values of resonant frequency remain the same whatever the applied voltage across the PMUTs piezoelectric layer. The amplitudes change with the applied voltage but those will be studied together with damping parameters in a further section below.

As an example the undamped amplitude for a PMUT model across which 14 V_{p-p} were applied was $1.21x10^{-6}$ m while the application of 7 V_{p-p} to the same PMUT model resulted in a displacement of $6.08x10^{-7}$ m. Also of importance is the fact that the frequency stepping for both models was set to 100 Hz. Using the same frequency stepping for all models is important to achieve reliable amplitude values which can then be compared. The reason being that as the frequency gets closer to resonance the higher the amplitude would be.

3.4 FEA III ~ Determination of the damping coefficients.

The next stage of mathematical modelling which was conducted was aimed to calibrate the finite element models' performance in terms of the maximum displacement, and velocity at the midpoint of the PMUT's membrane. This was done by comparing the values achieved from the Finite Element Models with those achieved from the laser vibrometer experimental data as outlined in Chapter 4.

The damping model used was Rayleigh Damping, the theory of which was discussed in Appendix C of this dissertation.

Through the calibration of the FEM the damping parameters were established. Since this project was mostly focusing on PMUTs operating in a frequency range at or below the 100 kHz region, this damping coefficient calibration, focused primarily on PMUTs having a minimum diameter of 700 μm.

A series of Finite Element Models were prepared and analysed as follows:

- Liquid (isopropanol) coupling fluid and Gas (air) filled cavity
- Liquid (isopropanol) coupling fluid and Liquid (Isopropanol) filled cavity

Each of these was modelled to achieve:

  - Maximum displacement of the diaphragm's midpoint with frequency
  - Maximum velocity of the diaphragm's midpoint with frequency

This was done by introducing the Beta coefficient of the Rayleigh damping parameters into the FEM to achieve displacement, and velocity values similar to those achieved with the laser vibrometer data achieved during the testing phase. As previously discussed in the Appendix C: Damping Theory, to simplify the model, the Alpha damping coefficient was set to zero with only the Beta coefficient being varied in the parametric sweep.

As can be seen in Figure 3.5 varying the damping parameters, in this case the Rayleigh Damping coefficient has a negligible effect on the value of the resonant frequency. On the other hand, it has a significant effect on the amplitude where one can see that the higher the damping coefficient, the lower the calculated displacement amplitude.

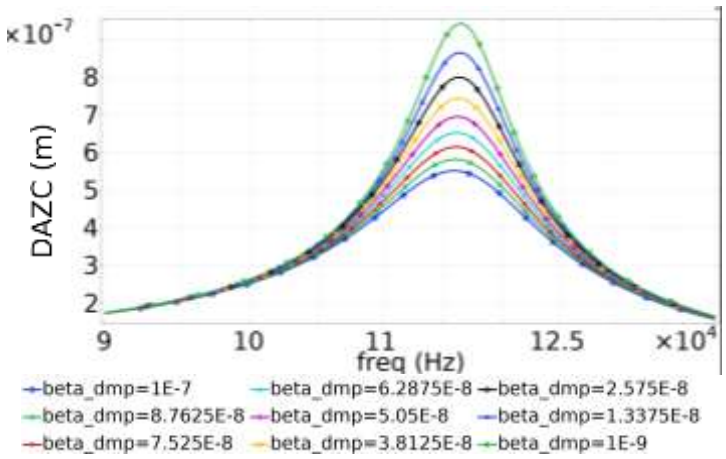

Figure 3.5 ~ Displacement Amplitude Z Component (DAZC) at the midpoint of the membrane in a 700 µm circular PMUT. Rayleigh Beta damping coefficient values were varied as indicated in the legend. Time steps of 500 Hz each. Excited with a 14 V_{p-p} sine wave signal.

To fine tune the frequency steps the frequency domain analysis was then focused on the frequencies between 1.158×10^5 Hz and 1.168×10^5 Hz. This resulted in the plot shown in Figure 3.6.which shows the behaviour of the circular 700 µm diameter device when varying the Beta Rayleigh damping coefficient at the smaller time steps of 10 Hz. Again the Alpha Rayleigh Coefficient was set to zero for simplification purposes.

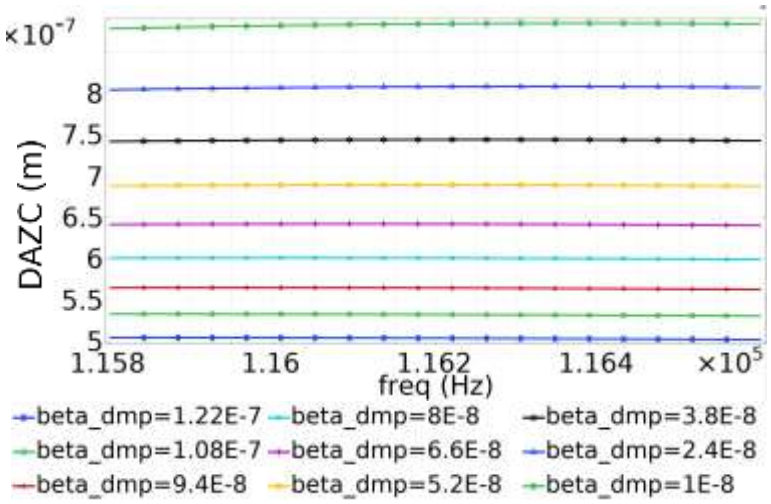

Figure 3.6 ~ Displacement Amplitude Z Component (DAZC) at the midpoint of the membrane of the 700 µm. Rayleigh Beta damping coefficient was varied as indicated in the legend. Time steps of 500 Hz each. Time steps of 10 Hz. Excited with a 14 V_{p-p} sine wave signal.

Table 3.5 shows the tabulation of the Rayleigh damping beta coefficients for a 700 µm PMUT which achieved the experimental parameters of displacement and velocity.

Table 3.5 ~ Beta Coefficient of the Rayleigh damping parameters for device 56, a 700 µm diameter PMUT with isopropanol coupling and air filled cavity. Steps of 50. Excited with a 14 V_{p-p} sine wave signal.

Parameter	**Vibrometer data for air filled cavity and isopropanol coupling fluid. Experimental value of resonance @ 111.09 kHz**	**Rayleigh damping Beta coeff. Resonance. FEM value of resonance 116.3 kHz**
Displacement	7.96×10^{-7} m	2.68×10^{-8}
Velocity	0.555 m/s	3.3×10^{-8}
Approximation as FEM loss factor values are not synchronised.		3×10^{-8}

The parametric sweep with the Rayleigh Beta damping coefficients was again repeated with the 900 µm PMUT. The resulting Displacement Amplitude Z Component vs frequency curves are shown in Figure 3.7.

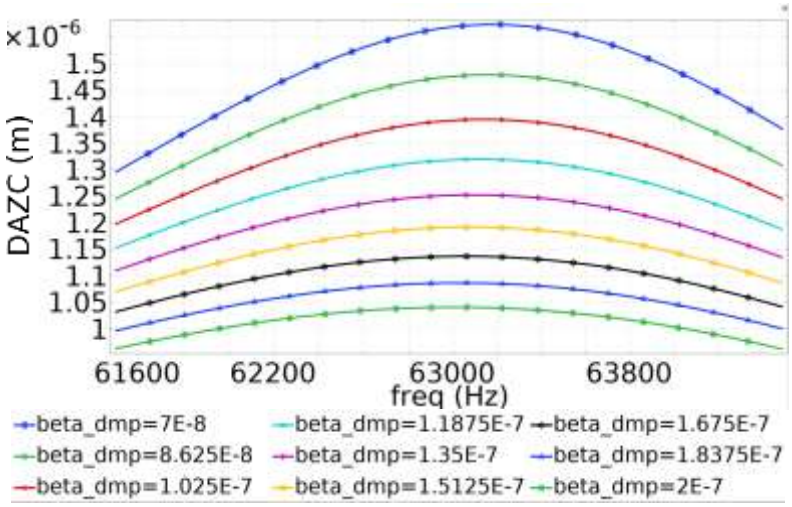

Figure 3.7 ~ Displacement Amplitude Z component (DAZC) at the centre of the membrane of the 900 µm. Isotropic Damping is being used with displacement at varying isotropic damping coefficients shown. Time steps of 10 Hz. Excited with a 14 V_{p-p} sine wave signal.

The results of the Beta coefficient which achieved diaphragm midpoint displacement and velocity parameters similar to the experimental data for a 900 µm PMUT are shown in Table 3.6

Table 3.6 ~ Rayleigh damping Beta coefficient parameters for Device 39, a 900 µm diameter PMUT with isopropanol coupling fluid and air filled cavity. Excited with a 14 V_{p-p} sine wave signal.

Parameter	**Vibrometer data for gas filled cavity and liquid isopropanol coupling fluid. Experimental value of resonance @ 62.03 kHz**	**Beta coefficient with alpha coef. = 0. FEM value of resonance @ 59.15 kHz**
Displacement	1.14×10^{-6} m	2.09×10^{-7}
Velocity	0.444 m/s	1.9×10^{-7}
Approximation between the two values to approach best value of Beta.		2×10^{-7}

A similar process was conducted to determine the Rayleigh Beta damping coefficient for a 600 µm PMUT and the results achieved after the FEA process were tabulated in Table 3.7.

Table 3.7 ~ Rayleigh damping Beta coefficient parameters determined through FEM for Device 39, a 600 μm diameter PMUT with isopropanol coupling fluid and air filled cavity. Excited with a 14 V_{p-p} sine wave signal.

Parameter	**Vibrometer data for gas filled cavity and liquid isopropanol coupling fluid Experimental value of resonance @ 153.12 kHz**	**Beta coefficient with alpha coef.= 0. FEM value of resonance @ 168.6kHz**
Displacement	$5.18x10^{-7}$ m	$1.375x10^{-8}$
Velocity	0.4987m/s	$1.75x10^{-8}$
Approximation between the two values to approach best value of Beta.		$1.5x10^{-8}$

The final device which was studied through the FEA was the 1,000 μm PMUT device for which the Beta Rayleigh damping coefficient results are tabulated in Table 3.8.

Table 3.8 ~ Beta Coefficient of the Rayleigh damping parameters for Device 27, a 1,000 μm diameter PMUT with Isopropanol coupling and air filled cavity. Excited with a 14V_{p-p} sine wave signal.

Parameter	**Vibrometer data for air filled cavity and isopropanol coupling fluid. Experimental value of resonance @ 53.28kHz**	**Rayleigh damping Beta coeff. Resonance. FEM value of resonance @ 46 kHz**
Displacement	$1.4621x10^{-6}$ m	$5x10^{-8}$
Velocity	0.48948 m/s	$2.675x10^{-8}$
Approximation between the two values to approach best value of Beta.		$3.5x10^{-8}$

3.5 FEA IV ~ Electrode radial coverage effect on PMUT dynamics.

Finite Element Analysis Study IV was conducted to review how the electrode coverage effects the PMUT dynamics including the velocity and maximum displacement of the diaphragm midpoint. As discussed in Chapter 2, reviewed literature indicated a maximization of PMUT diaphragm midpoint deflection at particular values of electrode radial coverage percentage.

The first model used in this analysis series was a frequency domain model based on a 700 μm diameter PMUT. In this model the coupling fluid used was isopropanol and the cavity fluid was air. The frequency domain model was coupled with a parametric sweep which step changed the electrode cover ratio from 44% to 99%. The setup of the 2D axisymmetric model is shown in Figure 3.8.

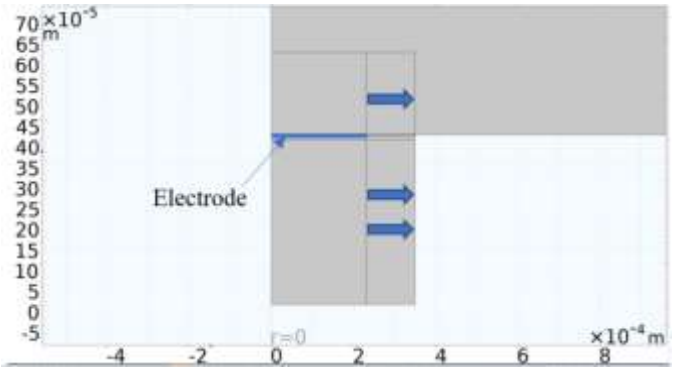

Figure 3.8 ~ Geometry of the model showing the operation of the parametric sweep mechanism through which the study of the electrode radial cover was conducted. The electrode size increased from 44% to 99% of the diaphragm.

The parameters shown in Table 3.9 were used to set up the model shown in Figure 3.8.

Table 3.9 ~ Table showing parameters utilised for this model.

Parameter	Value
Rayleigh Beta Coefficient	$3x10^{-8}$
Young's Modulus	120 GPa
Thermoviscous Acoustics	Not used as outlined in Appendix O.
Meshing method for the core area	Mapped meshing

Following the model set up, the frequencies were swept in frequency steps of 500 Hz. This frequency was selected to achieve a model which while being accurate solvable in a realistic time frame with computing power available. The response curves for the different electrode radial cover percentages are shown in Figure 3.9.

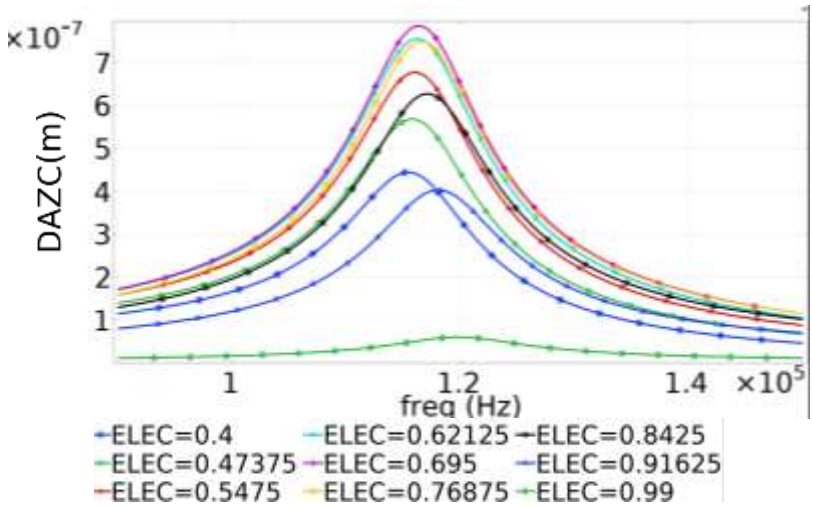

Figure 3.9 ~ Displacement Amplitude Z Component (DAZC) at the midpoint of the membrane for 700 µm diameter device. The finite element frequency stepping was conducted at 500 Hz steps. Coupling fluid was isopropanol and cavity fluid air. Values for electrode cover ratio (on diaphragm) varied between 0.4 and 0.99.

A further frequency domain finite element analysis was again conducted to fine tune the resolution. This time it was conducted using shorter time steps and focusing on the region closer to the resonant frequency. This was done to refine the results further and achieve the plots as shown in Figure 3.10.

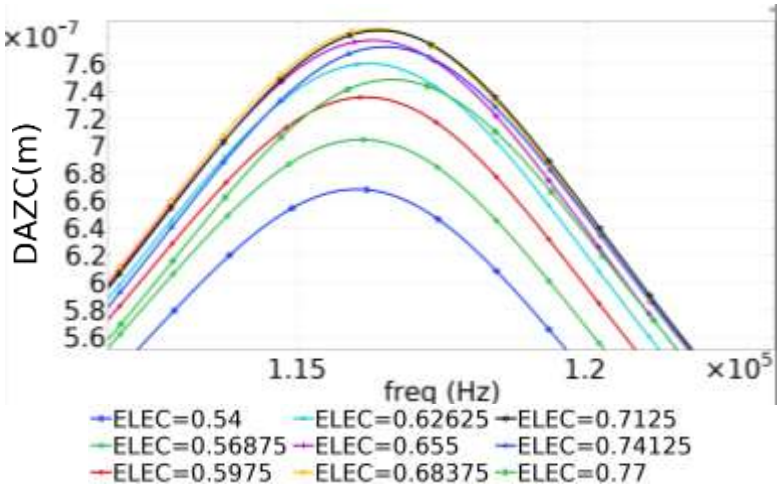

Figure 3.10 ~ Displacement Amplitude Z Component (DAZC) at the centre of the membrane for 700 μm diameter device. The finite element frequency stepping was conducted at 50 Hz steps. Coupling fluid isopropanol and cavity fluid air.

From this model it can be seen that the values for electrode cover which gave the best performance where between 65% and 74% radial cover. A further finite element analysis step was taken this time with time stepping of 10 Hz and further focusing of the electrode cover ratios as shown in Figure 3.11.

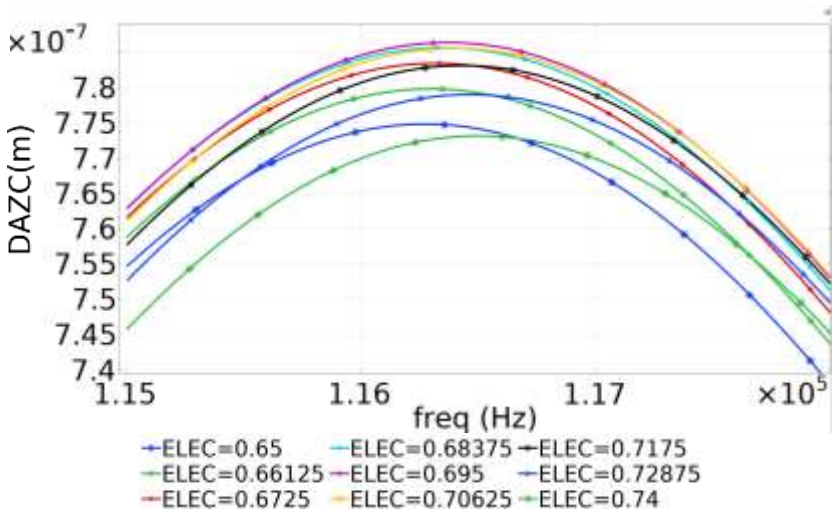

Figure 3.11 ~ Displacement Amplitude Z Component (DAZC) at the centre of the PMUT's diaphragm for 700 μm diameter device. The finite element frequency stepping was conducted at 50Hz steps. Coupling fluid isopropanol and cavity fluid air.

As can be seen in Figure 3.12, for a 700 μm PMUT, the best response was given by a PMUT with an electrode radial cover ratio of 69.5%. The simulation was again conducted, this time for a 900 μm PMUT to see if the same relationship between electrode radial cover and displacement of diaphragm at PMUT centre point still holds.

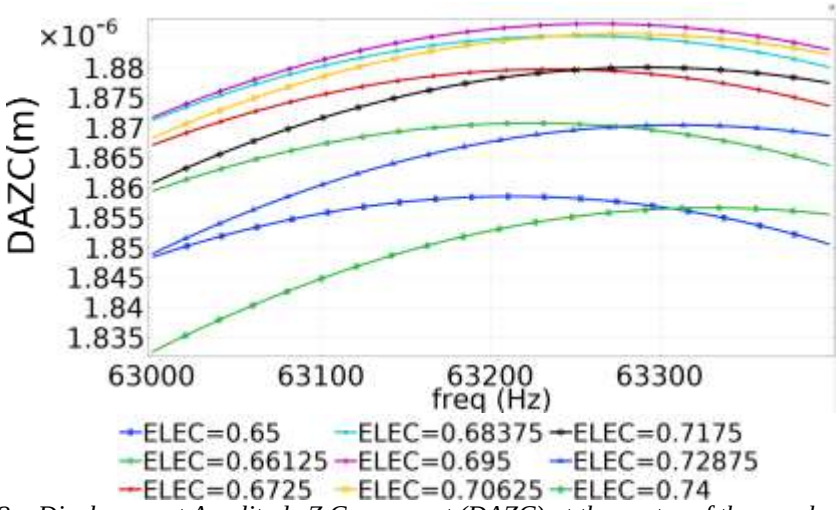

Figure 3.12 ~ Displacement Amplitude Z Component (DAZC) at the centre of the membrane for 700 μm diameter device. The finite element frequency stepping was conducted at 50 Hz steps. Coupling fluid isopropanol and cavity fluid air.

As can be seen in Figure 3.12 the resonant frequency was calculated at 63.30 kHz and the electrode radial cover which gave the best performance was again 69.5% for the 900 μm device similarly as that measured for the 700 μm device. Similar results were obtained from the Velocity Z- Component as shown in Figure 3.13.

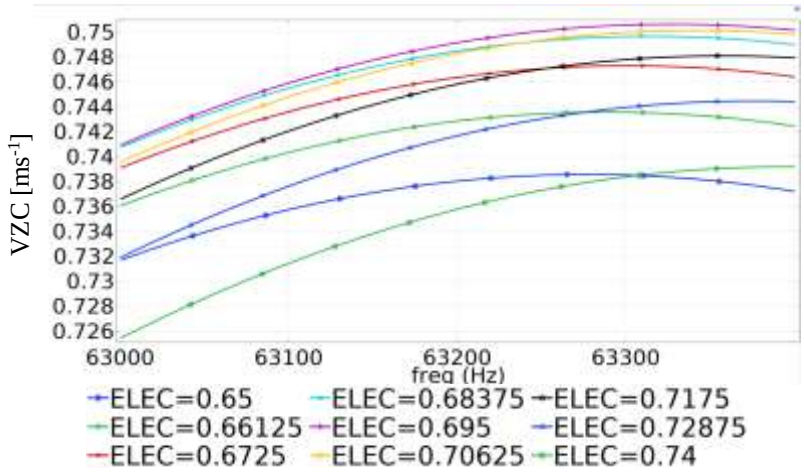

Figure 3.13 ~ Shows the Velocity, Z-component (VZC) for the displacement of the diaphragm at the midpoint in a 900 μm PMUT. The displacement is shown for different values of electrode coverage ratio.

From Finite Element Modelling results shown in Figure 3.11 and Figure 3.12 it was therefore evident that an electrode radial cover of 69.5 % gave the best performance irrespective of the diaphragm's diameter.

The next step of the Finite Element Analysis conducted in this area was to set up time domain studies through which to review the details of the diaphragm movement and therefore link the underlying physics to the relevant dynamics. The results were presented in Appendix H in which there are the time domain analysis which were conducted for devices with different electrode configurations. Through such time domain analysis the actual movement of the diaphragm at different points in time can be visualised an example of which is shown in Figure 3.14

Maximum Displacement ~ 1.16×10^{-9} m (a)

Maximum displacement ~ 5.8×10^{-9} m (b)

Figure 3.14~ Movement of the diaphragm for a PMUT with (a) device having 98% radial coverage electrode and (b) device having 66% radial coverage electrode. Both at taken at a time stamp of 1×10^{-6} seconds from start of excitation. The results have been magnified in the Z direction by 15,000 times.

Further details of the time domain sequence can also be reviewed in Appendix H. It is also important to note that since this finite element modelling was being conducted prior to the production of the prototypes a decision was taken for the experimental device to have an electrode radial coverage value of 66% rather than the 69.5% to be more anchored in the prior literature results. Two main points underpinning the decision were as follows:

- The FEM results and results in literature were close.
- The FEM results had not been calibrated with any experimental data at that point and therefore the comfort level was not high enough.

3.6 FEA V ~ Determination of the effect which the cavity fluid has on PMUT dynamics.

This FEA series was conducted to study how the cavity fluid effects the PMUT's dynamics especially the resonant frequency and diaphragm displacement at the point of resonance. The reason why this FEA was conducted was that preliminary analytic calculations indicated that the cavity fluid had a profound effect on the kinematics and dynamics of PMUT and consequently on its performance.

For the time domain modelling, a 900 μm diameter device was selected. To be able to study the propagation of the ultrasonic radiation in the coupling fluid, a larger coupling fluid area than what would normally be used in such an FEM, was set up as shown in Figure 3.15.

Before starting the time domain study a very accurate frequency domain analysis with a resolution at 1Hz time steps was carried out to establish the exact resonant frequency point. The excitation voltage used in this FEA was 14 $V_{p\text{-}p}$.

(a) *(b)* *(c)*

Figure 3.15 ~ Shows the (a) half model with sectional plane having as origin the midpoint and (b) and (c) showing closer views of the PMUT capsule including the cavity fluid shown in amber colour.

Following the establishment of the resonant frequency via the Finite Element Modelling, time domain studies were conducted through which detailed studies of PMUT dynamics with different coupling fluids were carried out. The results of these studies are shown in Appendix G. This appendix presents time domain studies conducted in nanosecond ($1x10^{-9}$ s) time periods through which the smallest details of the PMUT movements were studied.

The resonant frequency of the liquid filled cavity device was found to be much higher than the resonant frequency with a gas filled cavity device. Resonance was achieved when the signals shown in Figure 3.16 where applied for the gas and liquid filled cavity PMUTs respectively.

Frequency [Hz]: 59,800 Amplitude [V]: 14	Frequency [Hz]: 226,680 Amplitude [V]: 14
Isopropanol Coupling Fluid – Air Cavity Driving electric potential	Isopropanol Coupling Fluid – Isopropanol Cavity Driving electric potential
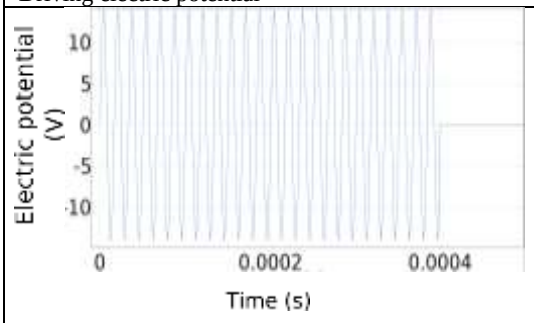	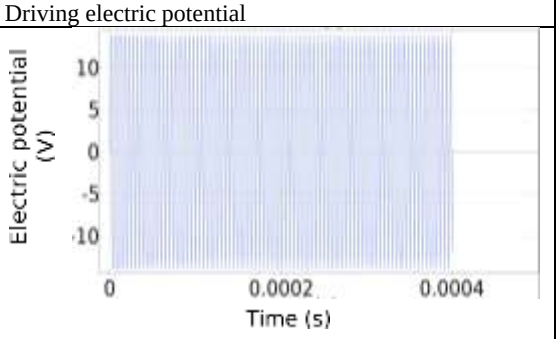
(a)	(b)

Figure 3.16 ~ Driving electric potential applies to the (a) air filled cavity PMUT and (b) the isopropanol filled cavity PMUT.

As can be seen the resonant frequency of a liquid filled cavity device at 226,680 Hz was much higher than that for an air filled cavity PMUT which resonated at 59,800 Hz. This produced the displacement curve for each of the two devices as shown in Figure 3.17.

Isopropanol Coupling Fluid – Air Cavity (Displacement field, Z component)	Isopropanol Coupling Fluid – Isopropanol Cavity (Displacement field, Z component)
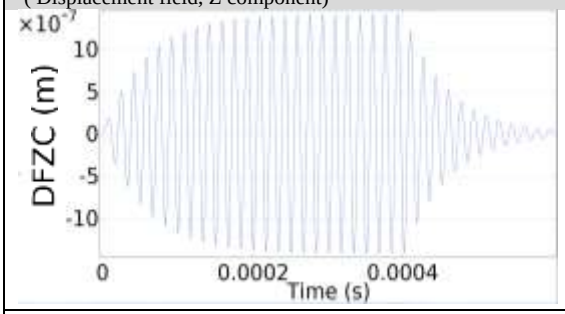	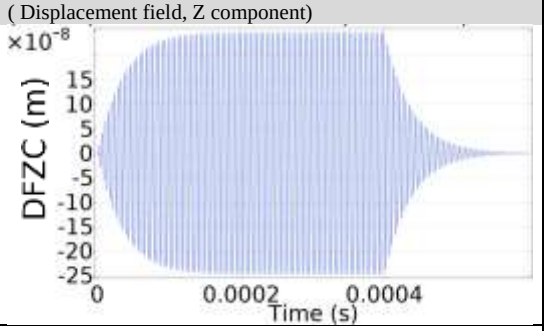
(a)	(b)

Figure 3.17~ Displacement field, Z component (DFZC) showing the displacement for the point "a" (with reference to Appendix D - Figure D.4). Graph (a) shows the displacement of a PMUT in an isopropanol environment and (a) air filled cavity (b) isopropanol filled cavity

On the other hand the velocity of the PMUT diaphragm mid-point displacement is shown in Figure 3.18.

Isopropanol Coupling Fluid – Air Cavity (Velocity, Z component)	Isopropanol Coupling Fluid – Isopropanol Cavity (Velocity, Z component)
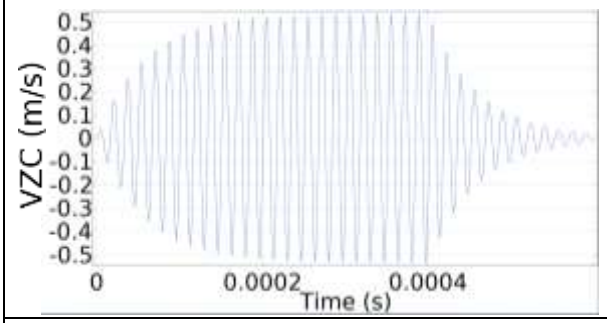	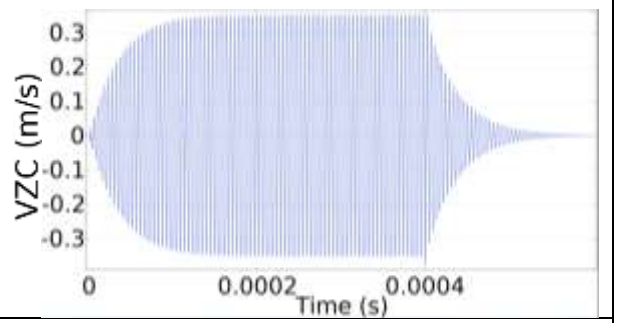
(a)	(b)

Figure 3.18 ~ Velocity, Z component (VZC) at point "a" (with reference to Figure D.4) on the membrane of a PMUT in isopropanol environment with an (a) air filled cavity and (b) liquid filled cavity.

The details of the time domain analysis can be reviewed in Appendix G where step by step time domain snapshots are taken showing the PMUT movement together with the pressures generated in the coupling and cavity fluids.

3.7 FEA VI ~ Acoustic pressure produced in the coupling fluid by various PMUT configurations.

One of the main scopes of this project was the production of a pressure wave in the coupling fluid. To review the effectiveness of the PMUT design it was therefore deemed essential to design FEMs through which the predicted coupling fluid pressures could be computed.

The first model developed was a frequency domain 2D axisymmetric model, having similar dimensions to the petri dish being used for the hydrophone experimental work outlined in Chapter 4. The model is shown in Figure 3.19. The numbered points marked in black and shown in the model are the points at which the pressure was calculated through the frequency domain model.

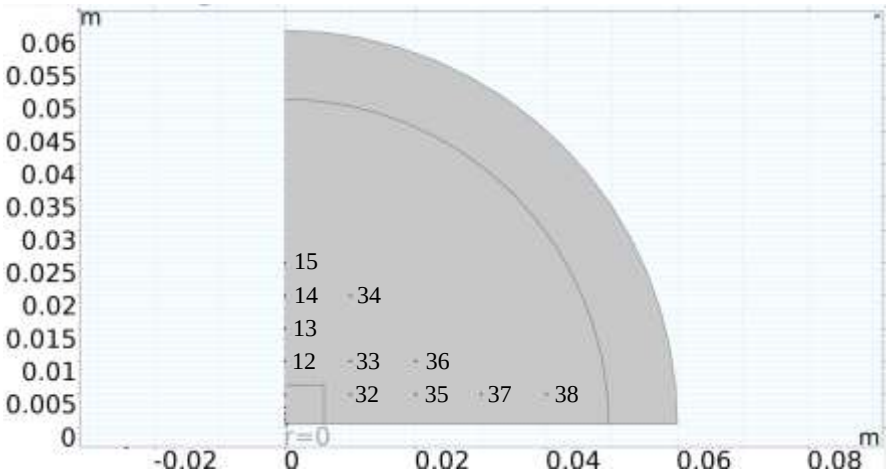

Figure 3.19 ~ Geometry of the axisymmetric model prepared for the sound pressure FEA.

Figure 3.20 presents a magnified view of the fluid area nearest to the PMUT including the details of the PMUT itself.

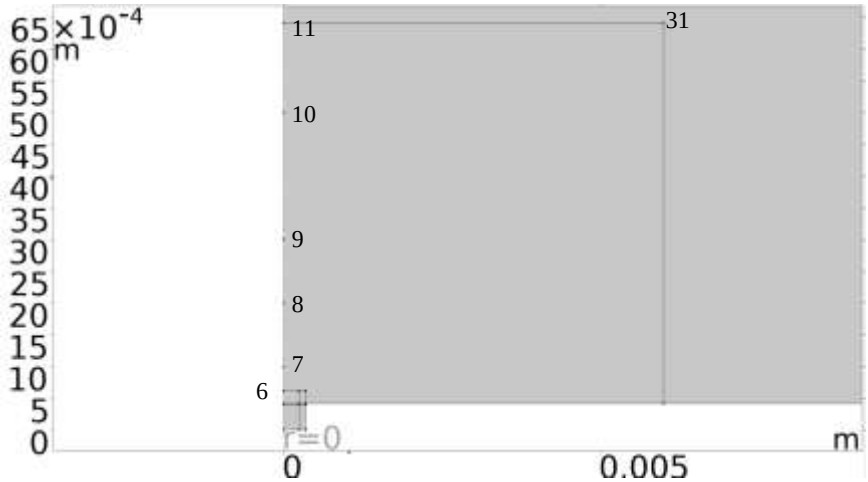

Figure 3.20 ~ A magnified view of the geometry for the axisymmetric model prepared for the sound pressure FEA showing the coupling fluid area nearest to the PMUT.

The PMUT which is situated at the point marked "r=0" in Figure 3.19 and Figure 3.20 was a 700 μm diameter circular diaphragm design. Coupling fluid used in this case was isopropanol and selected cavity fluid was air. The black dots shown in the model are the points at which the pressure readings were calculated through the FEA.

The first step was to run the model at frequencies between 115 kHz and 120 kHz in steps of 10 Hz. The voltage applied across the PMUT for this FEA was 14 $V_{p\text{-}p}$. The displacement vs frequency graph achieved is shown in Figure 3.21.

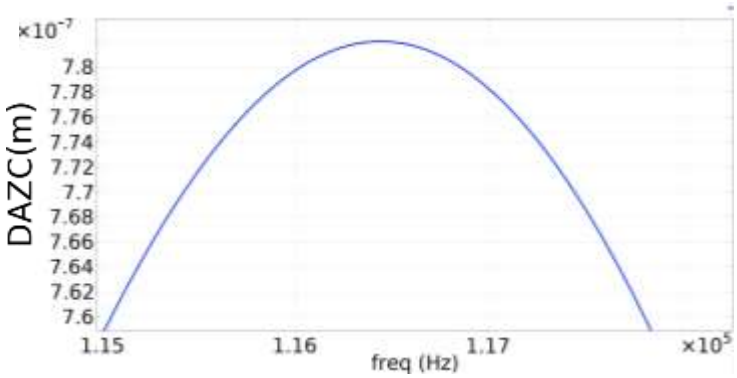

Figure 3.21 ~ Displacement Amplitude Z Component (DAZC) at the centre of the membrane for 700 µm showing PMUT's point of resonance.

The model was then fine-tuned with the frequency window set closer to the resonant point and smaller frequency steps taken. The new displacement vs frequency graph is shown in Figure 3.22.

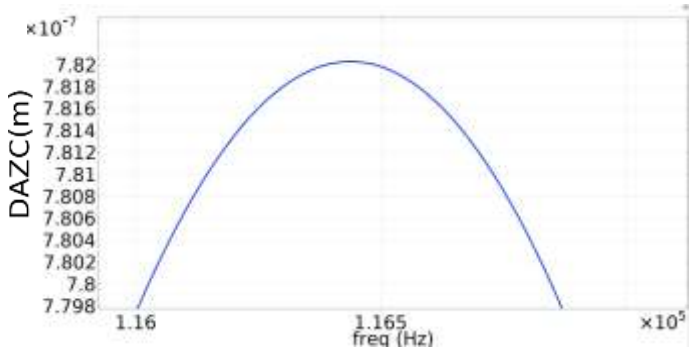

Figure 3.22 ~ Displacement Amplitude Z Component (DAZC) at the centre of the membrane for 700 µm point of resonance. Frequency steps of 1 Hz being taken for accuracy.

This model's exact point of resonance was 1.1644 x10^5 Hz. Important parameters were set as follows:

- Young's Modulus - 120 GPa
- Poisson ratio - 0.28
- Electrode radial cover percentage- 0.66
- Rayleigh Beta Damping Coefficient - 3x10^{-8}

The pressure values which were achieved through the simulations are presented in the sections below.

3.7.1 Lab testing position.

The lab test position was a point 0.04 m away in radius from the PMUT at a point 0.004 m above the PMUT. This is the position from where the acoustic experimental readings were taken in the lab. The point and the theoretical values of pressure obtained from the FEM are shown in Figure 3.23.

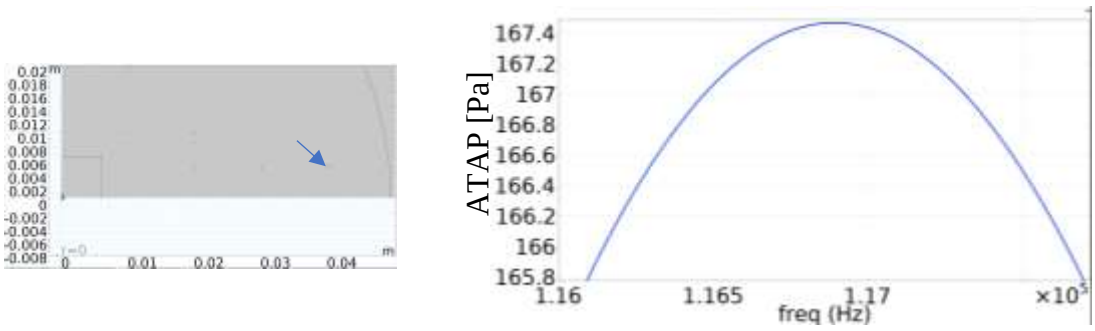

(a) (b)

Figure 3.23 ~ (a) Position were the hydrophone was placed during the acoustic experimental work also known as point 38 and (b)Absolute Total Acoustic Pressure (ATAP) calculated value (Pa)

This point is given the number 38 in the model and the calculated absolute total pressure at that point was 167.48 Pa.

3.7.2 Pressure values calculated at the reference points positioned in the coupling fluid. PMUT excitation at 14 $V_{p\text{-}p}$.

Further pressure values at points within the coupling fluid were also calculated and tabulated in Table 3.10.

Table 3.10 ~ Pressure calculated at various points in the PMUT's coupling fluid. Operating Voltage of 14 $V_{p\text{-}p}$

Point position from PMUT midpoint	**Point ref. number from simulation**	**Calculated Absolute Total Acoustic Pressure [Pa]**
Directly above midpoint of PMUT by 0.0144 m (1.44 cm)	13	464
Directly above midpoint of PMUT by 0.0194 m	14	349
Directly above midpoint of PMUT by 0.024 m	15	278
0.01m radially away from midpoint of PMUT and 0.0045 m higher	32	611
0.02m radially away from midpoint of PMUT and 0.0045 m higher	35	329
0.03 m radially away from midpoint of PMUT and 0.0045 m higher	37	222.7
0.04 m radially away from midpoint of PMUT and 0.0045 m higher _ (LAB TEST POSITION)	38	167.45

3.7.3 Pressure FEM results for coupling fluid region closest to PMUT. PMUT excitation at $14V_{p-p}$.

This section presents the pressures calculated closest to the PMUT device which are relevant when calculating the pressures inside an actual microscale device capsule. At the midpoint of the diaphragm the Absolute Total Acoustic pressure in the coupling fluid was calculated as being 62.2 kPa. This was therefore the maximum pressure produced by the PMUT at an operating voltage of 14 V_{p-p}.

Table 3.11 presents values of absolute total acoustic pressure calculated at some of the various pressure points outlined in this dissertation.

Table 3.11 ~ Calculated values of absolute total acoustic pressure at different points in the region closest to the PMUT. Operating voltage of $14V_{p-p}$

Point position from PMUT midpoint	**Point ref number from simulation**	**Calculated Absolute Total Acoustic Pressure [kPa]**
A point $2x10^{-4}$m or 0.2mm above the diaphragm midpoint	6	26.4
A point $5.8x10^{-4}$m or 0.58mm above the diaphragm midpoint	7	11
0.0015 m directly above the diaphragm midpoint.	8	4.23
0.0025 m directly above the diaphragm midpoint.	9	2.62
0.0045 m directly above the diaphragm midpoint.	10	1.48

3.7.4 Effect of PMUT signal voltage on Pressure.

The Finite Element Analysis series was then continued with another model having similar geometries but with the AlN being excited with a voltage of 20 V_{p-p}. This model was necessary to determine the peak PMUT diaphragm midpoint pressures which can be reached at the highest voltage which the PMUT can handle and at which it would conceivably be excited in a deployed device.

For this model the frequency was again parametrically scanned between 116 kHz to 118 kHz in steps of 1 Hz and the response was plotted in Figure 3.24.

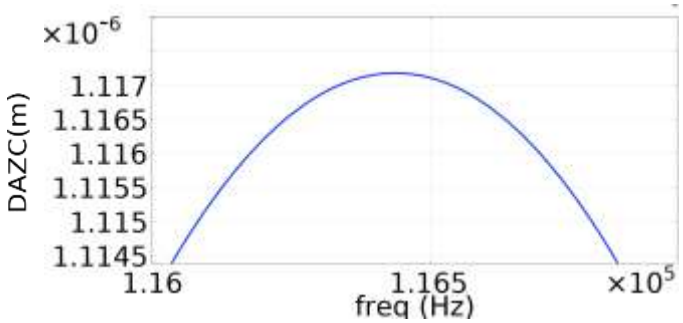

Figure 3.24 ~ Displacement Amplitude Z Component (DAZC) at the centre of the membrane for 700 µm diameter PMUT point of resonance at 20 V_{p-p}. Frequency steps of 1Hz.

The resonant frequency calculated through this accurate computation was found to be 116.44 kHz.

3.7.5 Pressure values calculated at reference points positioned inside the coupling fluid. PMUT excitation at 20 V_{p-p}.

The next involved conducting the same finite element process but using a 20 V_{p-p} excitation voltage. This voltage is the maximum voltage which can be handled by the PiezoMUMPS^{TM} device (as previously discussed). Therefore this FEM would indicate the maximum pressure which may be produced by the PMUT.

Table 3.12 ~ Pressure values calculated at specific points on the FEM. Operating voltage of 20 V_{p-p}

Point position from PMUT midpoint	Point ref number from simulation	Calculated Absolute Total Acoustic Pressure [Pa]
Directly above midpoint of PMUT by 0.0144 m or 1.44 cm	13	663.4
Directly above midpoint of PMUT by 0.0194 m	14	498.7
Directly above midpoint of PMUT by 0.024 m	15	397.7
0.01 m radially away from midpoint of PMUT and 0.0045 m higher	32	874
0.02 m radially away from midpoint of PMUT and 0.0045 m higher	35	470.5
0.03 m radially away from midpoint of PMUT and 0.0045 m higher	37	318.4
0.04 m radially away from midpoint of PMUT and 0.0045 m higher _(LAB TEST POSITION)	38	239.24

3.7.6 FEM Pressure results for coupling fluid region closest to PMUT. PMUT excitation at 20 V_{p-p}.

At the closest point to the midpoint of the diaphragm the Absolute Total Acoustic pressure in the coupling fluid was calculated to be 88.9 kPa from the FEM. This is the

maximum pressure induced by the PMUT at the maximum operating voltage of 20 V_{p-p}. These results were used to conduct the array pressure calculations.

Table 3.13 ~ Calculated values of Absolute total acoustic pressure at different points close to the PMUT. Operating voltage of 20V_{p-p}

Point position from PMUT midpoint	**Point ref number from simulation**	**Calculated Absolute Total Acoustic Pressure [kPa]**
A point $2x10^{-4}$ m or 0.2 mm above the diaphragm midpoint	6	37.8
A point $5.8x10^{-4}$ m or 0.58 mm above the diaphragm midpoint	7	15.75
0.0015 m	8	6.045
0.0025 m	9	3.741
0.0045 m	10	2.113

3.8 FEA VII ~ FEM of a novel multiple electrode design.

Apart from FEM (FEA IV) and experimental studies conducted to optimise the electrode's performance by determining the best radial cover percentage, multiple electrode designs concepts were also evaluated. Little evidence of multi electrode design were was reviewed in literature. The decision to conduct extensive finite element modelling in this field as to understand how multi electrode geometries behave in different fluidic environments was therefore taken.

In the reviewed literature no evidence of research work conducted on such devices was noted especially using the materials, fluids and frequencies used in this project. It was therefore necessary to design such a device from the ground up, with designs having to be first simulated through extensive Finite Element Modelling using parametric sweeps. The sweeps indicated the best designs which were selected to be fabricated. The multi electrode experimental devices were then benchmarked against a standard single electrode design.

For the final benchmarking two finite element models were designed. These were based on a circular PMUT geometry having a trench diameter of 600 μm. The diameter of 600 μm was selected due to space considerations on the test die.

The first of these devices which was to act as control device in the finite element pair, had a single electrode configuration designed at 66% radial cover (with respect to diaphragm) as shown in Figure 3.25. The 66% radial cover parameter was selected since literature and FEM (discussed in FEA IV) indicated this percentage cover as being at or near to the optimal electrode cover percentage.

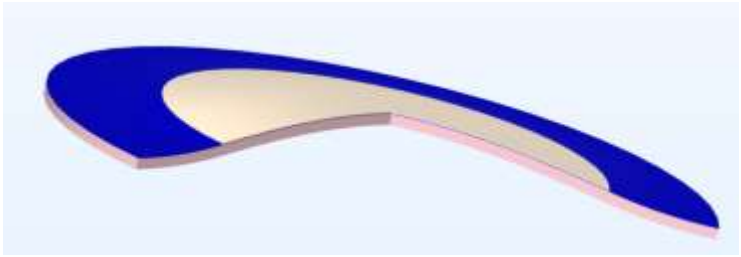

Figure 3.25 ~ Single electrode PMUT showing the electrodes on top in aluminium colour, the AlN layer in blue underneath and the pink silicon diaphragm.

The other device designed through the FEM process, was the multi electrode test device being benchmarked against the standard device. The specifically developed novel multi electrode device which is shown in Figure 3.26 was optimised for operation in an isopropanol, coupling fluid.

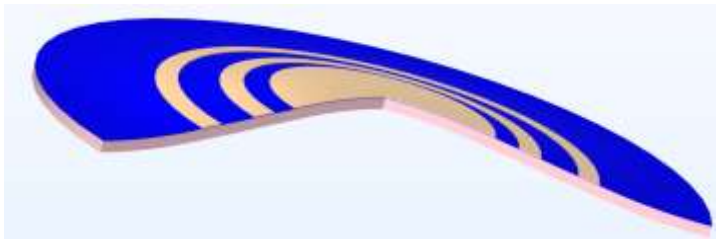

Figure 3.26 ~ Multiple electrode PMUT showing the electrodes on top in aluminium colour, the AlN layer in blue underneath and the pink silicon diaphragm.

The final optimised dimensions for the electrodes are shown in Table 3.14 with all dimensions being measured from the centre point.

Table 3.14 ~ Electrode parameters and measurements.

Electrode	**Position of the measurement point**	**Radius [μm]**	**Diameter [μm]**	**Percentage radial percentage (wrt diaphragm).**
Outer Electrode	Outer position	196.00	392.00	0.653
Outer Electrode	Inner position	176.00	353.40	0.589
Middle Electrode	Outer position	141.36	282.73	0.471
Middle Electrode	Inner position	121.34	242.68	0.404
Inner Electrode	N/A	99.00	198.00	0.330
Diaphragm diameter			600	

The FEA was conducted in the frequency domain on both models. The details of the finite element modelling which was conducted, included results are presented in Appendix J.

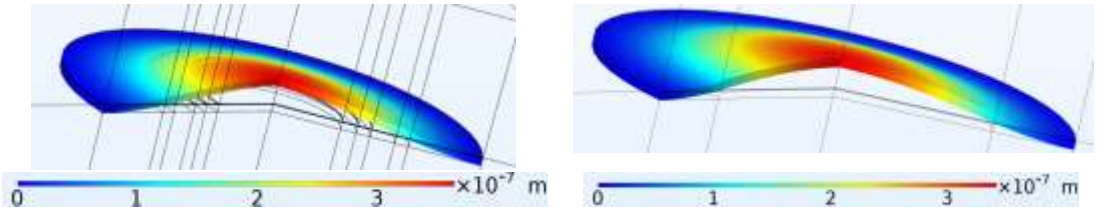

(a) (b)

Figure 3.27 ~ Shows the amplitude of the peak displacement of the Z component for (a) the multi electrode device and (b) the single electrode device.

The final results are tabulated in Table 3.15 showing the resonant frequency, peak displacement amplitude for the midpoint of the diaphragm, and peak velocity of oscillation for the same diaphragm midpoint.

Table 3.15 ~ Comparative analysis of experimental data achieved from multiple electrode and single electrode PMUTs.

Device Description	**FEM Resonant Frequency [Hz]**	**Peak Displacement Amplitude Z Component [m]**	**Peak Velocity Z Component [m/s]**	**Improvement in Amplitude [%]**	**Improvement in Velocity [%]**
600 µm diameter Multiple Electrode Device	1.686×10^{5}	3.64×10^{-7}	0.382	6.3	5.7
600 µm diameter Device with 66% electrode radial cover	1.685×10^{5}	3.42×10^{-7}	0.361		

Finite element modelling has therefore presented the opportunity of a 6% improvement in performance. For this reason it was decided to take this concept forward to experimental phase with Device 45 designed and placed in the test die as per Figure 3.28.

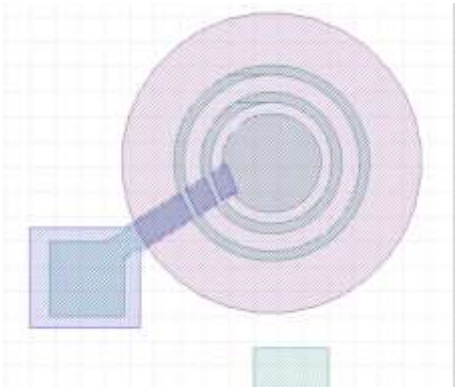

Figure 3.28 ~ Final mask design for Device 45 in the test die.

3.9 FEA VIII ~ FEM to determine effect on PMUT dynamics induced by diaphragm modifications.

This section describes the finite element analysis which was conducted to investigate how modifications to the diaphragm can affect the dynamics of the PMUT. Various finite element models with specific designs were simulated, built and some were eventually also tested experimentally.

The diaphragm modifications aimed to achieve the following:

- A reduction in the PMUT's resonant frequency thus enabling the PMUT to operate at a lower resonant frequency than would be expected for a PMUT with its diameter as discussed in FEA I were the relationship between diameter and resonant frequency was outlined.
- A higher sensitivity to incident ultrasonic radiation thus allowing it to detect lower intensity incident ultrasonic radiation.
- Possibility of achieving better dynamics when operating in high density fluids.

One of the designs which gave good results during finite element modelling is shown in Figure 3.29. This device was designed on a cavity diameter of 650 μm. This device was also prototyped and tested experimentally given the code number of Device 48.

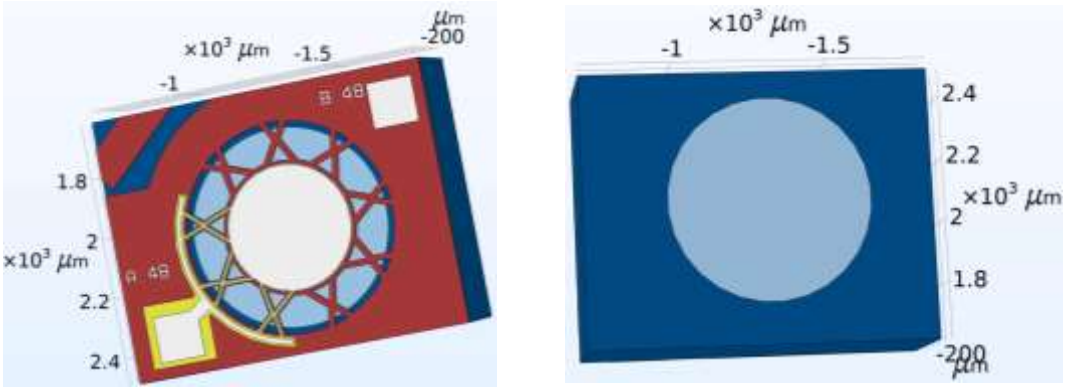

(a) (b)

Figure 3.29 ~ A FEM of a 650 μm circular diaphragm device showing (a) front side and (b) backside of design with central membrane supported via circumferential supports. Referred to as Device 48 in the experimental process.

At the centre of the design was a 410 μm diameter, 10 μm thick circular silicon membrane. The circular central membrane was kept in place, suspended and stretched by 18 suspension members as shown in Figure 3.29. This innovative design was based on the conceptual idea of a trampoline structure which is used for recreational purposes to amplify the amplitude of bouncing persons. The suspending members where designed to be 20 μm wide and 10 μm thick. The piezoelectric layer was deposited on the 410 μm diameter central membrane. One of the main complexities in view of the diaphragm discontinuity was the routing of the electrical paths to the central membrane.

The design of the path for the conductors feeding the top central electrode was more complex than the connection to the lower electrode. The electrical path was routed through six of the suspending members via 5 μm wide and 1 μm thick aluminium tracks. These aluminium tracks were patterned over a layer of silicon oxide which acted as an insulation layer between the upper (at signal potential) and lower (ground potential) tracks. The dimensions can be seen in Figure 3.30. The return electrical path was through the doped silicon and passed through all the suspending members.

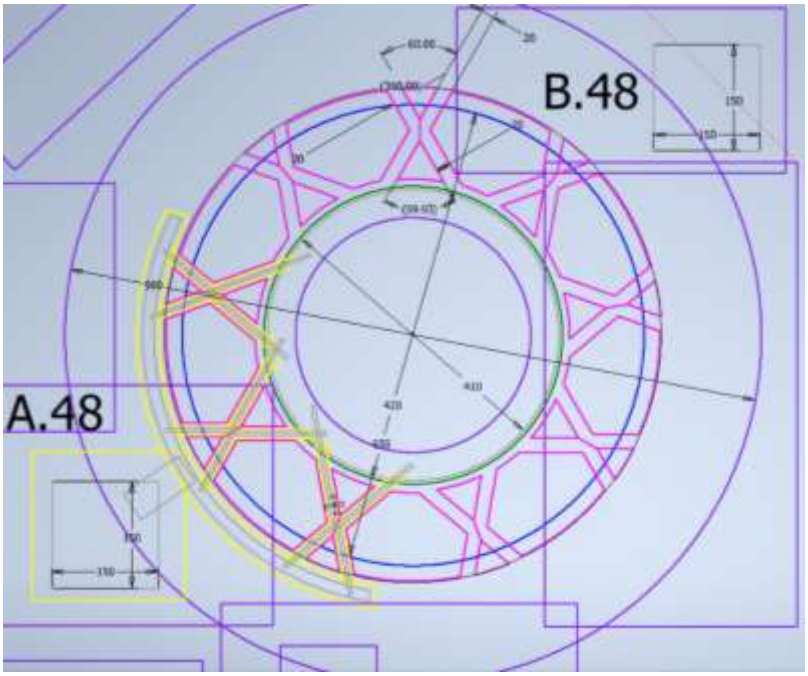

Figure 3.30 ~ Blueprints showing dimensions of the various masks of device 48.

To study the mechanics of this device and understand how the device performs in transmission mode, this model was first excited via a 14 $V_{p\text{-}p}$ sinusoidal electric signal applied to the piezoelectric layer. The device was simulated in an isopropanol coupling fluid and with an air filled cavity. The resonant frequency was fine-tuned through parametric sweeps with the final excitation sinusoid being cycled between 76,900 Hz and 77,100 Hz in steps of 1 Hz to achieve highly accurate resonant frequency values.

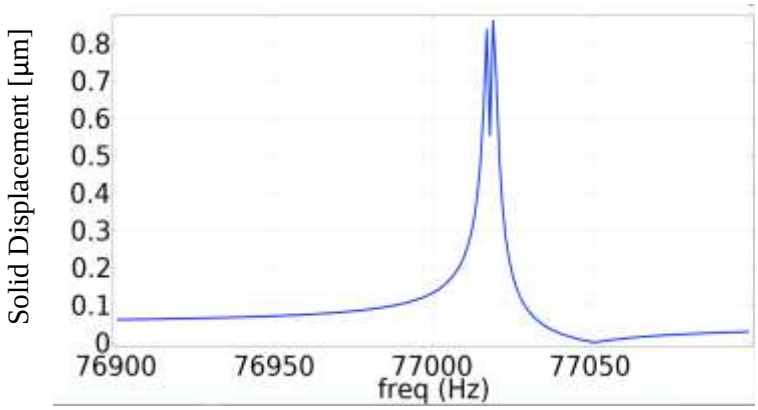

Figure 3.31 ~ Solid displacement at midpoint of diaphragm with PMUT being excited electrically. PMUT operating as transmitter.

As can be seen from Figure 3.31 the resonant frequency for the device when electrically excited and operating in transmission mode was 77.02 kHz. It was noted that while the resonant frequency of Device 48 occurred at 77.02 kHz, the control 650 μm PMUT device resonated at a frequency of 139 kHz. The important dynamic of the novel device's resonance at a lower frequency presented an important point of consideration which was deemed to warrant experimental testing. This reduction in resonant frequency made it possible to use smaller diameter devices to achieve operation at lower frequencies than would have been possible if a standard circular device had been used.

The PMUT was studied through FEM especially with regards to parameters such as displacement (shown in Figure 3.32), velocity, acceleration, stress levels, pressure induced in coupling fluids and many other parametric variables.

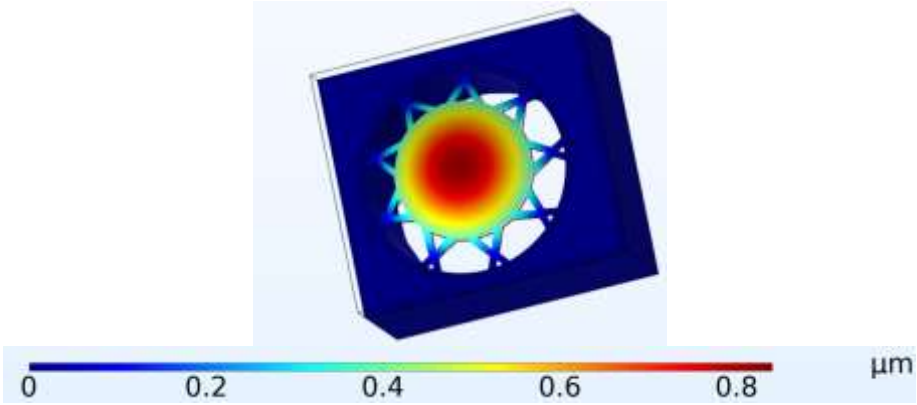

Figure 3.32 ~ Device 48 showing displacement at 77.017 kHz. Movements magnified by 100 times.

Apart from displacement of the diaphragm shown in Figure 3.32, identification of the stress points was a very important consideration to ensure reliability in operation. Figure 3.33 shows the misses stress levels on the device when operating in isopropanol coupling fluid.

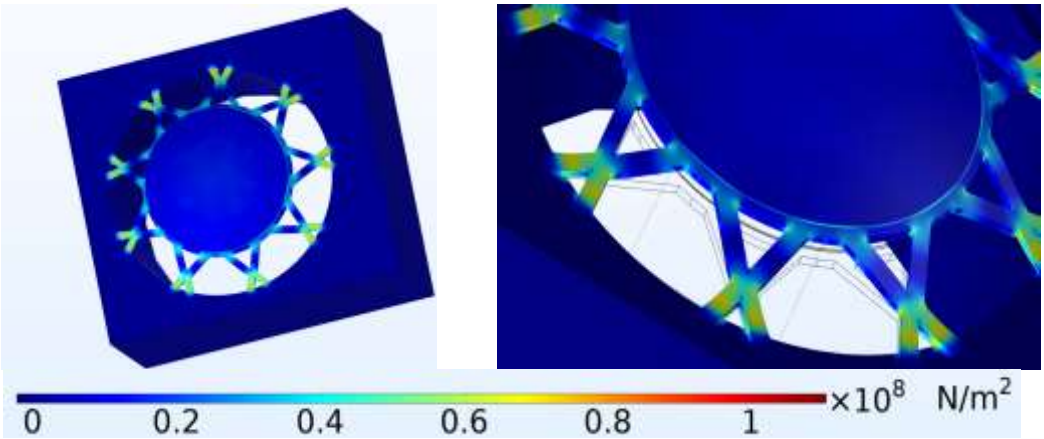

Figure 3.33 ~ FEM results showing Von misses Stress zones in the movement of the PMUT Device 48. Movements magnified by 100 times.

With reference to Figure 3.33 the maximum Von Mises stress levels when the device was deployed and excited in liquid isopropanol was 1.15×10^8 N/m^2. This maximum stress level may be observed to be reached by particular zones of the holding arms as shown in the figure. The Young's Modulus of the doped silicon used in this project was

calculated to be 120 GPa (as outlined in FEA I). It was therefore deemed that the stress levels reached by the silicon (as calculate by the FEM) clearly did not stress the silicon members beyond their elastic limit.

The next stage of modelling conducted for this device design was set up to study how the device operated as a receiver of ultrasonic radiation rather than as a transmitter.

This FEM incorporated modelling in the two physics areas of:

- Solid mechanics
- Pressure acoustics in the Frequency Domain

The pressure acoustics physics incorporated an incident spherical wave radiation component which developed an incident pressure field set up as planar waves. The reason for setting up the pressure field in this way was to conduct effective simulation of waves travelling through the concrete structures which would be incident on a PMUT operating in receiving mode. The first step was to determine the PMUT's points of resonance when operating in receiving mode. For this scope Finite Element Analysis was conducted in the frequency domain as will be outlined below.

This analysis was conducted primarily to identify the resonant point which would be the frequency at which the PMUT oscillates with the largest amplitude thereby having the highest displacement at the diaphragm's midpoint. A high level of displacement would be desirable as a higher level of displacement produces higher excitation of the AlN piezoelectric layer. This would in turn produce higher voltages by the PMUT.

The coupling fluid area was built up as a cuboid structure which in turn was composed of various smaller cuboid and cubic zones. These can be seen in Figure 3.34 and Figure 3.35. Each of the cuboids or cubes can be set up in various configurations, to act as coupling fluid, perfectly matched area or even as a radiating ultrasonic source.

In Figure 3.34 one may see the ultrasonic radiation being introduced into the model from the top face shaded in blue. However the model had the inbuilt flexibility which enabled each of the faces to be configurable in a way as to make them operate as ultrasonic sources if so required. This enables the model to be used for analysis where the ultrasonic radiation source could be simulated as coming from any direction including lateral directions so as to analyse how the PMUT device behaves under such excitation.

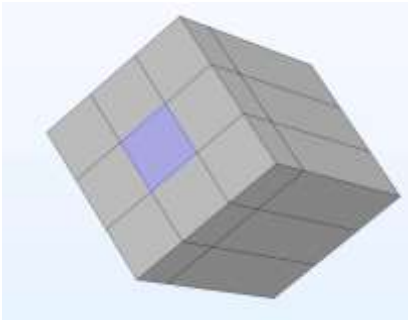

Figure 3.34 ~ Top view of the finite element model capsule showing the area where the incident ultrasonic wave was introduced into the coupling fluid.

With reference to Figure 3.35 it can be noted that the PMUT and cavity fluid reside in the smaller cube structure set up under the coupling fluid region. The two physics regions, namely the pressure acoustics and solid mechanics were coupled together through the acoustic - structure multi physics coupling boundary condition.

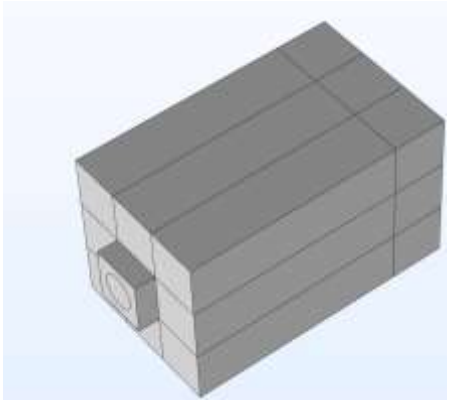

Figure 3.35 ~ Bottom side view of the Finite Element Model showing the PMUT cavity at the bottom.

The model also enabled the amplitude of the ultrasonic pressure waves to be set up as required. The design of the PMUT structure was conducted with meticulous detail to match the design of the actual PMUT and also match the fluidic volumes created between the supporting structural supports. Each of these supports was individually created and meshed as shown in Figure 3.36.

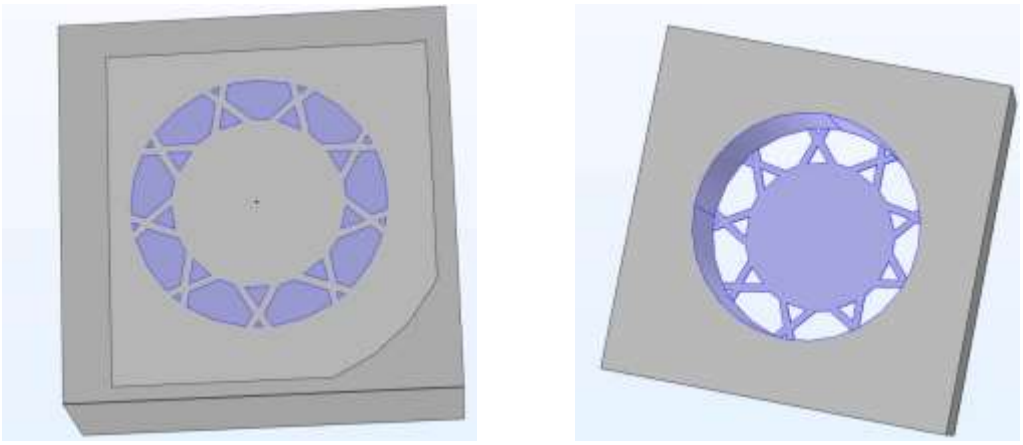

(a) (b)

Figure 3.36 ~ Views of the Device 48 FEM showing (a) the front side of the device with the fluid shown in blue between the supporting members holding the central membrane in place and (b) the backside of the device with the coupling fluid removed showing the empty cavity chamber.

The meshing conducted for this device was highly critical, especially due to the small size geometry of some of the features involved not least the supporting arms. The meshed device is shown in Figure 3.37. This was meshed using tetrahedral meshing with minimum element size set at 2 microns and an element growth rate set at 1.2. More detailed meshing with smaller mesh sizes could have been conducted to achieve greater accuracy. However it was seen to be a trade-off between accuracy and the possibility of resolving the models with the computing power available.

The mesh contained 500,523 elements and the final model took more than 40 hours to solve on a high performance computer. The accuracy achieved with these settings was deemed to be sufficient especially since at the stage at which it was conducted, the FEM was only required to indicate models which presented improvements warranting further studies through experimental work.

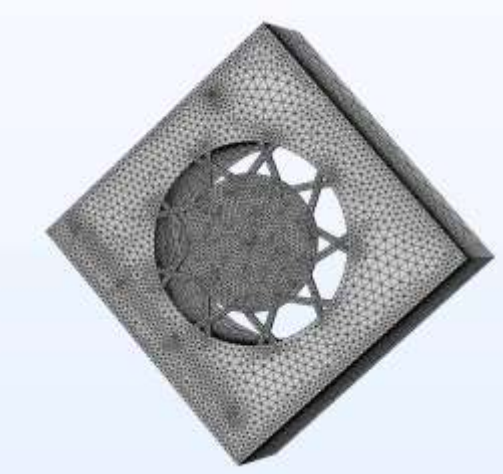

Figure 3.37 ~ The meshed PMUT structure for Device 48.

The analysis then continued with the ultrasonic radiation having a plane wave configuration at a peak pressure of 500 Pa being emanated from the area shown as the face shaded in blue in Figure 3.34. The pressure acoustics physics region was linked to the solid mechanics physics region via the acoustic-structure boundary coupling layer. The incident ultrasonic radiation interacted with the structural mechanics of the PMUT solid structure through the coupling mechanism. The ultrasonic radiation was cycled between 70 kHz and 160 kHz in increments of 500 Hz. The RMS solid displacement response is shown in Figure 3.38

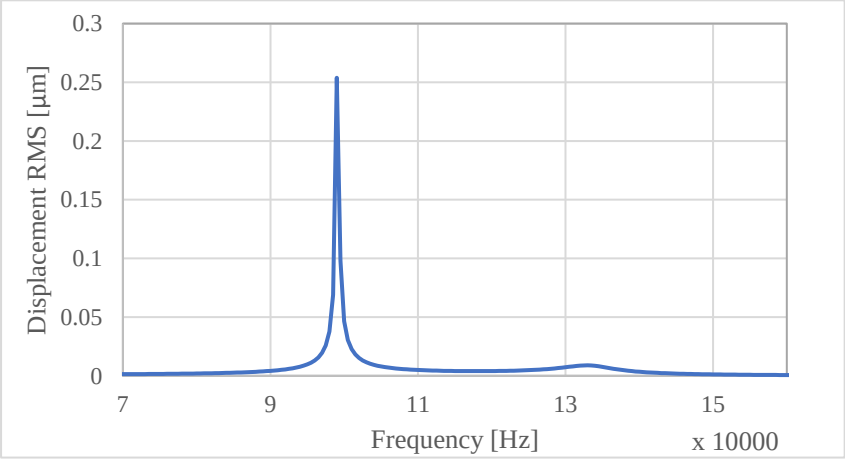

Figure 3.38 ~ Solid displacement (RMS) at the centre of the membrane for the control circular membrane device. The finite element frequency stepping was conducted at 500 Hz steps. Coupling fluid isopropanol and cavity fluid air.

The resonant frequency when the device was operating in reception mode was found to be 99 kHz as can be seen in Figure 3.38. The peak displacement exceeded 0.25 μm.

The next FEA step involved comparing the performance of Device 48's FEM with the FEM of a control device having similar diameter (650 μm) but with a standard circular diaphragm. The control device is shown in Figure 3.39.

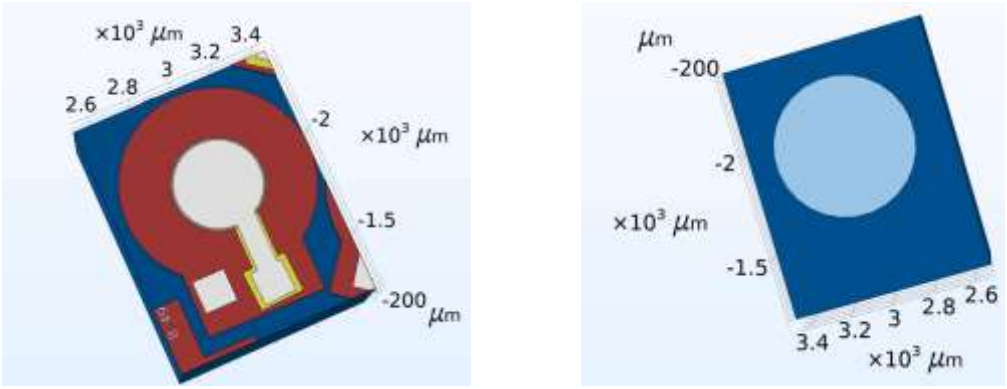

(a) (b)

Figure 3.39 ~ A FEM of a 650 μm circular diaphragm device with 66% electrode radial coverage showing (a) front side and (b) back side. Referred to as Device 49 in the experimental process.

The details of the control device are shown in Figure 3.40. To ensure that a like with like comparison was conducted, the benchmarking model was designed to be similarly sized to Device 48 with a silicon plate providing a solid surface for the diaphragm instead of the novel suspended structure presented in Figure 3.29.

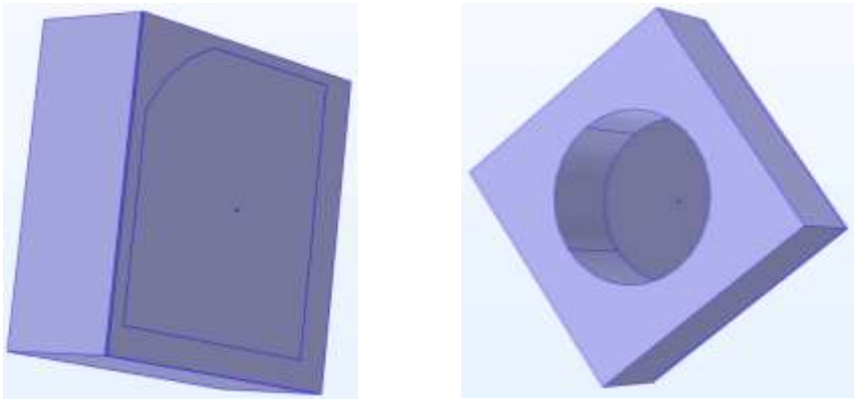

(a) (b)

Figure 3.40 ~ The 650 μm diameter PMUT structure acting as control showing (a) front side and (b) rear side of the PMUT.

The device was subjected to the same ultrasonic pressure wave frequency sweep as outlined above for Device 48. The calculated RMS displacement of the diaphragm midpoint for the control device is shown in Figure 3.41.

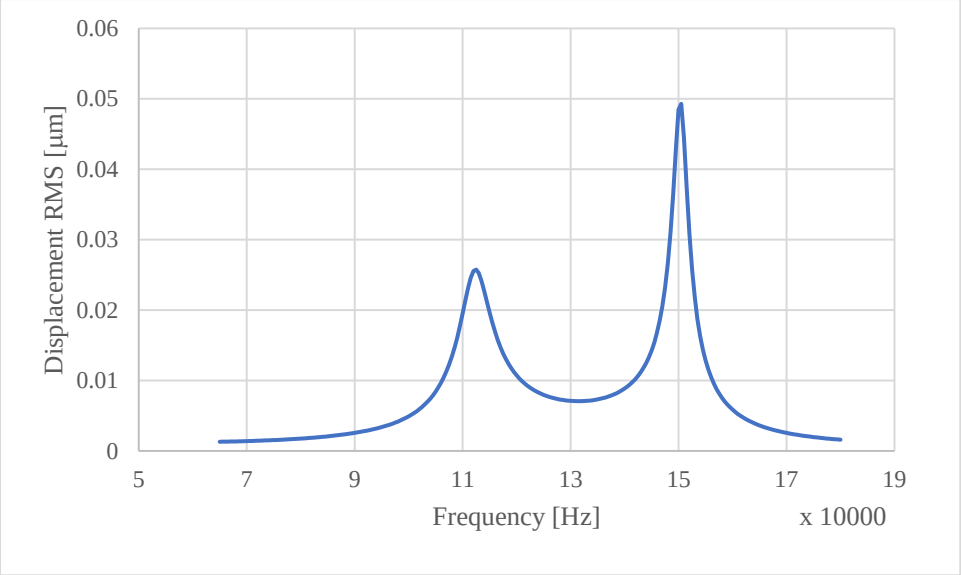

Figure 3.41 ~ Solid displacement (RMS) at the centre of the membrane for the control device. The finite element frequency stepping was conducted at 500Hz steps. Coupling fluid isopropanol and cavity fluid air.

As can be seen in Figure 3.41, the model frequency sweep showed two points of resonance for the control device. These occurred at 1.124 x10^5 Hz at which the RMS diaphragm midpoint displacement was 0.025 µm (shown in Figure 3.42) and at 1.505x10^5 Hz where the RMS diaphragm midpoint displacement was 0.0492 µm.

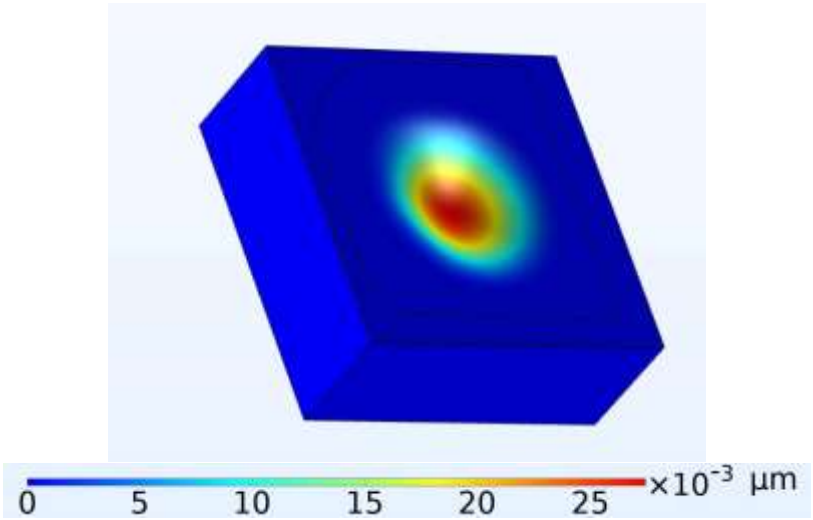

Figure 3.42 ~ FEM results showing the displacement of the 650 µm diameter circular PMUT structure acting as control with device 48.

The max stress levels at a frequency of 1.51x10^5 Hz was 2.17x10^6 N/m^2 as shown in Figure 3.43.

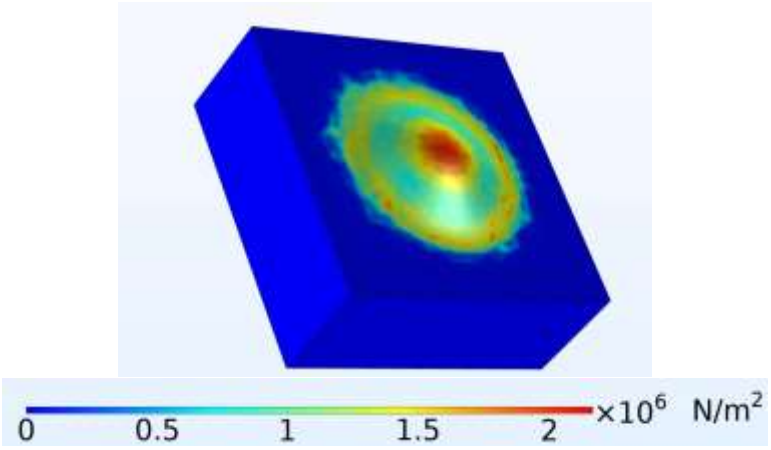

Figure 3.43 ~ Stress levels in the control device at the resonant frequency of 1.51x10^5 Hz.

The scope of t this simulation was to compare the performance of the modified Device 48 with the control device. Since these FEMs were conducted pre experimental phase before the damping coefficients were accurately established, Rayleigh damping was not included in the FEM. At this stage of the project absolute accurate displacement values were not required.

Table 3.16 presents a comparative assessment of the FEM results achieved for Device 48 and the control device when both were operating as receivers of ultrasonic radiation.

Table 3.16 ~ Comparison of parameters between Device 48 and the control device when acting as receivers of ultrasonic radiation.

	Device 48 with a diameter of 650 μm	**Circular 650 μm diameter diaphragm control Device**
Resonant Frequency	99 kHz	1.124x10^5 Hz and 1.505x10^5 Hz.
Solid Displacement (RMS)	0.25 μm	0.025 μm and 0.0492 μm

Taking the FEM midpoint displacement results achieved by Device 48 and comparing the 0.25 μm peak displacement result achieved with the 0.0492 μm peak midpoint displacement result achieved by the control device, it was noted that a 134% improvement in displacement performance was achieved when the novel designed device was operating as a receiver of ultrasonic radiation.

The novel FEM device presented good results when operating in both transmitting and receiving modes in issues such as a reduction in frequency. In view of these positive FEM results the device was progressed to the experimental phase and the lithography masks were subsequently prepared.

3.10 FEA IX ~ FEM to determine effect which an octagonal shaped diaphragm and cavity has on PMUT dynamics.

Another area studied through Finite Element Modelling was the relationship between the shape of the PMUT cavity and diaphragm's outer envelope with respect to the

PMUT's operational dynamics. Instead of a curved diaphragm as was the case for most of the other models an octagonal shape was designed and modelled in this case.

Since this model's geometry was not axisymmetric a 3D FEM of the octagonal shaped PMUT was set up. The diaphragm for this model was designed as shown in Figure 3.44.

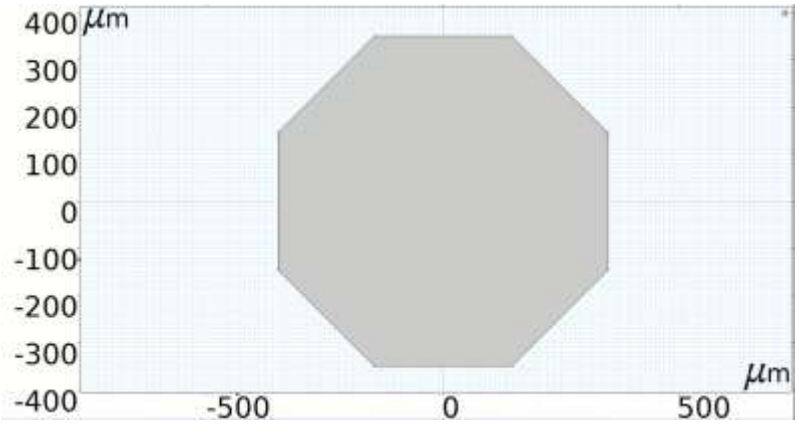

Figure 3.44 ~ 2D plot of the diaphragm used in this model.

The components making up the 3D FEM are shown in Figure 3.45. Figure 3.45 (a) shows the 3D cavity model including the diaphragm, electrodes and piezoelectric area while (b) shows the coupling fluid structure and perfectly matched layer.

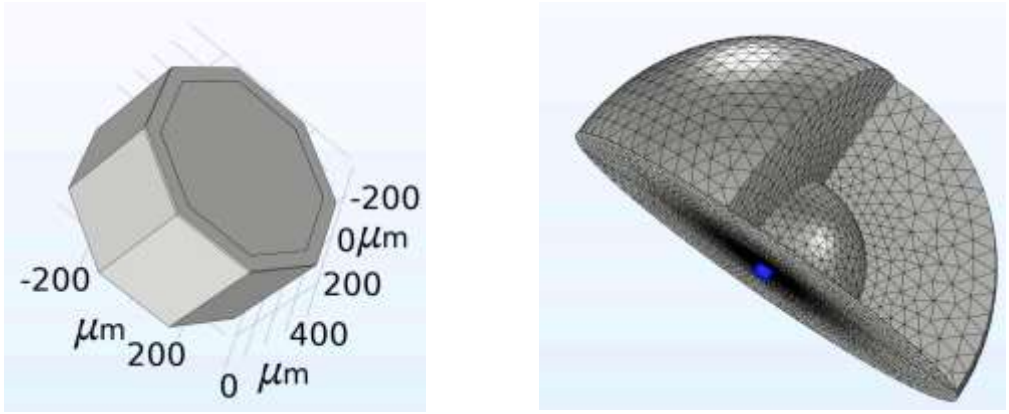

(a) (b)

Figure 3.45 ~ 3 D views showing (a) assembly of the PMUT structure including the cavity, diaphragm, piezo layer and upper electrode (b) the PMUT installed inside coupling fluid half sphere having 1 cm radius.

A frequency domain analysis was conducted. The result of the Finite Element Analysis is shown in Figure 3.46.

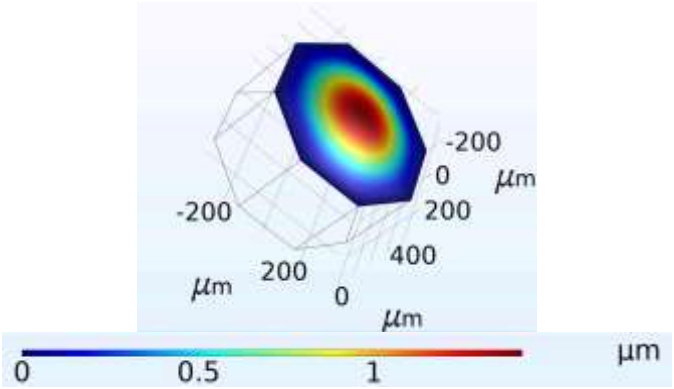

Figure 3.46 ~ Displacement of diaphragm at a resonant frequency of 96,300 Hz

The maximum displacement calculated by the Finite Element Modelling at the midpoint of the diaphragm was 1.4 µm. This value was obtained at a resonant frequency of 96,300 Hz. No Rayleigh beta damping coefficient was implemented.

With reference to FEA I the undamped coefficient for a benchmark 700 µm standard circular PMUT did not exceed the 1.2 µm mark for its maximum diaphragm midpoint displacement. The design of the octagonal configuration was therefore deemed to be imparting performance benefits to the PMUT without impacting the device's footprint on the die surface. It was therefore decided to take this design forward to experimental status.

To be able to compare the experimental results of the circular and the octagonal design, the experimental device was designed in such as a way as to be able to take the same die footprint which would be taken by a circular 700 µm diameter PMUT in an ultrasonic array as discussed in Appendix K. For this reason it was designed as an octagon circumscribed about a 700 µm circle as shown in Figure 3.47. The device was given the code name of Device 55 and the experimental work conducted on it can be viewed in Chapter 4.

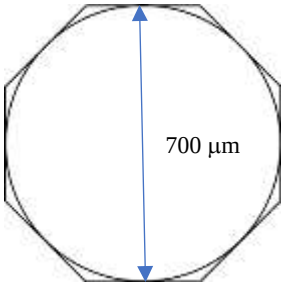

Figure 3.47 ~ The Octagon shaped PMUT Device 55 circumscribed about a 700 µm circle.

Since Device 55 circumscribed the area which is normally covered on the die by a 700 µm diameter circular PMUT, it would take the same die space in an array. The extra areas (compared to the circle) near each of the octagon's points would only cover die area which cannot be used anyway. A comparative assessment of the results will be discussed further in Chapter 5 ~ Conclusion 8.

3.11 FEA X ~ FEM of the array design

As discussed in the literature section, for the PMUTs to achieve an output through which significant transmission into the concrete structure would be achieved they must be set up in the form of arrays were potentially tens and up to hundreds of PMUTs can operate together.

Array concepts have also been modelled through MATLAB as shown in Appendix K. Here it was shown that with the incorporation of a multi element array system more effective beam directivity and waveform shaping could be achieved apart from the increase in the transmission ultrasonic pressures. Furthermore with a phased array ultrasonic beam steering could also be achieved through the incorporation of phase shifts.

Waveform steering opens up two important possibilities for the phased array namely:

- Achieving an optimal angle of incidence for onward travel into the concrete as discussed in the literature review section.
- Communicating with devices which are not directly in line with the transmitting device.

Appendix M presents a set of two finite element models through which the performance of an array in actual deployment was estimated. It must be stressed that this modelling was conducted as an estimation and the concrete structure did not have aggregate or rebar inside it. So it was essentially mortar.

Figure 3.48 show a result shot from the second array presented in Appendix M. In this model an array installed at the bottom of a 1 m high concrete block was transmitting to a capsule on the other side of the block. The FEM results shown in Figure 3.48 shows the early stages of the ultrasonic energy transmitting through the structure in the form of solid misses. The energy emanates in hemispherical fashion from the transmitting capsule.

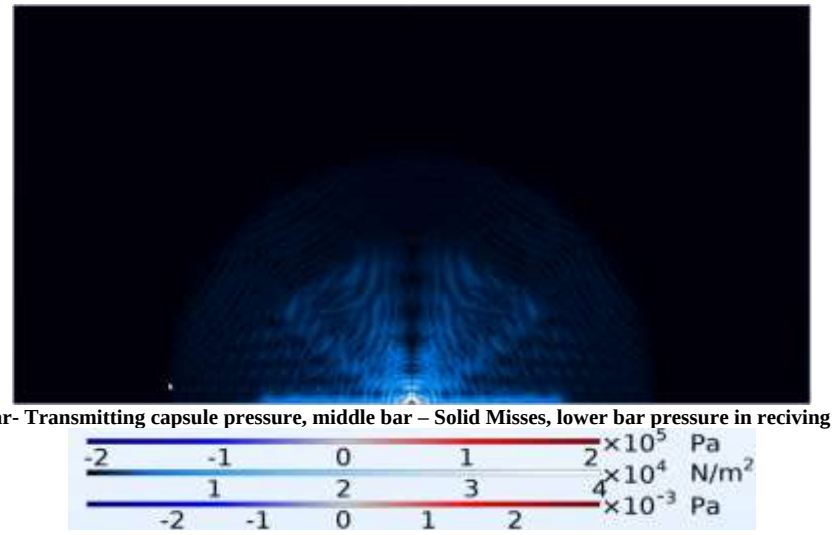

Upper bar- Transmitting capsule pressure, middle bar – Solid Misses, lower bar pressure in reciving capsule.

Figure 3.48~ Total Acoustic Pressure (Pa) in capsules and solid misses in solid at time $1.8x10^{-4}$ seconds.

The conclusions of this model which can be reviewed in more detail in Appendix M demonstrated that an array of PMUTs set up on a MEMs IC platform is capable of transmitting data over a 1 m range inside a concrete structure.

3.12 Glycerine as coupling fluid- conclusions.

When glycerine was used as a direct coupling fluid, it was noted that the PMUT's dynamics presented extensive deviation between the Finite Element Modelling results and the experimental data. Such deviations occurred with regards to the displacement of the midpoint of the PMUT's diaphragm and also the velocity and acceleration of the said point. On the other hand the resonant frequencies of PMUTs operating directly in contact with glycerine, calculated through FEM matched the resonant points obtained from the experimental work.

The main difference in the results obtained through the FEM and those obtained through experimental work was that experimental work with the laser vibrometer for devices using glycerine coupling fluid measured amplitudes of displacement and velocity which were much lower than those predicted by the finite element work.

Post experimental finite element modelling in COMSOL was also attempted with various parameters including thermoviscous acoustics physics. However even then the results were not sufficiently robust as to enable the building of reliable models through which coupling fluid pressure values could be computed.

At that point, further work in this area was not deemed necessary in view of the drastic reduction in dynamic performance experienced when PMUT was operating in glycerine as opposed to the less dense fluid, isopropanol. In the final design Glycerine was used as the second coupling fluid coupling the outside of the capsule with the concrete in a two fluid approach outlined in Appendix M and discussed in the conclusions to this dissertation.

3.13 Design and construction of the prototype experimental MEMs Integrated Circuit.

3.13.1 Integrating the experiments on the test device.

Following the conclusion of the finite element analysis, a prototype experimental IC was designed and produced incorporating the devices and concepts which were selected for further experimentation. The final designs which were produced for device manufacture continued to build on the work conducted and outlined in FEA I to FEA X. In this way the test devices could experimentally confirm and enhance the findings from the Finite Element Modelling.

The masks for each the five lithography levels namely Padoxide, PZfilm, Padmetal, SOI, and Trench were created to enable the prototype device IC to be manufactured. Appendix P outlines the mask design process.

This section will briefly outline the process undertaken to design the actual MEMs Integrated Circuit (IC). This IC integrated no fewer than 59 test devices on one die, each of required detailed geometry over five mask layers and therefore one may appreciate the required complexity. For this phase of the project the design work was started using CoventorWare® 2012 Finite Element Software. This finite element software was a specialised software optimised for MEMs fabrication processes.

One of the first steps involved the setting up of the PiezoMUMPS™ process in CoventorWare® . The reason for this was that the process was not yet available in the software library. The setup of the process can be seen in Figure 3.49.

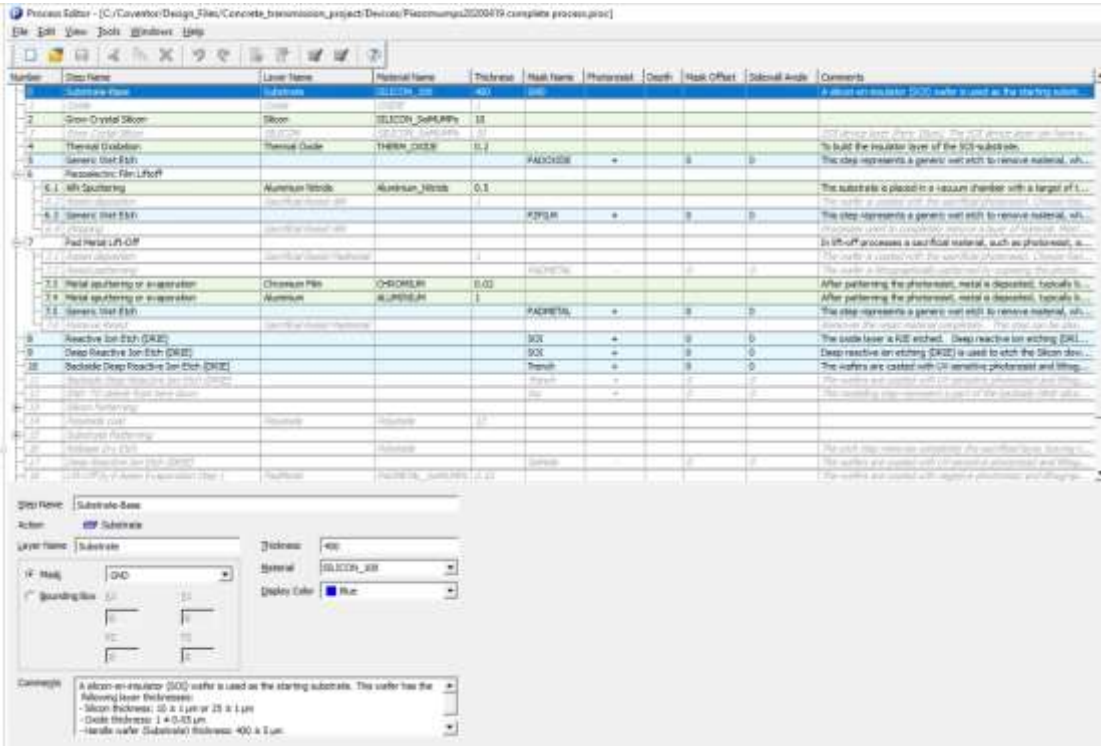

Figure 3.49 ~ The PiezoMUMPS™ process set up in the process editor.

To develop the process several items such as mask details, materials, geometries and layer thicknesses had to be researched and needed to be included and set up in the process editor. When the process was set up the actual mask design was started using the CoventorWare® geometry editor. Some of the devices had details which were too complex to be built on the geometry editor. These had to be developed through the use of the Autodesk Inventor and then transferred back to CoventorWare®. The first draft device was designed as shown in Figure 3.50.

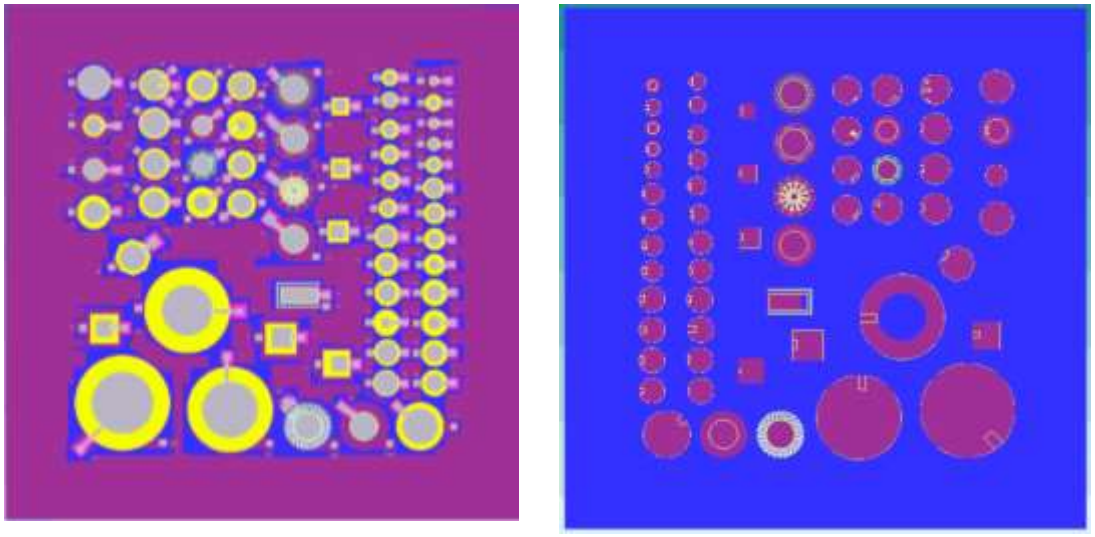

(a) (b)

Figure 3.50 ~ Early versions of the prototype experimentation device showing (a) the front side and (b) the backside of the die.

The design work proceeded through CoventorWare® with initial simulations conducted to study movements and establish primary workability of designs.

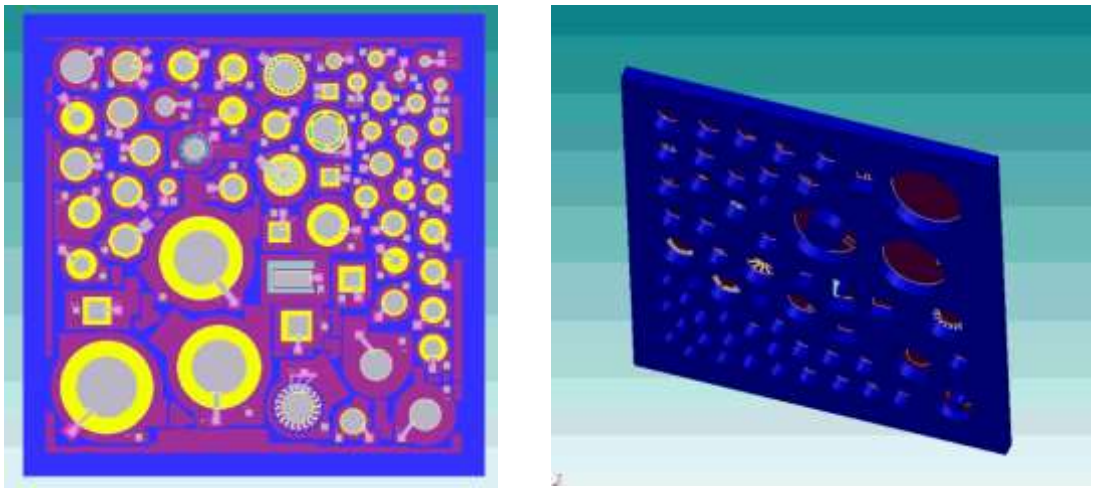

(a) (b)

Figure 3.51 ~ Final version of the prototype experimental design showing (a) front side and (b) back side of the die.

These simulations were however deemed to be insufficient in scope due to an inherent limitation of the CoventorWare® software being used. CoventorWare® limited the fluid which could be used, both as the cavity and the coupling fluid, to air only. This was not sufficient for this project as apart from air, various other fluids needed to be utilised including isopropanol, glycerine and distilled water.

This apart from the requirement to build a whole environmental envelope around the device which also included physics such as ultrasonic radiation within solids such as the concrete itself. Using ACAD, the IC design was transferred to COMSOL Multi-Physics software for further FEM conducted on it as a holistic die.

(a) (b)

Figure 3.52 ~ A view of the digitised IC showing (a) front side (b) rear side. This model was set up for transfer into COMSOL Multi-Physics for final Finite Element Analysis to be conducted prior to production of devices.

The mask design itself was continued on CoventorWare® after which it was fine tuned in KLayout, another die design software package. Work necessary to finalise the five mask designs was conducted through the use of this software. Klayout enabled extensive pre fabrication mask checking to be conducted especially with regards to the semiconductor fabrication design rules. Some of the work on the design rules and constraints imposed will be discussed in the subsections below.

3.13.2 The PiezoMUMPS™ Design Rules

The PiezoMUMPs™ process had a number of stringent design rules which needed to be followed when designing the device. The salient ones for the design process included the minimum features and spacing as well as the overlay tolerances.

3.13.3 Minimum features, spacing and tolerances.

As discussed, the production process to fabricate the prototype die, was based on lithography processes using masks. The photo masking processes impart tolerances to the feature geometry which must be followed. Hence design rules establish mandatory minimum feature and spacing sizes. The final designs had to incorporate these requirements also apart from the geometries established through the analytical computations and the finite element models. Table 3.17 shows these minimum sizes and spacing.

Table 3.17 ~ Table showing minimum feature sizes and minimum spacing [115].

Level Name	**Minimum Feature size** [µm]	**Minimum Spacing** [µm]
PADOXIDE	5	5
PZFILM	10	10
PADMETAL	3	3

SOI	2	2
SOIHOLE	3	3
TRENCH	200	200

The overlay tolerances which needed to be kept in mind during the design work are shown in Table 3.18.

Table 3.18 ~ Overlay tolerance between the various layers [115].

Layer combination	**Centre to centre Overlay Tolerance [µm]**	**Edge to Edge Bias [µm]**
PZFILM to SOI	±5	±5
PADMETAL to SOI	±3	±3
TRENCH to SOI	±5	<50

After the final adjustments for the die were conducted, surface scripts were set up and run to conduct extensive testing for any design rule violation which might have occurred. Such testing ensured that the design rules were being respected thus ensuring that the MEMs device received would operate in the correct planned way.

3.13.4 Design Rule Checking (DRC) and parametric testing.

Design rule checking was carried out extensively both through the local use of KLayout and also by IMEC using more sophisticated offsite tools. DRC scripts were obtained from IMEC and adjusted as necessary to test the required parameters. The masks were run through the scripts and then each result was looked at in detail with the required modifications being conducted. Samples of results obtained from the DRC process can be seen in Figure 3.53 and Figure 3.54.

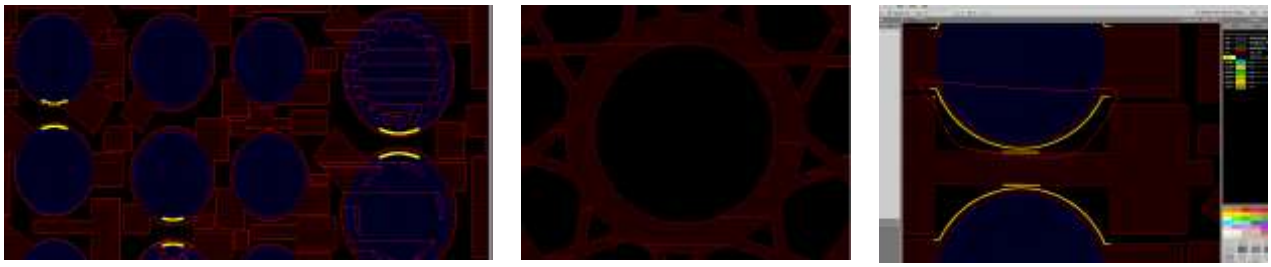

Figure 3.53 ~ Various results from design rule checking

The DRC process was quite intensive as the first runs resulted in hundreds of items being flagged. Each of these flags had to be looked at in detail and rectified, with the DRC file being run again on the modified maps. This went on until nothing further was flagged.

Figure 3.54 ~ Further results from design rule checking.

3.13.5 PADMETAL design to remove the effect of the conducting tracks from the experimental data thereby improving the accuracy.

One of the key considerations is ensuring that the tracks themselves do not excite the piezo layer thereby distorting the results from the experimental processes. The devices were designed in such a way that the track leading to electrode would have no actual effect on the PMUT dynamics by growing an oxide layer (PADOXIDE) under the track leading to the electrode structures. This concept is shown in Figure 3.55.

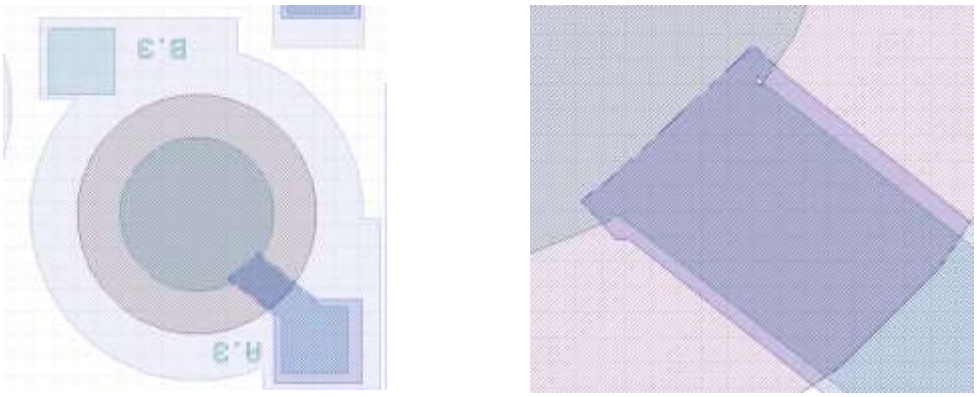

(a) (b)

Figure 3.55 ~ Designs showing (a) The layers in one of the devices designed for the experimentation and (b) Close up view showing the oxide insulation under the padmetal layer.

3.13.6 The final mask design process.

Five masks were then produced from the final model after the testing was concluded. These were sent for production as outlined in Appendix P. A frontal micrograph of the final MEMs IC is shown in Figure 3.56

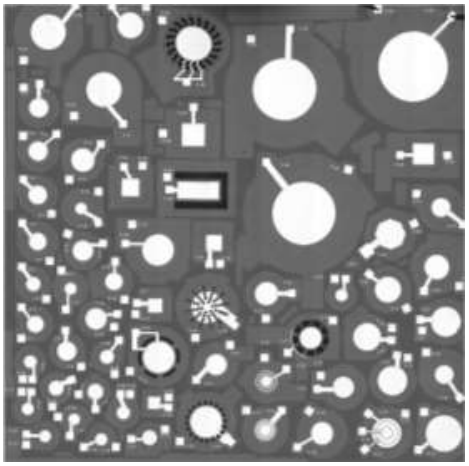

Figure 3.56 ~ Frontal micrograph of the MEMs test die produced for the experimental process.

3.14 Conclusions from the FEA work.

Through the work which was conducted, Finite Element Modelling has been shown to be a very useful, accurate and versatile tool for the design and simulation of PMUTs. Further Finite Element results are also outlined and elaborated upon in various appendices to this work. Finite Element Modelling was used not only to actually model the devices but to also aid in the derivation of parameters such as Young's modulus and damping coefficients.

FEM enabled detailed physics models to be developed through which the interaction between the solid structure and the surrounding fluid could be studied including the creation and propagation of the ultrasonic radiation. Such modelling was successfully created both in the time and frequency domains.

The final FEMs which were created were used in conjunction with lab work to determine parameters such as the pressures induced in the coupling and cavity fluids by the diaphragm's movements.

The next chapter outlines the experimental work which was conducted utilising laser diffraction, laser vibrometry and ultrasonic work.

Chapter 4: The experimental procedures conducted to study device mechanics and fluid dynamics.

4.1 Introduction to the experimental procedures.

Following the work on Finite Element Modelling, extensive experimental work had to be conducted through which the models could be verified. The experimental work conducted also allowed an extensive in depth look at PMUT dynamics. The microscale of the devices used in this project afford particular physics challenges to Finite Element Modelling, especially in the area of Computational Fluid Dynamics. Such challenge could only be unlocked and studied through an experimental process.

The experimental work was conducted in three main areas:

- Laser Vibrometer Experimentation
- Laser Diffraction Experimentation
- Acoustic Experimentation

4.2 Experimental Procedure I ~ Laser Vibrometer experimental work.

To accurately measure the vibrations induced in the PMUT a scanning Laser Doppler Vibrometer was used. This vibrometer operates by combining the interferometer with moving mirrors which direct the laser beam to the measurement points. The Laser Doppler Vibrometer is a transducer which analyses the frequency shift caused by the movement of a target surface.

The Laser Doppler Effect which is illustrated in Figure 4.1 is a measurable effect which is based on the frequency shift, Δf_D which occurs to a laser beam emitted by a source, denoted as S and reflected from a surface moving at a velocity v [116].

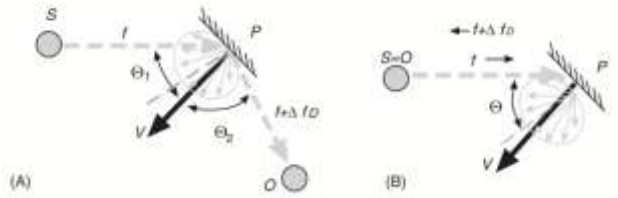

Figure 4.1 ~ (a) Illustration of The Doppler Effect (b) Doppler Effect when source of the light energy and Observer are at the same point [116].

The frequency shift Δf_D is given by equation (4.1) [116].

$$\Delta f_D = \frac{2v}{\lambda} cos\theta \tag{4.1}$$

where

λ is the source wavelength
θ is the angle between the line of motion of the surface and the observer
v is the velocity of motion of the surface being examined.

The phase shift $\Delta\phi$ due to the Doppler Effect and corresponding to the frequency shift discussed in the previous equation is being represented by equation (4.2) [116].

$$\Delta\phi = \frac{4\pi d}{\lambda}\cos\theta \tag{4.2}$$

where

$$d(t) = \int_0^{\tau} v(\tau)d\tau$$

The out of plane movement for the PMUTs which were the subject of this dissertation where in the submicron range. It is for this reason that specific equipment able to measure the minimal phase shifts expected, was needed for this project.

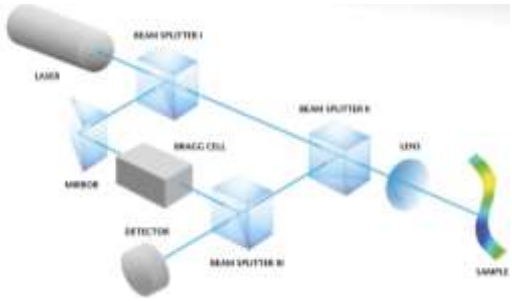

Figure 4.2 ~ The scanning laser Doppler vibrometer's operating principle [117].

It was prohibitively expensive to procure a laser vibrometer costing around a quarter of a million euros for this specific project. Instead, equipment at Polytec in Germany, was rented on need basis, together with a technician who carried out the detailed test procedures which were prepared by the author. Polytec was selected for this project as it was a world leader in laser vibrometer technology. The Polytec technical personnel were very knowledgeable on the use of the vibrometer, but not on MEMS or PMUTS and therefore sole technical expertise with regards to PMUT design, testing, and analysing of experimental data again rested with the author. This included decisions regarding which devices where to be tested, the test procedure to be followed including coupling fluids to be used, frequencies to be utilised, type of study, as well as the post processing and detailed analysis of the test data. During all the testing conducted the author joined the testing through online means and gave step by step instructions to the technician with regards to the procedure to be followed.

Laser vibrometer readings were taken with the device probed in a petri dish as shown in Figure 4.3. The coupling fluid, be it isopropanol or glycerine was poured over the device after probing.

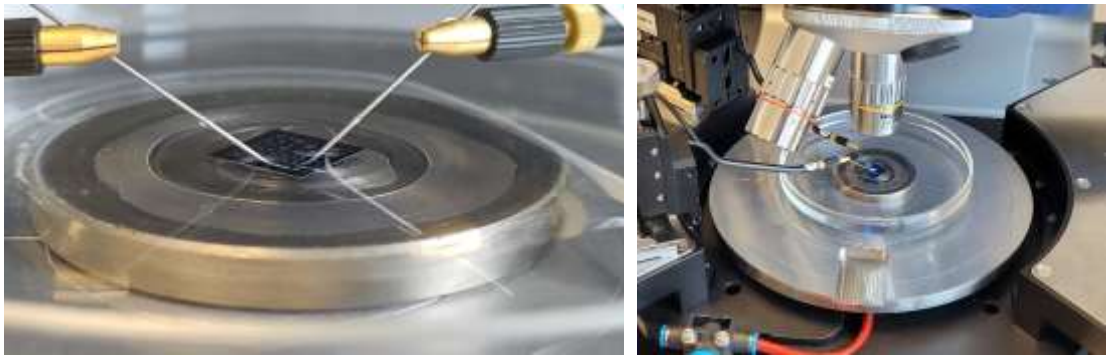

(a) (b)

Figure 4.3 ~ (a) Close up view showing probed die in petri dish with glycerine filled 2.5 mm height from Petri Dish bottom (b) view of the device petri dish loaded in the MSA 600 with close up view of the objective lenses.

Unless otherwise indicated below the petri dish was filled at a level of 4 mm of isopropanol or 2.5 mm of glycerine depending on the experiment. When probing the different devices on the test IC, the needles were always lifted and placed back in their new position one by one. The first needle was lifted and then touched down over the pads of the next device which was being studied. Similarly the second needle was then moved to the second device. This was done to ensure that the IC would not lift off from the petri dish bottom thereby allowing fluid to flow under the IC and into the cavities which would invalidate the experimental results.

4.2.1 The MSA 600 and MSA-100-3D Laser Vibrometers

The Polytec MSA 600 shown in Figure 4.4 (a), was the laser vibrometer which was used most extensively in the conduct of this experimental work. The reason for this, being its optimisation for 3D topographic measurements and system dynamic responses. Moreover one of the best points of this equipment was the head with variable magnification lenses which enabled optimal magnification to be used. The equipment could conduct characterisation of out of plane vibrations at frequencies of up to 25 MHz with picometer scale displacement through the use of laser Doppler vibration [117].

(a) (b)

Figure 4.4 ~ (a) The MSA 600 laser Doppler vibrometer equipment with the signal generating equipment set up below the stage (b) The MSA-100-3D Laser Vibrometer [117].

The MSA-100-3D laser vibrometer shown in Figure 4.4 (b) was also used in the laser Doppler vibrometer work. This vibrometer was optimised to conduct 3D vibration analysis.

4.2.2 Experimental work conducted through the use of laser vibrometer.

All the work conducted with laser vibrometers involved exciting PMUT devices with electric signals in different fluids and setup. For this reason various signal regimes were utilised depending on the scope of the individual test being conducted. The signals used for the experimental processes are briefly described in the following sections.

- **Periodic Chirp**
  This signal was used to conduct frequency response laser vibrometer experiments. The periodic chirp signal can be either a down chirp where the frequency reduces with time or an up chirp where the frequency increases with time as shown in Figure 4.5. During frequency sweeps the frequency response of the PMUT was monitored at each frequency step in order to determine the resonant frequency.

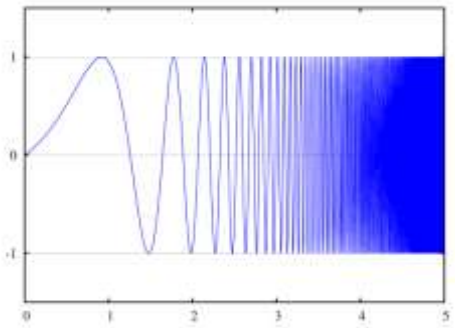

Figure 4.5 ~ The exponential chirp waveform showing how the frequency of a sinusoid increases with time [118].

- **Sine Excitation**
  Sine excitation signals were sinusoidal signals set at a particular frequency and amplitude. The sine excitation signal was utilised with the laser vibrometer to determine parameters such as the amplitude, velocity and acceleration. This signal type was also used in hydrophone acoustic experimentation to investigate ultrasonic power output from the PMUT.

- **Burst sine excitation**
  Burst sine excitation was the signal type utilised for both the time domain laser vibrometer characterisation work as well as the acoustic experimental work conducted. This signal involves transmitting specific frequencies at fixed time periods.

4.3 Experimental Procedure II ~ Laser diffraction experimental work for resonant frequency determination.

Laser beams are regularly used in the study of MEMS micro mirrors through processes known as laser fringing projections [119]. Laser fringe patterns are projected onto a screen through the scan of the MEMS micro-vibration mirror as shown in Figure 4.6.

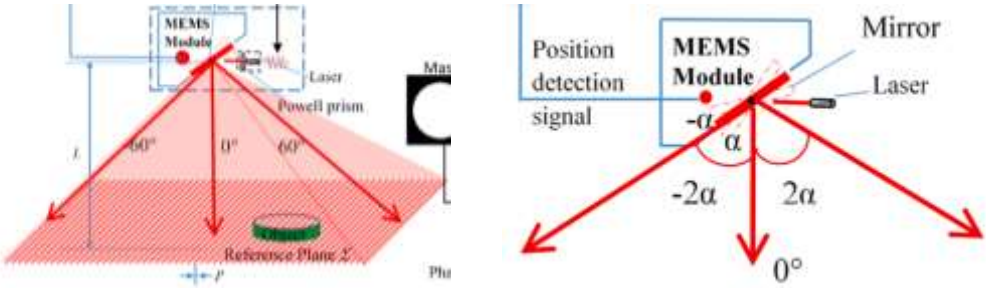

(a) (b)

Figure 4.6 ~ (a)Laser fringe pattern projection using MEMS micro-vibration mirror (b)Schematic diagram of the laser scanning [120].

If one refers to Figure 4.6 one may see that the larger the angle of movement of the micro vibration mirror the larger the scanning angle would be. Consequently the larger the magnitude of the scanning angle, the larger the surface area of the projected scan would be.

With respect to the project in hand it must be recalled that the PMUTs being designed in this project have an aluminium metal layer as the top layer which is meant to act as the upper electrode. This layer of aluminium is shiny and reflective to incident laser light thereby making the PMUT resemble a micro mirror in its optical physics characteristics. Therefore at the point of resonance, since the displacement of the membrane would be at its highest value, the projected surface area of the scan would be seen to increase in size showing the fringing. In the experimental processes conducted the projected image changed sharply as soon as the resonant point was reached making it easy to identify the resonant point. This made laser diffraction an important tool when used to detect resonant frequencies of PMUTs. High diameter PMUTs performed better with this method than smaller diameter ones.

Figure 4.7 (a) shows the setup for the laser diffraction experimentation with the laser beam being shown to the right of the photo. The collimated radiation from the laser beam is directed towards the PMUT and focused on the electrode. The beam hits the target electrode's aluminium surface after which it bounces off at an angle as shown in Figure 4.6 (b). Work was conducted in a dark lab as shown in Figure 4.7 (b) to enable the diffracted projected images to be observed better.

(a) (b) (c)

Figure 4.7 ~ Photo (a) shows a close up of the laser setup, with the laser diode on the right and the probes on the left (b) shows the collimated laser light shining on the device in darkened lab; (c) shows the reflected laser light with top image when device is off resonance and bottom with device at the point of resonance.

The laser used for this experimentation was a CPS532-Collimated Laser-Diode Pumped DPSS Laser Module with a 532 nm wavelength. It had a collimated 4.5 mw round beam, with an 11 mm diameter housing.

After impacting the target electrode surface the beam is reflected onto a white surface which acts as a screen. By referring to Figure 4.7 (c-top) one can see a photo of the projected area when the PMUT was not in resonance. Figure 4.7 (c-bottom) shows the much larger area with defined patterns covered by the PMUT when it was resonating.

4.4 Experimental Procedure III ~ Acoustic experimental work.

While laser beam experimentation enabled studies of PMUT dynamics to be conducted in detail it was through acoustic experimental work that it was possible to study the acoustic output from the PMUT devices. Acoustic experimentation complement the findings from the laser vibrometer work closing the loop between PMUT dynamics studied by the laser and acoustic output [121].

4.4.1 The hydrophone system.

High accuracy hydrophone systems were found to be very expensive and so extensive research was conducted to find the right probe which fitted the technical requirements and budget for this project. The probe selected had to operate over a wide bandwidth and be able to work in both transmission and receiving modes. Various different needle probes and hydrophones supplied by various potential supplier including “Precision Acoustics”, “Muller Probes”, “Neptune Sonar”, “Bruel and Kjaer” among others were reviewed.

Through extensive market research conducted with the various potential suppliers it was found that very few systems could deliver the required performance with one transducer and which fitted the project budget. The company selected to produce the equipment needed was "Benthowave Instrument Inc." from Canada. The selected hydrophone system had three main components as will be described below.

5 The BII-7001 hydrophone.

The BII-7001 hydrophone is shown in Figure 4.8. This hydrophone has low noise characteristics with a free voltage sensitivity of -202dBV/µPa±2dB at 1 kHz.

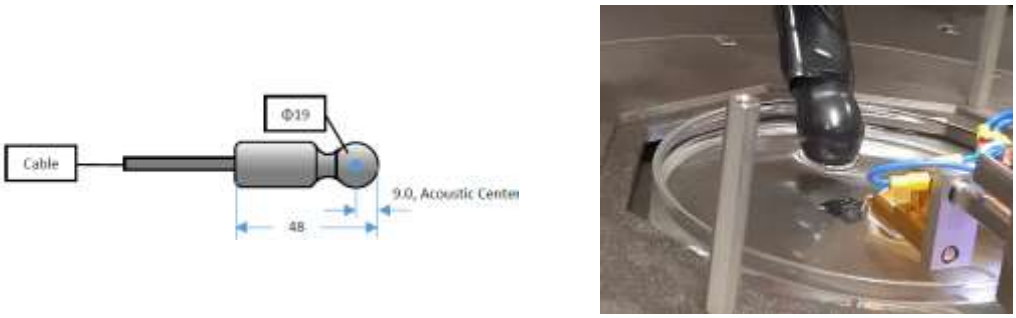

(a) (b)

Figure 4.8 ~ (a) Dimensions of the BII-7001 hydrophone including acoustic centre and (b) The BII-7001 hydrophone deployed in isopropanol coupling fluid [122].

Further views of the BII-7001 in the deployed state using a 3rd arm purposely procured can be seen in Figure 4.16. The BII-7001 has an operating frequency between 1 and 200 kHz in water and 1 to 5 kHz in air. The free field voltage sensitivity vs frequency is shown in Figure 4.9.

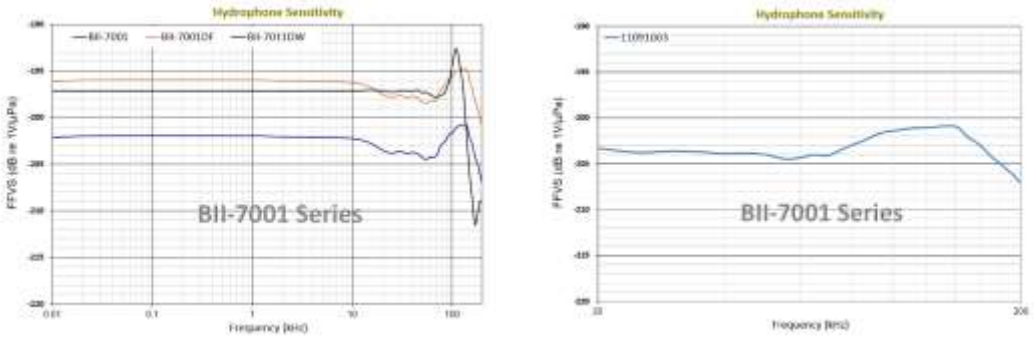

Figure 4.9 ~ Graphs showing the Free Voltage Sensitivity [122].

When working as a transmitter the hydrophone can take a maximum drive voltage of 300 V_{p-p} with a maximum pulse length of 100 ms at that voltage. The Transmitting Voltage Response curve is shown in Figure 4.10. For this hydrophone, the resonant frequency f_s was 110 kHz.

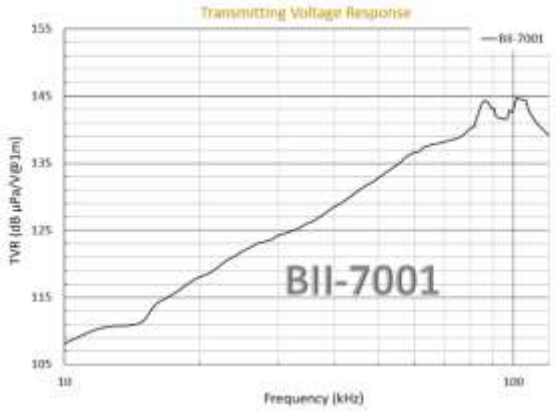

Figure 4.10 ~ Transmitting Voltage Response (TVR) curve [122].

The directivity patterns shown in Figure 4.11 were also crucial in selecting the hydrophone equipment. As can be seen the BII 7001 hydrophone is quite tolerant in directivity and is capable of picking or transmitting signals over a wide angle when signals are approaching from the forward direction.

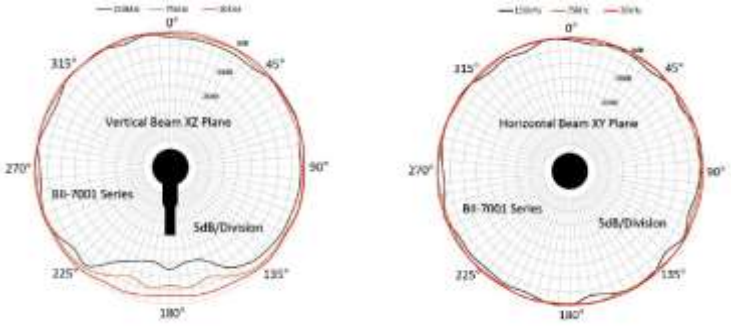

Figure 4.11 ~ Directivity patterns for hydrophone's vertical and horizontal beam planes [122].

6 BII-5023- Power Amplifier

The BII-5023 Power amplifier was selected to drive the BII-7001 when operating as an ultrasonic projector. It can be used in two configurations as shown in Figure 4.12. In this case the hydrophone was used directly without impedance matching since only low intensity sound waves needed to be produced to replicate the ultrasonic radiation which would be incident into a receiving device after transmission through concrete.

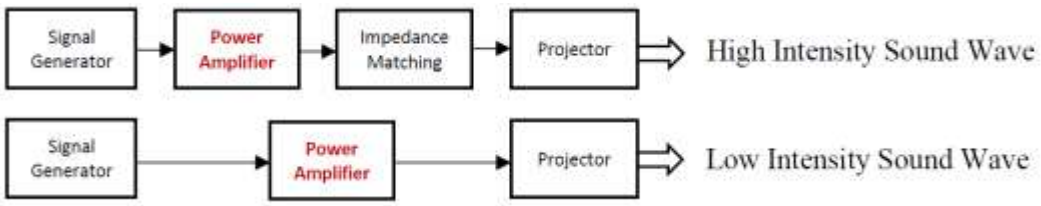

Figure 4.12 ~ System configuration for use of power amplifier stage [123].

The power amplifier operated on the frequency gain curves as per Figure 4.13 providing a gain of 42 dB in the operational range. It is also important to keep in mind that a maximum driving voltage of 300 V_{p-p} was needed to operate the hydrophone as a projector. A power amplifier was therefore required to raise the voltage of the signal received from the signal generator to the required high voltage.

Figure 4.13 ~ The frequency response of the BII-5023 Power Amplifier [123].

Due to the high voltage output the power amplifier was provided in a metal housing as shown in Figure 4.14 with all connections being set up via coaxial cables with a proper earthing point set up.

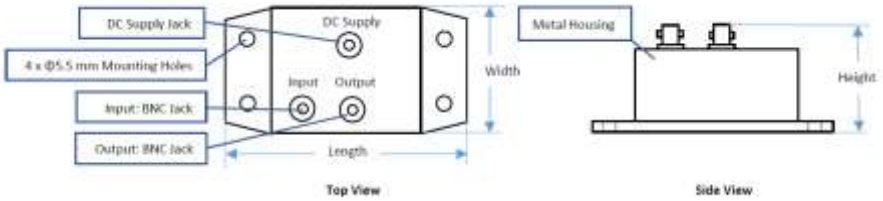

Figure 4.14 ~ Physical drawing of the metal enclosure [123].

7 BII-1064- Low Power Low Noise Preamplifiers

Incoming signals from the hydrophone when receiving ultrasonic signals emanating from the various PMUTs was envisaged to be of a low power. A low noise preamplifier was therefore required to suitably amplify the incoming signals in a usable way.

For this task the BII-1064 Low Power Preamplifier was selected. The -3dB bandwidth ranges for the power preamplifier were:

- 600 kHz at 60dB
- 900 kHz at 40dB
- 1.3 MHz at 20dB

A DC power supply to provide the required power to the preamplifier was also set up.

4.4.2 The procedure for the acoustic experimental processes.

Acoustic experimental processes are much more difficult to conduct than the counterpart optical experimental processes. For a start, ultrasonic radiation, is neither visible (unlike the laser radiation used for this project) nor audible. Sound waves have a much longer wavelength when compared to laser light. This meant that acoustic waves are much more prone to diffraction and it is also difficult to predict interference and reflection effects. The sound waves can cause constructive or destructive interference when interacting with each other which has an effect on the amplitudes measured.

Due to these issues each acoustic measurement shot needed to be set up in detail to ensure the set up details including needle positions which can interfere with the incident acoustic radiation. Many measurements were carried out however only the salient ones will be reproduced in this dissertation.

When the hydrophone was operated in transmission mode the gradient of the Transmitting Voltage Curve (TVR) shown in Figure 4.10 was considered such that as the frequency was increased from 10 to 80 kHz the voltage to the power amplifier has to be decreased to enable the hydrophone's power output to be kept constant notwithstanding the frequency. It was noticed that when operating the hydrophone at high voltage at low frequency, instabilities in the current input were noticed which were thought to result in fluctuations of sonic power output. This problem was observed to occur at frequencies of less than 60 kHz.

Unless otherwise indicated the pressure measurement point for the results mentioned below was taken at a point 4 cm away from the test devices at point 38 as indicated in Figure 3.32. The deployed device can be seen in Figure 4.8 (b) at the 3 cm point, but for the actual experimentation the hydrophone's position was further away from die to the 4 cm point.

It is important to stress that the scope of the hydrophone experimentation was not to have high accuracy absolute measurements. The acoustic experimentation was conducted to confirm minimum power outputs from the devices and also to act as a comparative process in which the output of different devices could be compared.

4.5 Test Equipment ~ Probe station and general setup of equipment

The experimental setup used to conduct laser diffraction and acoustic testing is shown in Figure 4.15. At the centre was of the experimental setup was the probe station which was required to probe the dies since these were not wire bonded. The dies were placed in a petri dish to enable the fluidic environment to be contained. Various microscopes could be used to observe and position the dies as well as electronic equipment through which to conduct the testing.

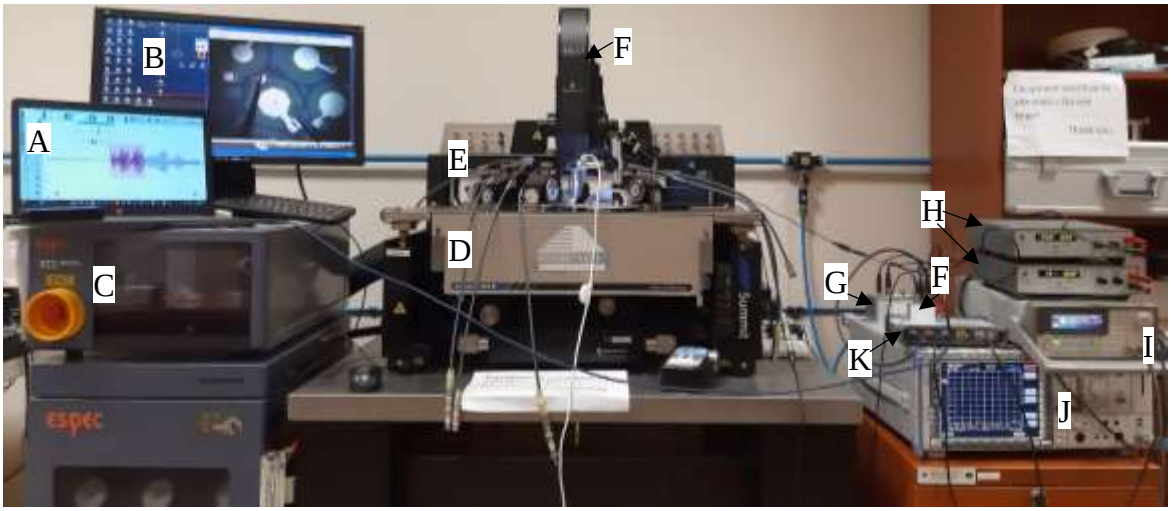

Figure 4.15 ~ Photo showing the setup of the test rig used to conduct acoustic, laser and optical characterisation.

Figure 4.15 presents the setup of the test rig. Through this test rig both laser diffraction resonant frequency detection and acoustic characterisation were carried out.

The components forming the test setup are marked with letters A to K

A	Display and processing for Pico Scope (item K below)
B	Display from microscope.
C	ESPEC ETC-200L control
D	Probe station – Cascade Microtech Summit 11000M
E	Test platform with details shown in Figure 4.16 (a).
F	Hydrophone Low Power Low Noise Preamplifier BII-1064
G	Hydrophone Power Amplifier BII-5023/6
H	Power Supplies Delta Elektronika ES030-5
I	Function Generator Agilent 33250A
J	Rohd and Schwarz FSU Spectrum Analyser
K	Picoscope 5000 Series

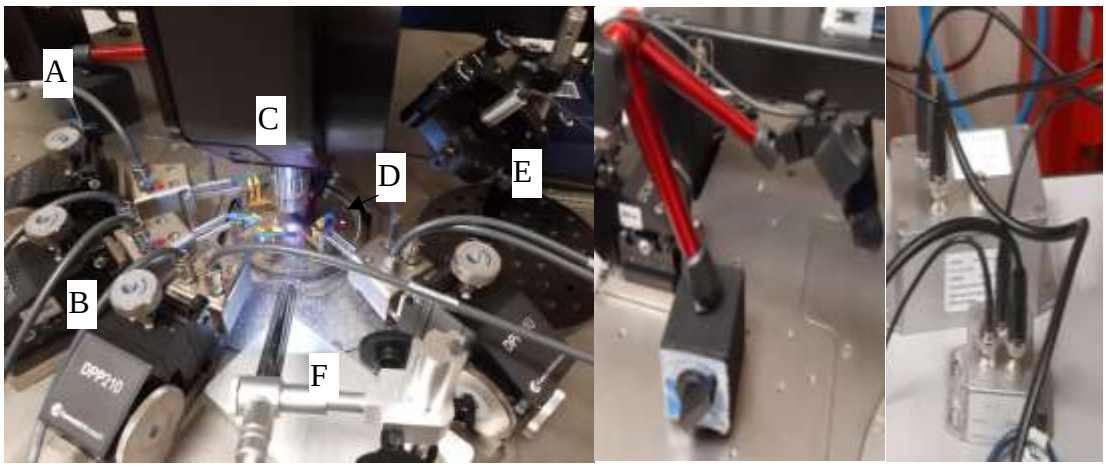

(a) (b) (c)

Figure 4.16 ~ (a) shows the details of the equipment on the test platform; (b) shows the details of the hydrophone arm and attachment; (c) shows the details of the hydrophone's power amplifier used for ultrasonic transmission at the rear and the Low power Amplifier used for ultrasonic reception at the front.

The equipment shown on the test platform is presented in close up view in Figure 4.16 (a) with the details being as follows:

A	Hydrophone attachment
B	Four DC probe positioners with magnetic mounting - DPP210
C	Main microscope
D	Petri dish to contain ICs in liquid environment.
E	532 nm laser for resonant frequency determination.
F	Lateral microscope

Figure 4.17 shows further views of electronic and fluid handling equipment.

(a) (b)

Figure 4.17 ~ Photos showing (a) Close up of the hydrophone control system (b) Coupling fluids and fluid handling systems.

4.6 The Experimental Results ~ optical and acoustic methods.

To make it easier for the reader to correlate the results to particular devices the results from the various experimental processes are collated together in this section. Hence the reader will be able to see the results of the various tests conducted, grouped together by device. Such would make it easier for the reader to follow the extensive and varied characterisation and testing conducted.

4.6.1 Device 10 ~ Circular PMUT with a Trench Diameter of 350 µm

The 350 µm device was the smallest device which was modelled in this experimental series. The scope of adding this device size to the prototype IC was to:

- Contribute to the experimental data through which the PMUT diameter vs resonant frequency of PMUTs in liquid coupling fluid was determined.
- Study the reliability and performance of a device which was capable of transmitting ultrasonic radiation at resonant frequencies above 400 kHz in liquids. In an RC SHM system such a device would be useful in detection of surface changes close to the device itself. Hence the integration of such a device into a system would add capabilities such as studying of SHM issues such as cracks, carbonation, rebar corrosion and other issues through ultrasonic methods.
- Calibrate the finite element modelling by aiding in the determination of the Silicon's young's modulus and the Rayleigh Beta coefficient.

A frontal micrograph of Device 10 is shown in Figure 4.18. The round electrode is shown in white colour with the piezoelectric layer being shown in green.

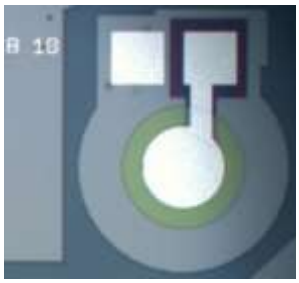

Figure 4.18 ~ Frontal micrograph of Device 10 – 350 µm diameter PMUT.

The specific dimensions for Device 10 are shown in Table 4.1. 66% electrode radial coverage was selected for optimal performance as calculated through finite element modelling.

Table 4.1 ~ Geometric data for Device 10

Nominal Trench Diameter [µm]	Padmetal Radial Cover [%]	Padmetal Diameter [µm]	Padoxide Diameter [µm]	Pzfilm Diameter [µm]	Specific Design Features
350	66	231	215	350	Circular PMUT

4.6.1.1 Laser Vibrometer testing of Device 10

Coupling Fluid: Isopropanol ~ Cavity Fluid: Air

The first stage of the test process was to excite the device with a periodic chirp signal to determine the resonant frequency of the device in isopropanol coupling fluid and air filled cavity. The velocity, displacement and acceleration response curves can be seen Figure 4.19.

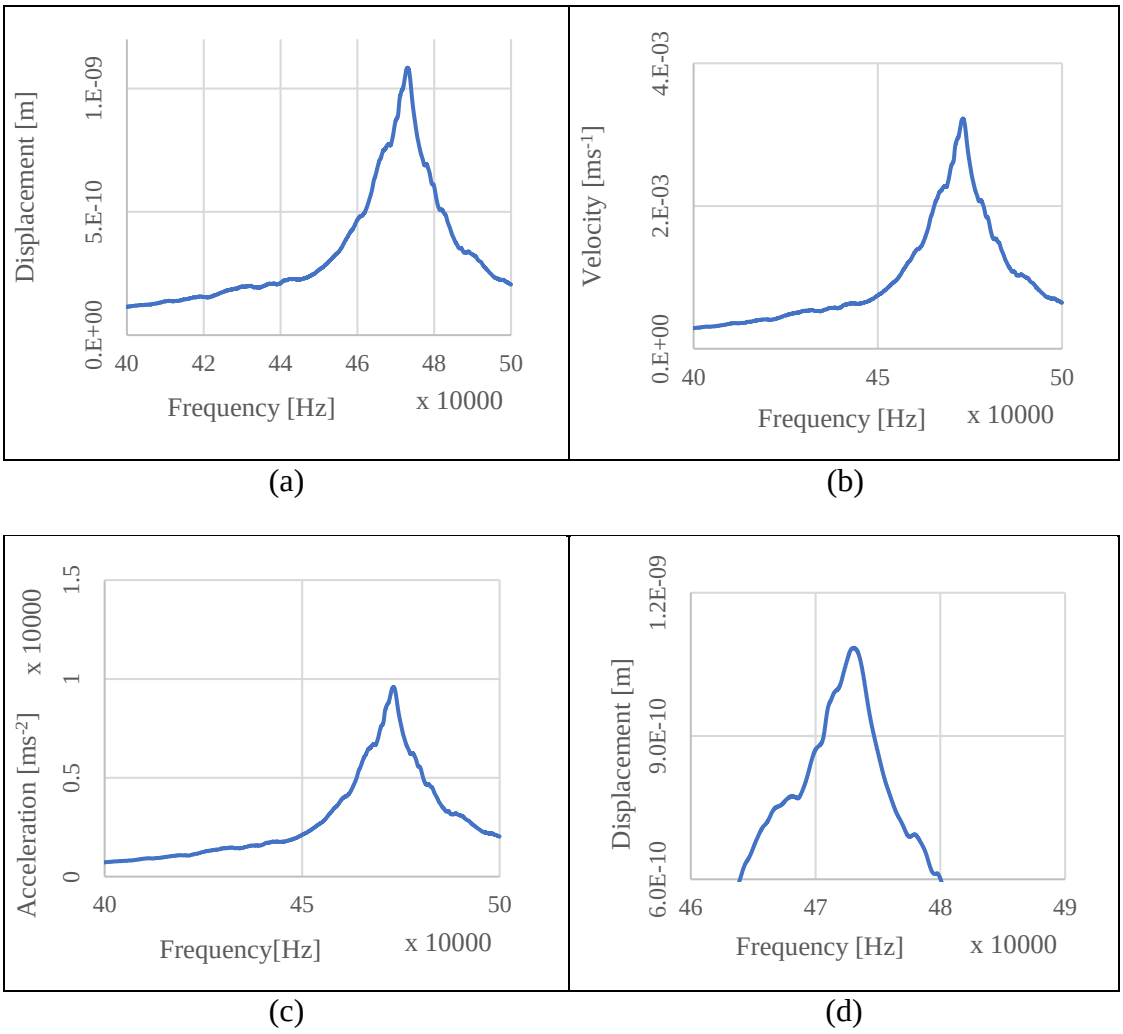

Figure 4.19 ~ Periodic Chirp frequency between 0 and 500 kHz with (a) Displacement, (b) Velocity and (c) acceleration values vs frequency for Device 10 in isopropanol coupling fluid and air filled cavity. (d) shows displacement vs frequency at a frequency between 460,000 Hz and 480,000 Hz. Values in these graphs have been adjusted for the fluid's refractive index.

One modes of oscillation was identified by Laser Vibrometer during Periodic Chirp excitation at the resonant frequency. The device was then sine excited at a voltage of 14 V_{p-p} as shown in Figure 4.20.

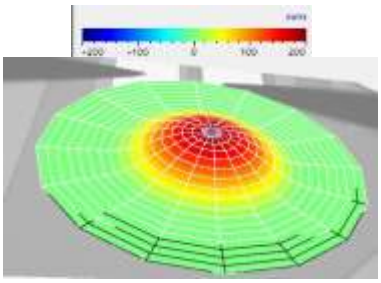

Figure 4.20 ~ Displacement of Device 10 excited with a 14 V_{p-p} sine wave signal at a frequency of 472.97 kHz. Device in an isopropanol coupling fluid & having an air filled cavity. Values shown are actual readings directly from vibrometer and not normalised with the fluid's refractive index.

The experimental values achieved for the diaphragm midpoint displacement, velocity and acceleration at an excitation sine wave with a voltage of 14 V_{p-p} are shown in Table 4.2.

Table 4.2 ~ Results of sine wave excitation with a sine wave signal having a 14 V_{p-p} amplitude for isopropanol coupling fluid & air filled cavity. Device operating at a resonant frequency of 472.97 kHz.

Monitored Parameter	**Values measured by vibrometer**	**Values normalised by the coupling liquid's refractive index†1.**
Displacement (Maximum)	183.6 nm	134.01 nm
Velocity (Maximum)	0.5455 m/s	0.3982 m/s
Acceleration (Maximum)	1621.11 km/s^2	1183.29 km/s^2

Note †1: Using ratio Isopropanol/Air ~ 1.37

4.6.2 Device 4 ~ Circular PMUT with a Trench Diameter of 550 µm

The 550 µm cavity diameter Device 4 was introduced in the experimental process for the following reasons:

- As part of the series to establish an equation describing the resonant frequency with respect to the device diameter for a device deployed in isopropanol.
- As part of a series of three devices with same diameter but different electrode radial cover, to study how the electrode radial cover effects the device's operational dynamics.
- To calibrate the finite element modelling by aiding in the determination of the Silicon's young's modulus and the Rayleigh Beta coefficient.

The device frontal micrograph is shown in Figure 4.21. The circular 66% radial cover electrode is visible in the middle of the device with the green piezoelectric layer showing the full extent of the diaphragm.

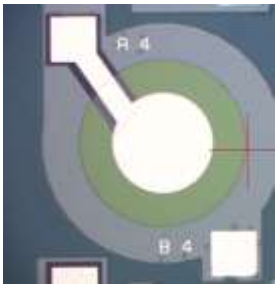

Figure 4.21 ~ Frontal device micrograph of Device 4, a 550 μm diameter circular PMUT.

The dimensions and parameters of Device 4 are shown in Table 4.3. The most important point is that Device 4 had a 66% (of the diaphragm) radial padmetal cover.

Table 4.3 ~ Geometric data for Device 4

Nominal Trench Diameter [μm]	Padmetal Cover [%]	Padmetal Diameter [μm]	Padoxide Diameter [μm]	Pzfilm Diameter [μm]	Special Design Features
550	66	363	314	550	Circular PMUT

4.6.2.1 Laser Vibrometer Testing of Device 4

Coupling Fluid: Isopropanol ~ Cavity Fluid: Air

Testing of Device 4 in an isopropanol coupling fluid and air filled cavity was conducted through laser vibrometer. The first stage was to proceed with device excitation with a scanning Periodic Chirp signal in order to determine the test device's resonant frequency.

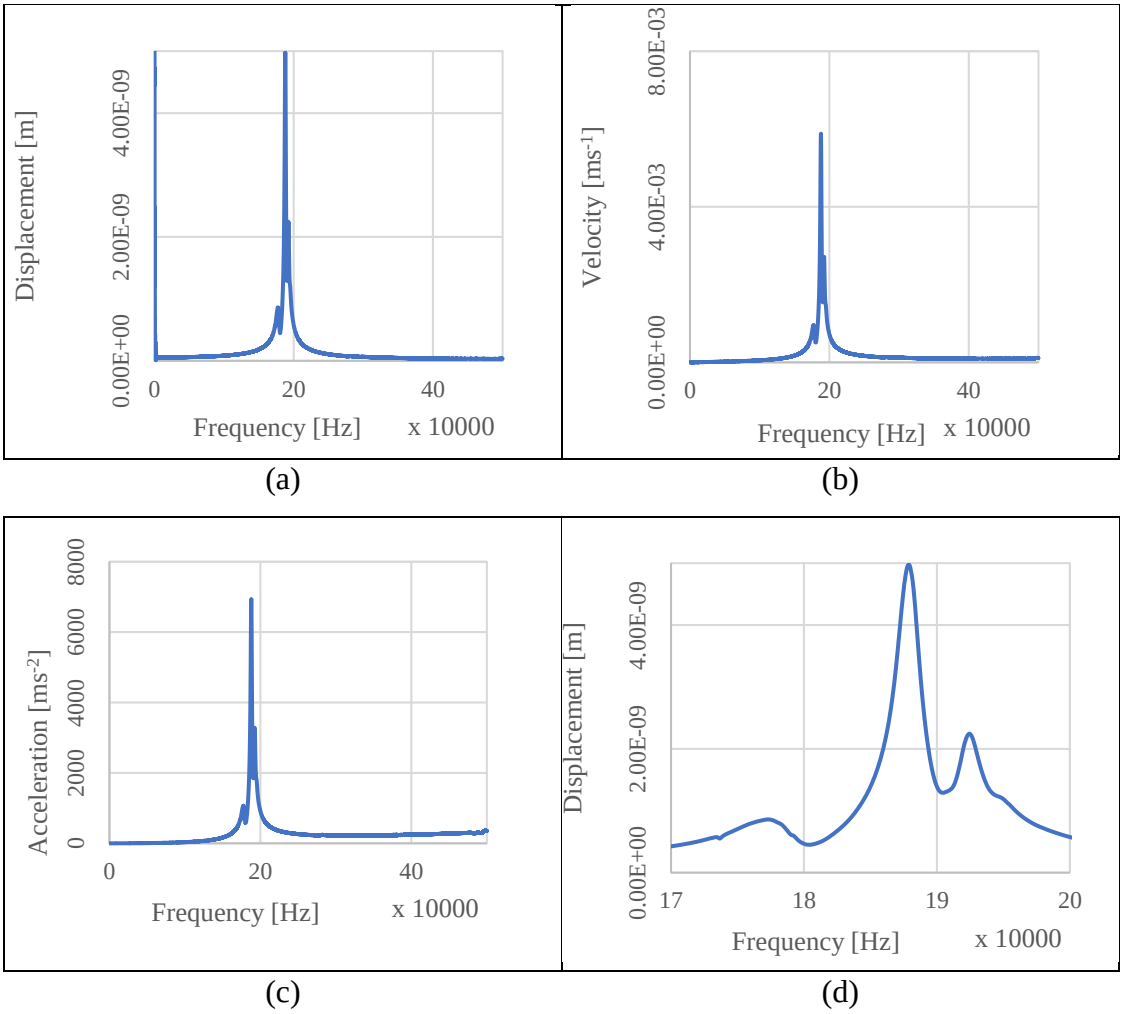

Figure 4.22 ~ Periodic Chirp frequency between 0 and 500 kHz with (a) Displacement, (b) Velocity and (c) acceleration values vs frequency for Device 16 in isopropanol coupling fluid and air filled cavity. (d) shows displacement vs frequency at a frequency between 100 kHz and 300 kHz. Device deployed in an isopropanol coupling fluid and having an air filled cavity.

Only one mode of oscillation was identified by the laser vibrometer during the Periodic Chirp excitation at which frequency the device was subsequently sine wave excited. Sine wave excitation was conducted at a voltage of 14 $V_{p\text{-}p}$ with the device still in an isopropanol coupling fluid & air filled cavity. The oscillation is shown in Figure 4.23.

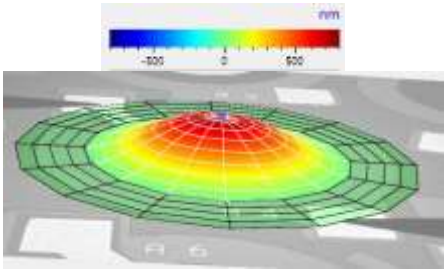

Figure 4.23 ~ Displacement of Device 4 when excited with a 14 $V_{p\text{-}p}$ sine wave signal at a frequency of 187.66 kHz. Device in an isopropanol coupling fluid & having an air filled cavity. Values shown are actual readings directly from vibrometer and not normalised with the fluid's refractive index.

The results achieved from the sine wave excitation at the resonant frequency are shown in Table 4.4.

Table 4.4- Results of Device excitation with sine wave signal at 14 V_{p-p} amplitude with device in an isopropanol coupling fluid and having an air filled cavity.

Monitored Parameter	Values measured by vibrometer	Values normalised by the coupling liquid's refractive index†1.
Displacement (Maximum)	727.1 nm	530.73 nm
Velocity (Maximum)	0.8573 m/s	0.626 m/s
Acceleration (Maximum)	1.011 Mm/s^2	0.738 Mm/s^2

Note †1: Using ratio Isopropanol/Air ~ 1.37

4.6.3 Device 14 ~ Circular PMUT with a Trench Diameter of 550 µm

Device 14 is the second of the 550 µm cavity diameter PMUT set and is shown in Figure 4.24. This device had a metal electrode with a 90% radial cover when compared to the diaphragm radius. This can be clearly seen in the figure where the metal layer nearly covers all the piezoelectric layer which is shown in green in the frontal micrograph.

This device was included in the experimental process to cover a number of functions namely:

- To corroborate the results, especially the resonant frequency, of Device 4.
- To act as part of the series studying the effect of electrode radial coverage percentage value, on the device's operation.
- To calibrate the finite element models by aiding in the determination of the doped silicon young's modulus and the determination of the Rayleigh Beta coefficient.

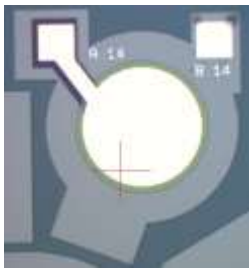

Figure 4.24 ~ Frontal device micrograph of Device 14 – 550 µm diameter PMUT.

Table 4.5 presents the salient parametric details for Device 14. The most salient difference between Device 14 and Device 4 was the electrode metal radial cover percentage which in this case was 90%.

Table 4.5 ~ Geometric data for Device 14

Nominal Trench Diameter [µm]	Padmetal Cover [%]	Padmetal Diameter [µm]	Padoxide Diameter [µm]	Pzfilm Diameter [µm]	Design Features
550	90	495	479	550	Circular PMUT

4.6.3.1 Laser Vibrometer Characterisation of Device 14

Coupling Fluid: Isopropanol ~ Cavity Fluid: Air

Laser vibrometer testing of Device 14 in an Isopropanol coupling fluid and air filled cavity was conducted. Experimentation commenced with the device being electrically excited via a Periodic Chirp signal. The PMUT's dynamic results of the periodic chirp excitation are shown in Figure 4.25.

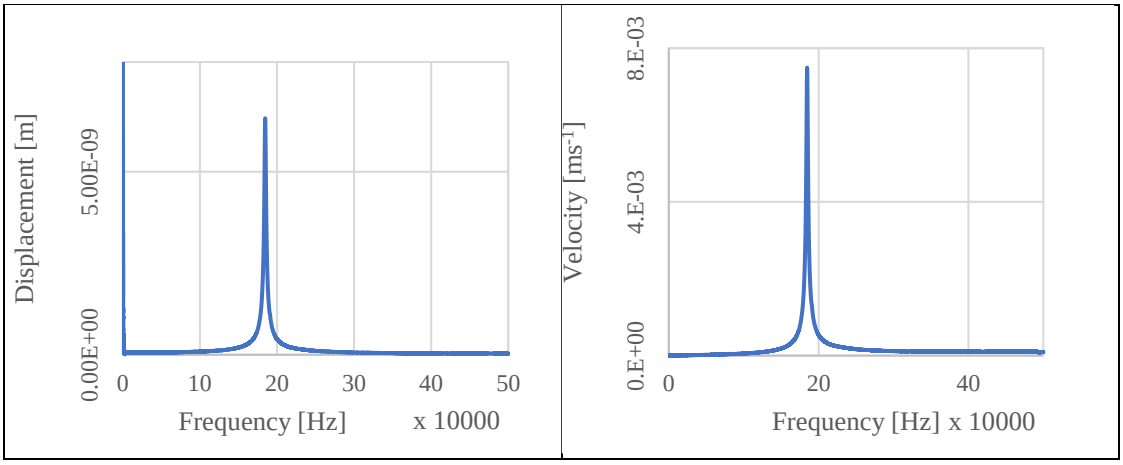

Figure 4.25 ~ Periodic Chirp frequency between 0 and 500 kHz with (a) Displacement, (b) Velocity and (c) acceleration values vs frequency for Device 14 in isopropanol coupling fluid and having an air filled cavity. (d) shows displacement vs frequency at a frequency between 180,000 Hz and 190,000 Hz.

Experimentation showed that there was only one mode of oscillation identified by the Laser Vibrometer during Periodic Chirp excitation at a frequency of 184.53 kHz. The device was excited with a sine wave excitation signal at a voltage of 14 $V_{p\text{-}p}$. The mode of vibration detected by the laser vibrometer is shown in Figure 4.26.

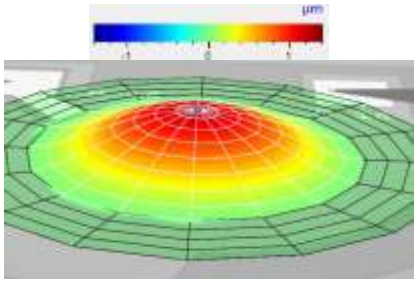

Figure 4.26 ~ Displacement of Device 14 excited with a 14 $V_{p\text{-}p}$ sine wave signal at a frequency of 184.53 kHz. Device in an isopropanol coupling fluid & with an air filled cavity. Values shown are actual readings directly from vibrometer and not normalised with the fluid's refractive index.

The parameters measured by the laser vibrometer are shown in Table 4.6.

Table 4.6 ~ Results of sine wave excitation at 14 $V_{p\text{-}p}$ amplitude with device in isopropanol coupling and air filled cavity.

Monitored Parameter	**Value measured by vibrometer**	**Values normalised by the coupling liquid's refractive index[†1].**
Displacement (Maximum)	1.201µm	0.8766 µm
Velocity (Maximum)	1.393 m/s	1.0168 m/s
Acceleration (Maximum)	1.615 Mm/s^2	1.1788 Mm/s^2

Note †1: Using ratio Isopropanol/Air ~ 1.37

4.6.4 Device 16 ~ Circular PMUT with a Trench Diameter of 550 µm

This device was the last of the trio of devices having a cavity diameter of 550 µm included together as a test series to study the effect of the electrode radial cover. The difference in design between this device and the other two 550 µm diameter devices discussed before (Device 4 and Device 14) was in the electrode radial cover percentage.

The device frontal micrograph is shown in Figure 4.27.

Figure 4.27 ~ Frontal device micrograph of Device 16 – 550 µm diameter PMUT.

The specific design parameters for Device 16 are tabulated in Table 4.7. As can also be seen in Figure 4.27, the electrode diameter in this particular device was reduced to cover

40% of the diaphragm's diameter. The diaphragm's diameter can be easily discerned through the green colour of the piezoelectric layer which covers the whole diaphragm. The difference in radial cover between Device 16 and Device 14 can easily be seen.

Table 4.7 ~ Geometric data for Device 16

Nominal Trench Diameter [µm]	Padmetal Cover [%]	Padmetal Diameter [µm]	Padoxide Diameter [µm]	Pzfilm Diameter [µm]	Special Design Features
550	40	220	204	550	Circular PMUT

4.6.4.1 Laser Vibrometer characterisation of Device 16

Coupling Fluid: Isopropanol ~ Cavity Fluid: Air

Testing of Device 16 in an Isopropanol environment and air cavity via device excitation was conducted with a Periodic Chirp signal. The results are shown in Figure 4.28.

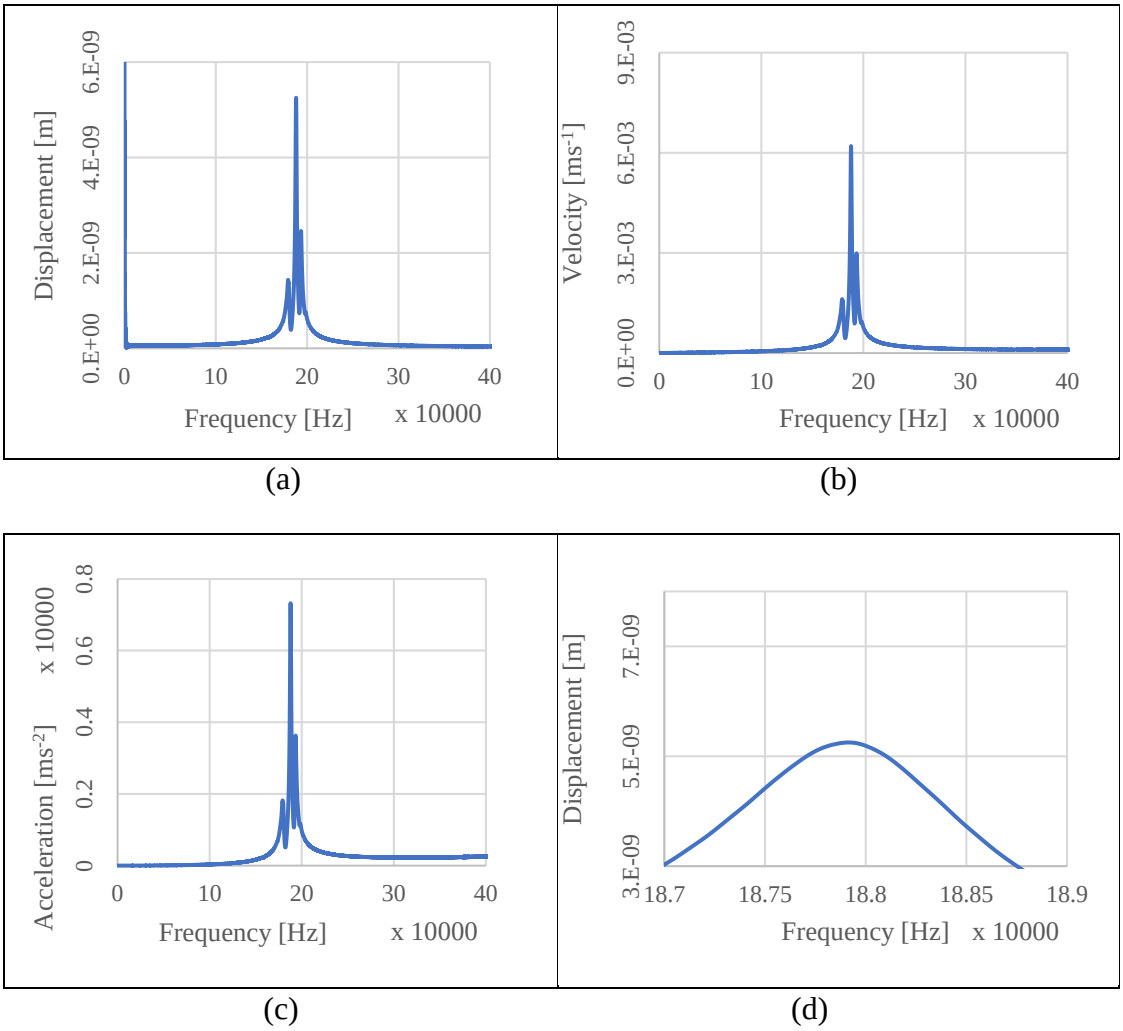

Figure 4.28 ~ Periodic Chirp frequency between 0 and 400 kHz with (a) displacement, (b) velocity and (c) acceleration values vs frequency for Device 16 in isopropanol coupling fluid and air filled cavity. (d) shows displacement vs frequency at a frequency between 187,000Hz and 189,000Hz.

In the frequency range scanned between 39 Hz and 500 kHz one predominant mode of oscillation was detected at a resonant frequency of 187.8 kHz. The device was subsequently excited with a sine wave signal having an amplitude of 14 V_{p-p} and the result is shown in Figure 4.29 showing the single mode of oscillation which was detected.

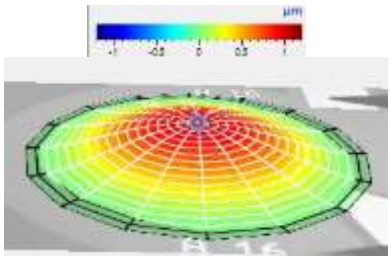

Figure 4.29 ~ Displacement of Device 16 excited with a 14 V_{p-p} sine wave signal at a frequency of 187.81 kHz. Device in an isopropanol coupling fluid & having an air filled cavity. Values shown are actual readings directly from vibrometer and not normalised with the fluid's refractive index.

The results achieved from the sine excitation at 14 V_{p-p} are shown in Table 4.8.

Table 4.8 ~ Results of Device excitation with Sine wave signal at 14 V_{p-p} amplitude with device in isopropanol coupling fluid and air cavity fluid.

Monitored Parameter	**Value measured by vibrometer**	**Values normalised by the coupling liquid's refractive index**[†1]
Displacement (Maximum)	1.023 µm	0.747 µm
Velocity (Maximum)	1.208 m/s	0.881 m/s
Acceleration (Maximum)	1.426×10^6 m/s^2	1.044×10^6 m/s^2

Note †1: Using ratio Isopropanol/Air ~ 1.37

4.6.5 Device 44 ~ Circular PMUT with a Trench Diameter of 600 µm

The 600 µm cavity diameter device was produced in the experimental test series for the following reasons namely to:

- act as part of the series set up to establish the relationship between PMUT diameter and resonant frequency.
- be used as a control device for other devices having special features which need to be evaluated, such as Device 45 covered in section 4.6.6.
- calibrate the finite element modelling by being part of the series determining the Young's Modulus of doped silicon as well as its Rayleigh Beta coefficient.

A frontal micrograph of the device is shown in Figure 4.30.

Figure 4.30 ~ Frontal device micrograph of Device 44 a 600µm diameter PMUT.

Parametric details are shown in Table 4.9, which shows the basic parameters for this device such as radial electrode coverage of 66%.

Table 4.9 ~ Geometric data for Device 44

Nominal Trench Diameter [µm]	Padmetal Cover [%]	Padmetal Diameter [µm]	Padoxide Diameter [µm]	Pzfilm Diameter [µm]	Special Design Features
600	66	396	380	600	Circular PMUT

4.6.5.1 Laser Vibrometer characterisation of Device 44

4.6.5.2 Coupling Fluid: Isopropanol ~ Cavity Fluid: Air

The next step in the experimental process was the testing of Device 44 in an isopropanol coupling fluid and having an air filled cavity through the application of a Periodic Chirp signal. This was conducted to establish the resonant frequency, with the device's dynamic response being shown in Figure 4.31.

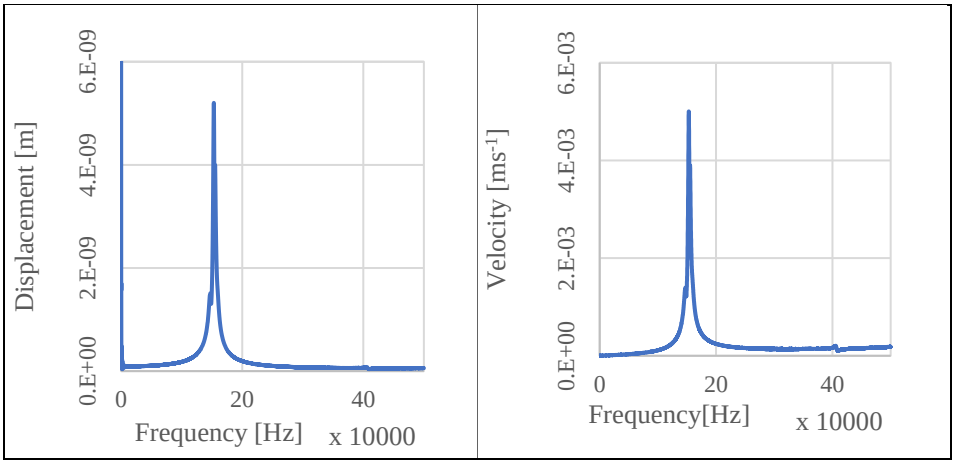

(a) (b)

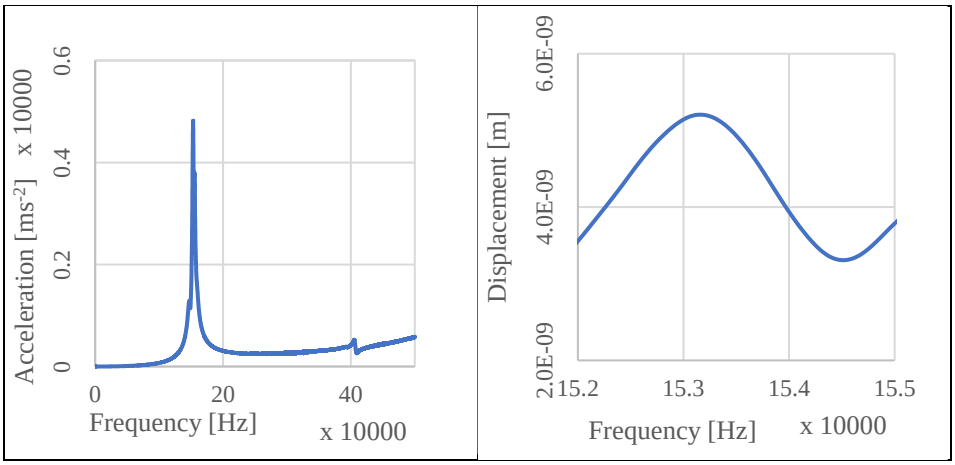

(c) (d)

Figure 4.31~ Periodic Chirp frequency between 0 and 500 kHz with (a) Displacement, (b) Velocity and (c) acceleration values vs frequency for Device 44 in isopropanol coupling fluid and air filled cavity. (d) shows displacement vs frequency at a frequency between 152,000Hz and 155,000Hz.

Two modes of oscillation identified were identified by the Laser Vibrometer during Periodic Chirp excitation as shown in Figure 4.32.

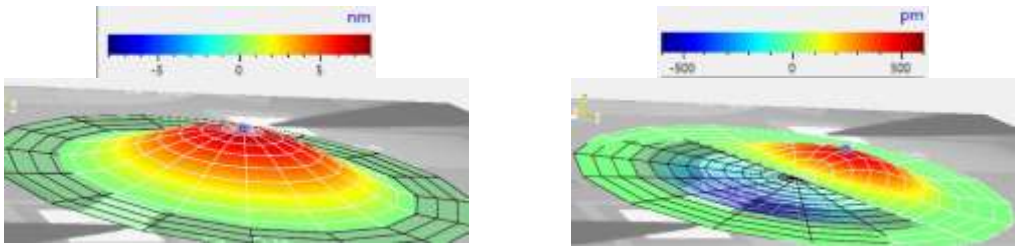

(a) (b)

Figure 4.32 ~ Displacement of Device 44 excited with a periodic chirp signal at a frequency of (a)153.12 kHz (b)406.48 kHz. Device in isopropanol coupling fluid & having an air filled cavity. Values shown are actual readings directly from vibrometer and not normalised with the fluid's refractive index.

The device was excited at its main mode of vibration through sine wave excitation via a signal at 14 $V_{p\text{-}p}$ amplitude in an isopropanol surrounding environment and air filled cavity as shown in Figure 4.33.

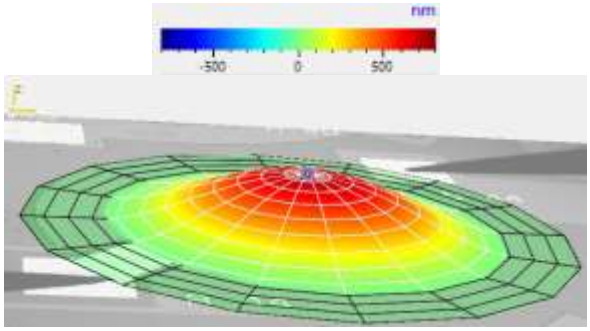

Figure 4.33 ~ Displacement of Device 44 excited with a 14$V_{p\text{-}p}$ sine wave signal at a frequency of 153.12 kHz. Device in an isopropanol coupling fluid & having an air filled cavity. Values shown are actual readings directly from vibrometer and not normalised with the fluid's refractive index.

The results achieved from the sine excitation process are tabulated in Table 4.10.

Table 4.10 ~ Results of Device 44 dynamic response when excited with a Sine wave signal at 14 $V_{p\text{-}p}$ amplitude with device in isopropanol coupling fluid & having air filled cavity.

Monitored Parameter	**Value measured by vibrometer**	**Values normalised by the coupling liquid's refractive index**[†1]
Displacement (Maximum)	710.2 nm	518.39 nm
Velocity (Maximum)	0.6833 m/s	0.4987 m/s
Acceleration (Maximum)	657.4 km/s^2	479.85 km/s^2

Note †1: Using ratio Isopropanol/Air ~ 1.37

4.6.6 Device 45 ~ Circular PMUT with special electrode design- Trench Diameter 600 µm

This novel device had a special electrode design as shown in Figure 4.34. This combined three basic electrode shapes at 33%, 47% and 66% radial coverage. The specific geometry was established through the finite element process discussed in Chapter 3. This device was placed in the test series to study the effect which the electrode shape would have on the device kinematics and performance.

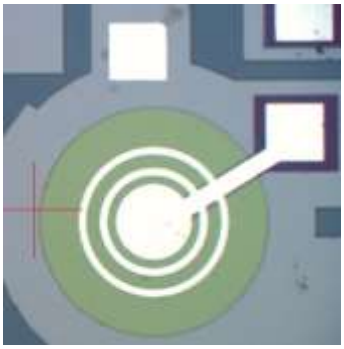

Figure 4.34 ~ Frontal device micrograph of Device 45 – 600 µm diameter PMUT with special electrode design.

The design parameters for Device 45 are shown in Table 4.11.

Table 4.11 ~ Geometric data for Device 45

Nominal Trench Diameter [µm]	Padmetal Cover [%]	Padmetal Diameter [µm]	Padoxide Diameter [µm]	Pzfilm Diameter [µm]	Special Design Features
600	33	198	182	600	Circular PMUT with a triple electrode design approach.

4.6.6.1 Laser Vibrometer characterisation of Device 45

Coupling Fluid: Isopropanol ~ Cavity Fluid: Air

Device 45 was tested in an isopropyl coupling fluid and air filled cavity with the device being excited through a Periodic Chirp signal. The PMUT's dynamic result are shown in Figure 4.35.

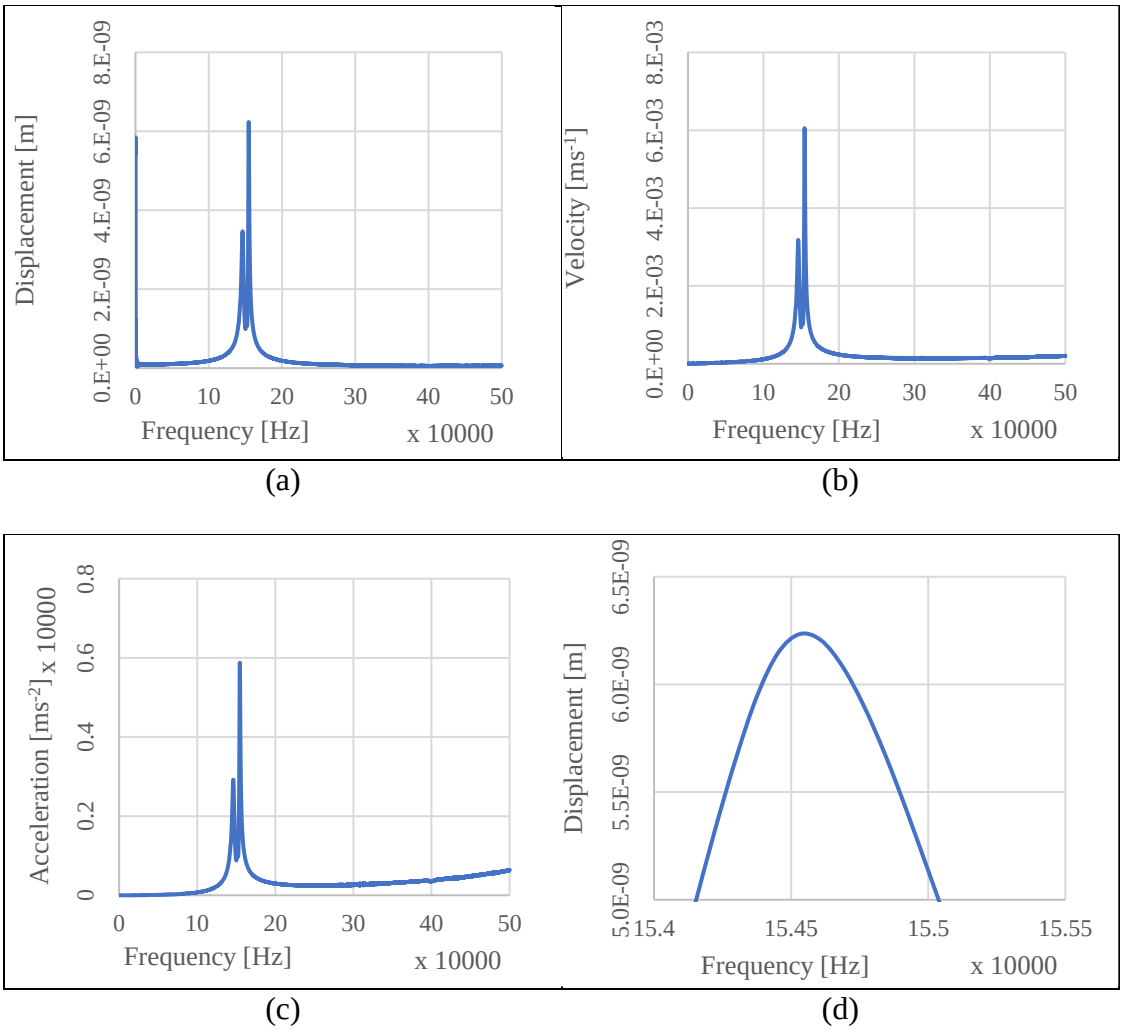

Figure 4.35- Periodic Chirp frequency between 0 and 500 kHz with (a) Displacement, (b) Velocity and (c) acceleration values vs frequency for Device 16 in isopropanol coupling fluid and air filled cavity, and (d) shows displacement vs frequency at a frequency between 154,000 Hz and 156,000 Hz.

Two resonant points were identified by the laser vibrometer during Periodic Chirp excitation with the principle one being at 146.09 kHz and the other being 154.53 kHz. These points are shown in Figure 4.36.

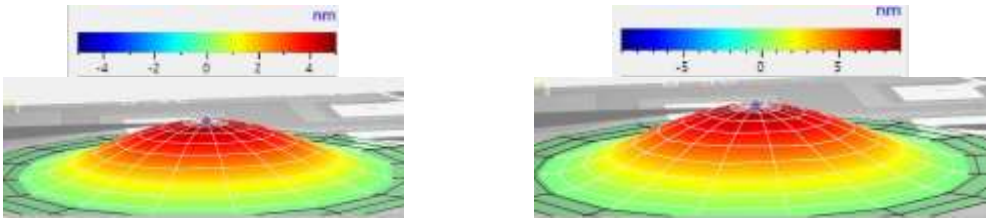

(a) (b)

Figure 4.36 ~ Displacement of Device 45 excited with a periodic chirp signal at a frequency of (a)146.09 kHz (b)154.53 kHz. Devices deployed in an isopropanol coupling fluid & having an air filled cavity. Values shown are actual readings directly from vibrometer and not normalised with the fluid's refractive index.

To review its performance dynamics the device was then excited at the established resonant frequency with a sine wave signal at 14 $V_{p\text{-}p}$ amplitude in an isopropanol coupling fluid and having an air filled cavity.

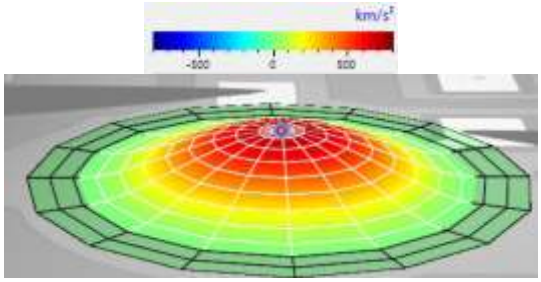

Figure 4.37 ~ Acceleration of points on device 45 excited with a 14$V_{p\text{-}p}$ sine wave signal at a frequency of 154.53 kHz in an isopropanol coupling fluid & having an air filled cavity. Values shown are actual readings directly from vibrometer and not normalised with fluid's refractive index.

The parametric data achieved from the sine wave excitation is shown in Table 4.12.

Table 4.12 ~ Results of Device excitation with Sine wave signal at 14 $V_{p\text{-}p}$ amplitude with device in isopropanol environment.

Monitored Parameter	**Value measured by vibrometer**	**Values normalised by the coupling liquid's refractive index**[†1]
Displacement (Maximum)	801.1 nm	584.7 nm
Velocity (Maximum)	0.7778 m/s	0.5677 m/s
Acceleration (Maximum)	755.2 km/s^2	551.24 km/s^2

Note †1: Using ratio Isopropanol/Air ~ 1.37

The values achieved with this special design electrode were superior to those achieved with Device 44 the single electrode having a 66% radial coverage electrode. The comparison between the two is tackled in Chapter 5 ~ Conclusion 6.

4.6.7 Device 48 ~ Slotted Device- Trench Diameter of 650 µm

This device was one of a number of devices designed with a modified diaphragm. The Finite Element Modelling and detailed designs underpinning this device where outlined in Chapter 2. As discussed previously the scope of this device was to develop devices which:

- could give an improved performance in ultrasonic radiation reception.
- enabled studies in the behaviour of device having a liquid filled cavity with fluids such as isopropanol.
- could perform better in more viscous fluids such as glycerine.

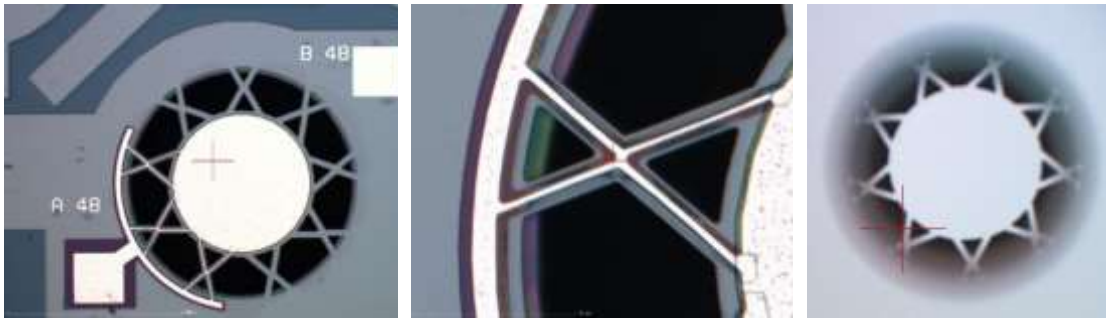

(a) (b) (c)

Figure 4.38 ~ Micrographs of Device 48 showing (a) front view showing whole device including pads and (b) high magnification detail of arms holding up the central membrane and (c) backside image through trench.

4.6.7.1 Laser Vibrometer characterisation of Device 48 - Trench Diameter of 650 µm

Coupling Fluid: Air ~ Cavity Fluid: Air

Testing started by operating Device 48 in an air coupling fluid and air filled cavity. The reason for this was to test its robustness in view of the extreme accelerations that the holding arms would be subjected to when operated in an air coupling environment. To find the resonant frequency when the device was operating in an air coupling fluid and having an air filled cavity, the device was excited with Periodic Chirp signal and with an excitation voltage of 14 $V_{p\text{-}p}$.

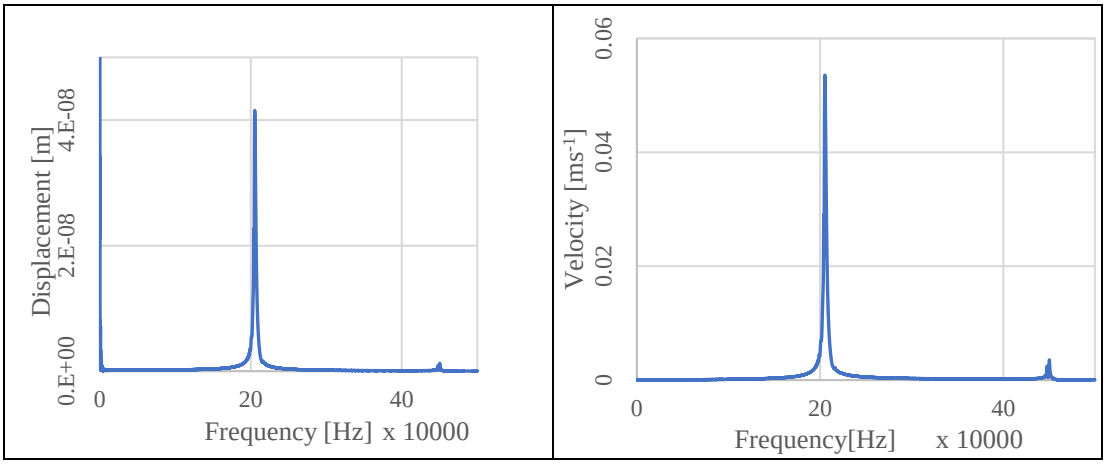

Figure 4.39 ~ Periodic Chirp frequency between 0 and 500 kHz with (a) Displacement, (b) Velocity and (c) acceleration values vs frequency for Device 48 in isopropanol coupling fluid and air filled cavity. (d) Shows displacement vs frequency at a frequency between 200,000 Hz and 209,000 Hz. Device deployed in an air coupling fluid & having an air filled cavity. Values shown are actual readings directly from vibrometer and not normalised with the fluid's refractive index.

The periodic chirp excitation pointed out two potential modes of oscillation identified by the Laser Vibrometer during Periodic Chirp excitation in an air coupling and air filled cavity device. These are shown in Figure 4.40.

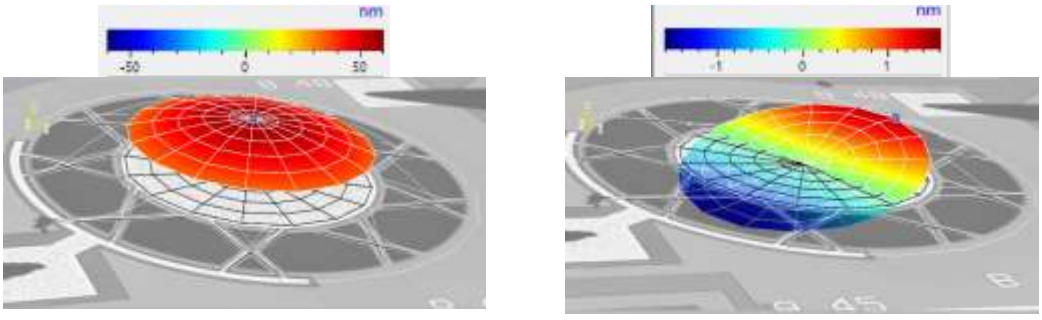

Figure 4.40 ~ Displacement of Device 48 excited with a periodic chirp signal at a frequency of (a) 205.273 kHz and (b) 450.1 kHz in air as coupling fluid & having an air filled cavity. Values shown are actual readings directly from vibrometer and not normalised with fluid's refractive index.

Sine wave excitation with Sine wave signal at 14 V_{p-p} amplitude was conducted on Device 48 which was deployed in air coupling fluid and having an air filled cavity. This was conducted at frequency of 205 kHz as indicated by the periodic chirp process. The displacement is shown in Figure 4.41

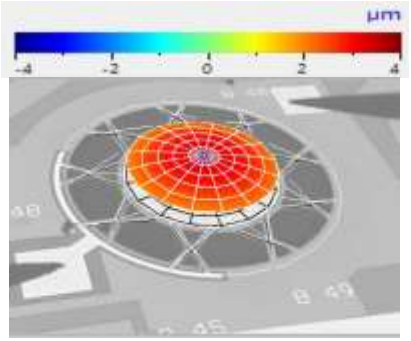

Figure 4.41- Displacement of Device 48 excited with a 14 V_{p-p} sine wave signal at a frequency of 205 kHz. In an air coupling fluid & having an air filled cavity. Values shown are actual readings directly from vibrometer and not normalised with the fluid's refractive index.

The results measured at the diaphragm midpoint during the sine excitation process are shown in Table 4.13. The voltage used was 14 V_{p-p}.

Table 4.13- Results of Device excitation with Sine wave signal at 14 V_{p-p} amplitude with device in air as coupling fluid and having an air filled cavity at 205 kHz.

Monitored Parameter	**Value measured by vibrometer†1**
Displacement (Maximum)	3.293 µm
Velocity (Maximum)	4.250 m/s
Acceleration (Maximum)	5.482 Mm/s^2

Note †1: Since air is used as coupling and cavity fluid, the values in this table do not need to be normalised.

Coupling Fluid: Isopropanol ~ Cavity Fluid: Air

The next step was to conduct periodic chirp excitation on Device 48 again, this time with an isopropanol coupling fluid and again with an air filled cavity. The results are shown in Figure 4.42.

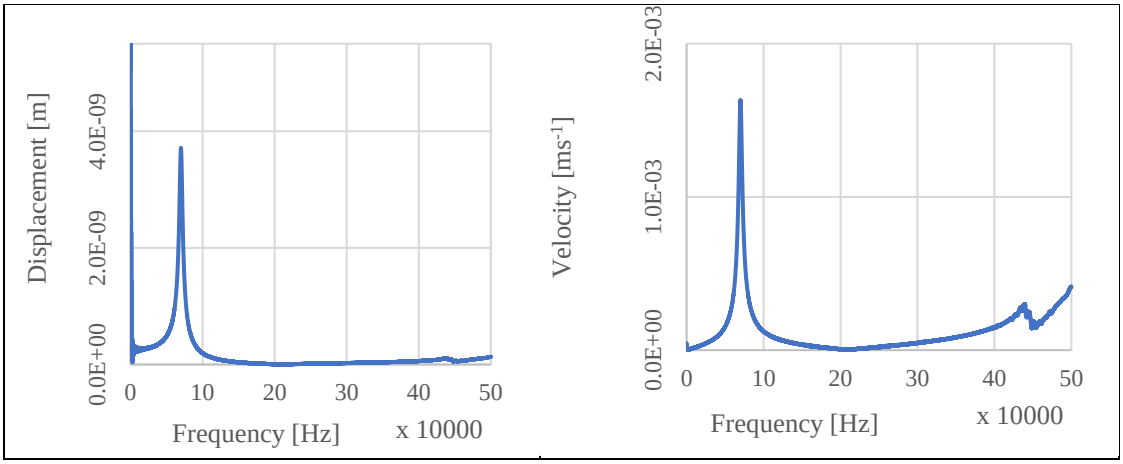

(a) (b)

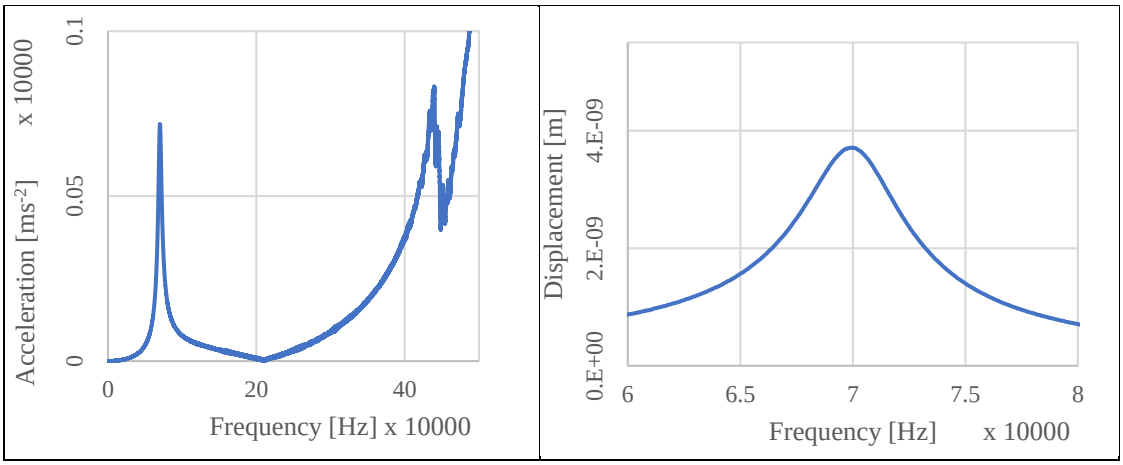

(c) (d)

Figure 4.42 ~ Periodic Chirp frequency between 0 and 500 kHz with (a) Displacement, (b) Velocity and (c) acceleration values vs frequency for Device 48. (d) Shows displacement vs frequency at a frequency between 60,000Hz and 80,000Hz. Device deployed in an isopropanol coupling fluid & with an air filled cavity. Values shown are actual readings directly from vibrometer and not normalised with the fluid's refractive index.

Two modes of oscillation were identified with the Laser Vibrometer during Periodic Chirp excitation for Device 48 deployed in an isopropanol coupling fluid and having an air filled cavity. The two modes of vibration are shown in Figure 4.43.

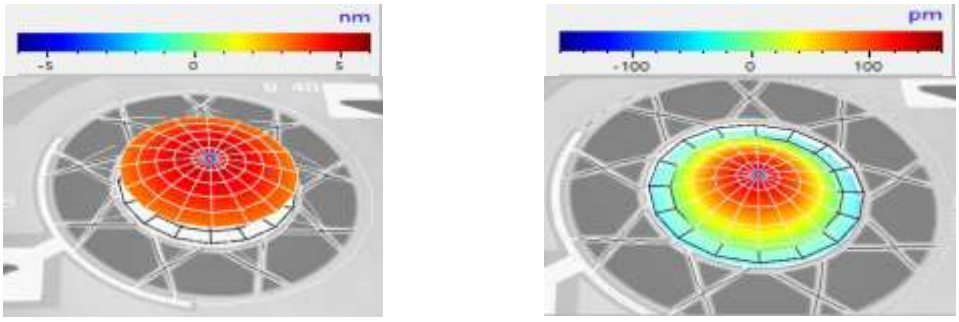

(a) (b)

Figure 4.43- Displacement of device 48 excited with a periodic chirp signal at a frequency of (a) 69.9 kHz (b) 438.98 kHz in an isopropanol coupling fluid and having an air filled cavity. Values shown are actual readings directly from vibrometer and not normalised with the fluid's refractive index.

The device was then subjected to excitation with a sine wave signal at an amplitude of 14 V_{p-p} in the isopropanol surrounding environment and an air filled cavity.

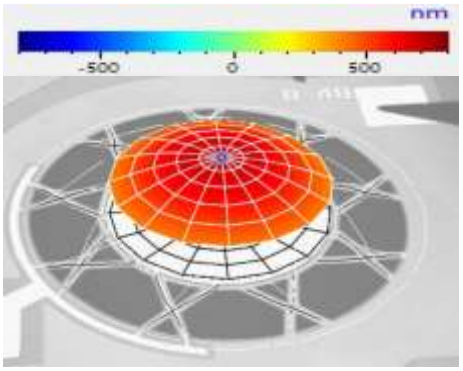

Figure 4.44 ~ Displacement of Device 48 excited with a 14 V_{p-p} sine wave signal at a frequency of 70 kHz and 14 V_{p-p} amplitude in an isopropanol coupling fluid and having an air filled cavity. Values shown are actual readings directly from vibrometer and not normalised with the fluid's refractive index.

The results from the sine excitation are tabulated in Table 4.14. It was also noted that the isopropanol did not readily seep into the cavity between the arms. This is an important consideration which is relevant when deciding the use, positioning and setup of modified diaphragm devices in a final deployable device package.

Table 4.14 ~ Results of Device 48 excitation with Sine wave signal at 14 V_{p-p} amplitude with device in isopropanol coupling fluid and air filled cavity at 70 kHz frequency.

Monitored Parameter	**Value measured by vibrometer**	**Values normalised by the coupling liquid's refractive index**[†1]
Displacement (Maximum)	724.3 nm	528.686 nm
Velocity (Maximum)	0.3186 m/s	0.233 m/s
Acceleration (Maximum)	140.1 km/s^2	102.26 km/s^2

Note †1: Using ratio Isopropanol/Air ~ 1.37

Coupling Fluid: Isopropanol ~ Cavity Fluid: Isopropanol

The device was then deployed in a way in which the cavity was filled with isopropanol thereby making it operate in an isopropanol coupling fluid and an isopropanol filled

cavity. The device was again excited through a periodic chirp signal to determine the resonant frequency and the results are shown in Figure 4.45.

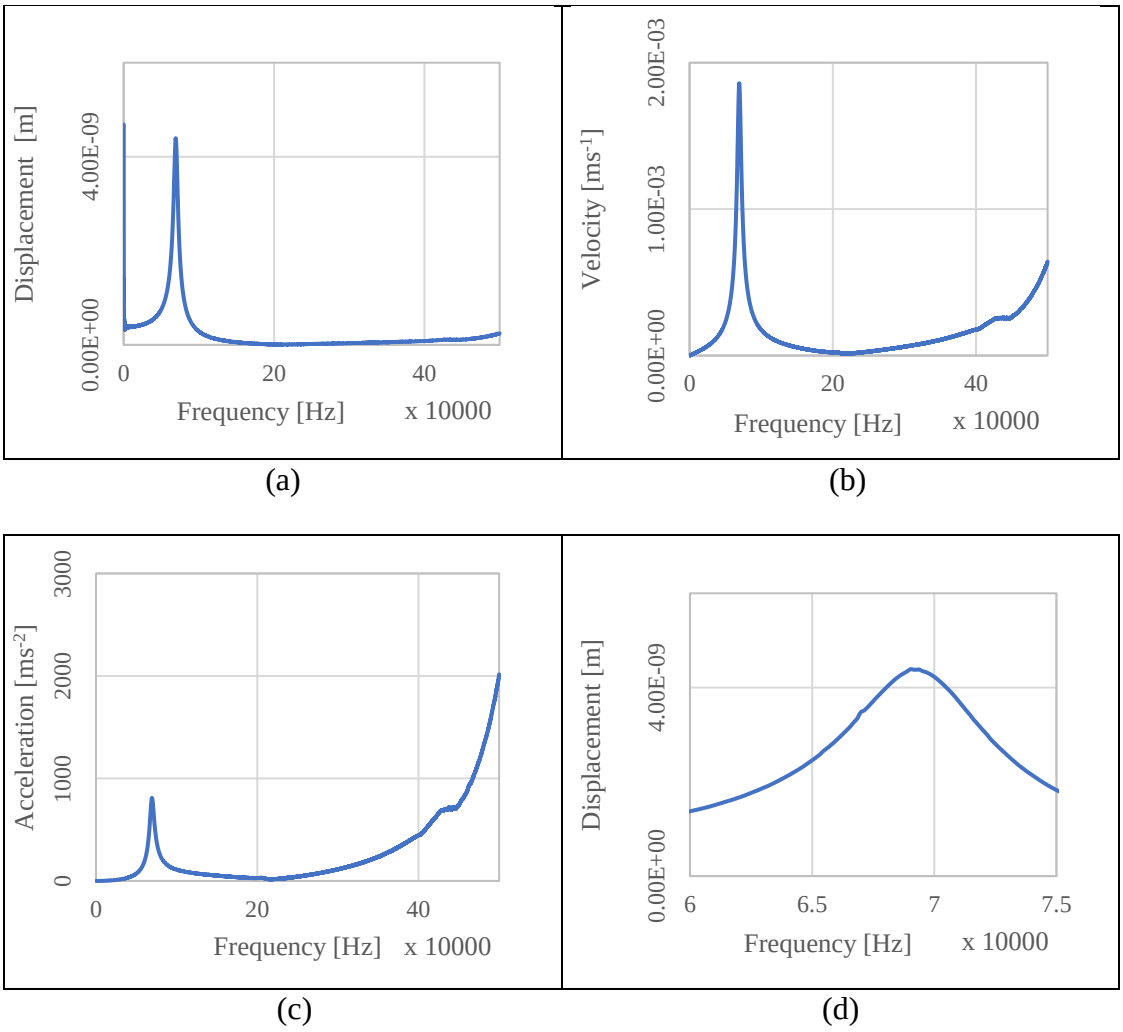

Figure 4.45 ~ Periodic Chirp frequency between 0 and 500 kHz with (a) Displacement, (b) Velocity and (c) acceleration values vs frequency for Device 48 in an isopropanol coupling fluid and having an air filled cavity. (d) Shows displacement vs frequency at a frequency between 60,000 Hz and 75,000 Hz. Values shown are actual readings directly from vibrometer and not normalised with the fluid's refractive index.

The device was deployed in isopropanol coupling fluid and isopropanol filled cavity and excited with a sine wave signal at 14 $V_{p\text{-}p}$ amplitude.

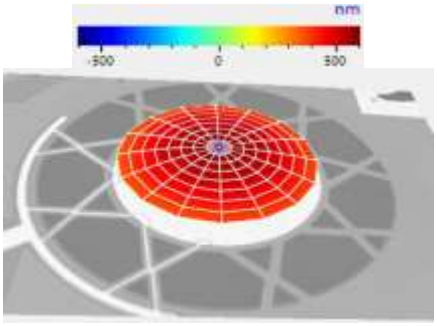

Figure 4.46 ~ Displacement of Device 48 excited with a 14 V_{p-p} sine wave signal at a frequency of 69.38 kHz in an isopropanol coupling fluid and isopropanol filled cavity. Values shown are actual readings directly from vibrometer and not normalised with the fluid's refractive index.

The parameters achieved during the sine wave excitation of the device in isopropanol coupling fluid and isopropanol filled cavity is shown in Table 4.15.

Table 4.15~ Results of Device excitation with Sine wave signal at 14 V_{p-p} amplitude with device in isopropanol coupling fluid and with an isopropanol filled cavity at 69.38 kHz.

Monitored Parameter	**Value measured by vibrometer**	**Values normalised by the coupling liquid's refractive index**[†1]
Displacement (Maximum)	577.7 nm	421.68 nm
Velocity (Maximum)	0.2518 m/s	0.184 m/s
Acceleration (Maximum)	109.8 km/s^2	80.15 km/s^2

Note †1: Using ratio Isopropanol/Air ~ 1.37

Coupling Fluid: Glycerine ~ Cavity Fluid: Air

The next series of experimental work conducted on Device 48 involved studying its operation when operating in a glycerine coupling fluid environment and having an air filled cavity. The device was excited via a periodic chirp signal to determine the resonant frequency when operating in glycerine as coupling fluid.

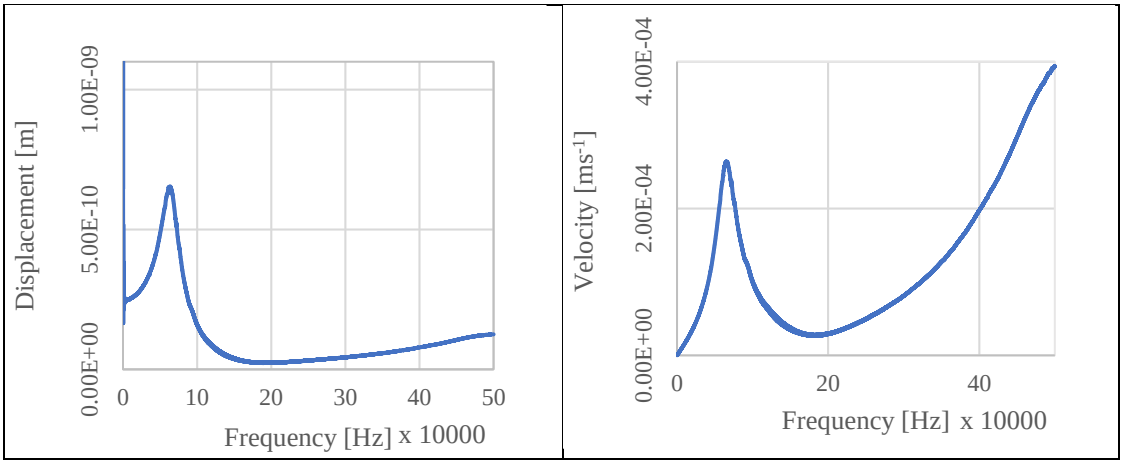

Figure 4.47 ~ Periodic Chirp frequency between 0 and 500 kHz with (a) Displacement, (b) Velocity and (c) acceleration values vs frequency for Device 48 in isopropanol coupling fluid and air filled cavity. (d) Shows displacement vs frequency at a frequency between 50,000 Hz and 80,000 Hz.

Two modes of oscillation were identified by Laser Vibrometer during Periodic Chirp excitation when the device was operating in a glycerine coupling fluid environment. The modes are shown in Figure 4.48.

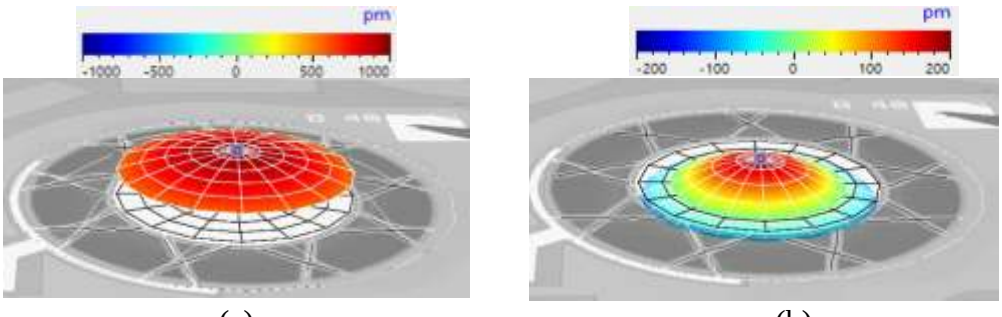

Figure 4.48 ~ Displacement of Device 48 excited with a periodic chirp signal at a frequency of a) 63.945 kHz (b) 500 kHz in glycerine coupling fluid with an air filled cavity. Values shown are actual readings directly from vibrometer and not normalised with the fluid's refractive index.

The Device 48 was then excited with a sine wave signal at the resonant frequency of 66.88 kHz at 14 V_{p-p}. The device at the point of maximum displacement is shown in Figure 4.49.

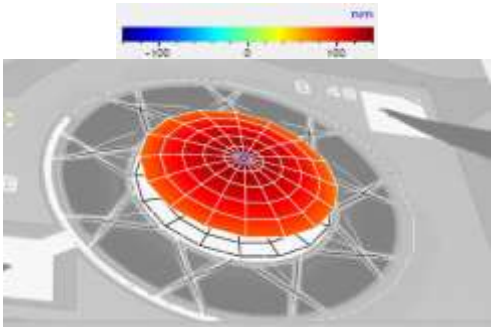

Figure 4.49 ~ Displacement of Device 48 excited with a 14V_{p-p} sine wave operating at a frequency of 66.88 kHz. Deployed in a glycerine coupling fluid and air filled cavity. Values shown are actual readings directly from vibrometer and not normalised with the fluid's refractive index.

The results of the diaphragm midpoint parameters when PMUT is undergoing sine wave excitation at 14V_{p-p} are tabulated in Table 4.16.

Table 4.16 ~ Results of sine wave excitation at an amplitude of 14 V_{p-p} and a frequency of 66.88 kHz. Deployment in glycerine coupling fluid & having an air filled cavity.

Monitored Parameter	**Value measured by vibrometer**	**Values normalised by the coupling liquid's refractive index**[†1]
Displacement (Maximum)	131.4 nm	90.62 nm
Velocity (Maximum)	55.19 mm/s	38.06 mm/s
Acceleration (Maximum)	23.19 km/s^2	15.99 km/s^2

Note †1: Using ratio Glycerine/Air ~ 1.45

4.6.7.2 Acoustic Experimental Data.

The device was next tested acoustically.

Device 48 acting as Transmitter

Step 1 - Setup

The experimental device was placed in a 10 cm diameter petri dish and the two metal pads of the Device 48 were probed. The petri dish was filled with isopropanol up to the 8 mm mark. The PMUT cavity was left air filled. The hydrophone system was set up as shown in Figure 4.16 and connected to the low noise preamplifier. The Device 48 was excited at different frequencies and the response measured on the hydrophone was noted.

Step2 Observing the PMUT as a transmitter.

A high amplitude was noticed at an excitation frequency of 92 kHz with the maximum amplitude out of the hydrophone being 10.69 V_{p-p} which worked out to a pressure of 95 Pa. The output voltage was so high that the system saturated as can be seen in Figure 4.50.

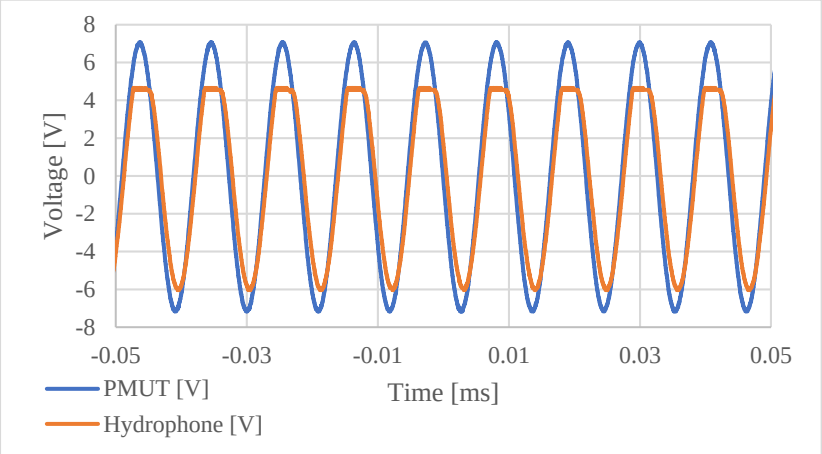

Figure 4.50 ~ Signal from hydrophone when the PMUT was excited at 92 kHz.

It was also notable to see that the two signals were in phase with the phase shift being 4 degrees. The hydrophone was then operated at the same frequency but without the pre-amp to obtain the voltage without saturation as shown in Figure 4.51.

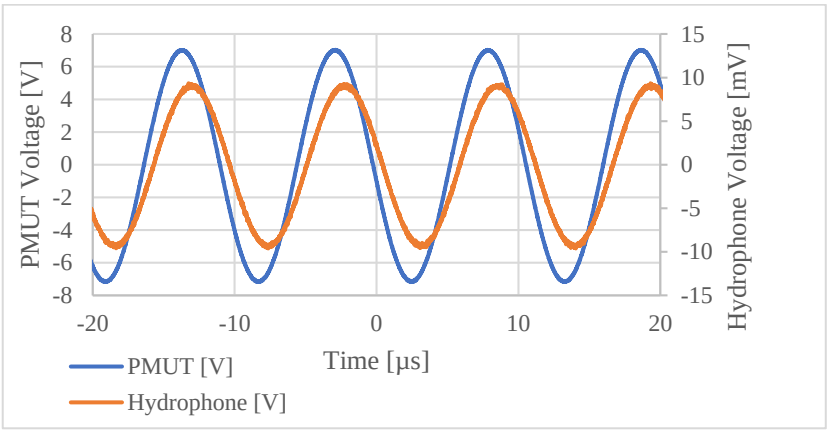

Figure 4.51 ~ Hydrophone being operated without pre-amp at 92.513 kHz.

In this case the measured voltage was 18.94 mV. This voltage output from the hydrophone works out to 169 Pa when the PMUT was operating in transmission mode. The PMUT continued to be excited at various other voltages. It can be noticed that at 93.29 kHz the voltage without amplifier was even higher than what was measured at 92.513 kHz. The results can be seen in Figure 4.52.

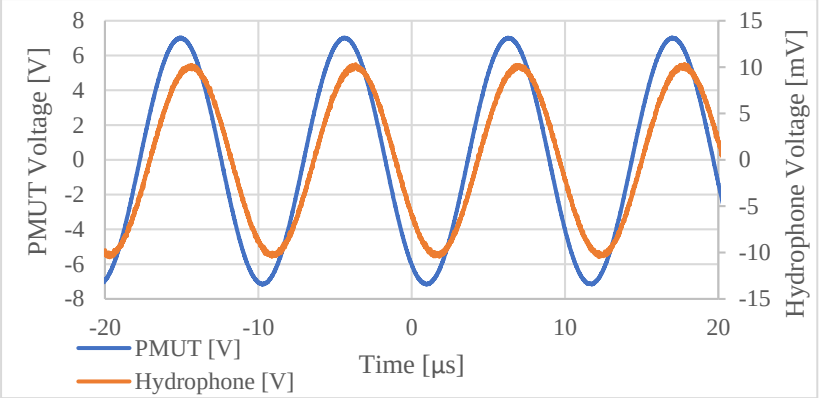

Figure 4.52 ~ Hydrophone being operated without pre amp at 93.29 kHz.

At this frequency the voltage from the hydrophone without preamp was 20.87 mV. This is a substantial increase in pressure with a measured output of 186 Pa. Another measurable output occurred, at a frequency of 82 kHz. This frequency presented a lower amplitude with the measured voltage being 4.34 V, this time with preamp. At this frequency the FFVS is 203 db re1V/µPa which works out to 43.35 Pa.

Another frequency which was substantially transmitted by Device 48 occurred at a frequency of 98.189 kHz. The plot of the hydrophone and PMUT signals are shown in Figure 4.53.

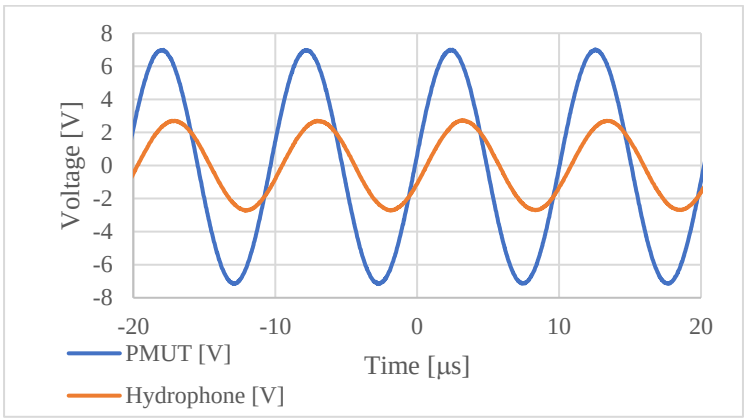

Figure 4.53 ~ Voltage output from hydrophone at 98.2 kHz against signal to PMUT.

At this transmitting frequency a voltage of 5.42 V_{p-p} was measured across the hydrophone. This translates to a pressure of 45.5 Pa at a point of measurement 4 cm laterally away from the PMUT

Device 48 acting as Receiver

Step 1 - Setup

The experimental device was placed in a 10 cm diameter petri dish and the two pads of the device 48 were probed. The petri dish was filled with isopropanol up to 8 mm. The

cavity was left air filled. Hydrophone system was set up as shown in Figure 4.8 and connected to the transmission power amplifier.

Step 2 – Examining the reception capabilities of the PMUT.

After connecting the PMUT to the transmission power amplifier a signal was applied from a signal generator. A signal from the signal generator was applied to the power amplifier and running it in continuous transmit mode. The transmitting power amplifier was provided with a DC voltage of 6 V and a current of 0.2 A. The signal fed to the power amplifier and the output from the PMUT where measured at various frequencies. The first frequency of interest at which a significant voltage output from the PMUT was measured was at 85.21 kHz and the waveforms are shown in Figure 4.54.

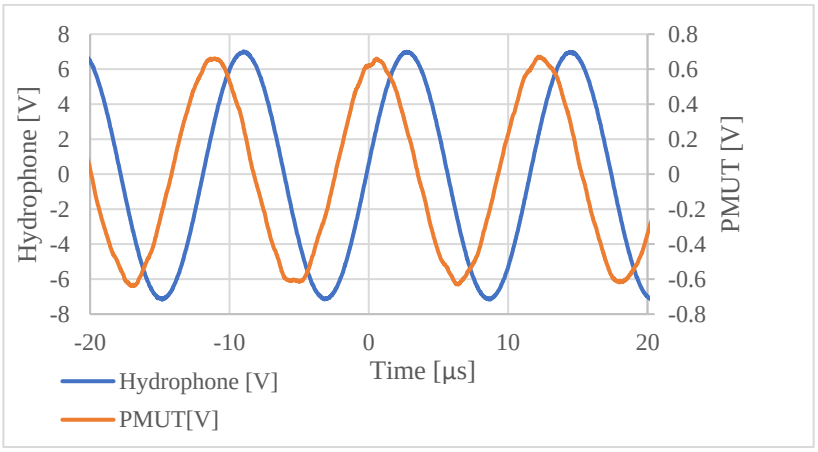

Figure 4.54 ~ Voltage output directly from PMUT and signal into hydrophone at 85.21 kHz.

The peak to peak voltage measured from across the PMUT in this case was 1.3 $V_{p\text{-}p}$. The PMUT voltage was 67.24 degrees lagging to the signal fed into the hydrophone. The device was observed to be able to detect a wide bandwidth. As an example another frequency at which the PMUT capture the received ultrasonic transmission excellently was at 94.1 kHz.

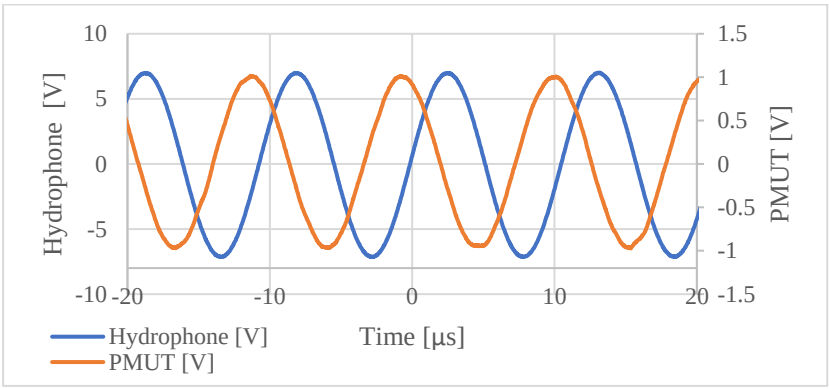

Figure 4.55 ~ Voltage output directly from PMUT and signal into hydrophone at 94.157 kHz.

A voltage of 1.971 $V_{p\text{-}p}$ was measured across the PMUT at 94.157 kHz with a leading phase shift of 107.5°. The PMUT was receptive to other ultrasonic frequencies. As an example one can refer to Figure 4.56 which shows the response at a frequency of 82.819 kHz.

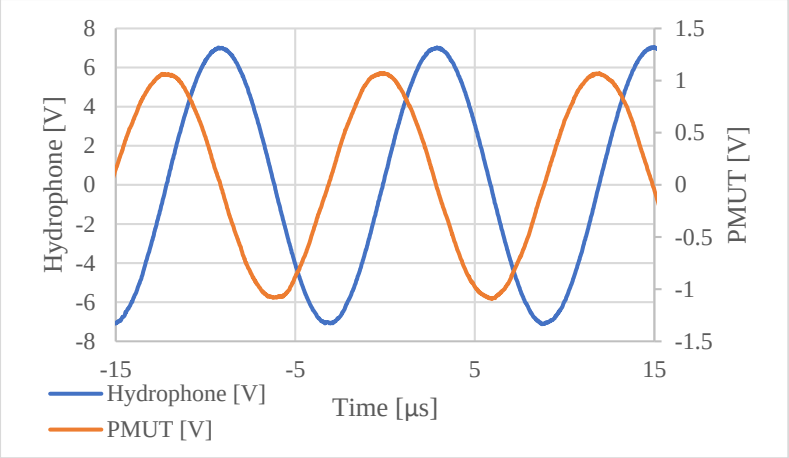

Figure 4.56 ~ Voltage output directly from PMUT and signal into hydrophone at 82.99 kHz.

As the hydrophone was being excited at a frequency of 82.99 kHz the voltage across the PMUT was measured at 2.183V. Apart from the frequencies mentioned here the PMUT also reacted to other frequencies albeit in a less pronounced way.

For this series of acoustic experiments carried out on Device 48 a low voltage of 6 V DC was used to power the transducer's high voltage amplifier. At hydrophone transmitting frequencies between 80 kHz and 100 kHz the transmitting voltage response varied slightly between141 dbµPa/V@1m and 143 dbµPa/V@1m. These values convert to a pressure output of between 47 Pa to 53 Pa.

Step 3 –Ultrasonic radiation reception with isopropanol filled cavity.

A further experimental process was held to determine the effect on ultrasonic reception which an isopropanol filled cavity has. At this stage the experimental device was inverted to allow liquid to freely flow into the cavity with the device being tapped to release any captured microbubbles. The device was then inverted back and probed again. The hydrophone was again used as ultrasonic excitation source as done in step 2 above. The reaction of the PMUT and the hydrophone's excitation at a frequency of 108.7 kHz is shown in Figure 4.57.

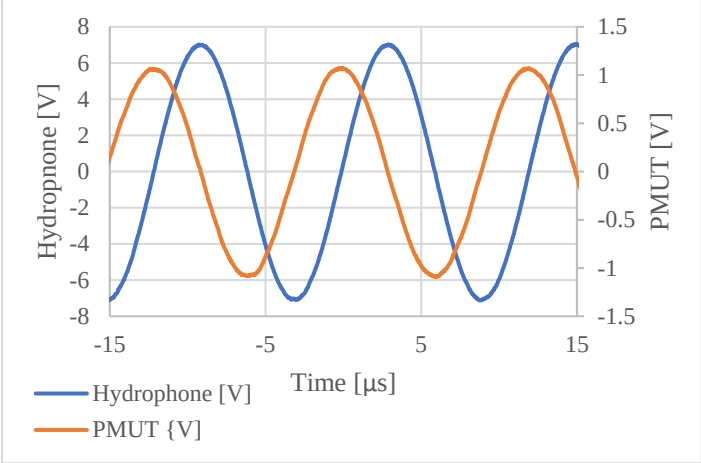

Figure 4.57 ~ Voltage output directly from PMUT and signal into hydrophone at 108.5 kHz.

The voltage measured in this case was 488.6 mV. It was noted that while the amplitude from the PMUT was lower in magnitude, the waveform was still close to sine wave shape.

Further voltage outputs across the PMUT were measured at further excitation frequency values as indicated below:

- 86.7 kHz - 430.8 mV_{p-p}
- 80.6 kHz - 225.9 mV_{p-p}
- 70.8 kHz - 225.9 mV_{p-p}
- 70.6 kHz- 225 mV_{p-p}

Voltages across the PMUT were also measured at higher frequency values:

- 108.7 kHz - 450 mV_{p-p}
- 123.6 kHz- 441 mV_{p-p}

4.6.7.3 Concluding point on Device 48's experimental process.

Device 48 performed very well in the experimental work conducted. This performance will be discussed further in Chapter 5.

4.6.8 Device 49 ~ Circular PMUT-Trench Diameter of 650 µm

This PMUT device was based on a circular diaphragm design with the padmetal electrode radial coverage being 66% of the diaphragm surface as shown in Figure 4.58.

Figure 4.58 ~ Frontal device micrograph of device 49 – 650µm diameter PMUT.

This device was put into the experimental cycle for the following reasons:

- To act as part of the series studying how diameter of PMUT effects the resonant frequency.
- To act as control device to benchmark PMUT devices which had a modified diaphragm.

The geometrical data for this device are tabulated in Table 4.17.

Table 4.17 ~ Geometric data for Device 49

Nominal Trench Diameter [µm]	Padmetal Cover [%]	Padmetal Diameter [µm]	Padoxide Diameter [µm]	Pzfilm Diameter [µm]	Design Features
650	66	429	413	650	Circular PMUT

4.6.8.1 Laser Vibrometer characterisation of Device 49

Coupling Fluid: Isopropanol ~ Cavity Fluid: Air

Device 49 was excited by a periodic chirp signal when deployed in an Isopropanol coupling fluid and having an air filled cavity.

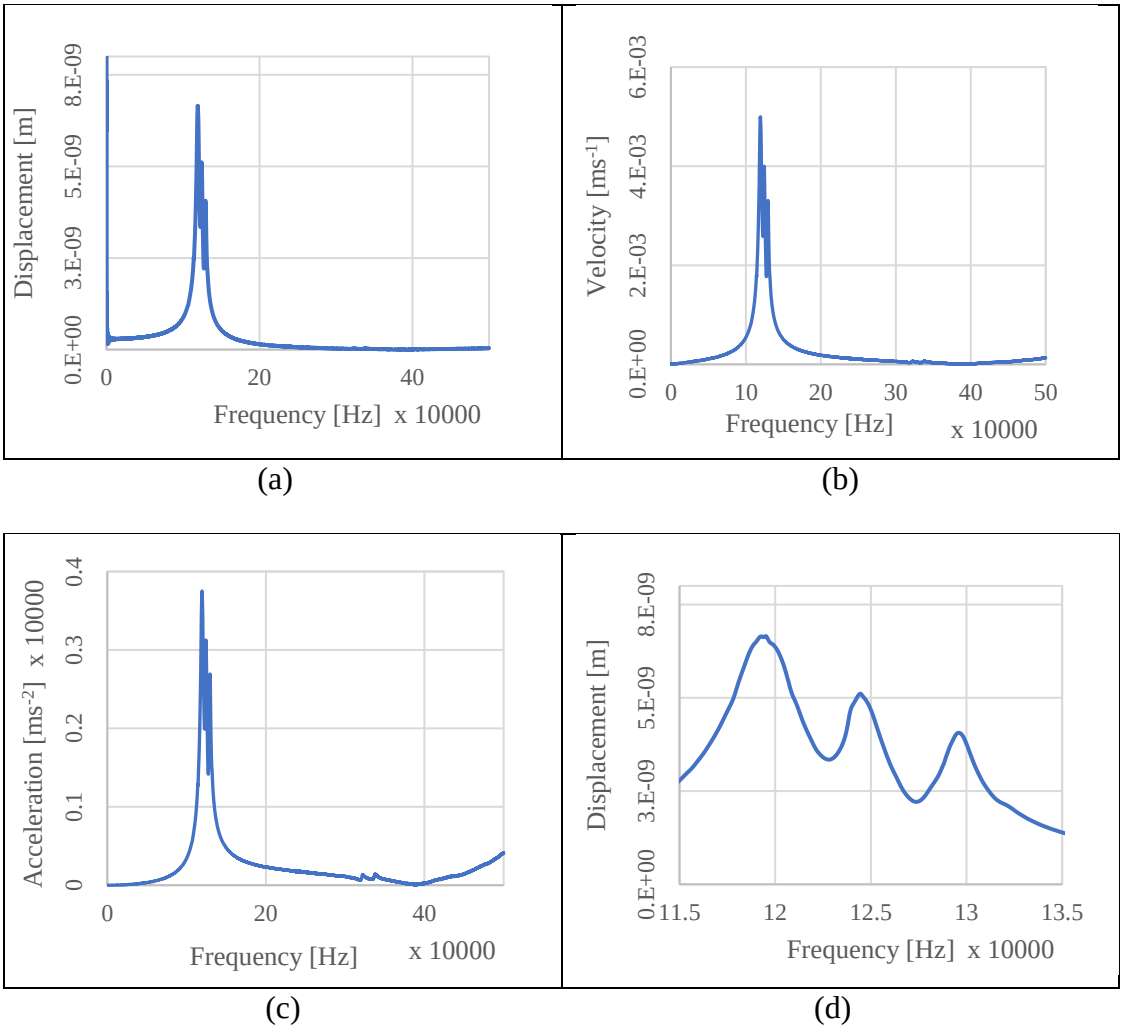

Figure 4.59 ~ Periodic Chirp frequency between 0 and 500 kHz with (a) Displacement, (b) Velocity and (c) acceleration values vs frequency for Device 49 in isopropyl alcohol surrounding and air filled cavity. (d) Shows displacement vs frequency at a frequency between 115,000 Hz and 135,000 Hz.

One modes of oscillation was identified by Laser Vibrometer during Periodic Chirp excitation. The output from the laser vibrometer is shown in Figure 4.60.

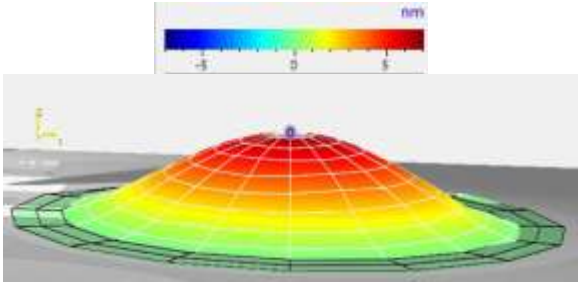

Figure 4.60 ~ Displacement of Device 49 excited with a 14V_{p-p} sine wave signal at a frequency of 119.53 kHz. Device deployed in an Isopropanol surrounding environment & with an air filled cavity. Values shown are actual readings directly from vibrometer and not normalised with the fluid's refractive index.

The results from the vibrometer analysis for Device 49 with sine excitation are tabulated in Table 4.18.

Table 4.18 ~ Results of Device 49 excitation with Sine wave signal at 14 V_{p-p} amplitude at frequency of 119.53 kHz. Device in an isopropanol coupling fluid and in an air filled cavity.

Monitored Parameter	Value measured by vibrometer	Values normalised by the coupling liquid's refractive index†1
Displacement (Maximum)	667 nm	486 nm
Velocity (Maximum)	501.3 mm/s	365.9 mm/s
Acceleration (Maximum)	376.472 km/s^2	274.797 km/s^2

Note †1: Using ratio Isopropanol/Air ~ 1.37

Coupling Fluid: Isopropanol ~ Cavity Fluid: Isopropanol

The Device 49 was next excited with a Periodic Chirp signal when deployed in an isopropanol coupling fluid environment and with an isopropanol filled cavity. The results are presented in Figure 4.61.

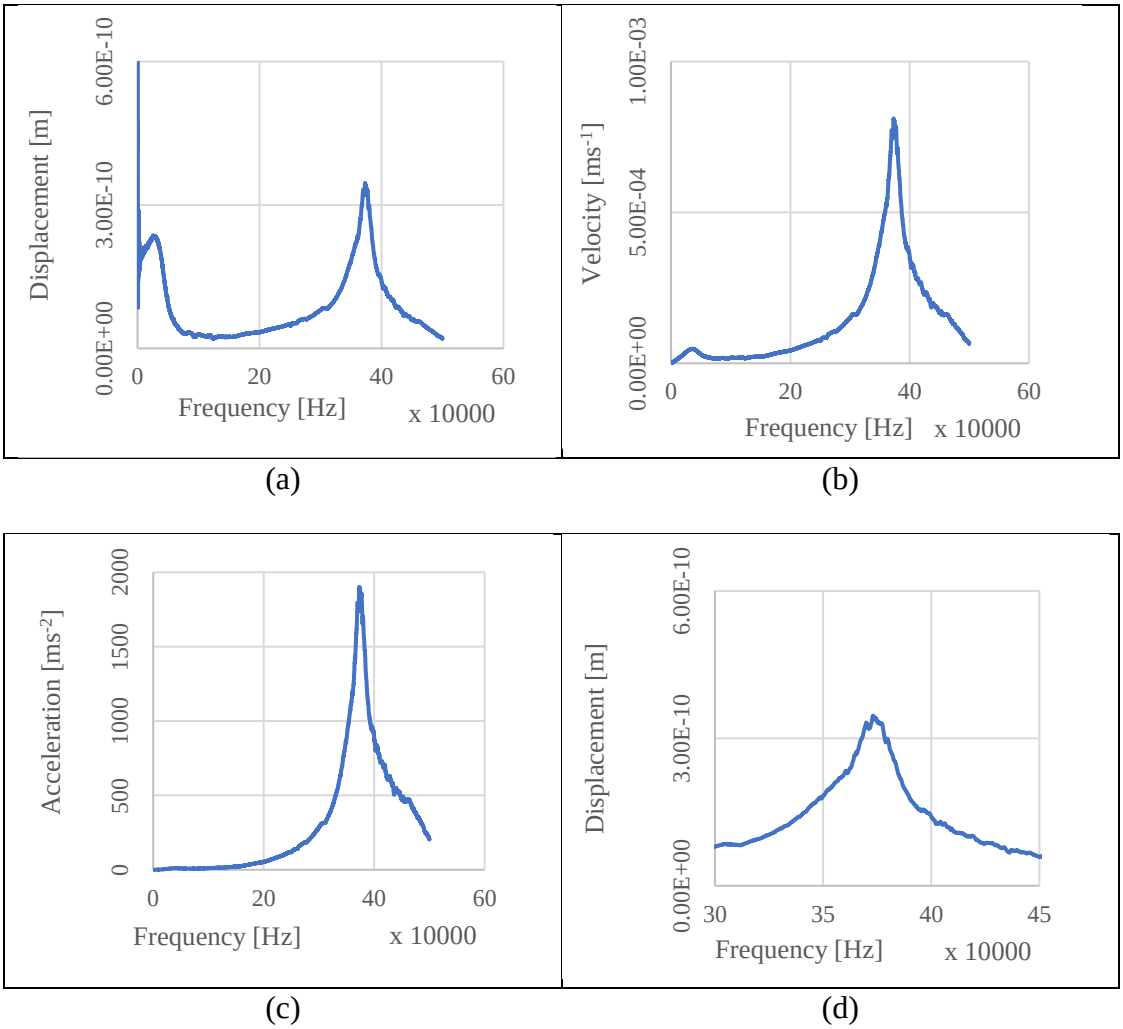

Figure 4.61 ~ Periodic Chirp frequency between 0 and 500 kHz with (a) Displacement, (b) Velocity and (c) acceleration values vs frequency for Device 49 in isopropanol coupling fluid and having an air filled cavity. (d) Shows displacement vs frequency at a frequency between 300,000 Hz and 450,000 Hz.

Two peaks were detected during device excitation with Sine wave signal at 14 V_{p-p} amplitude as shown in Figure 4.62.

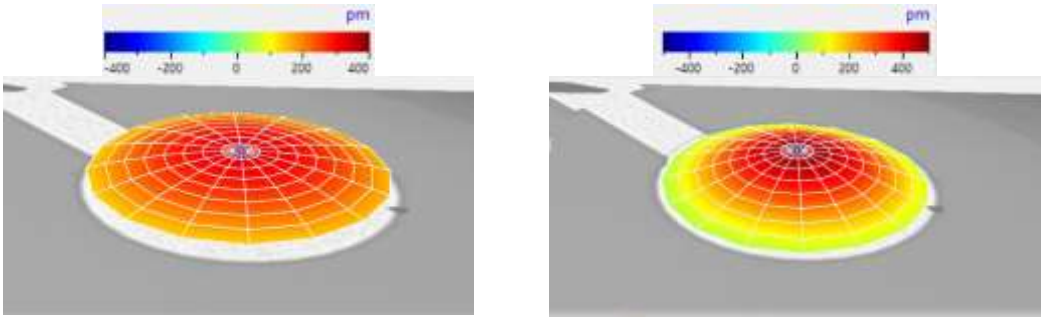

(a) (b)

Figure 4.62 ~ Displacement of Device 49 excited with a 14V_{p-p} sine wave signal at a frequency of (a) 27.11 kHz (b) 373.12 kHz. Deployed in an isopropanol coupling fluid & having an air filled cavity.

4.6.9 Device 50 ~ Circular PMUT Trench Diameter of 650 µm

Device 50 was based on a circular diaphragm design. The padmetal electrode radial coverage percentage was set at 70% of the diaphragm surface as shown in Figure 4.63.

Figure 4.63 ~ Frontal device micrograph of Device 50 – 650 µm diameter PMUT.

The geometrical data behind the design of Device 50 is tabulated in Table 4.19.

Table 4.19 ~ Geometric data for device 50

Nominal Trench Diameter [µm]	Padmetal Cover [%]	Padmetal Diameter [µm]	Padoxide Diameter [µm]	Pzfilm Diameter [µm]	Design Features
650	70	455	439	650	Circular PMUT

4.6.9.1 Laser Vibrometer characterisation of Device 50

Coupling Fluid: Isopropanol ~ Cavity Fluid: Isopropanol

Device 50 was excited with a Periodic Chirp signal when deployed in an isopropanol coupling environment and having an isopropanol filled cavity. The responses are seen in Figure 4.64.

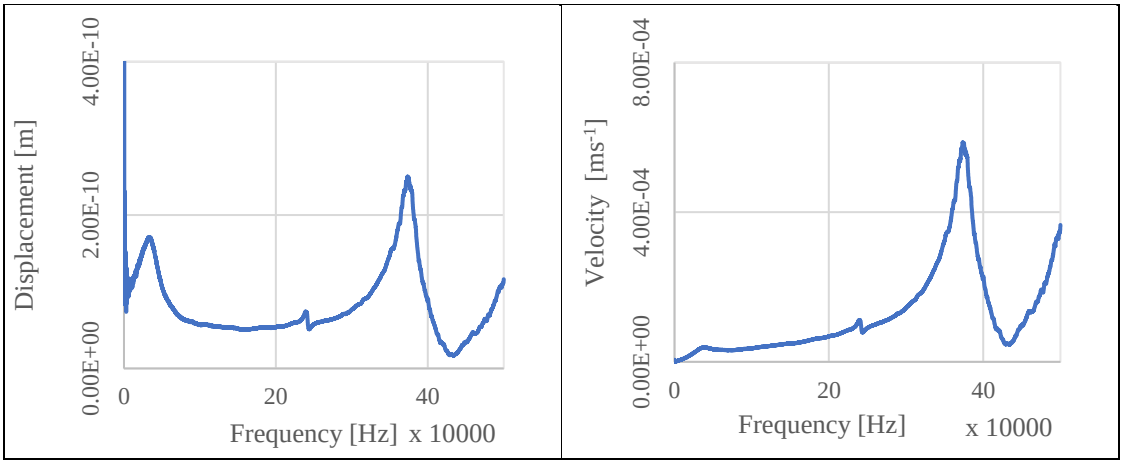

(a) (b)

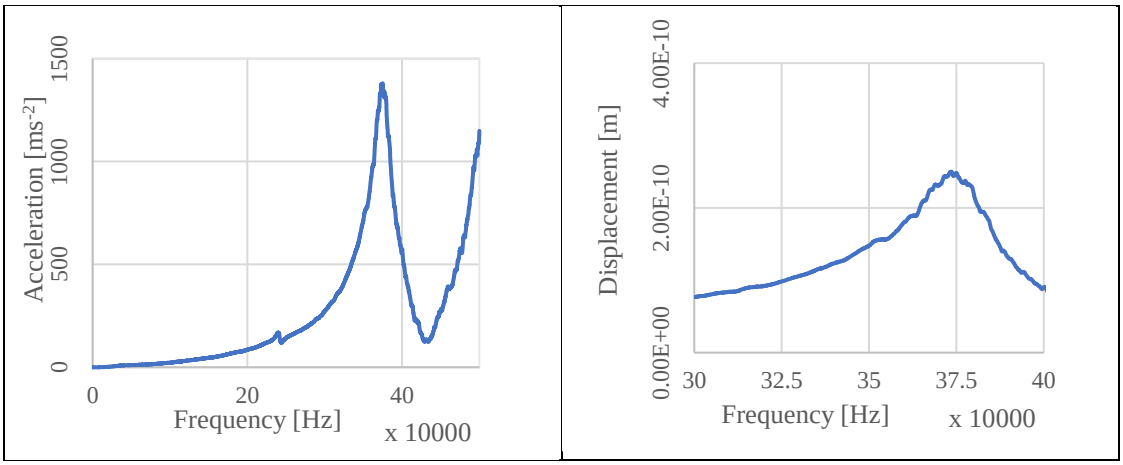

(c) (d)

Figure 4.64 ~ Periodic Chirp frequency between 0 and 500 kHz with (a) Displacement, (b) Velocity and (c) acceleration values vs frequency for Device 50. Device deployed in isopropanol coupling fluid and having an isopropanol filled cavity. (d) Shows displacement vs frequency at a frequency between 30 kHz and 40 kHz.

Significant responses were detected by the laser vibrometer at various frequencies during Periodic Chirp excitation as shown in Figure 4.65.

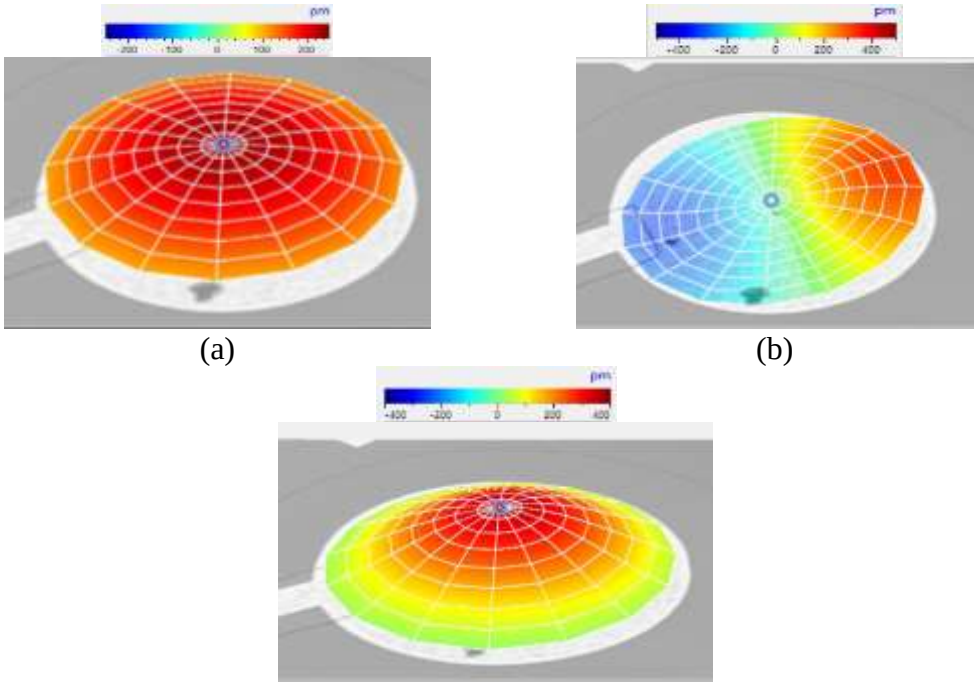

(a) (b)

(c)

Figure 4.65 ~ Displacement of device 50 excited with a periodic chirp signal at a frequency of a)33.44 kHz b)239.38 kHz c) 373.44 kHz. Deployed in an isopropanol coupling fluid and isopropanol filled cavity. Values shown are actual readings directly from vibrometer and not normalised with the fluid's refractive index.

The device was then subjected to sine excitation with a 14 $V_{p\text{-}p}$ signal at a frequency of 373.44 kHz. The displacement is shown in Figure 4.66.

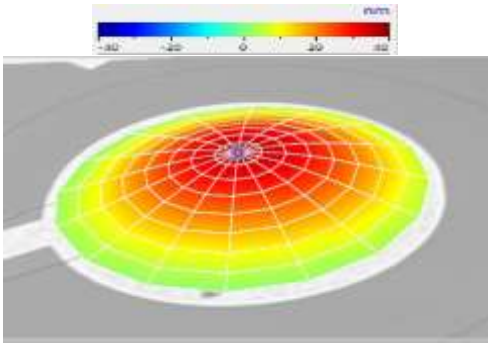

Figure 4.66 ~ Displacement of Device 50 excited with a 14$V_{p\text{-}p}$ sine wave signal at a frequency of 373.44 kHz when deployed in isopropanol coupling fluid and having an isopropanol filled cavity. Values shown are actual readings directly from vibrometer and not normalised with the fluid's refractive index.

The values measured during sine excitation are shown in Table 4.20

Table 4.20 ~ Results of device excitation with a Sine wave signal at 14 V_{p-p} amplitude at frequency of 373.44 kHz. Deployed in an isopropanol coupling fluid and isopropanol filled cavity.

Parameter	Value measured by vibrometer	Values normalised by the coupling liquid's refractive index†1
Peak Displacement	34.15 nm	23.55 nm
Peak Velocity	80.12 mm/s	55.26 mm/s
Peak Acceleration	188 km/s^2	129.66 km/s^2

Note †1: Using ratio Isopropanol/Air ~ 1.37

4.6.9.2 Acoustic Experimental Data for Device 50.

Device 50 acting as Transmitter

Step 1 - Setup

The experimental device was placed in a 10 cm diameter petri dish after which Device 50 was probed. The dish was filled with isopropanol coupling fluid up to the 8 mm depth mark. The PMUT cavity was left air filled. The hydrophone's electrical system was set up as shown in Figure 4.16 and connected to the low noise preamplifier.

Step 2 – Determining PMUT resonant frequency.

The first experimental procedure involved connecting the PMUT to a signal generator and running it in continuous transmit mode. The amplitude of the voltage applied across the PMUT was 14 V_{p-p}. Excitation signal to PMUT as well as signal from hydrophone preamplifier and are shown in Figure 4.67.

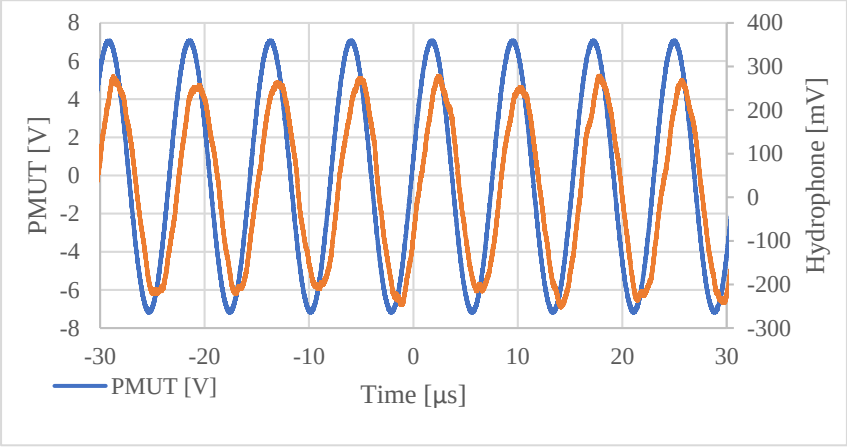

Figure 4.67 ~ Voltage applied across PMUT vs voltage measured out of PMUT pre amp for Device 50 operating as continuous sinusoidal waveform transmitter at 129.24 kHz.

The signal output from the hydrophone was a sine wave with a low amplitude of 525 mV_{p-p}. This equates to a sound pressure level of 4.165 Pa. Another point at which ultrasonic reception by the PMUT was at a significant level is shown in Figure 4.68. The excitation frequency was 116.8 kHz at an amplitude of 14 V_{p-p}.

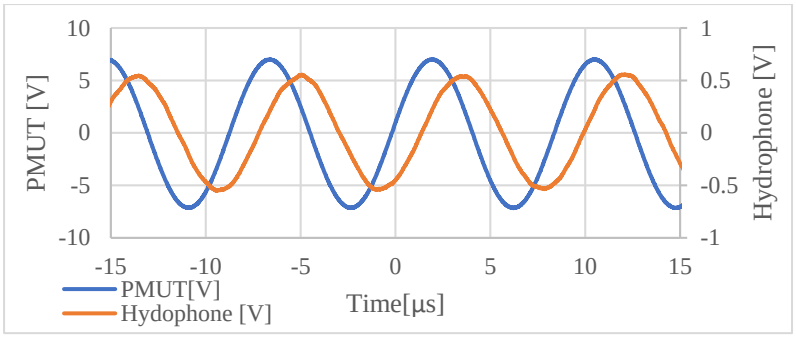

Figure 4.68 ~ Voltage applied across PMUT vs voltage measured out of PMUT pre amp for Device 50 operating as continuous sinusoidal waveform transmitter at 116.8 kHz.

In this case the peak to peak voltage was 1.089 V. The highest voltage measured by the hydrophone was at a frequency of 116.4 kHz as shown in Figure 4.69

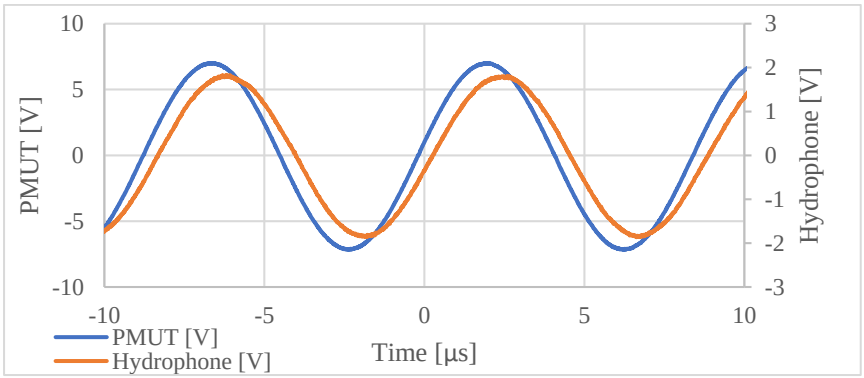

Figure 4.69 ~ Voltage applied across PMUT vs voltage measured out of PMUT pre amp for Device 50 operating as continuous sinusoidal waveform transmitter at 116.4 kHz.

At this frequency the measured voltage was 3.7 V. At this voltage the pressure detected by the hydrophone was calculated at a low 30 Pa.

4.6.10 Device 56 ~ Circular PMUT- Trench Diameter of 700µm

Device 56 a 700 µm PMUT shown in Figure 4.70 with a 66% electrode radial coverage was placed in the test series for the following reasons:

- To be part of the test series studying how diameter of PMUT effects the resonant frequency.
- To study the effect which electrode diameter has when device is operating in viscous fluid such as glycerine.

Figure 4.70 ~ Frontal device micrograph of Device 56 – 700µm diameter PMUT.

The geometric parameters relevant to Device 56 are listed in Figure 4.21.

Table 4.21 ~ Geometric data for device 56

Nominal Trench Diameter [µm]	Padmetal Cover [%]	Padmetal Diameter [µm]	Padoxide Diameter [µm]	Pzfilm Diameter [µm]	Design Features
700	66	462	446	700	Circular PMUT

4.6.10.1 Laser Vibrometer Characterisation of Device 56

Coupling Fluid: Isopropanol ~ Cavity Fluid: Air

Periodic Chirp excitation of Device 56 in an isopropanol coupling fluid and having an air filled cavity is shown in Figure 4.71.

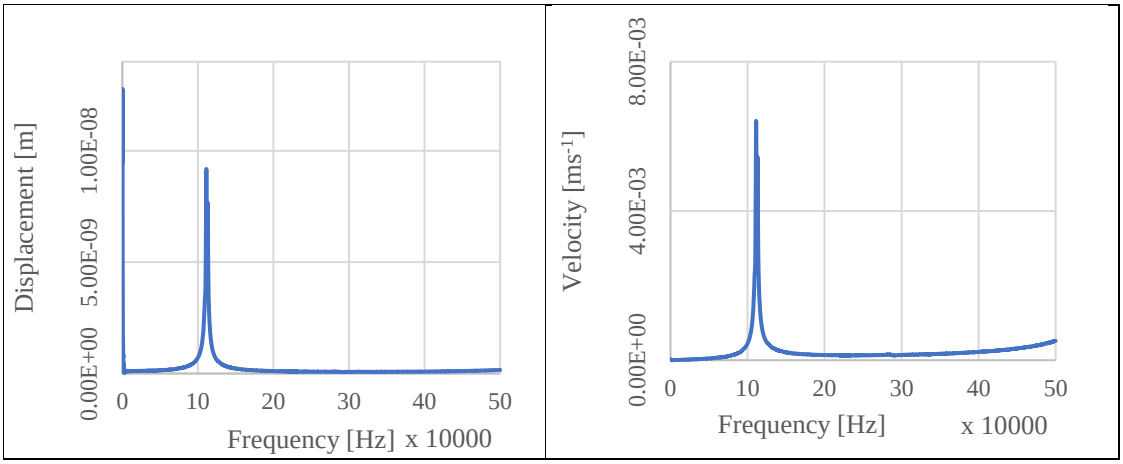

Figure 4.71 ~ Periodic Chirp frequency between 0 and 500 kHz with (a) Displacement, (b) Velocity and (c) acceleration values vs frequency for Device 56 in isopropanol coupling fluid and air filled cavity. (d) Shows displacement vs frequency at a frequency between 109 kHz and 115 kHz.

Two modes of oscillation were identified by Laser Vibrometer during Periodic Chirp excitation. These are shown in Figure 4.72.

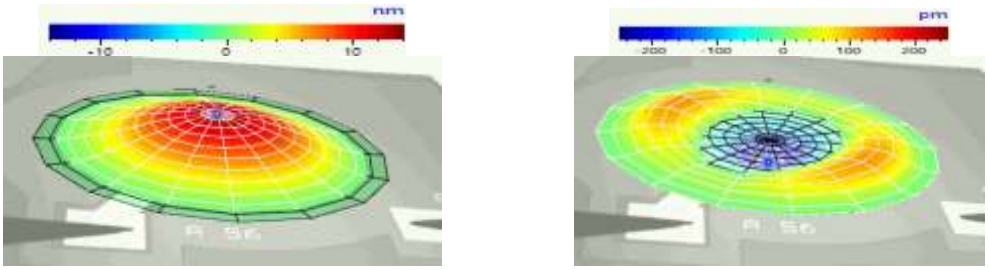

Figure 4.72 ~ Displacement of Device 56 excited with a periodic chirp signal at a frequency (a)111.17 kHz; (b)496.88 kHz. In isopropanol coupling fluid & having an air filled cavity. Values shown are actual readings directly from vibrometer and not normalised with the fluid's refractive index.

The device 56 was excited with sine wave signal having a 14 $V_{p\text{-}p}$ amplitude.

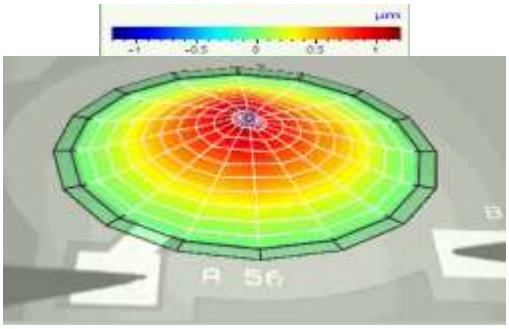

Figure 4.73 ~ Displacement of device 56 excited with a 14 V_{p-p} sine wave signal at a frequency 111.09 kHz. In an isopropanol coupling fluid & air filled cavity. Values shown are actual readings directly from vibrometer and not normalised with the fluid's refractive index.

The results achieved from the sine excitation at the resonant frequency are shown in Table 4.22.

Table 4.22 ~ Maximum values at device centre point for Device 56 in isopropanol coupling fluid and air filled cavity at a resonant frequency of 111.09 kHz

Parameter	**Value measured by vibrometer**	**Values normalised by the coupling liquid's refractive index**[†1]
Peak Displacement	1.09 µm	0.796 µm
Peak Velocity	0.76032 m/s	0.555 m/s
Peak Acceleration	530.721 km/s^2	387.39 km/s^2

Note †1: Using ratio Isopropanol/Air ~ 1.37

Coupling Fluid: Isopropanol ~ Cavity Fluid: Isopropanol

A Device 26 was tested experimentally to study its behaviour when it was inside isopropanol coupling fluid and had an isopropanol filled cavity. The device was excited by a periodic chirp frequency to achieve the plot shown in Figure 4.74.

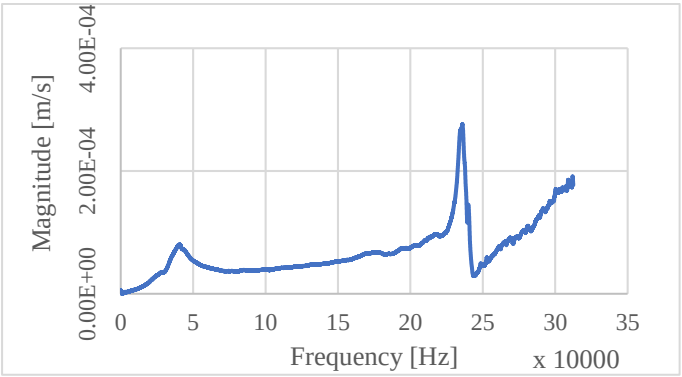

Figure 4.74 ~ The point of resonance for Device 56 at 235kHz.

The main resonant frequency was observed to be occurring at 235 kHz. Movement of the diaphragm was also observed at lower frequencies such as 13.91 kHz albeit to a lower amplitude. At the point of resonance, namely 235 kHz the diaphragmatic movement was observed to be following the mode shown in Figure 4.75.

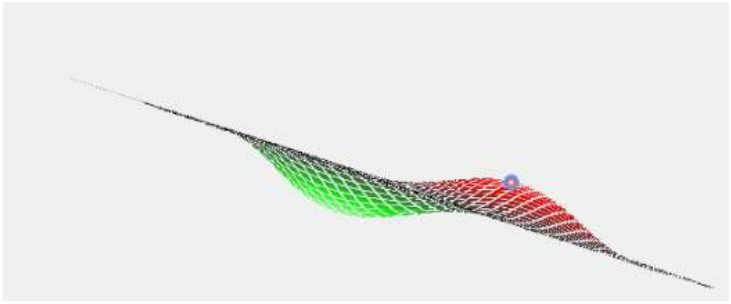

Figure 4.75 ~ Peak displacement of Device 56 during resonant frequency excited with periodic excitation.

Such an oscillatory mode made it evident that the movement of Device 56 when diaphragm is in liquid from both sides was unstable with various modes operating close to each other.

Coupling Fluid: Glycerine ~ Cavity Fluid: Air

The next phase of testing for Device 56 was conducted with glycerine coupling fluid and an air filled cavity. In this step the device was excited in the Time domain to produce a characterisation response. However before this was conducted excitation with a periodic chirp signal was carried out to determine the resonant frequency. The results are shown in Figure 4.76.

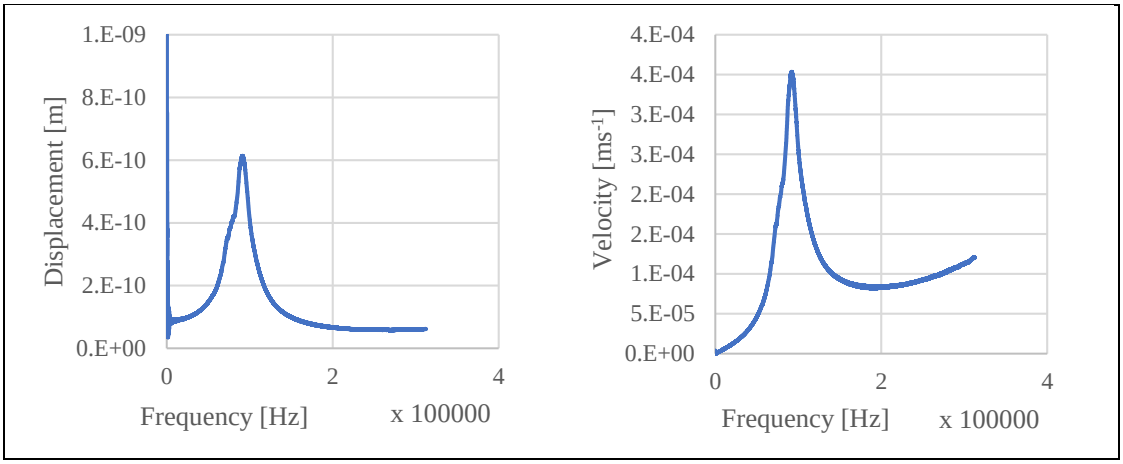

(a) (b)

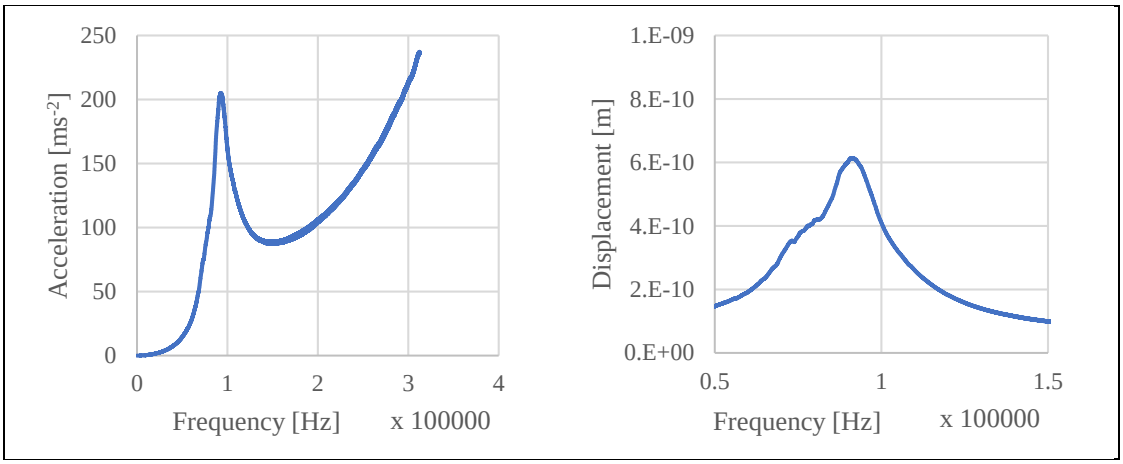

(c) (d)

Figure 4.76 ~ Periodic Chirp frequency between 0 and 40 kHz with peak midpoint (a) displacement, (b) velocity and (c) acceleration values vs frequency for Device 56 in glycerine coupling fluid and air filled cavity. (d) Shows displacement vs frequency at a resonant frequency between 50 kHz and 150 kHz.

After the periodic chirp followed the time domain analysis with the first part involving the excitation of the device with a burst sine excitation signal and the dynamic response of the PMUT was studied in the time domain.

The following parameters were used for this study:

Cavity fluid:	Air
Coupling Fluid:	Glycerine with height from petri dish bottom 2.5 mm
Excitation Signal:	Burst sine with amplitude of 18 V_{p-p}
Sampling Frequency:	6.250 MHz
Excitation frequency:	91.5 kHz

The burst sine excitation signal used is shown in Figure 4.77. The pulse frequency was set at 91.5 kHz which was determined to be the resonant frequency of the PMUT under test.

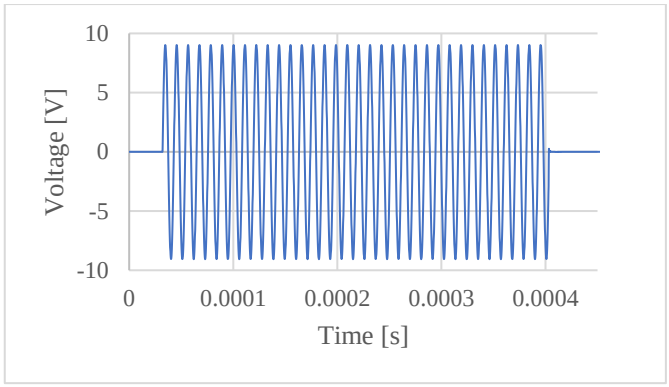

Figure 4.77 ~ The burst sine excitation signal at a frequency of 91.5 kHz

The velocity on the PMUT surface was measured at a number of points during the excitation process and the velocity vs time graph is being shown in Figure 4.78. The peak velocity reached was 0.06986 m/s.

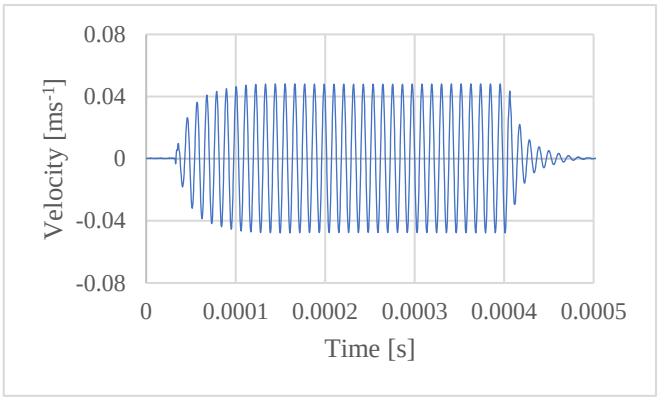

Figure 4.78 ~ The velocity of the diaphragm at the midpoint when subjected to the burst sine excitation.

The velocity data was then filtered and integrated to achieve the displacement data shown in Figure 4.79.

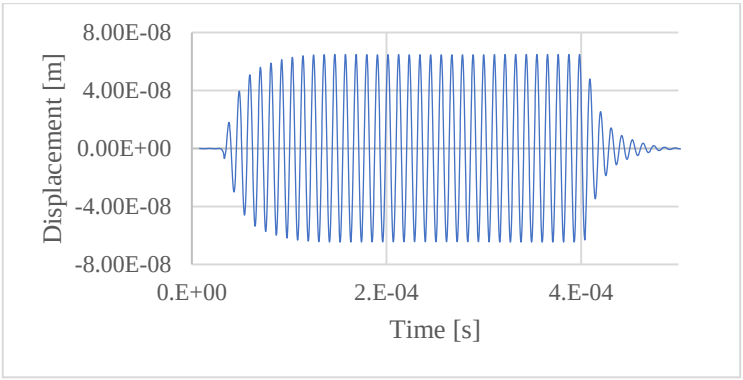

Figure 4.79 ~ The displacement of the diaphragm at the midpoint when subjected to the burst sine excitation.

The peak displacement of Device 56 when operating in glycerine was 6.49×10^{-8} m.

4.6.10.2 Acoustic Experimental Data for Device 56.

Device 56 acting as Transmitter

Step 1 - Setup

The experimental device was placed in a 10 cm diameter petri dish and Device 56 was probed. The dish was filled with isopropanol up to the 8 mm mark. The cavity for this test process was air filled. The hydrophone system was set up as shown in Figure 4.16 and connected to the low noise preamplifier.

Step 2 – Determining PMUT resonant frequency.

The first experimental procedure involved connecting the PMUT to a signal generator and running it in continuous transmit mode. The voltage applied across the PMUT was 14 $V_{p\text{-}p}$. The signal connected to the PMUT as well as that coming from hydrophone preamplifier are shown in Figure 4.80

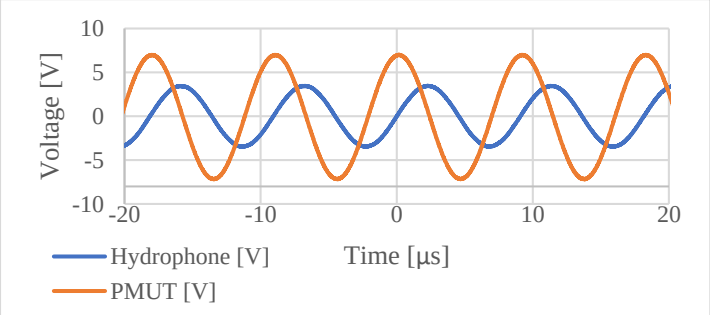

Figure 4.80 ~ Voltage applied across PMUT vs voltage measured out of PMUT pre amp for Device 56 operating as continuous sinusoidal waveform transmitter at 110.24 kHz.

The signal detected from then hydrophone was an undistorted sine wave with an amplitude of 6.955 $V_{p\text{-}p}$. This equated to a sound pressure level of 70 Pa. There was also an 84.57° phase shift between the signal input into the PMUT and the signal output from the hydrophone.

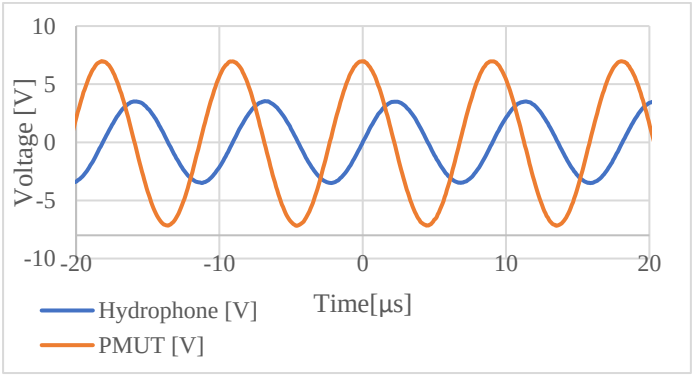

Figure 4.81 ~ Voltage applied across PMUT vs voltage measured out of PMUT pre amp for Device 56 operating as continuous sinusoidal waveform transmitter at 110.3 kHz.

The voltage output from the hydrophone at a frequency of 110.34 kHz was 7.04 V_{p-p} with a phase shift of 92.15°. This equates to a pressure of 70 Pa.

Step 3 – Analysing a trigger events.

The next step of the analysis involved setting up a triggered waveform study at 110 kHz. A 14 V_{p-p} sinusoidal pulse was applied for 730.7×10^{-6} seconds. The waveform shown in Figure 4.82 was achieved from the hydrophone.

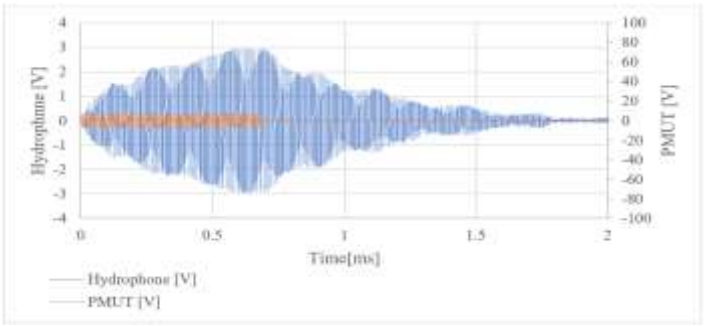

Figure 4.82 ~ Trigger with 14V_{p-p} sinusoidal signal applied across Device 56 for 770.7×10^{-6} seconds. The waveforms show the voltage across PMUT and voltage across hydrophone and the frequency was 110 kHz.

With reference to the Voltage measured 5.876 V_{p-p} at a point 0.627 ms after start of excitation.

4.6.11 Device 57 ~ Circular PMUT- Trench Diameter of 700 µm

This device was a 700 µm diameter circular PMUT device with the cavity being completely sealed from above via a full diaphragm. The device is shown in Figure 4.83.

Figure 4.83 ~ Device 57, a 700µm diameter, circular PMUT device.

The geometrical details for device's design are tabulated in Table 4.23.

Table 4.23 ~ Geometric data for Device 57

Nominal Trench Diameter [µm]	Padmetal Cover [%]	Padmetal Diameter [µm]	Padoxide Diameter [µm]	Pzfilm Diameter [µm]	Design Features
700	80	560	544	700	Circular PMUT

4.6.11.1 Laser Vibrometer Time domain characterisation of Device 57.

Coupling Fluid: Glycerine ~ Cavity Fluid: Air

Device 57 was characterised in the time domain when operating in a glycerine coupling fluid however the first step was the determination of the resonant frequency through a periodic chirp excitation process. The device's measured response is shown in Figure 4.84

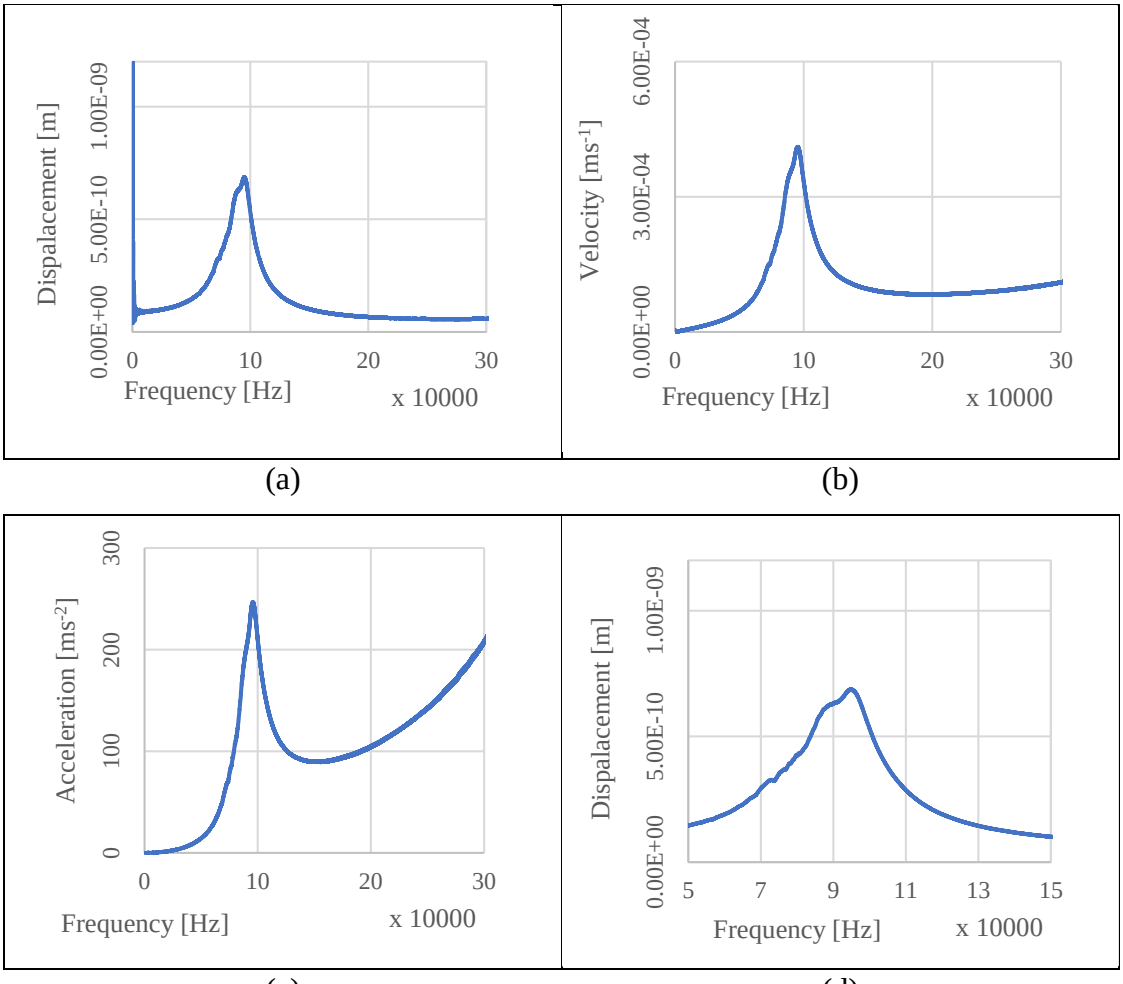

Figure 4.84 - Periodic Chirp frequency between 0 and 300 kHz with peak midpoint (a) displacement, (b) velocity and (c) acceleration values vs frequency for Device 57 in glycerine coupling fluid and air filled cavity. (d) Shows displacement vs frequency at a frequency between 50,000Hz and 150,000Hz.

The next step was to conduct the study in the time domain through the use of Burst Sine excitation.

The following parameters were used for this study:

Cavity fluid: Air

Coupling Fluid:	Glycerine with height from petri dish bottom 2.5mm
Excitation Signal:	Burst sine with amplitude of 18 V_{p-p}
Sampling Frequency:	6.250MHz
Excitation frequency:	95 kHz

The Burst Sine signal used to excite the Device 57 for the time domain studies is shown in Figure 4.85. The frequency utilised was 95 kHz which was determined as the device's resonant frequency via the periodic chirp excitation carried out previously.

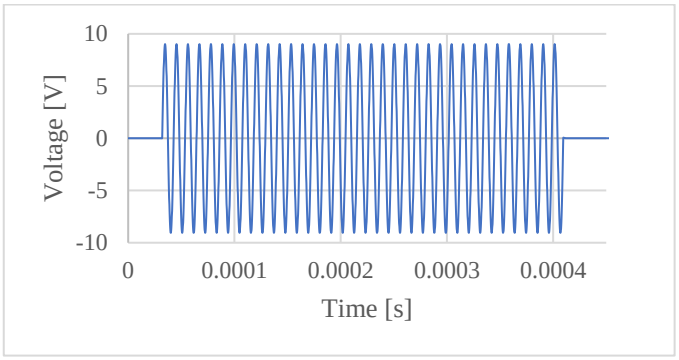

Figure 4.85 ~ The burst sine excitation signal at a frequency of 95 kHz.

The velocity on a number of points on the PMUT was measured with the laser vibrometer and the peak midpoint velocity is presented in Figure 4.86.

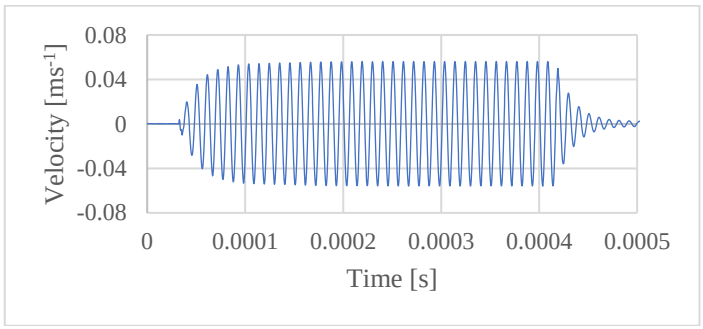

Figure 4.86 ~ The velocity of the diaphragm at the midpoint when subjected to the burst sine excitation.

The peak measured velocity of the diaphragm's midpoint was 0.081438 m/s. The velocity data was then filtered and integrated to obtain the displacement vs time curves as shown in Figure 4.87. This shows the displacement at the midpoint of the diaphragm.

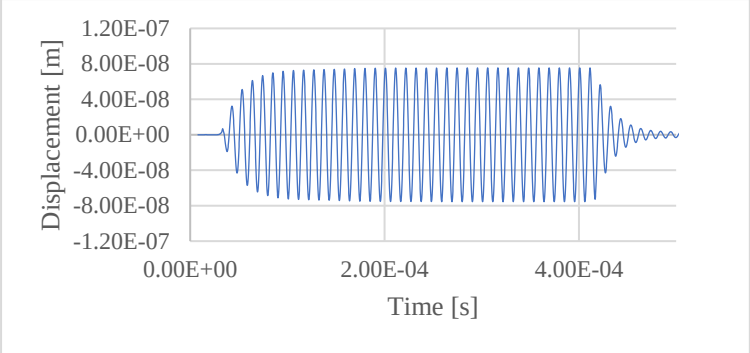

Figure 4.87 ~ The displacement of the diaphragm at the midpoint when subjected to the burst sine excitation.

The peak displacement of the diaphragm midpoint when operating in glycerine coupling fluid at the point of resonance was 7.55×10^{-8} m.

4.6.11.2 Acoustic Experimental Data for Device 57.

Device 57 acting as Transmitter

Step 1 - Setup

The experimental device was placed in a 10 cm diameter petri dish and Device 57 was probed after which the petri dish was filled with isopropanol with the hydrophone being submerged 4 mm below the surface of the fluid. The PMUT cavity was left air filled. The hydrophone's electrical system was set up as shown in Figure 4.16 and connected to the low noise preamplifier.

Step 2 – Determining PMUT resonant frequency.

The first experimental procedure involved connecting the PMUT to a signal generator and running it in continuous transmit mode. The voltage applied across the PMUT was 14 $V_{p\text{-}p}$. Frequencies were cycled and the output of the PMUT were observed. The first frequency with a significant output was 108 kHz with the signals being as shown in Figure 4.88.

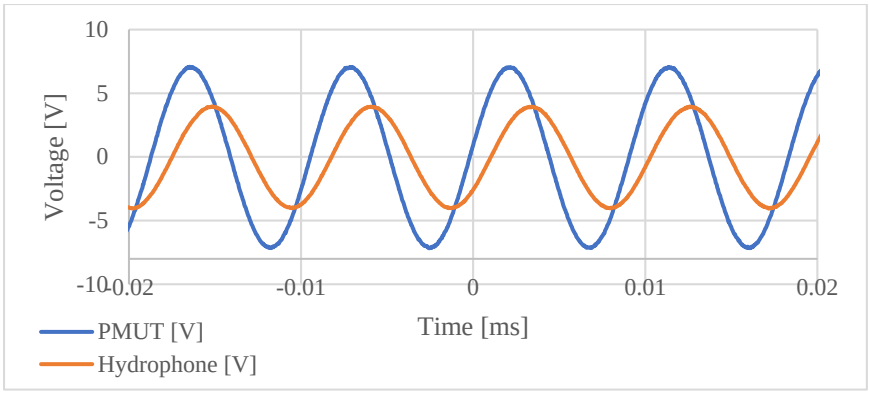

Figure 4.88 ~ Voltage applied across PMUT vs voltage measured out of PMUT pre amp for Device 57 operating as continuous sinusoidal waveform transmitter at 108 kHz

The voltage output from the hydrophone was 8.013 V_{p-p} with a phase shift of 48.10°. This worked out to a pressure of 63.57 Pa.

The excitation frequency was then changed to 110.5 kHz with the signal feed to the PMUT as well as the signal output from hydrophone preamplifier being shown in Figure 4.89.

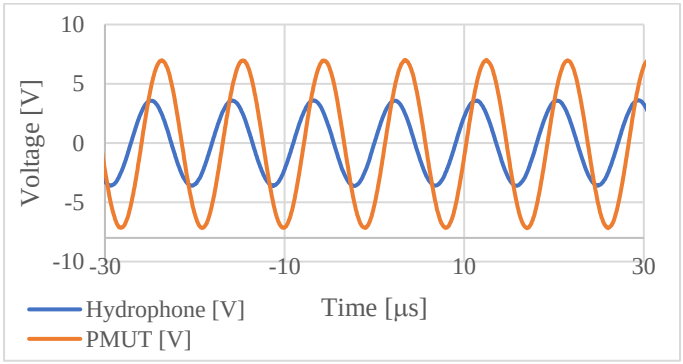

Figure 4.89 ~ Voltage applied across PMUT vs voltage measured out of PMUT pre amp for Device 57 operating as continuous sinusoidal waveform transmitter at 110.5 kHz.

The waveform of the signal from the hydrophone was an undistorted sine wave with an amplitude of 7.206 V_{p-p}. This equated to a sound pressure level of 57.17 Pa. There was also a 47.79° phase shift between the signal input into the PMUT and the signal output from the hydrophone.

The hydrophone was moved 0.5 cm closer to the experimental device and the reading retaken with the result shown in Figure 4.90.

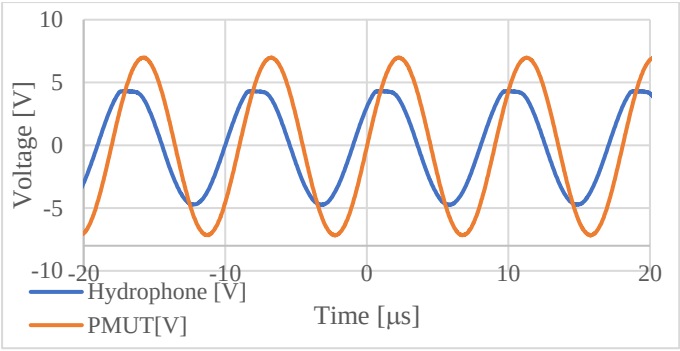

Figure 4.90 ~ Voltage applied across PMUT vs voltage measured out of PMUT pre amp for device 56 operating as continuous sinusoidal waveform transmitter at 110.5 kHz.

The voltage output from the hydrophone at 110.5 kHz was 9.107 V with a phase shift of 35.23°. This equated to an SPL of 72.25 Pa. It was actually higher than that as the amplifier was actually saturated. This can be seen in Figure 4.90

There were measurable outputs at other frequencies albeit at lower outputs such as 4.9 V_{p-p} at 94.5 kHz and 2.39 V_{p-p} at 120.6 kHz.

Step 3 – Analysing through trigger events.

The next step of the analysis involved setting up a triggered waveform to study how the PMUT behaves at 110 kHz with different time of excitation. In the first experiment with the signals being applied for 722.3×10^{-6} seconds, the response is shown in Figure 4.91.

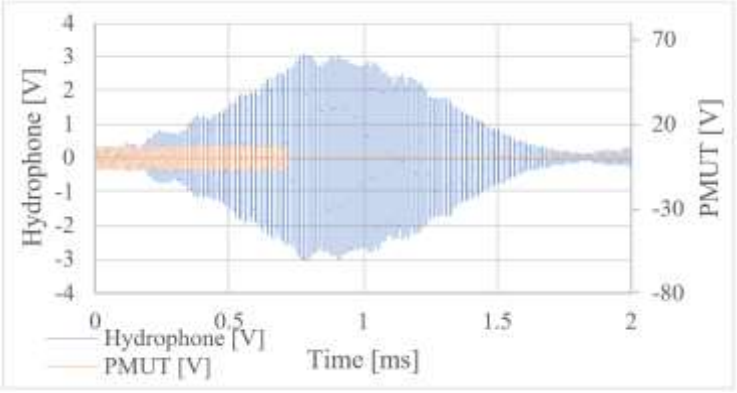

Figure 4.91 ~ Trigger with 14V_{p-p} sinusoidal signal applied across Device 57 for 770.7×10^{-6} seconds at 110 kHz. These waveforms show the voltage across PMUT and voltage across hydrophone.

The voltage achieved from this experiment was 5.763 V_{p-p} at a time 772.4 µs after the start of excitation. Such would work out to an SPL of 45.72 Pa. In the second experiment a 14 V_{p-p} sinusoidal pulse was applied for 1.899 ms.

The waveform shown in Figure 4.92 was achieved from the hydrophone.

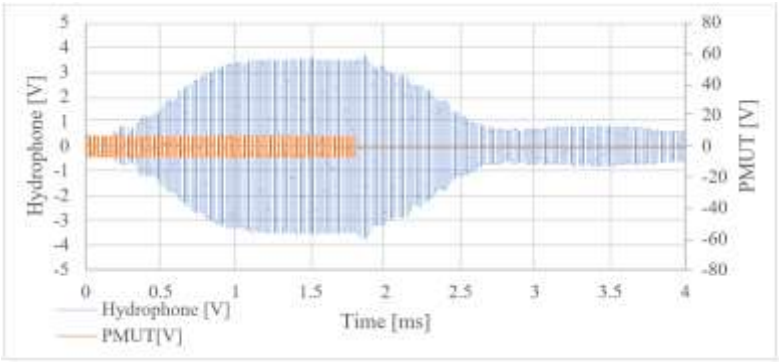

Figure 4.92 ~ Trigger at 110 kHz with 14 V_{p-p} sinusoidal signal applied across Device 57 PMUT for $770.7x10^{-6}$ seconds. These waveforms show the voltage across PMUT and voltage across hydrophone.

The measured voltage from the hydrophone was 7.081 V_{p-p} when this was situated at the experimental measurement point, 1.415 ms after start of excitation. This worked out to a SPL of 56.178 Pa.

Device 57 acting as receiver

This device was difficult to excite and it was impossible to achieve a notable output from the PMUT when operating the hydrophone in transmission mode. This can be seen in trend plot overlaying the low power output shown in Figure 4.93. The output voltage from the PMUT was 40 to 70mV.

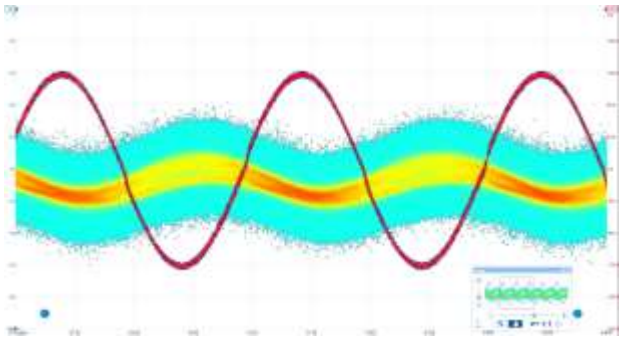

Figure 4.93 ~ Very low voltage output from PMUT when working in reception mode.

4.6.12 Device 58 ~ Circular PMUT- Trench Diameter of 700 µm

This device was a 700 µm diameter circular PMUT device with the cavity being completely sealed from the topside through a full diaphragm. The device frontal

micrograph is shown in Figure 4.94. This device was introduced into the experimental series for a number of reasons namely:

- To be part of the series studying how the resonant frequency varies with PMUT diameter.
- To be part of a series of devices studying how electrode radial cover effects PMUT kinematics and dynamics.

Figure 4.94 ~ Device 58 a 700 µm diameter circular PMUT device.

The specific details of the device's design are tabulated in Table 4.24.

Table 4.24 ~ Geometric data for Device 58

Nominal Trench Diameter [µm]	Padmetal Radial Cover [%]	Padmetal Diameter [µm]	Padoxide Diameter [µm]	Pzfilm Diameter [µm]	Design Features
700	50	350	334	700	Circular PMUT

4.6.12.1Laser Vibrometer characterisation of Device 58

Coupling Fluid: Isopropanol ~ Cavity Fluid: Air

The first step was to determine the device's resonant frequency when operating in an isopropanol environment and with an air filled cavity. This was conducted through device excitation with Periodic Chirp signal and the results are shown in Figure 4.95.

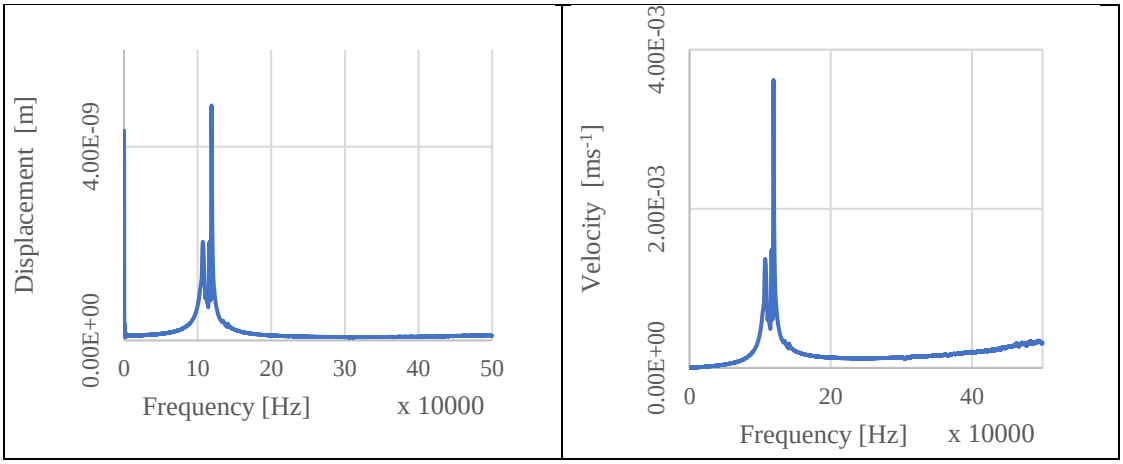

(a) (b)

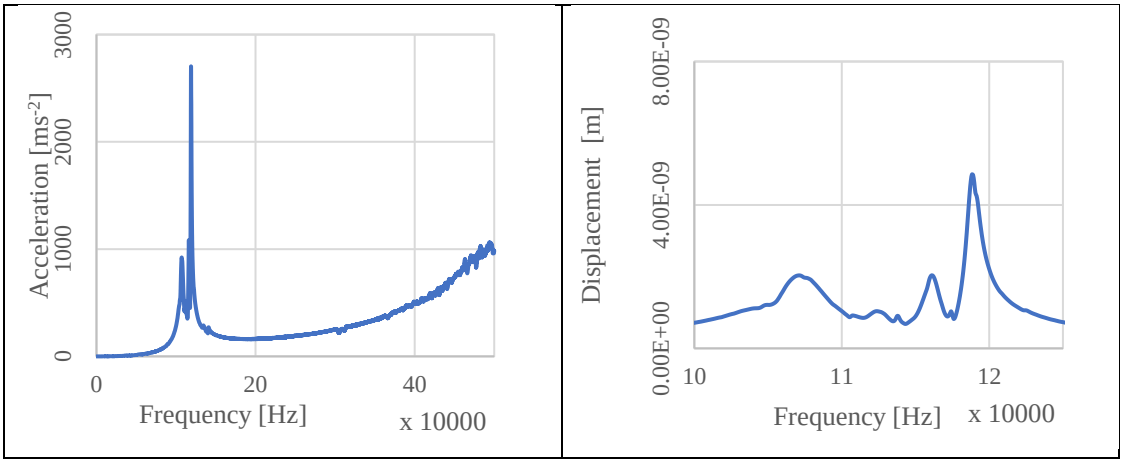

(c) (d)

Figure 4.95 ~ Periodic Chirp frequency between 0 and 50 kHz with (a) Displacement, (b) Velocity and (c) acceleration values vs frequency for Device 58 in isopropanol surrounding and air filled cavity. (d) Shows displacement vs frequency at a frequency between 100,000Hz and 125,000Hz.

Device 58 was then excited with a Sine wave signal at 14 V_{p-p} amplitude. The result of the displacement plot is shown in Figure 4.96.

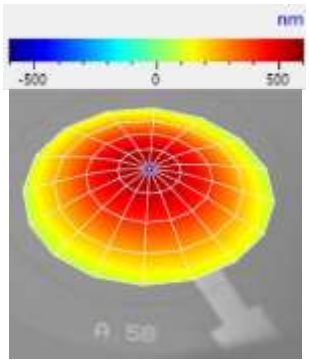

Figure 4.96 ~ Displacement of Device 58 excited with a 14 V_{p-p} periodic chirp signal at a frequency of 118.75 kHz in isopropanol coupling fluid and having an air filled cavity. Values shown are actual readings directly from vibrometer and not normalised with the fluid's refractive index.

The measured parameters for the diaphragm midpoint dynamics are tabulated in Table 4.25.

Table 4.25 ~ Results of Device excitation with Sine wave signal at 14 V_{p-p} amplitude at frequency of 373.44kHz. Deployed in an isopropanol coupling fluid & having an air filled cavity.

Parameter	**Value measured by vibrometer**	**Values normalised by the coupling liquid's refractive index**[†1]
Peak Displacement	584.51 nm	426.65 nm
Peak Velocity	436.12 mm/s	318.34 mm/s
Peak Acceleration	325.40 km/s^2	237.52 km/s^2

Note †1: Using ratio Isopropanol/Air ~ 1.37

Coupling Fluid: Glycerine ~ Cavity Fluid: Air

The Device 58 was then characterised in the time domain in a glycerine coupling fluid and an air filled cavity. The first step necessary was to determine the resonant frequency of the device when operating in this particular fluid excited by a periodic chirp signal. The results are shown in Figure 4.97.

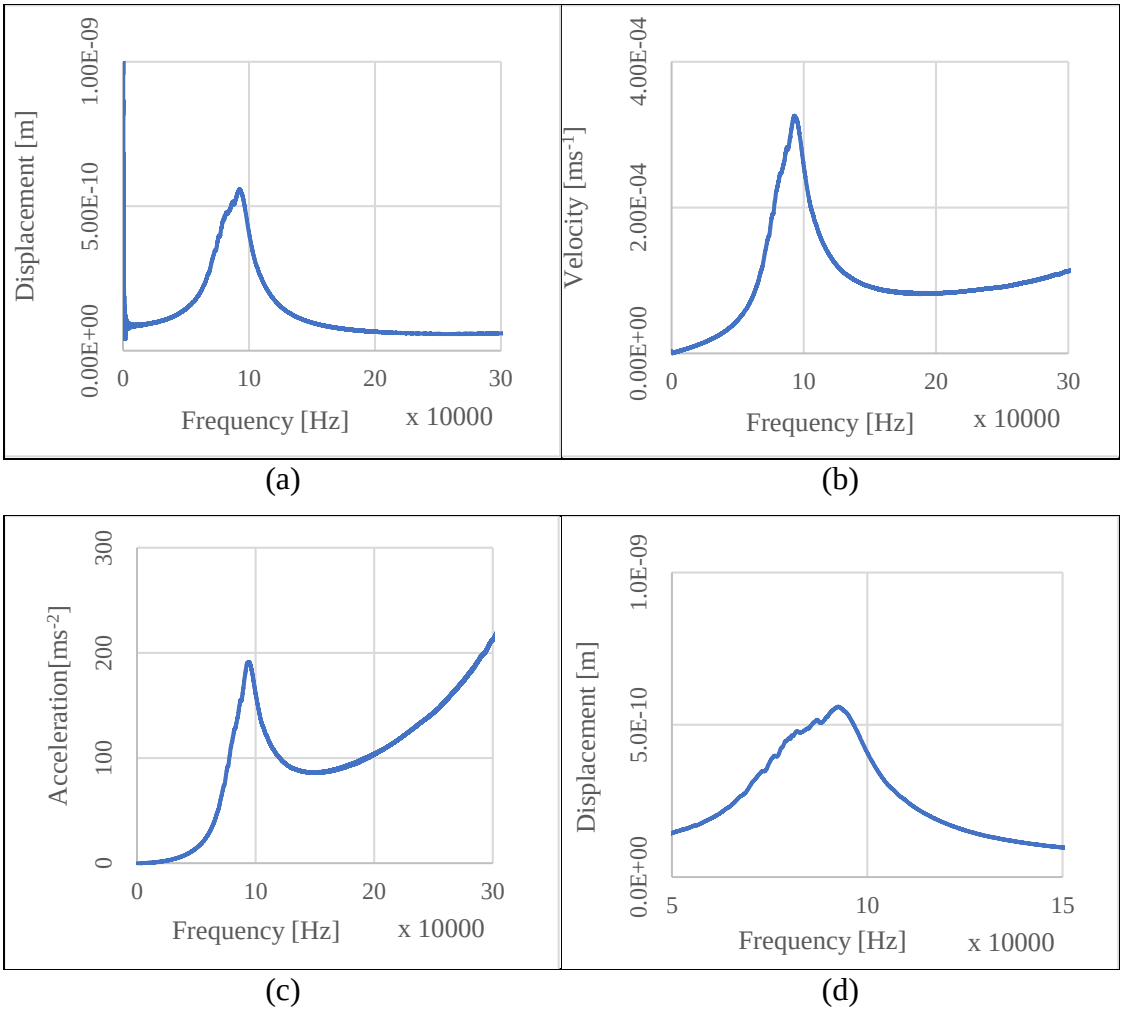

Figure 4.97 - Periodic Chirp frequency between 0 and 40 kHz with peak midpoint (a) displacement, (b) velocity and (c) acceleration values vs frequency for Device 58 in glycerine coupling fluid and air filled cavity. (d) Shows displacement vs frequency at a frequency between 50,000 Hz and 150,000 Hz.

After determining the resonant frequency the time domain study with burst sine excitation was conducted.

The following parameters were used for this study:

Cavity fluid:	Air
Coupling Fluid:	Glycerine with height from petri dish bottom 2.5mm
Excitation Signal:	Burst sine with amplitude of 18 V_{p-p}
Sampling Frequency:	6.250 MHz
Excitation frequency:	92.7 kHz

The burst sine excitation pulse used is shown in Figure 4.98. The peak voltage used was $18V_{p-p}$. This value was selected in view of the maximum voltage which could be handled by the PMUT and also the maximum voltage reached by the laser vibrometer signal generating equipment.

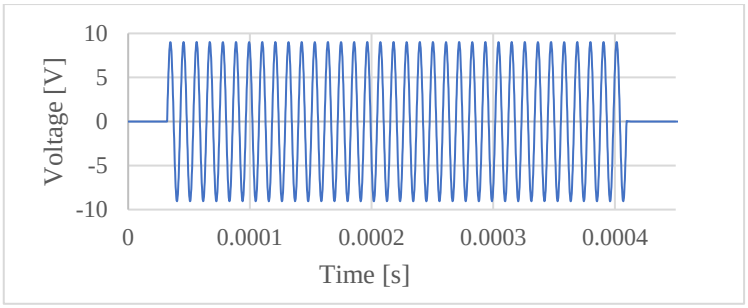

Figure 4.98 ~ The burst sine excitation signal at a frequency of 92.7 kHz

The velocity of the movements at multiple points on the PMUT surface were measured with the laser vibrometer and the resulting plot of the midpoint displacement is shown in Figure 4.99. The maximum velocity reached was 0.045 ms^{-1}.

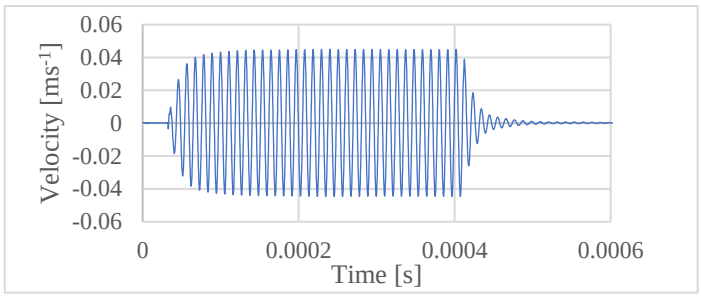

Figure 4.99 ~ The velocity of the diaphragm at the midpoint when subjected to the burst sine excitation.

The velocity data was filtered and integrated to achieve the displacement data for each point. The resultant peak diaphragm midpoint displacement is shown in Figure 4.100.

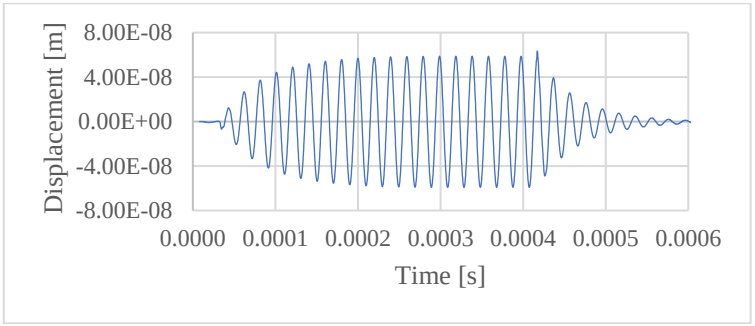

Figure 4.100 ~ The displacement of the diaphragm at the midpoint when subjected to the burst sine excitation.

The peak midpoint displacement on the diaphragm was measured at $6.34x10^{-8}$ m.

4.6.12.2 Acoustic experimental Data for Device 58

Device 58 acting as Transmitter

Step 1 - Setup

The experimental device was placed in 10 cm diameter petri dish and Device 58 was probed. The dish was filled with isopropanol with the hydrophone being submerged 4mm below the surface of the fluid. The cavity was left air filled and the hydrophone electrical system was set up as shown in Figure 4.16, with the hydrophone being connected to a low noise preamplifier.

Step 2 – Determining PMUT resonant frequency.

The first experimental procedure involved connecting the PMUT to a signal generator and running it in continuous transmit mode. The voltage applied across the PMUT was $14V_{p\text{-}p}$. Frequencies of the excitation signal were cycled and the output of the PMUT were observed. The first frequency with a significant output was 110.96 kHz with the signals being as shown in Figure 4.101.

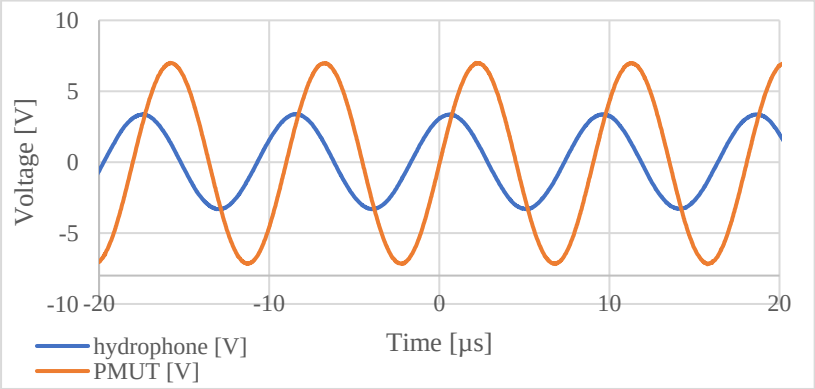

Figure 4.101 ~ Voltage applied across PMUT vs voltage measured out of PMUT pre amp for Device 58 operating as continuous sinusoidal waveform transmitter at 108 kHz

The voltage was 6.714 V with a phase shift of 67.79°. This worked out to a pressure of 53 Pa.

Step 3 – Analysing through trigger events.

The next step of the analysis involved setting up a triggered waveform study at 110.74 kHz. A 14 $V_{p\text{-}p}$ sinusoidal pulse was applied for $731x10^{-6}$ seconds. The waveform shown in Figure 4.102 was the output from the hydrophone.

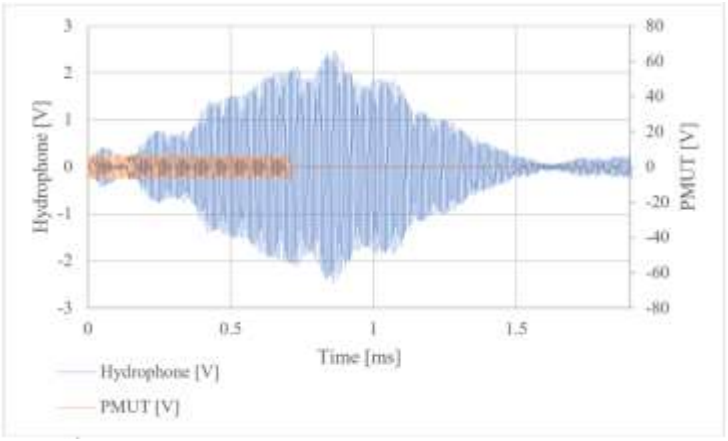

Figure 4.102 ~ Trigger with 14V_{p-p} sinusoidal signal applied across Device 58 PMUT for 731.1x10^{-6} seconds. Shows voltage across PMUT and voltage across hydrophone. Note discrepancy in scale on the y axis. Excitation frequency 110 kHz.

With reference to the voltage measured 4.193V at a point 0.731ms after start of excitation.

Device 58 acting as receiver

This device was found to be difficult to excite and no voltage output was noted even when the power supply to the hydrophone was increased to above 9V DC level. This continued to indicate towards the fact that solid diaphragm devices operated better when transmitting rather than when receiving ultrasonic radiation.

4.6.13 Device 59 ~ Circular PMUT-Trench Diameter of 700 µm

Device 59, the photo micrograph of which is being shown in Figure 4.103 was included to study the effect of having an electrode with a large radial cover percentage on device performance when operating in different fluids.

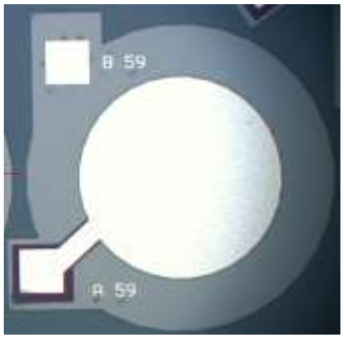

Figure 4.103 ~ Frontal device micrograph of Device 59, a 700µm diameter PMUT.

The geometrical parameters of Device 59 are shown in Table 4.26.

Table 4.26 ~ Geometric data for Device 59

Nominal Trench Diameter [µm]	Padmetal Cover [%]	Padmetal Diameter [µm]	Padoxide Diameter [µm]	Pzfilm Diameter [µm]	Design Features
700	98	690	674	700	Circular PMUT

4.6.13.1 Laser Vibrometer characterisation of Device 59

Coupling Fluid: Isopropanol ~ Cavity Fluid: Air

Testing of a Device 59 deployed in an isopropanol coupling fluid and air filled cavity was started through the use of a periodic chirp signal to determine the resonant frequency.

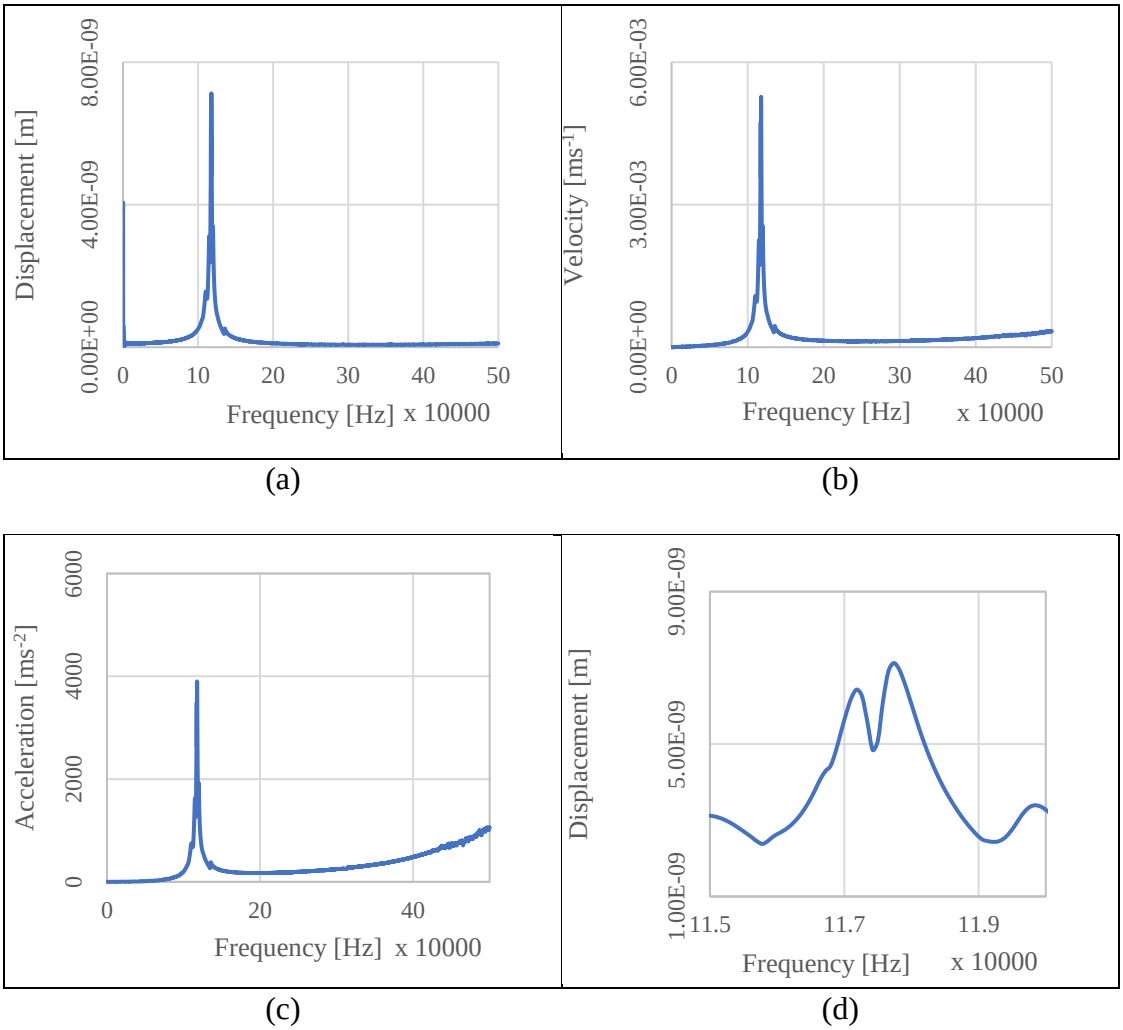

Figure 4.104- Periodic Chirp frequency between 0 and 500 kHz with (a) Displacement, (b) Velocity and (c) acceleration values vs frequency for Device 59 in isopropanol coupling fluid and air filled cavity. (d) Shows displacement vs frequency at a frequency between 115 kHz and 120 kHz. Values shown are actual readings directly from vibrometer and not normalised with the fluid's refractive index.

One mode of oscillation was identified by the laser vibrometer during Periodic Chirp excitation. The device was excited at this frequency through a Sine wave signal at an excitation voltage of 14 V_{p-p}. The result of the excitation is shown in Figure 4.105.

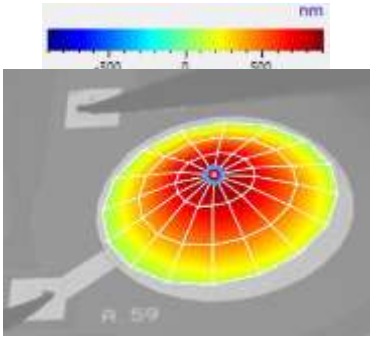

Figure 4.105 ~ Displacement of Device 59 excited with a 14V_{p-p} sine wave signal at a frequency of 117.66 kHz in isopropanol coupling fluid and air filled cavity. Values shown are actual readings directly from vibrometer and not normalised with the fluid's refractive index.

The results from the sine excitation are tabulated in Table 4.27.

Table 4.27 ~ Results of Device excitation with Sine wave signal at 14 V_{p-p} amplitude at frequency of 117.66 kHz in isopropanol coupling fluid & isopropanol filled cavity.

Parameter	**Value measured by vibrometer**	**Values normalised by the coupling liquid's refractive index**[†1]
Peak Displacement	888.5 nm	648.54 nm
Peak Velocity	0.6568 m/s	0.4794 m/s
Peak Acceleration	485.6 km/s^2	354.45 km/s^2

Note †1: Using ratio Isopropanol/Air ~ 1.37

The same Device 59 was then excited in the same set up with Sine wave signal this time with an amplitude of 19 V_{p-p}. The device was then subjected to Device excitation using an excitation frequency of 117.66 kHz. The displacement is shown in Figure 4.106.

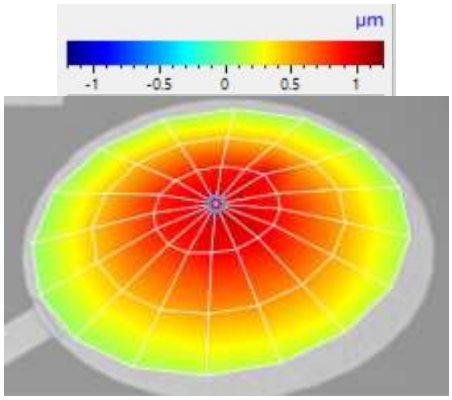

Figure 4.106- Displacement of Device 59 excited with a 19V_{p-p} sine wave signal at a frequency of 117.66 kHz. Device in isopropanol coupling fluid & air filled cavity.

The results of the sine wave excitation are shown in Table 4.28.

Table 4.28 ~ Results of Device excitation with Sine wave signal at 19 V_{p-p} amplitude at frequency of 117.66 kHz in isopropanol coupling fluid and isopropanol filled cavity.

Parameter	**Value measured by vibrometer**	**Values normalised by the coupling liquid's refractive index**[†1]
Peak Displacement	1.026 µm	0.749 µm
Peak Velocity	0.7583 m/s	0.554 m/s
Peak Acceleration	560.6 km/s^2	409.338 km/s^2

Note †1: Using ratio Isopropanol/Air ~ 1.37

The device was next tested in the time domain still in the isopropanol coupling fluid and air in cavity at a signal amplitude of 19V_{p-p}. The Device 59 was excited at its resonant excitation frequency of 117.66 kHz. The laser vibrometer measured the vibration velocity at the centre point of the PMUT and the resulting velocity - time relationship is shown in Figure 4.107.

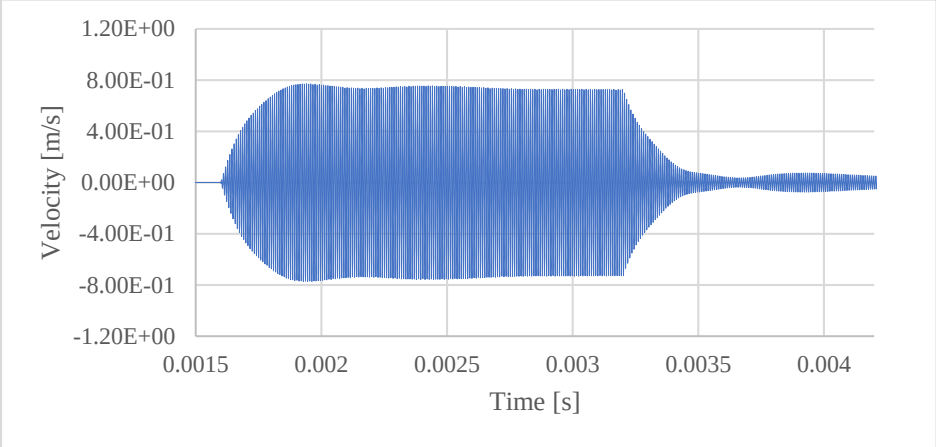

Figure 4.107 – Time domain laser vibrometer data for Device 59 in isopropanol as coupling fluid and an air filled cavity.

Through filtering and integration the displacement – time relationship shown in Figure 4.108 was derived.

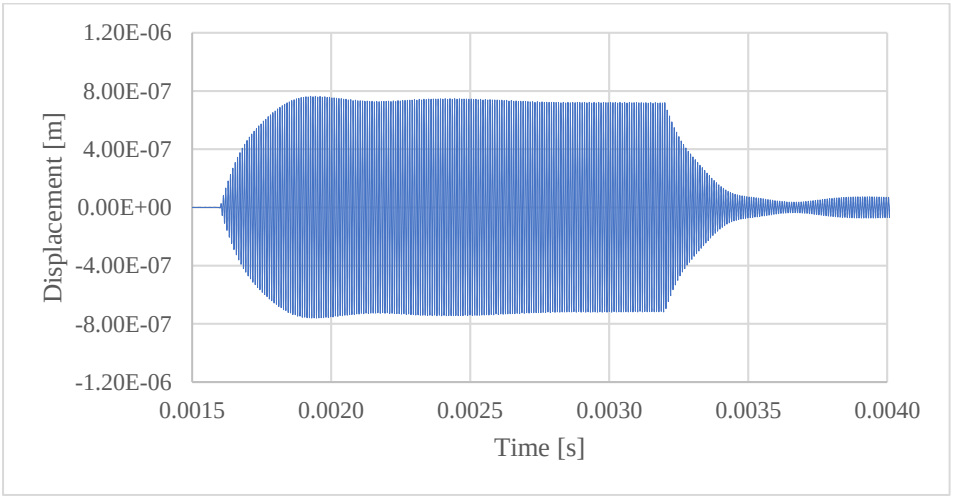

Figure 4.108 Displacement – time graph of device 55 derived by filtering and integrating the velocity – time results.

In this case the maximum vibration velocity reached was 0.563 m/s and maximum centre point displacement reached was 0.764×10^{-6} m.

Coupling Fluid: Glycerine ~ Cavity Fluid: Air

Device 59 was next tested with glycerine as coupling fluid and air as cavity fluid. To determine the resonant frequency the device was excited with a periodic chirp signal. The results are shown in Figure 4.109.

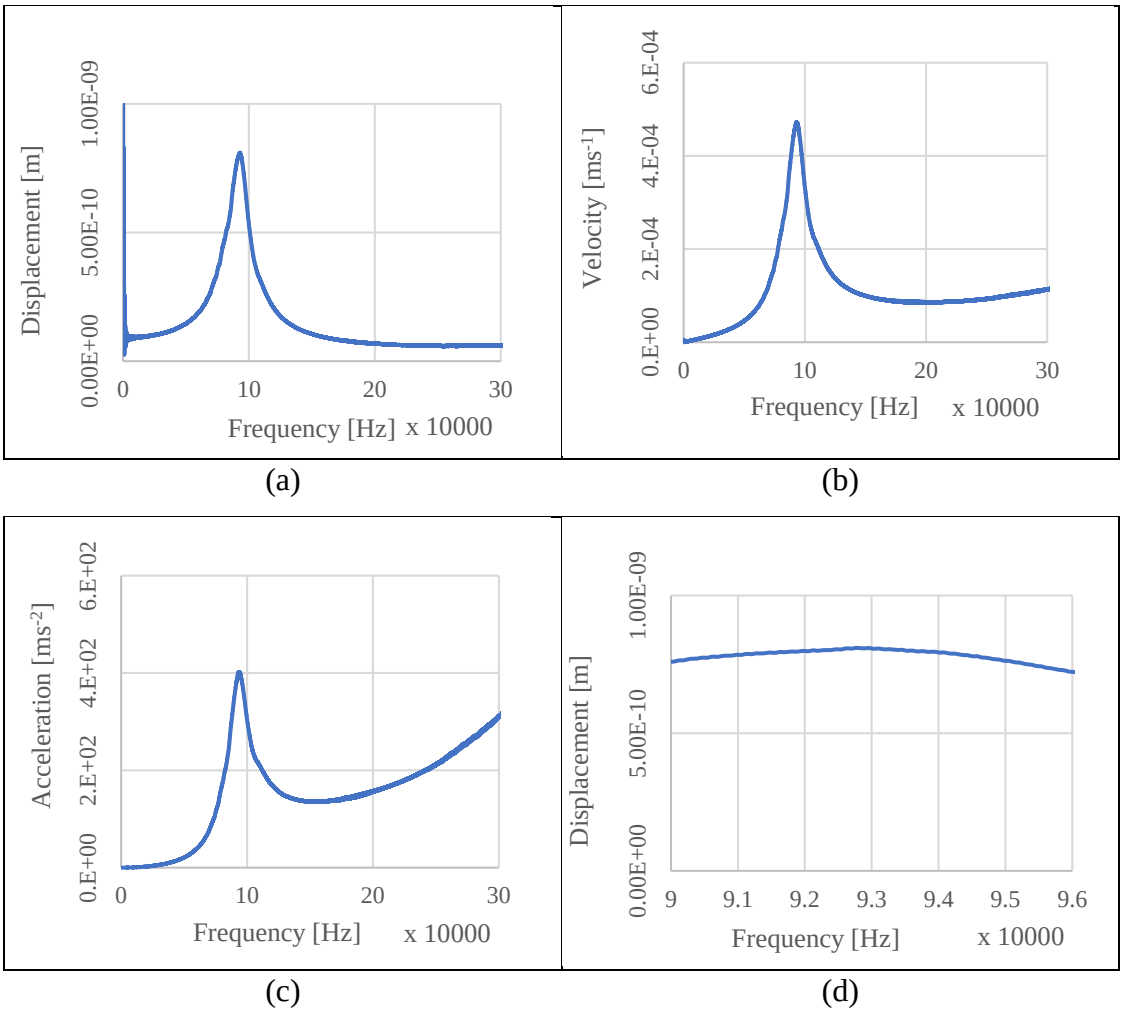

Figure 4.109 ~ Periodic Chirp frequency between 0 and 300 kHz with peak midpoint (a) displacement, (b) velocity and (c) acceleration values vs frequency for Device 59 in glycerine coupling fluid and air filled cavity. (d) Shows displacement vs frequency at a frequency between 90,000 Hz and 96,000 Hz.

The resonant frequency in glycerine was therefore established at 93.1 kHz. The mode of vibration at this frequency is shown in Figure 4.110.

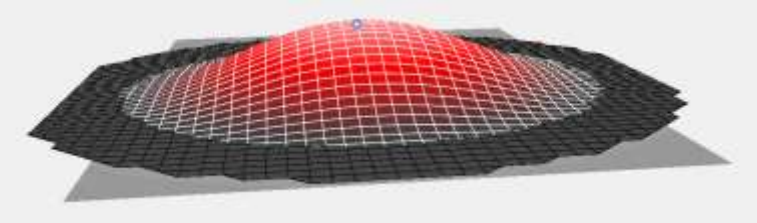

Figure 4.110 ~ Periodic chirp modal shape at resonant frequency

The next phase of the experimental process involved burst sine excitation at $18V_{p\text{-}p}$. The study was conducted in the time domain

The following parameters were used for this study:

Cavity fluid:	Air
Coupling Fluid:	Glycerine with height from petri dish bottom 2.5 mm
Excitation Signal:	Burst Sine with amplitude of 18 $V_{p\text{-}p}$
Sampling Frequency:	6.250 MHz
Excitation frequency:	93.1 kHz

The signal used to excite the PMUT is shown in Figure 4.111. It was a burst sine wave set at the frequency of 93.1 kHz which was determined to be the PMUT' s resonant frequency through the periodic chirp excitation process.

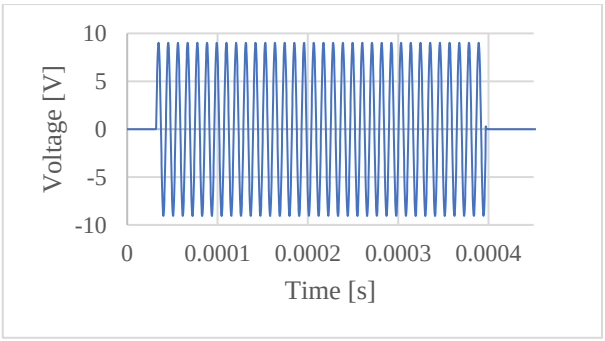

Figure 4.111 ~ The Burst Sine excitation signal at a frequency of 93.1 kHz

The vibrometer measured velocity of the points on the PMUT surface. In this experimental process the vibrometer measured velocity of movement on multiple points on the PMUT surface to get an accurate picture of the PMUT dynamics. The waveform is shown in Figure 4.112

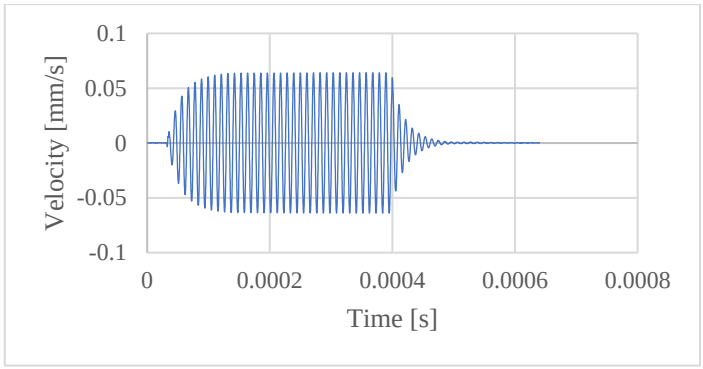

Figure 4.112 ~ The velocity of the diaphragm at the midpoint when subjected to the burst sine excitation.

The maximum velocity reached by the diaphragm midpoint was 0.0641m/s. By integrating the velocity the displacement was obtained which is in turn plotted in Figure 4.113.

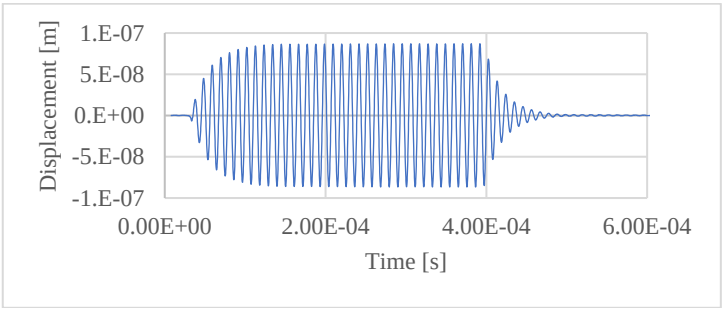

Figure 4.113 ~ The displacement of the diaphragm at the midpoint when subjected to the burst sine excitation.

The peak displacement reached at the diaphragm midpoint was 8.71×10^{-8} m.

4.6.13.2 Acoustic Experimental Data for device 59

Device 59 acting as Transmitter

Step 1 - Setup

The experimental device was placed in a 10 cm diameter petri dish and Device 59 was probed. The dish was then filled with isopropanol with the hydrophone tip being submerged under the surface of the fluid. The PMUT's cavity was left air filled. The hydrophone's electrical system was set up as shown in Figure 4.16 and connected to the low noise preamplifier.

Step 2 – Determining PMUT resonant frequency.

The first experimental procedure involved connecting the PMUT to a signal generator and running it in continuous transmit mode. The voltage applied across the PMUT was 14 $V_{p\text{-}p}$. Frequencies were cycled and the output of the PMUT was observed. The first

frequency with a significant output was 111 kHz with the signals being as shown in Figure 4.114.

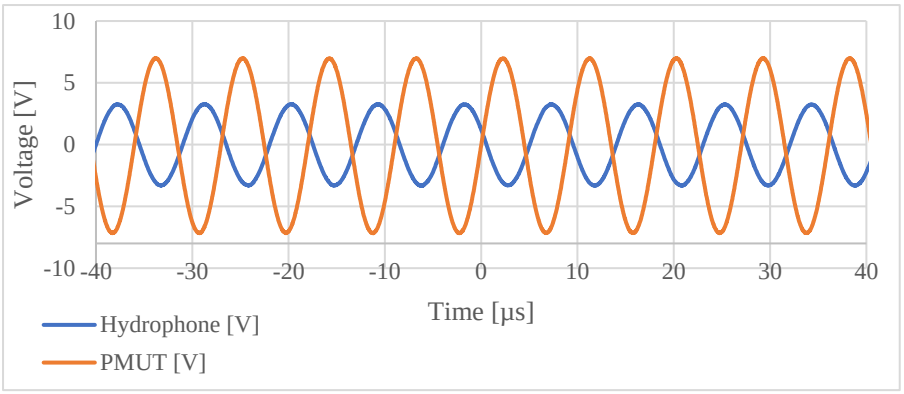

Figure 4.114 ~ Voltage applied across PMUT vs voltage measured out of PMUT pre amp for Device 59 operating as continuous sinusoidal waveform transmitter at 108 kHz

The voltage measured at the hydrophone was 6.592 V_{p-p} which worked out to an SPL of 55.39 Pa. The excitation frequency to the PMUT was changed to 110.8 kHz. The signal exciting the PMUT as well as that measured from hydrophone preamplifier are shown in Figure 4.115.

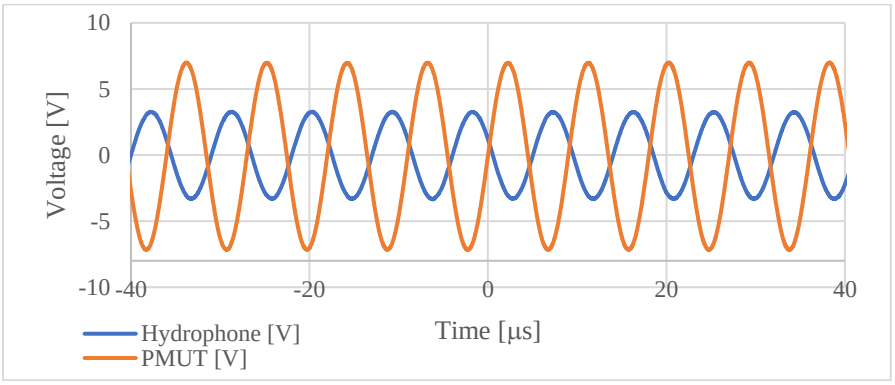

Figure 4.115 ~ Voltage applied across PMUT vs voltage measured out of PMUT pre amp for Device 59 operating as continuous sinusoidal waveform transmitter at 110.8 kHz.

The waveform measured from the hydrophone was an undistorted pure sine wave with 6.593V_{p-p}. This equated to a sound pressure level of 52 Pa. There is also a 158.9° phase shift between the signal input into the PMUT and the signal output from the hydrophone.

The best output measured from the PMUT occurred at a frequency of 116.8 kHz when a voltage of 22 mV was measured by the hydrophone without the pre amplifier. This worked out to 174 Pa. This value was noted to be very close to the value calculated through finite element modelling in section 3.7 (FEA VI) which was 167.48 Pa. It could therefore be concluded that the pressure values calculated through the FEA and those measured in the experimental process were broadly in line with each other. While it is also pertinent to point out that in this case the electrode coverage was different from that used in the FEA, experimental work had already demonstrated that the effect of electrode coverage on PMUT dynamics was less in practice than what was anticipated through the Finite Element Modelling.

Step 3 – Analysing through trigger events.

The next step of the analysis involved setting up a triggered waveform to study how the PMUT behaves at 110 kHz with different time of excitation. In the first experiment with the signals being applied for 722.3×10^{-6} seconds, response is shown in Figure 4.116.

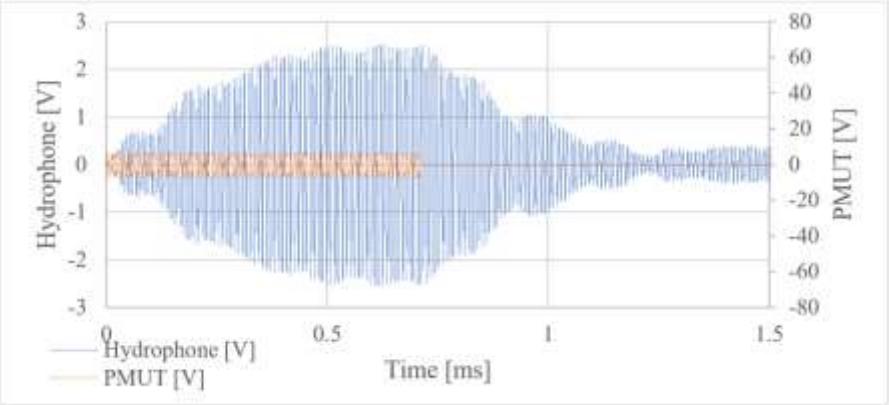

Figure 4.116 ~ Trigger with $14V_{p-p}$ sinusoidal signal applied across Device 59 PMUT for 719.3×10^{-6} seconds. Shows voltage across PMUT and voltage across hydrophone. At an excitation frequency of 110.8 kHz

The voltage achieved from this experiment was $4.833V_{p-p}$ at a time 509.6 µs after the start of excitation. Such would work out to an SPL of 38.344 Pa.

Device 59 acting as receiver

Device 59 did not excite easily. One of the frequencies at which the device was successfully excited was at 99 kHz. The voltage measured was 209.4 mV as can be seen in Figure 4.117.

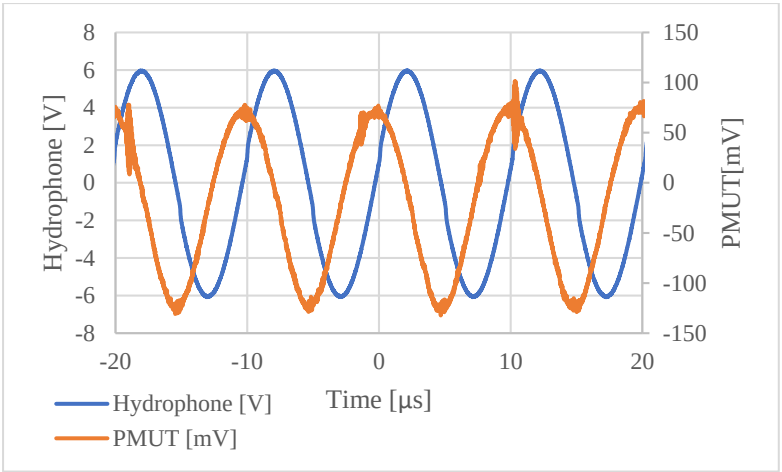

Figure 4.117 ~ PMUT voltage output when excited by hydrophone at 99 kHz.

4.6.14 Device 55 ~ Octagonal shaped PMUT with a 700 µm trench

As indicated in Chapter 3 FEM results pointed towards an improvement in PMUT dynamics through the use of an octagonal shaped PMUT design. It was therefore decided to build and test the eight sided PMUT device shown in Figure 4.118.

(a) (b)

Figure 4.118 ~ Micrograph showing (a) frontal side of Device 55 with the part in white shows padmetal, AlN is green and SiO is dark purple .

The PMUT dimensions are shown in Figure 4.119.

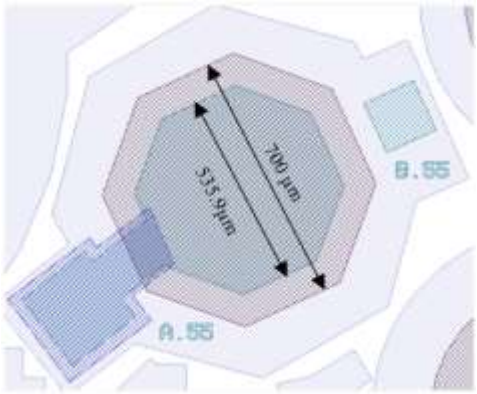

Figure 4.119 ~ Length of Hexagon 700µm with length of piezoelectric layer being 535.9 µm

Table 4.29 ~ Geometric data for device 55

Nominal Trench Diameter [µm]	Ratio Padmetal Cover:AlN [%]	Padmetal Length [µm]	Padoxide Diameter [µm]	Pzfilm Diameter [µm]	Special Design Features
700	76.4	535.9	N/A	700	Circular PMUT with holes around the electrode.

4.6.14.1Laser Vibrometer experimental data for Device 55

Coupling Fluid: Isopropanol ~ Cavity Fluid: Air

In a bid to find the resonant frequency the device was excited with Periodic Chirp signal when deployed in an isopropanol coupling fluid and air filled cavity. The results are shown in Figure 4.120.

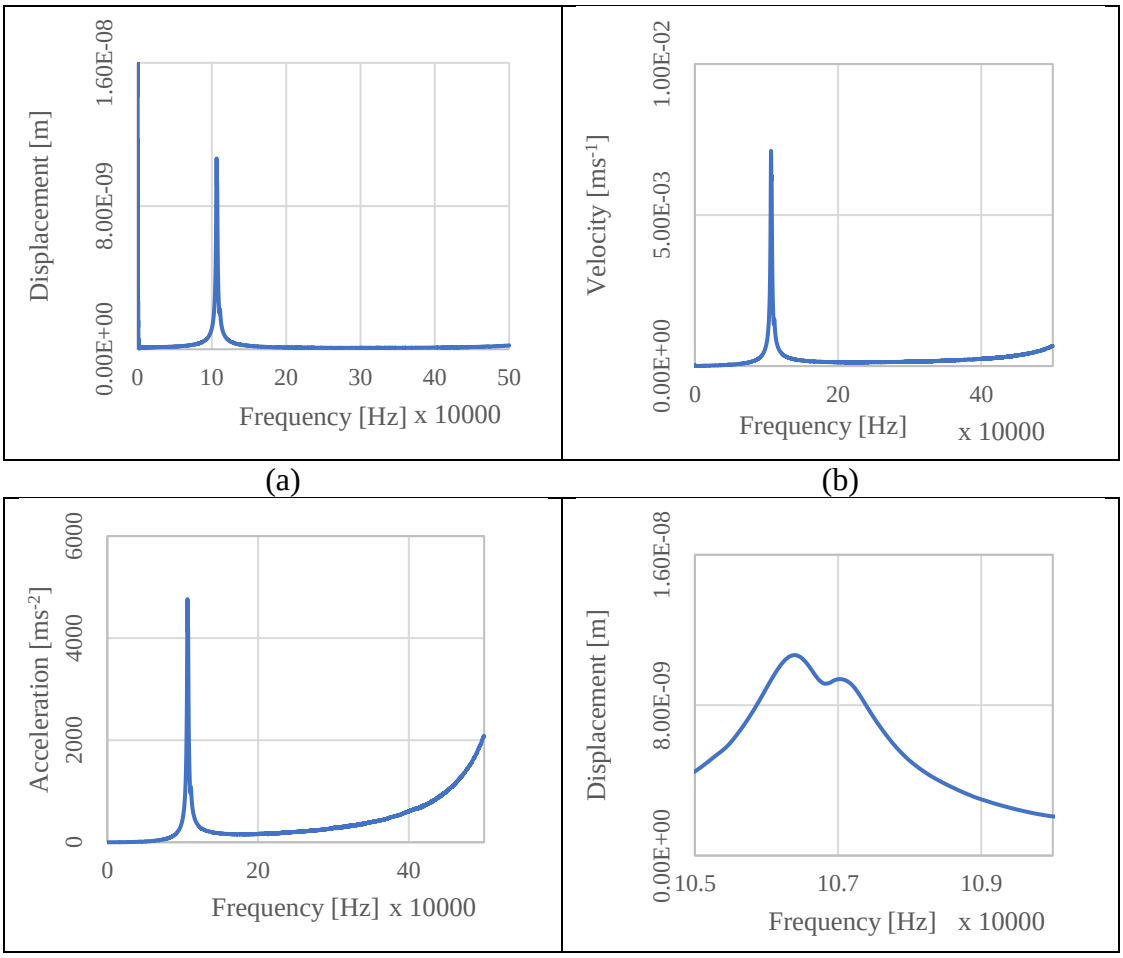

Figure 4.120 ~ Periodic Chirp frequency between 0 and 500 kHz with (a) Displacement, (b) Velocity and (c) acceleration values vs frequency for Device 55 in isopropanol coupling fluid and air filled cavity. (d) Shows displacement vs frequency at a frequency between 105 kHz and 110 kHz.

Two modes of oscillation where identified by Laser Vibrometer during Periodic Chirp excitation as shown in Figure 4.121.

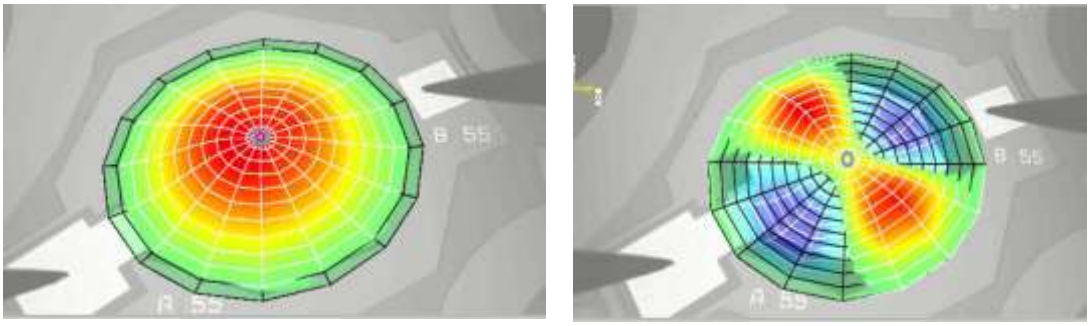

(a) (b)

Figure 4.121 ~ Displacement of Device 55 excited with a periodic chirp signal at a frequency (a)106.41 kHz; (b)500 kHz in isopropanol coupling fluid and air filled cavity. Values shown are actual readings directly from vibrometer and not normalised with the fluid's refractive index.

The device was subjected to sine wave excitation with 14 $V_{p\text{-}p}$ amplitude signal.

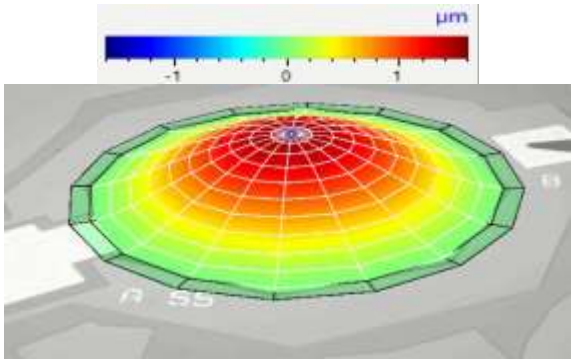

Figure 4.122 ~ Displacement of Device 55 excited with a 14 $V_{p\text{-}p}$ sine wave signal at a frequency 106.25 kHz in isopropanol coupling fluid and air filled cavity. Values shown are actual readings directly from vibrometer and not normalised with the fluid's refractive index.

The results from the sine wave excitation are shown in Table 4.30.

Table 4.30 ~ Maximum values at device centre point- frequency 106.25 kHz

Parameter	**Value measured by vibrometer**	**Values normalised by the coupling liquid's refractive index**[†1]
Peak Displacement	1.49 µm	1.087 µm
Peak Velocity	0.9960 m/s	0.727 m/s
Peak Acceleration	664.93 km/s^2	485.35 km/s^2

Note †1: Using ratio Isopropanol/Air ~ 1.37

Coupling Fluid: Glycerine ~ Cavity Fluid: Air

The device was next tested in glycerine to study how it behaves in viscous fluids. Laser Vibrometer Time domain experimental data for Device 55 with glycerine coupling fluid and an air filled cavity.

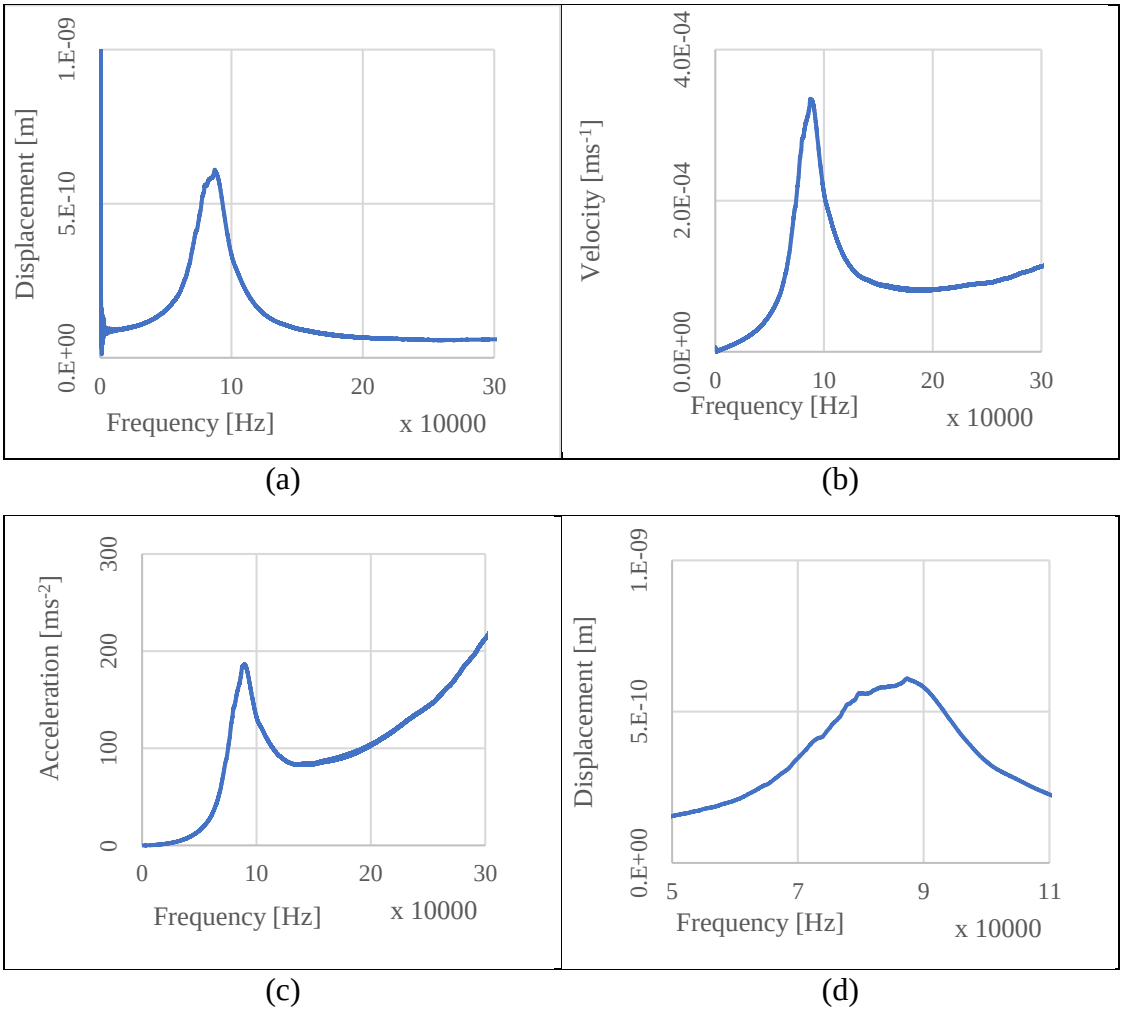

Figure 4.123 ~ Periodic Chirp frequency between 0 and 300 kHz with peak midpoint (a) displacement, (b) velocity and (c) acceleration values vs frequency for Device 55 in glycerine coupling fluid and air filled cavity. (d) Shows displacement vs frequency at a frequency between 50 kHz and 110 kHz.

The device was then studied in the time domain with the following parameters being used for this study:

Cavity fluid:	Air
Coupling Fluid:	Glycerine with height from petri dish bottom 2.5 mm
Excitation Signal:	Burst sine with amplitude of 18 V_{p-p}
Sampling Frequency:	6.250 MHz
Excitation frequency:	87.4 kHz

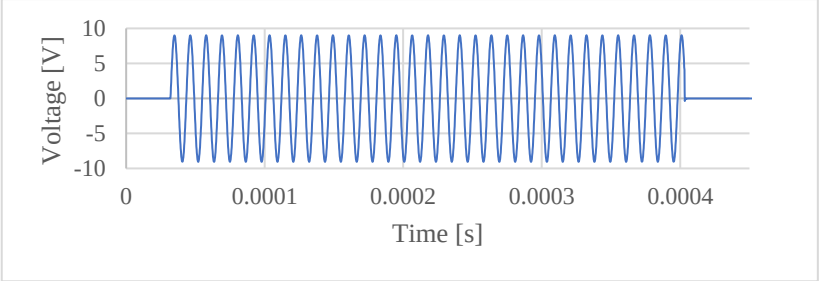

Figure 4.124 ~ The burst sine excitation signal used at a frequency of 87.4 kHz.

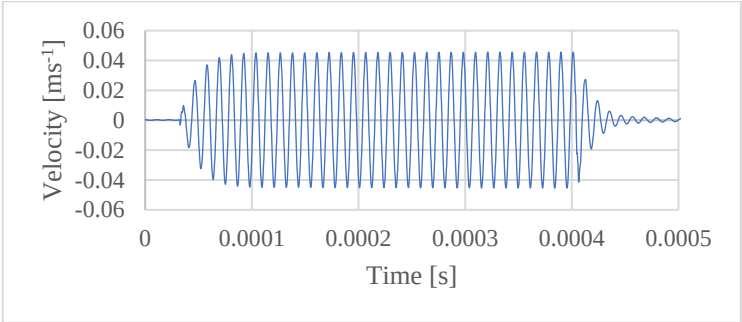

Figure 4.125 ~ The velocity of the diaphragm at the midpoint when subjected to the burst sine excitation.

The peak velocity was 0.0456 m/s.

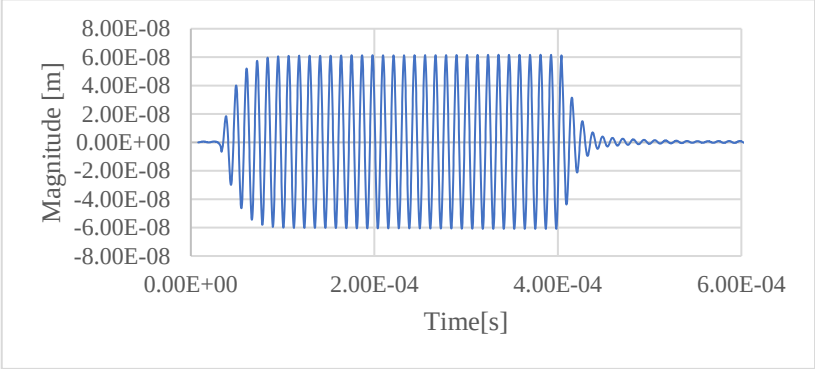

Figure 4.126 ~ The displacement of the diaphragm at the midpoint when subjected to the burst sine excitation.

The peak diaphragm midpoint displacement was 6.17×10^{-8} m when measured at the resonant frequency of 87.4 kHz.

4.6.14.2Acoustic Experimental Data.

Device 55 acting as Transmitter

Step 1 - Setup

The device was placed in a 10 cm diameter petri dish which was filled with isopropanol up to the 8 mm mark. The PMUT cavity was left air filled and the device was probed. The hydrophone system was set up as shown in Figure 4.16 and connected to the low noise preamplifier.

Step 2 – Determining PMUT resonant frequency.

The first experimental procedure involved connecting the PMUT to a signal generator and running it in continuous transmit mode. The voltage applied across the PMUT was 14 $V_{p\text{-}p}$. The signal being transmitted to the PMUT as well as that coming from hydrophone preamplifier and are shown in Figure 4.127

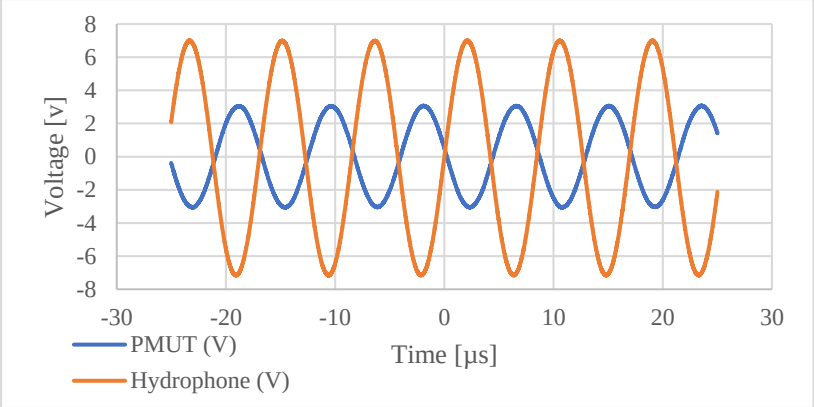

Figure 4.127 ~ Voltage applied across PMUT vs voltage measured out of PMUT pre amp for Device 55 operating as continuous sinusoidal waveform transmitter at 118 kHz.

The signal waveform coming from hydrophone was an undistorted sine wave with 6.15 $V_{p\text{-}p}$ which equated to 51.68 Pa. There was also a 190° phase shift. Another frequency was then selected namely 107 kHz and the response from the hydrophone was again reviewed as shown in Figure 4.128.

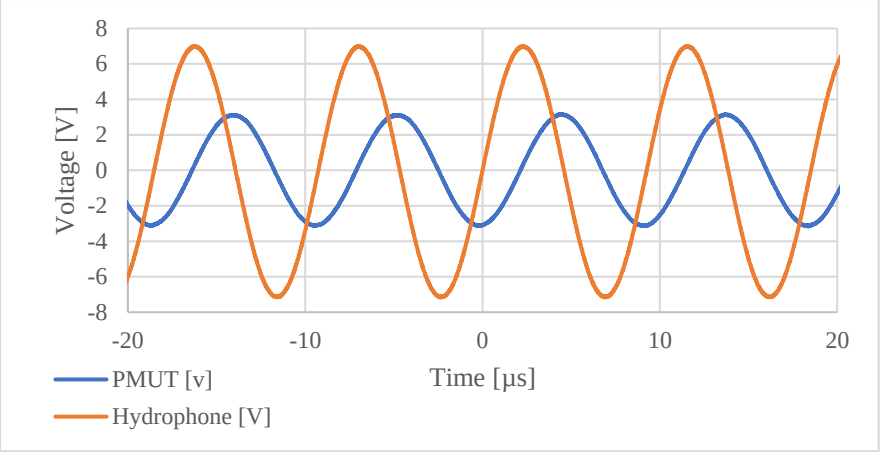

Figure 4.128 ~ Voltage applied across PMUT vs voltage measured out of PMUT pre amp for Device 55 operating as continuous sinusoidal waveform transmitter at 107 kHz

In this case the hydrophone output reached 6.30 V_{p-p} equating to 53 Pa. It was noted that the phase shift decreased to 84°. A further reading at 106 kHz was taken and is shown in Figure 4.129.

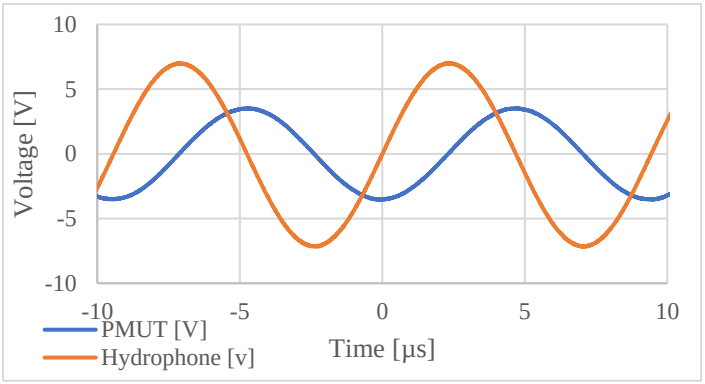

Figure 4.129 ~ Voltage applied across PMUT vs voltage measured out of PMUT pre amp for Device 55 operating as continuous sinusoidal waveform transmitter at 106 kHz.

The voltage in this case was 14 V_{p-p} which equated to a Sound Pressure Level of 112 Pa. The phase shift between the two signals was 89°.

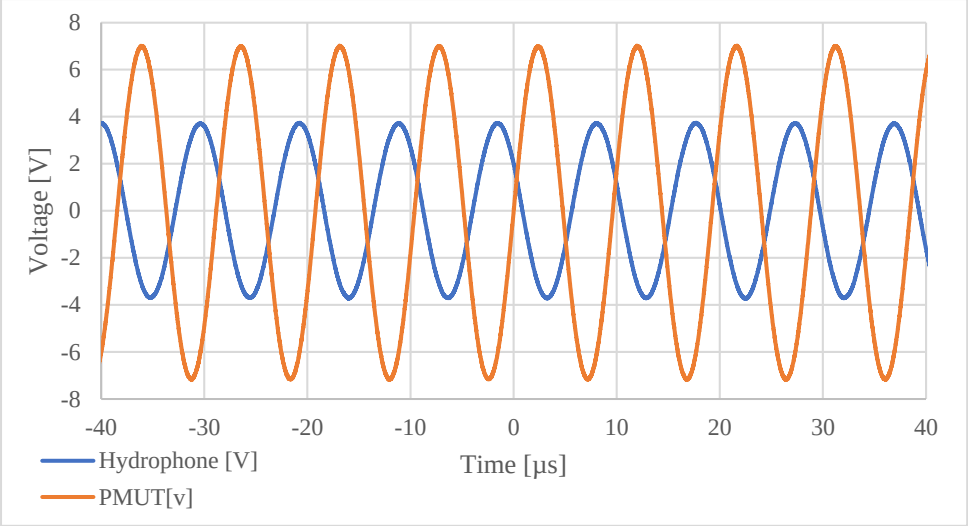

Figure 4.130 ~ Voltage applied across PMUT vs voltage measured out of PMUT pre amp for Device 55 operating as continuous sinusoidal waveform transmitter at 104 kHz

The highest voltage output by the hydrophone at 104 kHz was 7.43 Volts with a 147º phase shift. This equated to an SPL of 104.8Pa.

Lower voltages were measured at other frequencies as follows:

- At 100 kHz the measured voltage was 3V with a SPL of 26.7 [Pa]
- At 89 kHz the measured voltage was 1.2 V
- At 87 kHz the measured voltage was 2.1 V
- At 73 kHz the measured voltage was 2.23 V
- At 73 kHz the measured voltage was 2.076V

A higher ultrasonic power output value was detected at around 126.4 kHz as shown in Figure 4.131 below.

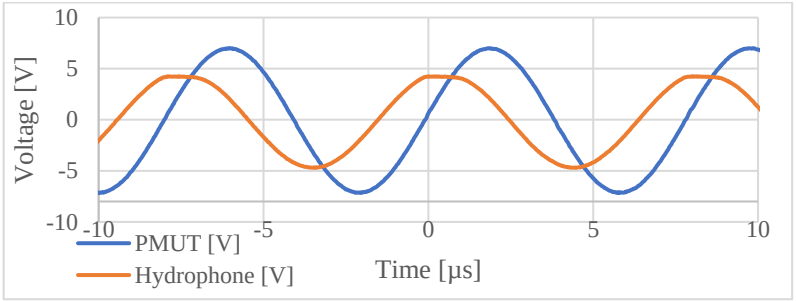

Figure 4.131 ~ Voltage applied across PMUT vs voltage measured out of PMUT pre amp for Device 55 operating as continuous sinusoidal waveform transmitter at 126.4 kHz

At the frequency of 126.4 kHz the hydrophone presented a $V_{p\text{-}p}$ of 8.967 V, equating to 71 Pa.

Step 3 – Analysing a trigger events.

The next step of the analysis involved setting up a triggered waveform at 104 kHz to further study. A 14 V_{p-p} sinusoidal pulse was applied for $773x10^{-6}$ seconds. The relationship shown in Figure 4.132.

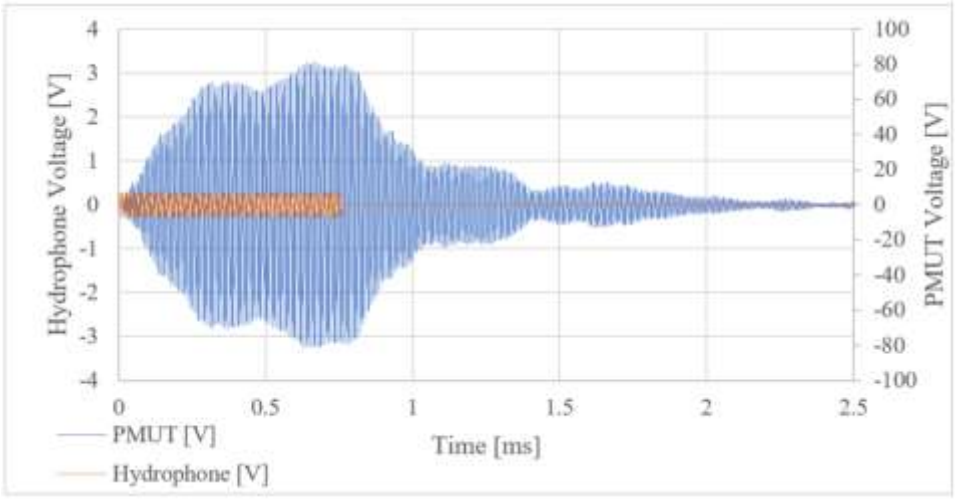

Figure 4.132 ~ Trigger with 14 V_{p-p} sinusoidal signal applied across Device 55 PMUT for $773x10^{-6}$ seconds. Shows voltage across PMUT and voltage across hydrophone. Note discrepancy in scale on the y axis. The excitation frequency was set at 104 kHz.

With reference to the voltage measured 6.428 V at a point 0.665 ms after start of excitation, with the measured voltage being 5.5 V at a point 0.376 ms after start of excitation.

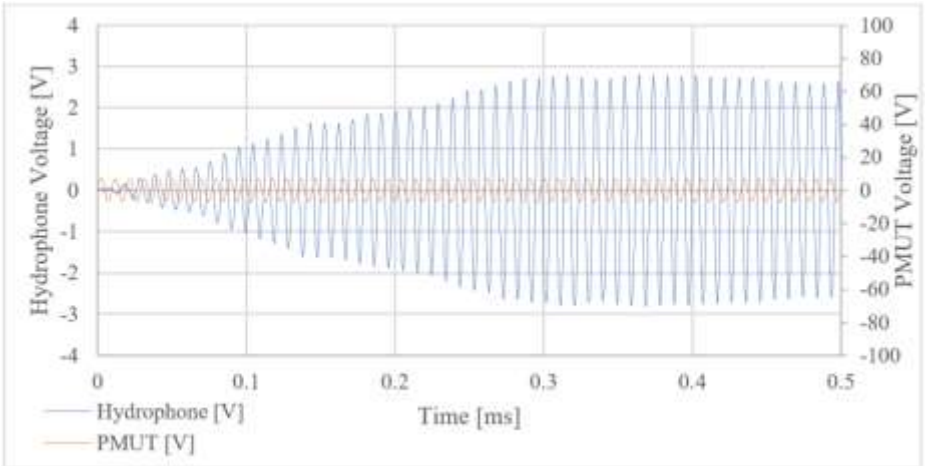

Figure 4.133~ Device 55 at 104 kHz studying the first 0.5 ms. Shows voltage across PMUT and voltage across hydrophone. Note discrepancy in scale on the y axis.

It is interesting to refer to Figure 4.134 where one can detect through the hydrophone the very first sonic waves of the PMUT as it starts to be excited electrically.

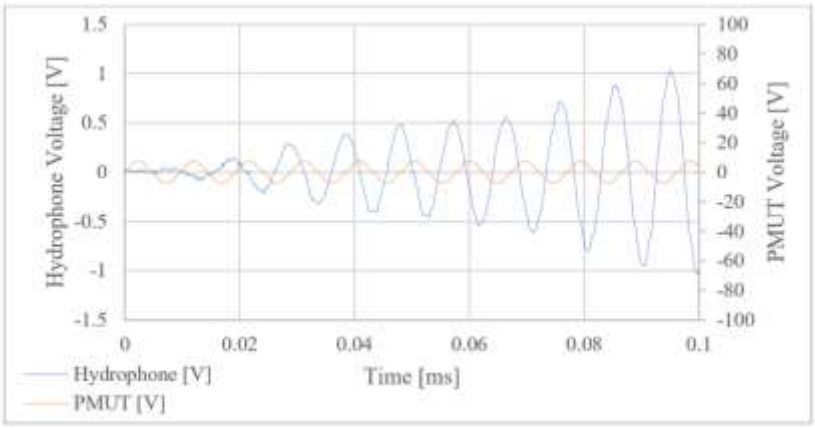

Figure 4.134 ~ Very first movements of PMUT Device 55 after start of excitation at 104 kHz. . Shows voltage across PMUT and voltage across hydrophone. Note discrepancy in scale on the y axis.

Following this a triggered timed pulse with frequency of 126.4 kHz was fed into the PMUT and the output of the hydrophone was studied as per Figure 4.135.

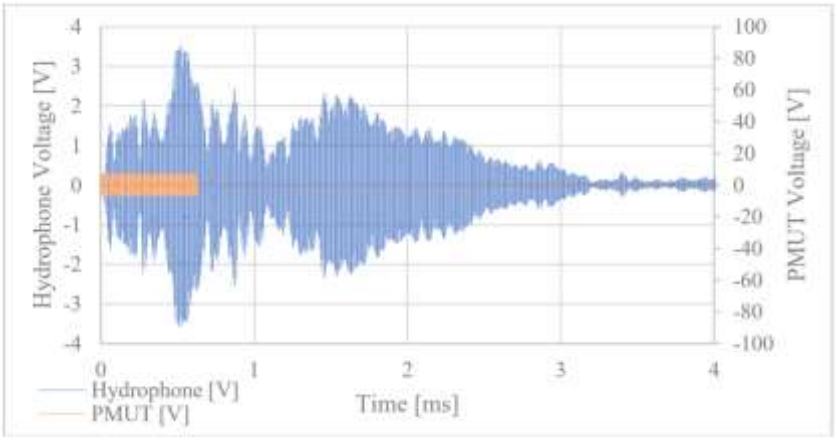

Figure 4.135 ~ Trigger with 14 V_{p-p} sinusoidal signal applied across Device 55 PMUT for 663.1x10^{-6} seconds. Shows voltage across PMUT and voltage across hydrophone. Note discrepancy in scale on the y axis. Excitation frequency was 126.4 kHz.

The signals at the initial time period after the start of excitation were examined in detail as per Figure 4.136

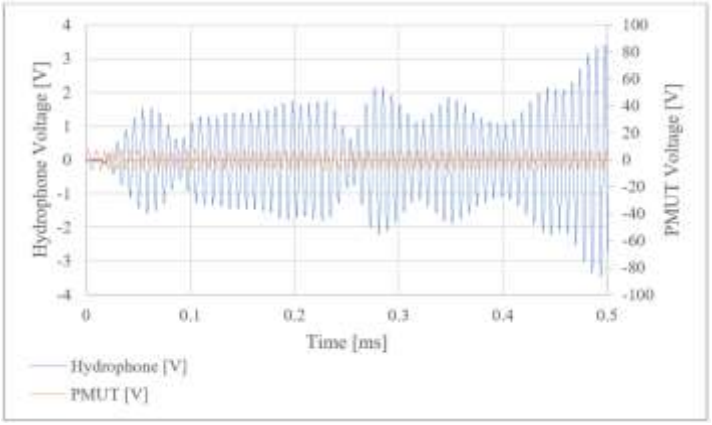

Figure 4.136 ~ Device 55 at 126 kHz studying the first 0.5 ms. Shows voltage across PMUT and voltage across hydrophone. Note discrepancy in scale on the y axis.

Step 4 conclusion from series

The acoustic experimental process presented the frequency of 104 kHz as the resonant frequency of PMUT Device 55. This was very close to the resonant frequency determined with the laser vibrometer which presented a resonant frequency of 106.25 kHz for a device in isopropanol coupling fluid and with an air filled cavity.

Table 4.31 ~ Voltage from hydrophone when operating Device 55 in transmission mode.

Frequency of signal to PMUT [Hz]	Voltage from hydrophone Pre amp [V]	Sound Pressure Level [Pa]
104.00	7.43	74
126.25	8.967	71

4.6.15 Device 39 ~ Circular PMUT- Trench Diameter of 900 µm

Device 39 was a 900 µm device shown in Figure 4.137.

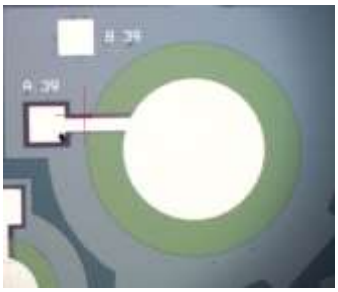

Figure 4.137 ~ Frontal device micrograph of Device 39 – 900µm diameter PMUT.

It was placed in the experimental work:

- As part of an experimental series to study the relationship between device diameter and resonant frequency.
- As a control for PMUT designs with modified diaphragm structure.
- As part of an experimental series to study the effect of having liquid in the cavity.
- To study the effect of high viscosity fluids such as glycerine on the movement of PMUTs.

The geometric parameters for Device 39 are shown in Table 4.32

Table 4.32 ~ Geometric data for Device 39

Nominal Trench Diameter [µm]	**Padmetal Cover [%]**	**Padmetal Diameter [µm]**	**Padoxide Diameter [µm]**	**Pzfilm Diameter [µm]**	**Design Features**
900	66	594	578	900	Circular PMUT

4.6.15.1 Laser Vibrometer characterisation of Device 39

Coupling Fluid: Isopropanol ~ Cavity Fluid: Air

Device 39 was excited with a Periodic Chirp signal in an Isopropanol environment and air cavity to determine the resonant frequency. The results are shown in Figure 4.138.

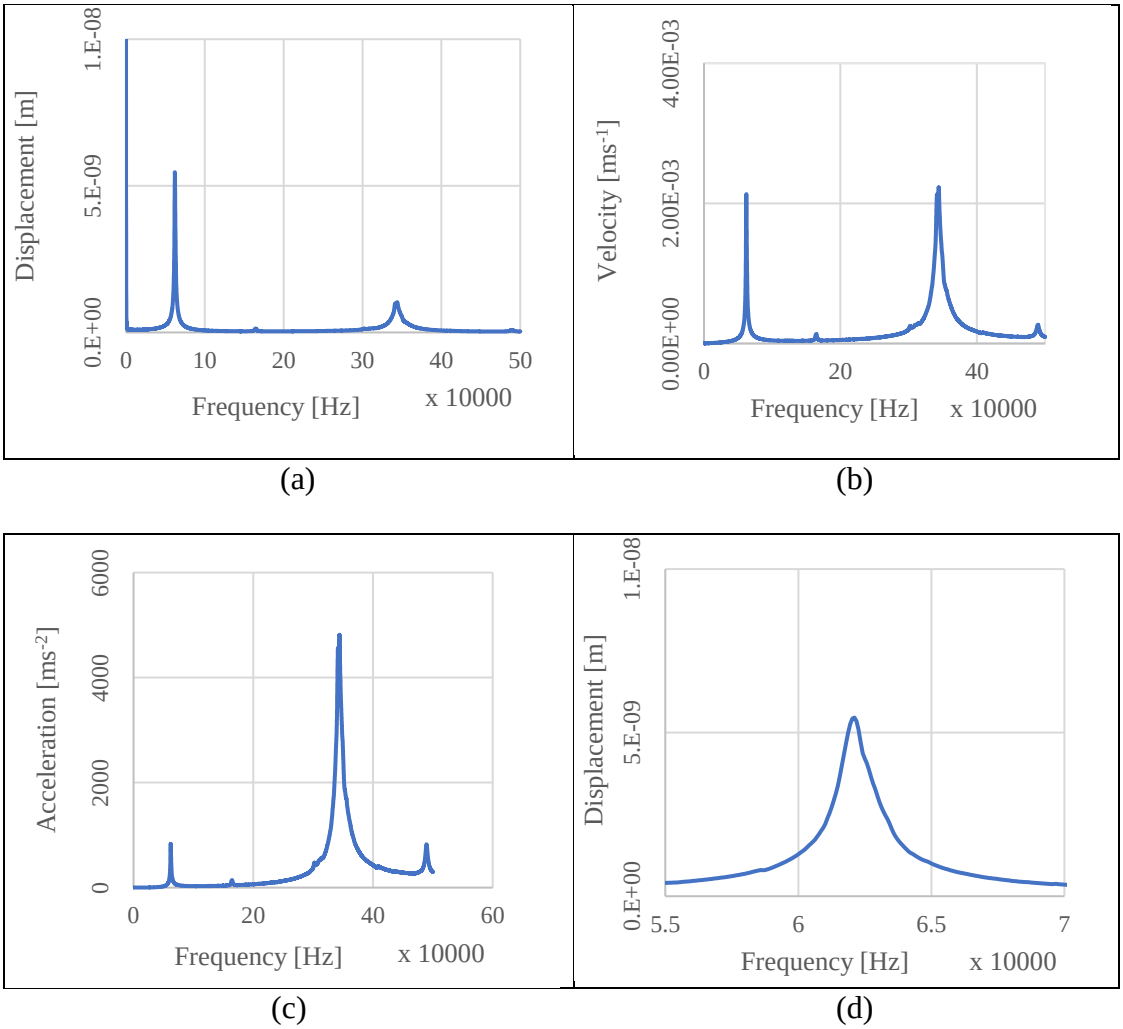

Figure 4.138 ~ Periodic Chirp frequency between 0 and 500 kHz with (a) Displacement, (b) Velocity and (c) acceleration values vs frequency for Device 39 in isopropanol coupling fluid and air filled cavity. (d) Shows displacement vs frequency at a frequency between 55,000 Hz and 70,000 Hz.

The periodic chirp exercise presented two modes of oscillation which were identified by laser vibrometer during periodic chirp excitation. These are shown in Figure 4.139.

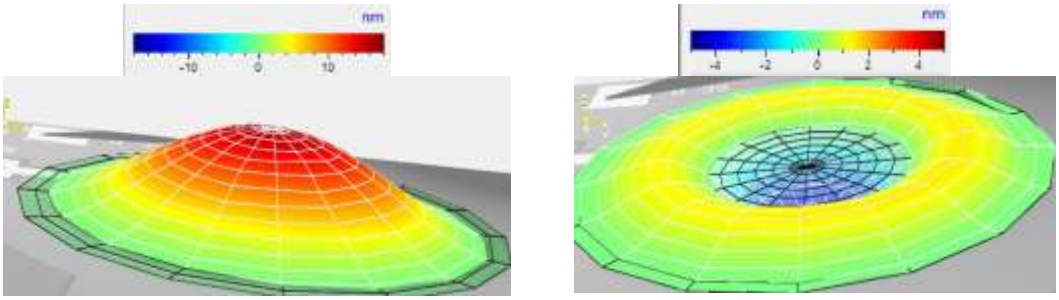

(a) (b)

Figure 4.139 ~ Displacement of Device 39 excited with a periodic chirp signal at a frequency (a) 62.03 kHz (b) 344.14 kHz isopropanol coupling fluid & air filled cavity. Values shown are actual readings directly from vibrometer and not normalised with the fluid's refractive index.

The device was excited at the established resonant frequency using sine wave excitation at 14 $V_{p\text{-}p}$ amplitude with the displacement shown in Figure 4.140.

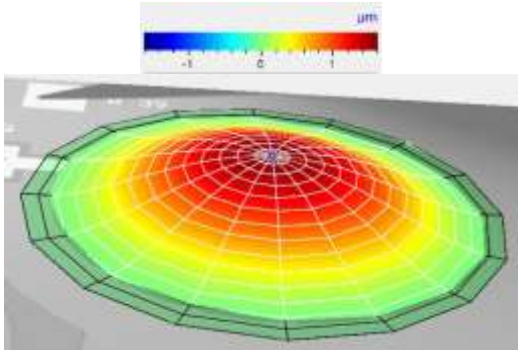

Figure 4.140 ~ Displacement of Device 39 excited with a 14$V_{p\text{-}p}$ sine wave signal at a frequency 62.03 kHz in isopropanol coupling fluid & air filled cavity. Values shown are actual readings directly from vibrometer and not normalised with the fluid's refractive index.

The peak values of the measured parameters at the device midpoint are shown in Table 4.33.

Table 4.33- Peak values at 62.03 kHz for device 39 in isopropanol environment and air filled cavity

Parameter	**Value measured by vibrometer**	**Values normalised by the coupling liquid's refractive index**[†1]
Peak Displacement	1.562 µm	1.14 µm
Peak Velocity	0.6087 m/s	0.444 m/s
Peak Acceleration	237.2 km/s^2	173.14 km/s^2

Note †1: Using ratio Isopropanol/Air ~ 1.37

Coupling Fluid: Isopropanol ~ Cavity Fluid: Isopropanol

Device 39 was excited with a periodic chirp signal in an Isopropanol environment and Isopropanol filled cavity. The results are shown in Figure 4.141.

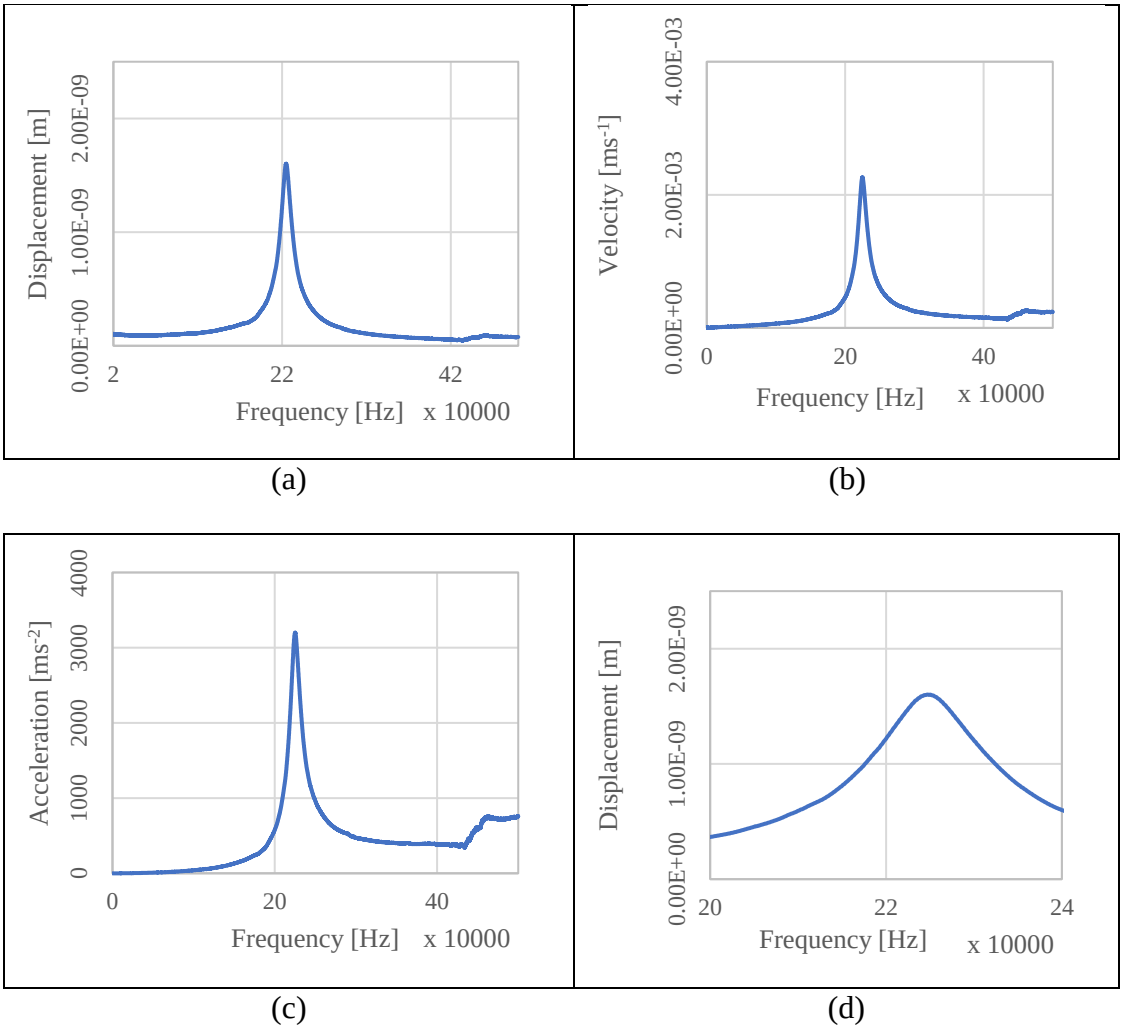

Figure 4.141- Periodic Chirp frequency between 0 and 500 kHz with (a) Displacement, (b) Velocity and (c) acceleration values vs frequency for Device 39 in isopropanol coupling fluid and isopropanol filled cavity. (d) Shows displacement vs frequency at a frequency between 200,000Hz and 240,000Hz. Values shown are actual readings directly from vibrometer and not normalised with the fluid's refractive index.

The device 39 was then excited with Sine wave signal at 14 V_{p-p} amplitude. The result is shown in Figure 4.142.

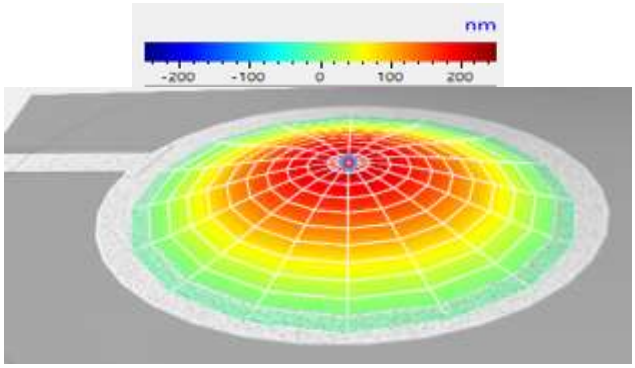

Figure 4.142 ~ Displacement of Device 39 excited with a 14 V_{p-p} sine wave signal at a frequency of 225 kHz with isopropanol coupling fluid & isopropanol filled cavity. Values shown are actual readings directly from vibrometer and not normalised with the fluid's refractive index.

The dynamic parameters measured during sine excitation are shown in Table 4.34.

Table 4.34 ~ Peak Values measured at 225 kHz

Parameter	Value measured by vibrometer	Values normalised by the coupling liquid's refractive index†1
Peak Displacement	2.13×10^{-7} m	1.55×10^{-7} m
Peak Velocity	0.301 m/s	0.220 m/s
Peak Acceleration	425.7 km/s^2	310.73 km/s^2

Note †1: Using ratio Isopropanol/Air ~ 1.37

Coupling Fluid: Glycerine ~ Cavity Fluid: Air

Time domain characterisation of Device 39 with glycerine coupling fluid and an air filled cavity was conducted. The first step was to find the resonant frequency through periodic chirp excitation. The results are shown in Figure 4.143.

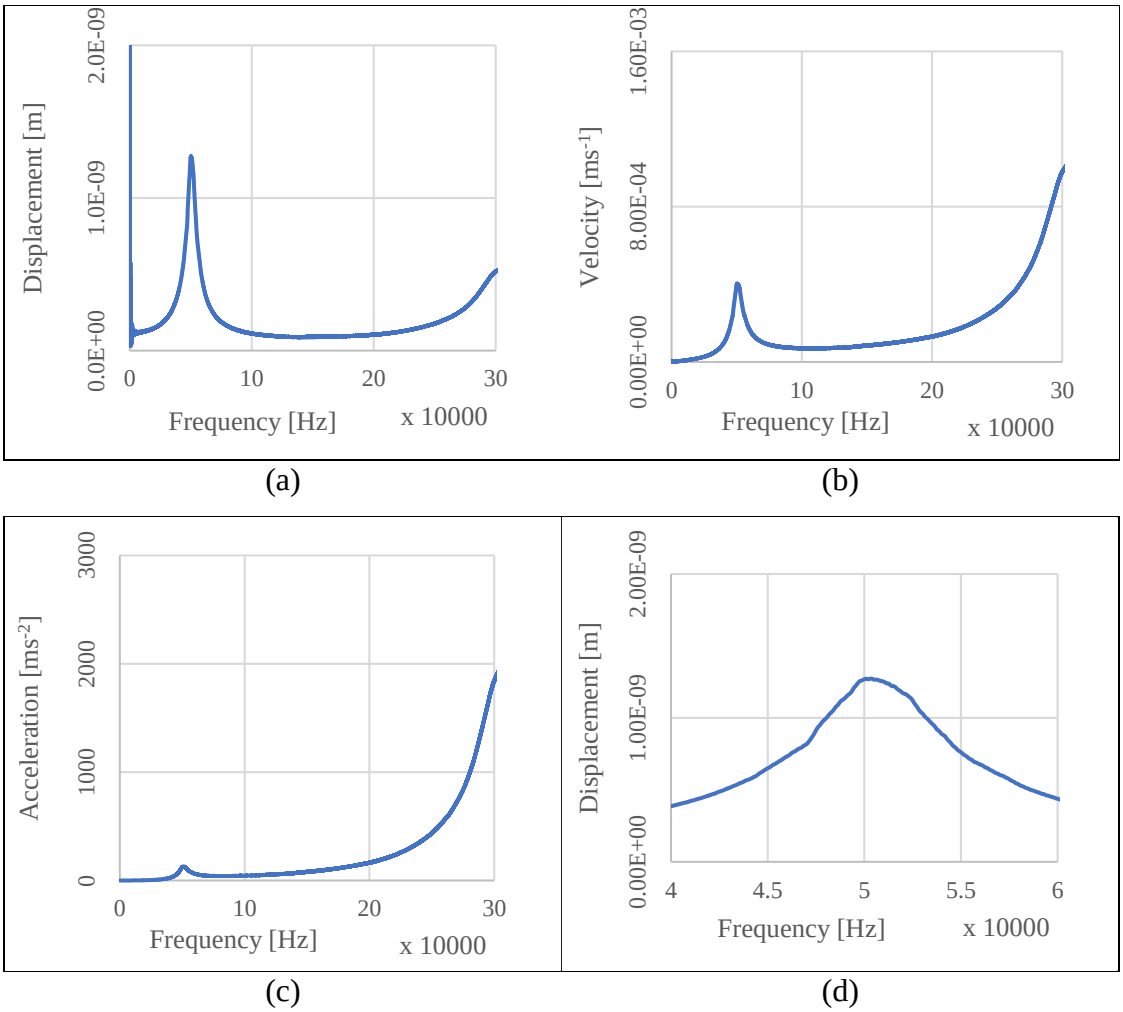

Figure 4.143 ~ Periodic Chirp frequency between 0 and 300 kHz with peak midpoint (a) displacement, (b) velocity and (c) acceleration values vs frequency for Device 39 in glycerine coupling fluid and air filled cavity. (d) Shows displacement vs frequency at a frequency between 40,000 Hz and 60,000 Hz.

The study was conducted in the time domain with the following parameters being used for this study:

Cavity fluid:	Air
Coupling Fluid:	Glycerine with height from petri dish bottom 2.5 mm
Excitation Signal:	Burst sine with amplitude of 14 V_{p-p}
Sampling Frequency:	6.250 MHz
Excitation frequency:	50.6 kHz

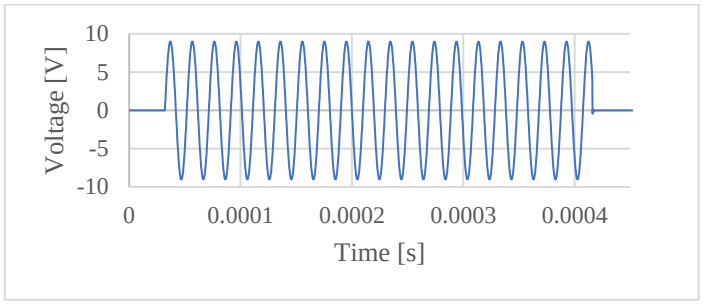

Figure 4.144 ~ The burst sine excitation signal at a frequency of 50.6 kHz

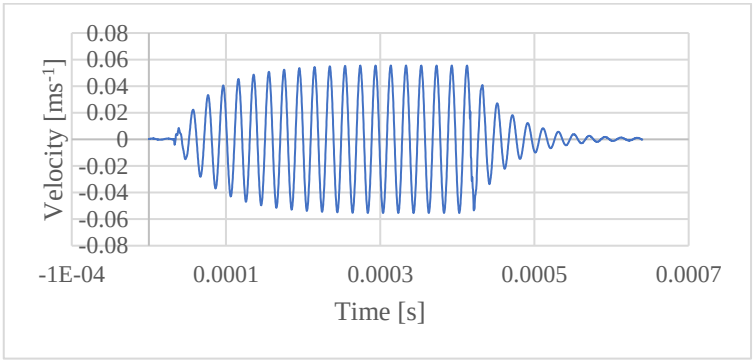

Figure 4.145 ~ The velocity of the diaphragm at the midpoint when subjected to the burst sine excitation.

The peak velocity measured in glycerine was 0.055571 m/s.

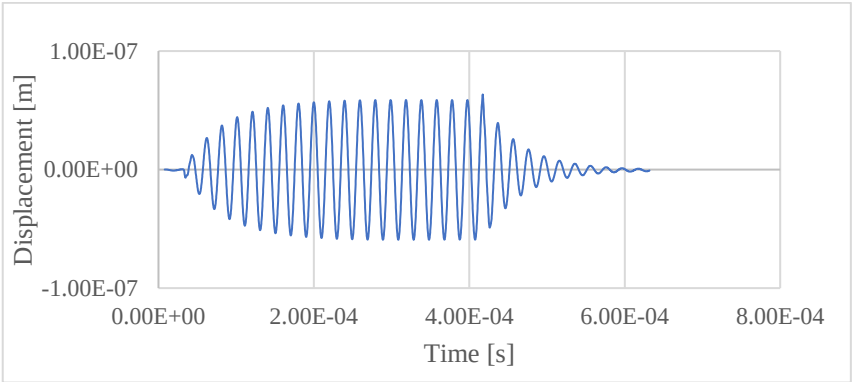

Figure 4.146 ~ The displacement of the diaphragm at the midpoint when subjected to the burst sine excitation.

The maximum displacement was 6.34×10^{-8} m.

4.6.16 Device 42 ~ PMUT with circumferential holes-Trench Diameter of 900 µm

Device 42 was a PMUT device which was specially designed for improved performance in transmission and reception. Micrographs of the device are shown in Figure 4.147.

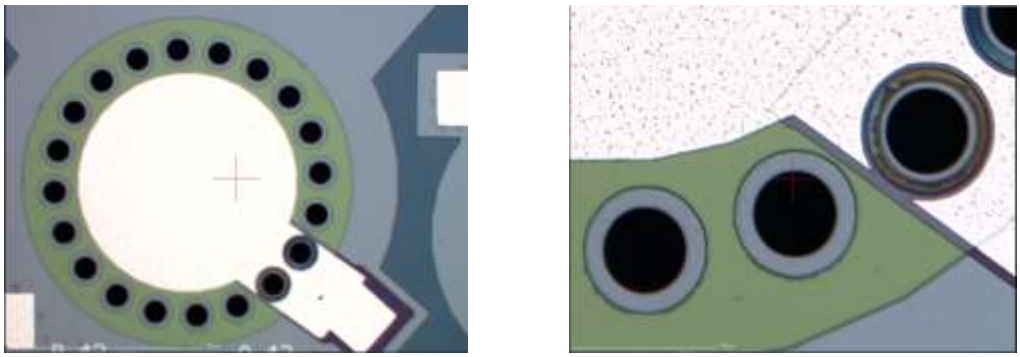

(a) (b)

Figure 4.147 ~ (a) Front View and (b) rear micrograph view of device 42

Parameters for device 39 are shown in Table 4.35.

Table 4.35 ~ Geometric data for Device 39

Nominal Trench Diameter [µm]	Padmetal Cover [%]	Padmetal Diameter [µm]	Padoxide Diameter [µm]	Pzfilm Diameter [µm]	Special Design Features
900	66	594	578	900	Circular PMUT with holes around the electrode.

4.6.16.1 Laser Vibrometer characterisation of Device 42

Coupling Fluid: Isopropanol ~ Cavity Fluid: Air

The device was excited with a periodic chirp signal when deployed in an isopropanol environment and air cavity. The results are shown in Figure 4.148.

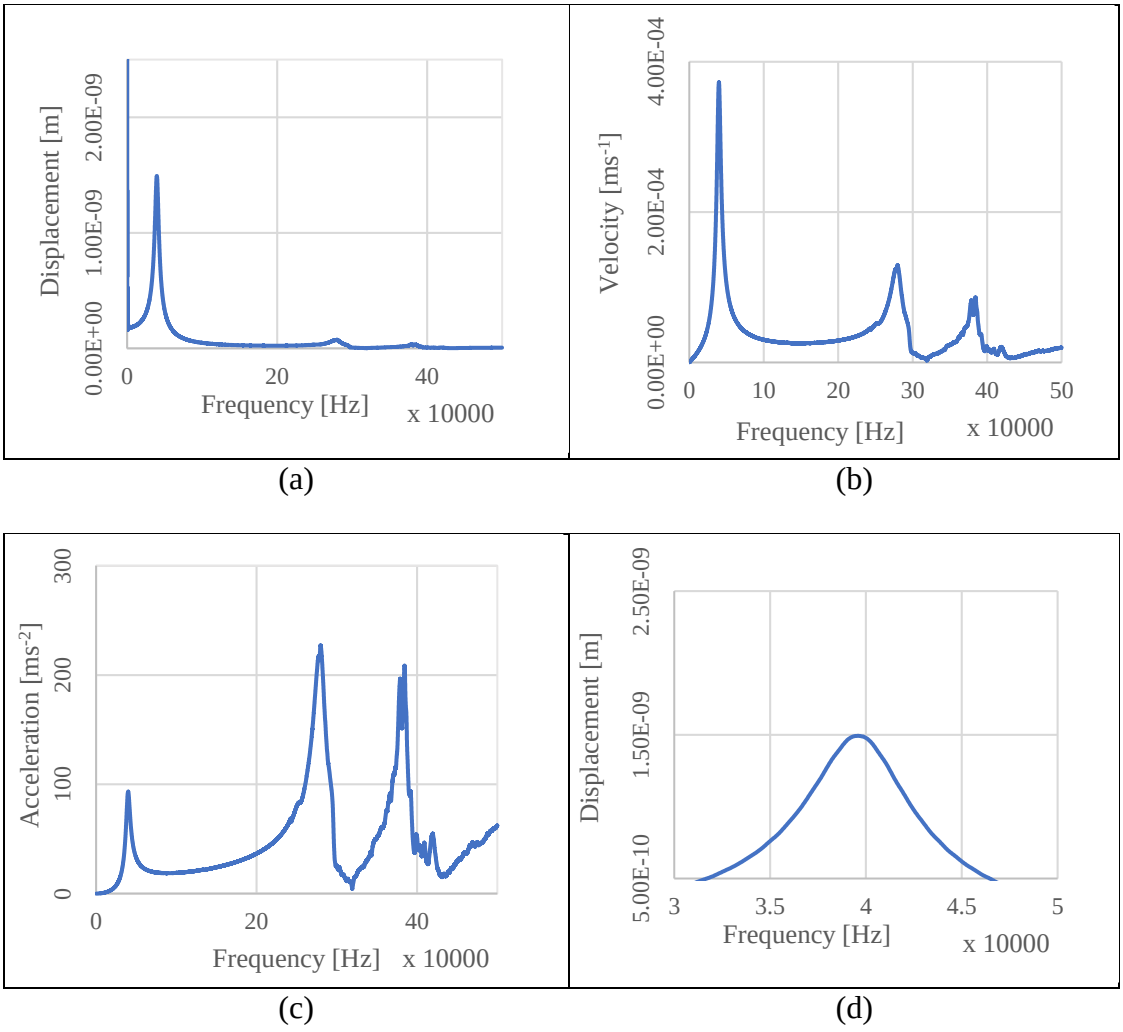

Figure 4.148 ~ Periodic Chirp frequency between 0 and 500 kHz with (a) Displacement, (b) Velocity and (c) acceleration values vs frequency for Device 42 in isopropanol coupling fluid and air filled cavity. (d) Shows displacement vs frequency at a frequency between 30,000 Hz and 50,000 Hz.

Various modes of oscillation were identified by Laser Vibrometer during Periodic Chirp excitation as shown in Figure 4.149.

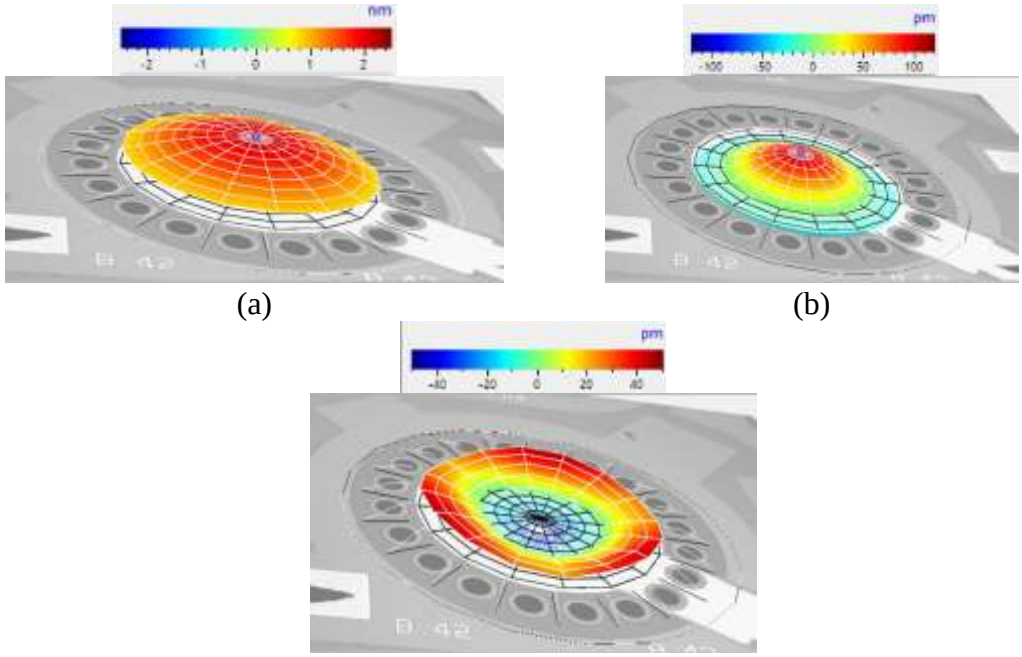

(a) (b)

(c)

Figure 4.149 ~ Displacement of Device 42 excited with a periodic chirp signal at a frequency (a)39.609 kHz (b)279.609 kHz (c) 384.336 kHz in isopropanol coupling fluid & Air filled cavity. Values shown are actual readings directly from vibrometer and not normalised with the fluid's refractive index.

Device excitation with Sine wave signal at 14 $V_{p\text{-}p}$ amplitude was conducted on the principle point of resonance as per Figure 4.150.

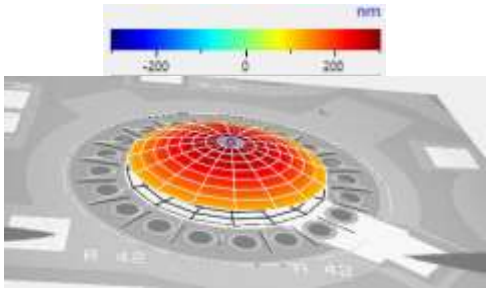

Figure 4.150- Displacement of Device 42 excited with a 14$V_{p\text{-}p}$ sine wave signal at a frequency 39.84 kHz in isopropanol coupling fluid & air filled cavity. Values shown are actual readings directly from vibrometer and not normalised with the fluid's refractive index.

The diaphragm midpoint dynamic parameters measured from the testing are shown in Table 4.36.

Table 4.36 ~ Maximum values at device centre point- frequency 39.84 kHz

Parameter	**Value measured by vibrometer**	**Values normalised by the coupling liquid's refractive index**[†1]
Peak Displacement	291 nm	212.41 nm
Peak Velocity	72.85 mm/s	53.18 mm/s
Peak Acceleration	18.24 km/s^2	13.31 km/s^2

Note †1: Using ratio Isopropanol/Air ~ 1.37

4.6.17 Device 41 ~ PMUT with slots - Trench Diameter of 900 µm

Device 41 was a PMUT device with special slots designed to optimise PMUT movements. The device was added to the experimental process to see if the slots improved performance or not.

(a) (b)

Figure 4.151 ~ (a) Frontal micrograph of Device 41 and (b) high magnification view of one of the slots around the central electrode.

Table 4.37 ~ Geometric data for Device 39

Nominal Trench Diameter [µm]	Padmetal Cover [%]	Padmetal Diameter [µm]	Padoxide Diameter [µm]	Pzfilm Diameter [µm]	Special Design Features
900	66	594	578	900	Circular PMUT with elliptical slots cut in area round the electrode.

4.6.17.1 Laser Vibrometer characterisation of Device 41

The device was tested in an isopropanol coupling fluid and air cavity with a periodic chirp signal to determine the resonant points. The results are shown in Figure 4.152.

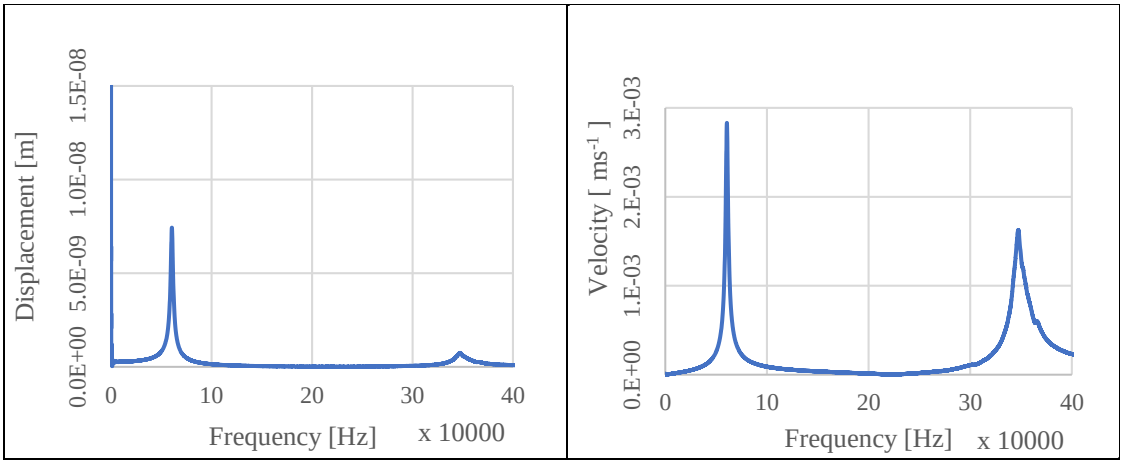

(a) (b)

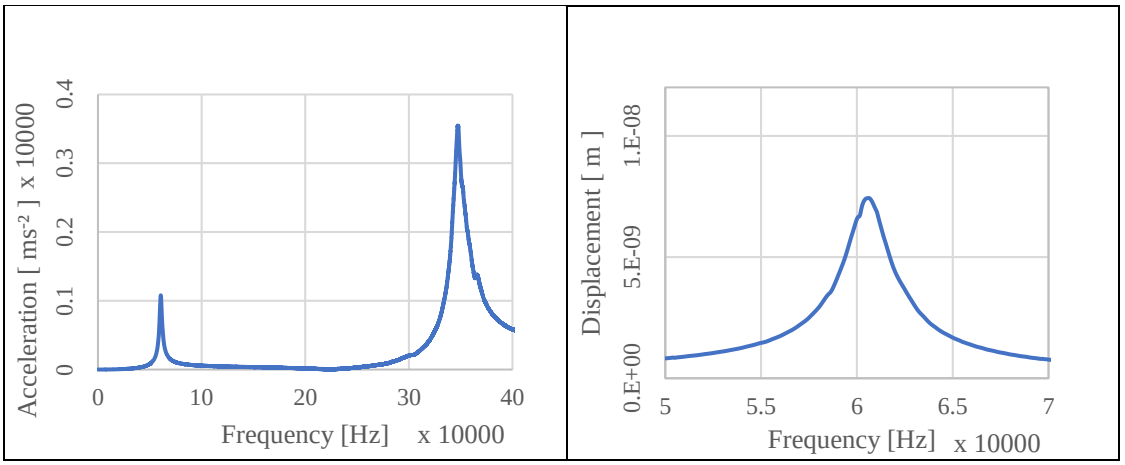

(c) (d)

Figure 4.152 ~ Periodic Chirp frequency between 0 and 400 kHz with (a) Displacement, (b) Velocity and (c) acceleration values vs frequency for Device 41 in isopropyl alcohol surrounding and air filled cavity. (d) Shows displacement vs frequency at a frequency between 50,000 Hz and 70,000 Hz.

The modes of oscillation identified by Laser Vibrometer during Periodic Chirp excitation are shown in Figure 4.153.

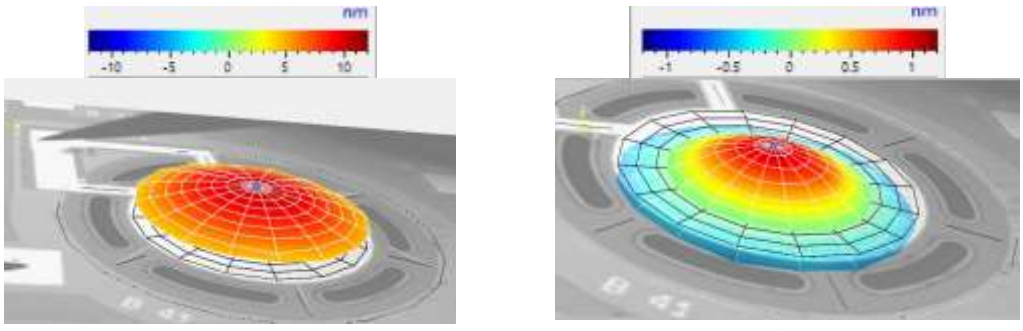

(a) (b)

Figure 4.153 ~ Displacement at device excitation with Sine wave signal with a frequency of (a) 60.5KHz (b) 347.1kHz in isopropanol coupling fluid & air filled cavity. Values shown are actual readings directly from vibrometer and not normalised with the fluid's refractive index.

Device excitation was conducted with a sine wave excitation signal at 14 V_{p-p} amplitude as shown in Figure 4.154.

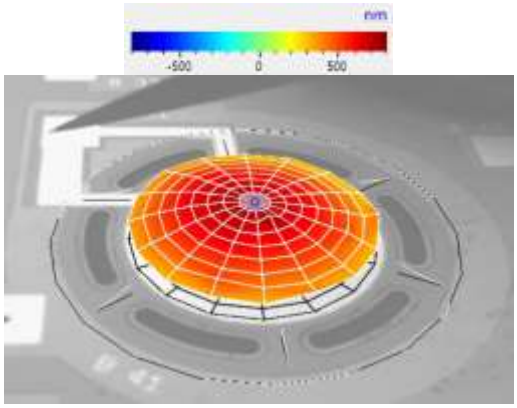

Figure 4.154~ Displacement of Device 41 excited with a periodic chirp signal at a frequency 60.62 kHz in isopropanol coupling fluid & air filled cavity. Values shown are actual readings directly from vibrometer and not normalised with the fluid's refractive index.

The results of the sine excitation are shown in Table 4.38.

Table 4.38 ~ Maximum values at device centre point- frequency 60.62 kHz

Parameter	**Value measured by vibrometer**	**Values normalised by the coupling liquid's refractive index**†1
Peak Displacement	699 nm	510.22 nm
Peak Velocity	0.2664 m/s	0.194 m/s
Peak Acceleration	101.5 km/s^2	74.09 km/s^2

Note †1: Using ratio Isopropanol/Air ~ 1.37

4.6.18 Device 26 ~ Circular PMUT- Trench Diameter of 1,000 µm

The device was designed with a suspended mass attached to the PMUT diaphragm, centred directly at the PMUT axis midpoint. The scope of the suspended mass was to study the effect which such design modifications may have on device performance including the resonant frequency.

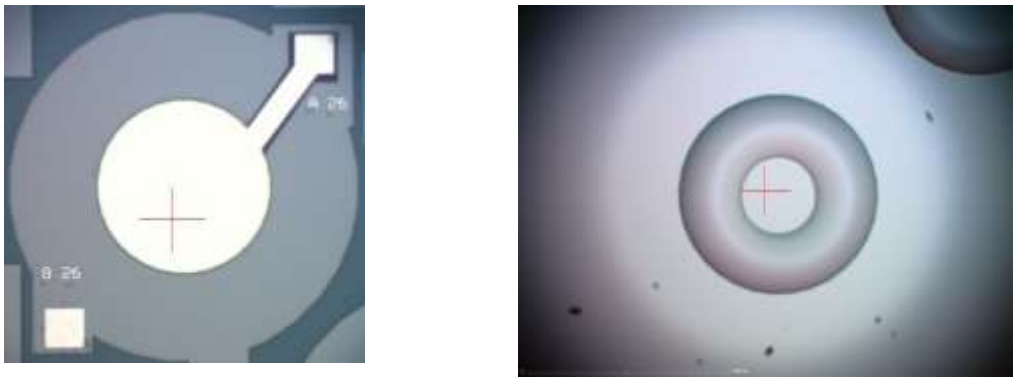

(a) (b)

Figure 4.155 ~ (a) Fronal Micrograph of Device 26 (b) Rear viewing micrograph of Device 26 showing the suspended mass.

The dimensions of Device 26 may be viewed in Table 4.39.

Table 4.39 ~ Geometric data for Device 26

Nominal Trench Diameter [µm]	Padmetal Cover [%]	Padmetal Diameter [µm]	Padoxide Diameter [µm]	Pzfilm Diameter [µm]	Design Features
1000	66	660	644	1000	Circular PMUT with a 200µm centre mass.

The mass suspended at the diaphragm midpoint had a diameter of 200 µm as can be seen in Figure 4.156.

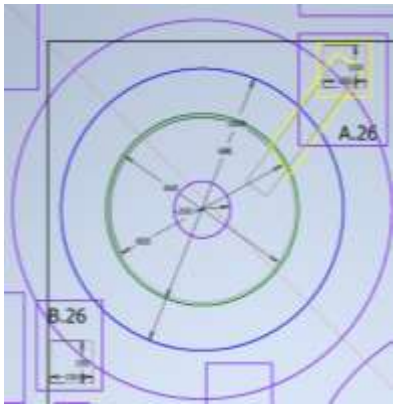

Figure 4.156 ~ Blueprint drawing of Device 26 showing the dimensions of the device including the centrally suspended mass.

4.6.18.1 Laser Vibrometer characterisation of Device 26

The device was first operated in an isopropyl coupling fluid and excited with both periodic chirp and sine wave excitation signals. The device tested however did not move at its midpoint which after investigation was found due to have been due to incomplete separation of the centre mass.

A fresh Device 26 was then tested in a glycerine coupling fluid and having an air filled cavity.

Coupling Fluid: Glycerine ~ Cavity Fluid: Air

Device 26 was excited with Periodic Chirp signal in a glycerine coupling fluid and air filled cavity. The PMUT dynamic response curves are shown in Figure 4.157.

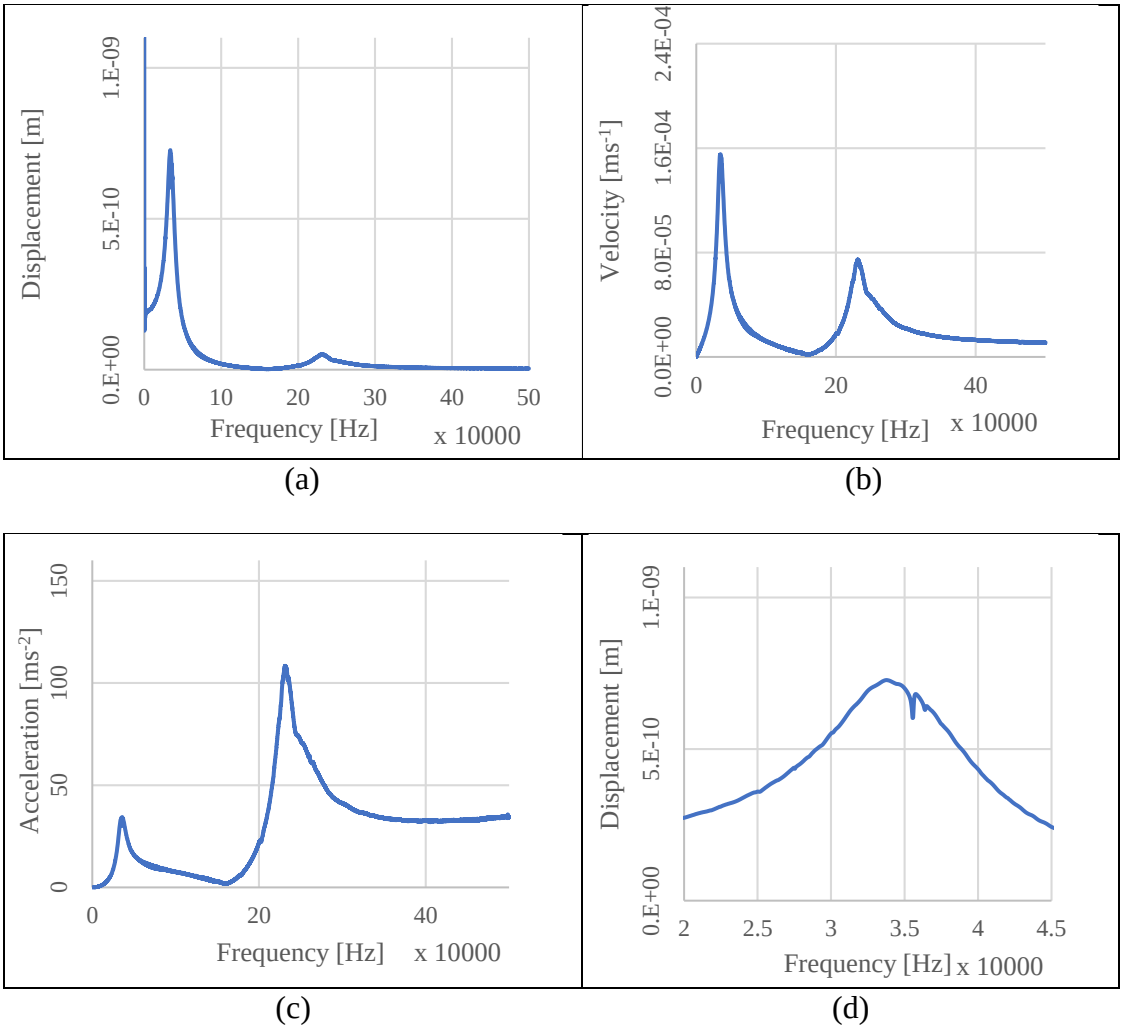

Figure 4.157 ~ Periodic Chirp frequency between 0 and 500 kHz with (a) Displacement, (b) Velocity and (c) acceleration values vs frequency for Device 26 in isopropanol coupling fluid and air filled cavity. (d) Shows displacement vs frequency at a frequency between 20,000 Hz and 45,000 Hz.

Two modes of oscillation were identified by the laser vibrometer during periodic chirp excitation with the device deployed in a glycerine coupling fluid surrounding environment and having an air filled cavity. These are shown in Figure 4.158.

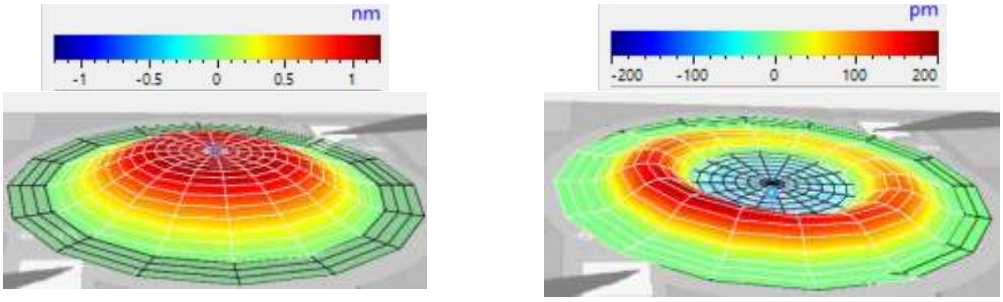

(a) (b)

Figure 4.158- Displacement of Device 26 excited with a periodic chirp signal at a frequency (a)34.69 kHz (b)230 kHz in glycerine coupling fluid and having an air filled cavity. Values shown are actual readings directly from vibrometer and not normalised with the fluid's refractive index.

The device was excited with a sine wave signal at 14 $V_{p\text{-}p}$ amplitude in glycerine coupling fluid and an air filled cavity. The diaphragm displacement when PMUT was under excitation is shown in Figure 4.159.

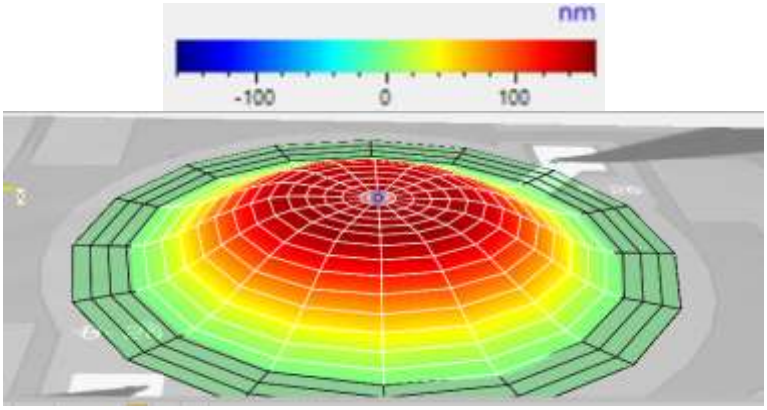

Figure 4.159 ~ Displacement of Device 26 excited with a 14$V_{p\text{-}p}$ sine wave signal at a frequency 34.69 kHz glycerine coupling fluid and air filled cavity. Values shown are actual readings directly from vibrometer and not normalised with the fluid's refractive index.

The measured values from the laser vibrometer are shown in Table 4.40.

Table 4.40 ~ Maximum values at the device' diaphragm mid-point when excited at a frequency of 34.69 kHz.

Parameter	**Value measured by vibrometer**	**Values normalised by the coupling liquid's refractive index**[†1]
Peak Displacement	146.7 nm	101.17 nm
Peak Velocity	31.97 mm/s	22.048 mm/s
Peak Acceleration	6.968 km/s^2	4.806 km/s^2

Note †1: Using ratio Glycerine/Air ~ 1.45

4.6.18.2 Acoustic experimental Data

Device 26 acting as Transmitter

Step 1 - Setup

The experimental device was placed in a 10 cm diameter petri dish and Device 26 was probed. The dish was filled with isopropanol with the hydrophone being submerged 4mm below the surface of the fluid. The PMUT cavity was air filled. The hydrophone's electrical system was set up as shown in Figure 4.16 and connected to the low noise preamplifier.

Step 2 – Determining PMUT resonant frequency.

The first experimental procedure involved connecting the PMUT to a signal generator and running it in continuous transmit mode. The voltage applied across the PMUT was 14 $V_{p\text{-}p}$. Frequencies were cycled and the output of the PMUT were observed. The first frequency with a significant output was 39.8 kHz with the signals being as shown in Figure 4.160.

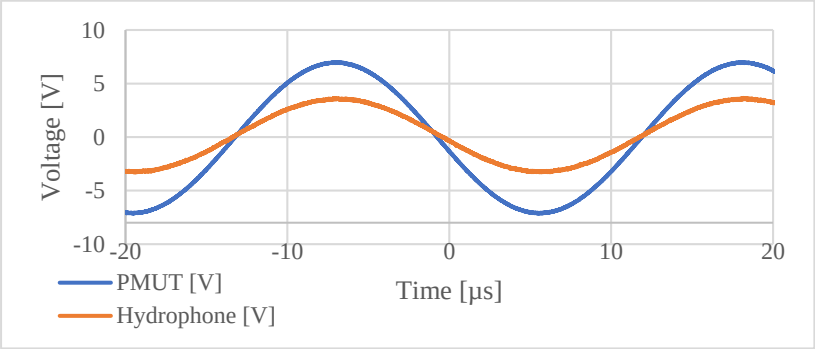

Figure 4.160 ~ Voltage applied across PMUT vs voltage measured out of PMUT pre amp for Device 26 operating as continuous sinusoidal waveform transmitter at 39.8 kHz

The voltage measured from the hydrophone with amplifier being used was 6.939 V with a phase shift of 4.51°. This works out to 62.1 Pa since the FFVS value was -202 dB re 1V/µPa at 39.8 kHz.

Another frequency of interest in terms of transmission was 44.9 kHz as shown in Figure 4.161.

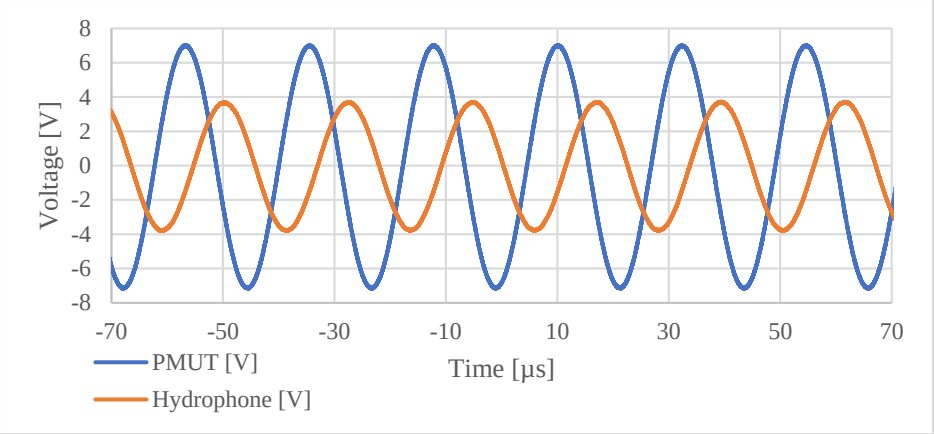

Figure 4.161 ~ Voltage applied across PMUT vs voltage measured out of PMUT pre amp for device 26 operating as continuous sinusoidal waveform transmitter at 44.9 kHz

The peak voltage measured across the hydrophone was 7.5 $V_{p\text{-}p}$ at 44.9 kHz with a phase shift of 112.2°. The pressure calculated at this frequency was therefore 84 Pa.

The device was then inverted to fill the cavity with liquid isopropanol. The resonant frequency at which a usable frequency was measured was 104.25 kHz and the response is shown in Figure 4.162.

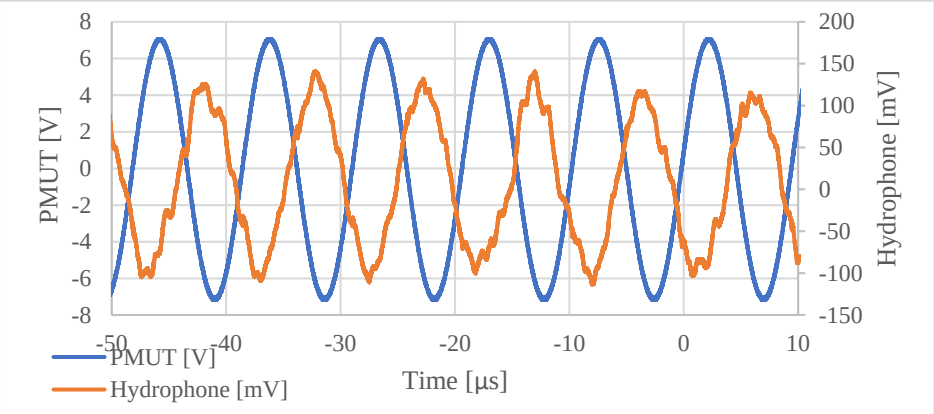

Figure 4.162 ~ Voltage applied across PMUT vs voltage measured out of PMUT pre amp for Device 26 operating as continuous sinusoidal waveform transmitter at 104.25 kHz. Cavity was isopropanol filled.

Step 3 – Analysing through trigger events.

A series of triggered waveform events was set up to see the effect which the input excitation pulse length has on the voltage achieved by the PMUT. The series was all conducted at an excitation frequency of 44.9 kHz.

The first shot was conducted with an excitation pulse of 223.7 µs as per Figure 4.163.

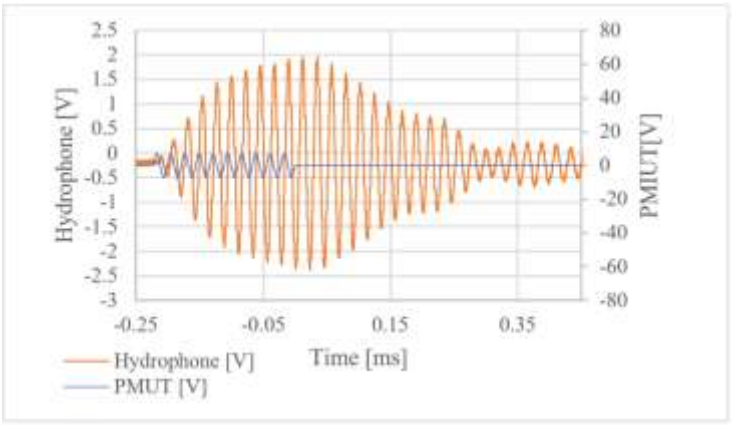

Figure 4.163 ~ At an excitation frequency of 44.9 kHz time period of 223.7 μs. Peak voltage achieved across hydrophone 4.36 V

The trigger event series shown between Figure 4.164 to Figure 4.167 shows an investigation of how the length of time of the application of the excitation signal has a direct effect on the acoustic pressures derived by the PMUT.

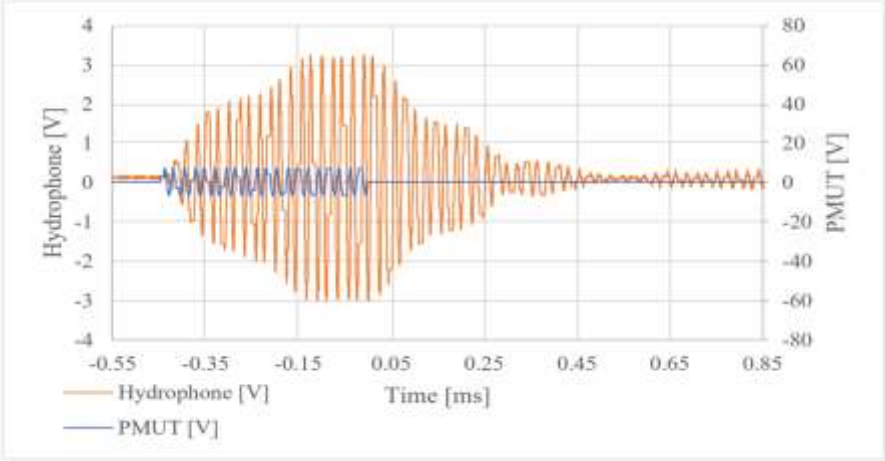

Figure 4.164 ~ Excitation pulse length on PMUT was 451.1 μs. The maximum voltage measured by hydrophone was 6.144 V.

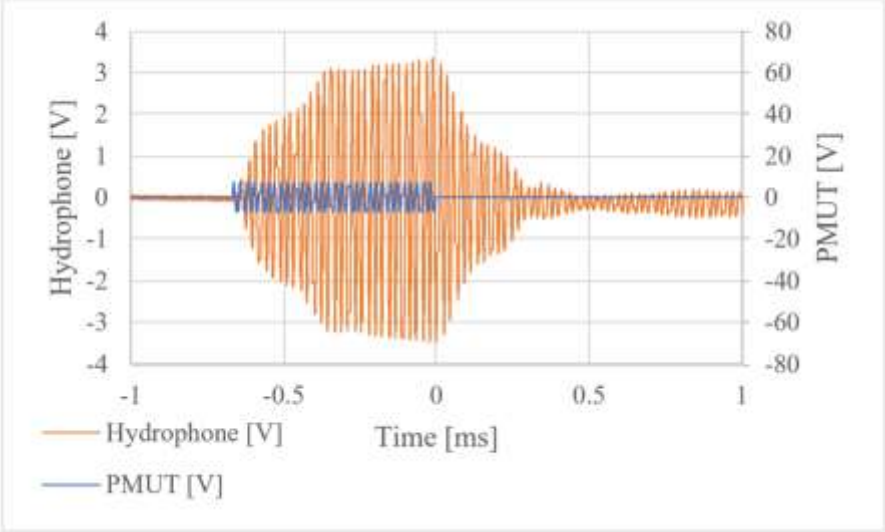

Figure 4.165 ~ Excitation frequency set at 44.9 kHz with excitation pulse length on PMUT 681μs of excitation. Peak voltage measured by the hydrophone was 6.814V.

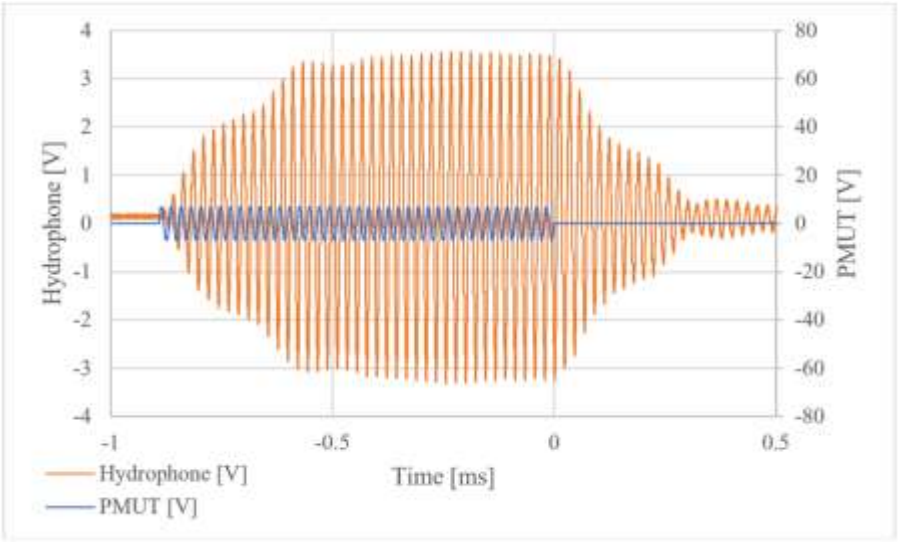

Figure 4.166 ~ Excitation frequency set at 44.9 kHz with excitation pulse length on PMUT being 902.1μs. Peak voltage measured by the hydrophone was 6.841V

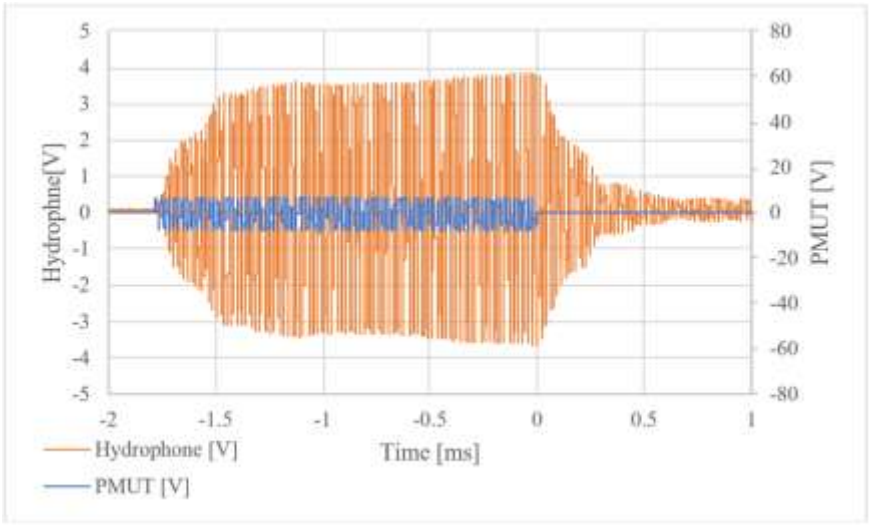

Figure 4.167 ~ Excitation frequency set at 44.9 kHz with excitation pulse length on PMUT being 1.79 ms. Peak voltage measured by the hydrophone was 7.451V

4.6.19 Device 27 ~ Circular PMUT- Trench Diameter of 1,000 μm

Device 27 was a 1,000 μm diameter circular PMUT device. Its diaphragm was solid and had no slots or cutouts. Padmetal cover was circular and had a diameter of 660 μm which was 66% of the diameter of the trench diameter. This device had no attached masses or any other special setup.

Figure 4.168 ~ Micrograph showing frontal side of device 27. Part in white shows padmetal.

The device parameters are tabulated in Table 4.41.

Table 4.41 ~ Geometric data for device 27

Nominal Trench Diameter [µm]	Padmetal Cover [%]	Padmetal Diameter [µm]	Padoxide Diameter [µm]	Pzfilm Diameter [µm]	Design Features
1,000	66	660	644	1,000	Circular PMUT

4.6.19.1 Laser Vibrometer Characterisation of Device 27

Coupling Fluid: Isopropanol ~ Cavity Fluid: Air

The device was deployed in an isopropanol environment with an air filled cavity and excited with a periodic chirp signal to determine the resonant point. The results are shown in Figure 4.169.

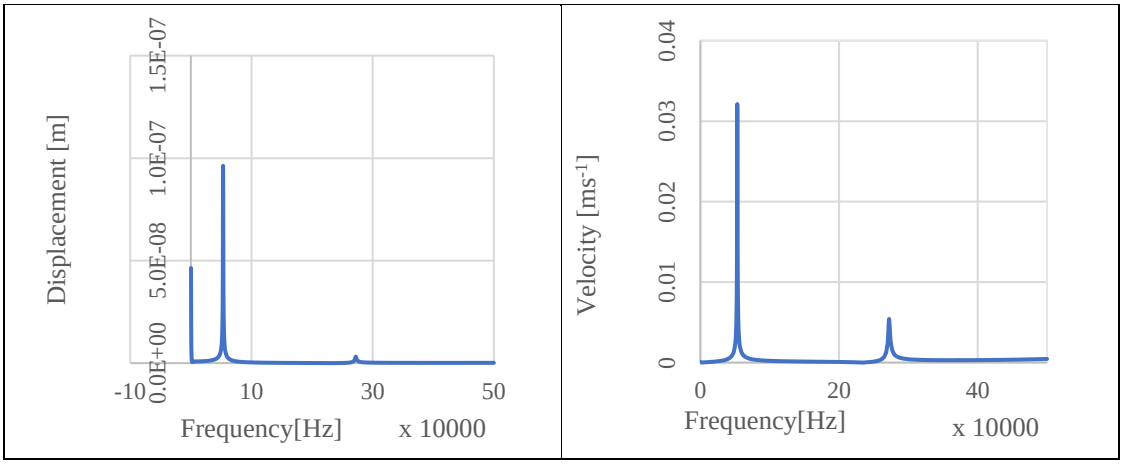

(a) (b)

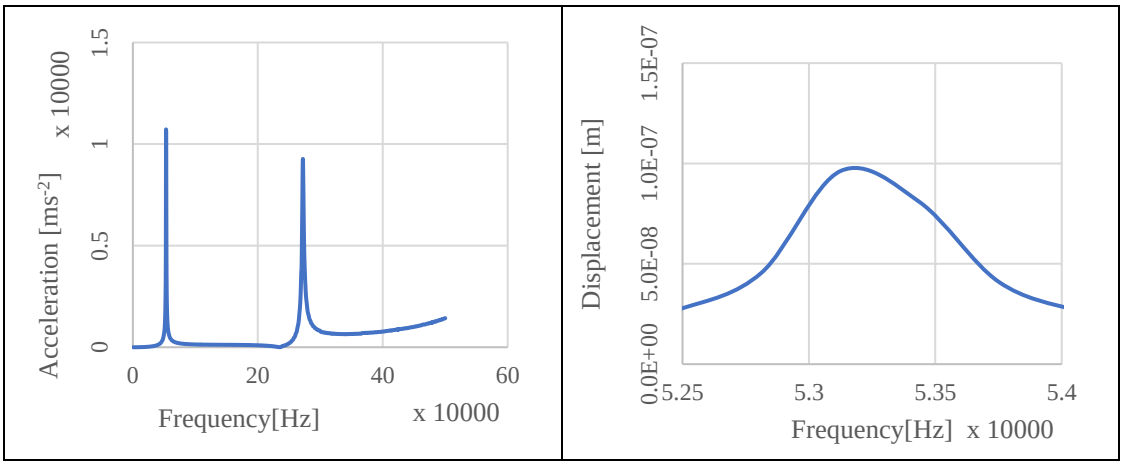

(c) (d)

Figure 4.169 ~ Periodic Chirp frequency between 0 and 500 kHz with (a) Displacement, (b) Velocity and (c) acceleration values vs frequency for Device 27 in isopropyl alcohol surrounding and air filled cavity. (d) Shows displacement vs frequency at a frequency between 52,500Hz and 54,000Hz. Isopropanol coupling fluid & Air filled cavity.

Modes of Oscillation identified by Laser Vibrometer during Periodic Chirp excitation are shown in Figure 4.170.

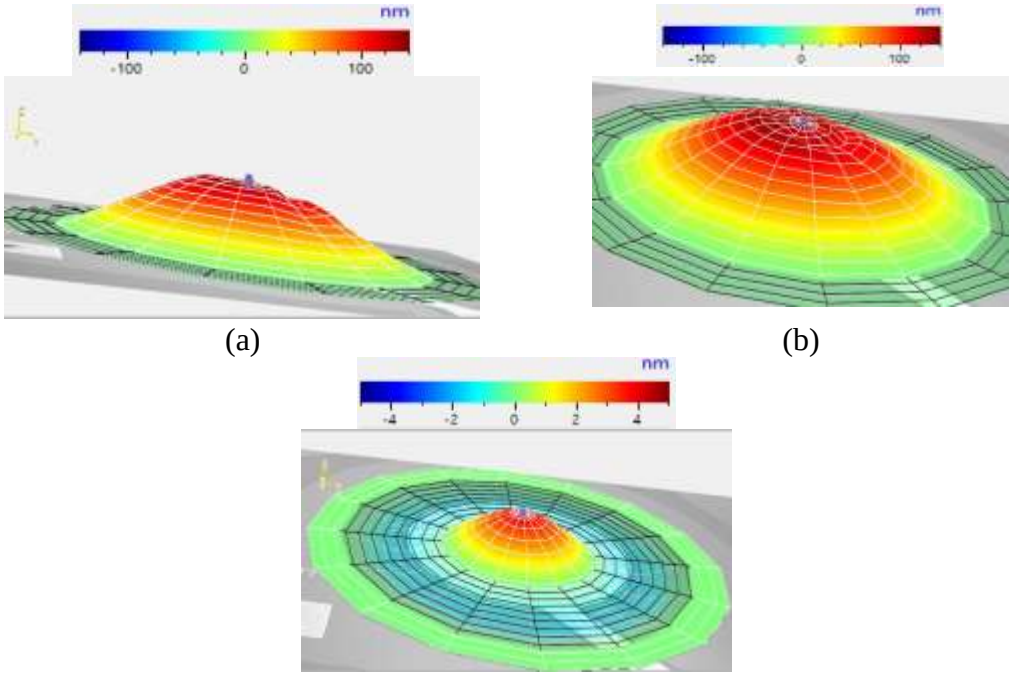

Figure 4.170 ~ Displacement of Device 27 excited with a periodic chirp signal at a frequency of 53.12 kHz shown in (a) and (b) and (c)271.88 kHz. Device was deployed in an isopropanol coupling fluid & had an air filled cavity. Values shown are actual readings directly from vibrometer and not normalised with the fluid's refractive index.

An issue that was noticed in the periodic chirp was that the device did not fully extend during the periodic chirp excitation as can be seen in Figure 4.171.

Device 27 was then excited with Sine wave signal at 14 V_{p-p} amplitude at the 53.12 kHz resonant point.

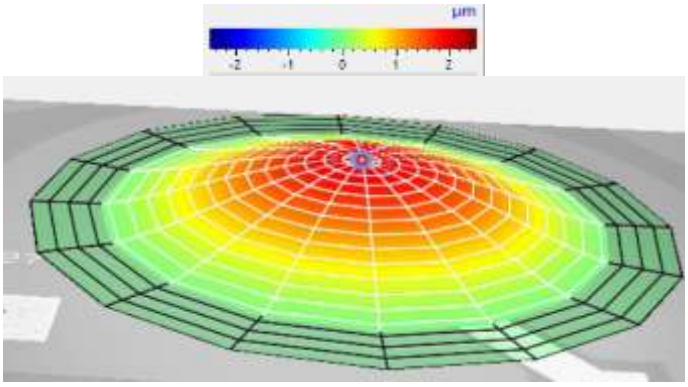

Figure 4.171 ~ Displacement of Device 27 excited with a periodic chirp signal at a frequency 53.28 kHz Deployed in an isopropanol coupling fluid & air filled cavity. Values shown are actual readings directly from vibrometer and not normalised with the fluid's refractive index.

The measured values achieved during the sine excitation exercise are tabulated in Table 4.42.

Table 4.42 ~ Maximum values at device centre point- frequency 53.28 kHz

Parameter	Value measured by vibrometer	Values normalised by the coupling liquid's refractive index†1
Peak Displacement	2.0031 µm	1.4621 µm
Peak Velocity	670.59 mm/s	489.48 mm/s
Peak Acceleration	224.50 km/s^2	163.868 km/s^2

Note †1: Using ratio Isopropanol/Air ~ 1.37

Coupling Fluid: Isopropanol ~ Cavity Fluid: Isopropanol

In the next step Device 27 was excited with a frequency at the point of resonance. The mode of vibration is shown in Figure 4.172 at a frequency of 195 kHz.

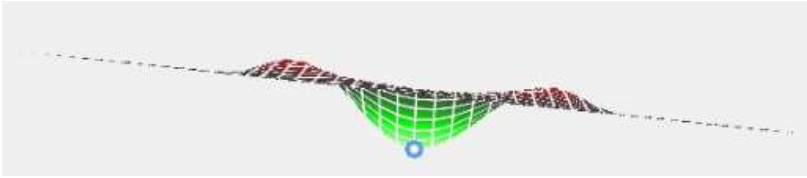

Figure 4.172 ~ Vibration mode for Device 27 at a resonant frequency of 195 kHz

Oscillation at the fundamental frequency were not sustained and it was clear that with the two sides in liquid, modes of vibration were too close together to separate. Investigation in this area was therefore not continued further in this dissertation. The reason for this decision was that the power output from such a device would be seriously reduced in a liquid filled cavity solution. There is potential for future research in such devices however especially when developing a device which has a limitation in terms of size and were the power output level is not top priority.

Coupling Fluid: Glycerine ~ Cavity Fluid: Air

The device was then deployed in a glycerine coupling fluid and with an air filled cavity and excited with a periodic chirp signal. The results are shown in Figure 4.173.

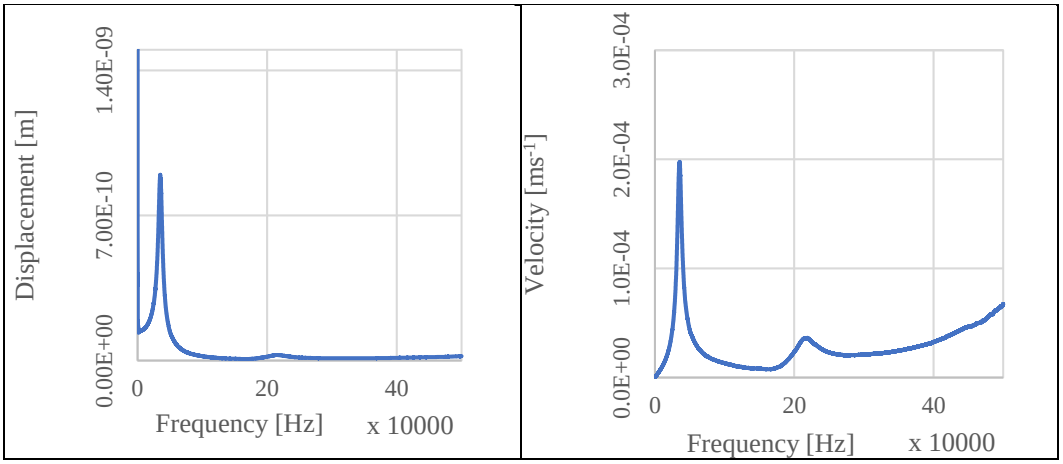

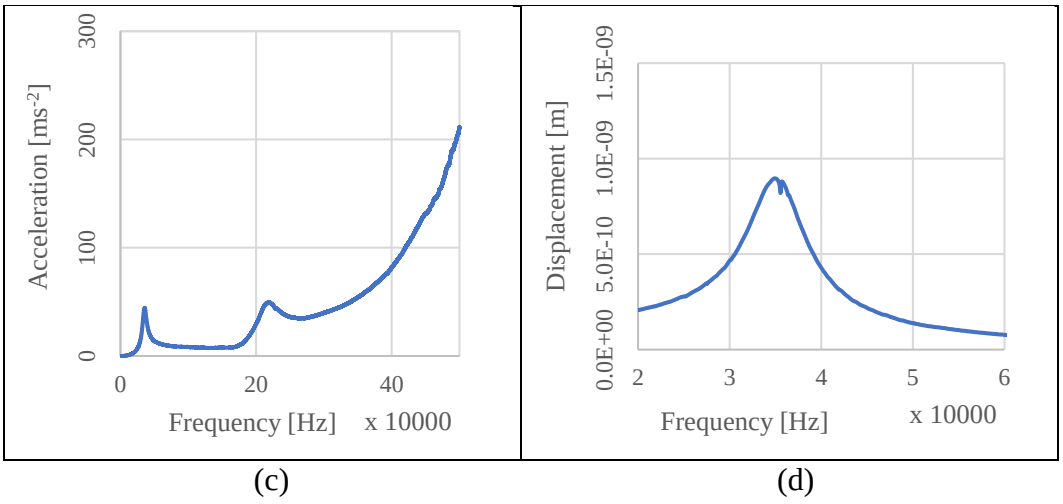

Figure 4.173- Periodic Chirp frequency between 0 and 500 kHz with (a) Displacement, (b) Velocity and (c) acceleration values vs frequency for Device 59 in glycerine coupling fluid and air filled cavity. (d) Shows displacement vs frequency at a frequency between 20,000Hz and 60,000Hz.

Two modes of oscillation were identified by the laser vibrometer during periodic chirp excitation as shown in Figure 4.174.

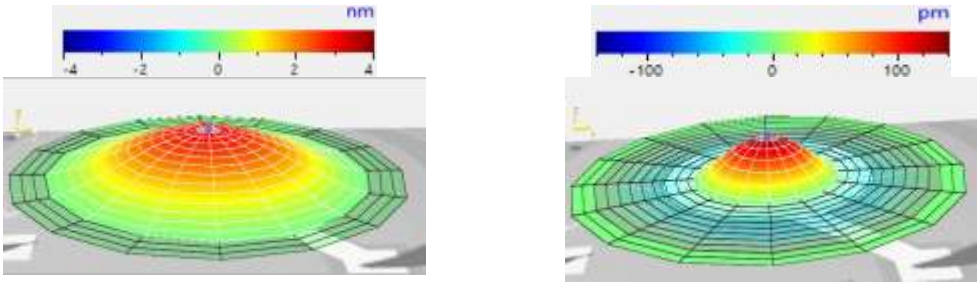

Figure 4.174 ~ Displacement of device 10 excited with a periodic chirp signal at a frequency (a)35.31 kHz (b)218.6 kHz in glycerine coupling fluid and air filled cavity.

The device was excited with a sine wave signal having a 14 $V_{p\text{-}p}$ amplitude in a glycerine coupling fluid and having an air filled cavity. The result is shown in Figure 4.175.

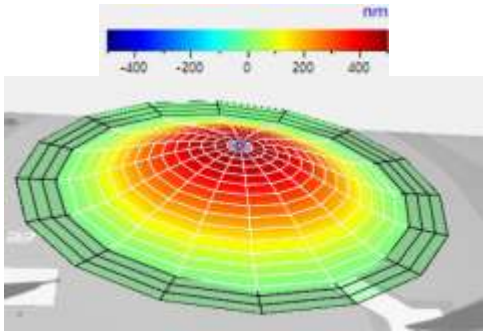

Figure 4.175 ~ Displacement of Device 27 excited with a 14 V_{p-p} periodic chirp signal at a frequency 35.31 kHz deployed in glycerine coupling fluid and having an air filled cavity. Values shown are actual readings directly from vibrometer and not normalised with the fluid's refractive index.

The detailed results from the sine wave excitation exercise are shown in Table 4.43.

Table 4.43 ~ Maximum values at device centre point- frequency 35.31 kHz in glycerine coupling fluid and air filled cavity.

Parameter	**Value measured by vibrometer**	**Values normalised by the coupling liquid's refractive index**†1
Peak Displacement	475.3 nm	327.79 nm
Peak Velocity	0.1055 m/s	0.07276 m/s
Peak Acceleration	23.40 km/s^2	16.14 km/s^2

Note †1: Using ratio Glycerine/Air ~ 1.45

4.6.19.2 Acoustic Experimental data for Device 27

Device 27 acting as Transmitter

Step 1 - Setup

The experimental device was placed in a 10 cm diameter petri dish and Device 27 was probed. The dish was filled with isopropanol coupling fluid with the hydrophone being submerged 4 mm below the surface of the fluid. The PMUT's cavity was air filled. The hydrophone's electrical system was set up as shown in Figure 4.16 and connected to the low noise preamplifier.

Step 2 – PMUT acting as transmitter.

The first experimental procedure involved connecting the PMUT to a signal generator and running it in continuous transmit mode. The voltage applied across the PMUT was 14 V_{p-p}. Frequencies were cycled and the output of the PMUT were observed. The first frequency with a significant output was 44.9 kHz with the signals being as shown in Figure 4.176.

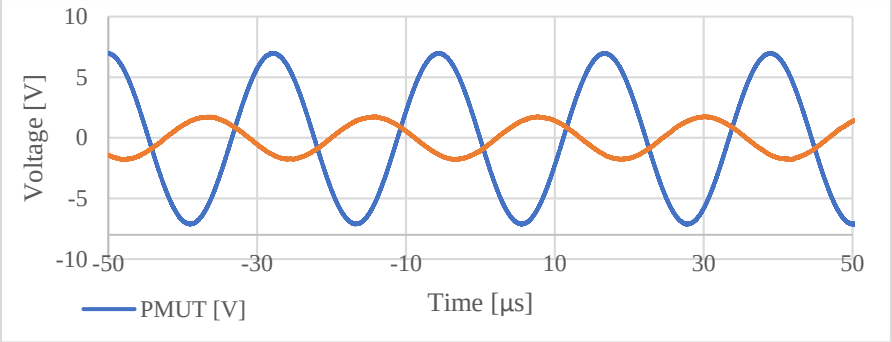

Figure 4.176 ~ Voltage applied across PMUT vs voltage measured out of PMUT pre amp for device 27 operating as continuous sinusoidal waveform transmitter at 44.9 kHz

The voltage measured from the hydrophone with amplifier being used was 3.476 V with a phase shift of 209.3°. This works out to 30.94 Pa since the FFVS was -202 dB re 1V/µPa at 44.9 kHz.

The device was then inverted to fill the cavity with liquid isopropanol and excited again. The response from the hydrophone is shown in Figure 4.177.

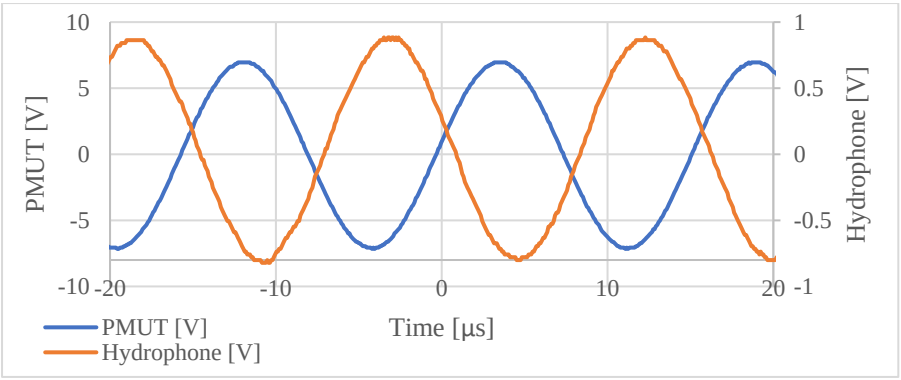

Figure 4.177 ~ Voltage applied across PMUT vs voltage measured out of hydrophone pre amp for device 26 operating as continuous sinusoidal waveform transmitter at 65 kHz. Cavity is filled with liquid isopropanol.

The peak voltage measured across the hydrophone was 1.633 V at 65 kHz with a phase shift of 205.1°. This 1,000 µm diameter PMUT was also observed to be able to transmit at higher frequencies presumably in high order modes. As an example the waveform shown in Figure 4.178 was detected by the hydrophone at a frequency of 111 kHz.

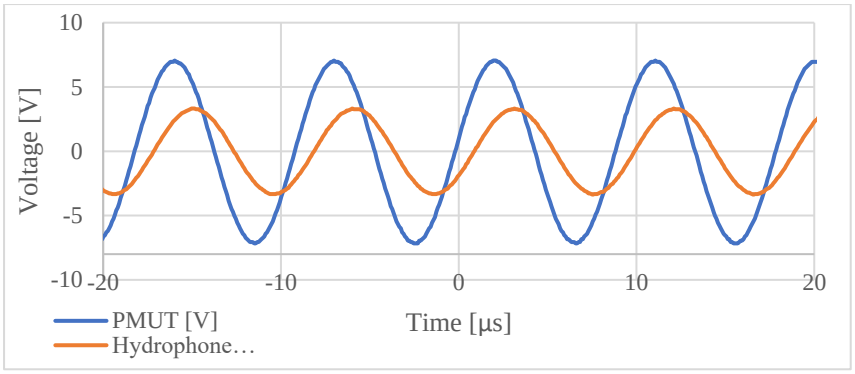

Figure 4.178 ~ Voltage applied across PMUT vs voltage measured out of hydrophone pre amp for Device 26 operating as continuous sinusoidal waveform transmitter at 111.1 kHz. Cavity was filled with liquid isopropanol.

The voltage across PMUT at a frequency of 111.1 kHz was 6.579 $V_{p\text{-}p}$. This translates to a pressure of 58 Pa.

Device 27 acting as receiver

The PMUT was tested in receiving mode whereby the hydrophone was operated in transmitting mode.

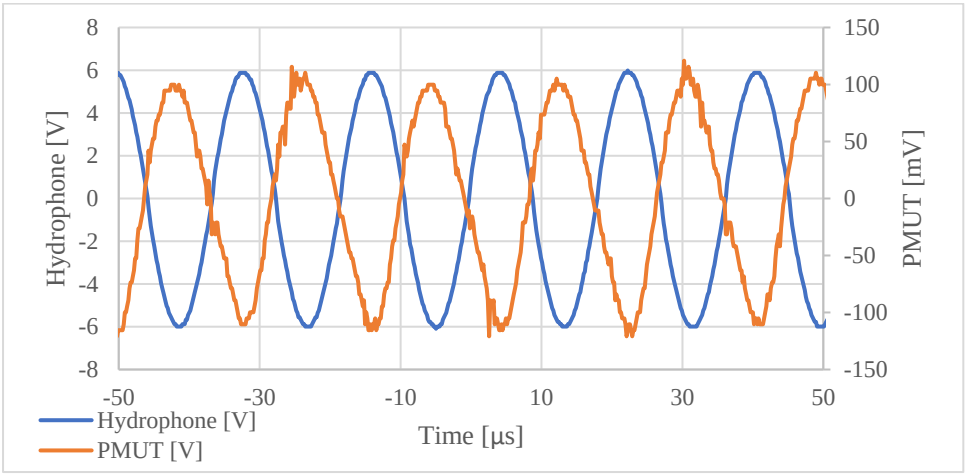

Figure 4.179 ~ Voltage applied across hydrophone vs voltage measured out of PMUT for device 27 operating as continuous sinusoidal waveform transmitter at 55 kHz. Cavity was isopropanol filled.

The voltage output from the PMUT was 213.8 mV with a phase shift of 242.4°. It was noted that the PMUT also picked up 55.9 kHz.

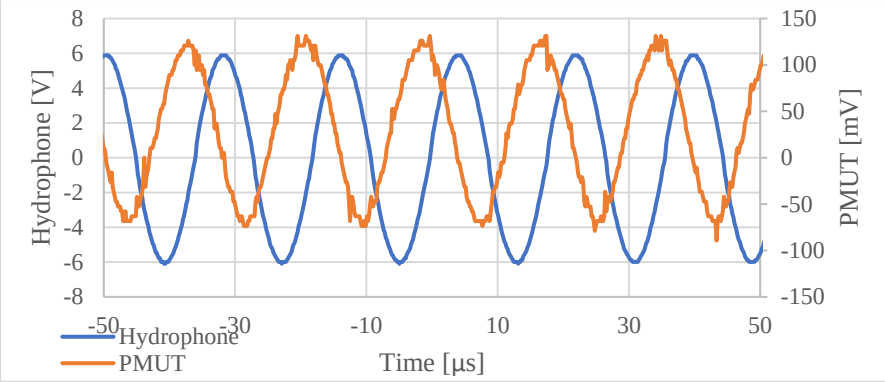

Figure 4.180 ~ Voltage applied across hydrophone vs voltage measured out of PMUT for Device 27 operating as continuous sinusoidal waveform transmitter at 55.9 kHz. Cavity was isopropanol filled.

4.6.20 Device 28 ~ Special design PMUT-Trench Diameter of 1,000 µm

Device 28 was another special design PMUT with slots in the diaphragm designed to optimise device performance and reduce the resonant frequency of the device.

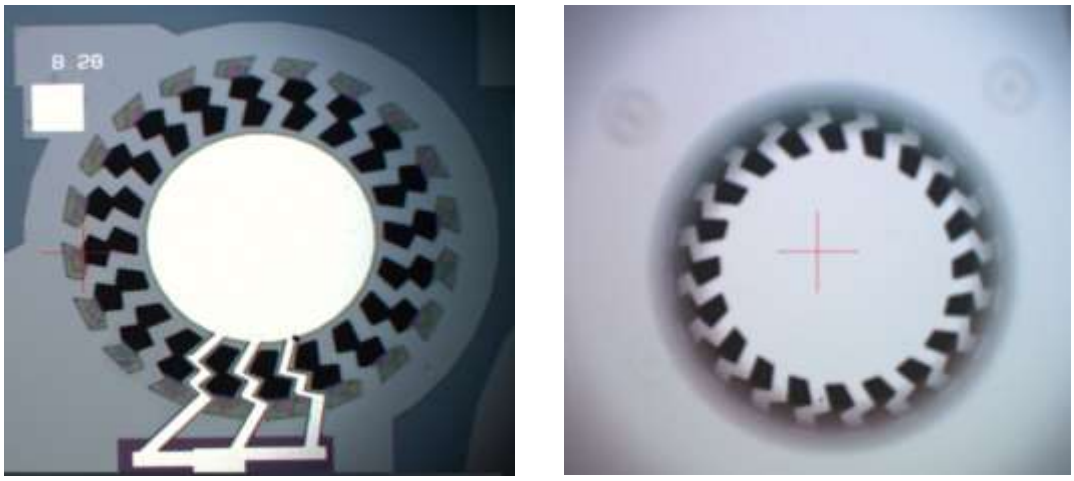

(a) (b)

Figure 4.181 ~ (a) Front View and (b) rear micrograph view of device 28

4.6.20.1 Laser Vibrometer characterisation of Device 28

Coupling Fluid: Isopropanol ~ Cavity Fluid: Air

The device was deployed in an isopropanol environment and with an air filled cavity and excited with a periodic chirp signal in which the resonant frequency was determined as per Figure 4.182.

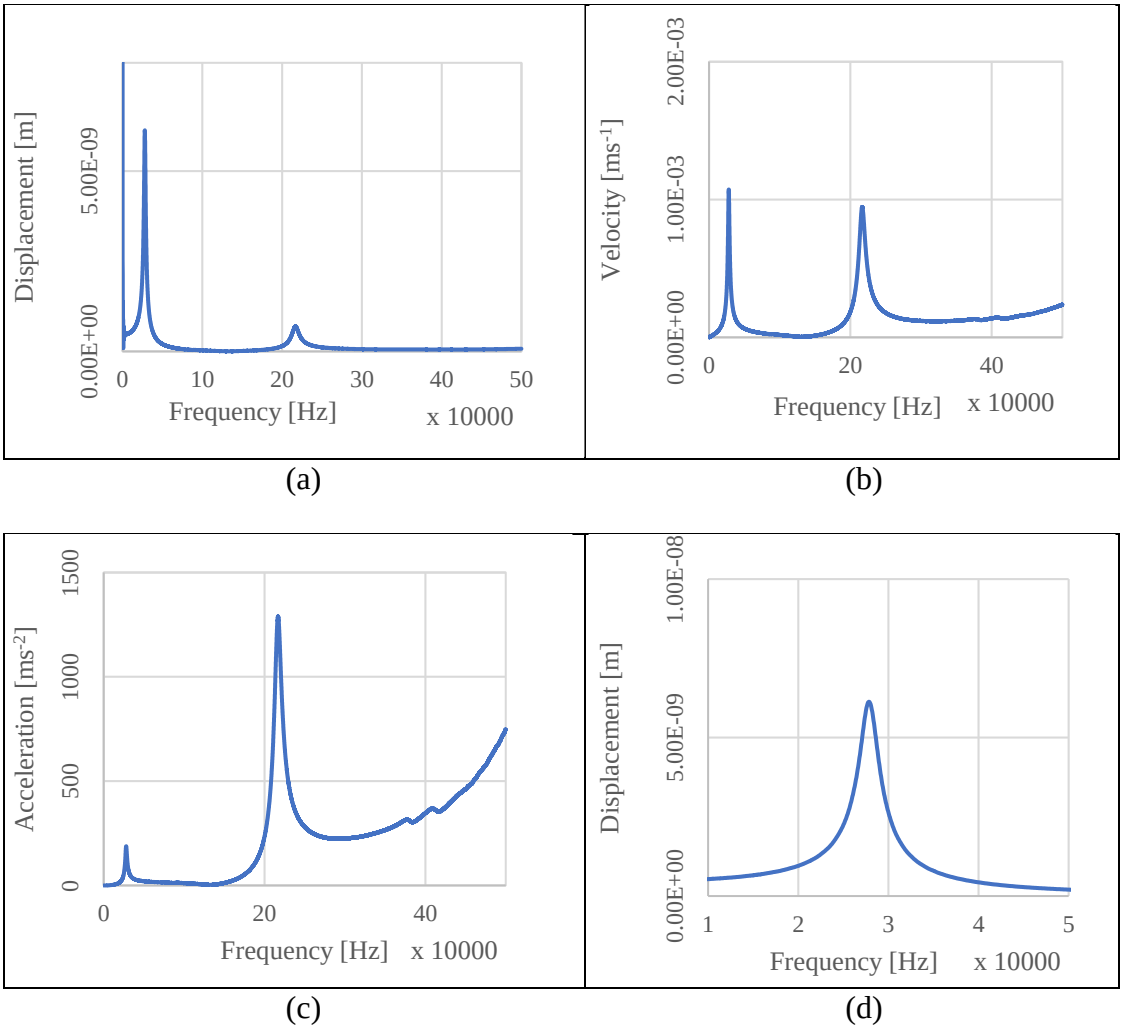

Figure 4.182 ~ Periodic Chirp frequency between 0 and 500 kHz with (a) Displacement, (b) Velocity and (c) acceleration values vs frequency for Device 28 in isopropanol coupling fluid and having an air filled cavity. (d) Shows displacement vs frequency at a frequency between 10,000 Hz and 50,000 Hz.

Two modes of oscillation where identified by the laser vibrometer during the periodic chirp excitation as shown in Figure 4.183

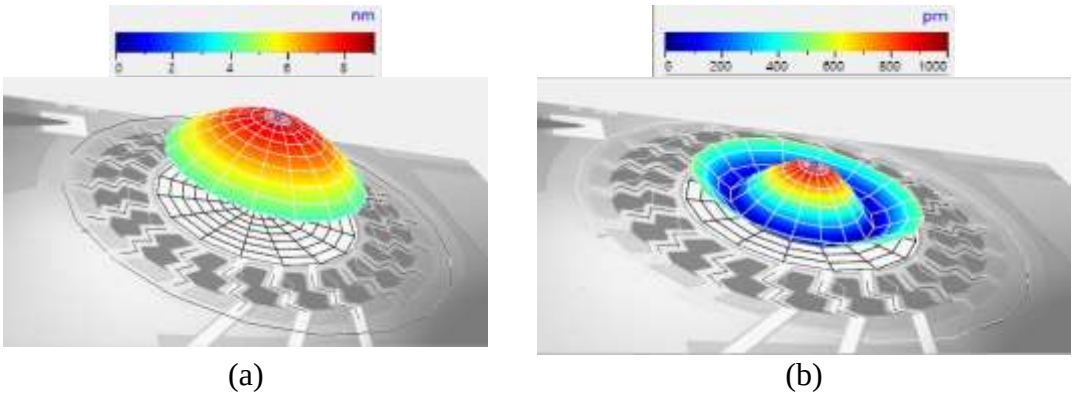

Figure 4.183 ~ Displacement of Device 28 excited with a periodic chirp signal at a frequency (a)27.85 kHz (b)216.6 kHz in isopropanol coupling fluid and air filled cavity.

Device 28 was then excited with Sine wave signal having a 14 V_{p-p} amplitude and the movements were observed as shown in Figure 4.184.

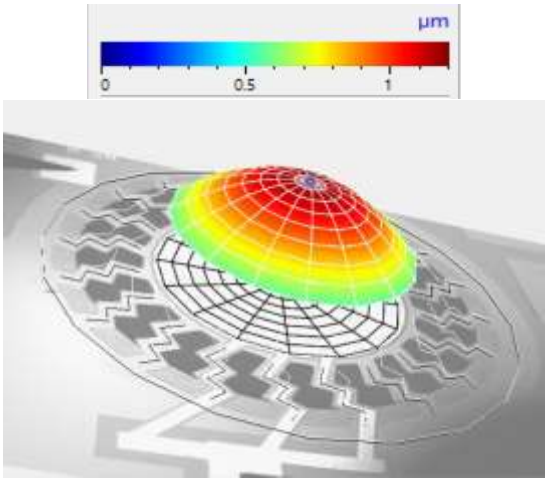

Figure 4.184 ~ Displacement of Device 28 excited with a periodic chirp signal at a frequency of 27.97 kHz. Values shown are actual readings directly from vibrometer and not normalised with the fluid's refractive index.

The details of the results obtained are tabulated in Table 4.44.

Table 4.44 ~ Maximum values at device centre point- frequency 27.97 kHz

Parameter	Value measured by vibrometer	Values normalised by the coupling liquid's refractive index†1
Peak Displacement	1.166 µm	0.851 µm
Peak Velocity	0.2049 m/s	0.149 m/s
Peak Acceleration	36 km/s^2	26.277 km/s^2

Note †1: Using ratio Isopropanol/Air ~ 1.37

Coupling Fluid: Glycerine ~ Cavity Fluid: Air

The next step involved testing the device in a Glycerine coupling fluid and an air cavity. Device excitation was conducted using a Periodic Chirp signal and the results are shown in Figure 4.185.

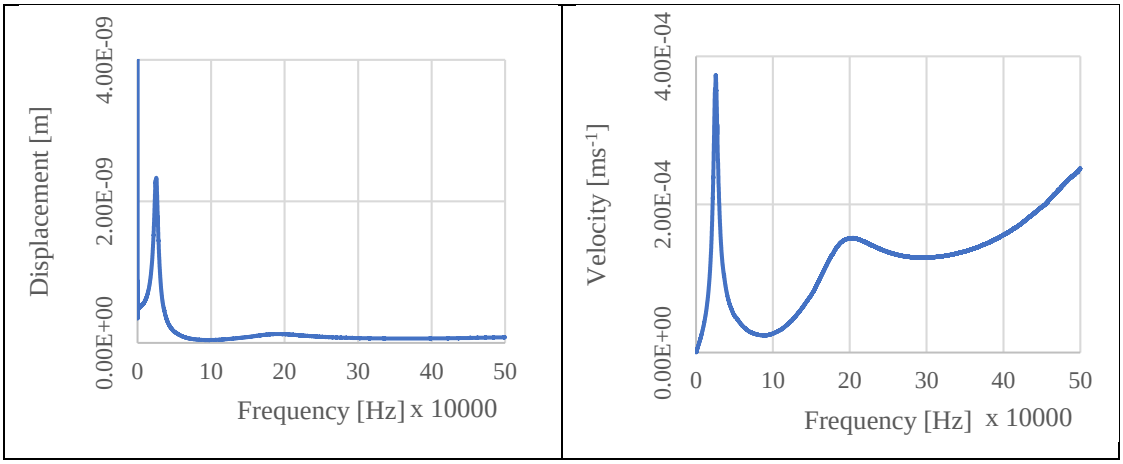

(a) (b)

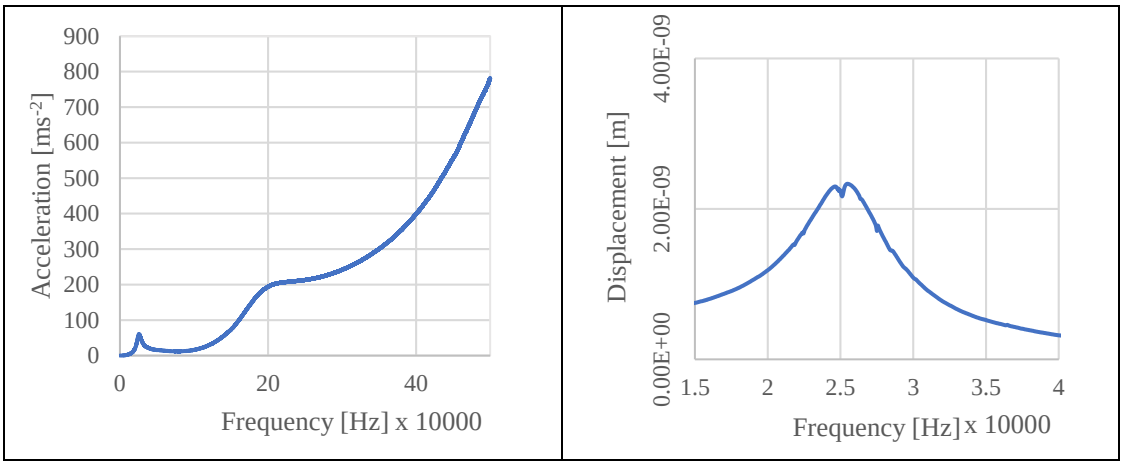

(c) (d)

Figure 4.185 ~ Periodic Chirp frequency between 0 and 500 kHz with (a) Displacement, (b) Velocity and (c) acceleration values vs frequency for Device 28 in glycerine coupling fluid and air filled cavity. (d) Shows displacement vs frequency at a frequency between 15,000 Hz and 40,000 Hz.

Two modes of Oscillation were identified by the laser vibrometer through the periodic chirp excitation process as seen in Figure 4.186.

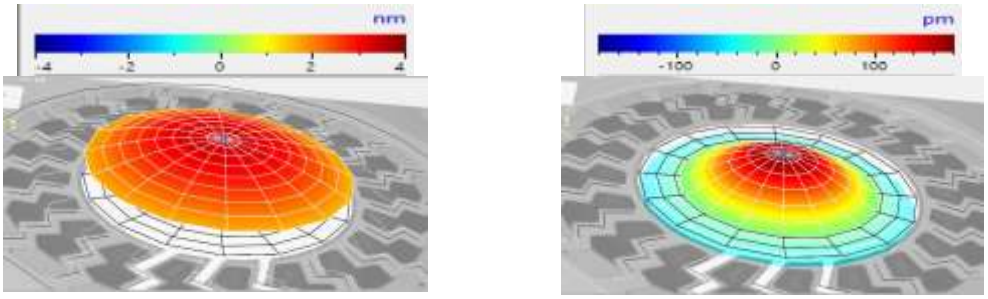

(a) (b)

Figure 4.186 ~ Displacement of Device 28 excited with a 14 V_{p-p} periodic chirp signal at a frequency (a)25.5 kHz (b)200 kHz in glycerine coupling fluid & air filled cavity. Values shown are actual readings directly from vibrometer and not normalised with the fluid's refractive index.

The Device 28 was then excited with a sine wave signal at its point of resonance. The sine wave signal had 14 V_{p-p} amplitude and the response is shown in Figure 4.187

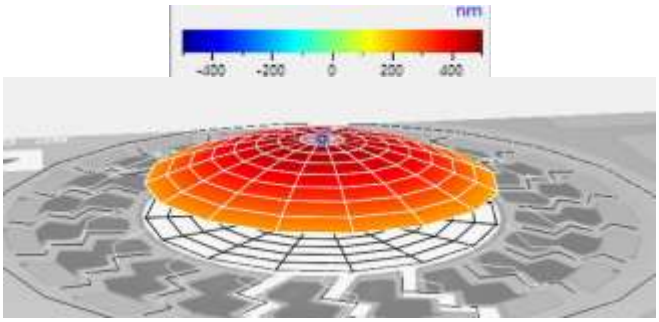

Figure 4.187 ~ Displacement of Device 10 excited with a 14 V_{p-p} periodic chirp signal at a frequency 25.62 kHz in glycerine coupling fluid and having an air filled cavity. Values shown are actual readings directly from vibrometer and not normalised with the fluid's refractive index.

The PMUT dynamics measured during excitation are tabulated in Table 4.45.

Table 4.45 ~ Maximum values at device centre point- frequency 25.5 kHz

Parameter	**Value measured by vibrometer**	**Values normalised by the coupling liquid's refractive index**[†1]
Peak Displacement	467.7 nm	322.55 nm
Peak Velocity	75.31 mm/s	51.94 mm/s
Peak Acceleration	12.13 km/s^2	8.655 km/s^2

Note †1: Using ratio Glycerine/Air ~ 1.45

4.6.21 Device 29 ~ Circular PMUT-Trench Diameter of 1,800 µm

Device 29 was a circular PMUT with a diameter of 1,800 µm. It was a large diameter PMUT included in the test sequence to:

- Contribute to the study of the relationship between resonant frequency and PMUT diameter for devices deployed in isopropanol.
- Contribute towards the study on how a liquid filled cavity effects ultrasonic transmission.

The frontal micrograph of the device is seen in Figure 4.188

Figure 4.188 ~ Micrograph showing frontal side of Device 29. Part in white shows padmetal.

The design parameters for Device 28 are tabulated in Table 4.46

Table 4.46 ~ Geometric data for device 29

Nominal Trench Diameter [µm]	Padmetal Cover [%]	Padmetal Diameter [µm]	Padoxide Diameter [µm]	Pzfilm Diameter [µm]	Design Features
1,800	66	1,188	1,172	1,800	Circular PMUT.

4.6.21.1 Laser Vibrometer Characterisation of Device 29

Coupling Fluid: Isopropanol ~ Cavity Fluid: Air

Device 29 was excited with a Periodic Chirp signal when deployed in isopropanol coupling fluid and having an air filled cavity. The resonant frequency was determined and the results can be reviewed in Figure 4.189.

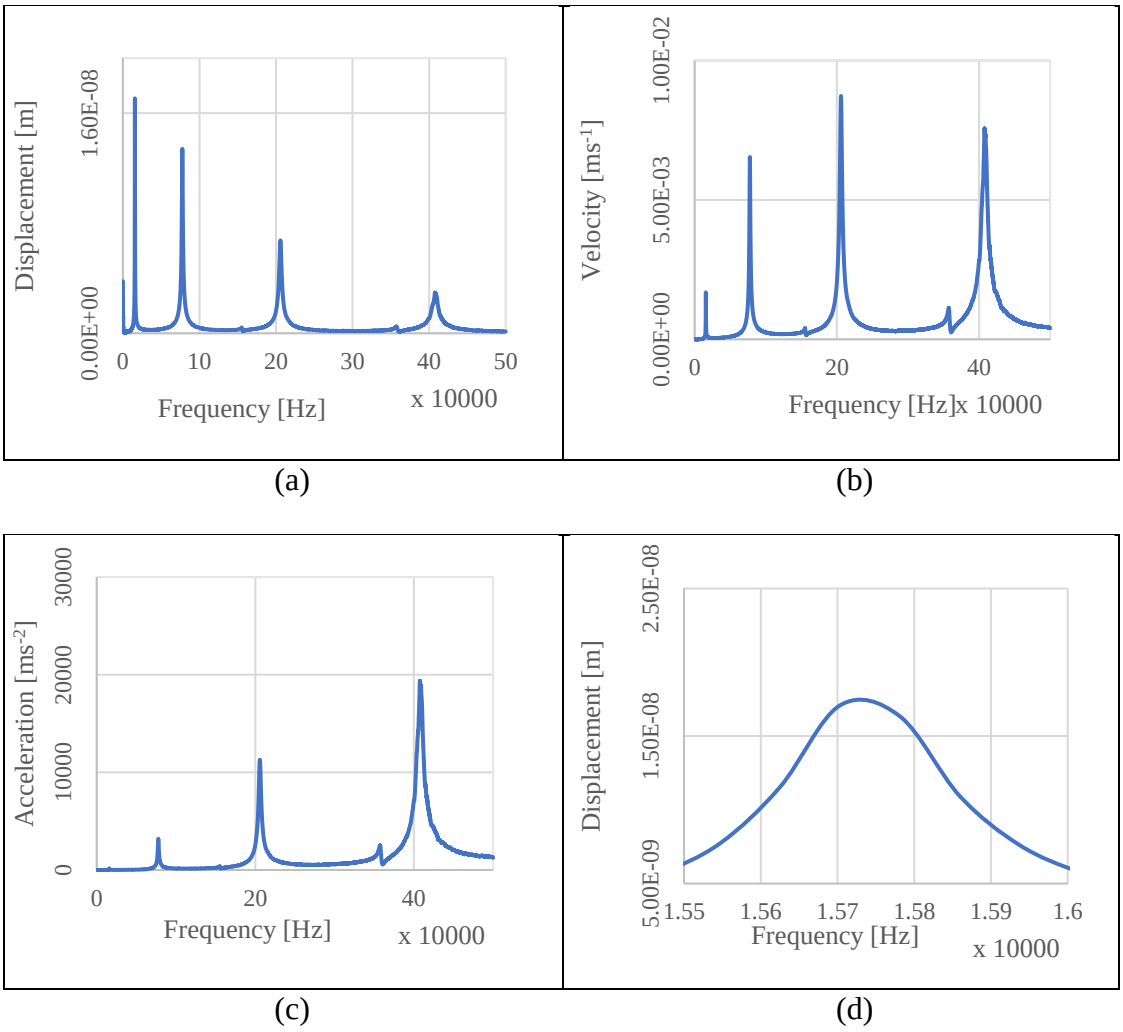

Figure 4.189 ~ Periodic Chirp frequency between 0 and 500 kHz with (a) Displacement, (b) Velocity and (c) acceleration values vs frequency for Device 29 in isopropanol and air filled cavity. (d) Shows displacement vs frequency at a frequency between 15,500 Hz and 16,000 Hz.

Various modes of oscillation at various points of resonance were identified by the laser vibrometer during the periodic chirp excitation process. These can be seen in Figure 4.190.

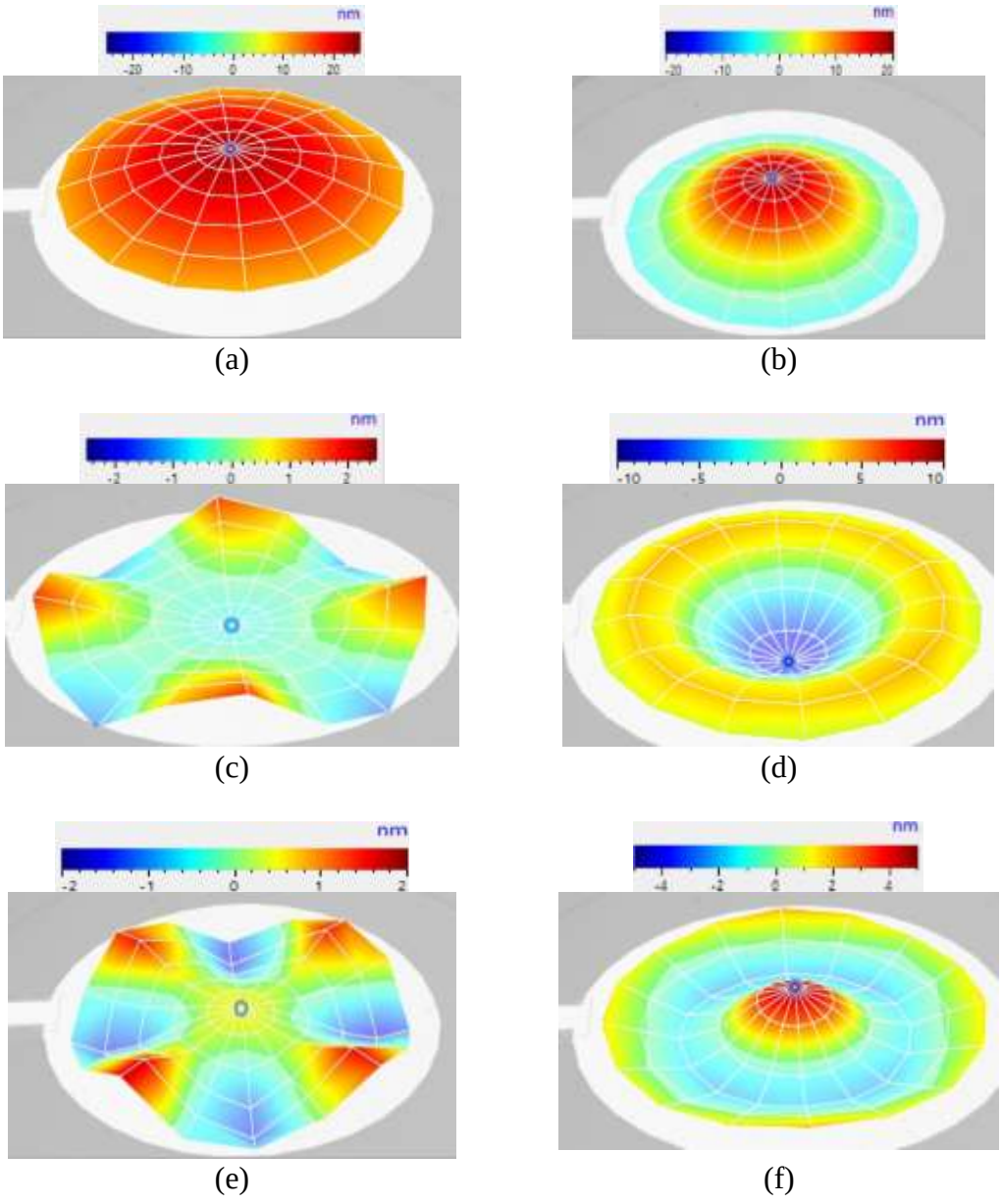

Figure 4.190 ~ Displacement of Device 29 excited with a periodic chirp signal at a frequency (a) 15.86 kHz;(b)77.73 kHz; (c)155.62 kHz (d)205.86 kHz (e)357.81 kHz (f)408.36 kHz in isopropanol coupling fluid and having an air filled cavity. Values shown are actual readings directly from vibrometer and not normalised with the fluid's refractive index.

The device was excited at the fundamental resonant point of 15.75 kHz with a sine wave signal having 14 $V_{p\text{-}p}$ amplitude. The device scanned during peak displacement at sine wave excitation can be seen in Figure 4.191.

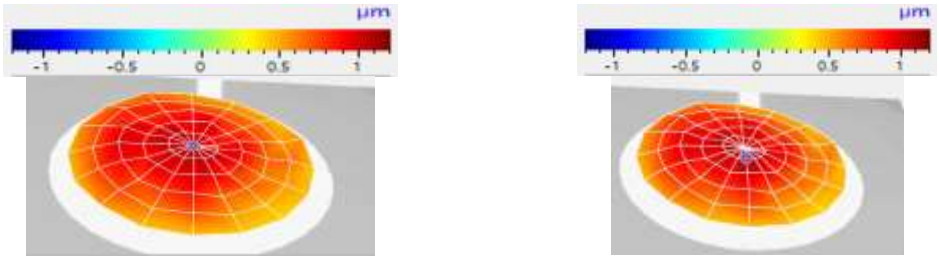

(a) (b)

Figure 4.191 ~ Displacement of Device 29 when excited. Device excitation with Sine wave signal at an amplitude of 7$V_{p\text{-}p}$ and at 15.78 kHz in isopropanol coupling fluid and having an air filled cavity. Values shown are actual readings directly from vibrometer and not normalised with the fluid's refractive index.

As can be seen in Figure 4.191 the displacement of the PMUT was irregular and at maximum displacement the diaphragm membrane looked warped. Readings at multiple points were taken in view of the shape and are tabulated in Table 4.47.

Table 4.47 ~ Maximum values at device centre point- frequency 15.78kHz

Parameter	**Value measured by vibrometer**	**Values normalised by the coupling liquid's refractive index**†1
Peak Displacement	994.2nm (point a) 1.076um (point b)	725.69nm (point a) 0.785um (point b)
Peak Velocity	95.58mm/s (point a) 0.1051m/s (point b)	69.766mm/s (point a) 0.0767m/s (point b)
Peak Acceleration	9.775km/s^2 (point a) 10.59km/s^2 (point b)	7.135km/s^2 (point a) 7.7299km/s^2 (point b)

Note †1: Using ratio Isopropanol/Air ~ 1.37

The voltage was increased further to see if the diaphragm can be made to be more stretched when in maximum displacement. Device 29 was then excited with a sine wave signal having an excitation voltage increased to 19 $V_{p\text{-}p}$. The frequency selected was again 15.78 kHz.

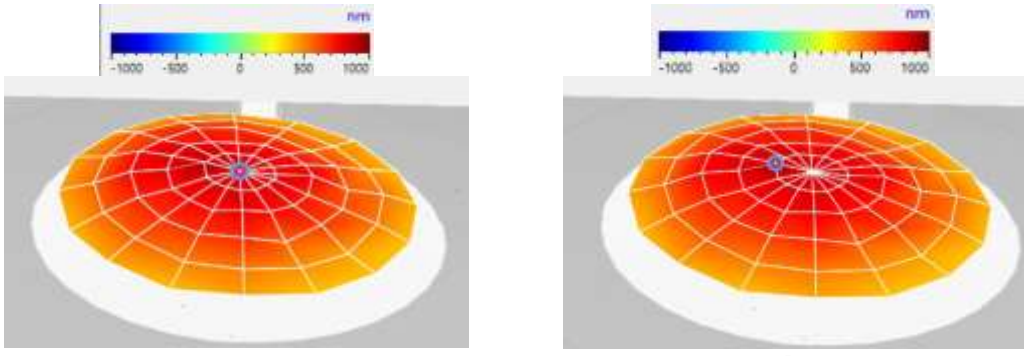

(a) (b)

Figure 4.192 ~ Displacement of Device 29 when excited. Device excitation with Sine wave signal of amplitude 19 $V_{p\text{-}p}$ and at 15.78 kHz. Diagram (a) indicates the location of point (a) and (b) indicates the location of point (b). Values shown are actual readings directly from vibrometer and not normalised with the fluid's refractive index.

From Figure 4.48 it was again evident that the membrane's surface topography remains warped and the measurements were tabulated in Table 4.48.

Table 4.48 ~ Maximum values at device centre point- frequency 15.78 kHz

Parameter	Value measured by vibrometer	Values normalised by the coupling liquid's refractive index†1
Peak Displacement	812.08nm (Point a) 926.5nm (Point b)	592.76nm (Point a) 676.28nm (Point b)
Peak Velocity	80.52mm/s (Point a) 92.25mm/s (Point b)	58.773mm/s (Point a) 67.33mm/s (Point b)
Peak Acceleration	7.984km/s^2 (Point a) 9.145 km/s^2 (Point b)	5.83km/s^2 (Point a) 6.675 km/s^2 (Point b)

Note †1: Using ratio Isopropanol/Air ~ 1.37

In view of these results and shapes obtained it was determined that the large diameter of the device must be having a detrimental effect on the PMUT's oscillatory movements resulting in distortions of the diaphragm.

Coupling Fluid: Isopropanol ~ Cavity Fluid: Isopropanol

A new device was again deployed in an isopropanol coupling fluid and this time with isopropyl filled cavity. Device excitation with a sine wave signal at 14 $V_{p\text{-}p}$ amplitude was conducted. The resonant frequency with both sides in isopropanol was 47.03 kHz.

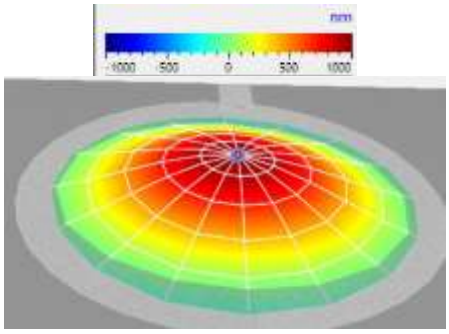

Figure 4.193 ~ Displacement of Device 29 excited with a 14 $V_{p\text{-}p}$ sine wave signal at a frequency 47.03 kHz in isopropanol coupling fluid & having an air filled cavity. Values shown are actual readings directly from vibrometer and not normalised with the fluid's refractive index.

The measured parameters from the midpoint of the moving diaphragm were tabulated in Table 4.49.

Table 4.49 ~Maximum values at device centre point at a frequency of 47.03 kHz

Parameter	Value measured by vibrometer	Values normalised by the coupling liquid's refractive index†1
Peak Displacement	970.3 nm	708.25 nm
Peak Velocity	0.2867 m/s	0.209 m/s
Peak Acceleration	84.73 km/s^2	61.85 km/s^2

Note †1: Using ratio Isopropanol/Air ~ 1.37

4.6.21.2 Acoustic Experimental data for Device 29

Device 27 Acting as Receiver

Step 1 - Setup

The experimental device was placed in a 10 cm diameter petri dish and Device 29 was probed. The petri dish was then filled with isopropanol with the hydrophone being submerged 4 mm below the surface of the fluid. The cavity was left air filled. The hydrophone's electrical system was set up as shown in Figure 4.16 and connected to the low noise preamplifier.

Step 2 – PMUT acting as receiver.

The acoustic pressure levels measured from this device when operating in receiving mode were not very high. As an example at 74 kHz the maximum output voltage from the hydrophone was 88 $mV_{p\text{-}p}$.

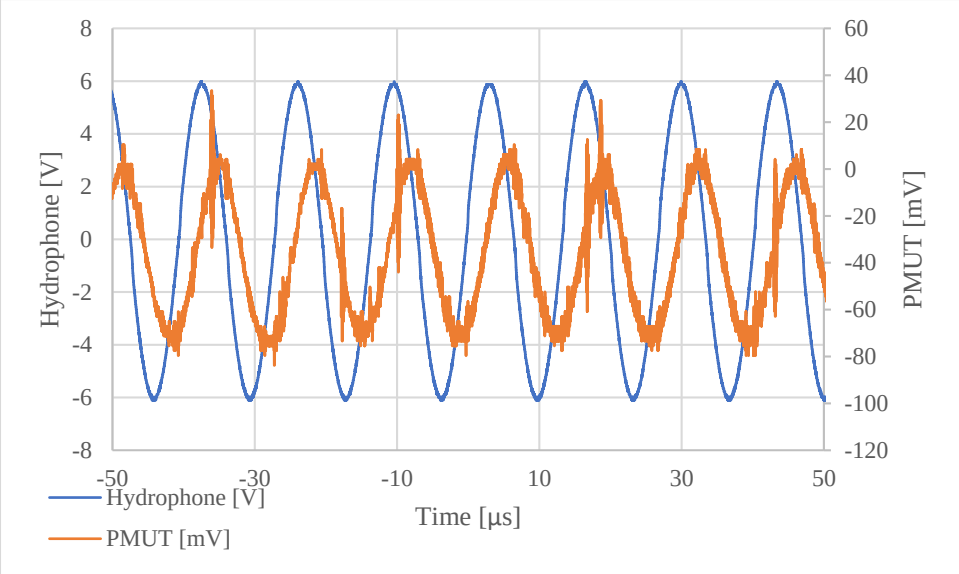

Figure 4.194 ~ PMUT receiving ultrasonic radiation at a frequency of 74 kHz. The maximum voltage across it was 88 $mV_{p\text{-}p}$.

An interesting result which may potentially lead to future research projects was noticed during testing. As Device 29 was probed in the coupling fluid it was noticed that the device tended to oscillate at a frequency of 3.319 kHz even when not excited directly by the hydrophone. This can be seen in Figure 4.195.

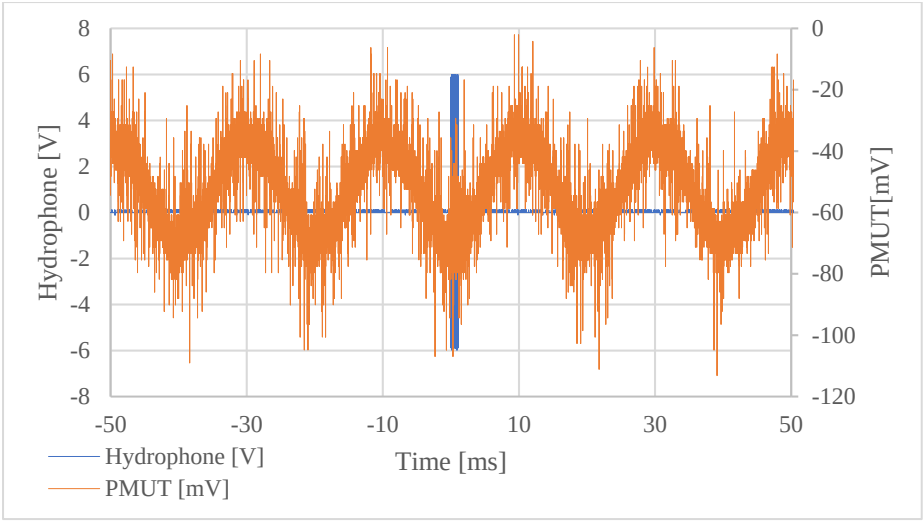

Figure 4.195 ~ Oscillation of Device 29 at a background frequency of 3.319 kHz continues without change even after the application of a burst signal having 159 wavelengths of 74 kHz ultrasonic radiation from the hydrophone with a pressure of 35 Pa.

Ultrasonic bursts at particular frequencies were introduced in the coupling fluid to observe how the PMUT's oscillatory behaviour was influenced and whether the background oscillations observed could be stopped. It was noted that even when excited at particular frequencies ranging between 10 and 80 kHz the oscillation still continued unabated as shown in Figure 4.195. This tendency to oscillate without external excitation was observed in the large diameter PMUTS especially the 1,800 µm and 2,000 µm PMUTs.

4.6.22 Device 33 ~ Circular PMUT- Trench Diameter of 2,000 µm

Device 33 was the largest diameter PMUT device of the test series. It was placed in the experimental series for a number of reasons particularly:

- To be part of the series establishing an equation linking PMUT diameter with resonant frequency.
- To review the durability and reliability of large diameter PMUTs. It is important to note that with the PiezoMUMPs^{TM} process the diaphragm thickness remains constant irrespective of the diaphragm diameter.

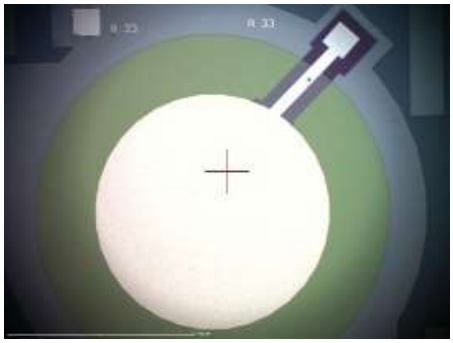

Figure 4.196 ~ Micrograph showing frontal side of Device 33. Part in white shows padmetal.

Table 4.50 presents the geometric data for Device 33.

Table 4.50 ~ Geometric data for Device 33

Nominal Trench Diameter [µm]	Padmetal Cover [%]	Padmetal Diameter [µm]	Padoxide Diameter [µm]	Pzfilm Diameter [µm]	Special Design Features
2,000	66	1,320	1,304	2,000	Circular PMUT

4.6.22.1 Laser Vibrometer Characterisation of Device 33

Coupling Fluid: Isopropanol ~ Cavity Fluid: Air

The device was excited with a periodic chirp signal when deployed in an Isopropanol coupling fluid environment and having an air filled cavity. The results of the periodic chirp signal are shown in Figure 4.197.

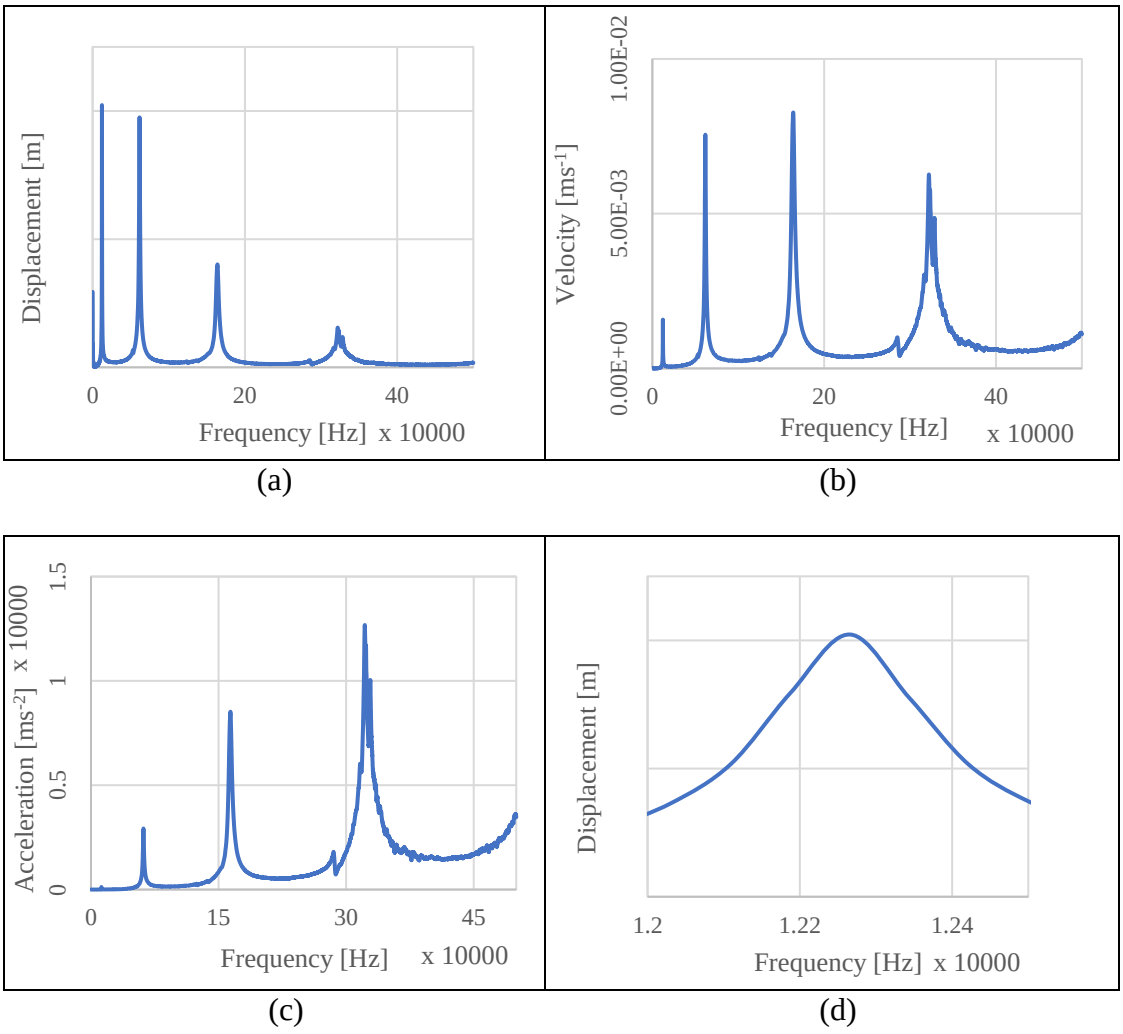

Figure 4.197 ~ Periodic Chirp frequency between 0 and 500 kHz with (a) Displacement, (b) Velocity and (c) acceleration values vs frequency for Device 33 in isopropanol coupling fluid and having an air filled cavity. (d) Shows displacement vs frequency at a frequency between 12,000 Hz and 12,500 Hz.

Various modes of oscillation were identified by the Laser Vibrometer during Periodic Chirp excitation. These are shown in Figure 4.198.

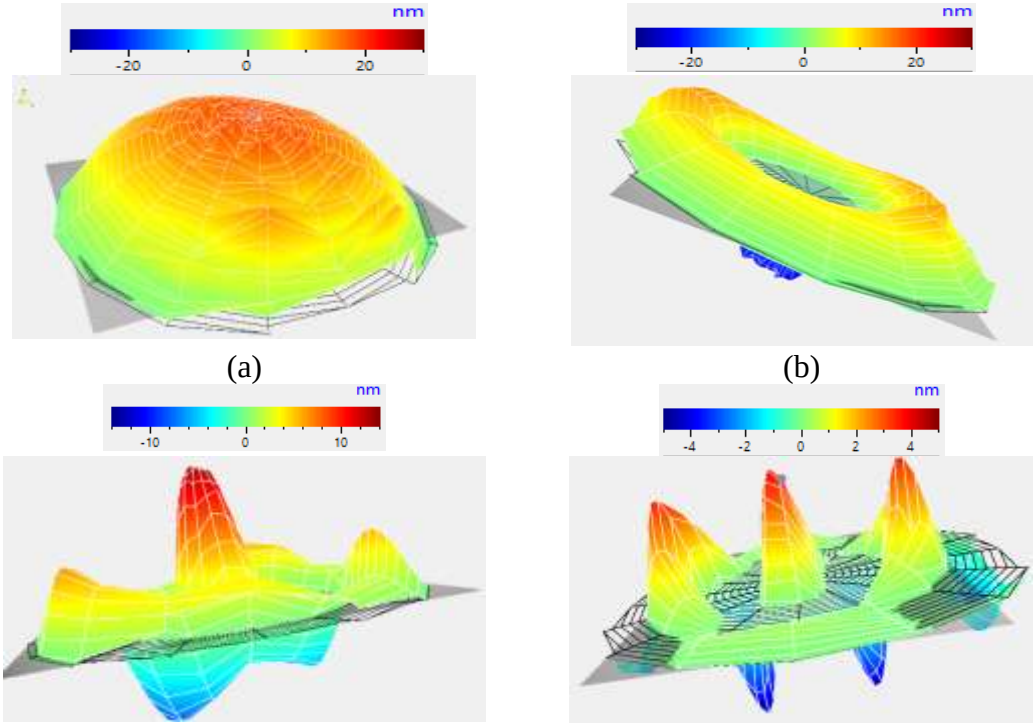

Figure 4.198 ~ Displacement of device 33 excited with a 14 $V_{p\text{-}p}$ periodic chirp signal at a frequency (a)12.27 kHz; (b)68.44KHz; (c)166.8 kHz; (d)314.69 kHz. Deployed in an isopropanol coupling fluid & having an air filled cavity. Values shown are actual readings directly from vibrometer and not normalised with the fluid's refractive index.

After establishing the resonant frequency the device was excited with a sine wave signal having an amplitude of 14 $V_{p\text{-}p}$.

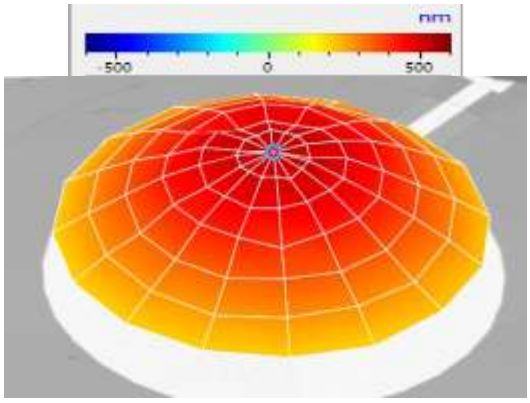

Figure 4.199 ~ Displacement of Device 33 excited with a 14 $V_{p\text{-}p}$ sine wave signal at a frequency 12.19 kHz. Device deployed in isopropanol coupling fluid and with an air filled cavity. Values shown are actual readings directly from vibrometer and not normalised with the fluid's refractive index.

The parameters measured at the diaphragm midpoint are tabulated in Table 4.51.

Table 4.51 ~ Maximum values at device centre point- frequency 12.19 kHz

Parameter	**Value measured by vibrometer**	**Values normalised by the coupling liquid's refractive index**†1
Peak Displacement	1.3 µm	0.95 µm
Peak Velocity	154.50 mm/s	112.77 mm/s
Peak Acceleration	18.494 km/s^2	13.499 km/s^2

Note †1: Using ratio Isopropanol/Air ~ 1.37

Coupling Fluid: Glycerine ~ Cavity Fluid: Air

Device 33 was next deployed in a glycerine coupling fluid and the cavity was left air filled. The device was then excited through a periodic chirp signal and the dynamic results are shown in Figure 4.200.

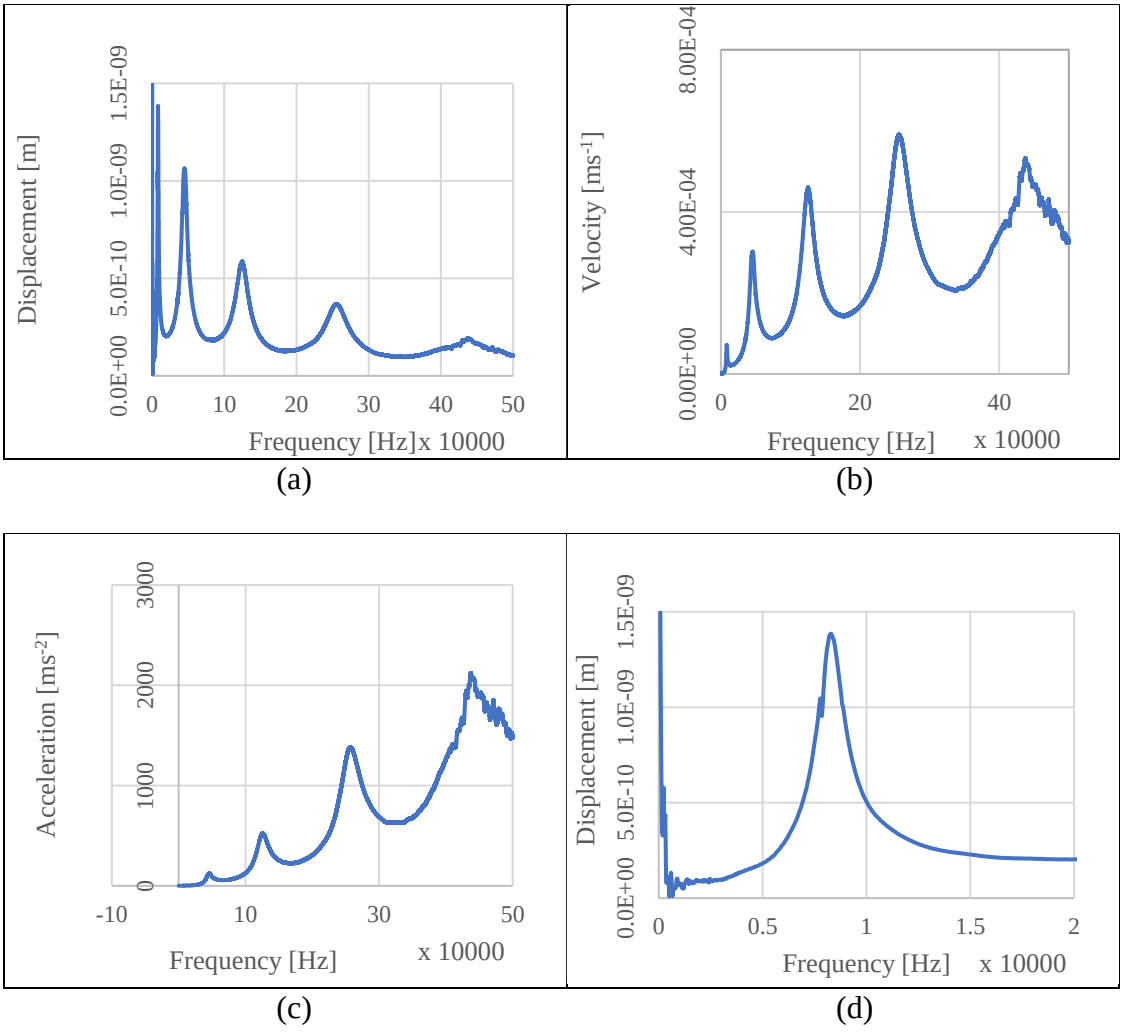

Figure 4.200 ~ Periodic Chirp frequency between 0 and 600 kHz with (a) Displacement, (b) Velocity and (c) acceleration values vs frequency for Device 33 deployed in glycerine coupling fluid and with air filled cavity. (d) Shows displacement vs frequency at a frequency between 4,000Hz and 10,000Hz.

Various modes of oscillation were identified by Laser Vibrometer during Periodic Chirp excitation. These are shown in Figure 4.201.

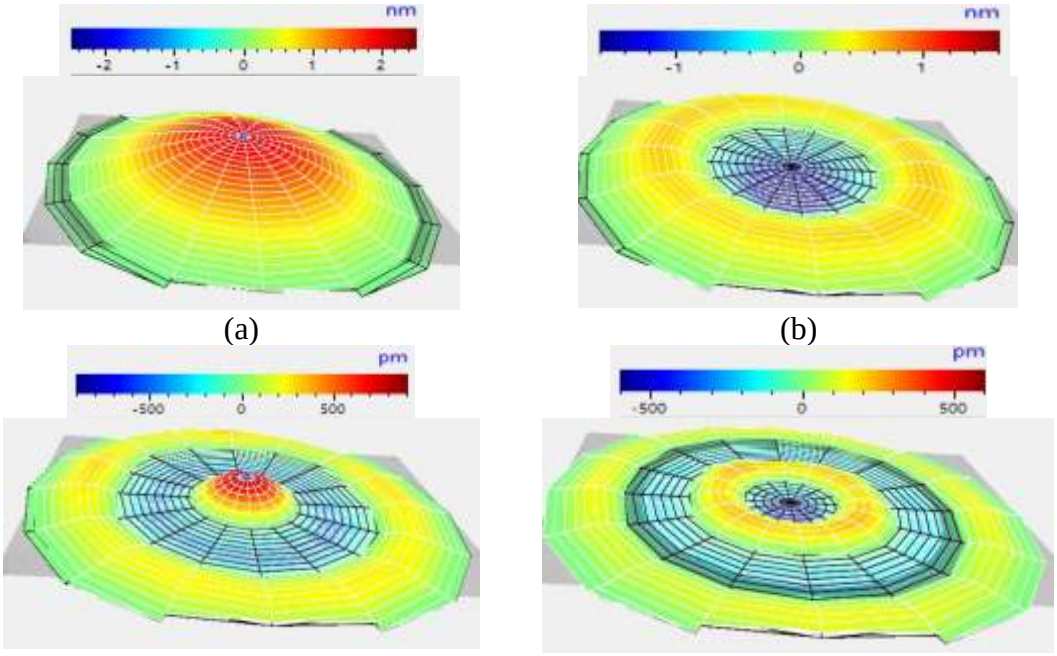

Figure 4.201 ~ Displacement of device 33 excited with a Periodic Chirp sine wave signal at a frequency of (a)8.281 kHz (b)44.961 kHz (c)124.688 kHz (d) 255.547 kHz. Deployed in glycerine coupling fluid and having an air filled cavity.

Device 33 was then excited with Sine wave signal with a 14 V_{p-p} amplitude. The maximum displacement point is shown in Figure 4.202.

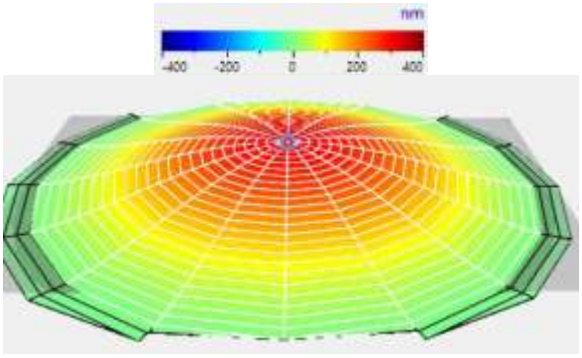

Figure 4.202- Displacement of Device 33 excited with a 7V_{p-p} sine wave signal at a frequency 8.28 kHz. Device deployed in glycerine coupling fluid and with an air filled cavity. Values shown are actual readings directly from vibrometer and not normalised with the fluid's refractive index.

The measured values of the PMUT movements are shown in Table 4.52

Table 4.52 ~ Maximum values at device centre point at a resonant frequency of 8.28 kHz

Parameter	**Value measured by vibrometer**	**Values normalised by the coupling liquid's refractive index**[†1]
Peak Displacement	309.2 nm	213.24 nm
Peak Velocity	16.10 mm/s	11.10 mm/s
Peak Acceleration	837.9 m/s^2	577.86 m/s^2

Note †1: Using ratio Glycerine/Air ~ 1.45

4.6.22.2 Acoustic Experimental data for Device 33.

Device 33 acting as Transmitter

Step 1 - Setup

The experimental device was placed in 10 cm diameter petri dish and Device 33 was probed after which the dish was filled with isopropanol and the hydrophone was submerged 4 mm below the surface of the fluid. The cavity was left air filled. Hydrophone electrical system was set up as shown in Figure 4.16 and connected to the low noise preamplifier.

Step 2 – PMUT acting as transmitter.

The hydrophone was excited at frequencies ranging from 7 to 15 kHz. The best transmission output was found to be at 13.27 kHz. The input from the hydrophone was found to be of very low power and a function to overlay low power inputs into a trend plot was used to observe the signal as shown in Figure 4.203.

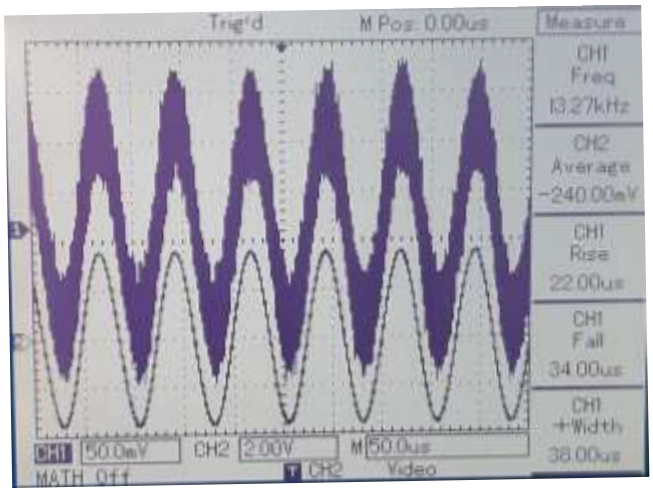

Figure 4.203 ~ Hydrophone output at a frequency of 13.27 kHz.

4.6.23 Laser Diffraction Measurements.

Detection of PMUT resonant frequency through the use of Laser diffraction was carried out to verify vibrometer reading for readings which either were not in line with FEM results or which appeared to have defective movements when observed with the vibrometer. The procedure for the laser diffraction process followed the method established in Chapter 4 – Experimental Procedure I.

Laser diffraction readings were conducted on at least five devices of the same design to ensure repeatability and reliability of results. The average value is reproduced below.

On the other hand laser vibrometer testing could only be carried out on one device due to cost since specialised equipment owned by Polytec had to be used.

Table 4.53 compares the resonant frequency results achieved from both the laser vibrometer and the laser diffraction procedures.

Table 4.53- Comparison between resonant frequency results achieved through Laser Vibrometer and Laser Diffraction procedures. Devices in isopropanol coupling fluid and with an air filled cavity.

Device number	**Diameter [μm]**	**Resonant Frequency results from Laser Vibrometer procedures [kHz]**	**Resonant Frequency result from Laser Diffraction procedure (average of five devices) [kHz]**
44	600	152	152
49	650	119.53	124
39	900	62.03	62
29	1,800	15.78	12.69
33	2,000	12	11

Laser diffraction measurements were found to be difficult to carry out on devices smaller the 600 μm with the laser equipment available.

4.7 Conclusions from the experimental work.

This chapter outlined and explained the experimental work conducted in this project. Three types of experimental procedures were conducted namely laser vibrometer, laser diffraction and ultrasonic work.

The main results achieved may be summarised as follows:

- The wider the PMUT's diameter, the lower its resonant frequency would be.
- A PMUT with a liquid filled cavity has a higher resonant frequency and a reduced amplitude of vibration when compared to a gas filled one.
- By modifying the diaphragm of a PMUT, such as by cutting holes in the diaphragm, the resonant frequency can be changed. The performance both in terms of transmission and reception of ultrasonic radiation can also be potentially enhanced. The geometry which needs to be used is however quite specific and an operational design was only achieved after extensive FEM was conducted.
- Multi electrode designs can also provide improvement to PMUT dynamics.
- PMUTs having relatively wide diameter significantly over the 1,000 μm diameter mark, were observed to be effected by intrinsic issues when transmitting or receiving ultrasonic data, such as picking up, locking to and resonating with the background ultrasonic radiation. Such radiation comes through the structure and is caused by vibrations.
- High density fluids such as glycerine drastically slowed down PMUT displacement and velocity.

Further to the detailed presentation of the results achieved for each device as outlined in this chapter, the next stage of the result analysis was a comparative assessment process of the results achieved. This comparative assessment in which the results achieved by one device were compared with those achieved by another benchmark device will be discussed in further detail in Chapter 5. That chapter will also outline the result analysis where the results achieved by a number of PMUT designs were studied together as a series.

From the analysis conducted and outlined in Chapter 5, conclusions were derived from which the ultimate PMUT geometries can then be derived.

Chapter 5: Result Analysis, Conclusions and Recommendations.

This chapter will conclude this dissertation by conducting a thematic analysis and discuss the results achieved from Finite Element Modelling and experimental work conducted. The results will be processed through comparative assessments where results achieved from different units will be compared together.

5.1 Conclusion 1 ~ Physical observations during the experimental process

The first experimental sessions carried out on receipt of the test MEMs devices, were conducted using distilled water as coupling fluid. Distilled water rather than tap water was selected, to lower the:

- ionic content thereby reducing the fluid's conductivity. Reduction in conductivity was deemed to be important in view that the distance between the probe needles during the experimentation process was only a few micrometres.
- quantity of impurities in the coupling fluid. Such impurities settle as residue on the PMUT thereby impacting the PMUT performance.
- chances of having chemical reactions between dissolved chemical species and the PiezoMUMPs^{TM} die material. Such chemical reactions may alter the nature and structure of the layers making up the device.

However it soon became evident that distilled water was not the ideal coupling fluid to use with PiezoMUMPs^{TM} devices. Figure 5.1, Figure 5.2, Figure 5.3 present micrographs showing damage which was noted on devices after experimental procedures were conducted in water coupling fluid.

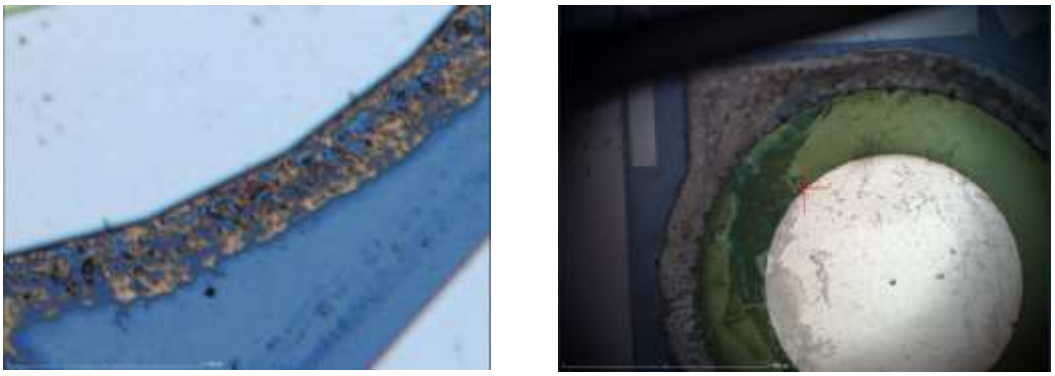

(a) (b)

Figure 5.1 ~ Micrographs (a) and (b) show damage due to water suffered by layers including the Piezolayer shown in green and the SOI layer shown as bubbling grey

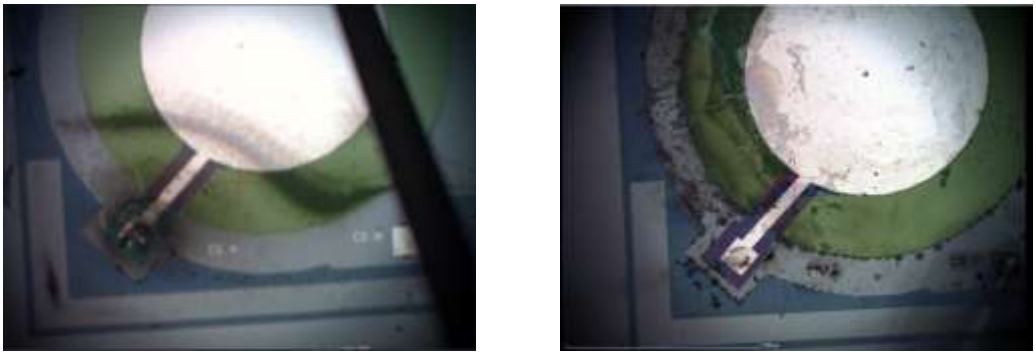

(a) (b)

Figure 5.2 ~ Micrographs showing (a) deterioration of probe pad together with residue and (b) showing residue left on device after experimental work conducted in distilled water.

(a) (b)

Figure 5.3 ~ Micrograph (a) shows complete oxidation and dissolution of a probe pad (b) view of test device after exposure to water showing residues and start of deterioration processes.

More serious damage was observed when the device was exposed to water and left under the influence of incoming ultrasonic radiation from hydrophone for an extended time period. Photomicrographs are shown in Figure 5.4.

(a) (b)

Figure 5.4 ~ Damage effects to (a) piezoelectric and (b) pad metal layers due to the combination of ultrasonic radiation and water.

Ultrasonic radiation was therefore shown to accelerate the water deterioration processes.

Due to the deteriorative effect of water it was decided to try out other potential coupling fluids which had similar acoustic properties as water but without having the same effect on the devices. Various substances were researched before the decision was taken to utilise isopropanol. Isopropanol is a covalent compound which has acoustic and density properties very close to those of water and can be bought in its pure state from chemical reagent suppliers. After the use of isopropanol as coupling fluid started, no further deterioration was noticed on test devices especially with regards to device layers dissolving.

Hence the first conclusion derived from the experimental work conducted was that distilled water should not be used as coupling fluid in conjunction with PiezoMUMPS^{TM} devices. A successful coupling fluid would be one based on isopropanol or other covalent compounds with a similar chemical structure.

5.2 Conclusion 2 ~ The PMUT's resonant frequency with respect to its diameter when using isopropanol coupling fluid.

One of the important areas covered by this dissertation was the establishment of an equation outlining the relationship between the PMUT's resonant frequency and its dimeter when operating in a liquid coupling fluid. Table 5.1 tabulates the PMUT cavity diameters against the resonant frequencies calculated via analytical and experimental methods achieved in this dissertation.

Table 5.1 ~ PMUT cavity diameter vs experimental and calculated resonant frequencies for PMUT devices in Isopropanol coupling fluid and air filled cavity *[124]*.

Trench Diameter [µm]	**Experimental Resonant Frequency [kHz]**	**Calculated Resonant Frequency through analytical method [kHz]**
550	187.66	212.233
600	153.12	172.929
650	119.53	143.114
700	111.09	120.033
900	62.03	65.827
1,000	53.28	51.081
1,800	12.65[†1]	11.029
2,000	9.4[†1]	9.446

Note†1 The vibrometer value for the resonant frequency achieved by the 2,000 µm ϕ device (12.27kHz) was discarded since laser diffraction as well as audio confirmation results together converged on the lower resonant point of 9.3kHz. The 1,800 µm ϕ device was treated similarly.

It can be seen that the analytical and experimental value are well correlated. The analytical values were then plotted together with the experimental values as shown in Figure 5.5.

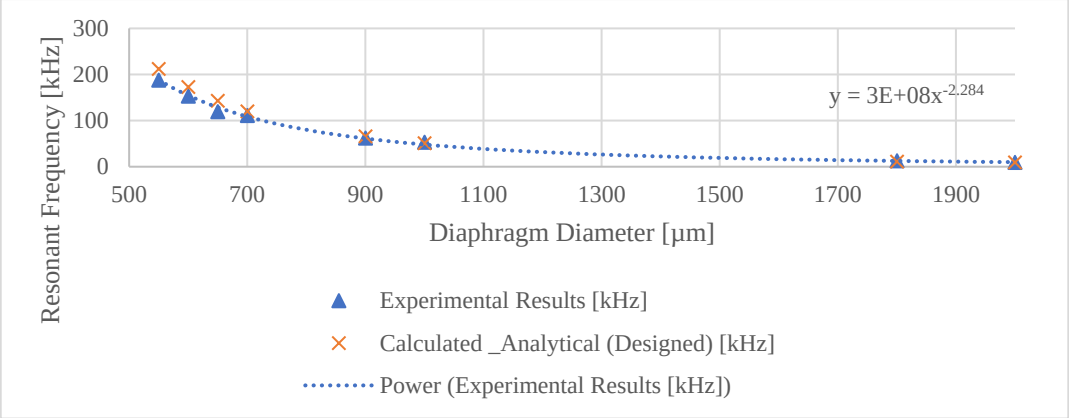

Figure 5.5 ~ Graph showing experimental and calculated (analytical) results [124].

Through graphical methods the equation linking resonant frequency with diaphragm diameter for PMUTs operating in isopropanol coupling fluid and air filled cavity is here being proposed in the form of equation (5.1)

$$f = 3x10^{8}D^{-2.284} \tag{5.1}$$

Where

f is the resonant frequency in kHz
D is the PMUT diaphragm's diameter in µm

This equation can be very useful for researchers designing PMUTs operating in the frequency range between 10 and 200 kHz operating in an isopropanol or water coupling fluid. As an example if one is targeting a resonant frequency of 90 kHz and using an isopropanol coupling fluid with an air filled cavity, the PMUT's diaphragm would require a diameter of 717.63 µm.

5.3 Conclusion 3 ~ How filling the cavity with a liquid or a gas filled effects the PMUT's dynamics including its resonant frequency.

Studying the dynamics of PMUTs with liquid filled cavities was deemed an important component for this project in view of the project scope itself, namely the development of PMUTs optimised to operate through concrete. If it could be shown that PMUTs could successfully operate with a liquid filled cavity it would present a possibility for devices to transmit and receive data in a bidirectional fashion i.e. both upwards and downwards perpendicularly to the device. The reason being that a device could potentially have coupling fluid on both sides by filling the cavity with liquid rather than air. A bidirectional device would be able to operate with only one PMUT die rather than two as presented in Figure 1.2.

Finite element modelling conducted and described in chapter 3 showed that having a liquid filled cavity would increase the resonant frequency and reduce the amplitude of vibration. This was confirmed experimentally as summarised below.

The vibrometer resonant frequency data obtained from PMUTs which were operated with liquid filled cavities was studied and tabulated against resonant frequency data achieved from PMUTs having an air filled cavity. The liquid used was isopropanol. The data is tabulated in Table 5.2.

Table 5.2 ~ Resonant frequency of PMUTs with liquid (isopropanol) filled cavity vs PMUT with air filled cavity.

	Resonant Frequency	
Trench Diameter [um]	**Liquid Filled Cavity [Hz]**	**Air Filled Cavity [Hz]**
650	373,440	119,530
700	235,000	111,090
900	225,000	62,030
1,000	195,000	53,280
1,800	47,030	12,650

This table clearly demonstrates the substantial increase in resonant frequency caused by having a liquid filled cavity instead of an air filled one. This is shown graphically in Figure 5.6.

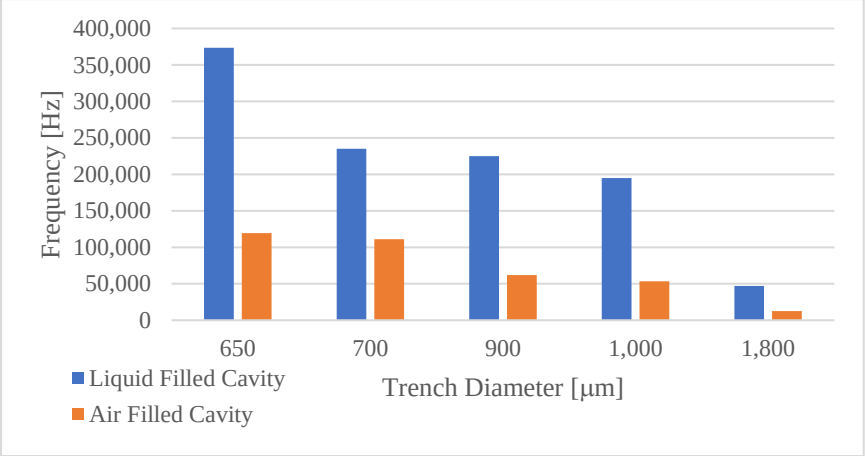

Figure 5.6 ~ Plot comparing the resonant frequency of PMUTs against trench diameter for devices with liquid or air filled cavities.

From a resonant frequency perspective, looking at these results clearly indicates that the cavity needs to be air filled to operate in the target resonant frequency region. For this project therefore, the cavity cannot be filled with a liquid coupling fluid. The reason being that as shown in Figure 5.6, the resonant frequency of a PMUT with liquid filled cavity would be too high for operations in concrete where the target frequencies for a proposed system are at or below 100 kHz. Experimentation and finite element modelling carried out in this project have made it clear that such frequencies could not be achieved by a PMUT having a liquid filled cavity unless one goes for a very large diameter cavity such as 1,800 µm. Having PMUTs with such a large diameter cavity

(such as the 1,800 μm diameter Device 29) would of course then present issues such as fragility, low reception, low amplitude of operation and oscillation with background ultrasonic radiation as shown in section 4.6.21.2 and as discussed further in conclusion 11.

5.4 Conclusion 4 ~ The effect which the density of the coupling fluid has on PMUT diaphragm midpoint velocity.

The next part of the conclusion involves a comparative assessment of the performance of PMUTs operating in high against those operating in low density coupling fluids. The high density coupling fluid used in this project was glycerine while the low density fluid used was isopropanol.

The values for peak midpoint displacement and velocity achieved by the PMUTs when excited in both the low density and the high density fluids are tabulated in Table 5.3. As can be seen in the table, the applied signal voltages to each of the PMUTs are not exactly the same since Devices 55, 56, 58, 59 had a higher voltages applied than the rest of the devices. The reason for this was that higher voltages were used in last laser vibrometer series in which Devices 55, 56, 58, and 59 were characterised in glycerine. This was done to observe the maximum PMUT output pressure output.

Table 5.3 ~ Table showing a comparative assessment of the effect of density on the PMUT diaphragm's midpoint velocity for devices deployed in isopropanol or glycerine.

			Air filled cavity		
Device number	**Diameter [μm]**	**Electrode cover or special shape**	**Diaphragm midpoint velocity in isopropanol coupling fluid [m/s]**	**Diaphragm midpoint velocity in glycerine coupling fluid [m/s]**	**Percentage difference [%]**
56	700	66%	0.555 ($14V_{p-p}$)	0.06986 ($19V_{p-p}$)	155.23
58	700	50%	0.318 ($14V_{p-p}$)	0.045 (18V)	150.41
59	700	98%	0.4794 ($14V_{p-p}$)	0.0641 ($18V_{p-p}$)	152.82
55	700	Octagon	0.727 ($14V_{p-p}$)	0.0456 ($18V_{p-p}$)	176.39
39	900	66%	0.444 ($14V_{p-p}$)	0.055571 ($14V_{p-p}$)	155.51
27	1,000	66%	0.48948 ($14V_{p-p}$)	0.07276 ($14V_{p-p}$)	148.24
33	2,000	66%	0.11277 ($14V_{p-p}$)	0.0111 ($14V_{p-p}$)	164.16

From the tabulated data it could be seen that all devices independently from electrode cover or diameter had a percentage difference reduction in velocity ranging from 148% to 176%. This happened even though in many of the devices (Devices 55, 56, 58, 59) a higher excitation voltage was used in glycerine than in isopropanol as discussed above.

Device 48, showed the lowest reduction in velocity when comparing its maximum diaphragm midpoint velocity in glycerine and in isopropanol. It presented a diaphragm midpoint velocity of 0.233 m/s when operating in isopropanol coupling fluid and

0.03806 m/s when operating in a glycerine coupling fluid with both instances being driven at an excitation voltage of 14 V_{p-p}. The reduction in velocity in this case was therefore 143.8% and while this meant that it had the lowest percentage reduction in diaphragm midpoint velocity between the two coupling fluid operation one must say that it still had a substantial reduction in performance.

Since a potential device would require two coupling fluids (one inside the capsule and one outside) as outline in Appendix M, the conclusion is therefore that the inside coupling fluid in contact with the PMUT should be a low density fluid. The outside coupling fluid should be a high density one to match the concrete's density and acoustic impedance.

5.5 Conclusion 5 ~ How PMUT dynamics are effected by the electrode percentage radial cover.

5.5.1 In low density fluids.

Literature reviewed in Chapter 3 has indicated that the electrode radial cover with respect to the diaphragm's diameter has an important effect on the PMUT's operating parameters. Through the FEM the electrode radial cover giving the best dynamic performance was calculated as being in the region of 66%. Table 5.4 presents experimental results achieved showing diaphragm dynamics for a 700 μm PMUT.

Table 5.4 ~ Table showing how Peak Displacement, Peak Velocity and Peak Acceleration vary with % electrode radial cover in a 700 μm PMUT device in isopropanol coupling fluid and air filled cavity. Excitation voltage 14 V_{p-p}

% cover	Peak displacement [μm]	Peak Velocity [mm/s]	Peak Acceleration [km/s^2]
50	0.42665	318.34	237.52
66	0.796	555	387.39
98	0.64854	479.4	354.45

The peak velocity plots achieved from the experimental process is shown in Figure 5.7 where it can be seen that the 66 % radial coverage device has shown the best performance for the 700 μm diameter set of devices. This when the PMUT was operating in isopropanol coupling fluid.

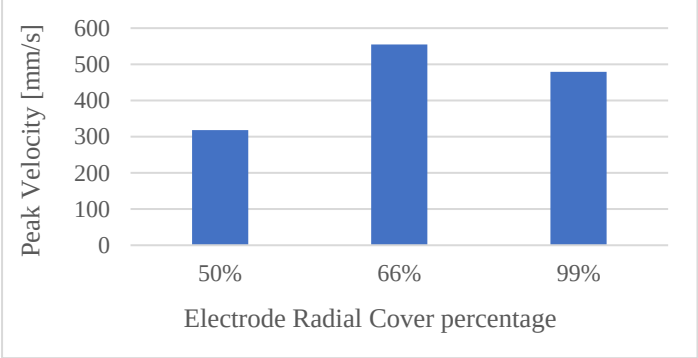

Figure 5.7 ~ Graph showing peak velocity vs Electrode radial cover for a 700μm PMUT deployed in isopropanol coupling fluid and air filled cavity.

The peak displacement vs the electrode radial cover for the same set of devices is shown in Figure 5.8.

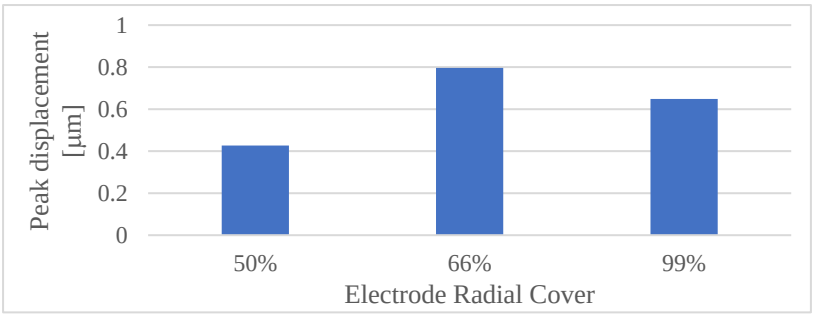

Figure 5.8 ~ Graph showing peak displacement vs Electrode Radial Cover for 700 µm PMUT deployed in isopropanol coupling fluid and air filled cavity.

As shown above, the experimental process presented a peak PMUT performance which was shown to occur at 66% radial coverage. However the values were not observed to be as clear cut as reviewed in literature and shown in Figure 2.12 especially with regards to the 98% electrode radial coverage which should have presented a diaphragm midpoint velocity close to zero. Finite element modelling results as shown in Figure 3.9 also tended to show that the values of the 98% radial coverage electrode were expected to be lower than what was achieved experimentally.

The relationship between electrode radial cover and PMUT dynamics was also experimentally explored in smaller diameter PMUTs having a diameter of 550 µm. At this diameter air filled cavity PMUTs where found to resonate at around 187 kHz in isopropanol coupling fluids. Although this frequency will not be used for the intra concrete ultrasonic transmission system a comparative analysis of experimental results was conducted for these PMUTs also such as to widen the electrode radial cover effect study. The tabulation of results is shown in Table 5.5.

Table 5.5 ~ Peak diaphragm midpoint displacement and velocity with 550 µm diameter PMUTs deployed in isopropanol coupling fluid and having an air filled cavity.

Device number	Electrode radial cover [%]	Resonant Frequency [kHz]	Peak displacement [mm]	Peak Velocity [mm/s]	Peak Acceleration [Mm/s^2]
4	66	187.66	0.53073	0.626	0.738
14	90	184.53	0.8766	1.0168	1.179
16	40	187.81	0.747	0.881	1.040

It was noted that the relationship between electrode radial cover and parameters such as peak displacement established with the 700 µm PMUT does not hold experimentally for the PMUTs having a 550 µm diameter. From the table one can see that peak velocity and displacement at the diaphragm's midpoint was achieved by the device with the 90% cover followed by the device with the 40% cover and then the 66% cover.

One of the reasons for the discrepancy between the experimental and FEM results could be due to residual stresses in the diaphragm [89] [125] [126]. Another factor which might have a bearing was the fact that the diaphragm's thickness was always the same

irrespective of diaphragm diameter, and therefore the geometries of the different diameter PMUTs are not actually growing in all directions proportionally.

5.5.2 In high density fluids

Studies on PMUT behaviour when deployed in high density fluids has shown a number of interesting points. A set of four 700 μm diameter PMUTs was deployed in glycerine coupling fluid and the experimental values measured are shown in Table 5.6.

Table 5.6 ~ Dynamics of 700 μm diameter PMUTs deployed in glycerine coupling fluid and with air filled cavities. Excitation voltage was 18 V_{p-p}

Device number	Electrode radial cover [%]	Resonant Frequency [kHz]	Peak displacement at diaphragm midpoint [mm]	Peak Velocity at diaphragm midpoint [mm/s]	Peak Acceleration [Mm/s^2]
56	66	91.5	0.0649	0.06986	66
57	80	95	0.0755	0.081438	80
58	50	92.7	0.0634	0.045	50
59	98	93.1	0.0871	0.0641	98

An important aspect which one notes from this table is that the device showing the highest displacement was Device 59 with an electrode radial cover of 98%. However peak velocity was measured on Device 57 (the 80% radial cover PMUT) followed by Device 56 (the 66%), then device 59 (the 98%) and finally device 50 (the 50% radial cover) in that order.

This experimentally demonstrates an important point which was also noticed through finite element modelling work, where it was identified that in high density coupling fluids the displacement and velocity peaks do not essentially track each other as frequency increases in a frequency sweep.

Velocity and displacement are linked to each other by the fact that velocity is the derivative of displacement in the time domain. The derivative in the time domain is achieved by multiplying the frequency domain spectrum by $j.\omega$ or $j2.\pi.f$, where f is the frequency. The fact that the velocity and displacement peaks were not tracking each other in the frequency domain indicates that while the amplitude of the diaphragm's midpoint displacement was indeed changing with frequency it was not doing so in a linear way and the slope was therefore not constant. Through Finite Element Modelling, it was therefore seen that at the very high damping levels imparted by the high density liquids, the frequencies at which maximum velocity and displacement occurred were shifted and did not track each other anymore. High damping levels were achieved by inserting very height damping coefficients in the FEM.

5.6 Conclusion 6 ~ Improvement of PMUT dynamic performance through the use of a custom multi electrode configuration design.

This was another important novel conclusion emanating from the work conducted. Both FEM (section 3.8-FEA VII) and experimental work with the laser vibrometer, was conducted to benchmark a device with a novel electrode design. The process conducted was described in Chapter 4 in which Device 45, the device with the novel multi electrode design was benchmarked against a standard electrode having 66% electrode coverage. The device diaphragm diameter selected for the benchmarking exercise was 600 μm and Table 5.7 shows the results of the benchmarking results.

Table 5.7 ~ Performance comparative assessment between the novel electrode design (Device 45) and benchmark device (Device 44). Both devices in isopropanol coupling fluid and have an air filled cavity.

Device Number	**44**	**45**	
Device Description	600 μm diaphragm diameter. Solid 66% electrode cover.	600 μm diaphragm diameter. A specially designed electrode with outer radii at 65.3%, 47.1%, and 33%.	
		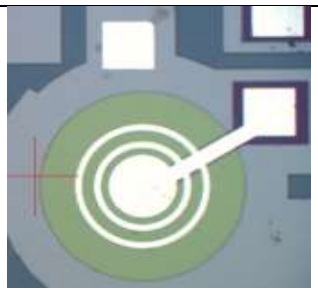	Performance Improvement
Peak Displacement [μm]	518.39	584.7	12.02 %
Peak Velocity [m/s]	0.4987	0.5677	12.94 %
Peak Acceleration [km/s^2]	479.858	551.24	13.85 %
Resonant Frequency [kHz]	153.12	154.53	

From these results it can therefore be concluded that the novel electrode design based on Device 45 does indeed enhance the performance of a 600 μm PMUT deployed in isopropanol by a significant amount as shown in the table. This design can be proliferated to other PMUTs having different diameters.

5.7 Conclusion 7 ~ The effect of the excitation voltage level on PMUT dynamics when PMUT is operating as an ultrasonic transmitter.

As discussed in this dissertation the establishment of the PMUT's operating voltage was not a very easy factor to establish since this data was not fully provided by the device manufacturer at project start and only rule of thumb data was available on enquiry. It was therefore deemed important to establish an understanding on how the signal voltage effects PMUT dynamics.

As described in the experimental data for Device 59 outlined in Chapter 4, a 700 μm device with a 98% padmetal radial cover was operated twice in an isopropanol coupling fluid, with an air filled cavity. In the first run it was operated with a 14 V_{p-p} excitation voltage and the second time it was operated with a 19 V_{p-p} excitation voltage. The comparative analysis is presented in Table 5.8.

Table 5.8 ~ Comparative analysis of PMUT operating at 14 V_{p-p} and 19 V_{p-p}

	Parameter value at the midpoint of the PMUT diaphragm when at a signal voltage of 14 V_{p-p}	Parameter value at the midpoint of the PMUT diaphragm when at a signal voltage of 19 V_{p-p}	% increase	% increase per volt
Displacement [μm]	0.64854	0.749	14.37669	2.875338
Velocity [m/s]	0.4794	0.554	14.43778	2.887556
Acceleration [km/s^2]	354.45	409.338	14.37257	2.874515

Through this work it was shown that for a more than 26% increase in voltage the performance improvement in performance was around 14%.

It could therefore be concluded that as the voltage increases the improvement in performance starts to taper off.

5.8 Conclusion 8 ~ How designing the PMUT's diaphragm and cavity in an Octagon shape improves the performance of the PMUT.

As discussed in Chapter 3 ~ FEA IX, an area which showed promise during Finite Element Modelling was a PMUT design with the diaphragm and cavity produced in an octagonal shape instead of the standard circular design.

The experimental work which was conducted confirmed the positive FEM results. The laser vibrometer results of Device 55 and three other 700 μm diameter PMUTs all deployed in isopropanol coupling fluid and having air filled cavities are being presented in Table 5.9. It can be seen that from the test series the octagonal shaped device achieved the best results in terms of dynamic performance.

Table 5.9 ~ Performance comparison for devices in isopropanol coupling fluid and air filled cavity. Voltage across PMUT was 14 V_{p-p}

Device nº	Diameter [µm]	Electrode radial cover [%]	Resonant Frequency [kHz]	Displacement [µm]	Velocity [m/s]	Acceleration [km/s^2]
59	700	98	117.66	0.64854	0.4794	354.45
56	700	66	111.09	0.796	0.555	387.39
58	700	50	118.75	0.42665	0.31834	237.52
55	Octagon shaped PMUT circumscribed about a 700 µm circle	76	106.25	1.087	0.727	485.35

If one compares Device 55 with Device 56, which was the highest performing 700 µm circular PMUT device, one can see a 30.9% improvement in the peak displacement of the diaphragm's midpoint at the resonant point and a 26.8% improvement in the peak velocity of the diaphragm midpoint at the same resonant point.

The scenario is different for PMUTs deployed in denser fluids. Experimental result data achieved from testing in high density fluid is shown in Table 5.10 which tabulates the peak diaphragm displacement and velocity of the diaphragm's midpoint at the point of resonance. This table collates data for Device 55 and four other 700 µm standard circular PMUTS when these are deployed in glycerine. This test series included all the devices which were in the first test series tabulated in Table 5.9.

Table 5.10 ~ Performance comparison for devices in glycerine coupling fluid and air filled cavity. Voltage across PMUT was 18 V_{p-p}

Device number	Diameter [µm]	Electrode radial cover [%]	Resonant Frequency [kHz]	Peak diaphragm midpoint Displacement at resonance [µm]	Peak diaphragm midpoint Velocity at resonance [m/s]
56	700	66	91.5	0.0649	0.06986
57	700	80	95	0.0755	0.081438
58	700	50	92.7	0.0634	0.045
59	700	98	93.1	0.0871	0.0641
55	Octagon shaped PMUT circumscribed about a 700 µm circle	76	91.5	0.0617	0.0456

In this scenario with glycerine as coupling fluid, Device 55 has actually achieved the worst performance results from the whole test series. Therefore the conclusion drawn from the Finite Element Modelling as well as the experimental work conducted has shown that an octagonal shaped PMUT imparts:

1) Improvements in transmission performance for PMUTs deployed in low density fluids.
2) Reduction in transmission performance for PMUTs deployed in high density fluids

5.9 Conclusion 9 ~ Improvement in PMUT dynamic performance by modifications to the diaphragm especially novel design presented through Device 48.

5.9.1 Device 48 operating in Transmission Mode

Most of the devices which were designed with a modified diaphragm did not show particular improvement in the transmission of ultrasonic radiation and actually the inverse was noticed to be true. Transmission was actually severely degraded when compared to devices with solid diaphragms.

However this was not the case with Device 48 which showed some interesting results.

Superior experimental results achieved by Device 48 for the diaphragm's midpoint, displacement and velocity experimental results, when compared to the results achieved by transducers having other designs, were noted. Keeping in mind that transducer diaphragm movement leads directly to the piezoelectric voltage generated, Device 48 would output a higher voltage for the same incident pressure waves when compared to other designs. This may allow two devices to transmit and receive data when spaced further apart in the concrete structure.

Coupled with the superior midpoint displacement and velocity values which directly lead to an improvement in the voltage output values, the significant lowering of the resonant frequency for Device 48 operating in reception mode was a very significant result. Table 5.11 presents a comparison of results achieved.

Table 5.11 ~ Comparative assessment of results from Device 48 and 49. Excitation voltage was 14 V_{p-p}

Device Number	49	48
Device Description	A 650 μm diaphragm diameter device with a 66% electrode cover.	A 650 μm diaphragm special design device.
Device image		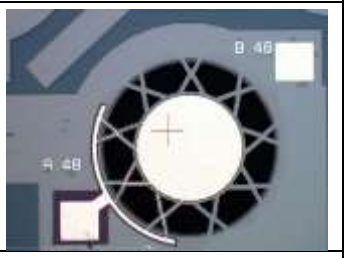
Peak Displacement [μm]	486 nm	528.686 nm
Peak Velocity [m/s]	0.3659 m/s	0.233 m/s
Peak Acceleration [km/s^2]	274.797 km/s^2	102.26 km/s^2
Resonant Frequency [kHz]	119.53	70

From this table it is interesting to note the significantly higher displacement achieved by Device 48 which presented an 8.4% increase over the displacement presented by Device 49.

Interestingly to note were the sound output pressures measured with the hydrophone from Device 48. At a frequency of 92 kHz the pressure output was 186 Pa. This was a very high power output which exceeded albeit marginally even the power outputs presented by solid 700 μm devices the highest output of which was 174 Pa.

Also one must note the lower transmitting frequency of operation of Device 48 when compared to similarly sized PMUTs which makes it better suited to operation inside a concrete environment. As discussed, this design allows the creation of more powerful transmitters provided means to block liquid ingress through the modified diaphragm can be developed.

Experimental work in reception of ultrasonic radiation has also shown significantly good results for this device also confirming the reduction in the operating frequency of Device 48. Keeping in mind that resonant frequency of a PMUT device decreases when the PMUT diameter increases, one can conclude that through the use of Device 48 (or similar device) a smaller PMUT diameter can be used than had a standard circular device been used. This would allow an array based on the Device 48 design to incorporate much more elements packed together than one using a standard circular diaphragm PMUT device since the former would have a smaller size.

5.9.2 Device 48 operating in a Receiving Mode

With respect to ultrasonic reception, Device 48, shown in Figure 4.38 presented very positive results. Finite element modelling discussed in Chapter 3 had predicted a 123% improvement in the reception of ultrasonic radiation when comparing Device 48 with a standard (control) circular diaphragm device.

Furthermore similarly to what was noted in transmission, the FEM also showed that this device resonated at a frequency of 99 kHz when receiving ultrasonic radiation which was significantly lower than the 150 kHz resonant frequency for a 650 μm diameter control device (which had a similar diameter).

Using a smaller diameter PMUTs for the same frequency would make an array more sensitive to ultrasonic radiation since it could potentially pack together more elements to set it up. Ultrasonic reception testing using the hydrophone has also shown that smaller diameter PMUTs are easier to excite through incoming ultrasonic radiation and therefore these benefits would accrue too.

The capability of Device 48 to operate notwithstanding flooding of the cavity with liquid had been demonstrated to occur during the laser vibrometer testing. However this could have occurred due to the fact that the vibrometer testing process did not exceed a few hour s at most which might not have given enough time for the liquid to flow into the cavity. It could also have been due to air which was still trapped in the cavity in the form of micro bubbles. In acoustic testing the procedure took a longer time span, in terms of hours/overnight rather than minutes. It was noticed that as time progressed in terms of hours the device's resonant frequency started to increase and the transmitting amplitudes dropped. This was an indication that liquid isopropanol was actually slowly and gradually displacing the air inside the cavity.

In terms of acoustic reception testing, Device 48 was very successful in reception. It presenting a 1.3 V_{p-p} amplitude signal when excited at 85.21 kHz, a 2.183V_{p-p} amplitude signal when excited at 82.99 kHz, and a1.971 V_{p-p} amplitude signal when excited at 94.2 kHz. In contrast the 700 μm diameter solid diaphragm PMUTs were found to be much more difficult to excite and when excitation did indeed occur, the voltage outputs were much lower.

Due to the good results achieved by this novel device, more experimental work and further updates to the designs would be warranted to study and optimise this concept for use in future projects.

An improvement which would need to be developed further would be a means of withholding liquid ingress through the gaps in the diaphragm created by the diaphragm modification. Research would need to develop methods such as the use of surface tension, and modifying the device design to reduce the opening sizes while retaining the same device dynamics. Experimentation using special fluids should also be studied.

When developing the package the positioning of the PMUT and the final device encapsulation design to avoid liquid ingress would need to be explored. This is discussed in section 5.10.

5.10 Conclusion 10 ~ Array design for intra concrete signal transmission.

Finite Element Modelling outlined in Appendix M has demonstrated that when multiple PMUT devices are assembled together and constructed as an array it is possible to achieve an effective ultrasonic transmission system.

An array would need to operate within an encapsulation system such as that found in literature and shown in Figure 5.9. Such a package allows the die to interact with the coupling fluid while being protected within the encapsulation.

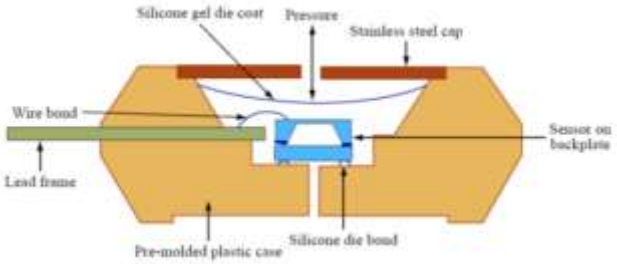

Figure 5.9 ~ A packaged pressure sensor [127].

In the Finite Element Analysis outlined in this section the encapsulation shown in Figure 5.10 was developed.

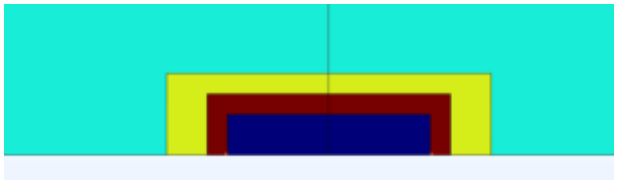

Figure 5.10 ~ The encapsulation developed for the Finite Element Analysis conducted to study the operation of an array designed for this project.

With reference to Figure 5.10 the lower capsule shaded in dark blue was the one which encapsulated the array and which was filled with the low density isopropanol coupling fluid. The capsule had a diameter of 10 mm and with a wall having a 1 mm thickness, shown shaded in red in the figure. The capsule was constructed from low density polyethylene.

The next layer shown shaded in yellow was a 1 mm (top) and 2 mm (sides) thick glycerine layer. The glycerine was modelled to be thicker on the sides to model a real life scenario. The turquoise layer shown in Figure 5.10 is the concrete with which the

glycerine layer couples. This was set up in the model as a 1 m high mortar cylinder with a 1 m radius.

The FEA was conducted using axisymmetric modelling, the details and results of which can be seen in Appendix M. Pressures in the receiving capsule calculated by the FEM were seen to be high enough to be detected by an array installed inside. This was established by the experimental work conducted with the hydrophone. The simulation considered all the acoustic complexities of the fluid- solid-fluid-solid interfaces [128] [129]. The conclusion from this section is that an array of PMUTs is capable of transmitting data through RC concrete for at least 1m. Even more effective transmission would be possible by optimising the array through phase shifting techniques which were not part of this project.

5.11 Conclusion 11 ~ Observations with respect to large diameter PMUTs.

In the experimental processes, PMUTs having large diameters especially in the region of 2,000 μm and 1,800 μm where found to present two issues which need to be noted.

- When excited electrically (working in transmission mode), these tend to suffer from distortions in their shape when at maximum displacement. Due to such distortion the PMUTs fail to reach their theoretical maximum displacements thereby reducing their performance.
- When excited acoustically (working in receiving mode), large diameter PMUTs tend to oscillate by capturing background frequencies without hydrophone excitation.

It would therefore seem that these diameters would be the upper limit of what can be built in terms of diameter for PMUTs which are designed for deployment in liquid coupling fluids. There can be various technical reasons underlying these two observations.

One issue which may have a bearing on large diameter PMUT dynamics is that while the diameter of the diaphragm is increasing its thickness remains constant at 10 μm. This would mean that the thickness to diameter ratio would continue to decrease to unsustainable levels where the PMUT would no longer be operating under the plate dynamics regime as discussed in Appendix B. These two issues would need to be studied further through more Finite Element Modelling and experimental work in future projects

On the positive side, the capability of capturing background radiation and oscillating by harnessing background vibration frequencies being transmitted through the structure could be studied further in view of building a potential energy harvesting system. Such a system embedded in a bridge deck, for example, could potentially harness traffic vibrations to oscillate and produce electrical energy which can be used to power a potential sensory device.

5.12 Final concluding statement and recommendations for future work.

5.12.1 Further work required

In view of the established viability of using PMUT technology for Structural Health Monitoring applications in RC structures work should be continued to develop and build future generations of devices based on the research results outlined in this dissertation. This project has identified the various areas which would need to be developed further and the equipment which would need to be procured to continue further research in this field.

- **Special anechoic test chamber.**

To improve the reliability and accuracy of results achieved through hydrophone testing it would be important to develop an anechoic tank which has special linings capable of absorbing incident ultrasonic radiation. Such linings would eliminate any echoes which would occur when radiation hits the tank boundary walls. Research in the lower frequency operating area ranging between 70 kHz and 5 kHz would also benefit from having fluid holding chambers which are significantly larger than the petri dish utilised in this project. The reason being that to operate at these frequencies the experimental process needs to handle wavelengths ranging between 0.017 m and 0.24 m when the ultrasonic radiation is travelling through the isopropanol coupling fluid. The test chamber should ideally also have motorised manipulator systems through which the hydrophones and needle probes can be positioned in exact positions. This would enable much better positional accuracy when analysing sound wave transmission than what was possible with the setup used in this project as shown in Figure 4.16.

It is also important to keep in mind that to operate in a larger chamber, devices need to be wire bonded to a PCB thus enabling the PMUT to be accessed via cables. The reason for this would be that it would be impossible to probe dies inside deep liquid filled tanks with probe needles as done in this project.

- **Needle probes.**

Needle probes are special thin probes which can be used to detect pressures at much closer distances to the devices themselves. Such close proximity improves the quality of pressure measurements. Research on the procurement of such devices was conducted during this project and it was established that needle probes are highly specialised (in terms of frequency spectrum covered) and expensive devices. Apart from budgetary considerations, another reason for not procuring needle probes for this project was that reviewed needle probes were found to be incapable of both transmitting and receiving ultrasonic radiation thereby requiring the procurement of even more probes to conduct both operations.

- **Laser vibrometer Equipment.**

Easy access to laser vibrometer facilities was found to be crucial in the development of PMUTs. In this project a laser vibrometer was not readily available but work was conducted through the hiring of the necessary facilities for half or full day experimental processes. An effective laser vibrometer optimised for micro devices is a very costly equipment component and therefore a cost effective method of utilisation would need to be established. Through laser vibrometry, PMUT dynamics can be intimately studied allowing both the calibration of Finite Element Models as well as the evaluation of the effectiveness of geometric modification implementations on particular PMUTs.

- **Access to other piezoelectric technologies such as PZT.**

Lead zirconate titanate (PZT) has a piezoelectric constant (e_{33}) equal to 23.3 which is much higher than the e_{33} of 1.55 for aluminium nitride. PZT based devices therefore have the potential of being able to transmit signals with a higher amplitude than AlN devices are capable of. Such would offer superior performance and demonstrate higher sensitivity in sensing applications [130]. On the down side, PZT is not readily incorporated in ICs as it requires processing temperatures over 600°C. This would mean that it would not be readily incorporated with ASIC devices on the same die area [131]. Further research in this area is therefore required with a possible solution being a multi die SIP package.

- **Deployment methodologies and packaging.**

Packaging of the MEMS devices is a very important component of a final design field deployable structural health monitoring device. The final package must be tough enough to resist the chemical and physical degradation it would be subjected to when embedded in a concrete structure. At the same time the encapsulation device must allow an unencumbered sonic transmission channel from the coupling fluid within the PMUTs' envelope to the outside. The encapsulation can be designed on the basic structure presented in Figure 5.10 with isopropanol coupling fluid inside, encapsulated in a low density polymer and with glycerine or another denser coupling fluid on the outside of the polymeric encapsulating material. The denser fluid would be able to couple the device acoustically to the concrete structure. The conceptual view of such a device was developed and is being shown in Figure 5.11 (a).

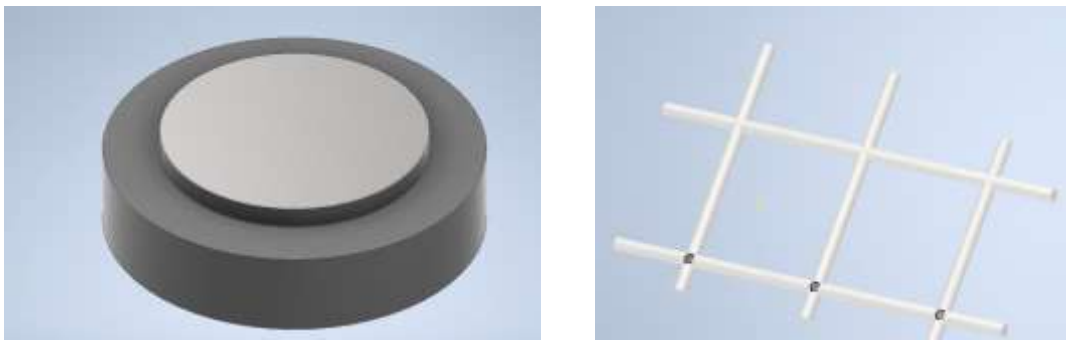

(a) (b)

Figure 5.11 ~ Concept for easy deployment showing (a) capsule and (b) capsule embedded in a grid.

The devices can be placed in position manually one by one in predetermined positions during the concrete pouring operations. This could be either in situ concrete pours or precast reinforced concrete products.

To enable rapid deployment of the SHM micro devices in a construction environment, by untrained personnel the author has also designed the innovative concept shown in Figure 5.11 (b). The proposal is to have the microscale devices preinstalled inside the mesh/rebar structure as shown in the figure. The cavity in which the microscale devices can be placed can either be positioned centrally as shown or else in lateral positions on the mesh nodes. The positioning would need to be studied further to ensure that no structural engineering impact such as reduction in structural tensile strength would occur.

The grid installation concept would mean that a whole array of devices can be positioned together as a group already positioned in grid formation thereby ensuring exact positioning. Such a system would also allow rapid installation by construction operatives who are untrained in the field of electronics. The grid concept can also be studied further for its use as a route through which inter device ultrasonic signals can be transmitted. As an example the grid could be made of structural steel. A metal grid being a homogenous solid provides a better ultrasonic transfer route than would concrete which is a composite structure as explained in Chapter 2. Steel being a dense solid material allows a potential route which allows sound to travel in a fast and more predictable fashion than would a non-homogenous material in which aggregate may disperse or distort the signals being transmitted.

A successful encapsulation device must also consider optimal methods for encapsulating PMUTs in a way which achieves the best performance out of them. As an example PMUTS with modified diaphragms having holes or slots in the diaphragm could be installed inverted and floating on the coupling fluid layer. This would allow them to receive and transmit data without the coupling liquid flowing into the cavity thereby reducing the device's effectiveness.

The work carried out in this dissertation through the conclusions derived from both the Finite Element Modelling and the experimental work, evidences that the proposed area of PMUT development holds a lot of promise for its adoption as a platform towards the implementation of an effective intra concrete transmission device. The results achieved point towards the viability of such micro devices as structural health monitoring systems which the author envisages would eventually replace all or most of the macro scale structural health monitoring systems currently in use today.

References

[1] X.-M. Wan, F. H. Wittmann, T.-J. Zhao and H. Fan, “Chloride content and pH value in the pore solution of concrete under carbonation,” *Journal of Zhejiang University,* vol. 14, no. 1, p. 71–78, 2013.

[2] A. Neville, “Chloride attack of reinforced concrete: an overview,” *Materials and Structures,* vol. 28, no. 2, p. 63–70, 1995.

[3] P. K. Mehta and P. J. Monteiro, Concrete: Microstructure, Properties, and Materials, vol. 3, New York, NY, USA: McGraw-Hill, 2006.

[4] M. Nokken and R. Hooton, “Using pore parameters to estimate permeability or conductivity of concrete(Article),” *Materials and Structures/Materiaux et Constructions,* vol. 41, no. 1, pp. 1-16, 2008.

[5] S. Sammut, E. Gatt and R. P. Borg, “Microscale miniaturisation of chloride ion detection sensors for long-term embedding in reinforced concrete structures.,” *Structural Control Health Monitoring,* 2021.

[6] S. Sammut, E. Gatt and R. P. Borg, “Chloride ion detection in concrete through Galvanic and Resistivity methods,” *JJCE Journal Jordan Journal of Civil Engineering,* vol. 11, no. 4, 2017.

[7] Go Global with kids, “Natchez Trace Parkway: Double Arch Bridge,” [Online]. Available: https://goglobalwithkids.com/natchez-trace-parkway-double-arch-bridge/. [Accessed 12 08 2023].

[8] “Rail Trailing,” [Online]. Available: http://www.railtrailing.com/2018/05/north-idaho-centennial-trail.html. [Accessed 12 08 2023].

[9] M. Iftissane, A. Mamouni and L. Zenkouar, “Conception of patch antenna at wide band.,” *International Journal of emerging sciences,* vol. 3, pp. 400-417, 2011.

[10] S. Jiang and S. V. Georgakopoulos, “Optimum Wireless Power Transmission through reinforced Concrete struture.,” *2011 IEEE International Conference on RFID,* vol. 4, pp. 50-56, 2011.

[11] K. K. Zhamova, “Small-Size X-Ray Sources for Medical Diagnosis,” *Biomedical Engineering,,* vol. 49, no. 6, pp. 354-356, 2016.

[12] S. Stankovica, R. Ilic, K. Jankovicb, D. Bojovic and B. Loncar, “Gamma Radiation Absorption Characteristics of Concrete with Components of Different Type Materials.,” *Acta Physica Polonica A,* vol. 117, pp. 812-816, 2010.

[13] S. Naqvi, S. Tahira, B. S. Warda, R. S. A. Hasan and F. Kinaan, “Awareness of Hazards of X-Ray Imaging and Perception Regarding Necessary Safety Measures to be Taken During X-Ray Imaging Procedures Among Patients in Public Sector Tertiary Hospitals of Karachi, Pakistan,” *Cureus,* vol. 11, no. 5, pp. 1-10, 2019.

[14] B. K. Dasa and A. Shyam, “Development of compact size penning ion source for compact neutron generator.,” *The Review of scientific instruments,* vol. 79, pp. 123305-1-4, 2009.

[15] E. Bezak, R. Takam, E. Yeoh and L. G. Marcu, “The risk of second primary cancers due to peripheral photon and neutron doses received during prostate cancer external beam radiation therapy.,” *Physica Medica,* vol. 42, pp. 253-258, 2017.

[16] E. Niederleithinger, J. Wolf, F. Mielentz, H. Wiggenhauser and S. Pirskawetz, “Embedded Ultrasonic Transducers for Active and Passive Concrete Monitoring.,” *Sensors,* vol. 15, pp. 9756-9772, 2015.

[17] R. Kessel, C. Hamm and V. Myers, “The safety of diver exposure to ultrasonic imaging sonars.,” in *UACE2017- 4th Underwater Acoustics Conference and Exhibition.*, Greece, 2017.

[18] E. Niederleithinger, J. Wolf, F. Mielentz, H. Wiggenhauser and S. Pirskawetz, “Embedded Ultrasonic Transducers for Active and Passive Concrete Monitoring,” *Sensors,* vol. 15, pp. 9756-9772, 2015.

[19] Y. Qiu, J. V. Gigliotti, M. Wallace, F. Griggio, C. Demore, E. M. Cochran and S. Trolier-McKinstry, “Piezoelectric Micromachined Ultrasound Transducer (PMUT) Arrays for Integrated Sensing, Actuation and Imaging.,” *sensors,* no. 15, pp. 8020-8041, 2015.

[20] A. Hajati, D. Latev, D. Gardner, A. Hajati and D. Imai, “Three- dimensional micro electromechanical system piezoelectric ultrasonic transducer.,” *Applied Physics Letters,* vol. 101, pp. 253101-1-5, 2012.

[21] Y.Lu, H. Tang, Q.Wang, S. Fung, J. Tsai, M. Daneman, B. Boser and D. Horsley, “Waveguide piezoelectric micromachined ultrasonic transducer array for short-range pulse-echo imaging.,” *Applied physics letters,* vol. 106, pp. 193506-1-4, 2015.

[22] T. Wang, T. Kobayashi and C. Lee, “Micromachined piezoelectric ultrasonic transducer with ultra-wide frequency bandwidth.,” *Applied Physics Letters,* vol. 106, pp. 1-5, 2015.

[23] M. Kabir, H. Kazari and D. Ozevin, “Piezoelectric MEMS acoustic emission sensors.,” *Sensors and Actuators.,* vol. 64, pp. 53-64, 2018.

[24] L. L. Wong, S. Na, A. I. Chen, Z. Li and M. Macecek, “A feasibility study of piezoelectric micromachined ultrasonic transducers fabrication using a multi- user MEMS process.,” *Sensors and Acuators,* vol. 247, pp. 430-439, 2016.

[25] F. Narvaez, S. Hosseini, H. Farkhani and F. Moradi, “Analysis and design of a PMUT based transducer for Powering Brain Implants.,” *Arxiv,* pp. 1-10, 2021.

[26] R. Przybyla, A. Flynn, V. Jain, S. Shelton, A. Guedes, I. Izyumin, D. Horsley and B. Boser, “A micromechanical ultrasonic distance sensor with >1 meter range.,” in *16th International Solid-State Sensors, Actuators and Microsystems Conference*, 2011.

[27] J. Krautkramer and H. Krautkramer, Ultrasonic Testing of Materials, Berlin: Springer Berlag, 1977.

[28] R. P. Hodges, Underwater Acoustics - Analysis, design and performance of sonar., UK: Wiley, 2023.

[29] Natioanl Physical Laboratory - UK, “National Physical Laboratory/acoustics/techguides,” [Online]. Available: http://resource.npl.co.uk/acoustics/techguides/concepts/siunits.html. [Accessed 13 09 2023].

[30] B. Carlin, Ultrasonics, New york: McGraw-Hill, 1960.

[31] P. P. Urone, R. Hinrichs, F. Gozuacik, D. Pattison and C. Tabor, Physics-High School, Texas: RICE University, 2020.

[32] M.Hertla and F.Mialhe, “On the replacement of water as coupling medium in scanning acoustic microscopy analysis of sensitive electronics components,” *Microelectronics Reliability,* vol. 114, no. 113860, 2020.

[33] Olympus, “Evident_Ultrasonic couplants,” [Online]. Available: https://www.olympus-ims.com/en/applications/ultrasonic-couplant/. [Accessed 7 1 2023].

[34] L. Yamus, “Pulsed Waves: Reflections and the speed of sound.,” *American Journal of Physics*, pp. 903-906, 1995.

[35] J. L. Rose, Ultrasonic waves in solid media., New York: Cambridge, 1999.

[36] E. D. Paul Regtien, “Acoustic sensors,” *Sensors for Mechatronics (second Edition),* 2018.

[37] A. D. Cedric Dumoulin, “Design optimization of embedded ultrasonic transducers for concrete structures assesment.,” *Ultrasonics,* vol. 79, pp. 18-33, 2017.

[38] L.F.Hutchins and D.A.Bresse, “Transient generation of elastic waves in solids by a disk shaped normal force source.,” *Journal of the acoustics society of America,* vol. 86, no. 2, pp. 810-817, 1989.

[39] R. T. Beyer and S. V. Letcher, Physical Ultrasonics, New york: Academic Press, 1969.

[40] T. M. Leo Beranek, Acoustics - Sound Fields, Transducers and Vibration, UK: Academic Press, 2019.

[41] D. Ozevin, “MEMS Acoustic Emission Sensors.,” *Applied Sciences,* vol. 10, pp. 1-14, 2020.

[42] C. Wilby, Structural Concrete, UK: Butterworth & Co, 1983.

[43] W. Punurai, J. Jarzhnski, K. K. J.Qu and L. Jacobs, “Characterization of dissipation losses in cement paste with diffuse ultrasound.,” *Mechanics,* vol. 34, pp. 289-294, 2006.

[44] T. S. Tie, K. H. Mo, A. Putra, S. C. Loo, U. J. Alengaram and T. C. Ling, “Sound absorption performance of modified concrete: A review.,” *Journal of Building Engineering,* vol. 30, 2020.

[45] X. Wu, Q. Yan, A. Hedayat and X. Wang, “The influenc law of concrete aggregate particle size on acoustic emission wave attenuation.,” *Nature,* pp. 1-14, 2021.

[46] T. Yua, J.-F. Chaix, L. Audibert, D. Komatitsch, V. Garnier and J.-M. Hénault, “Simulations of ultrasonic wave propagation in concrete based on a two- dmensional numerical model validated analytically and experimentally.,” *Ultrasonics,* no. 92, pp. 21-34, 2019.

[47] T. R. Naik, V. M. Malhotra and J. S. Popovics, “The Ultrasonic Pulse Velocity Method.,” in *Handbook on Nondestructive Testing of Concrete,* CRC press, 2014.

[48] P. Gaydecki, F. Burdekin, W. Damaj, D. John and P. Payne, “The propagation and attenuation of medium frequency ultrasonic waves in concrete: a signal analytical approach.,” *Measurement Science and Technology,* vol. 3, pp. 126-134, 1991.

[49] C. Glorieux, K. V. d. Rostyne, K. Nelson and W. Gao, “On the character of acoustic waves at the interface between hard and soft solids and liquids.,” *Journal of the Acoustical Society of America,* vol. 110, no. 3, pp. 1299-1306, 2001.

[50] E. Leinov, M. J. S. Lowe and P. Cawley, “Investigation of guided wave propagation in pipes fully and partially embedded in concrete.,” *The Journal of the Acoustical Society of America,* vol. 140, pp. 4528-4539, 2016.

[51] T. Watanabe, H. T. H. Trang, K. Harada and C. Hashimoto, “Evaluation of corrosion-induced crack and rebar corrosion by ultrasonic testing.,” *Construction and Building Materials,* vol. 67, pp. 197-201, 2014.

[52] B.-C. Kim and J.-Y. Kim, “Characterization of ultrasonic properties of concrete.,” *Mechanics Research Communications,* vol. 36, pp. 207-2014, 2008.

[53] Phlilps, “CMUT breakthrough ultrasound technology,” [Online]. Available: https://www.engineeringsolutions.philips.com/looking-expertise/mems-micro-devices/mems-micro-devices-applications/capacitive-micromachined-ultrasonic-transducers-cmut/. [Accessed 10 01 2023].

[54] M. Pekar, S. v. Nispen, R. Fey, S. Shulepov, N. Mihajlovic and H. Nijmeijer, “A fluid-coupled transmitting CMUT operated in collapse mode.,” *Sensors and Actuators,* vol. 267, pp. 474-484, 2017.

[55] E. B. Dew, A. K. Ilkhechi, M. Maadi, N. J. Haven and R. J. Zemp, “Outperforming piezoelectric ultrasonics with high reliability single membrane CMUT array elements.,” *Microsystems and Nanoengineering.,* pp. 2-15, 2022.

[56] M. d. Jong, W. Chen, H. Geerlings, M. Asta and K. A. Persson, “A database to enable discovery and design of piezoelectric materials,” *Nature,* pp. 1-13, 2015.

[57] J. Jung, “Review of piezoelectric micromachined ultrasonic transducers and their applications.,” *Journal of Micromechanics and Microengineering.,* vol. 27, 2017.

[58] V. M. Mastronardi, F. Guido, M. Amato, M. D. Vittorio and S. Petroni, “Piezoelectric ultrsonic transducer based on flexible AlN.,” *Microelectronic Engineering,* vol. 121, pp. 59-63, 2014.

[59] A. C. G. H. K. Glukh and B. Hardy, PiezoMumps Design Handbook Rev 1.3, MEMSCAP Inc., 2014.

[60] J. Wang, Z. Zheng, J. Chan and J. T. W. Yeow, “Capacitive micromachined ultrasound transducers for intravascular ultrasound imaging.,” *Micorsystems and Nanoengineering,* pp. 2-13, 2020.

[61] C. D.Herickhoff and R. v. schaijk, “CMUT technology developments.,” *Science Direct,* vol. 33, pp. 256-266, 2023.

[62] E. Hong, “Surface Micromachined Peristaltic Pumps Using Lead Zirconate Titanate Film, Ph.D. Thesis,” Pennsylvania USA, The Pennsylvania State University, 2004, pp. 1-195.

[63] S. Timoshenko and S. Woinowsky-Krieger, “Theory of Plates and Shells,” Singapore, McGraw-Hill, 1959, pp. 1-579.

[64] P. Morse and K. Ingard, “Theoretical Acoustics,” Princeton, NJ, USA, Princeton University Press, 1987, pp. 1-949.

[65] L. E. Kinsler, Fundamentals of Acoustics, New York: Wiley, 2000.

[66] D. R. Chou, Piezoelectric Micromachined Ultrasound Transducers for Medical Imaging., USA: Duke University, 2011.

[67] E. Serra, G. D. Giuseppe, M. Bawaj and N. Malossi, “MIcrofabrication of large-area circular high stress silicon nitride membranes for optomechanical applications.,” *AIP advances,* vol. 6, 2016.

[68] C. Ayela and L. Nicu, “Micromachined piezoelectric membranes with high nominal quality factors in newtonian liquid media: A Lamb’s model validation at the microscale.,” *Sensors and Actuators B: Chemical,* no. 123, pp. 860-868, 2006.

[69] H. Lamb, “On the vibrations of an elastic plate in contact with water.,” *Proceedings of the Royal Society of London,* vol. 98, no. 690, pp. 205-216, 1920.

[70] M. Olfatnia, Z. Shen, J. M. Miao, L. S. Ong and T. X. Ebrahimi., “Medium damping influences on the resonant frequancy and quality factor of peizoelectric circular

microdiaphragm sensors.," *Journal of Micromechanics and microengineering.*, pp. 1-9, 2011.

[71] A. W. Leissa, Vibration of Plates., Washington DC: NASA, 1969.

[72] R. Woltjer and e. al., "Optimization of piezo-MEMS layout for a bladder monitor.," in *2016 IEEE International Ultrasonics Symposium (IUS)*, Tours, France, 2016.

[73] T. D.Rossing, F. R. Moore and P. A. Wheeler, The Science of Sound Third Edition, St Francisco: Addison Wesley, 2002.

[74] Openstax, Physics for High School, XanEdu Publishing Inc., 2020.

[75] Y. Kerboua, A. Lakis and L. M. M. Thomas, "Vibration analysis of rectangular plates coupled with fluid," *Applied Mathematical Modelling,* vol. 32, pp. 2570-2586, 2008.

[76] J. Wang, M. Zhang, Z. Wang, S. S. Y. Ning, X. Yang and W. Pang, "An ultra- low power, small size and high precision Indoor Localization System Based on MEMS ultrasonic Transducer Chips.," *IEEE Transactions on Ultasonics, Ferroelectrics, and Frequency Control.*, vol. 69, no. 4, pp. 1469-1477, 2022.

[77] J. Kučan and M. Joler, "Impact of slot dimensions on the resonant frequencies of rectangular microstrip antennas.," *IEEE Xplore,* vol. ICECOM2013, 2013.

[78] J. Xue, M.-. Q. Niu, K. F. Xu and L. Q. Chen, "Reducing nonlinear vibration of locally resonant plates via multi frequency resonators.," *Archive of applied Mechanics,* pp. 1631-1646, 2023.

[79] S. Mondal, A. Patra, S.Chakraborty and N. Mitra, "Dynamic performance of sandwich composite plates with circular hole/cut-out: A mixed experimental–numerical study.," *Composite Structures,* vol. 131, pp. 479-489, 2015.

[80] Y. Li, M. Zhou and M. Li, "Analysis of the free vibration of thin rectangular plates with cut-outs using the discrete singular convolution method.," *Thin Walled Structures,* pp. 1-12, 2020.

[81] C. Bouy, "Free vibration of laminated composite plates with a central circular hole.," *Campos Struct,* vol. 35, no. 4, pp. 357-68, 1996.

[82] M.Vinyas, D. Harursampath and T. N. Thoi, "A higher order coupled frequency characteristics study of smart magneto-electro-elastic composite plates with cut-outs using finite element methods.," *Defence Technology,* vol. 17, pp. 100-118, 2020.

[83] L. Monahan, P. Nemergut and G. Maddux, "Natural frequencies and mode shapes of plates with interior cut-outs," *The Shock and Vibration Bulletin,* vol. 41, pp. 37-49, 1970.

[84] P. Paramasivam, "Free vibration of square plates with square opening," *Journal of Sound and Vibration,* vol. 30, pp. 173-178, 1973.

[85] G. Aksu and R. Ali, "Determination of dynamic characteristics of rectangular plates with cut-outs using a finite difference formulation.," *Journal of Sound and Vibration,* vol. 44, pp. 147-158, 1976.

[86] A. Rajamani and R. Prabhakaran, "Dynamic response of composite plates with cut-outs. Part I: Simply-supported plates," *Journal of Sound and Vibration,* vol. 54, pp. 549-564, 1977.

[87] S. H. Moon K. Kwaka, "Free vibration analysis of rectangular plate with a hole by means of independent coordinate coupling method.," *Journal of Sound and Vibration,* vol. 306, pp. 12-30, 2007.

[88] A.Lebedev, L.Smirnov and V.Alexandr, “Effect of the shape of a thin plate with cut-outs on natural frequencies.,” in *28th Nordic Seminar on Computational Mechanics*, Tallinn, 2015.

[89] K. Smyth and S.-G. Kim, “Experiment and Simulation Validated Analytical Equivalent Circuit Model for Piezoelectric Micromachined Ultrasonic Transducers.,” *IEEE Transactions Ultrasonic, Ferroelectric, Freqequency Control,* vol. 62, no. 4, pp. 744-765, 2015.

[90] F. Narvaez, S. Hosseini, H. Farkhani and F. Moradi, “Analysis and design of a PMUT based transducer for Powering Brain Implants.,” in *IEEE Ultrasonics Symposium*, 2022.

[91] Y. KUSANO, Large Amplitude Piezoelectric Micromachined Ultrasonic Transducers for Airborne Applications., California: University of California, 2019.

[92] L. Guo-Lun, Y. Kusano and D. A. Horsley, “Airborne Piezoelectric Micromachined Ultrasonic Transducers for Long-Range Detection.,” *Journal of Microelectromechanical Systems,* vol. 30, no. 1, pp. 81-89, 2021.

[93] I. O. Wygant and M. Kupnik, “An Equivalent Circuit Model of PMUTs with Clamped and Simply-Supported Plates,” in *2022 IEEE International Ultrasonics Symposium (IUS),* Venice, 2022.

[94] S. Akhbari, F. Sammoura and L. Lin, “Equivalent Circuit Models for Large Arrays of Curved and Flat Piezoelectric Micromachined Ultrasonic Transducers.,” *IEEE Transactions on Ultrasonics, Ferroelectrics, and Frequency Control.,* vol. 63, no. 3, pp. 432-447, 2016.

[95] C. Chare, P. Gijsenbergh, Y. Jeong, P. Heremans, D. Cheyns and J. Genoe, “Electromechanical Equivalent Circuit Model for Axisymmetric PMUTs With Elastic Boundary Conditions.,” *Journal of Microelectomechanical Systems,* vol. 31, no. 3, pp. 457-472, 2022.

[96] L. Wang, W. Zhu, Z. Wu, W. Liu and C. Sun, “A Novel Broadband Piezoelectric Micromachined Ultrasonic Transducer with Resonant Cavity.,” in *2021 IEEE International Ultrasonics Symposium (IUS),* Venice, 2021.

[97] Y. Birjis, S. Swaminathan, H. Nazemi, G. C. A. Raj, P. Munirathinam, A. A. Libdeh and A. Emadi, “Piezoelectric Micromachined Ultrasonic Transducers (PMUTs): Performance Metrics, Advancements, and Applications,” *Sensors,* vol. 22, no. 9151, pp. 1-29, 2022.

[98] I. Zamora, E. Ledesma, A. Uranga and N. Barniol, “Miniaturized 0.13-um CMOS Front-End Analog for AlN PMUT Arrays.,” *Sensors,* vol. 20, pp. 4-18, 2020.

[99] Magnetix/Shutterstock, Artist, [Art]. Science ABC.

[100] Y. Qiu, J. V. Gigliotti, M. Wallace, F. Griggio, C. E. M. Demore, S. Cochran and S. Trolier-McKinstry, “Piezoelectric Micromachined Ultrasound Transducer (PMUT) Arrays for Integrated Sensing, Actuation and Imaging Sensing, Actuation and Imaging.,” *Sensors,* no. 15, pp. 8020-8041, 2015.

[101] C. Buyle, L. d. strycker and L. V. d. Perre, “An accurately steerable, compact phased array system for narrowbeam ultrasound transmission,” *IEEE sensors journal,* vol. 22, no. 15, pp. 15385-15392, 1st aug 2022.

[102] V. G. Kartasheva, V. K. Kachanova, I. V. Sokolova, R. V. Kontsova and A. S. Fadina, “Choosing phased array pitch in Ultrasonic Tomography of materials with inhomogeneous structure.,” *Russian Journal of Nondestructive Testing,* vol. 54, no. 4, pp. 223-231, 2018.

[103] S. Sadeghpour, M. Ingram, C. Wang, J. D. Hooge and M. Kraft, “A 128x1 Phased array piezoelectric Micromachined Ultrasonic Transducer (PMUT) for Medical Imaging.,” in *International conference on solid-state Sensors, Actuators and Microsystems.,* 2021.

[104] Y. Qiu, J. Gigliotti, M. Wallace and e. al, “Piezoelectric Michromachined Ultrasound Trasducer (PMUT) arrays for integrated sensing, actuation and imaging.,” *Sensors,* vol. 15, no. 4, pp. 8020-8041, 2015.

[105] X. Jiang and J. M. Tsai, “Ultrasonic Fingerprint sensor with transmit beamforming Based on a PMUT array bonded to CMOS circuitry.,” *IEEE Transactions on Ultrasonics, Ferroelectics, and Frequency Control.,* vol. 64, no. 9, pp. 1401-2017, 2017.

[106] D. A. Horsley and e. al, “Ultrasonic fingerprint sensor based on a PMUT array bonded to CMOS circuitry,” *Proc. IEEE Int. Ultrasonic Symposium (IUS),* pp. 1-4, 2013.

[107] R.J.Ditchburn and M. Ibrahim, “Ultrasonic Phased Arrays for the inspection of thick section welds.,” Australian Government Department of Defence- Defence Science and Technology Organisation., Victoria, 2009.

[108] F. Lovholt and C. M. Karin Noren- Cosgriff, “Simulating low frequency sound transmission through walls and windows by a two- way coupled fluid structure interaction model.,” *Journal of Sound and Vibration.,* vol. 396, pp. 203-216, 2017.

[109] W. D. Callister, Materials science and engineering, New York: Wiley, 2003.

[110] L. Wang, W. Zhu, Z. Wu, W. Liu and C. Sun, “A novel broadband piezoelectric micromachined Ultrasonic Transducer with Resonant Cavity,” in *IEEE International Ultrasonics Symposium (IUS),* Venice, 2021.

[111] M. A. Hopcroft, W. D. Nix and T. W. Kenny, “What is the Young’s Modulus of Silicon?,” *Journal of Micro Electro Mechanical systems.,* vol. 19, no. 2, pp. 229-237, 2010.

[112] B. Bhushan and X. Li, “Micromechanical and tribological characterization of doped single-crystal silicon and polysilicon films for microelectromechanical systems devices.,” *Journal of Materials Research,* vol. 12, no. 1, p. 59, 1996.

[113] W. W. Zhang, H. Yu, S. Y. Lei and Q. A. Huang, “Modelling of the elastic properties of crystalline silicon using lattice dynamics.,” *Journal of Physics D: Applied Physics,* vol. 44, pp. 1-6, 2011.

[114] G. Weidmann, P. Lewis and N. Reid, Structural Materials, Oxford: The Open University, 1994.

[115] A. Cowen, G. Hames, K. Glukh and B. Hardy, “Piezomumps design handbook Rev 3.1,” MEMSCAP, 2014.

[116] E. Tomasini, G. Revel and P. Castellini, “Laser Based Measurements,” in *Encyclopedia of Vibration,* Ancona, Italy, Academic Press, 2002, pp. 729-710.

[117] Polytec, “MSA-600 Micro System Analyser- Measuring 3D dynamics and topography of MEMS and microstuctures.,” Germany, 2018.

[118] Creative Commons, [Online]. Available: https://creativecommons.org/licenses/by-sa/3.0/.

[119] H. Zuo, F. H. Nia and S. He, “SOIMUMPs micromirror scanner and its application in laser line gererator.,” *Journal Micro/Nanolith. MEMS MOEMS,* vol. 16, pp. 1-11, 2017.

[120] Y. W. Guowei Yang, “High resolution laser fringe pattern projection based on MEMS micro-vibration mirror scanning for 3D measurement.,” *Optics and Laser Technology,* pp. 1-7, 2021.

[121] Y. Chiba, M. Yoshioka and R. Horiunchi, “Measurement of instantaneious acoustic pressur for diagnostic ultrasound using frequency characteristics of amplitude and phase of

hydrophone sensitivity.," *Proceedings of Symposium on Ultrasonic Electronics,* vol. 39, pp. 29-31, 2018.

[122] Benthowave Instrument Inc., "Hydrophone Specification," Canada.

[123] Benthowave Instrument Inc., "BII-5020 Series Power Amplifier".

[124] S.Sammut, E.Gatt and R.P.Borg, "Low frequency Piezoelectric Micromachined Ultrasonic Transducers optimized for concrete structures.," in *Eurostruct 2023,* Vienna, 2023.

[125] S. Shelton and e. al, "CMOS compatible AlN piezoelectric micromachined ultrasonic transducers," in *IEEE international Ultrasonics Symposium,* 2009.

[126] P.Muralt and e. al, "Piezo electric micromachined Ultrasonic transducers based on PZT thin films.," *IEEE Transactions Ultrasonic Ferroelectric Frequency Control,* vol. 52, no. 12, pp. 2276-2288, 2005.

[127] Motorala, Sensor Device Data/Handbook 4th Edition., MIT Open Course Ware, 1998.

[128] D. Belgroune, J. F. d. Belleval and H. Djelouah, "A theroretical study of ultrasonic wave transmission through a fluid-solid interface.," *Ultraonics,* vol. 48, pp. 220-230, 2008.

[129] S. Hoche, M. Hussein and T. Becker, "Density, ultraound velocity, acoustic impedance, reflection and absorption, coefficient determination of liquids via multiple reflection method.," *Ultrasonics,* vol. 57, pp. 65-71, 2014.

[130] Y. He, H. Wan, X. Jiang and C. Peng, "Piezoelectric Micromachined Ultrasound Transducer Technology: Recent Advances and Applications.," *Biosensors,* vol. 13, no. 55, pp. 2-26, 2023.

[131] M. Fraga, H. Furlan, R.S.Pessoa and M. Massi, "Wide bandgap semiconductor thin films for piezoelectric and piezoresistive MEMS sensors applied at high temperatures: an overview.," *Microsystems Technology,* vol. 20, pp. 9-21, 2014.

[132] H. L. Ming, X. W. Jiang, Y. Wang, J. Zhou and J.-Y. Ren, "Sensitivity—Bandwidth Optimization of PMUT with Acoustical Matching Using Finite Element Method," *Sensors,* vol. 22, no. 2307, 2022.

[133] M. Gad-el-Hak, MEMS design and fabrication., London: Taylor & Francis Group, 2006.

[134] M. Kabir, H. Kazari and D. Ozevin, "Piezoelectric MEMS acoustic emission sensors," *Sensors and Actuators A: Physical,* vol. 279, pp. 53-64, 2018.

[135] "Materials Explorer app.," The Materials Project.

[136] Department of Energy, "Materials Poject Documentation," [Online]. Available: https://docs.materialsproject.org/. [Accessed 12 02 2023].

[137] COMSOL, "Comsol Material Database," COMSOL, 2020.

[138] Eurocode 2 - Table of concrete design properties, "Design aid - Table of concrete design properties including strength properties (fck, fcd, fctm, fctd) elastic deformation properties (Ecm), minimum longitudinal reinforcement against brittle failure, and minimum shear reinforcement," [Online]. Available: https://eurocodeapplied.com/design/en1992/concrete-design-properties. [Accessed 04 09 2023].

[139] rshydro, "Sound Speeds in Water, Liquid and Materials," [Online]. Available: https://rshydro.co.uk/sound-speeds/. [Accessed 23 May 2023].

[140] V. K. Kachanov, I. V. Sokolov, R. V. Kontsov and A. A. Sinitsyn, "Using Antenna Arrays for Reference-Free Measurement of Speed of Ultrasound and Thickness of Concrete Articles.," *Russian Journal of Nondestructive Testing,* vol. 53, no. 1, pp. 23-31, 2017.

[141] “The Engineering Toolbox,” 2001. [Online]. Available: https://www.engineeringtoolbox.com/water-dynamic-kinematic-viscosity-d_596.html. [Accessed 12 09 2023].

[142] “What is Poisson's Ratio: Definition, Formula, Examples.,” [Online]. Available: https://www.smlease.com/entries/mechanical-design-basics/what-is-poisson-ratio/. [Accessed 27 06 2023].

[143] M. A. Hopcroft, W. D. Nix and T. W. Kenny, “What is the Young's Modulus of Silicon?,” *Journal of Microelectromechanical Systems,* vol. 19, no. 2, pp. 229-238, 2010.

[144] A. H. Meitzler, “Poisson’s Ratio for Polycrystalline Silicon Used in Disk-Shaped Microresonators.,” *IEEE transactions on ultrasonics, ferroelectrics, and frequency control,* vol. 53, no. 2, p. 264, 2006.

[145] L. Zhang, R. Barrett, P. Cloetens, C. Detlefs and M. S. d. Rio, “Anisotropic elasticity of silicon and its application to the modelling of X-ray optics.,” *Journal of Synchrotron Radiation,* no. 21, pp. 507-517, 2014.

[146] L. E. Kinsler and A. R. Frey, “Circular Membranes and Plates,” in *Fundamentals of acoustics*, New York, Wiley, 1962, pp. 81-107.

[147] C. Beards, Structural Vibration - Analysis and Damping, London: Wiley, 1996.

[148] D. Ewins, “Damping measurement,” in *Encyclopedia of Vibration*, London, Imperial College of Science, Technology and Medicine, London, 2001, pp. 321-438.

[149] S. Kelly, Fundamentals of Mechanical Vibrations., New York: MCGraw Hill, 1993.

[150] COMSOL, “Comsol Documentation,” 2022. [Online]. Available: https://doc.comsol.com/6.1/docserver/#!/com.comsol.help.comsol/helpdesk/helpdesk.html. [Accessed 30 05 2023].

[151] H. Hariri, Design and realization of a piezoelectric mobile for cooperative use., Paris: Universite Paris Sud, 2012.

[152] J. A. Krupka, P. Kaminski, R. Kozlowski and B. Surma, “Dielectric properties of semi-insulating silicon at microwave frequencies.,” *Applied physics letters,* vol. 107, pp. 082105-1-3, August 2015.

[153] Comsol, Structural Mechanics Module User's Guide, Comsol, 2018.

[154] Computer Simulation Technology, “Understanding Time Domain Meshing in CST Microwave Studio,” 2010.

[155] L. W. Schmerr, Fundamentals of Ultrasonic Phased Arrays, USA: Springer, 2020.

[156] P. Delos, B. Broughton and J. Kraft, “Phased Array Antenna Patterns- Part 1: Linear Array Neam Characteristics and Array Factor,” *Analog Devices,* vol. 54, no. 2, pp. 1-7, 2019.

[157] M. H. Jensen, “Theory of Thermoviscous Acoustics: Thermal and Viscous Losses.,” COMSOL, 2014. [Online]. Available: https://www.comsol.com/blogs/theory-of-thermoviscous-acoustics-thermal-and-viscous-losses/. [Accessed 03 08 2023].

[158] Polytec, “Under water measurements with laser vibrometers.,” Germany.

[159] Monument Chemical, “Isopropyl Alcohol - Technical product information”.

[160] “Hyperphysics,” Department of Physics and Astronomy,Georgia state Univerasity, Georgia USA.

[161] T.G.Leighton, The Acoustic Bubble, Cambridge: Academic Press, 1994.

[162] R. Szilard, Theories and applications of plate analysis., United States of America: John WIley and Sons Inc, 2004.

[163] A. F. Bower, Applied Mechanics of Solids, Boca Raton: Taylor and Francis Group, 2010.

[164] Mini Physics, “Refraction of Light.,” [Online]. Available: https://www.miniphysics.com/refraction-of-light.html. [Accessed 19 08 2023].

[165] “FNBW vs HPBW- Difference between FNBW and HPBW.,” Test and measurement world terminology section., [Online]. Available: https://www.test-and-measurement-world.com/Terminology/FNBW-vs-HPBW.html. [Accessed 26 08 2023].

Appendix A: Material Parameters used in FEM and experimental processes.

This appendix presents the parametric data for the material used in the Finite Element Modelling and the experimental processes.

Material Parameters for PiezoMUMPS^{TM} devices.

The PiezoMUMPS^{TM} device used, was composed of various layers each of which was composed from different materials. All of these materials needed to have the correct parameters in place to be correctly modelled as close to a real life set up as possible.

Silicon- The material making up the PMUT's diaphragmatic structure.

In view of the PMUT's operation as a plate (as discussed in Appendix B), the stiffness of the plate's diaphragm's material is of crucial importance for the determination of the PMUT's operational characteristics including its resonant frequency, and amplitude of diaphragm displacement as well as the velocity of such displacement.

These characteristics of the diaphragm's dynamics then result in the ultrasonic waves' parameters such as in the pressure raised in the coupling fluid and the frequency of the ultrasonic transmission.

Two important characteristics would be the silicon's young's modulus, E, and the Poison ratio v.

The wafers used for the process are n-type Silicon on Insulator (SOI) which is a brittle material. The silicon layer of the SOI wafer is doped with phosphorus to obtain the n-type Si. The silicon used for MEMs processes is single crystal silicon material. It is doped by annealing at a high temperature of 1,050°C in inert Argon gas for 1 hour after phosphosilicate glass has been deposited on it. This annealing is conducted to drive the phosphorous into the silicon itself thus doping it.

The elasticity matrix

The elasticity matrix for Silicon is shown in (A.1). The relative permittivity is 12.7 and the density is 2,330 kg/m^3 [132].

$$\begin{bmatrix} 194.5 & 35.7 & 64.1 & 0 & 0 & 0 \\ 35.7 & 194.5 & 64.1 & 0 & 0 & 0 \\ 64.1 & 64.1 & 165.7 & 0 & 0 & 0 \\ 0 & 0 & 0 & 79.6 & 0 & 0 \\ 0 & 0 & 0 & 0 & 79.6 & 0 \\ 0 & 0 & 0 & 0 & 0 & 50.9 \end{bmatrix} \quad (A.1)$$

Silicon Oxide - The material used to build the electrical insulation.

SiO_2 is grown thermally on the Si. In the case of PiezoMUMPs™ the thickness of the oxide layer is 2,000Angstrom. Figure A.1 presents the thermal oxide layer.

Figure A.1 ~ Thermal oxide layer shown in yellow over the silicon layer.

The thermal oxidation process involves high temperatures which can be up to 1,000°C. The thermal oxide's dielectric strength is 1.1×10^6 V/cm [133].

Aluminium nitride- The material causing the piezoelectric forces

There are a number of piezoelectric materials which can be used in MEMs devices such as lead zirconate titanate PZT. The piezoelectric material used in the PiezoMUMPs™ process is AlN as shown in Figure A.2.

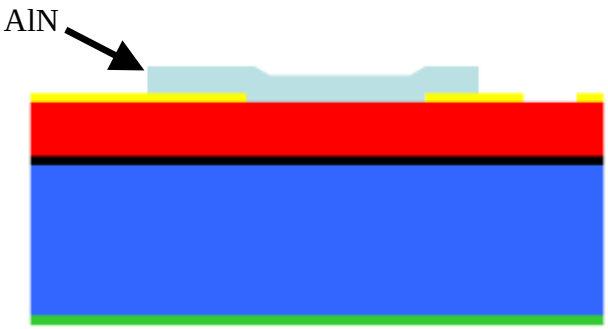

Figure A.2 ~ The aluminium nitride layer being shown deposited.

The coefficient $\frac{e_{31,f}}{\varepsilon_0 \varepsilon_{33,f}}$ for AlN is higher than that achieved by PZT and therefore for the sensing part of the micro device it would be preferable to use AlN [135].

$e_{31,f}$ is the intrinsic effective piezoelectric coefficient
ε_0 is the permittivity of vacuum
$\varepsilon_{33,f}$ is the relative dielectric coefficient

Aluminium Nitride, a ceramic, is the polar piezoelectric compound used in PiezoMUMPs™ in which a 0.5µm thick layer is used [99]. The structure is shown in Figure A.3.

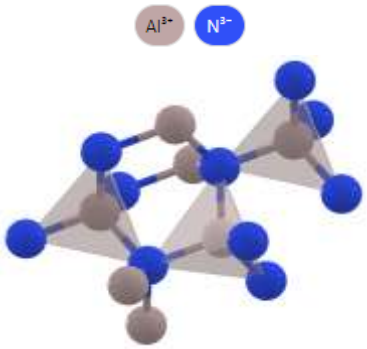

Figure A.3 ~ AlN Wurtzite structured crystal. Crystallized in the hexagonal P6_3mc space group [135].

The piezoelectric layer is the driving layer for PMUT and as such one of the most important layers.

Piezoelectric Tensor

Parameters for the AlN used in the PiezoMUMPs^{TM} process were not very accessible. There are various ways of mathematically describing piezoelectric tensors. A 3x3 matrix representation [d_{11}- d_{33}] can be used to describe the relationship between the strain and the actual polarisation of the material through the direct piezoelectric effect, with the change in polarisation brought about by specific directional strains.

AlN is anisotropic and highly so, with the d_{33} coefficient having a much higher value than the other coefficients. The latter being much smaller typically having a magnitude of less than 1 pC/N. According to the PiezoMUMPs^{TM} handbook the AlN used had a piezoelectric strain coefficient, d_{33}, ranging between 3.4 and 6.5 (pC/N) [115]. In the piezoelectric tensor the coefficient d_{33} shows the change in polarisation in the third axis' direction when a strain is present along the same axis. The 3x3 tensor therefore only represents direct piezoelectric effects.

Another more comprehensive way of describing the piezoelectric tensor is through a 6x3 tensor showing converse and direct piezoelectric effects. This tensor is good for substances which have hexagonal or tetragonal crystals and is shown in (A.2) [32]. Aluminium Nitride has a hexagonal structure [136].

$$\begin{bmatrix} 0 & 0 & 0 & 0 & e_{15} & 0 \\ 0 & 0 & 0 & e_{15} & 0 & 0 \\ e_{31} & e_{31} & e_{33} & 0 & 0 & 0 \end{bmatrix} \quad (A.2)$$

The total piezoelectric tensor represents in a comprehensive way the piezoelectric properties of the material being used. The total Piezoelectric Tensor for AlN with all the relevant values is shown in (A.3) with units of the piezoelectric voltage coefficients e_{ij} being C/m^2 [136] [56].

$$\begin{bmatrix} 0 & 0 & 0 & 0 & -0.2893 & 0 \\ 0 & 0 & 0 & -0.2893 & 0 & 0 \\ -0.5801 & -0.5801 & 1.461 & 0 & 0 & 0 \end{bmatrix} \quad (A.3)$$

The voigt notation representation of the coupling matrix used in the FEM for AlN was obtained from the COMSOL materials database as no information was obtained from the die manufacturer [137].

Other parameters for AlN used in the simulations.

The voigt notation representation of the elasticity matrix for AlN used in the FEM is given in (A.4). Similarly as what was the case for the coupling matrix, the data was obtained from the COMSOL materials database as no information was obtained from the die manufacturer [56].

$$\begin{bmatrix} 410 & 149 & 99 & 0 & 0 & 0 \\ 149 & 410 & 99 & 0 & 0 & 0 \\ 99 & 99 & 389 & 0 & 0 & 0 \\ 0 & 0 & 0 & 125 & 0 & 0 \\ 0 & 0 & 0 & 0 & 125 & 0 \\ 0 & 0 & 0 & 0 & 0 & 130.5 \end{bmatrix} \text{GPa} \qquad (A.4)$$

The Stress-charge form was used.

The density of Aluminium Nitride used was 3,300kg/m^3. The relative permittivity used was 9 [56].

Chrome and aluminium -The materials used for the electrical contacts-Metal layers

The metal layer in the simulations which are the subject of this dissertation are not used as electrical paths but are only placed in the model to simulate the mechanical aspects which affect the PMUT dynamics. A two metal layered process was used Figure A.4.

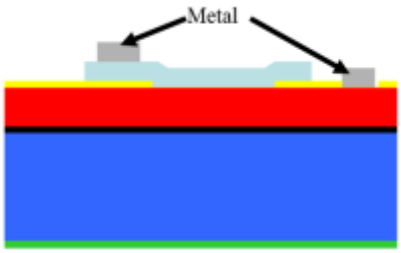

Figure A.4 ~ The metal contacts shown in grey.

The aluminium layer is the other significant layer in terms of Young's modulus. This layer would be significant in view that it is the second thickest layer at 1.02 µm thick. The value of young's modulus for this layer was taken from the COMSOL materials database where equation (A.5) outlines the equation used in the derivation of the modulus.

$$E_{silicon} = 7.659324\text{x}10^{10} + 2007396.0\text{x}T^{1-186458.4}\text{x}T^{2+419.2175}\text{x}T^{3-0.3495083}\text{x}T^{4} \qquad (A.5)$$

Where T is the temperature which is being used at 293.15K or 20°C for the modelling in this dissertation. This was the temperature setting in the laboratory where the experimental work was conducted.

Using the value of T given above, the value of Young's modulus used for aluminium in these models was 69.1 GPa.

The density of aluminium is calculated by COMSOL using either of two equations, (A.6) and (A.7).

If the ambient temperature is between 20 and 130 Kelvin, equation (A.6) was used as presented here:

$$\rho_{Al} = 2734.317-0.02751647T+0.001016054T^2-1.700864x10^{-5}T^3+5.734155x10^{-8}T^4 \quad (A.6)$$

However in the case of this project since the lab was kept at a temperature of 20 degrees C the density equation used was (A.7) which referred to temperatures between 130 and 933 degrees Kelvin.

$$\rho_{Al} = 2736.893-0.006011681T-7.012444x10^{-4}T^2+1.3582x10^{-6}T^3-1.367828x10^{-9}T^4+ 5.177991x10^{-13}T^5 \quad (A.7)$$

At 20° C the density of aluminium is therefore 2,700kgm^{-3}

Further data for Finite Element Modelling of reinforced concrete.

For finite element modelling of concrete various other parameters where required to set up a complete solid mechanics model. These parameters were obtained through the Eurocodes which are the industry standard. The young's modulus for concrete was obtained from Table A.1 and the Poisson's ratio *v* for intact concrete was 0.2 [138].

Table A.1 ~ Concrete parametric properties according to EN1992-1-1 [40]

Symbol	**Description**	**C20 /25**	**C25 /30**	**C30 /37**	**C35 /45**	**C40 /50**	**C45 /55**	**C50 /60**	**C55 /67**	**C60 /75**
Ecm (MPa)	Elastic modulus	299 62	314 76	328 37	340 77	352 20	362 83	372 78	382 14	391 00

The speed of sound of substances used in this project is shown in Table A.2.

Table A.2 ~ Table denoting the speed of sound in materials mentioned in this dissertation.

Substance	**Phase**	**Speed of sound [m/s]**	**Note**	**Reference**
Mild Steel	Solid	3,235		[139]
316 Stainless Steel	Solid	3,272		[139]
Concrete	Solid	3,300		[140]
Isopropanol	Liquid	1,207	At 20°c	[137] [28]
Distilled Water	Liquid	1,498		
Glycerine	Liquid	1,964		[137]

Air	Gas	343.2		[137]†1
Note†1: This is calculated by COMSOL at 20°C				

The dynamic viscosity values were also needed when modelling thermal and viscous losses through the Thermoviscous Acoustic physics module. Table A.3 presents the values for the dynamic viscosities of the liquids used in this project.

Table A.3~ Table of Dynamic Viscosity of liquids used in the simulation and experimental processes.

Substance	**Phase**	**Dynamic Viscosity [Pa s]**	**Note**	**Reference**
Isopropanol	Liquid	0.00192	At 20°c	[139] [137]
Distilled water	Liquid	0.001	At 20°c	[141]
Glycerine	Liquid	0.950	300K	[137]

Density of Isopropanol

The density of isopropanol was calculated by the COMSOL materials database. The equation worked for temperatures between 274 and 333 Kelvin. The actual isopropanol density was calculated using the equation (A.8).

$$1044.556-0.8201473xT^{1} \quad (A.8)$$

Hence at 20°C the density is 804.1298kgm^{-3} [137].

Density of Glycerine

The density of glycerine used in the simulations was 1,260 kgm^{-3} [137].

Poisson's Ratio

Material submitted to uniaxial loading generally responds in a triaxial fashion with three dimensional deformation occurring. Figure A.5 represents a conceptual illustration outlining the principles underpinning the Poisson ratio.

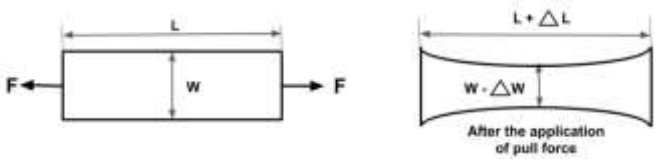

Figure A.5 ~ Illustration of the concepts of Lateral and Longitudinal strain underpinning the Poisson Ratio [142].

In the case of an isotropic material, the expression for the Poisson's ratio is shown in (A.9)

$$Poisson's\ Ratio = v = \frac{Lateral\ Strain}{Longitudinal\ Strain} = -\frac{\Delta w/w}{\Delta l/l} \quad (A.9)$$

From literature one can see various values of the Poisson's ratio of silicon. A reviewed paper stated that polysilicon semiconductor structures present average values of Poisson's ratio of 0.22. Such values are however dependent on the deposition process [111]. Further literature studied indicate that possible values of the Poisson's ratio varying between 0.048 and 0.40 [143].

The SOI wafer orientation used for the PiezoMUMPs^{TM} process was <100> with values of Poisson's ratio for such an orientation being found to be 0.29 [144] and 0.2783 [145] in literature. The value of the Poisson's Ratio used for the Finite Element Modelling conducted in this dissertation was that of 0.28.

Appendix B: Configuration- Uniformly Stretched Circular Membrane vs Thin Circular Plate.

This appendix presents important theory central to the analysis of PMUTs and the design of mathematical models representing them.

The vibration systems of plane surfaces has a range complex mechanisms which can be acting to produce the movements. Detailed analysis of each mechanism is beyond the scope of this dissertation. This text will therefore look into two vibration systems namely:

- Uniformly Stretched Circular Membrane (USCM)
- Thin Circular plate (TCP)

Uniformly Stretched Circular Membrane (USCM)

In a Uniformly Stretched Circular Membrane the restoring forces are due to tension rather than stiffness of the membrane. The latter may be considered negligible in the case of a USMC. Microphone diaphragms and drum membranes can be considered as falling in this category [146].

The derivation of the wave equation for a membrane assumes a perfectly elastic membrane which is assumed to be uniformly thin (with respect to the diameter) therefore having negligible stiffness. USMCs vibrate with small displacement amplitudes where the transverse displacement can be expressed with the equation (B.1) [146].

$$y = y(x, z, t) \tag{B.1}$$

The force acting to restore any element making part of the membrane which is away from the equilibrium plane is shown in (B.2) [146].

$$Tdz\left[\left(\frac{\partial y}{\partial \mathrm{x}}\right)_{x+dx} - \left(\frac{\partial y}{\partial \mathrm{x}}\right)_{x}\right] = T\left(\frac{\partial^2 y}{\partial \mathrm{x}^2}\right)dxdz \tag{B.2}$$

Where

T is the tension at which the membrane's edge is stretched. Since the tension is uniformly distributed through the membrane matter on opposing sides of a line ds will be pulled apart with a tensional force equivalent to Tds.

The other terms are shown in Figure B.1.

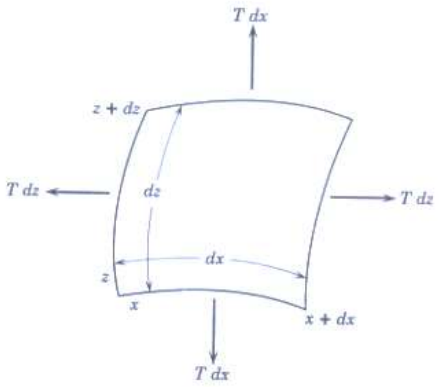

Figure B.1 ~ A vibrating rectangular membrane [146].

Equation (B.3) is obtained from the expression of the restoring forces which are acting on membrane elements.

$$T\left(\frac{\partial^2 y}{\partial x^2}+\frac{\partial^2 y}{\partial z^2}\right)dxdz = sdxdz\frac{\partial^2 y}{\partial t^2} \qquad (B.3)$$

Where

s	is the mass per unit area of the element
$sdxdz$	is the mass of the element
$\frac{\partial^2 y}{\partial t^2}$	is the acceleration of the element.

$$\frac{\partial^2 y}{\partial x^2} = c^2\left(\frac{\partial^2 y}{\partial x^2}+\frac{\partial^2 y}{\partial z^2}\right) \qquad (B.4)$$

Where:

$$c = \sqrt{\frac{T}{s}}$$

The membrane practically vibrates in a symmetric way which means that the equation simplifies to (B.5)

$$\frac{\partial^2 y}{\partial x^2} = c^2\left(\frac{\partial^2 y}{\partial x^2}+\frac{\partial^2 y}{\partial z^2}\right) \qquad (B.5)$$

Equation (B.5) can be expressed in the general form as shown in (B.6)

$$\frac{\partial^2 y}{\partial t^2} = c^2\nabla^2 y \qquad (B.6)$$

For the circular membrane the equation can be expressed as (B.7).

Where

$x = rcos\theta$
$z = rsin\,\theta$

$$\frac{\partial^2 y}{\partial t^2} = c^2\left(\frac{\partial^2 y}{\partial t^2} + \frac{1}{r}\frac{\partial y}{\partial r} + \frac{1}{r^2}\frac{\partial^2 y}{\partial \theta^2}\right) \quad (B.7)$$

Membrane vibration is symmetrical and therefore the equation can be simplified to $y = y(r,t)$ which is independent of θ, the azimuth. The equation simplifies to that shown in (B.8).

$$\frac{\partial^2 y}{\partial t^2} = c^2\left(\frac{\partial^2 y}{\partial r^2} + \frac{1}{r}\frac{\partial y}{\partial r}\right) \quad (B.8)$$

Thin Circular Plate (TCP)

Thin Circular Plates' main difference from a USCM is the fact that stiffness plays an important part in the plates' movement mechanics. Examples of TCPs would be telephone diaphragms or the circular plates fronting the face of some sonar systems [146].

TCPs differ from membranes in one key way namely that the restorative force on the plate is due to the diaphragm's stiffness rather than due to the tension applied to the USCM. The equation of motion applicable for thin circular plates is shown in (B.9) [146].

$$\frac{\partial^2 y}{\partial t^2} = -\frac{k^2 Y}{\rho(1-\sigma^2)}\nabla_r^4 y \quad (B.9)$$

Where

ρ is the material's volume density
σ is the poisson ratio for the material
Y is the Young's modulus for the material
k is a constant which for a uniform thickness plate $k = \frac{plate\ thickness}{\sqrt{12}}$

Appendix C: Damping Theory.

This appendix explains the damping theories necessary to calibrate the FEMs with the experimental data thus making them more accurate. Through the application of this theory the acceleration, displacement, velocity and vibration modes of the FEM could be set to approach and match experimental data. This would in turn make them more reliable when used to design further devices.

Solid structural damping is usually of a low value when compared to other diaphragm dynamics. This means that at most frequencies the difference in performance between a damped and undamped system is low enough as to present negligible performance differences between damped and undamped structures. However as the structural vibrating frequency starts to approach the resonant point, damping starts having an incrementally more important effect on the structure's performance characteristics. Damping models can be highly complex and hence the structural model needs to be reduced to the lowest number of degrees of freedom possible. Figure C.1 show a model with a single degree of freedom [147].

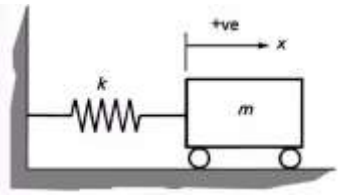

Figure C.1 ~ Model of structural vibration with single degree of freedom [147].

The model shown in Figure C.1 represents the mass of the body with the component "m" which may move in one direction over a surface. The mass is held by a spring which has the stiffness parameter k. The spring is attached to the body from one end and to a fixed point from the other. The spring provides a restorative force to the mass when it is pulled to the right which pulls and accelerates the body to the left when the body is eventually released. The body overshoots the mark and is then slowed down by the spring which acts as retarding mechanism as soon as the body passes the equilibrium position. The oscillations go on until the body should theoretically reach its original position. In reality this is not reached due to the fact that the some of the kinetic energy would have been dissipated through damping [147].

It is very difficult to predictively model damping of a vibrating structure in an accurate way [148]. The reason being that many mechanisms are operating such as losses intra element connections, and the internal friction due to deformation. There is also the fluid structure interaction which need to be considered especially in the case of fluids which are denser than air and where the oscillations are occurring at high frequencies. These structure to fluid interactions will be discussed in subsequent theory sections as these are far too complex to be modelled through the simple models outlined in this section. There are various damping models which may be used and are reviewed briefly here.

Viscous Damping

In the case of viscous damping the model is adjusted as shown in Figure C.2

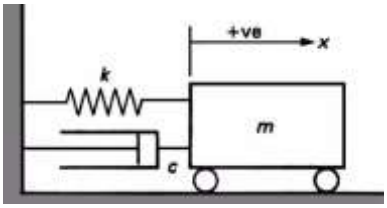

Figure C.2 ~ Model showing a viscous damping model with movement in a single degree of freedom [147].

This includes the addition of a viscous damper which is also fixed to the same support as the spring k. In this case the equation of motion is shown in (C.1) [147].

$$m\ddot{x} + c\dot{x} + kx = \text{Fsinvt} \tag{C.1}$$

The differential equation which directs the movement of a body in a single degree of freedom system which, is excited by a single frequency is shown in (C.2) [149]

$$\ddot{x} + 2\zeta\omega_n\dot{x} + \omega_n^2 x = \frac{F_0}{\tilde{m}}\sin(\omega t+\psi) \tag{C.2}$$

The equations (C.3) and (C.4) are achieved from equation (C.2).

$$X = \frac{F_0}{\tilde{m}\left[\left(\omega_n^2-\omega^2\right)^2+(2\zeta\omega\omega_n)^2\right]^{1/2}} \tag{C.3}$$

$$\phi = tan^{-1}\left(\frac{2\zeta\omega\omega_n}{\omega_n^2-\omega^2}\right) \tag{C.4}$$

For viscous damping the COMSOL modelling uses two constants namely:

η_b	Bulk Viscosity
η_v	Shear Viscosity

The Bulk Viscosity Coefficient is proportional to changes in the volume while the shear viscosity is proportional to the change in the shape [150].

COMSOL can use various damping types to model the frictional damping intrinsic to the material itself. The structural mechanics interface which is used to in the models has three explicit models to choose from including viscous damping, and loss factor models based on Isotropic, anisotropic parameters as well as Rayleigh damping which is the Damping type used in most of the models underpinning this dissertation unless otherwise specified.

Rayleigh Damping

To understand the parameters underlying Rayleigh damping one needs to look at a simplified mode with a single degree of freedom. The dynamics of the system is described by the equation of motion shown in equation (C.5) [150].

$$m\frac{d^2u}{dt^2} + c\frac{du}{dt} + ku = f(t) \qquad (C.5)$$

Where

u is the displacement
m is the mass
c is the damping parameter
k is the system stiffness
f(t) is the time dependent function

The equation of motion can then be presented as shown in (C.6) [150].

$$\frac{d^2u}{dt^2} + 2\zeta\omega_0\frac{du}{dt} + \omega_0^2 u = \frac{f(t)}{m} \qquad (C.6)$$

Where

ζ is the damping ratio with a value of 1 for a critically damped system and is equal to $c/(2m\omega_0)$

ω_0 is the resonant frequency of an undamped system

c is a parameter defined in terms of mass fraction and stiffness through the two parameters as shown in (C.7), one α_{dM} being the mass parameter and the other β_{dK} being the stiffness parameter.

$$c=\alpha_{dM}m+\beta_{dK}k \qquad (C.7)$$

Obtaining optimal values for the parameters α_{dM} and β_{dK} can be complicated. On the other hand values of the damping ratio ζ which gives the ratio between the critical and actual damping values can be found in literature as a percentage of critical damping. Figure C.3 shows the Rayleigh damping representation.

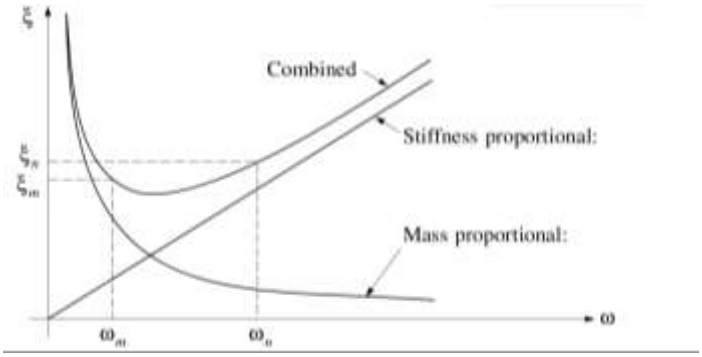

Figure C.3 ~ Representation for Rayleigh Damping showing the damping ratio on the y axis vs the frequency on the x axis [151].

Rayleigh damping does have another drawback namely instances where experimental results may not agree with results from the model. This is due to the fact that damping forces related to the material are similar to forces of friction in their behaviour and therefore increase linearly with frequency. The damping ratios are shown in (C.8) and (C.9) below [150].

$$\alpha_{dM}=4\pi f_1 f_2 \frac{\zeta_n f_m-\zeta_n f_m}{f_n^2-f_m^2} \qquad (C.8)$$

$$\beta_{dK}=\frac{\zeta_n f_m-\zeta_n f_m}{\pi(f_n^2-f_m^2)} \qquad (C.9)$$

Both α_{dM} and β_{dK} cannot be negative and actually for modelling purposes α_{dM} can be set to zero and only the β_{dK} used to model the damping.

In this type of damping COMSOL allows the two damping coefficients to be set. The Beta damping coefficient provides a stronger damping effect at the higher frequencies. On the other hand the Alpha term which is mass proportional is stronger acting at low frequencies as it acts on the structure's velocity component.

Isotropic loss factor

The isotropic loss factor or loss tangent tanδ, measures the energy which is dissipated in the material itself when it is subjected to oscillatory movements. It is therefore an important parameter as it defines the amount of kinetic oscillatory energy which is transformed to heat inside the substance itself thereby damping the oscillations. The loss factor which is both temperature and frequency dependent is also strongly dependent on the composition and microstructure of the semiconducting material itself. The relationship between loss tangent and frequency is shown in Figure C.4.

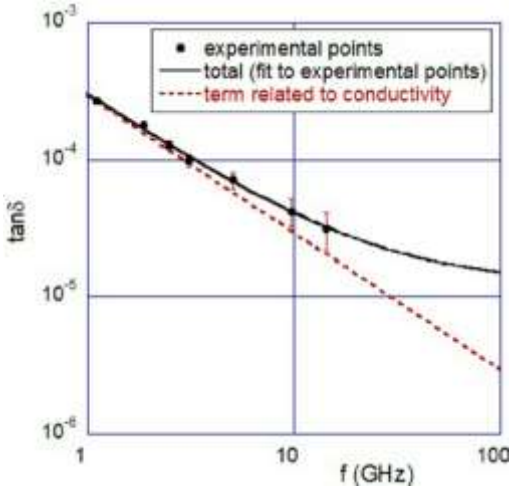

Figure C.4 ~ Graph showing the loss tangent versus the frequency. The material is high purity semiconductor silicon [152].

Since the frequency being used in this project is less than 1 GHz, the value of tan δ used in the FEM was started at $1x10^{-4}$. Damping time domain modelling was challenging especially with regards to the introduction of the damping coefficients. System damping could occur due to the interaction of various sources. These included material dissipation such as hysteresis damping, or to thermodynamic effects such as thermoelectric damping. Other important sources of damping included Isotropic Loss factor damping was not found to introduce damping in the time domain and hence not used.

Rayleigh damping on the other hand produced good results in the time domain too and therefor was used to produce the models shown in this dissertation.

Appendix D: Finite Element Modelling (FEM) details.

This appendix complements the work outlined in Chapter 3 with further background material.

Frequency Domain modelling

The frequency domain modelling carried out using COMSOL was used to compute the frequency response for each PMUT when excited through a range of frequency deployed in the correct fluids.

Three physics interfaces were used to conduct the frequency domain studies namely:

- Solid Mechanics interface
- Electrostatics interface
- Pressure Acoustics interface

Solid Mechanics

The solid mechanics interface was used to calculate the frequency response of the structure when loaded and excited at particular frequencies. The steady state structural response to the excitation prevails when the transients are damped with the response being predominantly linear to achieve a pure response.

The solid mechanics interface models the deformation and motion of structures in 2 or 3 dimensional spatial frame. Apart from the spatial coordinates **x**, y, z for 3D models and r, φ and z for 2D axisymmetric models.

In the case of this dissertation the study is based on the deformation of PMUT structures. COMSOL keeps the same material coordinates **X** which is the coordinate vector made use of by the continuum mechanics theory operated in the calculation. X is part of a reference set (also called material coordinates) which includes Y, Z, φ, R, and Z. The relationship is shown in (D.1) [150].

$$x = x(X, t) = X + u(X, t) \tag{D.1}$$

where u is the displacement vector which determines the instantaneous spatial position of the point **X**.

The material coordinates are constant and dependent on the geometry designed. On the other hand the spatial coordinates depicted in capital letters are dependent on the solutions of the finite element analysis. The spatial coordinate x is therefore linked to the material coordinate **X** through equation (D.2) [150]:

$$x=X+u(X,t) \tag{D.2}$$

The displacement u is shown in Figure D.1.

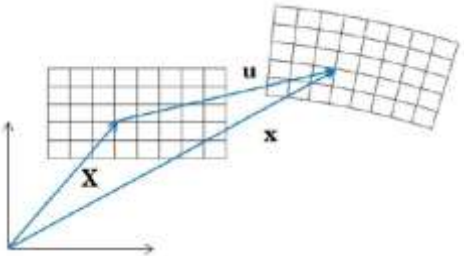

Figure D.1 ~ Representation showing the relationship between the coordinates X, x, and u [150].

The silicon and aluminium layers were modelled as isotropic linear elastic materials having the same properties in all directions. The aluminium nitride layer on the other hand was set up as piezoelectric material under the structural mechanics interface. The discretization chosen for the displacement field was Quadratic Lagrange.

Acoustic Structure Boundary

The Acoustic Structure Interface, models the region in which the ultrasonic energy is actually created in the model by coupling the two fields of structural mechanics and acoustics. This is where rapid changes in acoustic pressure are induced into the fluid by the vibrating structure which in the case of this dissertation is the PMUT's diaphragm structure. The induced pressures may be both above and below atmospheric pressure depending on the diaphragm's direction of movement.

The Acoustic Structure Interaction may operate in both directions with pressure waves also travelling into the coupling fluid from the surrounding solid structure and being capable of inducing oscillations in the PMUT's diaphragm. This causes the PMUT to work as a receiving device instead of as a transmitting device.

The axisymmetric 2D model

The first set of finite element models were meant to study how a PMUT behaves in fluid in both the time and the frequency domains. As discussed in the underpinning theory, a PMUT's performance is greatly affected by the fluids surrounding it both in terms of the coupling fluid and also the fluid medium filling the cavity such as for example if the cavity is filled with liquid or gas.

The axisymmetric model is shown in Figure D.2. The model is based on the cylindrical coordinates using the variables Z, φ and r to describe points within the 3D space.

Figure D.2 ~ Creating a 3D solid from the 2D geometry [153].

The technique of using 2D axisymmetric modelling sets out the geometry on a half plane with r≥0 and the rotation angle φ being equal to zero. The full geometry is then created by having the 2D geometry being rotated around the z-axis point. In view of the symetricity requirement for 2D axisymetric loading, this modelling type was only used for plane circular PMUT structures. For other non axisymetric device structures, where loads are not indipendent of the rotation angle φ, 3 D modelling techniques were used as explained further in the dissertation. The geometry of the main model used throughout this dissertation is shown in Figure D.3 and Figure D.4. Figure D.3 (a) shows the whole model with the PMUT (and cavity) in the lower left hand corner. It also shows the coupling fluid including the perfectly matched layer (PML). Figure D.3 (b) shows a closer view of the PMUT and the cavity filled with the cavity fluid.

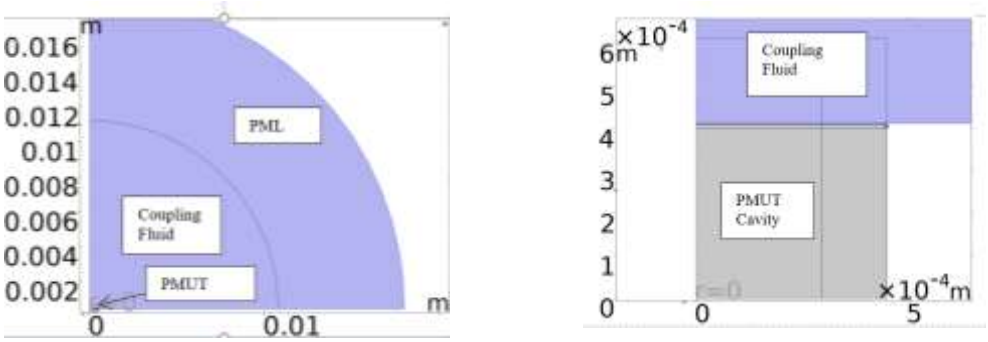

(a) (b)

Figure D.3 ~ The 2D-Axysymetric model showing the (a) whole model with fluid layer over the PMUT, PML and cavity under the PMUT (b) Close up view of PMUT with PMUT cavity under the PMUT.

Figure D.4 presents a close view of the PMUT's solid structure FEM with the various layers forming it.

Figure D.4 ~ Close up of the PMUT solid structure (shaded in blue) including the Silicon Diaphragm, AlN piezoelectric layer, and the Al metal contact. The lower grey area shows the fluid in the cavity while the upper grey area shows the coupling fluid.

Appendix E: Creating the Finite Element Models – Meshing.

Meshing of the 2D models

Meshing is crucial to achieve accurate results from the FEMs. The meshing process took a lot of effort and testing to ensure that the best meshing strategies were developed. One of the principle difficulties for effective meshing to be developed was the mismatch in thickness between the various layers making up the model.

As an example the AlN piezoelectric layer at a thickness of 0.5 μm is much thinner than the other layers especially the fluid layers and the concrete structures which are measured in meters. The AlN layer is naturally a critical element for the correct operation of the model and therefore it is crucial to ensure that the meshing is carried out in the best possible way.

The full mesh can be seen in Figure E.1 which shows a full view of the meshed 2D section.

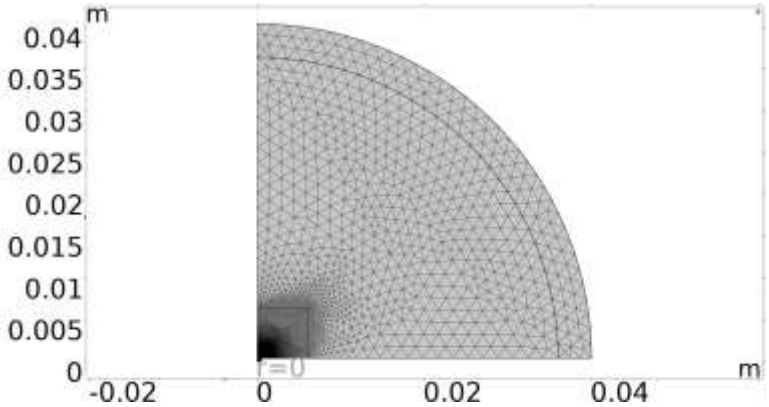

Figure E.1 ~ A view of the 2D meshing for the system.

PMUT and Cavity fluid ~ Mapped or tetrahedral meshing

In view of the criticality of this region, two methods of meshing were separately tried out for this area. These were mapped meshing and tetrahedral meshing. The results from the two meshing types were compared as will be seen further below.

Meshing Method 1- Mapped meshing.

The area marked in blue ink in Figure E.2 shows the region which was meshed using mapped meshing. It encompasses the area of the cavity fluid and the PMUT itself including the 0.5 μm thick aluminium nitride layer.

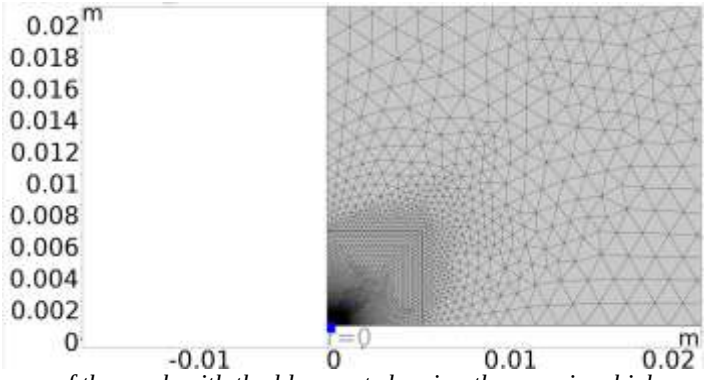

Figure E.2 ~ Close up of the mesh with the blue part showing the area in which mapped mapping was conducted.

Mapped meshing was selected for this particular area to create a quadrilateral mesh which is structured on the domains themselves. COMSOL documentation rates the mapped mesh as potentially able to create the highest quality of surface meshes [150]. Since the elements created were all of a rectangular shape having 90^{o} angles, all skewness issues were avoided. Trials also found that this meshing provided the best control on size and elemental growth rate thereby again resulting in high quality in this, crucial, area of the model.

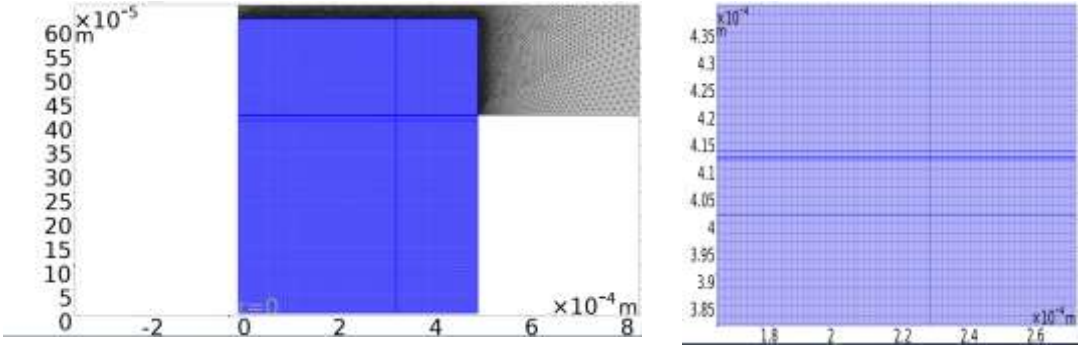

(a) (b)

Figure E.3 ~ Mapped meshing carried out in the region encompassing the PMUT, cavity and coupling fluid area immediately above the PMUT.

The element sizes were not left in the default physics controlled mode. They were set at customized settings to enable full customization of the FEM. The maximum element size for the mapped area was 1.68×10^{-6} m while the minimum element size used was 8×10^{-7} m. Maximum element growth rate was set at 1.01 and the curvature factor was 0.2.

Meshing Method 2- Tetrahedral Meshing.

This area contained no less than 12 regions each with different parameters including thickness. This makes tetrahedral meshing for this area a challenging undertaking. The tetrahedral meshing system used for this area was based on a three level system as shown in Table E.1.

Table E.1~ The parameters for the three level tetrahedral meshing used.

	Max element size [m]	**Minimum element size [m]**	**Maximum element growth rate**	**Curvature facture**	**Resolution of narrow regions**
Level 1	$2x10^{-6}$	$4.41x10^{-7}$	1.08	0.25	1
Level 2	0.00112	$1.6x10^{-5}$	1.1	0.25	1
Auto calibration for finer fluid dynamics meshing.					
Level 3	0.0018	$8x10^{-5}$	1.15	0.3	1
Auto calibration for normal size fluid dynamics meshing.					

Level 1 was reserved for the smallest and most delicate areas with submicron mesh sizes being utilised. Naturally such intensive meshing could not be used to mesh the whole model as it would be prohibitively complex for the model to be solved in a reasonable time period.

It was therefore decided to mesh the other two regions using physics set meshing specialised for fluid dynamics. In the region closest to the piezoelectric area the meshing was set to fine while in the other region it was set to normal as shown in Figure E.4.

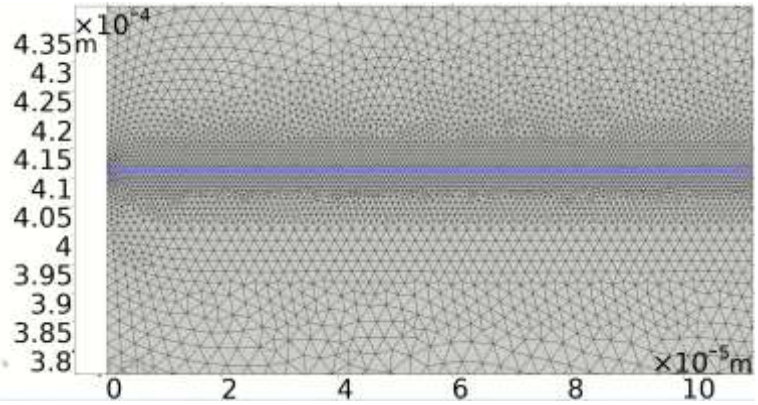

Figure E.4 ~ The meshing used in the PMUT area showing the very finely meshed AlN layer (shown in blue).

The comparison of the results obtained from the two meshing types is outlined in the section below.

Comparing results achieved with mapped mapping with those obtained using tetrahedral mapping.

As discussed previously the core area was meshed using two methodologies, namely mapped and tetrahedral meshing. A comparative assessment was conducted and tabulated in Table E.2 to study the effect which meshing type has on the accuracy of the FEM.

Table E.2 ~ Comparative analysis between mapped and tetrahedral meshing in the PMUT core region.

PMUT Diameter [μm]	Experimental Value of resonant frequency at E= 140 GPa [kHz]	FEM Value of resonant frequency at E= 140 GPa using mapped meshing [kHz]	FEM Value of resonant frequency at E= 140 GPa when using Tetrahedral meshing [kHz]	Percentage difference between the resonant frequency values achieved through FEM mapped mashing and FEM tetrahedral meshing [%]	Percentage difference between the resonant frequency achieved by FEM using mapped meshing and experimental values [%]	Percentage difference between the resonant frequency achieved by FEM using tetrahedral meshing and experimental values [%]
550	187.70	219.80	216.30	1.61	-15.75	-14.16
700	111.00	123.00	107.70	13.26	-10.26	3.02
900	57.50	63.70	66.90	-4.90	-10.23	-15.11
1800	12.69	12.50	12.40	0.80	1.51	2.31
2000	10.20	9.80	10.20	-4.00	4.00	0.00

From the table it could be seen that the percentage difference was within tolerance ratios which one can see in FEMs.

The coupling fluid in the region close to the PMUT

The next part of the meshing process involved the area indicated in blue ink in Figure E.5. The meshing for this area was developed carefully in view of the sensitivity of this region since it is close to the PMUT structure itself.

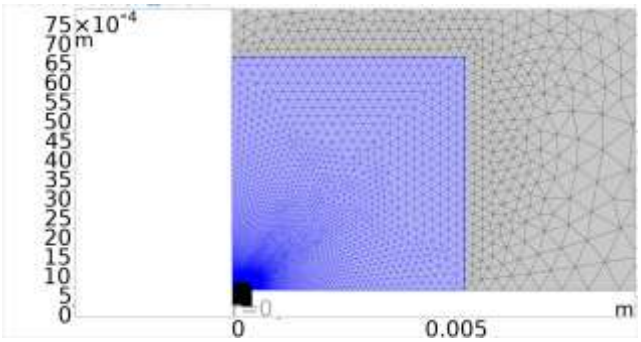

Figure E.5 ~ Tetrahedral meshing for the box demarcating the fluid nearest to the PMUT.

Through various trials it was determined that this area could not be practically meshed through a mapped meshing system. It was therefore decided that for the scope of the project the meshing was conducted through the use of tetrahedral meshing.

The coupling fluid outer zone and the perfectly matched layer.

This area is the zone which incorporates the outer fluid region including the perfectly matched layer. It is shown shaded in blue in Figure E.6 with the PML being the outer edge of the zone.

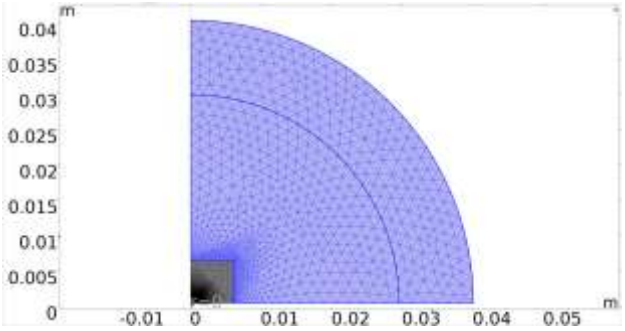

Figure E.6 ~ Meshing of the fluid outer zone and the Perfectly Matched Region (PML).

This fluidic area was on the outer region of the model and therefore the meshing did not require the same level of stringent parameters used for the inner regions. However it still was still passed through an intensive testing process as will be described below.

Mesh Quality testing.

The meshes which were produced were subjected to rigorous testing for various parameters to ensure that in all cases the mesh quality was of a high standard. Since a low resolution of the mesh produces results which are not accurate. Poor quality meshing may also result in inverted elements and cause non convergence due to high Jacobian condition numbers. The testing procedure below is shown for one example, however this process was conducted for each of the models presented in this dissertation.

COMSOL uses a dimensionless system to represent the mesh quality parameters where 1 indicates a perfect mesh element while 0 denotes a degenerate element. The first parameter test conducted in each of the meshes was a test to determine the amount of skewness present in each element. Skewness is defined by equation (E.1) [150].

$$1 - max\left(\frac{\theta - \theta_e}{180 - \theta_e}, \frac{\theta_{e-} - \theta}{\theta_e}\right) \tag{E.1}$$

where

θ is the vertex angle for a 2D model or the edge angle in a 3D model,
θ_e is the corresponding edge or vertex angle in an ideal element,

The skewness plot is shown in Figure E.7 which shows all mesh elements coded in green thereby signifying high quality (0.5 upwards) for each of the elements.

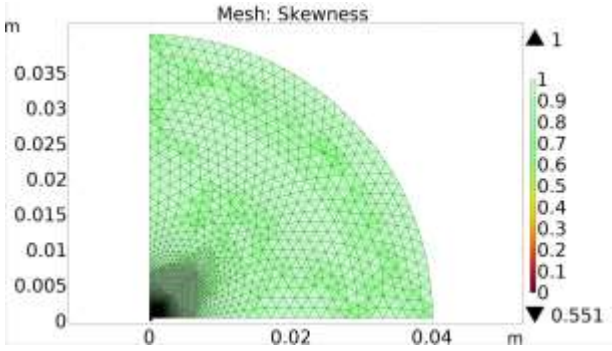

Figure E.7 ~ Mesh Plot showing the skewness factor for the elements in the mesh.

The second meshing parameter quality test was for the maximum angle. The plot for this is shown in Figure E.8. This parameter takes the largest angle in an element returning a score of "1" if no angle is larger than the angles of the ideal element or else provides a measure depending on how much larger the elemental angle is from the ideal.

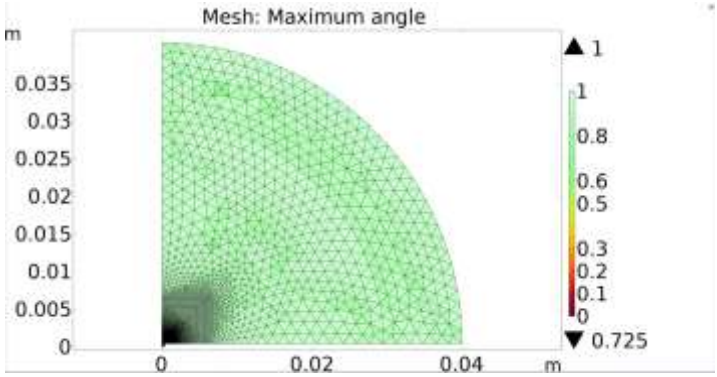

Figure E.8 ~ Mesh Plot showing the maximum angle factor for the elements in the mesh.

Other mesh quality parameters which were similarly checked were:

- *Volume vs circumradius* ~ is the parameter which looked at the volume of the element and the radius of the sphere circumscribed by it.
- *Volume vs length* ~ is the parameter which looked at a quotient made up of the length of the elemental edge and volume.
- *Conditional Number* ~ is the parameter which looked at the elemental dimension divided by the transforming matrix number. The transforming matrix transforms the element to the reference element.

In this example being presented as illustration the constructed mesh consisted of 106,367 elements with an average quality above 0.9743 and with no element going below the 0.55 average quality score. Hence from a meshing perspective this model was deemed to be reliable. All models used in this project be they 2D or 3D were similarly tested in all quality parameters.

Modelling in the Frequency Domain

Modelling in the frequency domain was conducted when the scope was the determination of parameters such as the resonant frequency of particular PMUTs. In the frequency domain FEM, the model's responses to steady state excitation at the particular frequencies as determined by the frequency sweep were measured.

Modelling in the time domain

Time domain modelling especially at the minute timestamps required for this project presented a very challenging FEM scenario. Time domain Finite Element Modelling was carried out using a high performance processors such as an Intel i9 processor with 64 GB RAM, and various 10^{th} generation i7 high spec machines to adequately handle the models with the required accuracy and resolution.

Time domain modelling was also found to be very onerous in terms of file sizes. Various mechanisms were utilised to reduce the model sizes although to reach the level of detail needed most of the files exceeded 20 GB of data with some even exceeding the 100 GB mark.

The axisymmetric models were coupled with the time domain multi physics equations whereby the system's dynamics were explained through differential equations which were either linear or non-linear depending on the dynamic which was being measured at that particular point.

The time domain models were operated through the application of external excitation signals across the AlN piezo layer through which the diaphragm structure was submitted to a system of forced vibrations. The interaction of the diaphragm with the fluids below and above it were then modelled as were the sonic wave output which was produced. When the external signal was discontinued the diaphragm vibrated freely (as opposed to forced) [149] and thereafter decelerated. The cycle then repeats itself periodically tied to the resonant frequency which is obtained from the frequency domain models.

Appendix F: Determination of the Young's modulus for SOI process phosphorous doped silicon.

This appendix presents further results from the young's modulus finite element analysis. Similar effects were viewed in the 1,000 μm device as seen in Figure F.1. Steps of 100 Hz each were taken for each of the models.

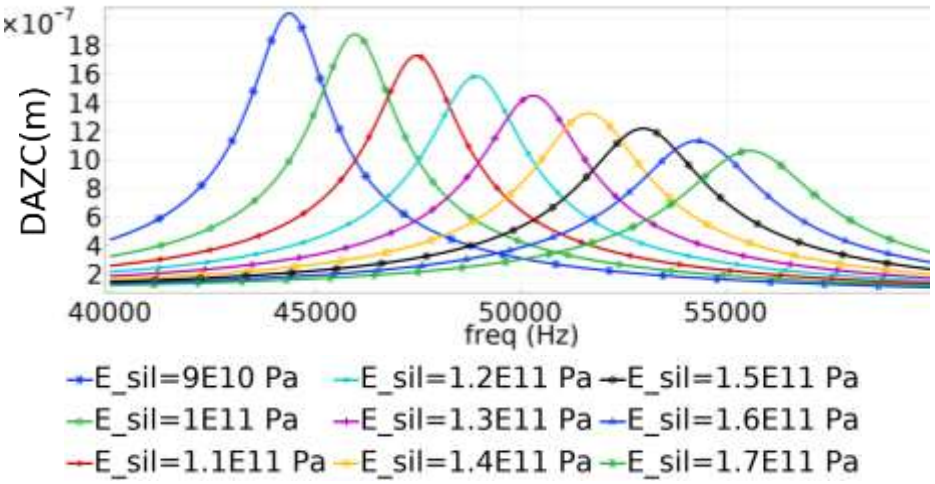

Figure F.1 ~ Displacement Amplitude Z Component (DAZC) at the centre of the membrane for a 1000 μm diameter device. Damping was set to zero and Poisson ratio of Silicon was set to 0.28. The finite element frequency stepping was conducted at 30Hz steps. Coupling fluid was isopropanol and cavity fluid was air.

The next parametric and frequency sweep presented in Figure F.2 was a 1,800 μm diameter PMUT, a larger diameter PMUT. Since the differences in the resonant frequency for each value of Young's modulus was smaller than those for the 1,000 μm PMUT in this case the frequency steps taken were also smaller, at 50 Hz to keep an adequate resolution for the resonant frequency.

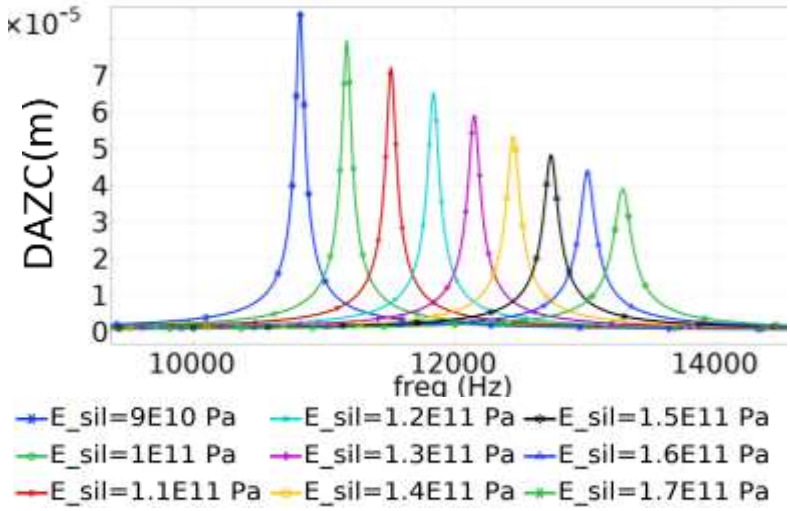

Figure F.2 ~ PMUT Displacement Amplitude Z Component (DAZC) at the centre of the membrane for 1,800 μm diameter device. Damping was set to zero and Poisson ratio of Silicon was set to 0.28. The finite element frequency stepping was conducted at 10Hz steps. Coupling fluid was isopropanol and the cavity fluid was air.

Appendix G: Time domain FEM used to study the effect on resonant frequency by having a gas or liquid filled cavity.

This appendix presents Finite Element Modelling in the time domain which was conducted to present the underlying issues and be able to explain the dynamics behind the difference in performance of the models. One of the models had a liquid filled cavity and the other had a gas filled cavity. The two were contrasted and the results are outlined in this Appendix G.

This Appendix will therefore delve into the computational fluid dynamic studies through which the movement of the PMUT diaphragm was studied by a set of two very high resolution time domain models, namely:

Model 1 - Coupling fluid was isopropanol and the cavity was air filled. Hereafter called "***Model_iso_air_900μmϕ***" in this Appendix.

Model 2 - Coupling fluid was isopropanol and the cavity was filled with isopropanol. Hereafter called "***Model_iso_iso_900μmϕ***" in this Appendix.

The Finite Element Analysis studied the minute movements of the diaphragm during the first instances of the initiation of electrical excitation. These two models were constructed to model the complex mechanics underpinning the operation of the PMUT and the interaction of the diaphragm with the coupling fluids. The model set studied the kinematics of the PMUT diaphragm including parameters such as displacement, velocity and acceleration. This was done in conjunction with the computational fluid dynamics carried out on both the coupling and the cavity fluids from time equal to 0 seconds up to time equal to $2x10^{-5}$ seconds, after start of excitation.

This limited time period allowed a detailed time domain study in which the time stepping was conducted in the nanosecond (at $1x10^{-9}$ seconds) scale although only the time periods in steps of $1x10^{-8}$ seconds were saved. This was done to keep the models from exceeding the 30 GB mark while at the same time achieving the necessary resolution. Having small time stepping allowed the FEA to benefit from the small mesh size. In order as to have accurate representations, for small mesh sizes the time step need to be small in order to satisfy the Courant stability condition [154].

The PMUT diameter for these finite element model set was 900 μm with the electrode diameter having a diameter 66% of the PMUT's diameter. The two models were excited at the same frequency of 59,800 Hz which was the resonant frequency determined previously by the frequency domain modelling for a PMUT with a liquid isopropanol coupling fluid and an air-filled cavity.

Figure G.1 shows the initiation of acceleration for each of the two models when excited.

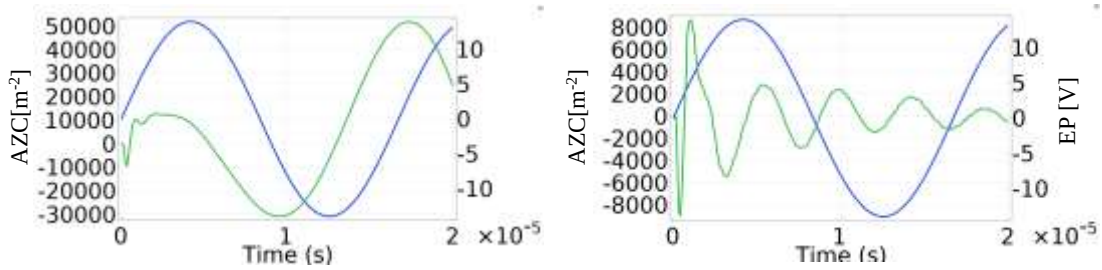

(a) (b)

Figure G.1 ~ Shows the Acceleration, Z-component (AZC) in green and the Electric Potential (EP) in blue ink for the instant between 0 to 2x10^{-5} seconds when the PMUT starts to displace under the influence of the voltage exciting the piezoelectric AlN layer. Graph set (a) is for ***Model_iso_air_900μmϕ*** *and graph set (b) is for* ***Model_iso_iso_900μmϕ***

Figure G.2 shows displacement of the PMUT's diaphragm midpoint plotted against electrical potential for both models.

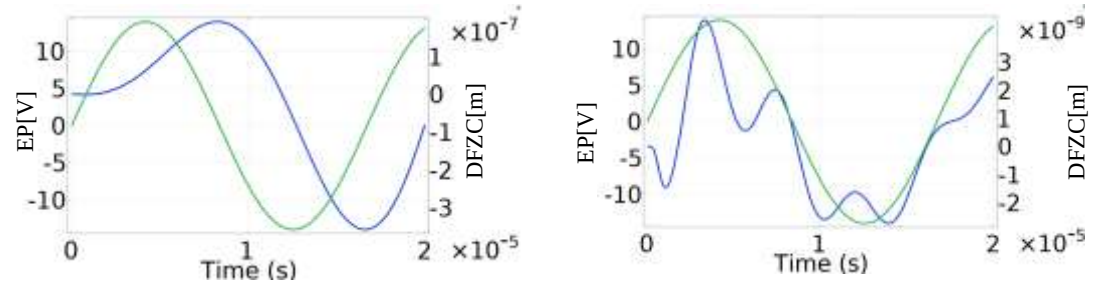

(a) (b)

Figure G.2 ~ Shows the Electrical potential (EP) in green and the Displacement Field Z component (DFZC) in blue ink for the instant between 0 to 2x10^{-5} seconds when the PMUT starts to displace under the influence of the voltage exciting the piezoelectric AlN layer. Figure (a) are the graphs for ***Model_iso_air_900μmϕ*** *and figure (b) are the graphs for* ***Model_iso_iso_900μmϕ****.*

Figure G.2 shows the very different reaction of **Model-iso-iso-900 *μmϕ*** and ***Model-iso-air-900μmϕ*** to the excitation voltage. The displacement of ***Model-iso-air-900μmϕ****'s* diaphragm shows a displacement reaction which mirrors the excitation frequency's sinusoidal shape but with a significant phase shift. With respect to the displacement of **Model-iso-iso-900 *μmϕ*** the reaction of the diaphragm to the excitation voltage is much more complex and it is clear that the device is not in resonance.

Figure G.3. shows the displacement and velocity graphs plotted together.

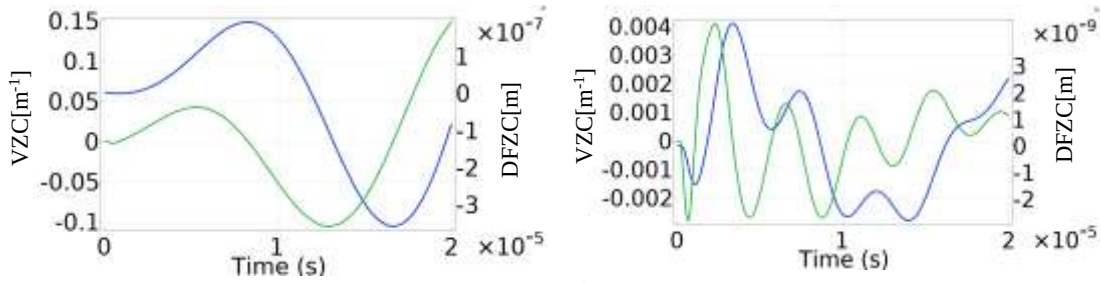

(a) (b)

Figure G.3 ~ Shows the Velocity, Z-component (VZC) in green and the Displacement Field Z component (DFZC) in blue ink for the instant between 0 and 2x10^{-5} seconds when the PMUT starts to

*displace under the influence of the voltage exciting the piezoelectric AlN layer. Figure (a) is them graph for **Model_iso_air_900µmϕ** and figure (b) is the graph for **Model_iso_iso_900µmϕ**.*

The below stages will look at the two PMUT models under excitation which initiates at the time stamp of 0 seconds.

At time = $1x10^{-8}$ seconds

The first figure of the series namely Figure G.4 shows a close view of the diaphragm at the initial point of $1x10^{-8}$ seconds after the start of the application of the excitation signal for ***Model_iso_air_900µmϕ***. Unless otherwise indicated, the time stamps given in this FEM sequence were with reference to time 0 seconds which indicated the start of the application of the excitation signal.

The coupling fluid, isopropanol, was situated on top of the diaphragm and the cavity fluid underneath the diaphragm was air. Therefore the fluidic system in this case presented a complex dynamic for the diaphragm balanced between a liquid and gas. At this point in time the diaphragm incurred a maximum displacement of $5.29x10^{-13}$ m and created a localised area of high pressure in the cavity fluid of $8.29x10^{-3}$ Pa. Initially these zones of high pressure were only in very small submicron sized areas of the cavity.

The main moment of the PMUT is most pronounced to the PMUT sides as shown in Figure G.4 although one needs to keep in mind that the movement has been scaled up by a factor of $10x10^{6}$. The pressure in the coupling fluid started to build all along the PMUT surface on both sides with the coupling fluid side reaching a maximum pressure of 0.98 Pa and a minimum pressure of -59.5 Pa.

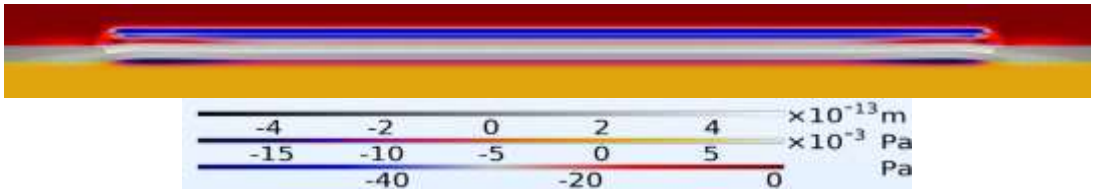

Top Bar ~ Diaphragm displacement / Middle Bar ~ Cavity pressure / Bottom Bar ~ Coupling fluid pressure

Maximum Velocity of diaphragm = $4.6x10^{-5}$ m/s
Maximum Acceleration of diaphragm = $7.51x10^{3}$ m/s^2

Figure G.4 ~ FEM showing the movement of the diaphragm of a 900 µm diameter PMUT with isopropanol as coupling fluid shown above the diaphragm (silver colour) and air filled cavity below the diaphragm. This diagram represents the system at time $1x10^{-8}$ seconds. Diaphragm movements are scaled (magnified) by a factor of 10,000,000.

Figure G.5 shows ***Model_iso_iso_900µmϕ*** *with* the PMUT diaphragm having same setup as the previous one with the singular difference of having isopropanol as both coupling and cavity fluids. The peak displacement (again on the lateral sides of the diaphragm) for this case was $5.36x10^{-13}$ m with the pressure of the cavity fluid reaching 18.2 Pa and a minimum pressure of -36.4 Pa along the length of the diaphragm.

The pressure in the coupling fluid on the other hand reached 0.93 Pa in the fluid just above the diaphragm with a low pressure point of -60.2 Pa.

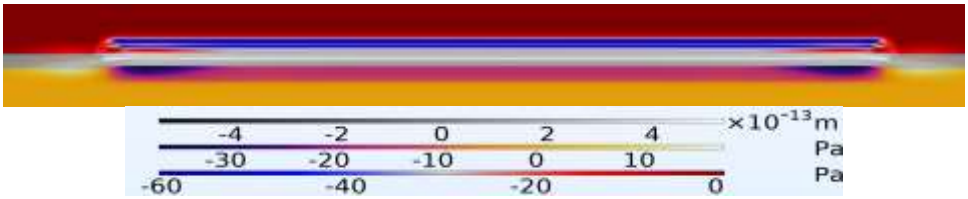

Top Bar ~ Diaphragm displacement / Middle Bar ~ Cavity pressure / Bottom Bar ~ Coupling fluid pressure

Maximum Velocity of diaphragm = 4.09×10^{-5} m/s
Maximum Acceleration of diaphragm = 7.61×10^{3} m/s^2

Figure G.5 ~ FEM showing the movement of the diaphragm of a 900 µm PMUT with isopropanol as coupling fluid shown above the diaphragm (silver colour) and isopropanol filled cavity below the diaphragm. This diagram represents the system at time 1×10^{-8} s. Diaphragm movements are scaled (magnified) by a factor of 10,000,000.

At time = 2×10^{-8} seconds

The next figure, Figure G.6, depicts the situation of ***Model-iso-air-900µmϕ*** at time 2×10^{-8} s after initiation of electrical excitation of the piezo layer. It shows a maximal displacement of 1.35×10^{-12} m with pressure in coupling fluid increasing to 34.2 Pa and the pressure in the cavity fluid falling to 0.02 Pa.

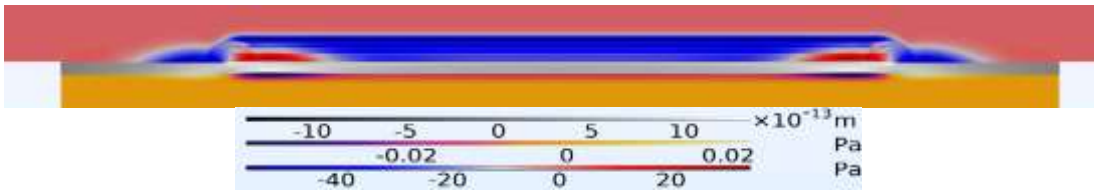

Top Bar ~ Diaphragm displacement / Middle Bar ~ Cavity pressure / Bottom Bar ~ Coupling fluid pressure

Maximum Velocity of diaphragm = 9.51×10^{-5}m/s
Maximum Acceleration of diaphragm = 7.53×10^{3} m/s^2

Figure G.6 ~ FEM showing the movement of the diaphragm of a 900µm PMUT with isopropanol as coupling fluid shown above the diaphragm (silver colour) and air filled cavity below the diaphragm. This diagram represents the system at time 2×10^{-8}s. Diaphragm movements are scaled (magnified) by a factor of 2,000,000.

The next step presented in Figure G.7 shows ***Model_iso_iso_900µmϕ*** with a maximum midpoint displacement of 1.37×10^{-12} m, and with a maximum pressure of 21.3Pa reached by the coupling fluid. A maximum pressure of 45.4 Pa was calculated in the cavity.

At this stage the main notable difference between ***Model_iso_iso_900µmϕ*** and **Model-*iso-air-900µmϕ*** is in the cavity pressure with ***Model_iso_iso_900µmϕ*** producing a pressure of 45.4Pa directly under the laterally flexing parts. In Figure G.7 one may see the high pressure areas in white colour under the extreme left and right areas of the diaphragm. This does not occur in ***Model-iso-air-900µmϕ*** where the maximum induced pressure was just 0.02 Pa.

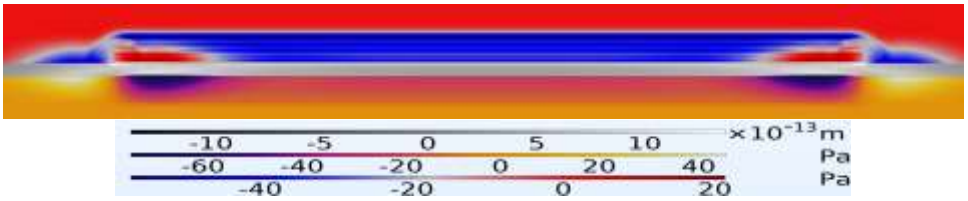

Top Bar ~ Diaphragm displacement / Middle Bar ~ Cavity pressure / Bottom Bar ~ Coupling fluid pressure

Maximum Velocity of diaphragm = 7.98×10^{-5}m/s
Maximum Acceleration of diaphragm = 6.69×10^{3}m/s^2

Figure G.7 ~ FEM showing the movement of the diaphragm of a 900µm PMUT with isopropanol as coupling fluid shown above the diaphragm (silver colour) and isopropanol filled cavity below the diaphragm. This diagram represents the system at time 2×10^{-8}s. Diaphragm movements are scaled (magnified) by a factor of 2,000,000.

At time= 4×10^{-8} seconds

The next pair of figures, namely Figure G.8 and Figure G.9 show the diaphragm-pressure dynamics at time 4×10^{-8} seconds. With regard to the diaphragm maximum displacement, ***Model_iso_air_900µmϕ*** and ***Model_iso_iso_900µmϕ*** show similar parameters with the former showing a maximum displacement of 4.76×10^{-12} m and the latter presenting a maximum displacement of 4.63×10^{-12} m.

Model_iso_air_900µmϕ presents coupling fluid pressure maximum value of 128 Pa and minimum value of -117 Pa. On the other hand cavity pressure continues to show very low values with a maximum pressure of 0.06 Pa and minimum of -0.09 Pa.

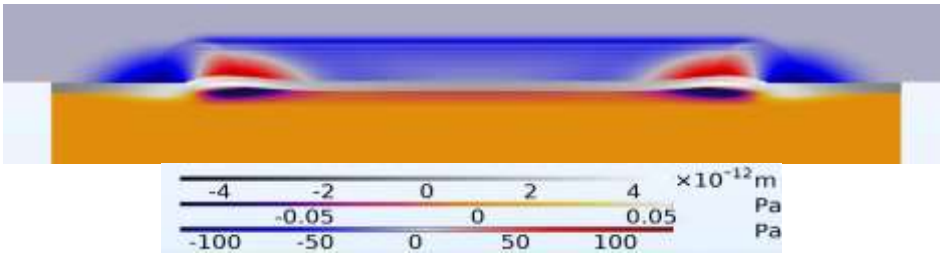

Top Bar ~ Diaphragm displacement / Middle Bar ~ Cavity pressure / Bottom Bar ~ Coupling fluid pressure

Max Velocity=2.08×10^{-4}m/s
Maximum Acceleration= 6.55×10^{3} m/s^2

Figure G.8 ~ FEM showing the movement of the diaphragm of a 900 µm PMUT with isopropanol as coupling fluid shown above the diaphragm (silver colour) and air filled cavity below the diaphragm. This diagram represents the system at time 4×10^{-8}s. Diaphragm movements are scaled (magnified) by a factor of 2,000,000.

The ***Model_iso_iso_900µmϕ*** shown in Figure G.9, on the other hand continue to demonstrate higher cavity pressures fluctuating between a maximum value of 90.4 Pa and a minimum value of -138 Pa. The pressure in the coupling fluid fluctuates between a maximum value of 88.2 Pa and a minimum value of -97.4 Pa.

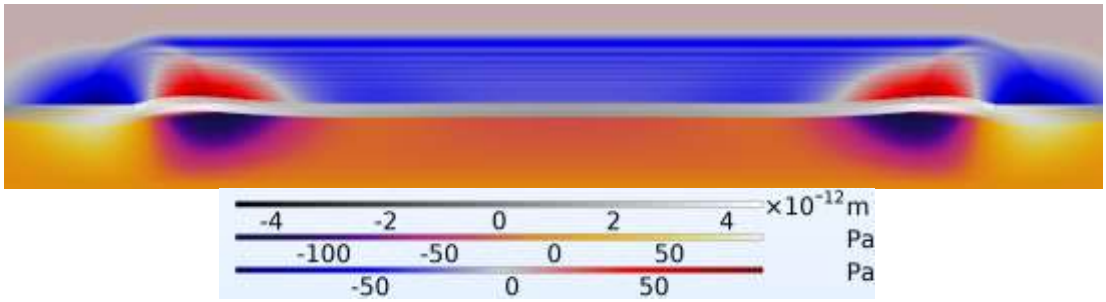

Top Bar ~ Diaphragm displacement / Middle Bar ~ Cavity pressure / Bottom Bar ~ Coupling fluid pressure

Max velocity of diaphragm = 1.65×10^{-4} m/s
Maximum acceleration of diaphragm = 5.36×10^{3} m/s^2

Figure G.9 ~ FEM showing the movement of the diaphragm of a 900µm PMUT with isopropanol as coupling fluid shown above the diaphragm (silver colour) with (a) air and (b) isopropanol filled cavity below the diaphragm. This diagram represents the system at time 4×10^{-8} s. Diaphragm movements are scaled (magnified) by a factor of 2,000,000.

At time= 9×10^{-8}seconds

Model_iso_iso_900µmϕ presents further increase in cavity fluid pressures with a maximum pressure of 141 Pa and minimum pressure of -219 Pa being produced in the fluidic volume under the PMUT. This can be seen in Figure G.10 (b). Again, as discussed in the previous time stamp, this is much higher than the pressures produced in the air filled chamber of ***Model_iso_air_900µmϕ*** which only reaches a maximum pressure of 0.14Pa and a minimum pressure of -0.2Pa as seen in Figure G.10 (a).

The air filled cavity PMUT achieves a maximum coupling fluid pressure of 278 Pa (with a minimum of -197 Pa) or 100 Pa higher than the isopropanol filled one which reaches a maximum of 178 Pa (with a minimum of -151 Pa). Clearly the pressure underlying and overlying the PMUT diaphragm in the isopropanol filled diaphragm example starts to present a clamping effect on the diaphragm, which affects the net movement possible. In the PMUT with an air filled cavity diaphragm the maximum displacement achieved by the membrane was 2.49×10^{-11} m as compared to 2.12×10^{-11} m for the isopropanol filled cavity PMUT.

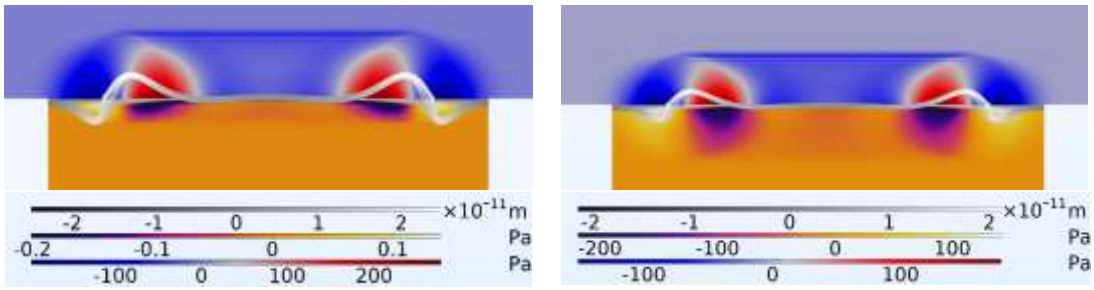

Top Bar ~ Diaphragm displacement / Middle Bar ~ Cavity pressure / Bottom Bar ~ Coupling fluid pressure

Maximum velocity of diaphragm
5.04×10^{-4} m/s
Max Acceleration of diaphragm
6.52×10^{3} m/s^2

(a)

Maximum Velocity of diaphragm
3.92×10^{-4} m/s
Max Acceleration of diaphragm
5.27×10^{3} m/s^2

(b)

Figure G.10 ~ FEM showing the movement of the diaphragm of two 900 µm PMUTs with isopropanol as coupling fluid shown above the diaphragm (silver colour) with (a) air and (b) isopropanol filled cavity below the diaphragm. This diagram represents the system at time $9x10^{-8}$ s. Diaphragm movements are scaled (magnified) by a factor of 2,000,000.

At this point this point this text also provides the reader with Figure G.11 which shows a FEM presenting the peak points of flexion of the PMUT's diaphragm overlaid over the extents of the AlN layer. From this figure one can clearly see that the peak of the diaphragm's flexion coincides with the extent of the AlN layer. It is to be remembered that in this model set the AlN diameter is set at 66% of the PMUT's diaphragm.

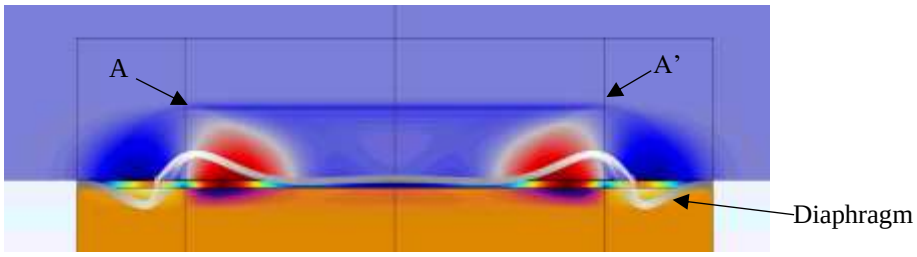

*Figure G.11 ~ FEM showing diaphragm of **Model_iso_air_900µmϕ** with edge lines showing the extent of the AlN piezoelectric layer between lines A and A'. Diaphragm movements are scaled (magnified) by a factor of 2,000,000.*

<u>At time= $1.9x10^{-7}$ seconds</u>

At this time stamp by looking at Figure G.12 one can note the continued development of a high pressure zone ring formed in the coupling fluid over the lateral region of the PMUT. In the case of the PMUT with the isopropanol filled cavity the area with minimum pressure continued to extend much further than that visible in the coupling fluid of ***Model_iso_air_900µmϕ.***

It is also important to point out to the reader that with regards to the diaphragm's displacement, comparing with the magnification scale of the former was reduced to 20,000. The diaphragm for the isopropanol filled cavity PMUT continues to deflect less than that for the air filled one with a peak displacement of $9.22x10^{-11}$ m as compared to $1.12x10^{-10}$ m for the air filled cavity PMUT.

For ***Model_iso_air_900µmϕ*** the pressure achieved in the cavity continued to be very low with a maximum pressure of 0.27 Pa and a minimum pressure of -0.42 Pa. This when compared to the ***Model_iso_iso_900µmϕ*** shown in Figure G.12 which presented a maximum pressure of 211 Pa and a minimum of -298 Pa in the cavity fluid. Maximum coupling fluid maximum pressure on the other hand was higher in the air filled cavity device with a maximum pressure of 410 Pa being calculated as compared to 266 Pa for the isopropanol filled cavity PMUT.

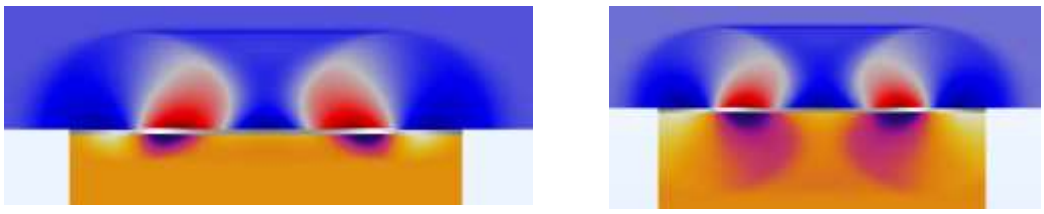

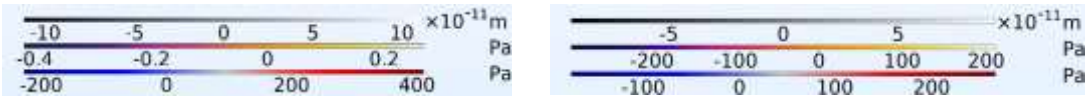

Top Bar ~ Diaphragm displacement / Middle Bar ~ Cavity pressure / Bottom Bar ~ Coupling fluid pressure

Max & Min Velocity of diaphragm = 1.14×10^{-3} m/s and -7.96×10^{-4} m/s
Max Acceleration of diaphragm = 7.1×10^{3} m/s^2
(a)

Max & Min Velocity of diaphragm = 8.98×10^{-4} m/s -6.65×10^{-4} m/s
Max Acceleration of diaphragm = 5.63×10^{3} m/s^2
(b)

Figure G.12 ~ FEM showing the movement of the diaphragm of a 900 µm PMUT with isopropanol as coupling fluid shown above the diaphragm (silver colour) with (a)air and (b) isopropanol filled cavity below the diaphragm. This diagram represents the system at time 1.9×10^{-7}s. Diaphragm movements are scaled (magnified) by a factor of 20,000.

The high pressure ring described above can be visualised better in 3D view via Figure G.13. The high pressure ring can be seen to point inwards towards the top of the hemispherical high pressure are being formed.

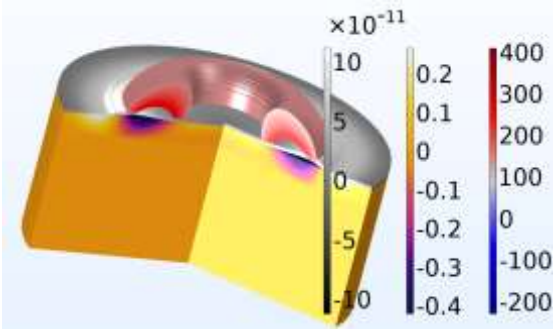

Figure G.13 ~ A 3-dimensional model showing the formation of the high pressure ring around the diaphragm's point of flexion. Legend~ Left bar- diaphragm displacement [m], middle bar- cavity pressure [Pa] & right bar coupling fluid pressure [Pa]. At time 1.9×10^{-7} seconds. Diaphragm movement magnified by 2×10^{5} times.

<u>At time= 2.8×10^{-7} seconds</u>

At this point in time in both models shown in Figure G.14 the reader can see the two high pressure zones in the coupling fluid start to interact with each other and join together at the midpoint, thus starting the formation of the ultrasonic pressure wave in the coupling fluid.

Again the ***Model_iso_air_900µmϕ*** presents a much lower cavity fluid pressure level and higher coupling fluid pressure level when compared with ***Model_iso_iso_900µmϕ.*** The former presenting a coupling fluid maximum pressure of 497 Pa and the latter 33 Pa. In terms of cavity pressure one may compare the maximum pressure of 208 Pa in ***Model_iso_iso_900µmϕ*** when compared with 0.45 Pa for ***Model_iso_air_900µmϕ.***

The isopropanol cavity filled PMUT was calculated to present a midpoint displacement of 1.98×10^{-10} m while the air filled one continued to add to the gap in midpoint displacement between the two with a displacement of 2.42×10^{-10} m.

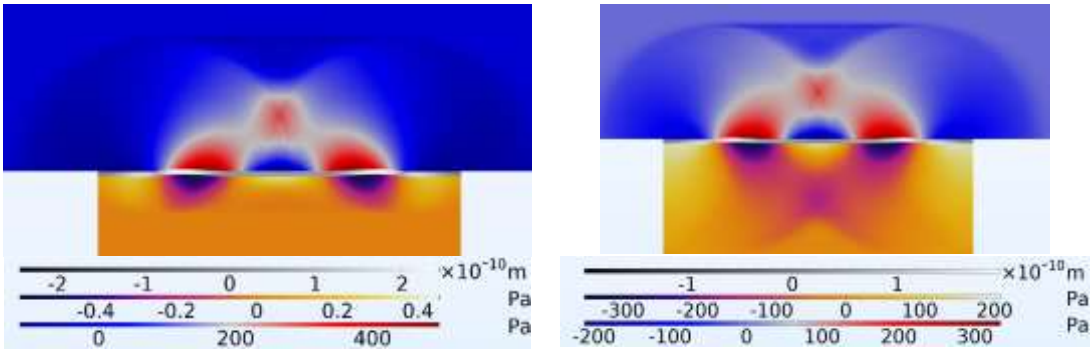

Top Bar ~ Diaphragm displacement / Middle Bar ~ Cavity pressure / Bottom Bar ~ Coupling fluid pressure

MaxVelocity of diaphragm =1.71x10^{-3} m/s
Max Acceleration of diaphragm = 1.02x10^{4} m/s^{2}
(a)

Max Velocity of diaphragm = 1.36x10^{-3} m/s
Max Acceleration of diaphragm = 8.21x10^{3} m/s^{2}
(b)

Figure G.14 ~ FEM showing the movement of the diaphragm of a 900µm PMUT with isopropanol as coupling fluid shown above the diaphragm (silver colour) and (a)air (b) isopropanol filled cavity below the diaphragm. This diagram represents the system at time 2.8x10^{-7}s. Diaphragm movements are scaled (magnified) by a factor of 20,000.

Figure G.15 presents a 3-dimensional model showing the initiation of the formation of the high pressure fluid dome over the PMUT diaphragm. This helps the reader understand the dynamics of the early stages of the formation of a pressure wave in the coupling fluid.

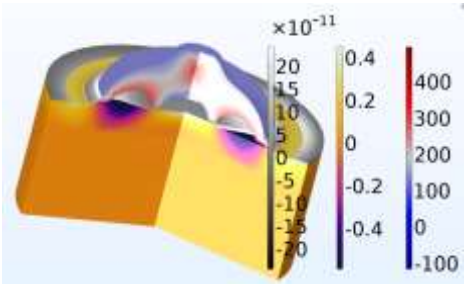

Figure G.15 ~Legend~ Left bar- diaphragm displacement, middle bar- cavity pressure & left bar coupling fluid pressure. FEM of air filled cavity at 2.8x10^{-7} seconds. Diaphragm movement magnified 2x10^{5}times.

<u>At time= 3.8x10^{-7} seconds</u>

Figure G.16 shows the PMUT continue to build pressure in the coupling fluid as the diaphragm accelerates upwards.

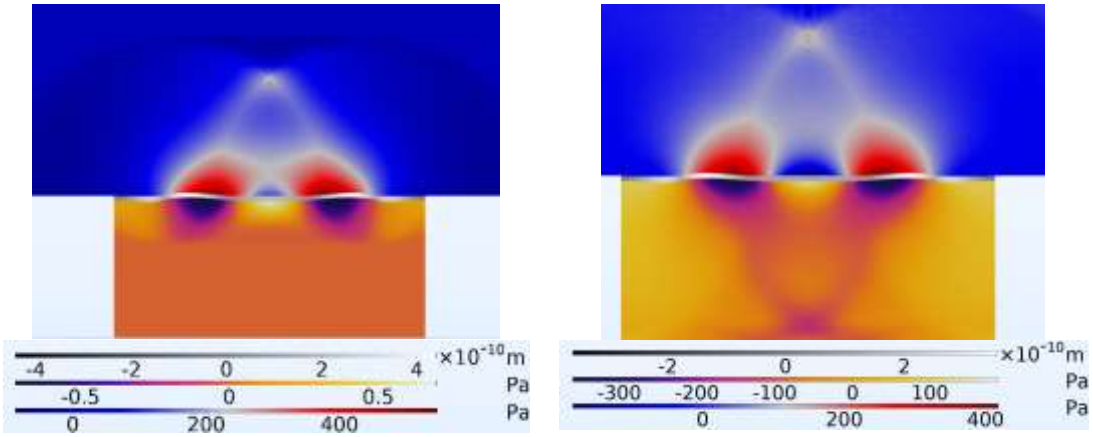

Top Bar ~ Diaphragm displacement / Middle Bar ~ Cavity pressure / Bottom Bar ~ Coupling fluid pressure

Max Velocity of diaphragm =2.3x10^{-3} m/s
Max Acceleration of diaphragm = 6.19x10^{3} m/s^{2}
(a)

Max Velocity of diaphragm = 1.87x10^{-3} m/s
Max Acceleration of diaphragm = 9.19x10^{3} m/s^{2}
(b)

Figure G.16 ~ FEM showing the movement of the diaphragm of a 900 µm PMUT with isopropanol as coupling fluid shown above the diaphragm (silver colour) and (a)air (b) isopropanol filled cavity below the diaphragm. This diagram represents the system at time 3.8x10^{-7}s. Diaphragm movements are scaled (magnified) by a factor of 20,000.

Table G.1 presents the critical parameters comparing the two models.

*Table G.1 - Parameters for **Model_iso_air_900µmϕ** and **Model_iso_iso_900µmϕ** at time 3.8x10^{-7} seconds*

PMUT	Displacement [m]	Max & Min Cavity Fluid Pressure [Pa]	Max & Min Coupling Fluid Pressure [Pa]
Model_iso_air_900µmϕ	4.42x10^{-10}	0.7/-0.72	546/-85.8
Model_iso_iso_900µmϕ	3.6x10^{-10}	187/-360	418/-184

<u>At time= 4.8x10^{-7} seconds</u>

At this point from Figure G.17 (a) ***Model_iso_air_900µmϕ*** one can see that the two lateral high pressure zones seen in Figure G.16 have now combined to start the formation of a high pressure wave front with a maximum pressure of 576 Pa in the coupling fluid. With respect to ***Model_iso_iso_900µmϕ*** seen in Figure G.17 (b) the high pressure volumes are still distinct and have not merged.

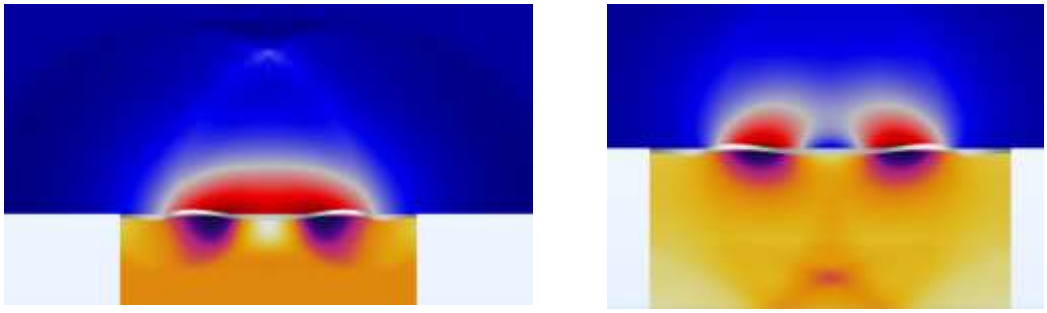

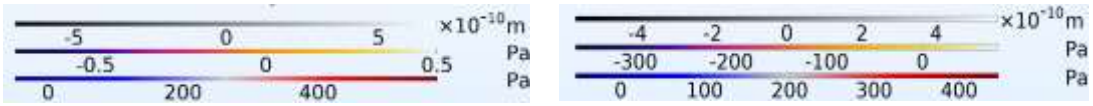

Top Bar ~ Diaphragm displacement / Middle Bar ~ Cavity pressure / Bottom Bar ~ Coupling fluid pressure

Max Velocity of diaphragm =2.75x10^{-3}m/s
Max Acceleration of diaphragm = 4.65x10^{3}m/s^{2}
(a)

Max Velocity of diaphragm = 2.33x10^{-3}m/s
Max Acceleration of diaphragm = 6.52x10^{3}m/s^{2}
(b)

Figure G.17 ~ FEM showing the movement of the diaphragm of a 900µm PMUT with isopropanol as coupling fluid shown above the diaphragm (silver colour) with (a)air and (b) isopropanol filled cavity below the diaphragm. This diagram represents the system at time 4.8x10^{-7}s. Diaphragm movements are scaled (magnified) by a factor of 20,000.

The important parameters for both models is seen in Table G.2.

*Table G.2 ~ Parameters for **Model_iso_air_900µmϕ** and **Model_iso_iso_900µmϕ** at time 4.8x10^{-7} seconds.*

PMUT	Displacement [m]	Max & Min Cavity Fluid Pressure [Pa]	Max & Min Coupling Fluid Pressure [Pa]
Model_iso_air_900µmϕ	6.92x10^{-10}	0.5/-0.74	576/-48.9
Model_iso_iso_900µmϕ	5.66x10^{-10}	79/-363	446/-53.3

<u>At time=5.8x10^{-7} seconds</u>

At this point one can see that in ***Model_iso_air_900µmϕ*** the embryonic wave front is formed and it continues to build up pressure at an increased rate. Similarly the ***Model_iso_iso_900µmϕ*** also builds up a wave front albeit with a pressure value which is half that calculated for the air filled cavity PMUT as can be seen in Figure G.18.

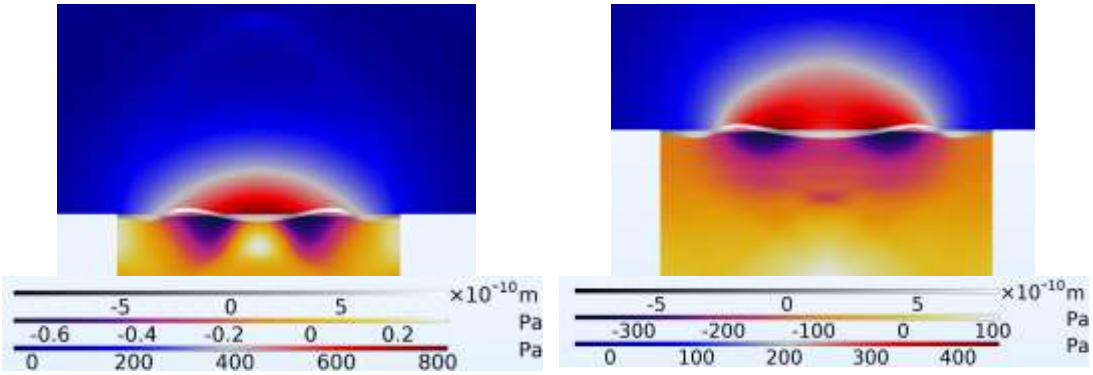

Top Bar ~ Diaphragm displacement / Middle Bar ~ Cavity pressure / Bottom Bar ~ Coupling fluid pressure

Max Velocity of diaphragm =3.08x10^{-3}m/s
Max Acceleration of diaphragm = 5.55x10^{3}m/s^{2}
(a)

Max Velocity of diaphragm = 2.7x10^{-3}m/s
Max Acceleration of diaphragm = 3.96x10^{3}m/s^{2}
(b)

Figure G.18 ~ FEM showing the movement of the diaphragm of a 900µm PMUT with isopropanol as coupling fluid, shown above the diaphragm (silver colour) with (a) air and (b) isopropanol filled cavity below the diaphragm. This diagram represents the system at time 5.8x10^{-7}s. Diaphragm movements are scaled (magnified) by a factor of 20,000.

Table G.3 presents the critical parameters underlining the PMUT's operating parameters. The pressure in the coupling fluid for **Model_iso_air_900µmϕ** starts to demonstrate a higher lever while the pressure in the cavity fluid is higher for ***Model_iso_iso_900µmϕ***. The latter is naturally expected as the cavity is filled with liquid rather than compressible gas.

*Table G.3 ~ Parameters for **Model_iso_air_900µmϕ** and **Model_iso_iso_900µmϕ** at time 5.8x10^{-7} seconds*

PMUT	Displacement [m]	Max & Min Cavity Fluid Pressure [Pa]	Max & Min Coupling Fluid Pressure [Pa]
Model_iso_air_900µmϕ	9.81x10^{-10}	0.31/-0.68	819/-35.9
Model_iso_iso_900µmϕ	8.11x10^{-10}	107/-366	447/-40.3

At time = 6.8x10^{-7} seconds

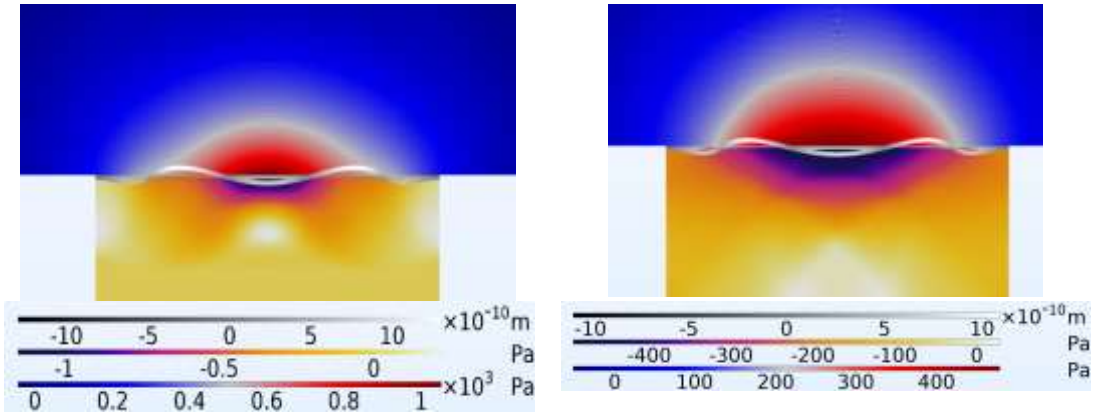

Top Bar ~ Diaphragm displacement / Middle Bar ~ Cavity pressure / Bottom Bar ~ Coupling fluid pressure

Max Velocity of diaphragm =3.29x10^{-3} m/s
Max Acceleration of diaphragm = 9.05x10^{3} m/s^{2}

(a)

Max Velocity of diaphragm = 2.93x10^{-3} m/s
Max Acceleration of diaphragm = 1.76x10^{3} m/s^{2}

(b)

Figure G.19 ~ FEM showing the movement of the diaphragm of a 900 µm PMUT with isopropanol as coupling fluid shown above the diaphragm (silver colour) with (a) air and (b) isopropanol filled cavity below the diaphragm. This diagram represents the system at time 6.8x10^{-7}s. Diaphragm movements are scaled (magnified) by a factor of 20,000.

Table G.4 presents the parameters showing that the coupling fluid pressure in the air filled cavity model continues to increase reaching more than double the pressure level at time 6.8x10^{-7} seconds.

*Table G.4 ~ Parameters for **Model_iso_air_900µmϕ** and **Model_iso_iso_900µmϕ** at time 6.8x10^{-7} seconds*

PMUT	Displacement [m]	Max & Min Cavity Fluid Pressure [Pa]	Max & Min Coupling Fluid Pressure [Pa]
Model_iso_air_900µmϕ	1.3x10^{-9}	0.22/-1.15	1.05x10^{3}/-46.4
Model_iso_iso_900µmϕ	1.09x10^{-9}	28/-493	479/-54.2

At time= $1.18x10^{-6}$ seconds

With reference to Figure G.20 it can be seen that while the diaphragm of the air filled cavity model has a general movement upwards, the diaphragm in the liquid filled cavity model flexes around the midpoint.

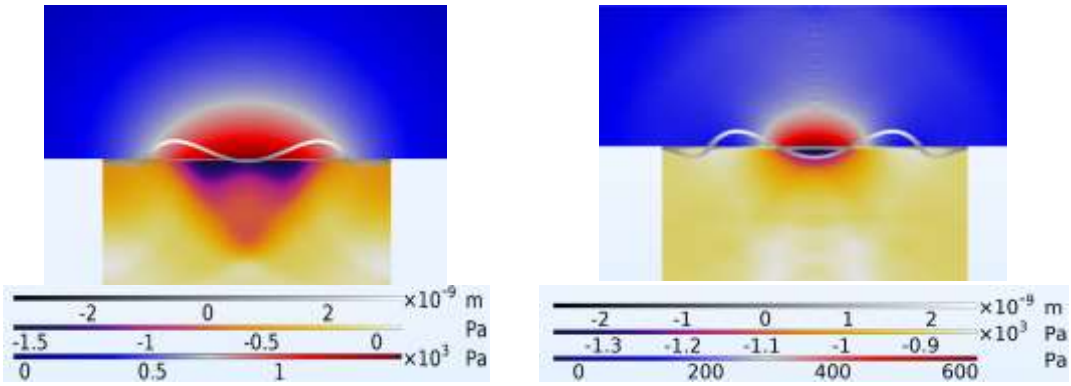

Top Bar ~ Diaphragm displacement / Middle Bar ~ Cavity pressure / Bottom Bar ~ Coupling fluid pressure

Max Velocity of diaphragm =$4.85x10^{-3}$ m/s
Max Acceleration of diaphragm = $8.26x10^{3}$ m/s^2
(a)

Max Velocity of diaphragm = $2.77x10^{-3}$ m/s
Max Acceleration of diaphragm = $7.86x10^{3}$ m/s^2
(b)

Figure G.20 ~ FEM showing the movement of the diaphragm of a 900µm PMUT with isopropanol as coupling fluid shown above the diaphragm (silver colour) with (a) air and (b) isopropanol filled cavity below the diaphragm. This diagram represents the system at time $1.18x10^{-6}$s. Diaphragm movements are scaled (magnified) by a factor of 20,000.

The relevance of this movement by the diaphragm can be seen in Table G.5 where the coupling fluid pressure in the air filled cavity model continues to increase at a much faster rate than in the liquid filled one.

*Table G.5 ~ Parameters for **Model_iso_air_900µmϕ** and **Model_iso_iso_900µmϕ** at time $1.18x10^{-6}$ seconds*

PMUT	Displacement [m]	Max & Min Cavity Fluid Pressure [Pa]	Max & Min Coupling Fluid Pressure [Pa]
Model_iso_air_900µmϕ	$3.22x10^{-9}$	0.11/-1.57	$1.48x10^{3}$/-42.5
Model_iso_iso_900µmϕ	$2.56x10^{-9}$	-829/$-1.36x10^{3}$	627/-39.3

The next time stamps from t= $1.38x10^{-6}$ seconds onwards continue to show this relationship where the pressure reached in the coupling fluid by ***Model_iso_air_900µmϕ*** continues to reach higher levels than that reached by ***Model_iso_iso_900µmϕ***.

The next time stamps in this dissertation continue to show the stages of the PMUT movements and the development of pressure in both the coupling and cavity fluids.

At time=$1.38x10^{-6}$ seconds

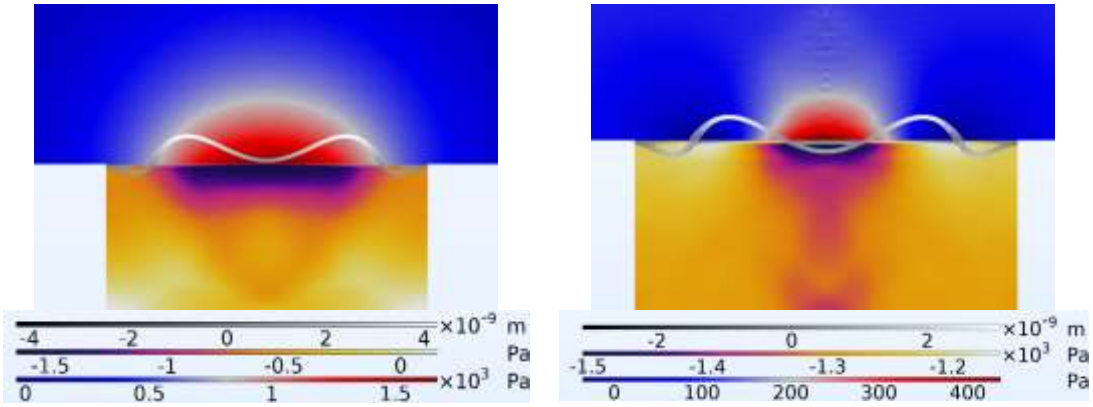

Top Bar ~ Diaphragm displacement / Middle Bar ~ Cavity pressure / Bottom Bar ~ Coupling fluid pressure

Max Velocity of diaphragm =6.16x10^{-3} m/s
Max Acceleration of diaphragm = 9.17x10^{3} m/s^{2}

(a)

Max Velocity of diaphragm = 2.7x10^{-3} m/s
Max Acceleration of diaphragm = 5.52x10^{3} m/s^{2}

(b)

Figure G.21 ~ FEM showing the movement of the diaphragm of a 900 µm PMUT with isopropanol as coupling fluid shown above the diaphragm (silver colour) with (a) air and (b) isopropanol filled cavity below the diaphragm. This diagram represents the system at time 1.38x10^{-6} s. Diaphragm movements are scaled (magnified) by a factor of 20,000.

*Table G.6 ~ Parameters for **Model_iso_air_900µmϕ** and **Model_iso_iso_900µmϕ** at time 1.38x10^{-6} seconds*

PMUT	Displacement [m]	Max & Min Cavity Fluid Pressure [Pa]	Max & Min Coupling Fluid Pressure [Pa]
Model_iso_air_900µmϕ	4.27x10^{-9}	0.16/-1.65	1.67x10^{3}/-38
Model_iso_iso_900µmϕ	3.09x10^{-9}	-1.16x10^{3}/-1.5x10^{3}	437/-35.6

At time= 1.48x10^{-6} seconds

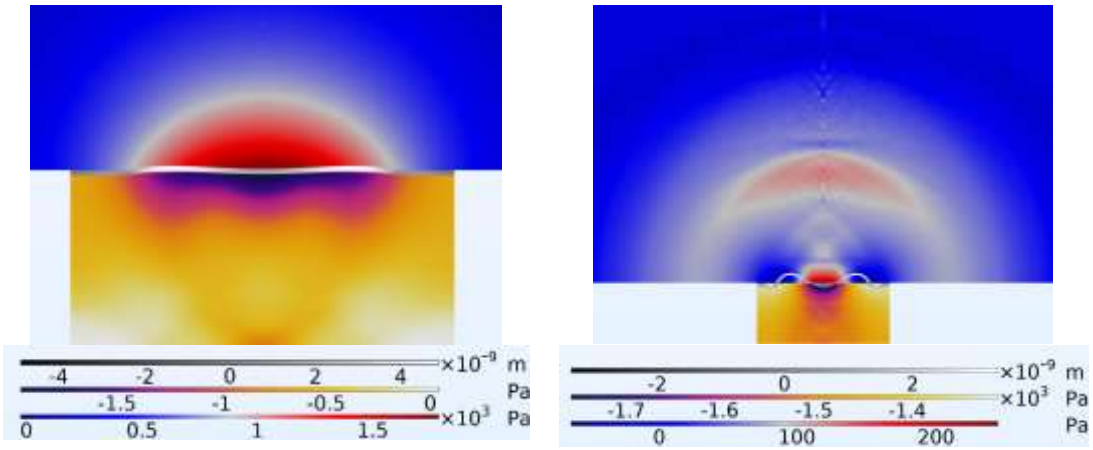

Top Bar ~ Diaphragm displacement / Middle Bar ~ Cavity pressure / Bottom Bar ~ Coupling fluid pressure

Max Velocity of diaphragm =6.93x10^{-3} m/s
Max Acceleration of diaphragm = 1.01x10^{4} m/s^{2}

(a)

Max Velocity of diaphragm = 2.72x10^{-3} m/s
Max Acceleration of diaphragm = 7.36x10^{3} m/s^{2}

(b)

Figure G.22 ~ FEM showing the movement of the diaphragm of a 900 µm PMUT with isopropanol as coupling fluid shown above the diaphragm (silver colour) and (a)air (b) isopropanol filled cavity below

the diaphragm. This diagram represents the system at time 1.48x10^{-6} s. Diaphragm movements are scaled (magnified) by a factor of 20,000.

*Table G.7 ~ Parameters for **Model_iso_air_900µmϕ** and **Model_iso_iso_900µmϕ** at time 1.48x10^{-6} seconds*

PMUT	Displacement [m]	Max & Min Cavity Fluid Pressure [Pa]	Max & Min Coupling Fluid Pressure [Pa]
Model_iso_air_900µmϕ	4.89x10^{-9}	0.04/-1.96	1.78x10^{3}/-24.4
Model_iso_iso_900µmϕ	3.34x10^{-9}	-1.3x10^{3}/-1.76x10^{3}	245/-63.7

At time = 1.68x10^{-6} seconds

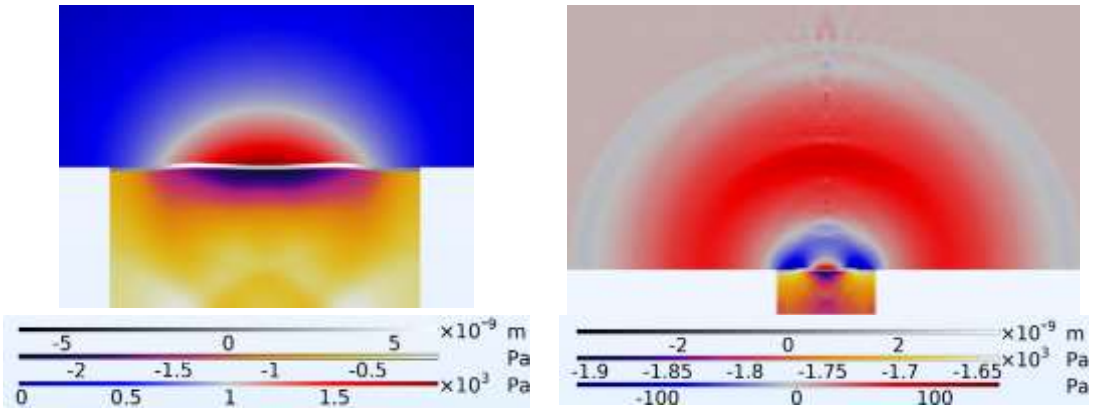

Top Bar ~ Diaphragm displacement / Middle Bar ~ Cavity pressure / Bottom Bar ~ Coupling fluid pressure

Max Velocity of diaphragm = 8.71x10^{-3}m/s
Max Acceleration of diaphragm = 1.18x10^{4}m/s^{2}
(a)

Max Velocity of diaphragm = 3.26x10^{-3}m/s
Max Acceleration of diaphragm = 3.11x10^{3}m/s^{2}
(b)

Figure G.23 ~ FEM showing the movement of the diaphragm of a 900µm PMUT with isopropanol as coupling fluid shown above the diaphragm (silver colour) and (a)air (b) isopropanol filled cavity below the diaphragm. This diagram represents the system at time 1.68x10^{-6}s. Diaphragm movements are scaled (magnified) by a factor of 20,000.

*Table G.8 ~ Parameters for **Model_iso_air_900µmϕ** and **Model_iso_iso_900µmϕ** at time 1.68x10^{-6} seconds*

PMUT	Displacement [m]	Max & Min Cavity Fluid Pressure [Pa]	Max & Min Coupling Fluid Pressure [Pa]
Model_iso_air_900µmϕ	6.3x10^{-9}	-0.14/-2.3	1.99x10^{3}/-34.4
Model_iso_iso_900µmϕ	3.83x10^{-9}	-1.64x10^{3}/-1.91x10^{3}	146/-158

At time= 1.98x10^{-6} seconds

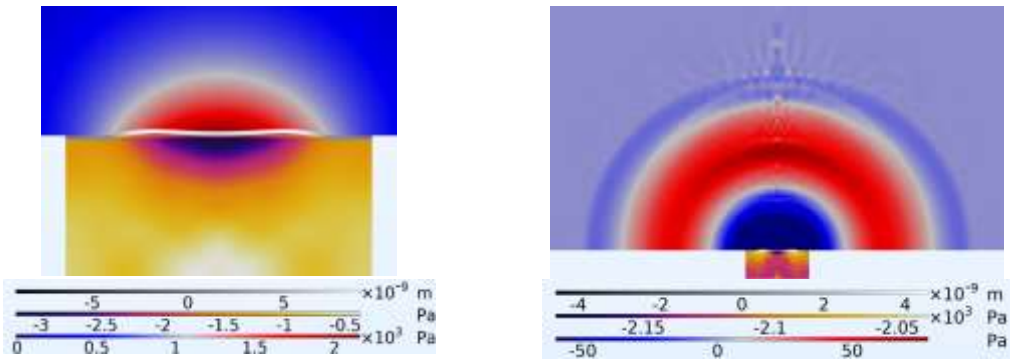

Top Bar ~ Diaphragm displacement / Middle Bar ~ Cavity pressure / Bottom Bar ~ Coupling fluid pressure

Max Velocity of diaphragm = 0.01×10^{-3} m/s
Max Acceleration of diaphragm = 1.28×10^{4} m/s^2
(a)

Max Velocity of diaphragm = 3.89×10^{-3} m/s
Max Acceleration of diaphragm = 1.74×10^{3} m/s^2
(b)

Figure. G.24 ~ FEM showing the movement of the diaphragm of a 900 µm PMUT with isopropanol as coupling fluid shown above the diaphragm (silver colour) and (a)air (b) isopropanol filled cavity below the diaphragm. This diagram represents the system at time 1.98×10^{-6}s. Diaphragm movements are scaled (magnified) by a factor of 2,000.

*Table G.9 ~ Parameters for **Model_iso_air_900µmϕ** and **Model_iso_iso_900µmϕ** at time 1.98×10^{-6} seconds*

PMUT	Displacement [m]	Max & Min Cavity Fluid Pressure [Pa]	Max & Min Coupling Fluid Pressure [Pa]
Model_iso_air_900µmϕ	8.97×10^{-9}	-0.38/-3.21	2.16×10^{3}/-10.9
Model_iso_iso_900µmϕ	4.55×10^{-9}	-2.04×10^{3}/-2.18×10^{3}	80.5/-197

At time = 2.28×10^{-6} seconds

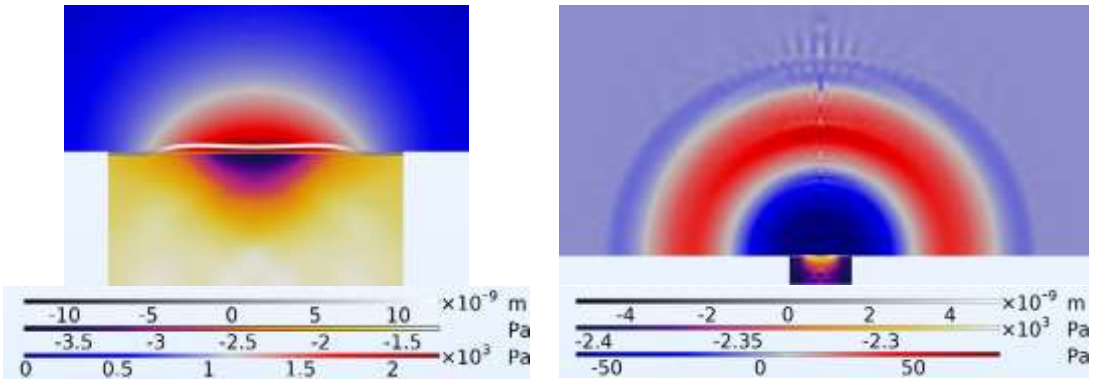

Top Bar ~ Diaphragm displacement / Middle Bar ~ Cavity pressure / Bottom Bar ~ Coupling fluid pressure

Max Velocity of diaphragm = 0.02×10^{-3} m/s
Max Acceleration of diaphragm = 1.25×10^{4} m/s^2
(a)

Max Velocity of diaphragm = 4.15×10^{-3} m/s
Max Acceleration of diaphragm = 1.31×10^{3} m/s^2
(b)

Figure G.25 ~ FEM showing the movement of the diaphragm of a 900 µm PMUT with isopropanol as coupling fluid shown above the diaphragm (silver colour) with (a) air and (b) isopropanol filled cavity below the diaphragm. This diagram represents the system at time 2.28×10^{-6}s. Diaphragm movements are scaled (magnified) by a factor of 2,000.

*Table G.10 ~ Parameters for **Model_iso_air_900µmϕ** and **Model_iso_iso_900µmϕ** at time 2.28x10^{-6} seconds*

PMUT	Displacement [m]	Max & Min Cavity Fluid Pressure [Pa]	Max & Min Coupling Fluid Pressure [Pa]
Model_iso_air_900µmϕ	1.24x10^{-10}	-1.28/-3.8	2.26x10^{3}/-12.5
Model_iso_iso_900µmϕ	5.22x10^{-9}	-2.26x10^{3}/-2.41x103	70.4/-200

<u>At time = 2.48 x10^{-6} seconds</u>

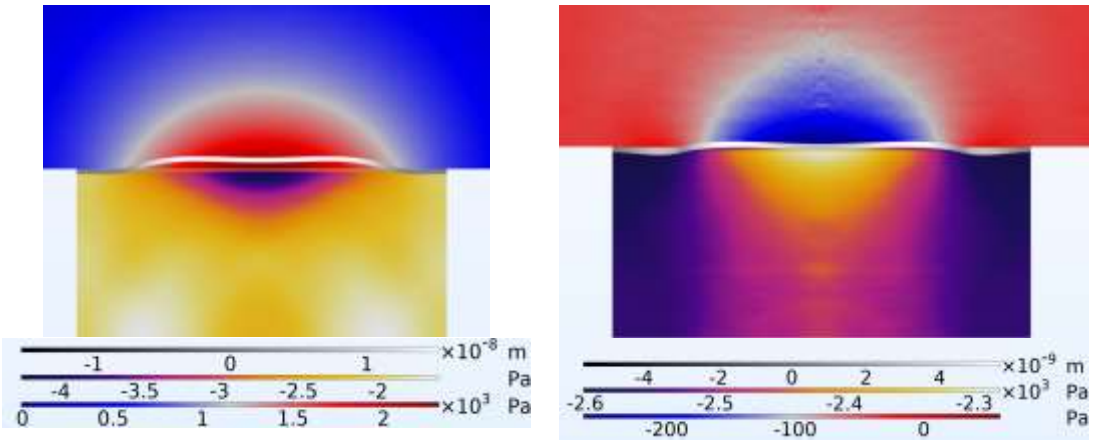

Top Bar ~ Diaphragm displacement / Middle Bar ~ Cavity pressure / Bottom Bar ~ Coupling fluid pressure

Max Velocity of diaphragm = 0.02 m/s
Max Acceleration of diaphragm = 1.25x10^{4} m/s^{2}
(a)

Max Velocity of diaphragm = 3.92x10^{-3} m/s
Max Acceleration of diaphragm = 2.19x10^{3} m/s^{2}
(b)

Figure G.26 ~ FEM showing the movement of the diaphragm of a 900 µm PMUT with isopropanol as coupling fluid shown above the diaphragm (silver colour) and (a)air (b) isopropanol filled cavity below the diaphragm. This diagram represents the system at time 2.48x10^{-6}s. Diaphragm movements are scaled (magnified) by a factor of 2,000.

*Table G.11 ~ Parameters for **Model_iso_air_900µmϕ** and **Model_iso_iso_900µm ϕ** at time 2.48x10^{-6} seconds*

PMUT	Displacement [m]	Max & Min Cavity Fluid Pressure [Pa]	Max & Min Coupling Fluid Pressure [Pa]
Model_iso_air_900µmϕ	1.53x10^{-8}	-1.61/-4.25	2.31x10^{3}/-8.05
Model_iso_iso_900µmϕ	5.63x10^{-9}	-2.28x10^{3}/-2.6x10^{3}	59.2/-265

<u>At time= 2.78x10^{-6} seconds</u>

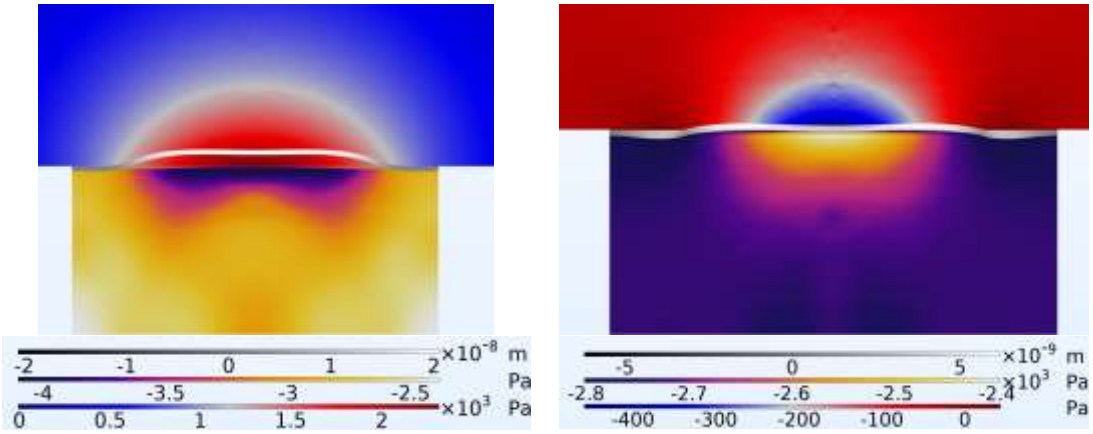

Top Bar ~ Diaphragm displacement / Middle Bar ~ Cavity pressure / Bottom Bar ~ Coupling fluid pressure

Max Velocity of diaphragm = 0.02 m/s
Max Acceleration of diaphragm = 1.23×10^4 m/s^2

(a)

Max Velocity of diaphragm = 2.83×10^{-3} m/s
Max Acceleration of diaphragm = 4.82×10^3 m/s^2

(b)

Figure G.27 ~ FEM showing the movement of the diaphragm of a 900 µm PMUT with isopropanol as coupling fluid shown above the diaphragm (silver colour) and (a)air (b) isopropanol filled cavity below the diaphragm. This diagram represents the system at time 2.78×10^{-6}s. Diaphragm movements are scaled (magnified) by a factor of 2,000.

*Table G.12 ~ Parameters for **Model_iso_air_900µmϕ** and **Model_iso_iso_900µmϕ** at time 2.78×10^{-6} seconds*

PMUT	Displacement [m]	Max & Min Cavity Fluid Pressure [Pa]	Max & Min Coupling Fluid Pressure [Pa]
Model_iso_air_900µmϕ	2.05×10^{-8}	-2.38/-4.1	2.32×10^3/-6.41
Model_iso_iso_900µmϕ	6.19×10^{-9}	-2.4×10^3/-2.8×10^3	42.5/-458

At time = 3.38×10^{-6} seconds

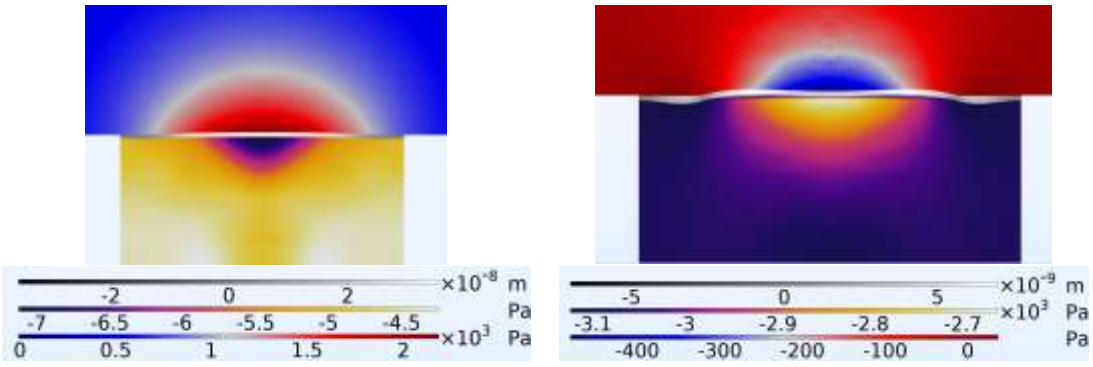

Top Bar ~ Diaphragm displacement / Middle Bar ~ Cavity pressure / Bottom Bar ~ Coupling fluid pressure

Max Velocity of diaphragm = 0.03 m/s
Max Acceleration of diaphragm = 1.17×10^4 m/s^2

(a)

Max Velocity of diaphragm = 8.69×10^{-4} m/s
Max Acceleration of diaphragm = 4.81×10^3 m/s^2

(b)

Figure G.28 ~ FEM showing the movement of the diaphragm of a 900µm PMUT with isopropanol as coupling fluid shown above the diaphragm (silver colour) and (a)air (b) isopropanol filled cavity below

the diaphragm. This diagram represents the system at time 3.38x10^{-6}s. Diaphragm movements are scaled (magnified) by a factor of (a) 200 times and (b) 2,000 times.

*Table G.13 ~ Parameters for **Model_iso_air_900µmϕ** and **Model_iso_iso_900µmϕ** at time 3.38x10^{-6}seconds*

PMUT	Displacement [m]	Max & Min Cavity Fluid Pressure [Pa]	Max & Min Coupling Fluid Pressure [Pa]
Model_iso_air_900µmϕ	3.55x10^{-8}	-4.24/-7.12	2.19x10^{3}/-5.5
Model_iso_iso_900µmϕ	6.97x10^{-9}	-2.66x10^{3}/-3.12x10^{3}	40.4/-481

At time= 4.28x10^{-6} seconds

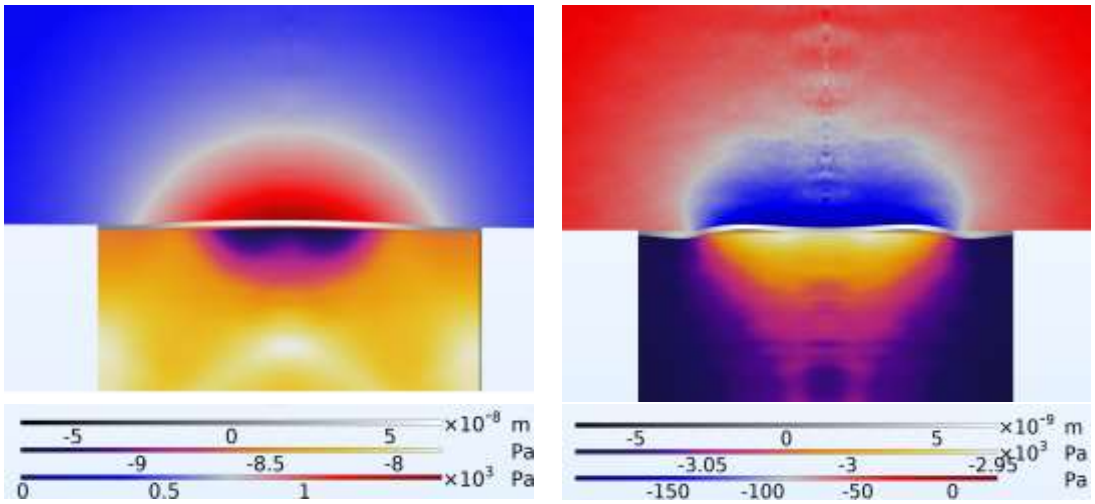

Top Bar ~ Diaphragm displacement / Middle Bar ~ Cavity pressure / Bottom Bar ~ Coupling fluid pressure

Max velocity of diaphragm=0.04 m/s
Max acceleration of diaphragm= 8.17x10^{3} m/s^{2}

(a)

Max Velocity of diaphragm = 4.14x10^{-4} m/s
Max Acceleration of diaphragm = 1.19x10^{3} m/s^{2}

(b)

Figure G.29 ~ FEM showing the movement of the diaphragm of a 900µm PMUT with isopropanol as coupling fluid shown above the diaphragm (silver colour) and (a)air (b) isopropanol filled cavity below the diaphragm. This diagram represents the system at time 4.28x10^{-6}s. Diaphragm movements are scaled (magnified) by a factor of (a) 200 times and (b) 2000 times.

*Table G.14 ~ Parameters for **Model_iso_air_900µmϕ** and **Model_iso_iso_900µmϕ** at time 4.28x10^{-6} seconds*

PMUT	Displacement [m]	Max & Min Cavity Fluid Pressure [Pa]	Max & Min Coupling Fluid Pressure [Pa]
Model_iso_air_900µmϕ	6.63x10^{-8}	-7.81/-9.45	1.48x10^{3}/-6.86
Model_iso_iso_900µmϕ	7.01x10^{-9}	-2.95x10^{3}/-3.09x10^{3}	23.7/-199

Figure G.30 presents a 3-dimensional model showing the layers of high pressure fluid as the fluid moves outwards from the PMUT surface over the PMUT diaphragm.

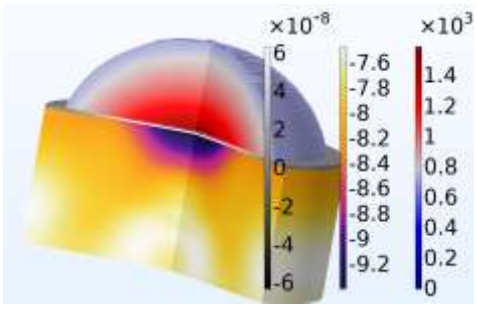

*Figure G.30 ~ 3D view of model **Model_iso_air_900µmϕ** at 4.2x10^{-6} seconds. Diaphragm movement magnified by 200times. Legend~ Left bar- diaphragm displacement [m], middle bar- cavity pressure [Pa] & left bar coupling fluid pressure [Pa].*

At time= 4.58x10^{-6} seconds

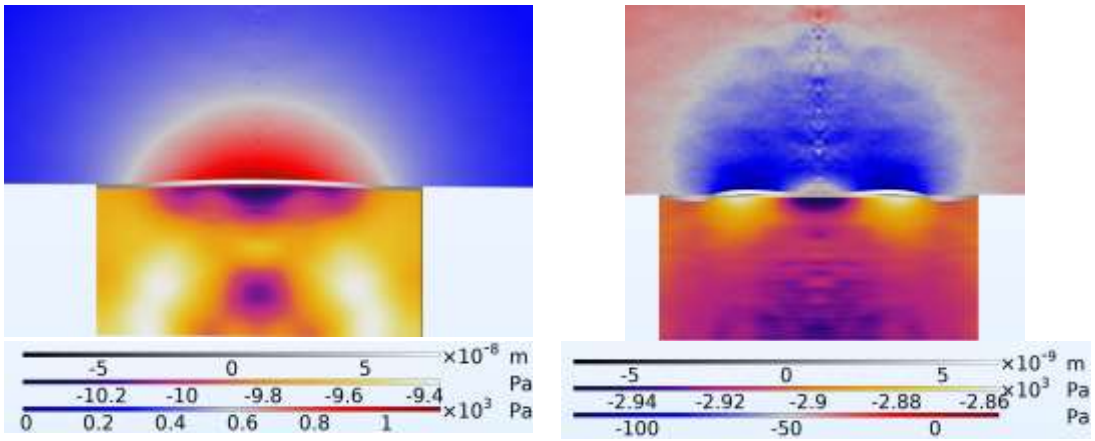

Top Bar ~ Diaphragm displacement / Middle Bar ~ Cavity pressure / Bottom Bar ~ Coupling fluid pressure

Max velocity of diaphragm = 0.04 m/s
Max acceleration of diaphragm = 5.88x10^3 m/s^2

(a)

Max Velocity of diaphragm = 4.98x10^{-4} m/s
Max Acceleration of diaphragm = 1.05x10^3 m/s^2

(b)

Figure G.31 ~ FEM showing the movement of the diaphragm of a 900 µm PMUT with isopropanol as coupling fluid shown above the diaphragm (silver colour) and (a)air (b) isopropanol filled cavity below the diaphragm. This diagram represents the system at time 4.58x10^{-6}s. Diaphragm movements are scaled (magnified) by a factor of (a) 200 times and (b) 2,000 times.

*Table G.15 ~ Parameters for **Model_iso_air_900µmϕ** and **Model_iso_iso_900µmϕ** at time 4.58x10^{-6}seconds*

PMUT	Displacement [m]	Max & Min Cavity Fluid Pressure [Pa]	Max & Min Coupling Fluid Pressure [Pa]
Model_iso_air_900µmϕ	7.82x10^{-8}	-9.36/-10.4	1.15x10^3/-9.04
Model_iso_iso_900µmϕ	6.8x10^{-9}	-2.86x10^3/-2.95x10^3	22.8/-121

At time = 4.88x10^{-6} seconds

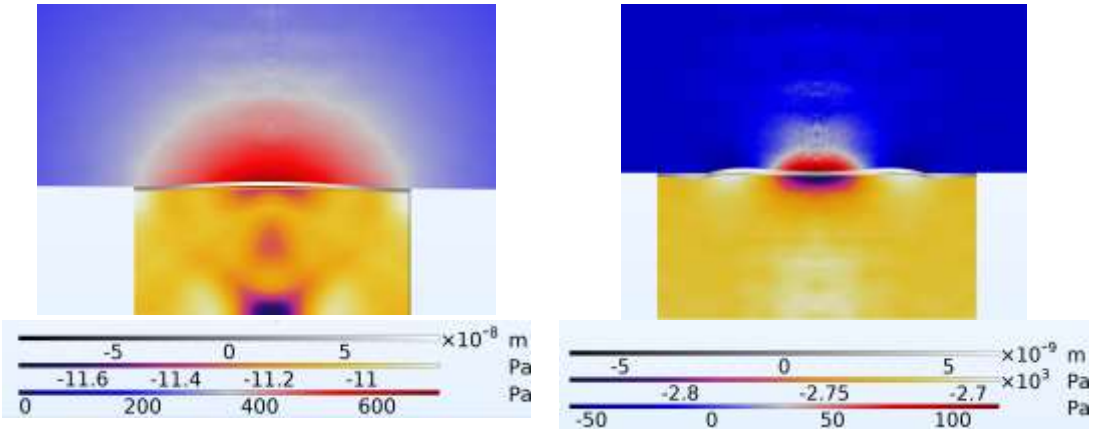

Top Bar ~ Diaphragm displacement / Middle Bar ~ Cavity pressure / Bottom Bar ~ Coupling fluid pressure

Max velocity of diaphragm=0.04 m/s
Max acceleration of diaphragm= 3.22×10^{3} m/s^2

(a)

Max Velocity of diaphragm = 5.41×10^{-4} m/s
Max Acceleration of diaphragm = 1.64×10^{3} m/s^2

(b)

Figure G.32 ~ FEM showing the movement of the diaphragm of a 900µm PMUT with isopropanol as coupling fluid shown above the diaphragm (silver colour) and (a)air (b) isopropanol filled cavity below the diaphragm. This diagram represents the system at time 4.88×10^{-6} s. Diaphragm movements are scaled (magnified) by a factor of (a) 200 times and (b) 2,000 times.

*Table G.16 ~ Parameters for **Model_iso_air_900µmϕ** and **Model_iso_iso_900µmϕ** at time 4.88×10^{-6} seconds*

PMUT	Displacement [m]	Max & Min Cavity Fluid Pressure [Pa]	Max & Min Coupling Fluid Pressure [Pa]
Model_iso_air_900µmϕ	9.06×10^{-8}	-10.8/-11.7	706/-11.3
Model_iso_iso_900µmϕ	6.52×10^{-9}	-2.69×10^{3}/-2.84×10^{3}	119/-59

At time= 4.97×10^{-6} seconds

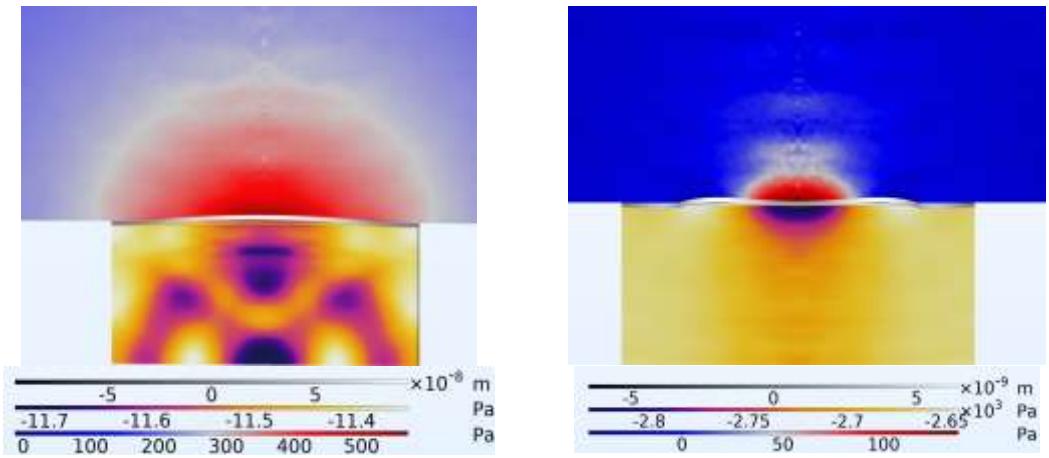

Top Bar ~ Diaphragm displacement / Middle Bar ~ Cavity pressure / Bottom Bar ~ Coupling fluid pressure

Max velocity of diaphragm=0.04 m/s
Max acceleration of diaphragm= 2.41×10^{3} m/s^2

(a)

Max Velocity of diaphragm = 5.58×10^{-4} m/s
Max Acceleration of diaphragm = 1.98×10^{3} m/s^2

(b)

Figure G.33 ~ FEM showing the movement of the diaphragm of a 900µm PMUT with isopropanol as coupling fluid shown above the diaphragm (silver colour) and (a) air (b) isopropanol filled cavity below the diaphragm. This diagram represents the system at time 4.97x10^{-6}s. Diaphragm movements are scaled (magnified) by a factor of (a) 200 times (b) 2000 times.

*Table G.17 ~ Parameters for **Model_iso_air_900µmϕ** and **Model_iso_iso_900µmϕ** at time 4.97x10^{-6} seconds*

PMUT	Displacement [m]	Max & Min Cavity Fluid Pressure [Pa]	Max & Min Coupling Fluid Pressure [Pa]
Model_iso_air_900µmϕ	9.44x10^{-8}	-11.3/-11.7	568/-12.3
Model_iso_iso_900µmϕ	6.43x10^{-9}	-2.63x10^{3}/-2.81x10^{3}	126/-57.3

At time= 5.17x10^{-6} seconds

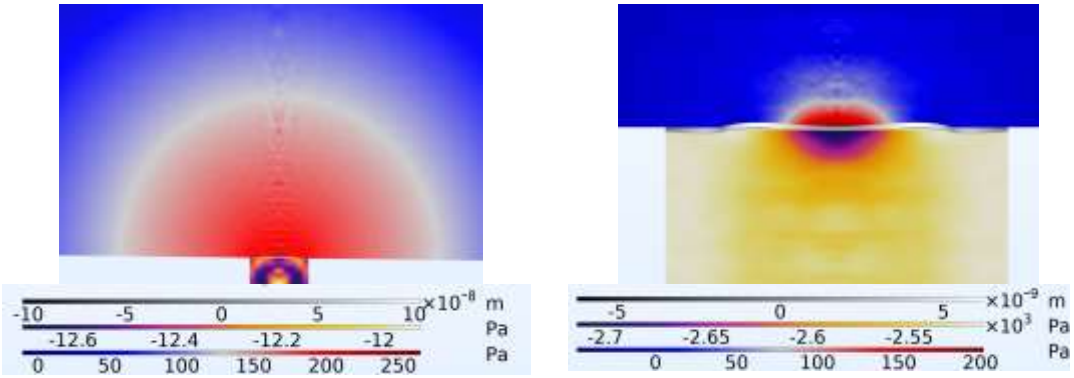

Top Bar ~ Diaphragm displacement / Middle Bar ~ Cavity pressure / Bottom Bar ~ Coupling fluid pressure

Max velocity of diaphragm=0.04 m/s
Max acceleration of diaphragm= 431 m/s^2

(a)

Max Velocity of diaphragm = 5.95x10^{-4} m/s
Max Acceleration of diaphragm = 2.77x10^3 m/s^2

(b)

Figure G.34 ~ FEM showing the movement of the diaphragm of a 900µm PMUT with isopropanol as coupling fluid shown above the diaphragm (silver colour) and (a) air (b) isopropanol filled cavity below the diaphragm. This diagram represents the system at time 5.17x10^{-6}s. Diaphragm movements are scaled (magnified) by a factor of (a) 200 times (b) 2,000 times.

*Table G.18 ~ Parameters for **Model_iso_air_900µmϕ** and **Model_iso_iso_900µmϕ** at time 5.17x10^{-6} seconds*

PMUT	Displacement [m]	Max & Min Cavity Fluid Pressure [Pa]	Max & Min Coupling Fluid Pressure [Pa]
Model_iso_air_900µmϕ	1.03x10^{-7}	-11.9/-12.7	265/-10.7
Model_iso_iso_900µmϕ	6.22x10^{-9}	-2.51x10^{3}/-2.71x10^{3}	202/-48.4

At time= $5.34x10^{-6}$ seconds

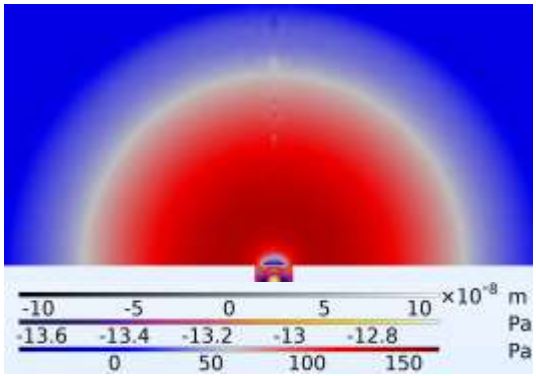

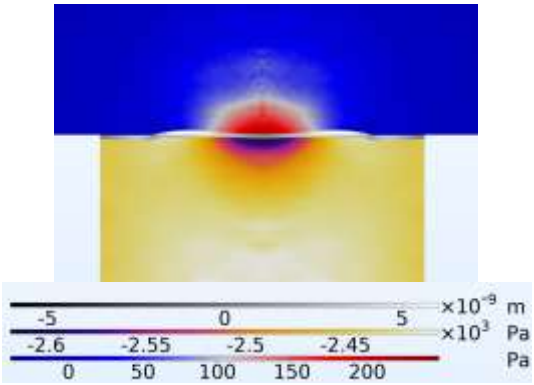

Top Bar ~ Diaphragm displacement / Middle Bar ~ Cavity pressure / Bottom Bar ~ Coupling fluid pressure

Max velocity of diaphragm=0.04 m/s
Max acceleration of diaphragm= $1.36x10^{3}$ m/s^2

(a)

Max Velocity of diaphragm = $6.09x10^{-4}$ m/s
Max Acceleration of diaphragm = $3.13x10^{3}$ m/s^2

(b)

Figure G.35 ~ FEM showing the movement of the diaphragm of a 900µm PMUT with isopropanol as coupling fluid shown above the diaphragm (silver colour) and (a) air (b) isopropanol filled cavity below the diaphragm. This diagram represents the system at time $5.34x10^{-6}$s. Diaphragm movements are scaled (magnified) by a factor of (a) 200 times (b) 2,000 times.

*Table G.19 ~ Parameters for **Model_iso_air_900µmϕ** and **Model_iso_iso_900µmϕ** at time $5.34x10^{-6}$ seconds*

PMUT	Displacement [m]	Max & Min Cavity Fluid Pressure [Pa]	Max & Min Coupling Fluid Pressure [Pa]
Model_iso_air_900µmϕ	$1.1x10^{-7}$	-12.6/-13.7	178/-49.5
Model_iso_iso_900µmϕ	$6.04x10^{-9}$	$-2.4x10^{3}$/$-2.62x10^{3}$	248/-38.7

At time= $5.37x10^{-6}$ seconds

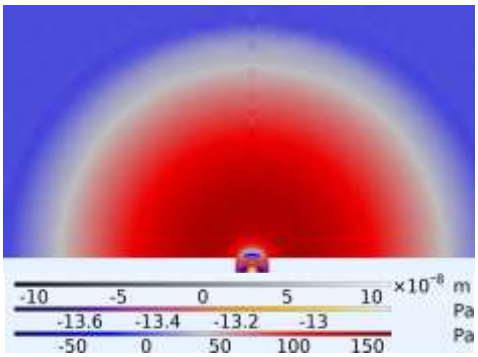

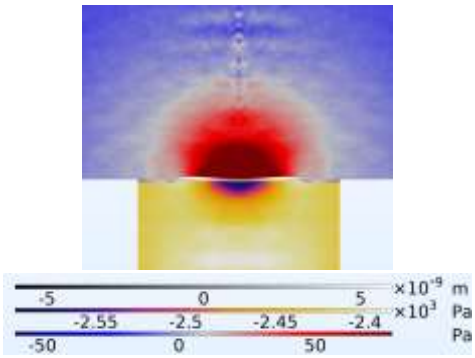

Top Bar ~ Diaphragm displacement / Middle Bar ~ Cavity pressure / Bottom Bar ~ Coupling fluid pressure

Max velocity of diaphragm=0.04 m/s
Max acceleration of diaphragm= $1.58x10^{3}$ m/s^2

(a)

Max Velocity of diaphragm = $6.1x10^{-4}$ m/s
Max Acceleration of diaphragm = $2.61x10^{3}$ m/s^2

(b)

Figure G.36 ~ FEM showing the movement of the diaphragm of a 900 µm PMUT with isopropanol as coupling fluid shown above the diaphragm (silver colour) and (a)air (b) isopropanol filled cavity below the diaphragm. This diagram represents the system at time $5.37x10^{-6}$ s. Diaphragm movements are scaled (magnified) by a factor of (a) 200 and (b) 2,000 times.

Table G.20 presents the parametric values at time 5.37x10^{-6} s

*Table G.20 ~ Parameters for **Model_iso_air_900 µmϕ** and **Model_iso_iso_900 µmϕ** at time 5.37x10^{-6} seconds*

PMUT	Displacement [m]	Max & Min Cavity Fluid Pressure [Pa]	Max & Min Coupling Fluid Pressure [Pa]
Model_iso_air_900µmϕ	1.11x10^{-7}	-12.8/-13.8	166/-89.3
Model_iso_iso_900µmϕ	6x10^{-9}	-2.38x10^{3}/-2.59x10^{3}	252/-40.2

Appendix H: Time domain analysis of different electrode configuration.

This appendix presents a time domain analysis of PMUT dynamics when movement is driven by electrodes having different radial cover configurations. To explore the effect of the electrode radial cover in detail, two time domain models were set up to model the electrode movements and pressures raised in microsecond resolution. For comparability, both models had a diameter of 700 μm. One of them had an electrode radial cover percentage of 66% while the other carried a radial cover percentage of 98%. The two time domain models were set up through a three step process to achieve steady state conditions with a reasonable amount of computational time. The step set up was as follows:

- Step 1 was set up to range between 0 and 0.0004 seconds in steps of $1x10^{-6}$ seconds.
- Step 2 was set up to range between 0.0004 and 0.000440 seconds in steps of $1x10^{-7}$ seconds.
- Step 3 was the concatenation step. This step combines the other two together into one single model.

Conducting the whole time domain analysis in time steps of $1x10^{-7}$ s would take many days of computer analysis. Hence this approach was designed in a way which used larger time steps of $1x10^{-6}$ seconds for a total of 0.0004 seconds in which time the PMUT accelerates to its steady state speed utilising reasonable computing time. In the final 0.00004 s of the simulation when the PMUT would have reached its steady state operating parameters the FEA enters step 2 in which the PMUT movements are studied at time steps of $1x10^{-7}$ seconds. This generates hundreds of GB of analytical data through which the minutest simulated movements and fluid dynamics of the FEM could be studied. The third step was the concatenation step, in which the data from the two previous steps was concatenated together into one set of results ready for final analysis. Figure H.1 shows the displacement of the PMUT midpoint in the time domain following the two step set up to conduct the time domain analysis.

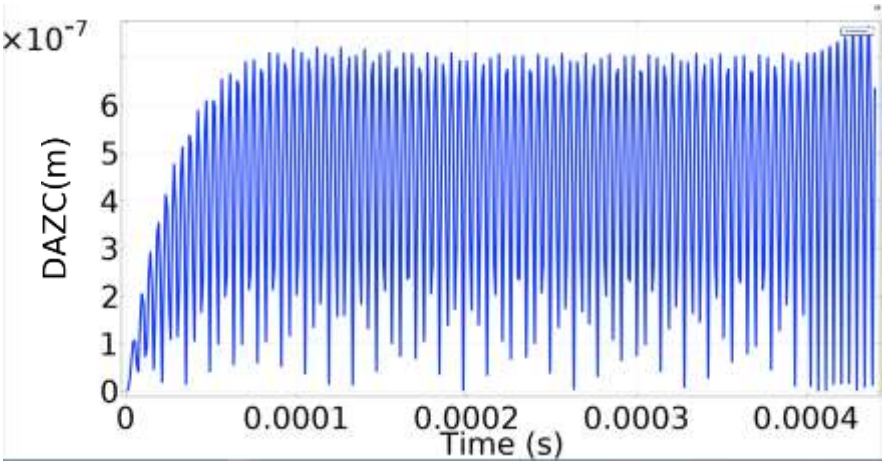

Figure H.1 ~ Displacement Amplitude Z Component (DAZC) at the centre of the membrane for 700 μm diameter device showing step 1 up to 0.0004 s and step 2 from 0.0004 s onwards.

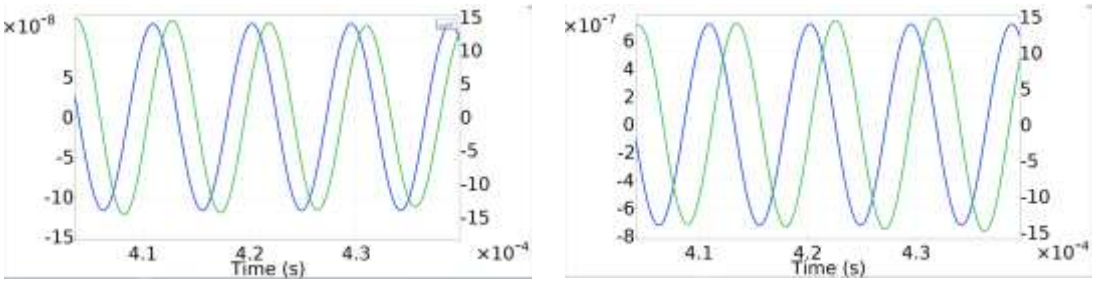

(a) (b)

Figure H.2 ~ Displacement field, Z-component (m) Electric potential (V) (a) 98% radial coverage (b) 66% radial coverage

As one can see from Figure H.3 the diaphragm midpoint displacement in the PMUT having an electrode with radial dimensions of 66% is much more pronounced than the PMUT which has an electrode that has a radius of 98% that of the diaphragm.

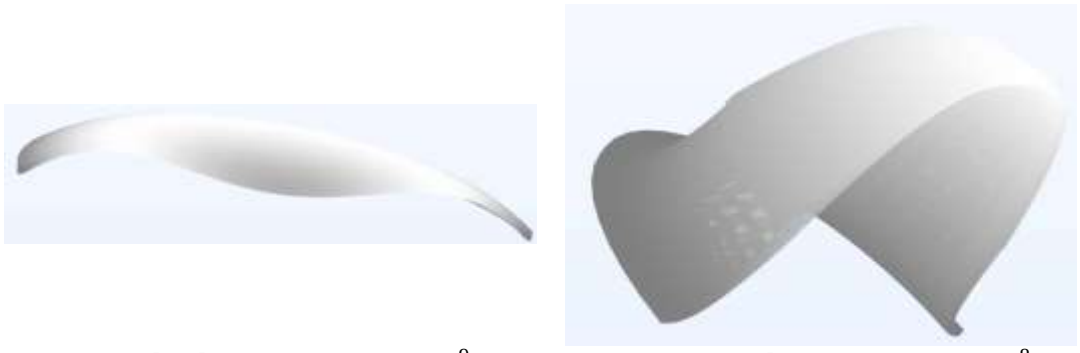

Maximum displacement ~3.19x10^{-9} m Maximum Displacement ~2.75x10^{-8} m

(a) (b)

Figure H.3 ~ At time t=2x10^{-6} s. PMUT(a)has radial electrode cover of 98% that of diaphragm (b) has radial cover of 66% that of diaphragm. Both displacements are magnified by 15,000 times in the z dimension.

Figure H.4 presents two PMUTs deployed in an isopropanol coupling fluid and air filled cavity environment. One of the devices, shown as device (a) has an electrode radial cover of 98% that of the PMUT's diaphragm while that shown as (b) has an electrode radial cover equal to 66% that of the PMUT diaphragm.

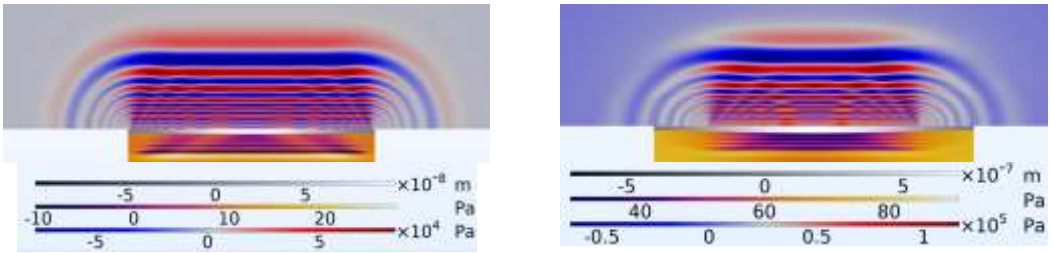

(a) (b)

Figure H.4 ~ Time domain FEM showing diaphragm displacement, pressure in coupling and cavity fluids for (a) 98% and (b) 66% radial coverage devices. At t= 4.002x10^{-4}s. Scale factor 10.

It can be seen from Figure H.5 that the in the 66% radial cover device the ultrasonic pressure is focused towards the central part of the waves being emitted into the coupling and cavity fluids. In the case of the 98% radial cover device this focus seems to occur

to a much lesser extent and the waves pressure distribution continues homogenously around the PMUT.

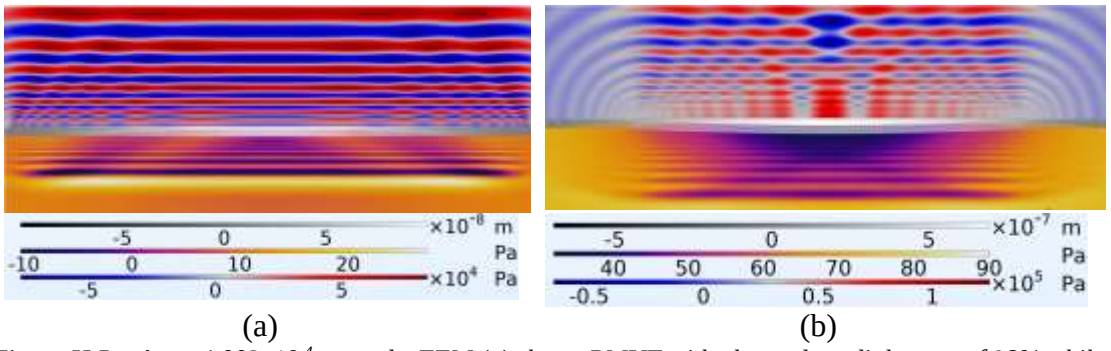

(a) (b)

Figure H.5 ~ At t= 4.003x10^{-4} seconds. FEM (a) shows PMUT with electrode radial cover of 98% while FEM (b) shows PMUT with an electrode radial cover of 66% that of the diaphragm. Both FEMs are scaled by a factor of 10 in the z dimension.

The 98% electrode radial coverage device reached a maximum pressure of 8.38x10^{4} Pa in the coupling fluid at a displacement of 9.97x10^{-8} m. The cavity fluid pressure remained low with the maximum at 27.3 Pa. The 66% electrode radial coverage device reached a pressure of 1.25x10^{5} Pa at a PMUT midpoint displacement of 6.93x10^{-7} m. The pressure reached in the cavity fluid for the 66% electrode radial cover device was 90.1 Pa. The formation of the pressure waves and the high pressure concentration at PMUT midpoint can be seen in Figure H.6.

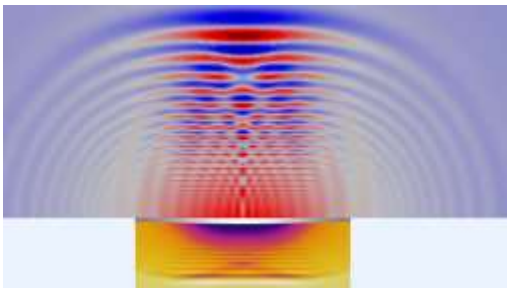

Figure H.6 ~ Focusing of ultrasonic beam towards the midpoint of the waveforms seen in greater detail for the 66% electrode radial cover device. FEM at t= 4.006x10^{-4} s. Scaled in the Z direction by a factor of 10.

The next FEM pair which can be seen in Figure H.7 continued to show a comparative view between the dynamics of a PMUT with a 66% radial cover electrode and a PMUT with a 98% radial cover electrode. Through this one can continue to see that the PMUT with a 66% electrode radial cover demonstrates:

- More focusing of the high pressure points in the coupling fluid
- Much more pronounced high pressure zones in the coupling fluid

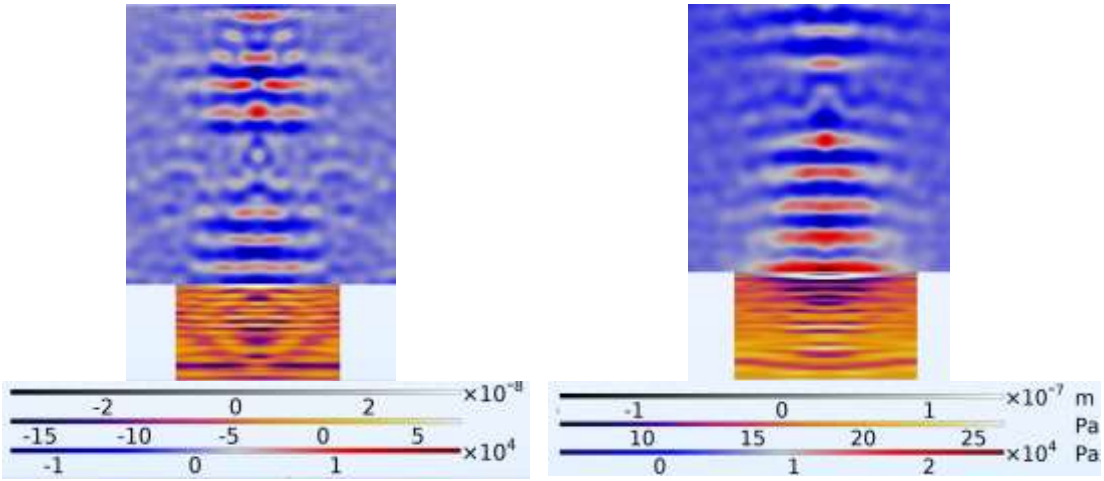

(a) (b)

Figure H.7 ~ (a) 98% electrode radial coverage (b) 66% electrode radial coverage of diaphragm. At t= 4.109x10^{-4} s. Scale factor 100.

With reference to Figure H.7 the maximum coupling fluid pressure reached by the PMUT with the 98% electrode radial coverage PMUT device was 1.88x10^{4} Pa at a maximum diaphragm midpoint displacement of 3.38x10^{-8} m. The maximum cavity pressure was 7.26 Pa. On the other hand in the PMUT with a 66% electrode radial cover electrode, the coupling fluid pressure at a diaphragm midpoint displacement of 1.5x10^{-7} m reached 2.56x10^{4} Pa.

Next on the series is Figure H.8 where one can see the diaphragm midpoint start to retract again as the cycle proceeds. With the receding of the diaphragm midpoint the pressure in the coupling fluid then starts to decrease.

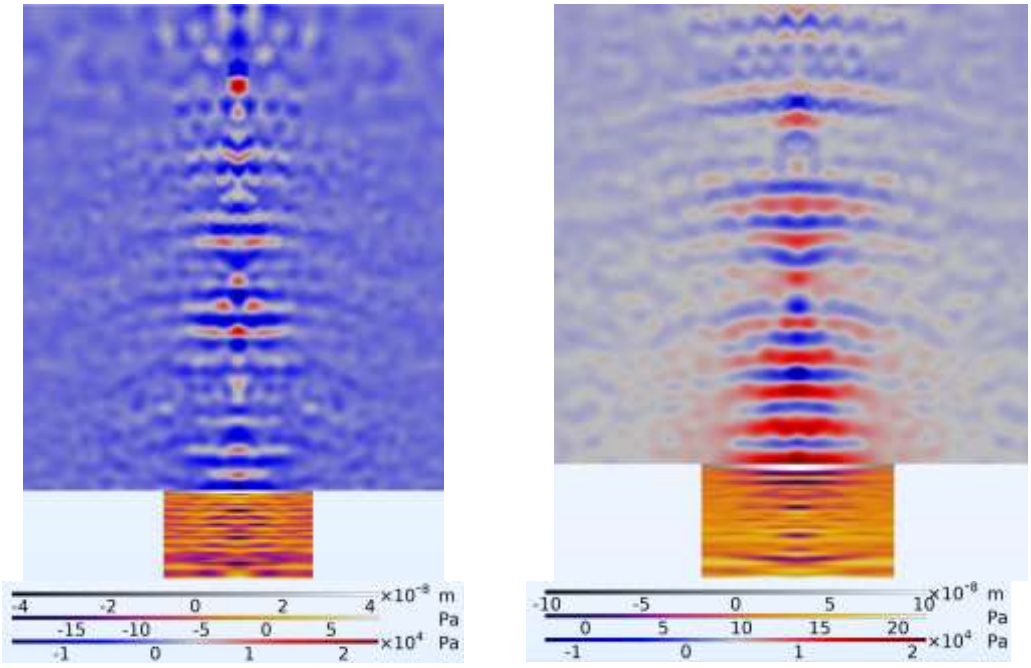

(a) (b)

Figure H.8 ~ Dynamics and pressures induced by PMUTs having electrodes with (a) 98% electrode radial coverage of diaphragm and (b) 66% electrode radial coverage of diaphragm. At t = 4.11x10^{-4} s. Scale factor of 10.

With reference to Figure H.8 for the PMUT with a 98% electrode radial coverage the maximum PMUT midpoint displacement was $4.19x10^{-8}$ m which induced a maximum coupling fluid pressure of $2.37x10^{4}$ Pa. In the case of the 66% electrode radial cover device, the peak coupling fluid pressure reached was $2.12x10^{4}$ Pa at a peak diaphragm midpoint displacement of $1.01x10^{-7}$ m.

At the next time stamp of $4.112x10^{-4}$ s from start of excitation, the maximum displacement reached by the device with the 98% radial cover electrode was $4.19x10^{-8}$ m with the pressure inside the coupling fluid reaching the $2.37x10^{4}$ Pa mark. The maximum displacement in the 66% device was $3.29x10^{-9}$ m with a maximum pressure of $1.68x10^{4}$ Pa being reached. This is shown in Figure H.9.

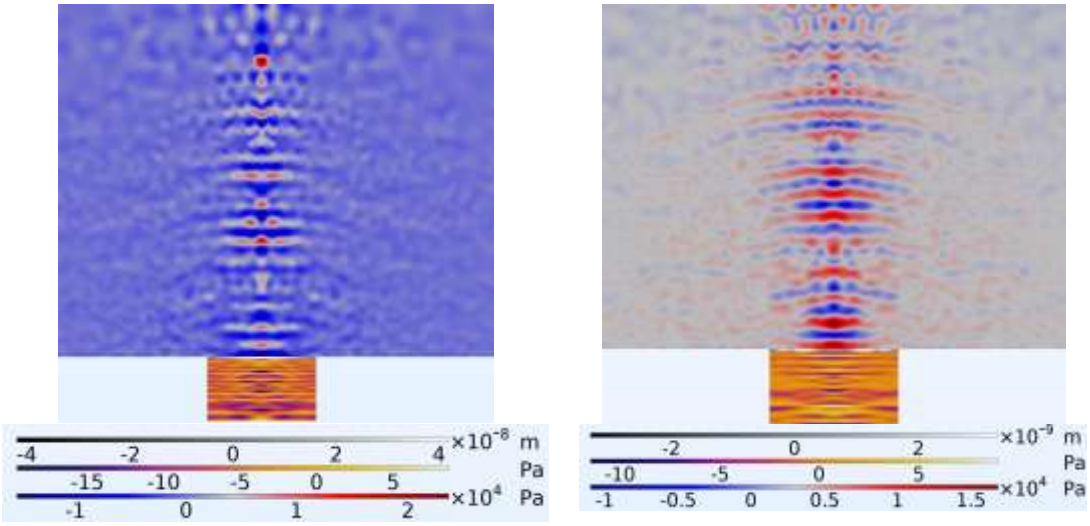

(a) (b)

Figure H.9 ~ Two PMUTS transmitting in isopropanol coupling fluid with (a) PMUT having an electrode with a 98% radial coverage and (b) having an electrode with 66% radial coverage. At t = $4.112x10^{-4}$ s. Scaled by a factor of 10 in the z direction. Both having air filled cavities.

With reference to Figure H.10 in the 66% radial coverage device the maximum amplitude at the diaphragm's midpoint which was reached was 9.9 $x10^{-8}$ m thereby continuing to show the diaphragm movement downwards after having reached the peak earlier in the series. The maximum coupling fluid pressure at this point in time was $1.15x10^{4}$ Pa. In the 98% electrode radial coverage device the maximum amplitude reached was $7.17x10^{-8}$ m and the coupling fluid maximum pressure reached was $1.52x10^{4}$ Pa.

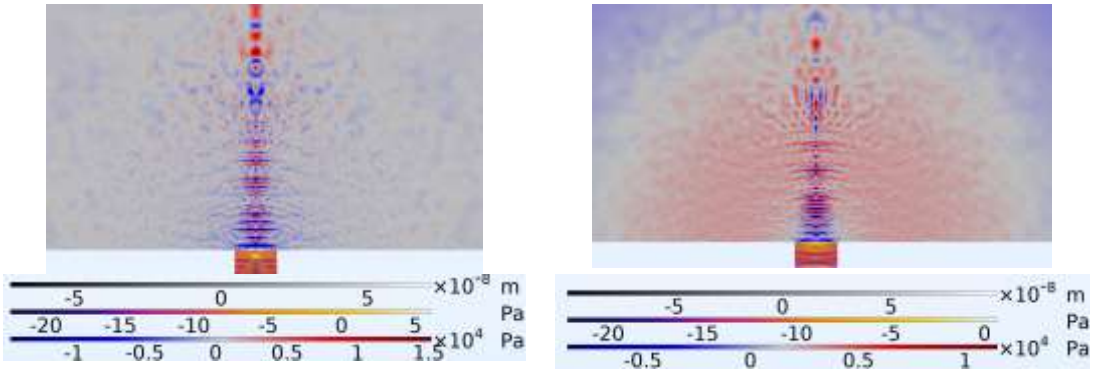

(a) (b)

Figure H.10 ~ Two PMUTS transmitting in isopropanol coupling fluid with (a) PMUT having an electrode with a 98% radial coverage and (b) having an electrode with 66% radial coverage. At a time stamp of 4.114x10^{-4} s. Scale factor of 10.

Appendix I: The Cavity - Studying the wave dynamics of the cavity - the kettle drum effect.

Through this appendix, the reader is presented with the time domain modelling which captures the steady state conditions showing the operation of the PMUT's cavity as a kettle drum whereby the waves being reflected back inside the cavity interact with the PMUT diaphragm thereby effecting its dynamic response. To approach this in a highly accurate way which was achievable with the computational power available a two-step model was set up with concatenation as used and explained in detail in Appendix H. The air cavity is shown in Figure I.1.

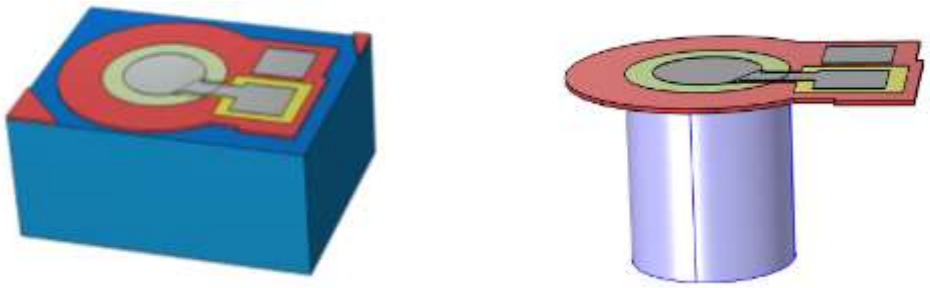

(a) (b)

Figure I.1 ~ Finite element model showing (a) the complete device and (b) the silicon PMUT structure removed to show the fluid column inside the cavity.

To understand the gas dynamics occurring inside the PMUT cavity a series of finite element images was created showing a full cycle of diaphragm movement from its highest to its lowest points.

The first image of the series presented as Figure I.2 shows the pressure gradients inside the cavity at the instant when the diaphragm had reached the highest point. As can be seen the cavity is in a state of low pressure which state has been brought about due to the diaphragm's upward movement during the previous cycle.

The calculated maximum height reached by the diaphragm shows that the finite element parameters are accurately tuned with the experimental data.

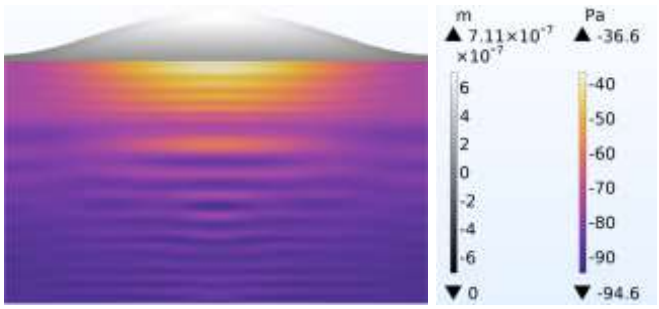

Figure I.2 ~ Acoustic pressure waves in the air filled PMUT cavity at a time stamp of $4.045x10^{-4}$ s. Diaphragm displacement magnified by a factor of 100.

Figure I.3 presents the diaphragm at the point at which it is starting on its downward movement and causing a pressure increase in the cavity fluid. A wave front, which will be followed in this series and which is marked with the black arrow, was created and started moving downwards in parallel with the diaphragm's own centre point movement but with a much higher velocity.

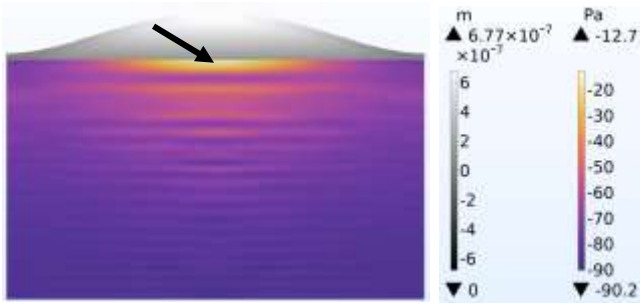

Figure I.3 ~ Acoustic pressure waves in the air filled PMUT cavity at a time stamp of $4.049x10^{-4}$ seconds. Diaphragm displacement magnified by a factor of 100.

In Figure I.4 and Figure I.5 it can be seen that the movement of the waveform being followed continued in its downward path.

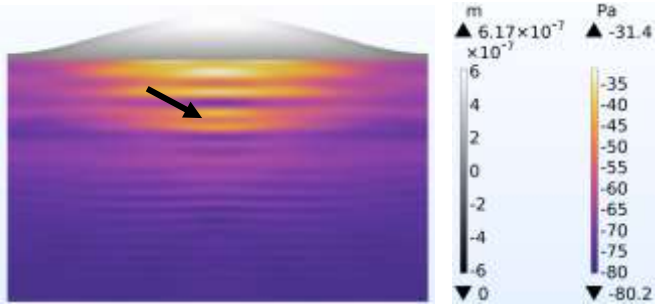

Figure I.4 ~ Acoustic pressure waves in the air filled PMUT cavity at a time stamp of $4.052x10^{-4}$ seconds. Diaphragm displacement magnified by a factor of 100.

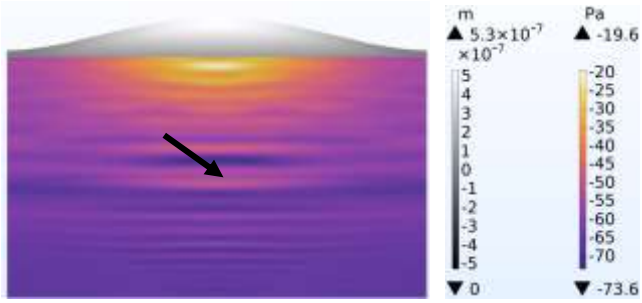

Figure I.5 ~ Acoustic pressure waves in the air filled PMUT cavity at a time stamp of $4.055x10^{-4}$ seconds. Diaphragm displacement magnified by a factor of 100.

Figure I.6 shows the wave's continued movement downwards.

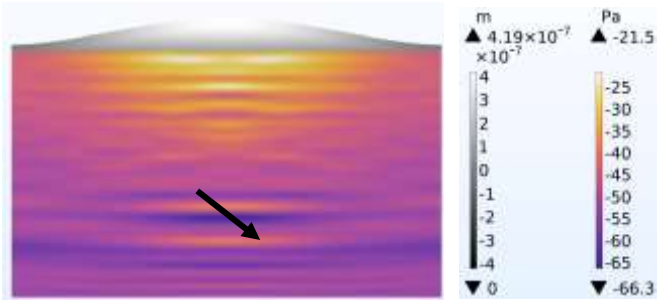

Figure I.6 ~ Acoustic pressure waves in the air filled PMUT cavity at a time stamp of $4.058x10^{-4}$ seconds. Diaphragm displacement magnified by a factor of 100.

The waveform finally impacts the bottom of the cavity as can be seen in Figure I.7.

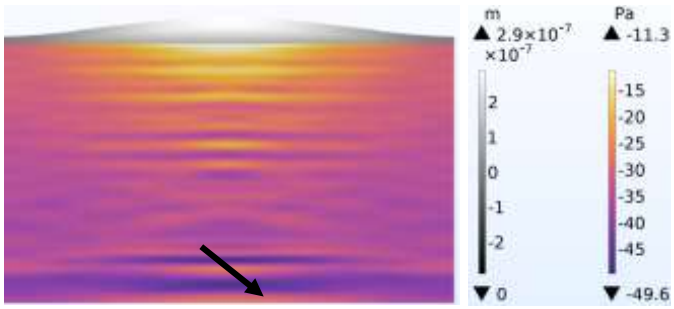

Figure I.7 ~ Acoustic pressure waves in the air filled PMUT cavity at a time stamp of $4.061x10^{-4}$ seconds. Diaphragm displacement magnified by a factor of 100.

After impacting the cavity bottom, reflection of the wave front back up into the cavity can be followed as shown in Figure I.8

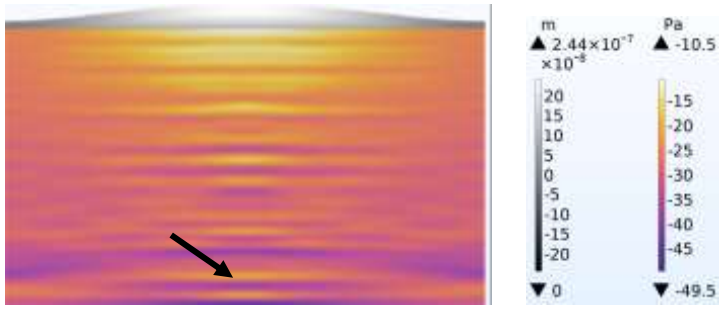

Figure I.8 ~ Acoustic pressure waves in the air filled PMUT cavity at a time stamp of $4.062x10^{-4}$ seconds. Diaphragm displacement magnified by a factor of 100.

Figure I.9 to Figure I.14 present sequence of stages showing the movement of the reflected ultrasonic base from the base of the cavity until it arrives to a position close to the diaphragm.

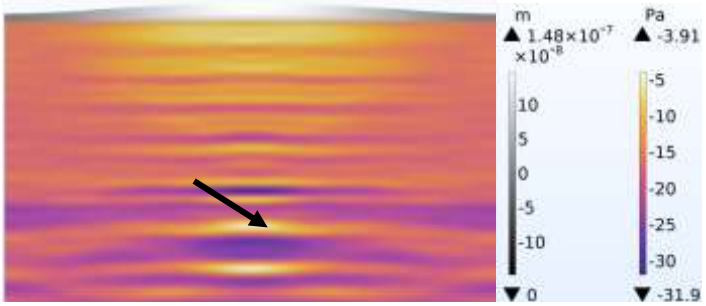

Figure I.9 ~ Acoustic pressure waves in the air filled PMUT cavity at a time stamp of $4.064x10^{-4}$ seconds. Diaphragm displacement magnified by a factor of 100.

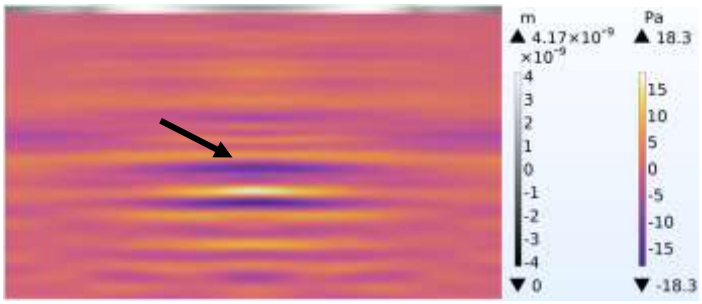

Figure I.10 ~ Acoustic pressure waves in the air filled PMUT cavity at a time stamp of $4.067x10^{-4}$ seconds. Diaphragm displacement magnified by a factor of 100.

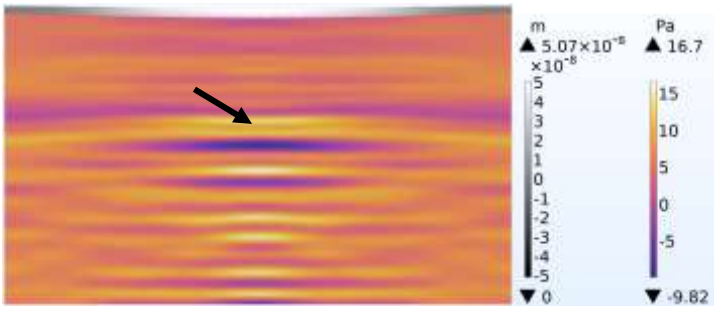

Figure I.11~ Acoustic pressure waves in the air filled PMUT cavity at a time stamp of $4.068x10^{-4}$ seconds. Diaphragm displacement magnified by a factor of 100.

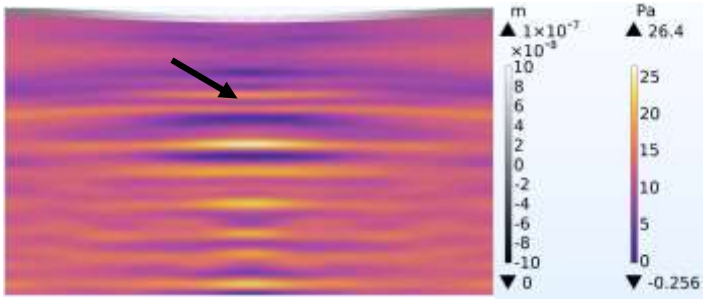

Figure I.12 ~ Acoustic pressure waves in the air filled PMUT cavity at a time stamp of $4.069x10^{-4}$ seconds. Diaphragm displacement magnified by a factor of 100.

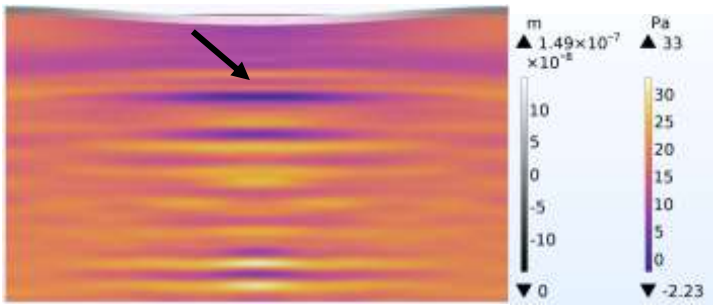

Figure I.13 ~ Acoustic pressure waves in the air filled PMUT cavity at a time stamp of 4.07x10^{-4} seconds. Diaphragm displacement magnified by a factor of 100.

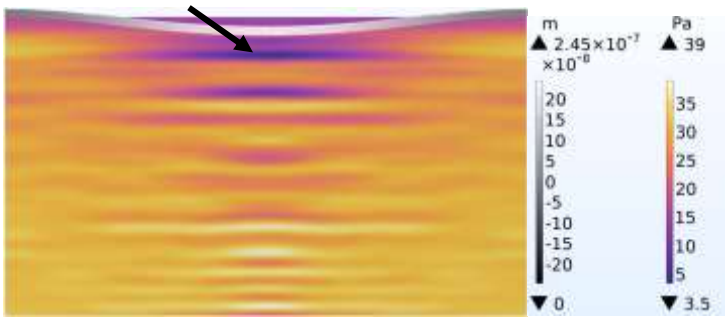

Figure I.14 ~ Acoustic pressure waves in the air filled PMUT cavity at a time stamp of 4.072x10^{-4} seconds. Diaphragm displacement magnified by a factor of 100.

At the point shown in Figure I.15 the rising wave front being followed in this series impacts the diaphragm.

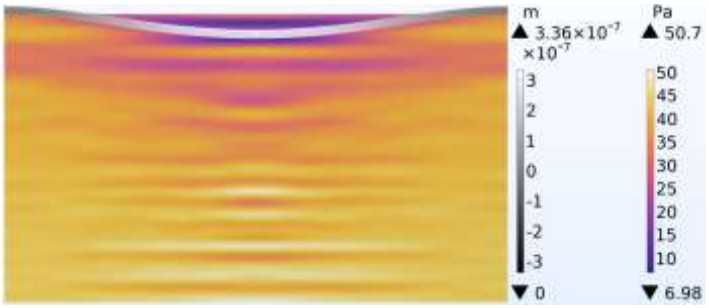

Figure I.15 ~ Acoustic pressure waves in the air filled PMUT cavity at a time stamp of 4.074x10^{-4} seconds. Diaphragm displacement magnified by a factor of 100.

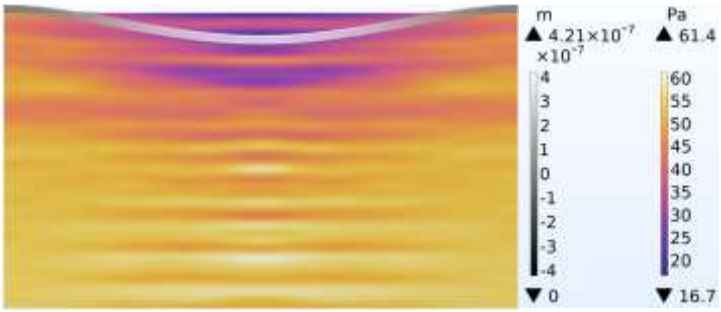

Figure I.16 ~ Acoustic pressure waves in the air filled PMUT cavity at a time stamp of 4.076x10^{-4} seconds. Diaphragm displacement magnified by a factor of 100.

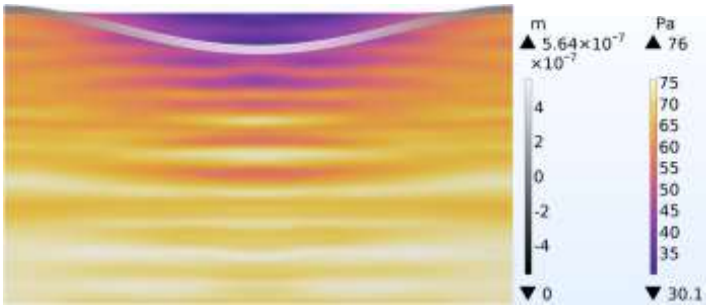

Figure I.17 ~ Acoustic pressure waves in the air filled PMUT cavity at a time stamp of 4.08x10^{-4} seconds. Diaphragm displacement magnified by a factor of 100.

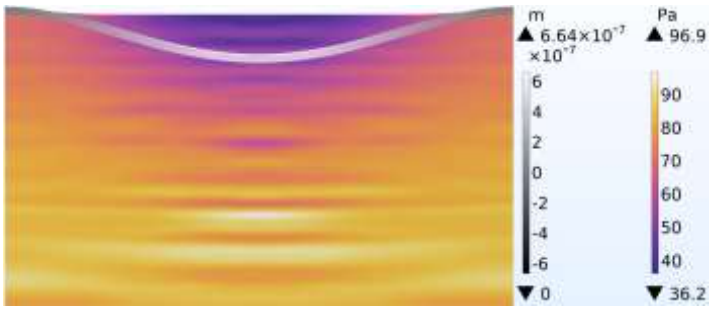

Figure I.18 ~ Acoustic pressure waves in the air filled PMUT cavity at a time stamp of 4.084x10^{-4} seconds. Diaphragm displacement magnified by a factor of 100.

This continues until the diaphragm reaches the lowest position of 7.16x10^{-7} m at which point a pressure of 108 Pa was reached in the cavity fluid.

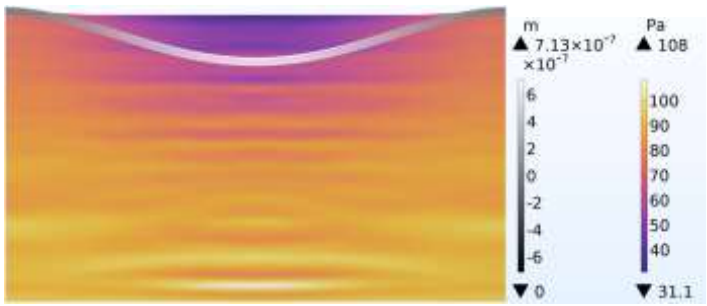

Figure I.19 ~ Acoustic pressure waves in the air filled PMUT cavity at a time stamp of 4.088x10^{-4} seconds. Diaphragm displacement magnified by a factor of 100.

As the waves move up and down they interact with each other in constructive and destructive interference. Further work would need to be conducted to establish the best cavity depth at which the reflected and incident waves would interact and interfere in a way as to improve PMUT performance. For this project the cavity height was fixed to 400 μm irrespective of the PMUT diameter.

Appendix J: The modelling processes for multiple electrode PMUT designs.

This appendix provides further details with regards to the Finite Element Modelling and design of a multi electrode PMUT device (numbered Device 45 in the prototype IC) to complement the material provided in Chapter 3.

This special multiple electrode device was a 600 μm PMUT excited by a specially designed electrode made up of 3 concentric electrodes. Due to the complexity of the model and the many parameters involved, finite element modelling was needed to study the interaction of the electrodes with the piezo layer and ultimately determine the dynamics of operation of the PMUT in isopropanol coupling fluid and with an air filled cavity.

To understand the PMUT electrode kinematics and review if PMUT dynamics can be improved with the multi electrode configuration, the special electrode model was benchmarked with a single electrode 600 μm PMUT acting as standard. Figure J.1 shows a 3D view of the finite element model built to model the multi electrode device.

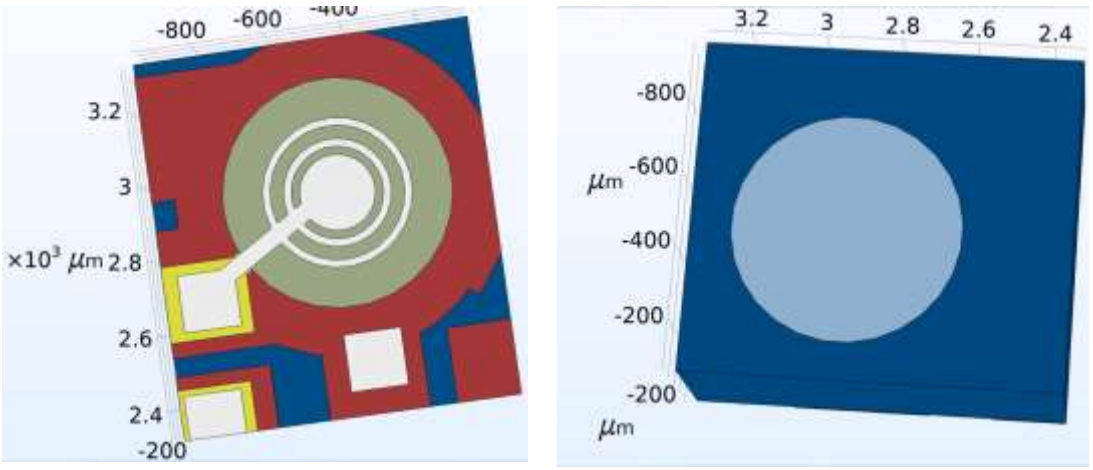

(a) (b)

Figure J.1 ~ FEM showing (a) Front side and (b) backside of a 600 μm diameter device with triple electrode at 33%, 44% and 66% positions with reference to diaphragm. Referred to as Device 45 in the experimental MEMS device.

A similar FEM was built for the single electrode device. An electrode radial percentage cover of 66% was selected for the benchmark as discussed in the literature review Chapter 2, which results were confirmed (to an extent) by finite element modelling outlined in Chapter 3.

The models were built using 2D axisymmetric geometry so as to minimise the device geometry and allow the model to be solvable with available computing power. This follows the geometry shown in Chapter 3. Even so the model for the multi electrode model had 331,953 degrees of freedom and took a number of hours to solve.

Since this model set, was a comparative exercise, the absolute value of each of the results were not important as such. Damping coefficients were therefore not set in both of the models as these could only be established after experimental work was conducted with which to calibrate the model. This finite element modelling set, being a feasibility exercise was conducted before the test devices were built. The coupling fluid dome was set with a radius of 0.04 m and the PML layer was set at 12 times the PMUT diaphragm diameter to ensure that it acted effectively and absorbed all the reflected radiation. The piezoelectric layer was set up with additive strain decomposition enabled. This enables decomposition of strains to be used in this geometrically non-linear analysis.

A frequency domain sweep of two models was conducted at 10 Hz steps to ensure that the peak displacement and velocity values were captured correctly at their points of resonance. The values achieved for the two models are being shown here with the first set of results pertaining to the multi electrode model. The first value being shown in Figure J.2 is the Displacement Amplitude Z Component for the multi electrode model.

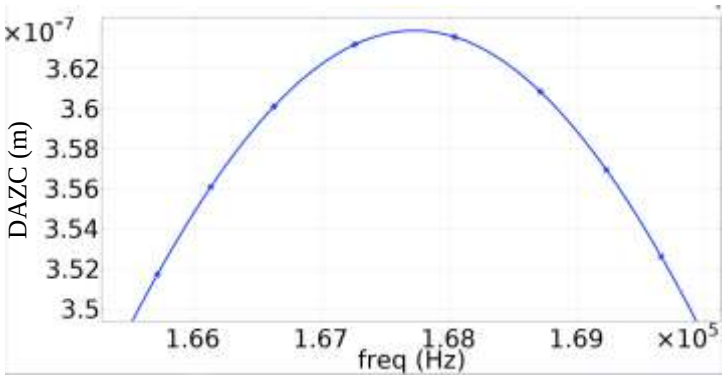

Figure J.2 ~ Displacement amplitude, Z component (DAZC) (m) for multiple electrode PMUT. Peak displacement for the diaphragm midpoint was 3.639x10^{-7} m occurring at a frequency of 1.677x10^{5} Hz

Figure J.3 in turn presents the Velocity Z component (m/s) for the multi electrode PMUT showing the maximum velocity reached by the PMUT diaphragm plotted against frequency. In this case the peak velocity was 0.382 m/s.

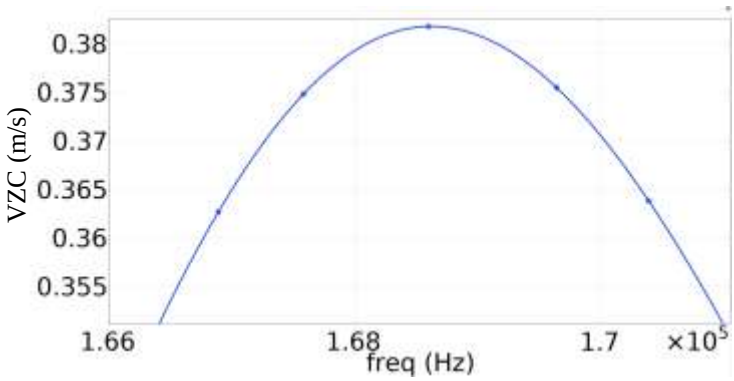

Figure J.3 ~ Velocity, Z Component (VZC) in m/s for multiple electrode PMUT. Peak velocity was 0.382 m/s at 1.686x10^{5} Hz

It can be seen that peak velocity and displacement did not occur at exactly the same resonant frequency.

Figure J.4 presents a pictorial view of the diaphragm's displacement at the point of resonance which occurred at $1.677x10^5$ Hz.

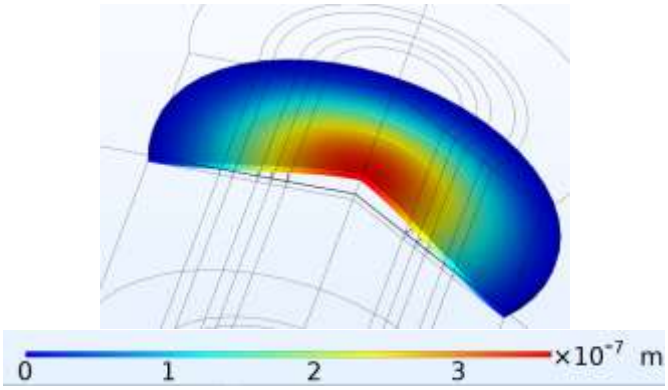

Figure J.4 ~ Displacement at $1.677x10^5$ Hz

Figure J.5 showed the solid mises stress levels on the diaphragm structure. This shows the distortion energy present in the material. In this case the maximum mises level reached at resonance was $5.21x10^{-7}$ and the minimum value was $3.59x10^4$ N/m^2.

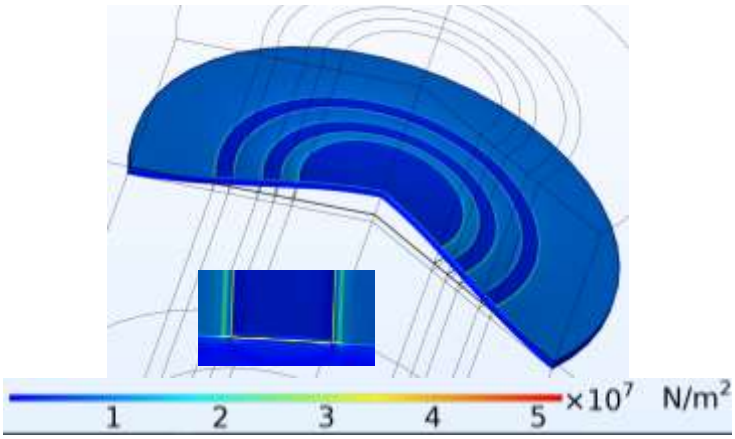

Figure J.5 ~ Solid mises stress levels for multiple electrode PMUT. At $1.677x10^5$ Hz

The ZZ piezoelectric strain tensor is shown in Figure J.6. The maximum value of the strain tensor was $7.19x10^{-5}$ and the minimum value was $-3.96x10^{-4}$.

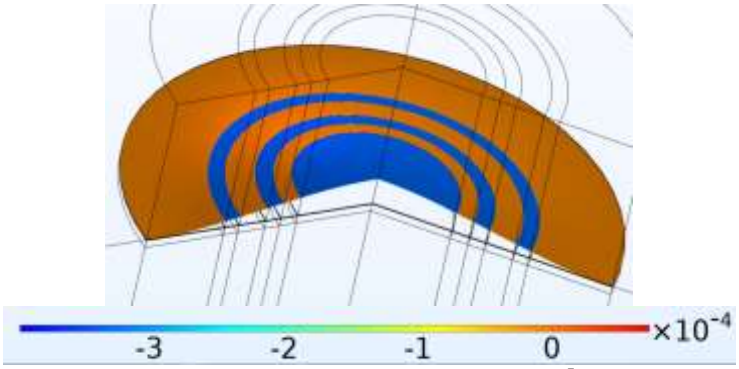

Figure J.6 ~ Piezoelectric Strain tensor, ZZ component. At 1.6775 $x10^5$ Hz. Minimum tensor reached at this frequency was $-3.96x10^{-4}$

The next group of results pertain to the single electrode design acting as benchmark. Figure J.7 shows the displacement amplitude for the single electrode PMUT design which presented a peak displacement of $3.4x10^{-7}$ m at the midpoint of the diaphragm. The resonant frequency was $1.68x10^{5}$ Hz.

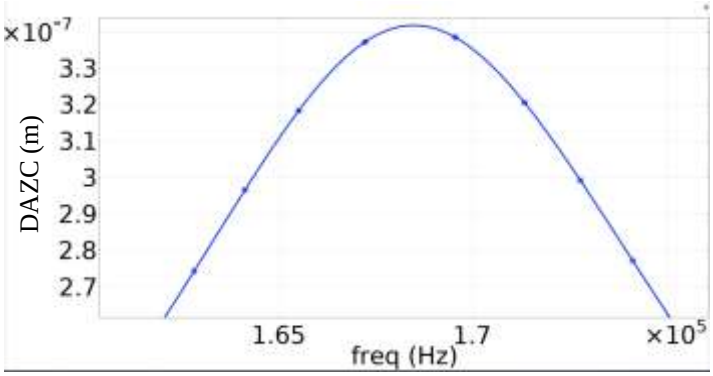

Figure J.7 ~ Displacement amplitude, Z component (DAZC) (m) for single electrode PMUT. Peak displacement was $3.4171x10^{-7}$ m at $1.685x10^{5}$ Hz

Figure J.8 shows the velocity Z component in m/s for the single electrode PMUT showing a peak velocity of 0.361 ms^{-1}.

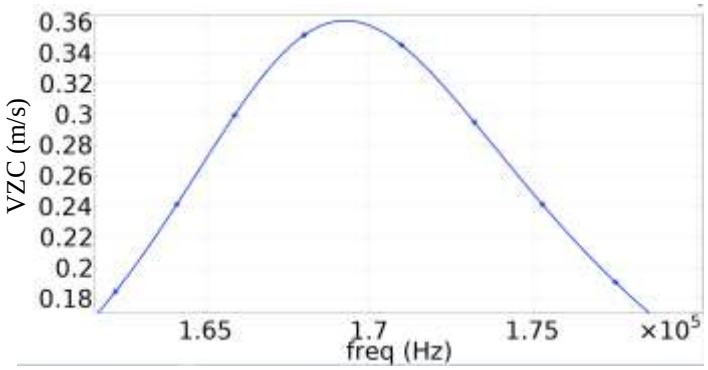

Figure J.8 ~ Velocity, Z component (VZC) (m/s) for single electrode PMUT. Peak velocity was 0.361 ms^{-1} at $1.6925x10^{5}$ Hz

Figure J.9 shows the RMS displacement for the single electrode device.

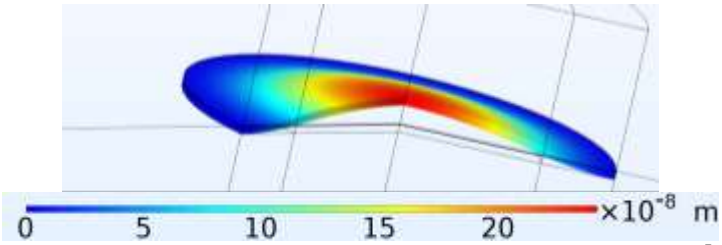

Figure J.9 ~ RMS Displacement of diaphragm midpoint at $1.685x10^{5}$ Hz

Figure J.10 shows the solid mises plot for the diaphragm structure of the single electrode device. In this case the peak stress level was $2.9x10^{7}$ N/m^2 and the minimum was $7.01x10^{-4}$ N/m^2. Comparing these values with those achieved for the multi electrode model, indicated that the lower limit for the single electrode model was higher than that

achieved for the multi electrode model. On the other hand the upper solid mises stress level achieved by the multi electrode model was higher.

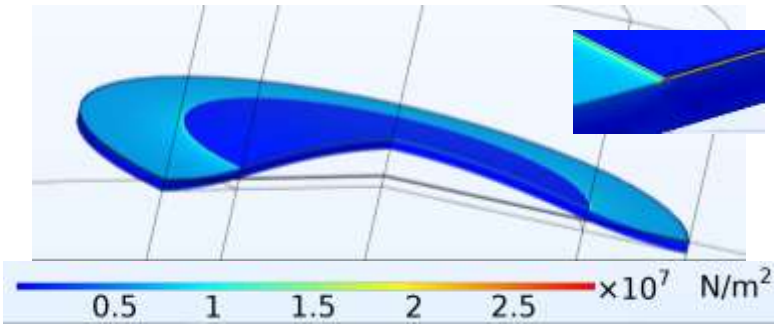

Figure J.10 ~ Solid mises stress levels for single electrode PMUT. At 1.685x10^{5} Hz

Figure J.11 shows the plot of the piezoelectric strain tensor at the resonant point. The minimum value of the strain tensor was -1.36x10^{-4} and the maximum value at the resonant point was 2.17x10^{-5}.

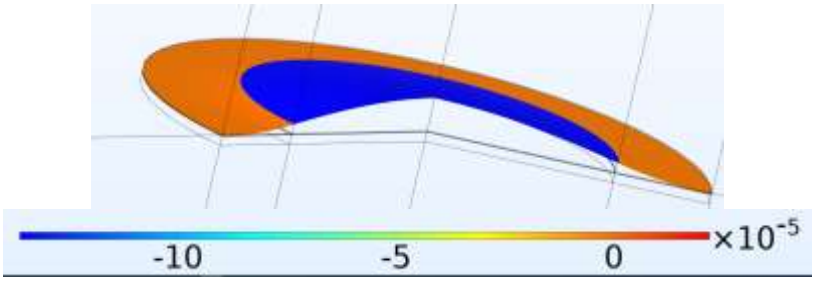

Figure J.11~ Plot of the piezoelectric strain tensor at the point of resonance. The minimum piezoelectric strain tensor reached at this frequency was -1.36x10^{-4}

A comparative analysis between the multi electrode and single electrode designs are shown in Table J.1.

Table J.1 ~ Comparison between multi electrode and single electrode designs.

	Displacement [m]	**Velocity [m/s]**	**Resonant frequency [Hz]**
Multi Electrode	3.64x10^{-07}	0.382	1.68x10^{+05}
Control 66% Cover Electrode	3.40x10^{-07}	0.361	1.68x10^{+05}
Percentage Improvement [%]	6.79	5.65	

This table clearly shows that the multi electrode design imparted improvements to the PMUT's dynamics. Following the Finite element model conducted the detailed geometric designs were conducted as shown in Figure J.12.

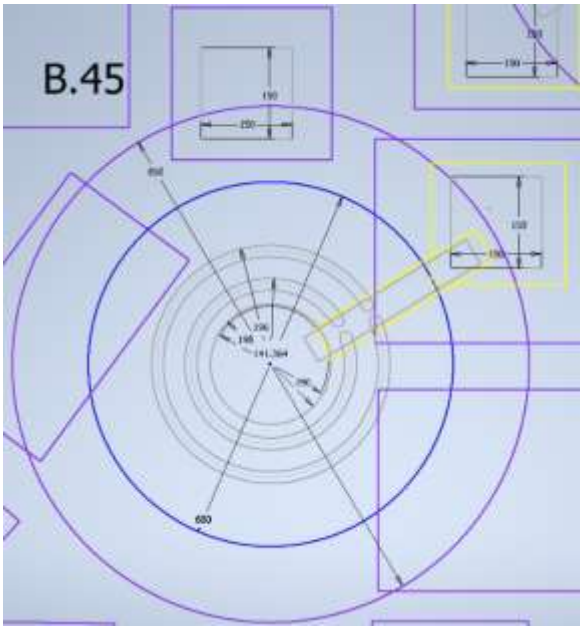

Figure J.12~ Pre stencil design blueprint of Device 45.

In this project other potential multi electrode designs were developed from the finite element modelling as shown in Figure J.13. However these were not tested with the laser vibrometer and therefore will not be discussed further in this text.

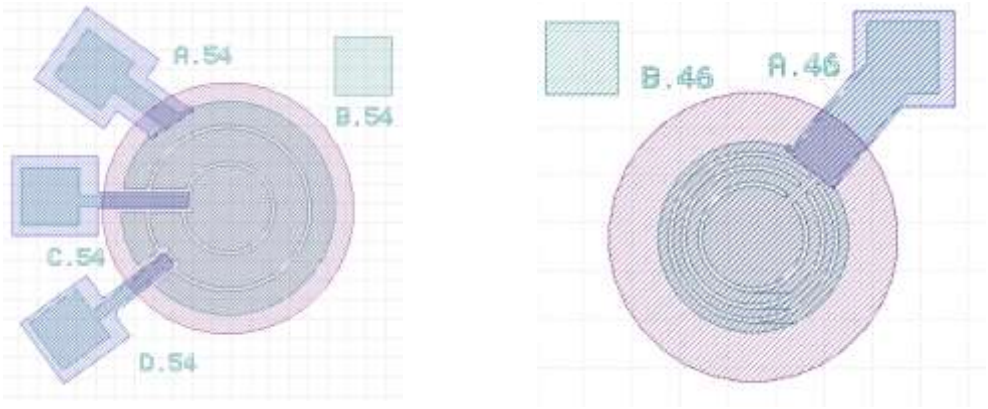

(a) (b)

Figure J.13~ Two PMUT devices with (a) being a device where electrodes are triggered with phase shifts and (b) another three electrode design.

Appendix K: Ultrasonic array theory and the array factor.

This appendix outlines the theory essential to understand the principles underlying ultrasonic transmission.

The orientation of the Beam.

The incident angle at which incident radiation passing through a medium hits the second medium is critical. Similarly to a beam of light, sound is also refracted as shown in Figure K.1.

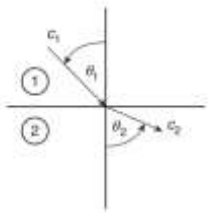

Figure K.1 ~ The process of refraction at a boundary between interfaces having a different refractive index [35].

The relationship between θ_1 and θ_2 is determined by snell's law as per (K.1) [27]

$$\frac{\sin\theta_1}{\sin\theta_2} = \frac{c_1}{c_2} \qquad (K.1)$$

Where

> θ_1 *and* θ_2 are the angle of incidence and of refraction respectively
> c_1 and c_2 are the speed of sound in the first medium and in the second medium respectively

For a liquid to solid interface the angle would normally be around 15°. In macro scale ultrasonic transducers, wedges made of solid or liquid material are used to provide this angle [30]. A portion of the incident radiation is reflected back into the first medium. The other portion enters the second medium.

The portion of the ultrasonic radiation which enters into the second medium is again portioned into different energy types when it acts on an interface. This complicates the wave motion analysis due to the fact that one needs to consider the wave motion as a conglomerate of two components, one having normal wave propagation and the other having shear wave propagation. This concept is presented in Figure K.2.

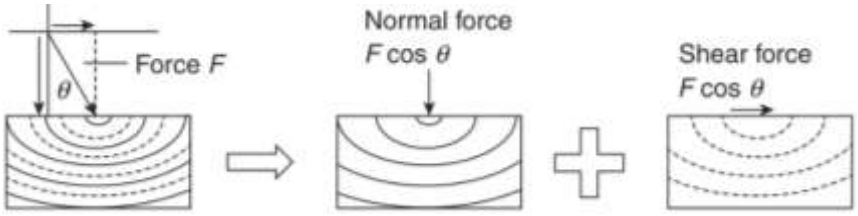

Figure K.2 ~ Energy conversion diagram for ultrasonic shear forces.

This complex waveform production and propagation will be studied closely through Finite Element Modelling.

Reflection of Ultrasonic Radiation

Objects also tend to reflect the incident ultrasonic radiation. A large object compared to the wavelength tends to strongly reflect the incident beam. However if the object is small (compared to the wavelength) the incident beam advances round the obstacle coming back together after surpassing the obstacle without any interference. Many obstacles can induce scattering to occur instead of reflection [30].

The interface between two materials is critical to the transfer of ultrasonic energy. This holds true as only part of the incident wave travels into the second material with the other part of the incident radiation being reflected back. The ratio between the two is provided by (K.2) [30].

$$A_r = \frac{R_1 - R_2}{R_1 + R_2} \qquad (K.2)$$

Where

A_r is the ratio between the reflected and incident wave pressure or amplitude.
R_1 which is the acoustic impedance of the first material is calculated by multiplying the density of the first material with the sonic velocity in the first material.
R_2 which is the acoustic impedance of the second material is calculated by multiplying the density of the second material with the sonic velocity in the second material. R is calculated (K.3).

$$R = R_0 \left(\frac{\rho_1 C_1 - \rho_2 C_2}{\rho_1 C_1 + \rho_2 C_2}\right)^2 \qquad (K.3)$$

R is the ultrasonic energy which is reflected
R_0 is the ultrasonic energy which is incident

The reflected energy percentage can be as high as 100% in the case of a gas to solid boundary also keeping in mind that in a transmitter - receiver set up the boundary layer needs to be traversed by the sonic energy twice [30]. In the case of boundary involving a liquid and a solid such as steel the energy transmitted through the boundary would equate to circa 12% which would equate to 1.4% of the energy arriving at the receiver

if one considers that there would be two boundaries in a system. This computation equates to a perfect boundary system as in reality this would further reduce if one equates energy lost in other ways such as dispersion. Liquids are therefore used as coupling fluids in view that air boundaries reflect close to 100% of the incident radiation. Different liquids have different acoustic impedances.

Focusing and steering the sonic beam.

The time delay for the propagation of the wave from the transducer to a point x in the fluid as shown in Figure K.3 is outlined by equation (K.4) [155].

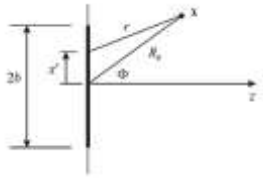

Figure K.3 ~ Focusing one element to a point x [155].

$$\Delta t = \frac{r - R_0}{c} = \frac{\sqrt{R_0^2 + (x')^2 - 2x'R_0 sin\Phi} - R_0}{c} \qquad \text{(K.4)}$$

Where

R_0 is the distance to the focal point x at an angle Φ
c is the speed of sound in the fluid

The two subsections below will show concretely how the waveforms may interact with each other constructively or destructively by changing the phase and weighting of the signal arriving to each element.

Transmission

Figure K.4 presents a concept of a phased array with five transmitters each of which can be driven with an electrical excitation signal. In this case the five transmitters are being operated with exactly the same excitation signal.

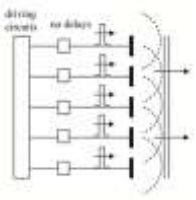

Figure K.4 ~ A phased array in which the driving electrical are not delayed with reference to each antenna – i.e. no phase shift [155].

The excitation signal causes each of the transmitters to radiate a spherical wave as shown by the spherical dashed lines. By implementing delays in the signal being fed to each of the transmitters the spherical waves from each would no longer be emanated at the same time as shown in Figure K.5.

(a) (b)

Figure K.5 ~ Beam being steered through specific delays introduced in the signal to each of the transmitters [155].

In this case the beam is effectively being steered and focused without any actual physical movement of the antennas.

Such beam manipulations can be conducted by introducing delays into the signal being fed into each of the PMUTs as shown in Figure K.6.

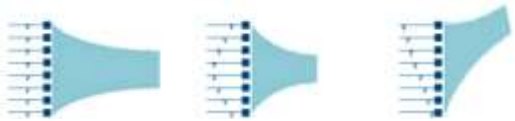

Figure K.6 ~ A schematic which shows the principles of ultrasonic beam steering and focusing in an array system [100].

Through a studied and exact manipulation of the signal being provided to each of the elements forming up the phased array various scanning techniques can be achieved as shown in Figure K.7.

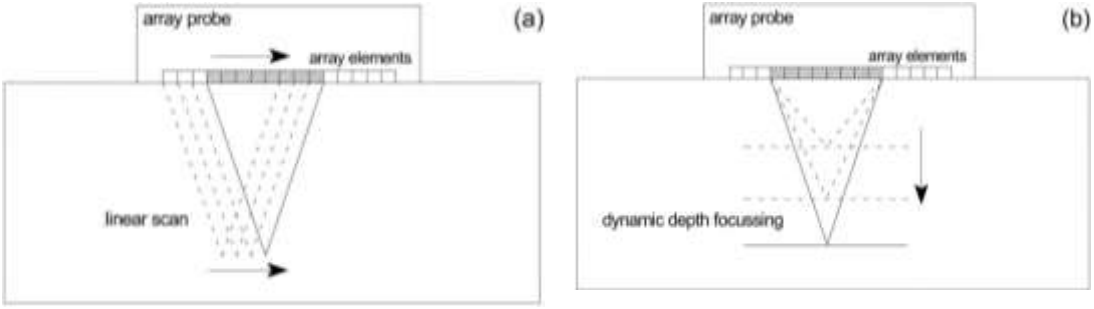

Figure K.7 ~ Phased array performing (a) A linear Scan, and (b) Dynamic depth focusing [155].

Through dynamic phase shifting sectoral scanning as shown in Figure K.8 can be conducted thus enabling cross communication between devices. This enables them to circumvent any acoustic obstacles which might be in the communication paths.

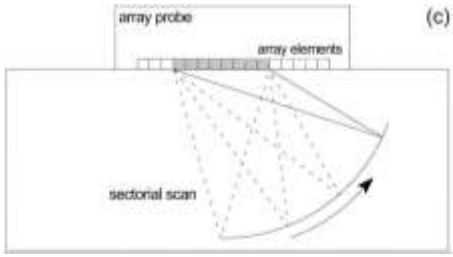

Figure K.8 ~ Phased array performing beam sweeping [155].

Reception

The phased array is also very useful for the reception component of the system as shown in Figure K.9.

(a) (b)

Figure K.9 ~ The phased array operations in receiving mode. It can be seen that (a) the array enhances signals received at an angle through the application of delays and summation and (b) signals being received from a shaped wave front are also similarly enhanced [155].

As can be seen in through the application of delays and a summation a signal arriving at an angle to the array can be enhanced with a single high amplitude signal being produced from the multitude of received small amplitude signals. This high amplitude signal would be similar to what would have been received by one transducer had it been facing the incoming waveform directly.

Array shapes

Literature has in indicated that individual ultrasonic transmitters have been set up in various array set ups, two of the simplest being the linear and the 2D arrays as shown in Figure K.10.

(a) (b)

Figure K.10 ~ Schematics showing (a)A linear array (b) A 2D array with uniform spacing [134].

The 2D phased arrays may also be organised in various patterns as shown in Figure K.11.

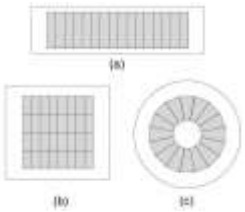

Figure K.11 ~ Phased array patterns with (a) Linear array with 16 elements, (b) Matrix array with 32 elements, and (c) annular array with 16 elements [107].

Through beam steering carried as outlined here the point of focus and direction of the beam may also be altered in such a way as to achieve optimal angles to deliver the incident sonic energy into the structure as outlined in Figure K.12.

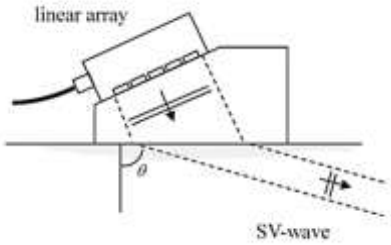

Figure K.12 ~ Shear Waves created with an array system. The angle can be varied by the phase difference.

At this stage it is essential to look closer at the mathematics needed to enable the calculation of the phase shifts which are so crucial for the phased array to operate. As discussed above in a phased array, time delays need to be implemented for each element. This is possible to be emulated by implementing phase shifts and indeed this is the common approach in many practical applications as reviewed in literature [156].

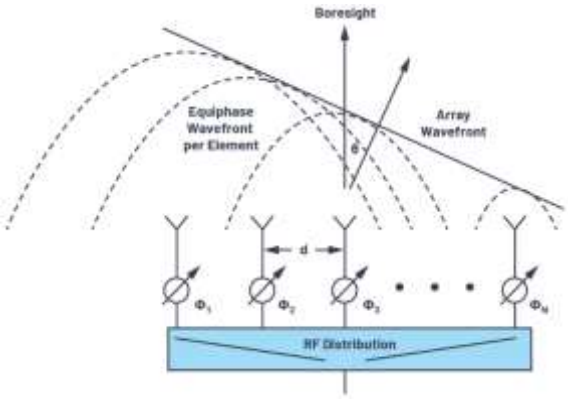

Figure K.13 ~ Concept of a phased array using phase shifting. This example utilises RF however similar geometries hold for ultrasonic physics. [156].

Figure K.14 (a) shows an array transmitting a wave front which was steered to an angle θ. The next step is to use geometrical manipulations to determine the phase shift ΔΦ.

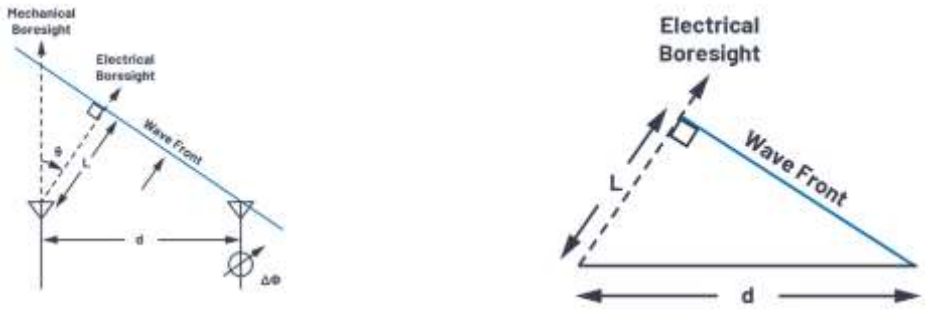

(a) (b)

Figure K.14 ~ Diagram (a) shows a two element array with a phase shift implemented in one of the elements (b) geometric manipulation of the wave front [156].

From the system shown in Figure K.14 the geometrically constructed triangle shown in Figure K.15 can be derived.

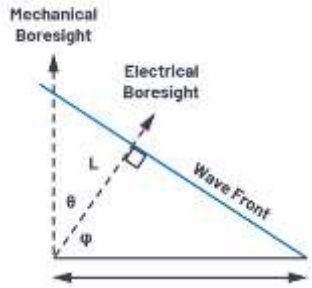

Figure K.15 ~ Geometrical derivation of phase shifts needed to achieve the beam steering angle [156].

From Figure K.15 one can derive the phase shift starting by equation (K.5) below [156].

$$cos\varphi = \frac{L}{d} \tag{K.5}$$

Where

$\varphi + \theta = 90^o$

$cos\varphi = \cos(90^o - \theta) = sin\theta$

$I = dsin\theta, \Delta t = \frac{L}{c}$

Where c is the wave propagation speed

$\Delta\Phi = dsin\theta, \Delta t = \frac{2\pi L}{\lambda} = \frac{2\pi dsin\theta}{\lambda}$

If $d = \frac{\lambda}{2}, \Delta\Phi = \pi sin\theta$

To be able to manipulate the whole antenna gain as a pattern one needs to keep in mind both the Element Factor (G_E) which is the gain of each individual element making up the array and the Array Factor (G_A). The latter is a function of the impact pertaining from the beamforming capabilities of the array. The concepts are shown in Figure K.16.

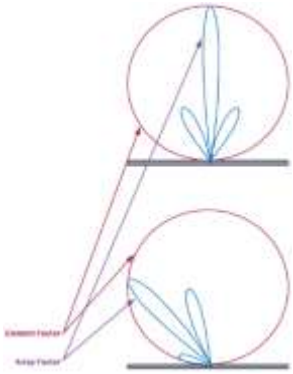

Figure K.16 ~ Diagram showing the Element and array factors [156].

The equation for the phase array hydrophone gain pattern is given by (K.6)

$$G(\theta) = G_E(\theta) + G_A(\theta) \tag{K.6}$$

$G_E(\theta)$ is defined by the PMUT geometries and materials and therefore the focus here would be on the array factor. The array factor is expressed as per (K.7) [156].

$$AF[\theta] = \frac{sin\left(\frac{N\pi d}{\lambda}[sin(\theta) - \sin(\theta_0)]\right)}{Nsin\left(\frac{\pi d}{\lambda}[sin(\theta) - \sin(\theta_0)]\right)} \tag{K.7}$$

Where

θ_0 is the beam angle.

Therefore the Array Factor in terms of phase difference would be as shown in (K.8)

$$\mathrm{AF}[\theta, \Delta\Phi] = \frac{sin\left(N\left[\frac{\pi d}{\lambda}\sin(\theta) - \frac{\Delta\Phi}{2}\right]\right)}{Nsin\left(\frac{\pi d}{\lambda}\sin(\theta) - \frac{\Delta\Phi}{2}\right)} \tag{K.8}$$

Appendix L: Array Design and spacing of the elements.

This appendix will provide an overview of the simulations and studies conducted to study the geometries needed for the array design. The next part of the dissertation will look at how to integrate the selected PMUT design to operate together with other PMUTs in the form of a steerable phased array. For the theory underlying the below one needs to refer to the theory section in Appendix K.

When operating in transmission mode the phased array needs to:

- Achieve a focused beam with a small width, hence requiring a large number of transducers.
- The beam should also be steerable to enable the device to reach out to devices which are not directly perpendicular over the transmitting device.
- Achieve the highest power density possible from the limited die size available.

To understand how arrays function one needs to look at how the various antenna elements interact with each other. This was conducted theoretically from first principles by building arrays starting from 2 x 1 up to 20 x 20.

The first array geometry simulated with MATLAB, with the result being shown in Figure L.1 shown in consisted of an array with two elements being spaced ½λ apart. Coupling fluid was selected as being isopropanol meaning that the propagation speed was set at 1207 m/s. The frequency of operation was set at 90 kHz. The spacing in this case is 6.71 mm.

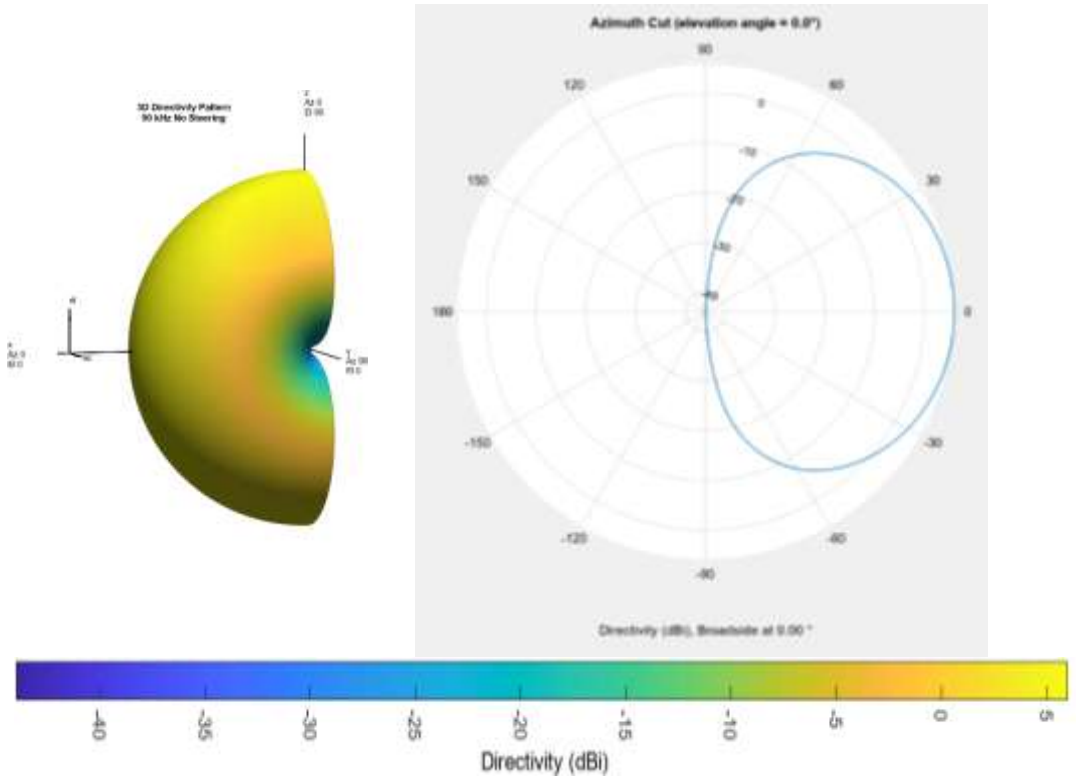

Figure L.1 ~ Two elements set at ½ wavelength away from each other showing both the Azimuth pattern and the array geometry.

The next model set up in MATLAB was of a Uniform Linear Array (ULA) made up four element with the array span being a total of 20.12 mm. The azimuth pattern and azimuth pattern are shown in Figure L.2.

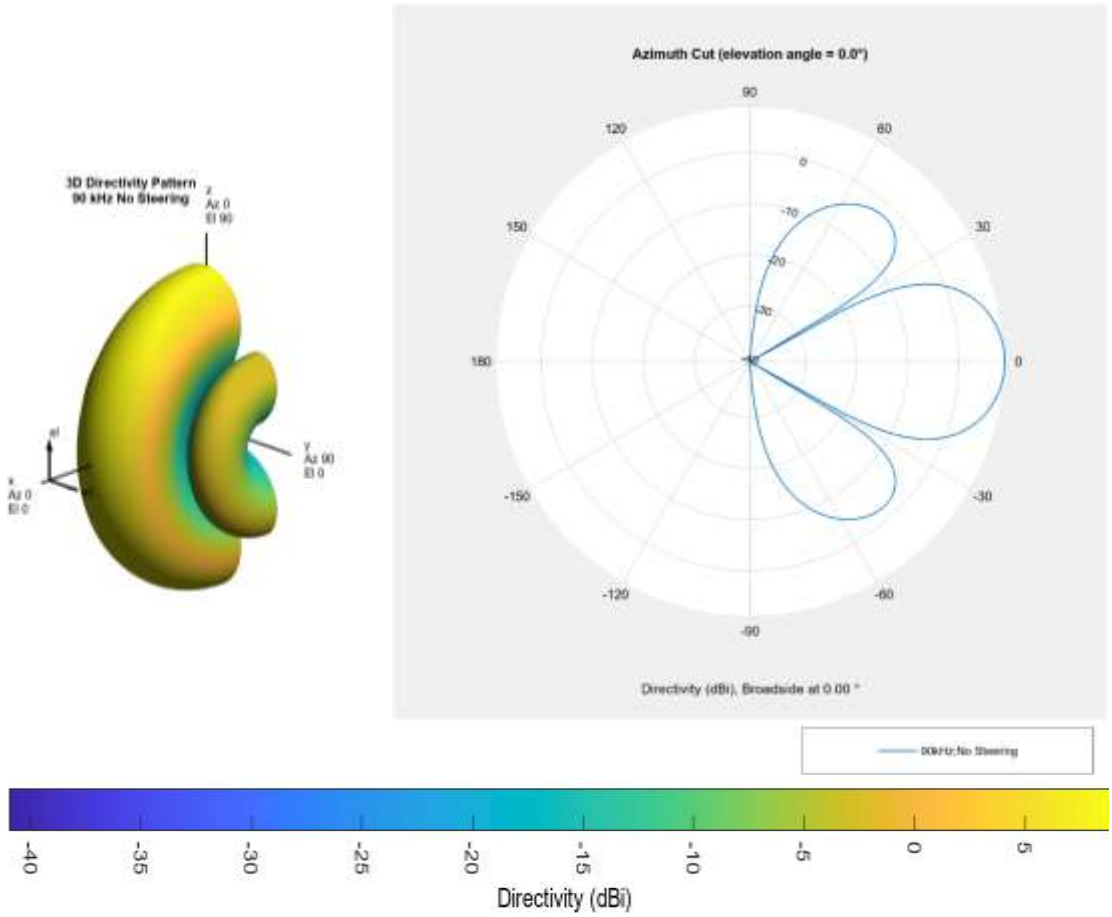

Figure L.2 ~ A 4 element in Line Uniform Linear array.

By implementing phase delays to individual elements the beam can be steered as outlined in the theory Appendix K. In this model, the beam was shifted by 20° on the azimuth as shown in Figure L.3. One can see how the main lobe moves by 20°. The main lobe is still quite wide for an effective beam.

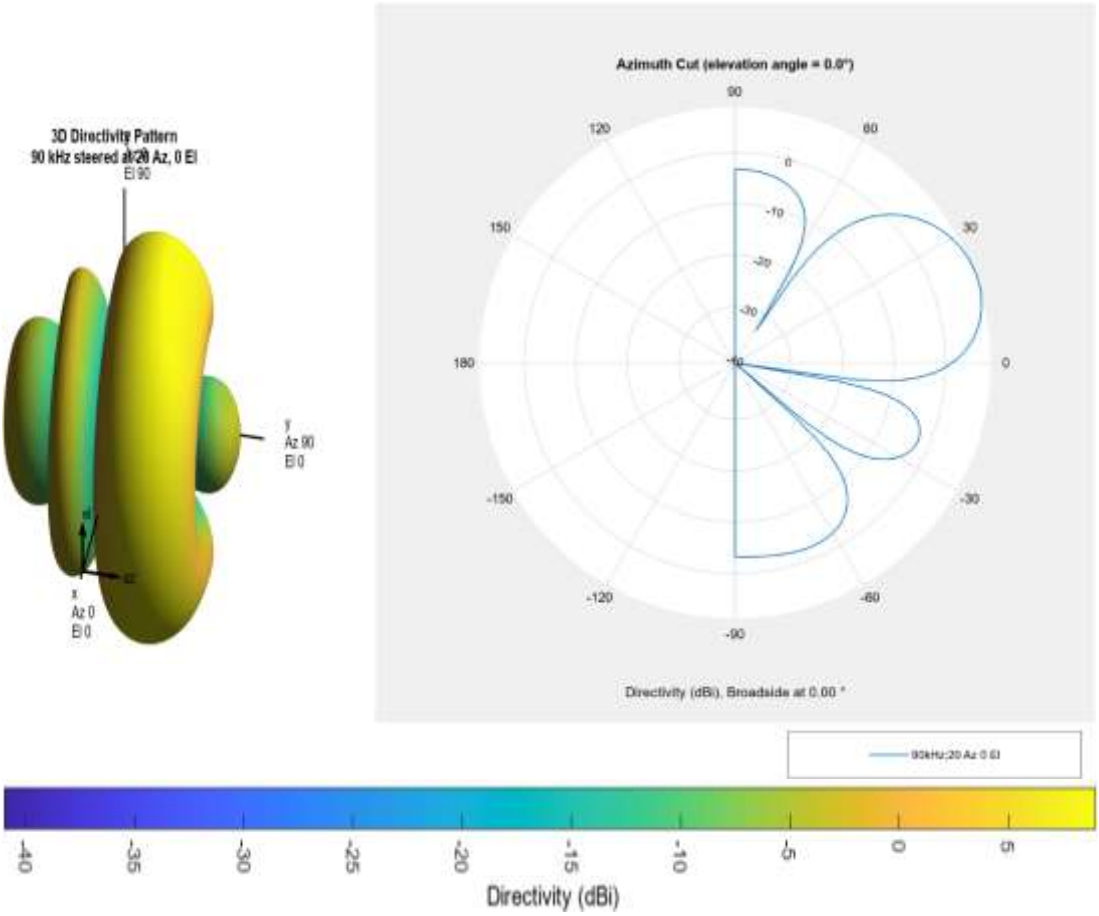

Figure L.3 ~ A 4 element Uniform Linear Array with beam shifted by 20°. Simulation conducted on MATLAB.

In this case the Half Power Beam Width (HPBW) was 26.30° Azimuth and 180° elevation. The HPBW is the angular width of the main lobe at the half power point. The First Null Beam Width (FNBW) on the other hand is an angular width measurement, taken between the first side lobes (or nulls).

These concepts can be seen explained further in Figure L.4.

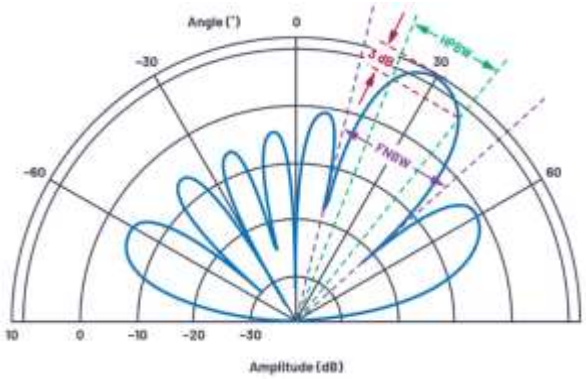

Figure L.4 ~ Diagram showing the lobe diagram depicting the First Null Beam Width and the Half Power Beam Width [156].

The next model set up and simulated on MATLAB was an evolution of the Uniform Linear Array into a Uniform rectangular array. In this case the model was an array

having a square structure with a four by four array with point source isotropic sources. The array has a dimension of 20.12 mm by 20.12 mm. The result of the MATLAB simulation can be seen in Figure L.5

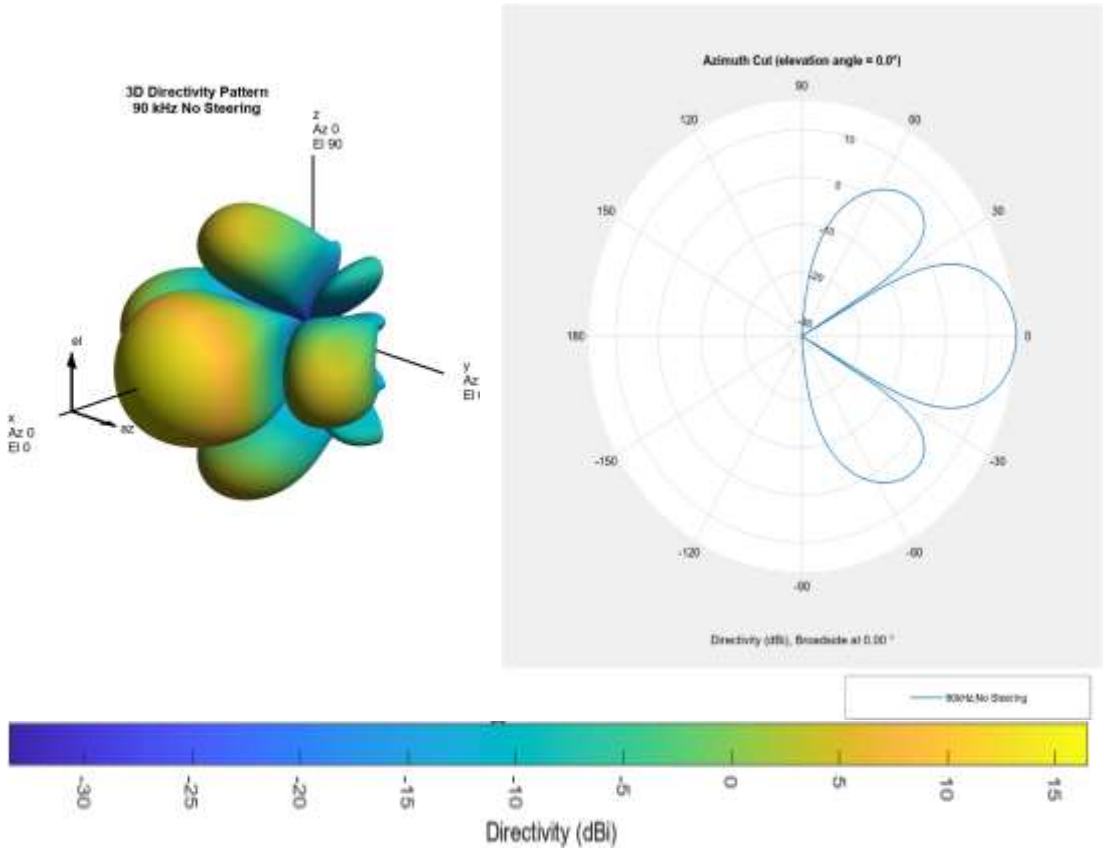

Figure L.5 ~ Azimuth Pattern and 2D pattern from a four by four Universal Rectangular Array. Simulation conducted on MATLAB.

The 4 by 4 isotropic source transducer array was next enhanced to a 10 by 10 isotropic source array on MATLAB. The dimensions for these point sources making up the array would be 60.35 mm x 60.35 mm as can be seen in Figure L.6.

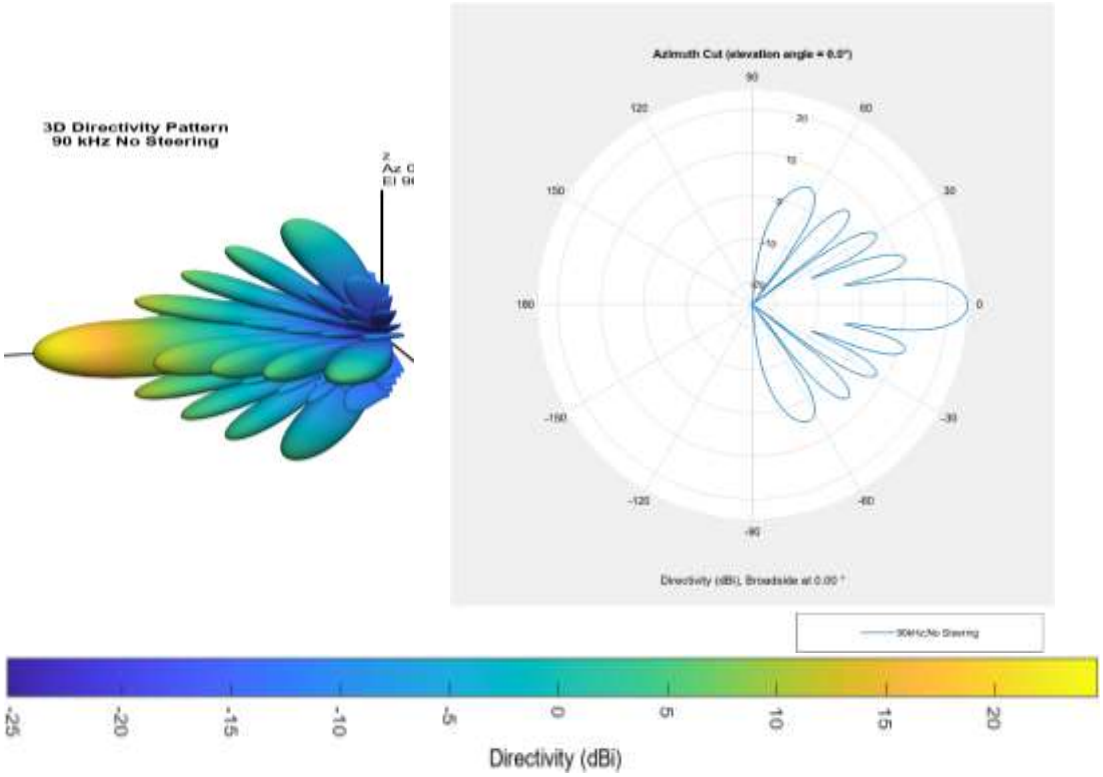

Figure L.6 ~ 3D and azimuth patterns of a 10x10 isotropic ultrasonic emitter array. Simulation conducted on MATLAB.

The next model demonstrate a 20 x 20 array again with ½ λ wavelength spacing showing the further narrowing of the beam. This would have 400 separate single point isotropic elements as shown in Figure L.7.

Figure L.7 ~ The geometric formation of the 10x10 array.

In this case the array directivity would be 30.86 dBi at 0° Azimuth.

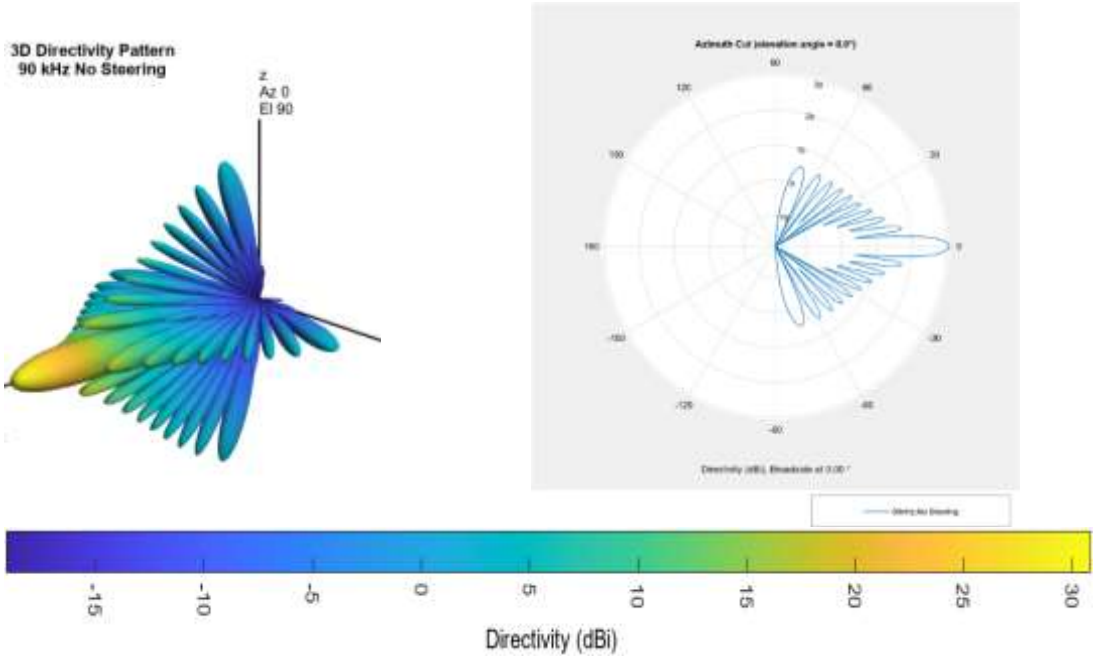

Figure L.8 ~ 3D and azimuth patterns of a 20 x 20 array having ½ λ spacing. Simulation conducted on MATLAB.

As can be seen with the response in U space achieved from the MATLAB simulation as shown in Figure L.9 is sharp and focused. The conclusion from this simulation is that the more elements that are added to the array the more focused the beam would be.

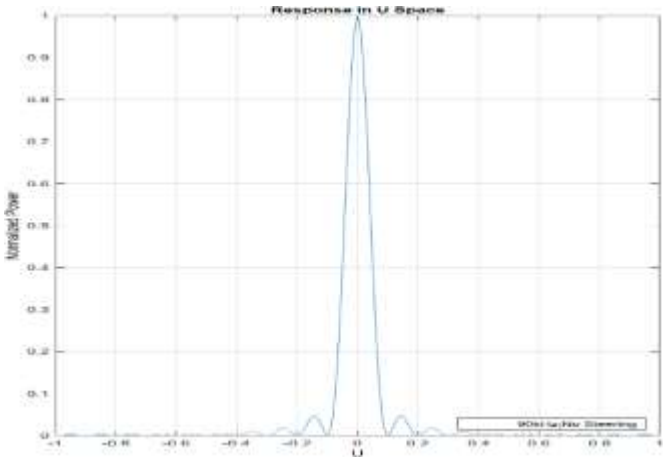

Figure L.9 ~ Response in U space for the 20 x20 array. Simulation conducted on MATLAB.

A contrasting example also simulated on MATLAB shown below in Figure L.10 presents the same number of elements but with ¼ λ separation. The size of the array would be 63.7 mm x 63.7 mm. The array directivity would be 24.94 dBi at 0 azimuth.

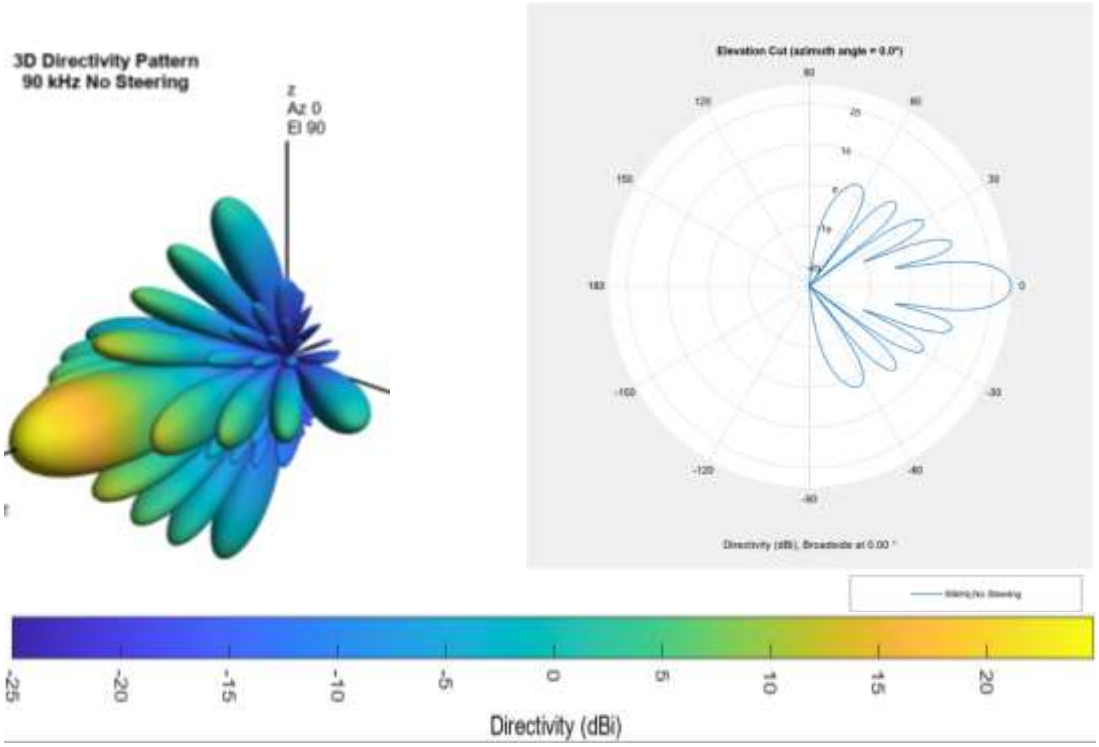

Figure L.10 ~ 3D and azimuth patterns of a 20x20 array with ¼ λ spacing. Simulation conducted on MATLAB.

The 20 by 20 isotropic array shown in Figure L.11 presents the MATLAB result of a simulation presenting the concept of beam steering with the main lobe shifted by 20 azimuth.

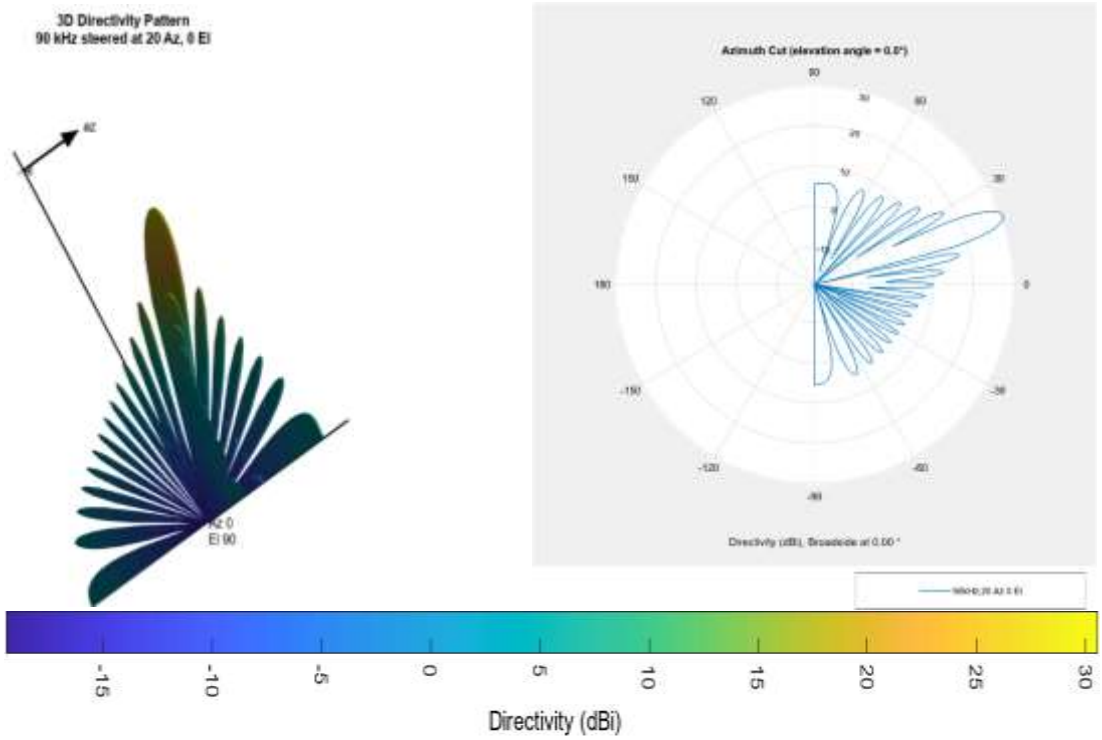

Figure L.11 ~ The 3D and azimuth patterns of a 20 x 20 array with ½ λ spacing but with beam shifted by 20° azimuth. Simulation conducted on MATLAB.

Beam forming is a very important concept as simply packing in elements without the necessary beam forming being conducted would not only be a waste of expensive die surface but actually impact performance such as impacting the beam geometry itself.

To illustrate this a 30 x 30 isotropic element array was designed with a spacing of 0.1 λ as shown in Figure L.12. This 30 by 30 isotropic element array had a total of 900 elements making it up.

Figure L.12 ~ A 30x30 array with 0.1 λ spacing

By comparing this array to arrays having fewer elements but with ½ λ spacing presented before one can see that the output beam energy is less focused than for example the 20 by 20 element array. As can be seen in the array directivity for this particular example was 20.57 dBi at 0° azimuth and elevation. This was clearly less effective in terms of transducer utilisation than the 24.94 dBi achieved on the 20x20 element array with ½ λ spacing presented earlier in this dissertation.

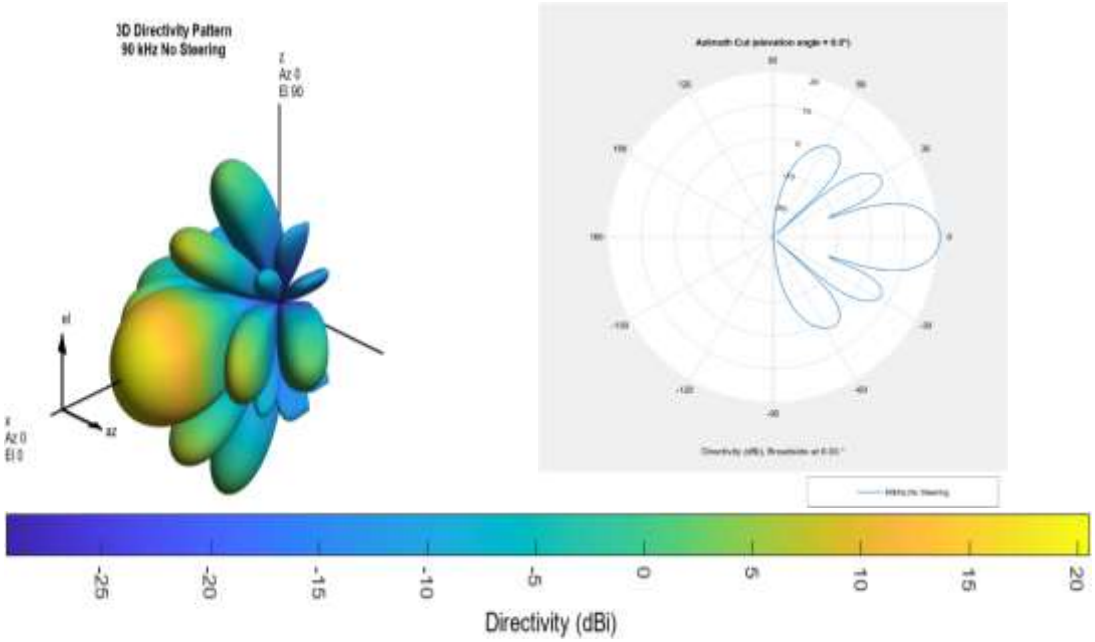

Figure L.13 ~ 3D and azimuth patterns of a 30x30 array with a 0.1λ spacing

For this particular example The HPBW was calculated on MATLAB at 16.98° Azimuth and 18º Elevation. The FNBW was 38.94° Azimuth and 38° Elevation.

MATLAB scripts were designed to be able to create the steering vectors needed to steer arrays. The script used the PHASED.URA class found in the MATLAB Phased Array System toolbox. This is typically used to create uniform rectangular arrays made up of elements. The URA is a 2D structure. The MATLAB scripts were then run to provide matrices with the element phase shifts however research in phase shift optimization was not continued as it was deemed beyond the scope of this dissertation.

Appendix M: Finite Element Analysis of an array deployed in concrete.

This appendix outlines finite element analysis conducted to establish how an array would perform when embedded in mortar. Two models were utilised as will be described below.

The first model was a 3D finite element model having a 100 mm^3 mortar cube with a transmitting and receiving device embedded on opposite sides of the mortar cube. This model is simplified and contains no aggregate, or rebar. This model was built to calculate the total pressure produced inside the transmitting capsule by the array. Figure M.1 shows the model.

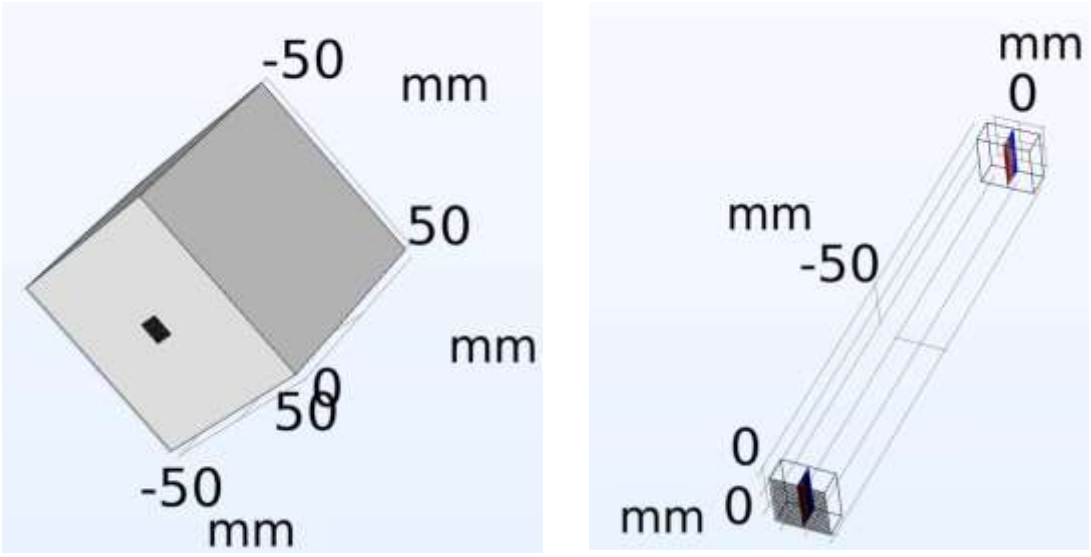

(a) (b)

Figure M.1 ~ (a) 100 mm^3 cube with one of the isopropanol filled capsules visible in the lower face and (b) dimension details of two capsules facing each other.

The two capsules with dimensions 11x11x5 mm where filled with isopropanol. They were set up on opposite sides of the mortar block. A 13 x 13 PMUT array was set up in the transmitting capsule. The frequency utilised was 90,000 Hz and the output from one PMUT was 88,900 Pa. This pressure value was taken from the pressure values achieved from calculations presented in this dissertations.

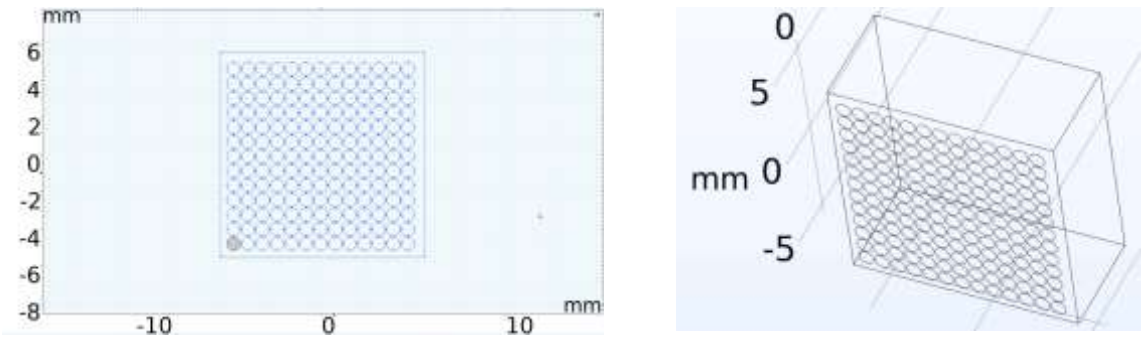

(a) (b)

Figure M.2 ~ (a) Work plane showing the 13x13 PMUT array and (b) the array inside the transmitting isopropanol capsule.

The diameter of the PMUTs used to form the array was 718 μm which diameter was calculated from the diameter vs frequency equation calculated in this dissertation. The Total Acoustic Pressure calculated at the outside envelope of the transmitting capsule is shown in Figure M.3.

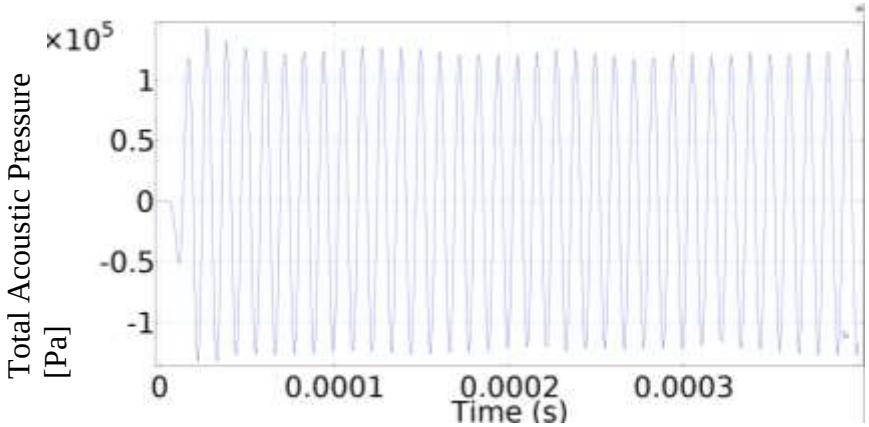

Figure M.3 ~ The total acoustic pressure measure at the outside envelope of the transmitting capsule in the 100 mm^3 cube model.

From Figure M.3 it can be seen that the pressure created in the transmitting capsule was above the 1.2 x10^5 Pa mark. This value was then used to set the second finite element model.

The second model design to study array performance in concrete is shown in Figure M.4.

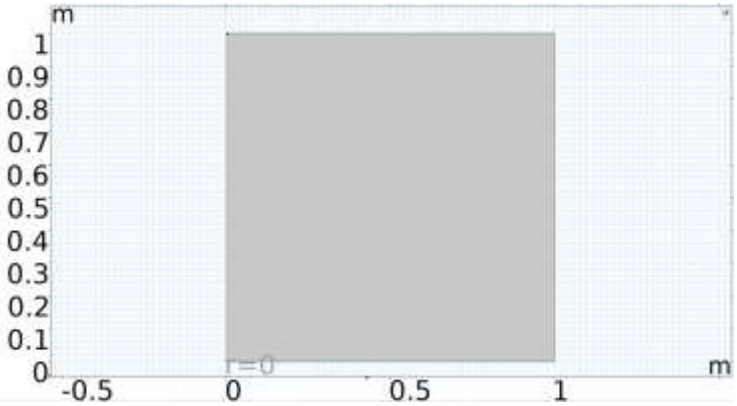

Figure M.4 ~ The 2D axisymmetric model showing the 1 m long mortar cylinder and the upper and lower encapsulated devices.

It was constructed out of a 1 m high mortar cylinder having a 1 m radius with the midpoint being the capsules' centre point. A section through the transmitting and receiving capsules is shown in Figure M.5 showing the outgoing ultrasonic radiation. The capsules were made from polyethylene having a 10 mm diameter with a 1 mm capsular wall thickness. The capsule was filled with isopropanol with a glycerine layer placed over the capsule to couple the capsule with the concrete structure in which the capsule was embedded.

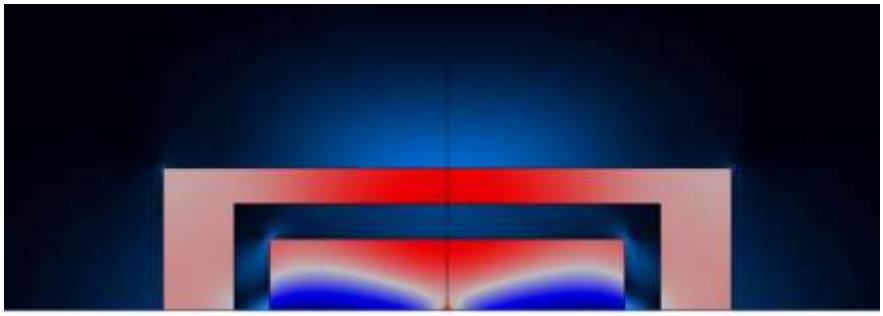

Figure M.5 ~ Section through the concrete, and the transmitting device's encapsulation.

Due to the axisymmetric nature of the model an array could not be created but instead was modelled by an incident pressure field having an amplitude of $1x10^5$ Pa at a frequency of 90 kHz. This amplitude was selected based on the results achieved from the first model. Figure M.6 shows the calculated pressure values at the bottom and top of the capsule.

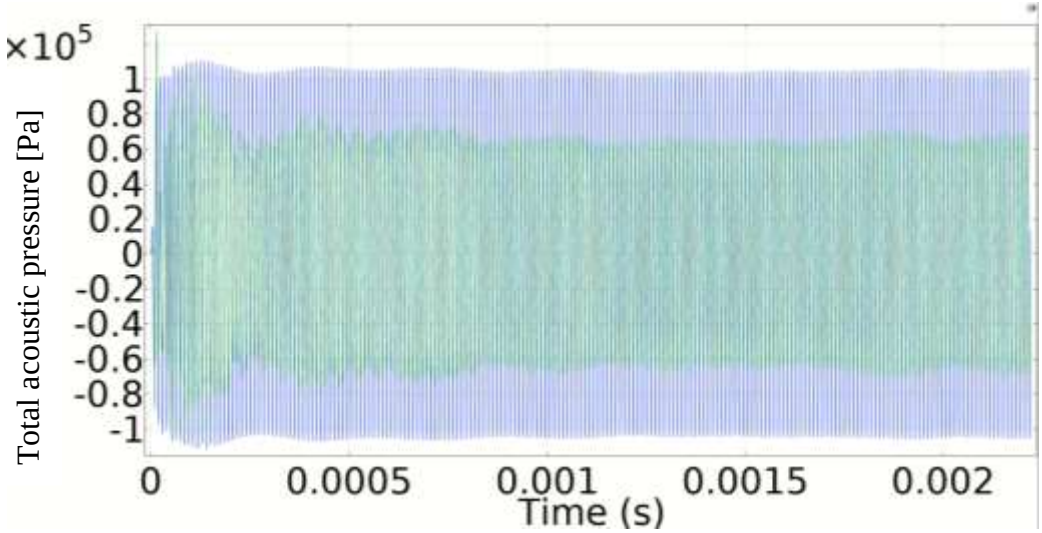

Figure M.6 ~ Total acoustic pressure (Pa) calculated in the transmitting capsule.

Figure M.7 shows the full transmission path through the mortar between the transmitting and receiving capsules.

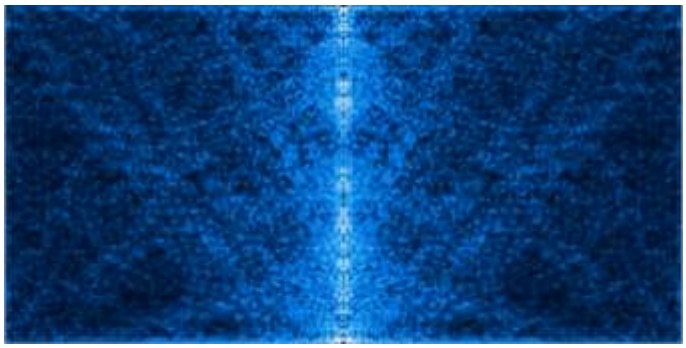

Upper bar- Transmitting capsule pressure, middle bar – Solid Misses, lower bar pressure in reciving capsule.

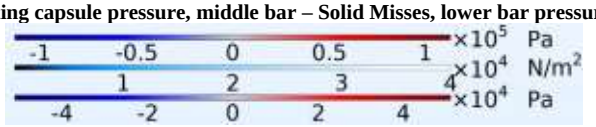

Figure M.7 ~ Total Acoustic Pressure (Pa) and solid misses at 0.0022222 seconds since start of excitation.

The operation of the transmitting and receiving capsules is shown in more detail in Figure M.8.

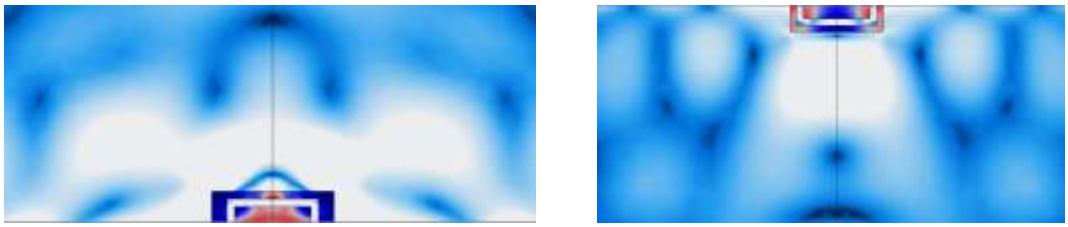

(a) (b)

Upper bar- Transmitting capsule pressure, middle bar – Solid Misses, lower bar pressure in reciving capsule.

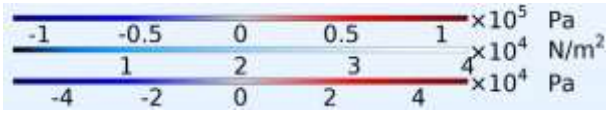

Figure M.8 ~ Total acoustic pressure (Pa) and solid misses through solids at time 0.0022222 seconds from start of excitation. Figure (a) shows the transmitting capsule and (b) shows the receiving capsule.

The total acoustic pressure in the receiving capsule is shown in Figure M.9 showing the increase in pressure inside the receiving capsule.

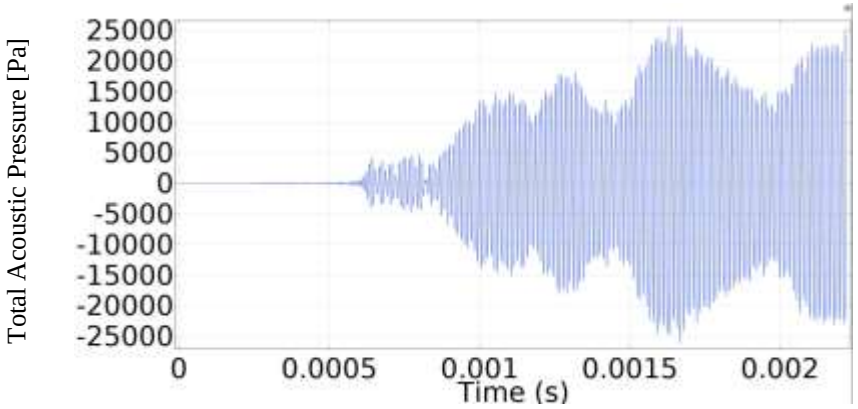

Figure M.9 ~ Total acoustic pressure calculated at the receiving capsule (Pa).

This figure and the results of this finite element modelling therefore demonstrate that it is theoretically possible to achieve pressures exceeding 20 kPa in a receiving capsule situated a meter away with both transmitting and receiving capsules embedded in reinforced concrete. This shows the technical feasibility of having such a system

Appendix N: Further modified diaphragm conceptual devices which were developed.

This appendix will outline and present other modified diaphragm designs that were modelled and tested experimentally. They will not be covered in detail in this text given that they were not seen as having achieved significant performance improvements over simpler, axisymmetric devices presented in this dissertation. However they are being mentioned to present the reader with the extent of the research areas covered to develop new innovative designs and improve design performance. These devices can also be the basis of future development of new devices having particular properties. All the devices presented in this section of the dissertation, including Device 48 are novel designs.

Figure N.1 shows a 900 μm cavity diameter device with holes fabricated through the electrode, piezo layer and diaphragm.

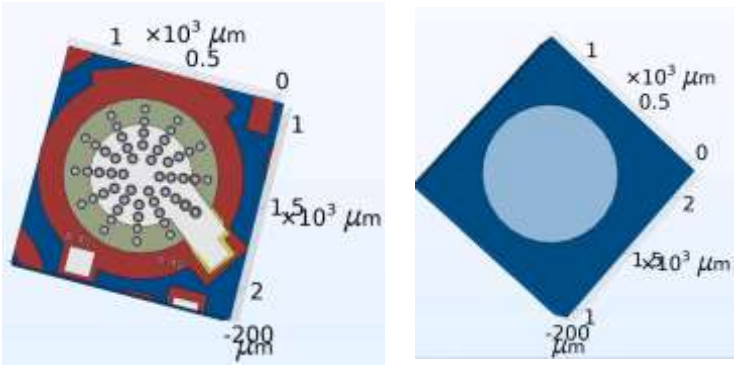

(a) (b)

Figure N.1 ~ FEM showing (a) Front side and (b) backside of a 900 μm device with holes through diaphragm. Referred to as Device 40 in the experimental MEMS device.

The holes were 40 micron in diameter. However as shown in Figure N.2 each of the holes had a complex deign since they needed to be constructed in a way which ensured separation between the upper and lower electrodes.

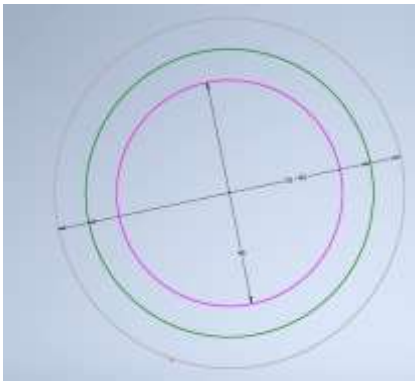

Figure N.2 ~ Dimensions of hole structure through the various layers. The inside hole marked in purple had a diameter of 40 μm. That hole passed right through the SOI layer right into the trench. The next opening with a diameter of 51 μm opened up the AlN layer. The final opening at 62 μm opened the pad metal layer.

Figure N.3 shows another experimental design with holes produced around the central electrode.

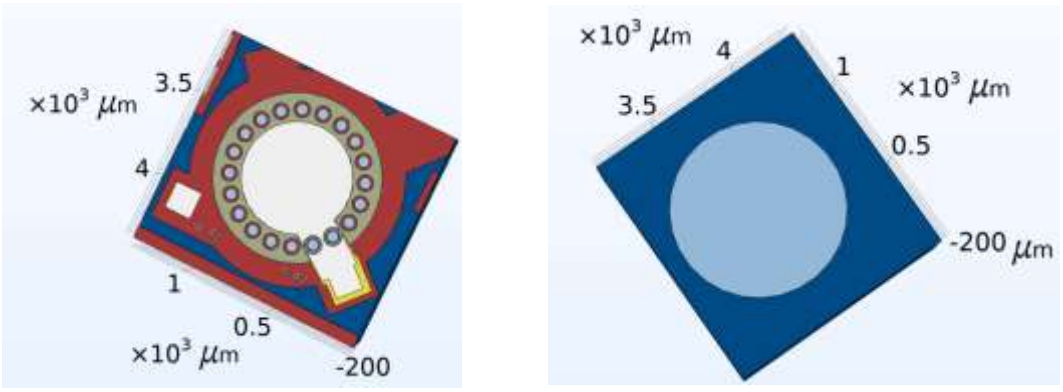

(a) (b)

Figure N.3 ~ FEM showing (a) Front side and (b) backside of a 1,000 µm device with slots through diaphragm. Referred to as Device 42 in the experimental MEMS device.

In this case the holes are 60 microns in diameter. The holes in Device 42 are more complex than those of Device 40 shown in Figure N.2 since these also have the oxide layer incorporated. The detail of these holes are shown in Figure N.4.

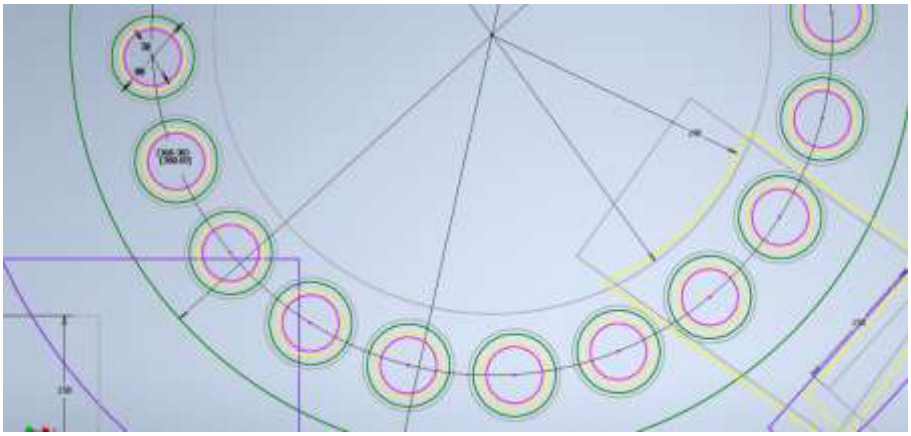

Figure N.4 ~ Details of Device 42 showing the blueprint details of the hole structure.

Figure N.5 shows a 1,000 µm device modified with a different supporting structure than that presented for Device 48.

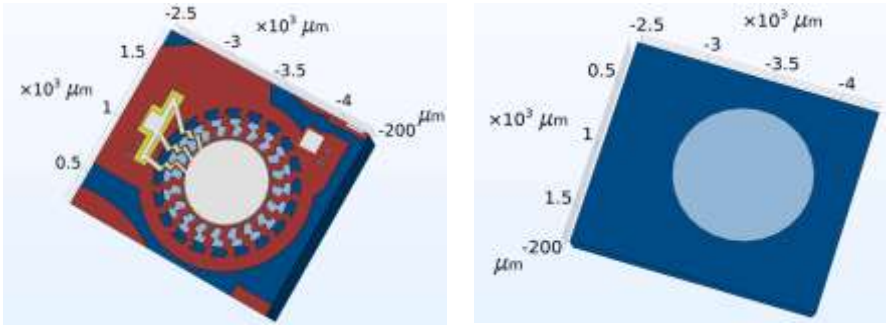

(a) (b)

Figure N.5 ~ FEM showing (a) Front side and (b) backside of a 1,000 µm device with slots through diaphragm. Referred to as Device 28 in the experimental MEMS device.

The details of the design is shown in Figure N.6.

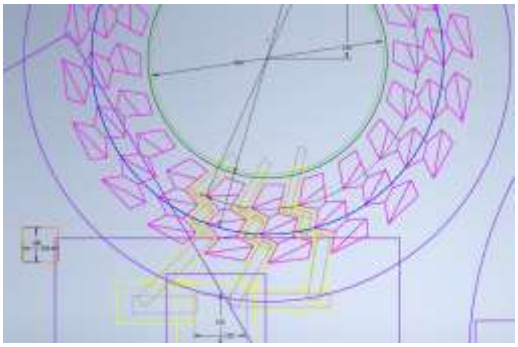

Figure N.6 ~ Design showing dimensions of device 28 including details of the support and electrical conduction.

Figure N.7 shows the 3 D image of a device with slots cut out around the central electrode. This was given the number of Device 41.

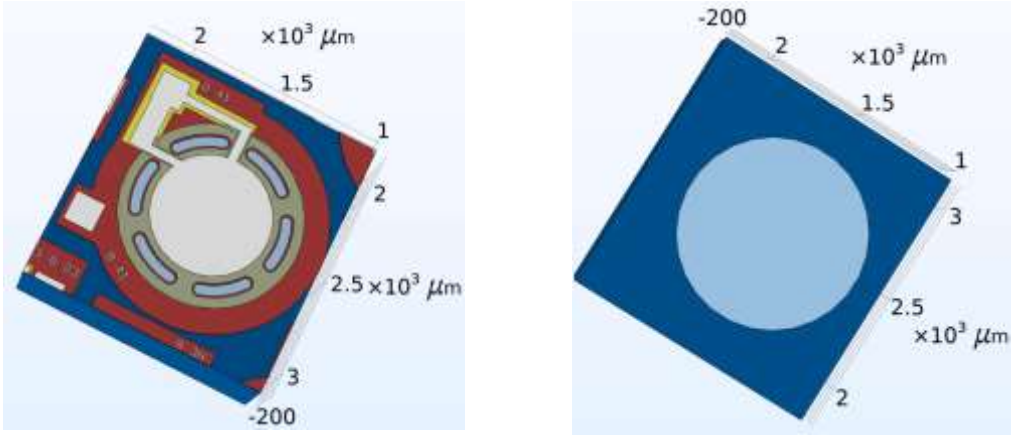

(a) (b)

Figure N.7 ~ FEM showing (a) Front side and (b) backside of a 900 μm diameter device with elliptical slots cut into the area around the electrode. Referred to as Device 41 in the experimental MEMS device.

The details of the geometry involved is shown in Figure N.8.

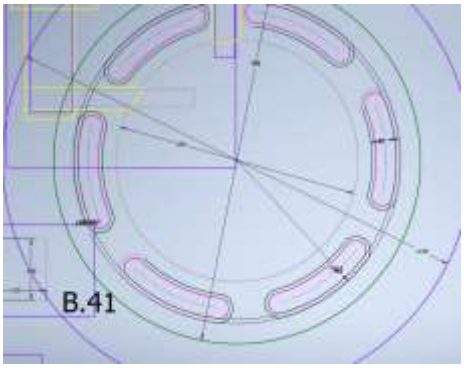

Figure N.8 ~ Details of the slot structure of Device 41

Appendix O: Modelling thermal and viscous losses through the Thermoviscous Acoustics module.

This appendix outlines the FEM process behind the decision taken on whether to include a thermoviscous layer in the final model. In geometrically small structures the attenuation of sound waves due to thermal and viscous effects may be pronounced and therefore need to be investigated. The effect due to these two effects can lower the resonant frequency and amplitude. In such case the equations for Thermoviscous acoustics would be solved through the Navier Stokes equations apart from the equations for mass (continuity) as well as energy conservation [157].

The length of the viscous and thermal layers are equated together by the Prandtl number as shown in equation (O.1) [150]

$$\delta_{visc} = \sqrt{Pr}\,\delta_{therm} \tag{O.1}$$

where

$$P_r = \frac{C_p \mu}{k} \tag{O.2}$$

and

- C_p is the heat capacity of the fluid measured at constant pressure
- μ is the dynamic viscosity of the fluid measuring the resistance of the fluid to shearing.
- k is the coefficient of thermal conduction

The viscous boundary layer thickness can be found shown in equation (O.3) [150]:

$$\delta_{visc} = \sqrt{\frac{2\mu}{\omega \rho_0}} \tag{O.3}$$

While the thermal boundary layer thickness can be found in equation (O.4) [150]

$$\delta_{therm} = \sqrt{\frac{2k}{\omega \rho_0 C_p}} \tag{O.4}$$

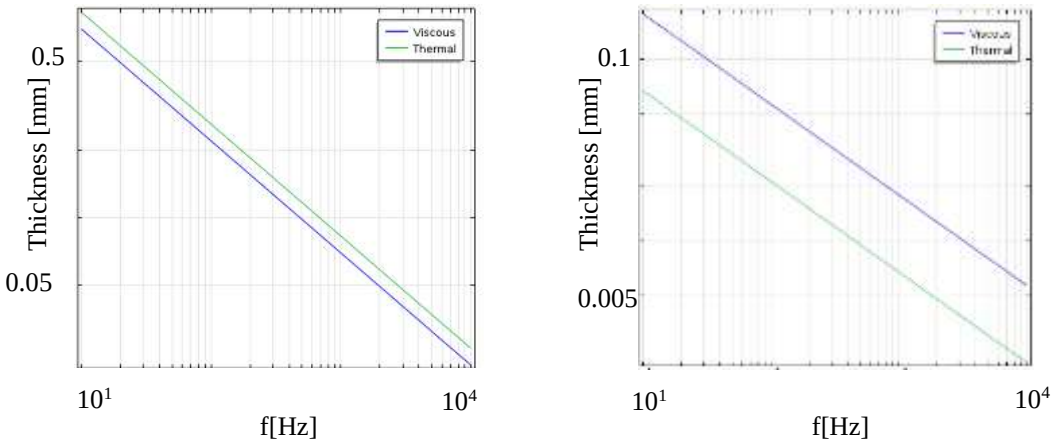

(a) (b)

Figure O.1 ~ Graphs showing the thickness of the thermal and viscous boundary layers for (a) air (b) water as fluids [157].

In the case of this project we are looking at frequencies predominantly between 70 kHz and 100 kHz. With reference to Figure O.1, since the project is therefore focusing on the $1x10^5$ Hz frequency region, the boundary layer in a liquid filled cavity or coupling fluid can be disregarded as its thickness would be in the submicron region. For air, the viscous boundary region would be in the region between 5 to 8 μm and the thermal boundary region at 1.4 times more, would equate to around 10 μm. Hence keeping in mind that the PMUT's diameter of circa 700 μm thermoviscous acoustics was deemed as not being applicable and therefore not implemented in the final model dynamics.

To verify the theory and be sure that thermoviscous physics is not required to achieve an accurate model, two models were set up and the results compared. The first model was built including the thermoviscous damping physics module and the other was set up without the module. The two models were set up in the frequency domain with the value of young's modulus being parametrically swept between 90 GPa and 170 GPa. The model with the thermoviscous physics contained a 0.5 μm thick thermoviscous layer in the liquid coupling fluid.

Figure O.2 and Figure O.3 show the results achieved from the two models. The resonant frequencies presented in these two figures were slightly different from those presented in the main text as the tetrahedral meshing was used for these two models instead of mapped meshing used in the rest of the text.

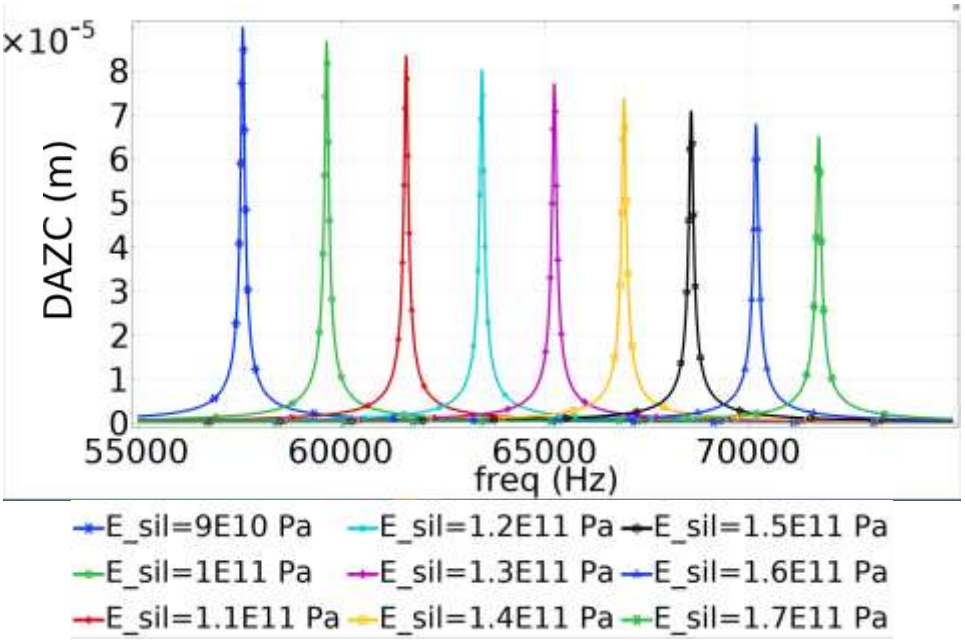

Figure O.2 ~ Frequency domain modelling of a 900 μm PMUT without a 0.5 μm thermoviscous layer included and values of young's modulus swept parametrically in the range from 90 GPa to 170 GPa. Frequencies swept from 40 kHz to 80 kHz in steps of 10 Hz.

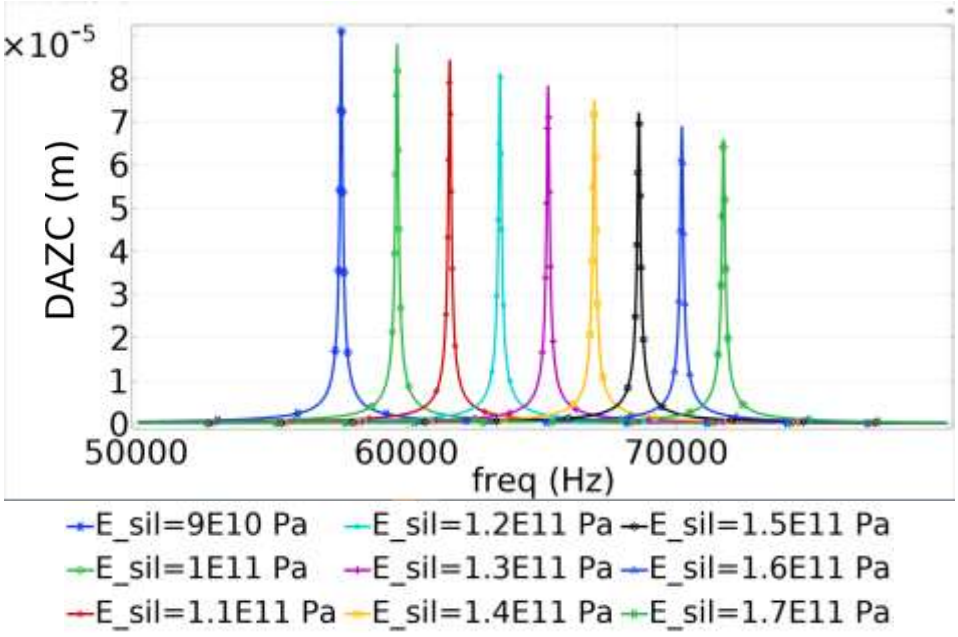

Figure O.3 ~ Frequency domain modelling of a 900 μm PMUT with thermoviscous physics included and values of young's modulus swept parametrically in the range from 90 GPa to 170 GPa. Frequencies swept from 40 kHz to 80 kHz in steps of 10 Hz.

As can be seen in Figure O.3 the maximum displacement of the model without thermoviscous acoustics in the model and with a young's Modulus of 90 GPa was 9.003×10^{-5} m. On the other hand the model presented in Figure O.2 without thermoviscous acoustics returned a displacement of 9.1128×10^{-5} m. This works out to a difference of 1.21% between the two models.

Comparison between the two results therefore show only marginal differences between the two models which therefore confirm that there is no scope to utilise thermoviscous acoustics for the models set up using isopropanol as fluid. The reason being that this would complicate the mathematics needlessly. Suffice it to say that the model with the thermoviscous physics integrated in it, took no less than 42 hours to resolve. Such minute differences in maximum displacement can easily be accounted for through the damping coefficients rather than using thermoviscous damping.

Appendix P: Mask design for the fabrication of the MEMS IC.

This appendix provides details on the lithography work conducted to prepare the masks necessary to fabricate the device. The details of each of the masks will be presented here.

Mask 1 – Lithography level name ~ PADOXIDE

CIF Level name:	POX
GDS Level number:	10
Colour(right):	Yellow

The mask shown in Figure P.1 was designed to indicate the areas where the 2,000 Angstrom thermal oxide is to remain in place.

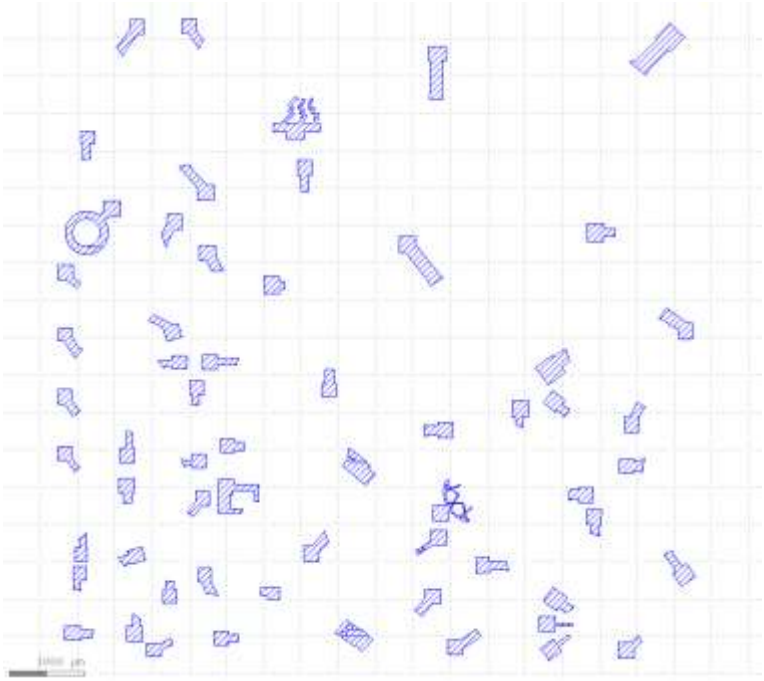

Figure P.1 ~ The final Padoxide lithography mask as designed and sent to the MEMS production facility.

The silicon oxide layer is grown throughout the die at a uniform thickness and the process to remove the desired areas starts by coating the die with a photoresist layer after which the mask is used to pattern this layer through the use of light. A wet etching process removes the unwanted oxide and a follow up acid strip process removes the remaining photoresist.

Mask 2 – Lithography level name ~ PZFILM

CIF Level name: PZF
GDS Level number: 20
Colour (right): Sky Blue

The piezoelectric aluminium nitride is deposited over the entire die through a reactive sputtering process. The wafer is then again coated in photoresist which is then exposed to light through the mask shown in Figure P.2.

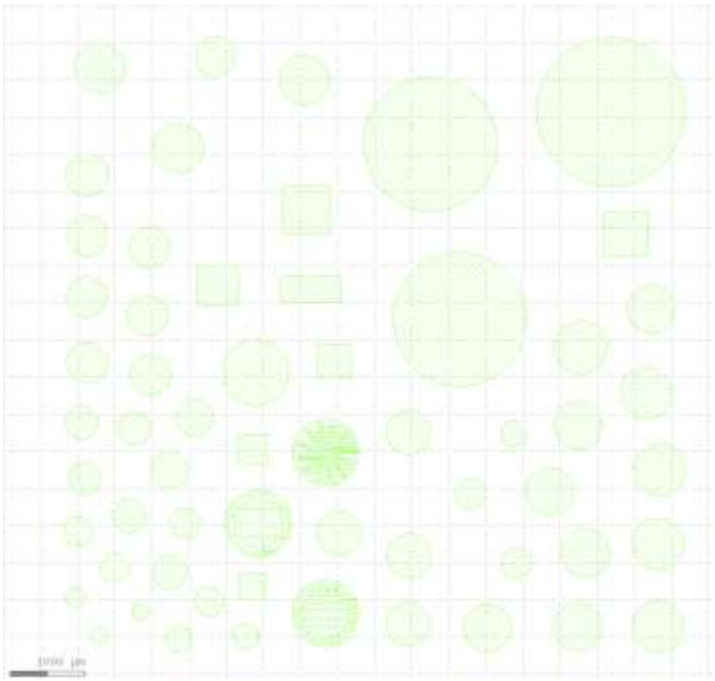

Figure P.2 ~ The final PZfilm lithography mask as designed and sent to the MEMS production facility.

The photoresist layer was then developed, and the wafer wet etched to remove the extra AlN. A solvent strip was then done to remove the remaining photoresist.

Mask 3 – Lithography level name ~ PADMETAL

CIF Level Name: PAD
GDS Level Number: 30
Colour (right): Grey

In this case a negative photoresist was used to coat the entire wafer after which this was lithographically patterned using the mask shown in Figure P.3.

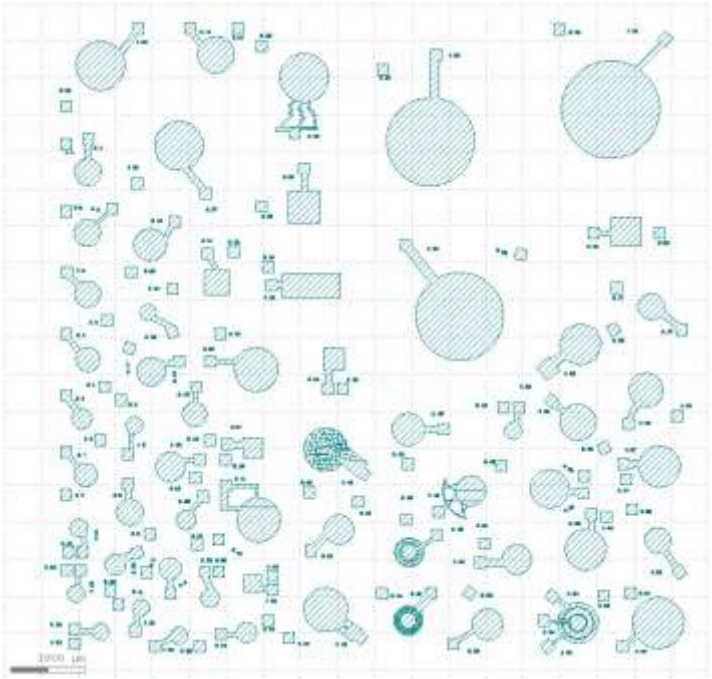

Figure P.3 ~ The final Padmetal lithography mask as sent to the MEMS production facility.

After the photoresist was developed the metal stack, with a 29 nm chrome layer and a 1,000 nm aluminium layer was deposited in the open areas left in the photoresist after it was developed. As done in the other processes the photoresist was then dissolved and removed.

Mask 4 – Lithography level name ~ SOI

CIF Level Name: SOI
GDS Level Number: 40
Colour(right): Pattern in red area

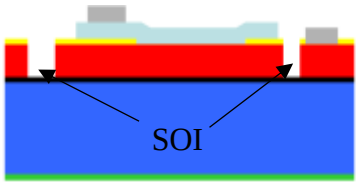

In the silicon patterning process the wafer was again coated in photoresist. This time the 4th mask shown in Figure P.4 was used to pattern the photoresist with UV light. After this patterning, the exposed photoresist was removed with the patterned photoresist being etched through reactive ion etching. A deep reactive ion etching followed to etch right down to the oxide layer.

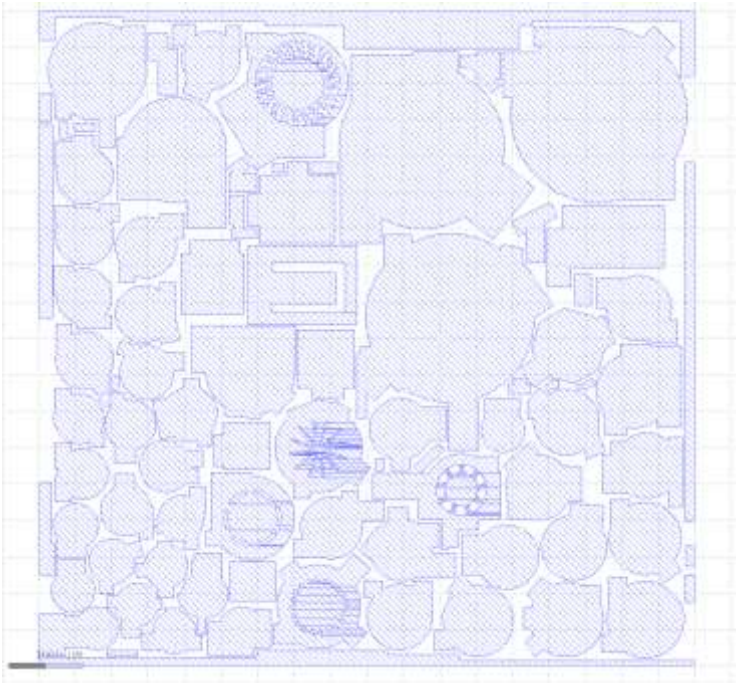

Figure P.4 ~ The final SOI lithography mask as sent to the MEMS production facility.

The photoresist was then again chemically stripped away.

Mask 5 – Lithography level name ~ TRENCH

CIF Level Name: TRCH
GDS Level Number: 50
Colour: Cut in navy blue area

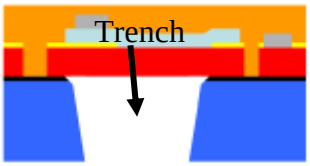

The next step is to apply a coat of polyimide as shown in Figure P.5 to keep the wafer intact, when the trench etching is carried out.

Figure P.5 ~ The polyimide coat is shown in orange.

The bottom was then covered with photoresist and lithographically patterned using the last mask as shown in Figure P.6. Reactive Ion Etching (RIE) followed by DRIE (Deep Reactive Ion Etching) was then used, to remove the bottom side layer thus opening up

the trenches stopping at the oxide layer. This layer was then removed in the open areas defined by the TRENCH mask via a wet etch process.

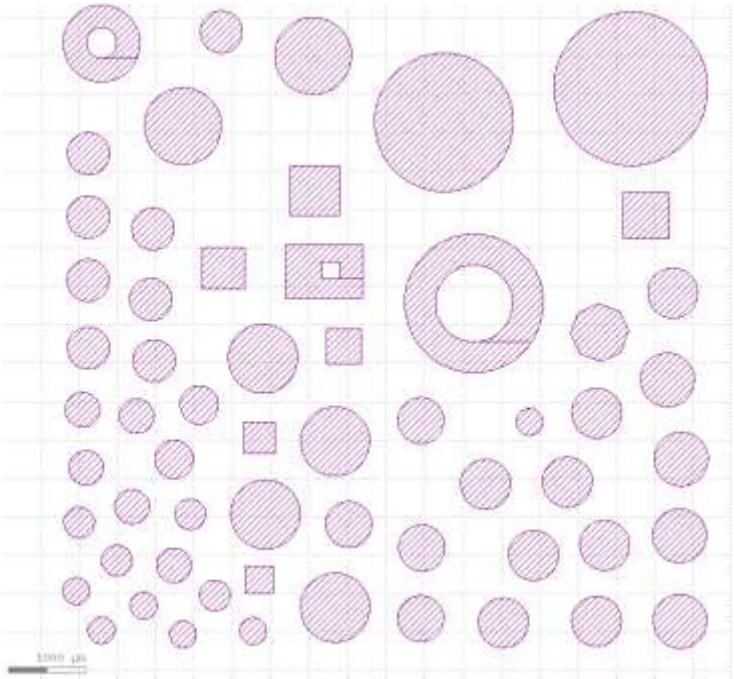

Figure P.6 ~ The final Trench lithography mask as sent to the MEMS production facility.

The TRENCH process to SOI overlay tolerances are described further in Chapter 3 ~ Table 3.18. The "Centre to Centre" overlay tolerance accounts for the bottom side to top side lithography alignment between the TRENCH and SOI mask levels. The TRENCH to SOI "Edge to Edge" bias accounts for the etch profile of the through holes in the Substrate layer and the "blow-out" of the etch profile at the Substrate – Oxide interface. This is shown in Figure P.7.

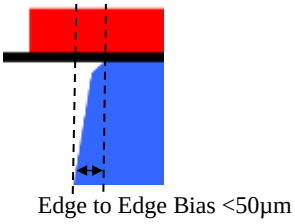

Figure P.7 ~ Cross section showing tolerances between the trench and the SOI layer [101].

The TRENCH mask process is not really meant for applications requiring tight tolerances and is only capable of etching features which are coarse in terms of alignment [115]. However in the case of this project this was really the only option available for an affordable IC to be produced. The trench sizing tolerances were naturally taken into account when analysing the results achieved.

Prod*ucing the final prototype experimental device*

The final set of masks, shown in combined form in Figure P.8, was then sent to IMEC for the production of the prototype experimental devices to proceed.

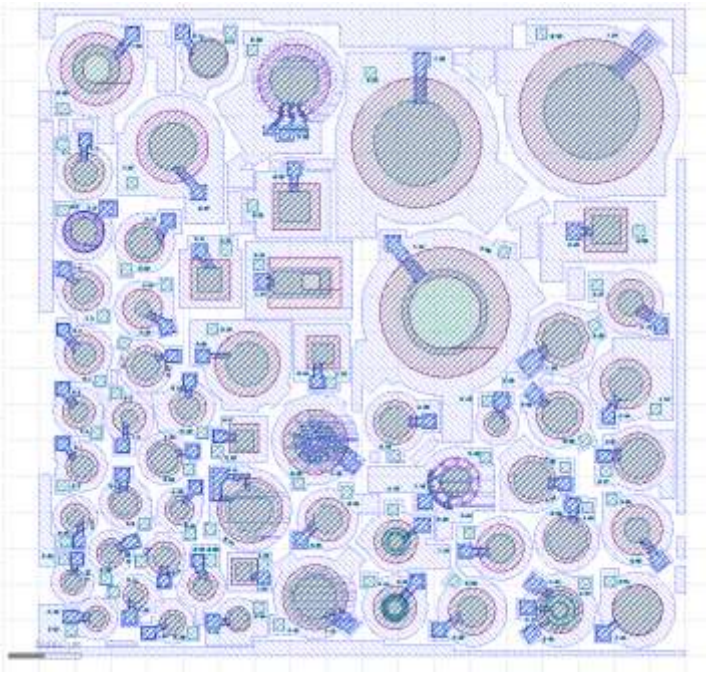

Figure P.8 ~ The final Padoxide lithography mask as sent to the MEMS production facility.

Fifteen finished ICs where received, attached on heat sensitive die attach tape as shown in Figure P.9.(b)

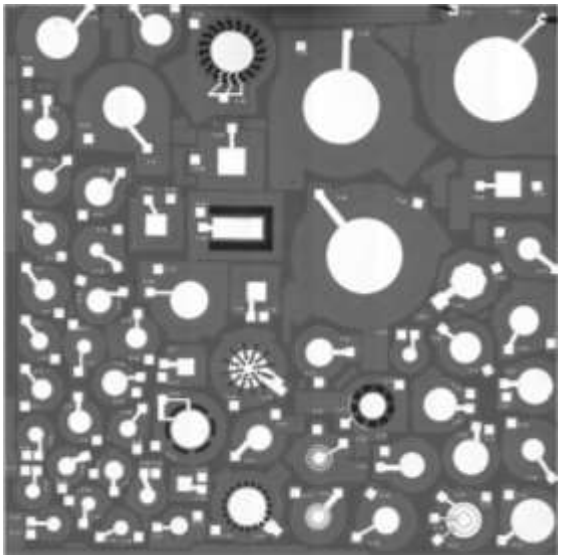

(a)

(b)

Figure P.9 ~ (a)Front micrograph of the prototype experimental device, and (b) 15 devices as received mounted on die attach tape and ring.

Dimensional checks.

Once the devices were received rigorous micrographic inspection was conducted. This included measurement of key areas to be sure that the devices were created as designed. In this case measurement of key areas was especially important given that in this case the devices' operating parameters was geometrically sensitive.

The dimensions of the diaphragm are very dependent on the Trench to SOI overlay tolerance especially the edge to edge bias presented in Figure P.10.

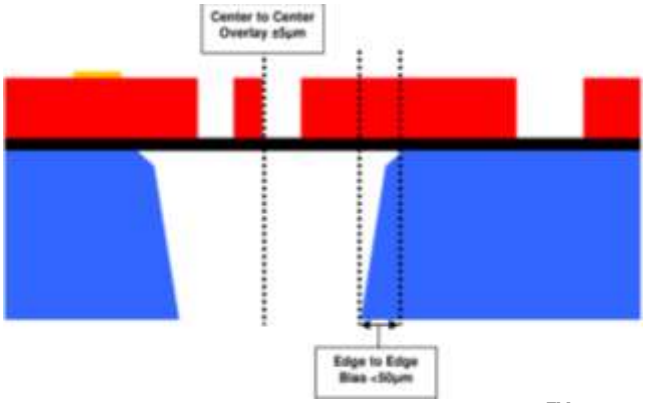

Figure P.10 ~ Drawing showing the tolerances which the PiezoMUMPs™ process imparts between the trench and SOI

Detailed measurements of features such as the trench diameter measurements were conducted through the use of digital micrographs and specialised software such as Fiji. Figure P.11 outlines the measurement procedure for a trench opening diameter.

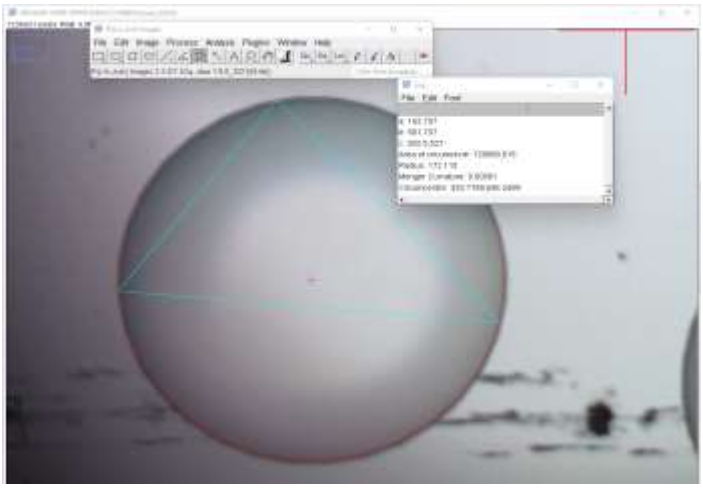

Figure P.11 ~ Measurement of the trench opening diameter.

Appendix Q: The effect of liquids on laser vibrometer optical physics.

Liquids interact with light in a different way than would gases such as air, which is the medium, most of the laser vibrometer technology in use today are optimised to work in. One of the most important effects which liquids have on the laser beam is the absorption of the laser beam itself. Due to this absorption laser vibrometers using an infrared laser source in the 1,550 nm region could not be utilised, as electromagnetic radiation with this wavelength is absorbed quickly in water. While such lasers allow higher power output in the region of 10mW and therefore have a better signal to noise ratio they could not be used in this project due to the absorption.

On the other hand lasers operating within the visible spectrum were utilised such as a helium neon sources operating at 633 nm. At such a wavelength, water is not readily attenuated and therefore was used in the conduct of vibration measurements in liquids. Its power had to be limited to 1mW to be eye safe.

This appendix explains procedures needed to utilise laser vibrometer results which have been measured in water rather than air. Since the vibrometers used were calibrated for operations in air, literature by the vibrometer manufacturer indicated that the measured readings for amplitude and velocity needed to be adjusted to account for the differences between the refractive index of the different fluids [158]. For this adjustment, equations (Q.1) and (Q.2) were to be used.

$$\text{Displacement}_{(\text{actual value in liquid})} = \text{Displacement}_{(\text{measured value in liquid})} / \text{refractive-index} \qquad (Q.1)$$

$$\text{Velocity}_{(\text{actual value in liquid})} = \text{Velocity}_{(\text{measured value in liquid})} / \text{refractive-index} \qquad (Q.2)$$

Due to the fact that this was a crucial point effecting the correctness of published results a short experimental process, using the vibrometer, was conducted by Polytec (the laser vibrometer manufacturer) to confirm equations (Q.1) and (Q.2) for the liquids used in this project, namely isopropanol and glycerine. It is important to note that the procedure outlined in this section was not part of the PMUT experimental procedures designed by the author but an important process set up by Polytec to ensure the accuracy of the result conducted.

The experimental set up used for this procedure is shown in Figure Q.1, with a source of vibration producing a vibrating frequency shown in the top right corner. This source of vibration caused vibration in a metal pin bent at 90° into a cup containing the coupling liquid.

Figure Q.1 ~ Concept of the frequency adjustment procedure showing source of vibration at the top right hand corner with metal vibrating laser target in the fluid test container.

The vibrating metal pin was set up to act as a target for the incident laser beam incoming from the vibrometer as shown in Figure Q.2. The red or green dots shown on the laser target indicate the point at which the laser impacts the metal.

Figure Q.2 ~ Side view showing the metal vibrating laser target partially in liquid and partially in air.

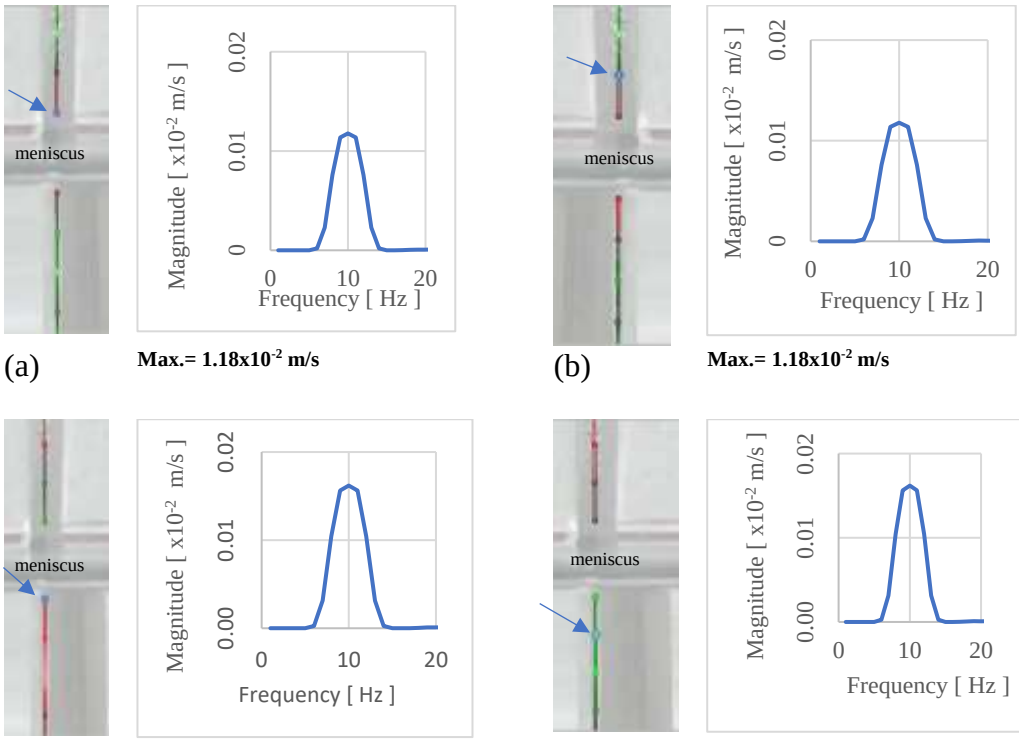

(c) **Max.= 1.62x10^{-2} m/s** (d) **Max.= 1.62x10^{-2} m/s**

Figure Q.3 ~ FFT amplitudes of velocity at different points on the target. (a) and (b) are for readings in air while (c) and (d) are for readings taken under the liquid level when the target is resonating at 11Hz.

Similarly further FFT results were measured for displacement and acceleration of the laser target in air and isopropanol. The values are tabulated in Table Q.1.

Table Q.1~ Values of displacement, velocity and acceleration for laser target in air and in isopropanol

	Air	**Isopropanol**	**Isopropanol/Air**
Displacement	2.01x10^{-4} m	2.76x10^{-4} m	1.38
Velocity	1.18x10^{-2} ms^{-1}	1.62x10^{-2} ms^{-1}	1.37
Acceleration	7.85x10^{-1}ms^{-2}	1.08 ms^{-2}	1.38

The procedure was then repeated for the liquid glycerine, again measuring the displacement, velocity and acceleration of the laser target in air and liquid. The results are tabulated in Table Q.2.

Table Q.2~ Values of displacement, velocity and acceleration for laser target in air and in glycerine

	Air	**Glycerine**	**Glycerine/Air**
Displacement	2.01x10^{-4} m	2.92x10^{-4} m	1.45
Velocity	1.18x10^{-2} ms^{-1}	1.71x10^{-2} ms^{-1}	1.45
Acceleration	7.86x10^{-1} ms^{-2}	1.14 ms^{-2}	1.45

The refractive index of isopropanol at 20^{o}C is 1.3776 [159] while that for glycerine also at 20^{o}C is in the range of 1.47 to 1.46 (changing slightly for different wavelengths of light) [160]. It is therefore evident that the values of the liquid/air ratios outlined in Table Q.1and Table Q.2 are very close to the refractive index values obtained from literature.

As final verification of equations (Q.1) and (Q.2), readings in the time domain were also taken to verify that adjustments required for the FFT readings would also need to be conducted for time domain readings. This verification is shown in Figure Q.4 and Figure Q.5.

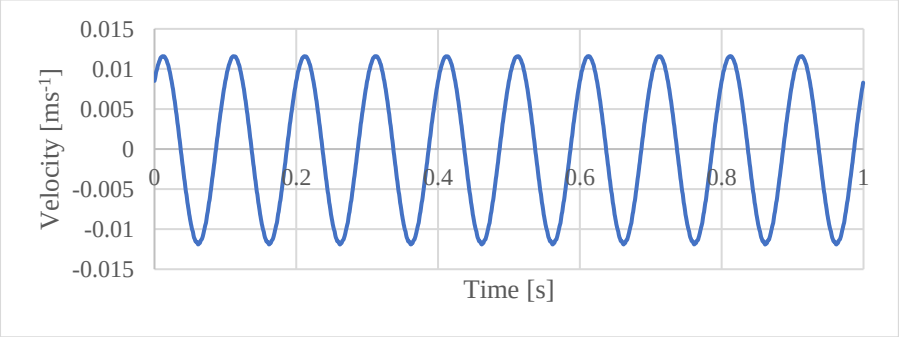

Figure Q.4 ~ Time domain plot of the laser target in air.

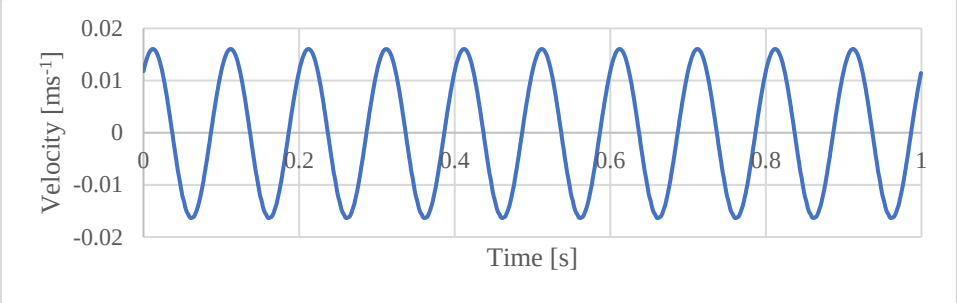

Figure Q.5 ~ Time domain plot of the vibration velocity of the laser target in liquid isopropanol.

The results achieved by the vibrometers will therefore be normalised using equations (Q.1) and (Q.2) . The ratios used to correct the vibrometer data achieved (both FFT and time domain) will be the experimentally derived values rather than the literature values as follows:

- **Isopropanol/Air ~ 1.37**
- **Glycerine/Air ~ 1.4**